The Electronic Structure and Optoelectronic Processes at the Interfaces in Organic Solar Cells Composed of Small Organic Molecules – A Computational Analysis of Molecular, Intermolecular, and Aggregate Aspects

Dissertation zur Erlangung des naturwissenschaftlichen Doktorgrades

der Julius-Maximilians-Universität Würzburg

vorgelegt von

Charlotte Brückner

aus
Marburg

Würzburg, 2016

Eingereicht bei der Fakultät für Chemie und Pharmazie am

_____

Gutachter der schriftlichen Arbeit

    1. Gutachter: _____

    2. Gutachter: _____

Prüfer des öffentlichen Promotionskolloquiums:

    1. Prüfer: _____

    2. Prüfer: _____

    3. Prüfer: _____

Datum des öffentlichen Promotionskolloquiums:

_____

Doktorurkunde ausgehändigt am

_____

Contents

Abbreviations

ADC(2)	algebraic diagrammatic construction to second order
AIMD	*ab initio* molecular dynamics
AM1	Austin Model 1
AMOEBA	atomic multipole optimized energetics for biomolecular applications
AO	atomic orbital
ASC	apparent surface charge
BDT	benzo[1,2-b:4,5-b']dithiophene
BHJ	bulk heterojunction
BLA	bond length alternation
BSE	Bethe-Salpeter
BSSE	basis set superposition error
CASPT2	complete active space second-order perturbation theory
CASSCF	complete active space self-consistent field
CC	coupled cluster
CC2	second-order approximate coupled-cluster singles and doubles
CCSD	coupled cluster singles doubles
c-DFT	constrained density functional theory
CI	configuration interaction
CIS	configuration interaction singles
CIS(D)	configuration interaction singles with perturbative doubles correction
CISDTQ	CI singles-doubles-triples-quadruples
CM5	charge model 5
CNDO	complete neglect of differential overlap
COSMO	conductor-like screening model
C-PCM	conductor-PCM
CSF	configuration state function
CT	charge transfer
CV-DFT	constricted variational DFT
D3	Grimme's dispersion correction D3
DF	density functional
DFA	density functional approximation
DFT	density functional theory
DFTB	tight-binding DFT
DIP	diindenoperylene
DMA	distributed multipole analysis
DOS	density of states
DPCM	dielectric-PCM
DPP	diketopyrrolopyrrole
DSSC	dye-sensitized solar cell
EA	electron affinity
ECP	effective core potential
EDA	energy decomposition analysis
EE	excitation energy
EOM	equation of motion
EQE	external quantum efficiency
ESP	electrostatic potential
F8BT	poly(9,9-dioctylfluorene-co-benzothiadiazole)
fcc	face-centered cubic
FCI	full configuration interaction
GBA	generalized Born approximation
GGA	generalized gradient approximation
GLPT	Görling-Levy perturbation theory
GMH	generalized Mulliken-Hush
GUGA-CI	graphical unitary group approach – CI
HF	Hartree-Fock
HOMO	highest occupied molecular orbital
IEF	integral equation formalism
IMC	image charge method
INDO	intermediate neglect of differential overlap
INDO/S	spectroscopically orientated INDO
IP	ionization potential
IQE	internal quantum efficiency
IR	infrared
ISC	intersystem crossing
ITO	indium tin oxide
J_{sc}	short-circuit current
k_b	Boltzmann factor
KMC	kinetic Monte Carlo
KS	Kohn-Sham
LDA	local density approximation

LJ	Lennard-Jones
LMO-EDA	local molecular orbital energy decomposition analysis
LR	linear response
LUMO	lowest unccoupied molecular orbital
MAE	mean absolute error
MC	Monte Carlo
MCRPA	multiconfigurational random phase approximation
MD	molecular dynamics
MIM	metal-insulator-metal
MM	molecular mechanics
MM3	molecular mechanics 3
MNDO	modified neglect of differential overlap
MO	molecular orbital
MP2	Møller-Plesset perturbation theory to second order
MR	multireference
MRCI	multireference configuration interaction
MS-CASPT2	multistate CASPT2
MSIE	many-electron self-interaction error
NDDO	neglect of diatomic differential overlap
NIR	near-infrared
OFET	organic field-effect transistor
OLED	organic light-emitting diodes
OMx	orthogonalization model x
OPLS-AA	optimized potentials for liquid simulations – All-Atom
OPV	organic photovoltaics
OSC	organic solar cell
P3HT	poly(3-hexylthiophene-2,5-diyl)
PBI	perylene-3,4:9,10-tetracarboxylic acid bisimide
$PC_{61}BM$	phenyl-C_{61}-butyric acid methyl ester
$PC_{71}BM$	phenyl-C_{71}-butyric acid methyl ester
PCE	power conversion efficiency
PCM	polarizable continuum model
PDDG	Pairwise directed distributed Gaussians
PEDOT	poly(3,4-ethylenedioxythiophene)
PES	potential energy surface
PFB	poly(9,9-dioctylfluorene-co-bis-N,N-(4-butylphenyl)-bis-N,N-phenyl-1,4-phenylenediamine)
PM3	Parameterization Model 3
PPP	Pariser-Pople-Parr
PSS	polystyrene sulfonate
PTCDA	perylenetetracarboxylic dianhydride
QM	quantum mechanics
QM/MM	hybrid quantum mechanics/molecular mechanics
RASSCF	restricted active space self-consistent field
RI	resolution of the identity
RMSD	root mean square deviation
RPA	random-phase approximation
SA-CASSCF	state-averaged CASSCF
SAPT	symmetry-adapted perturbation theory
SAS	solvent accessible surface
SCC-DFTB	self-consistent charge density DFTB
SCF	self-consistent field
SCRF	self-consistent reaction field
SCS	spin-component scaling
SES	solvent excluded surface
SF-TD-DFT	spin-flip TD-DFT
SOPPA	second-order polarization propagator approximation
SOS	spin-opposite scaling
SS	state specific
TADF	thermally activated delayed fluorescence
TDA	Tamm-Dancoff approximation
TD-DFT	time-dependent density functional theory
TD-HF	time-dependent Hartree-Fock
UV	ultraviolet
vdW	van-der-Waals
VIS	visible
V_{oc}	open-circuit voltage
ZDO	zero differential overlap
ZINDO	"Zerner's" extension of INDO/S

1   Acknowledgments

2 Introduction

The exploitation of solar energy as a renewable, carbon neutral energy resource[1] has turned into a promising technology to cover a part of the globally increasing energy consumption.[2] Compared with their inorganic counterparts, organic solar cells stand out due to their low fabrication cost, low weight, and mechanical flexibility,[3] but have long lagged behind in terms of efficiency. Meanwhile, constant progress has brought about device performances beyond the milestone[4] of 10%[5] that begin to be competitive with first-generation silicon-wafer based cells and especially with second-generation silicon thin-film photovoltaics.[2,6] While long-term stability is still an issue,[7,8] encapsulation techniques are steadily improving,[9] and new device architectures with longer lifetimes have been introduced.[10] A particular advantage of solution-processed organic solar cells is the possibility of roll-to-roll production.[11,12] As recently outlined, the large-scale energy production via so-called third-generation solar cells seems therefore feasible[13] although neither organic solar cells nor the so-called dye-sensitized solar cells,[14,15] which were developed in parallel,[1] have reached a noticeable degree of commercialization until now.[16] Yet, compared with perovskite cells, the most recent solar cell type, the environmentally unproblematic composition of organic solar cells offers the opportunity for a truly sustainable energy production. In fact, while the perovskite solar cell[17] has shown an incredible performance increase in only a few years,[18] sealing techniques for this cell - due the toxicity of Pb(II), a degradation product of its key component $[CH_3NH_3]PbI_3$ - still need to be brought to perfection until perovskite cells can conquer the market.[13,16]

The key process in all solar cells is the generation of charge carriers upon light absorption.[5] In contrast to traditional silicon-based cells, the crucial charge-transfer step, where an exciton dissociates, occurs in organic, dye-sensitized, and perovskite solar cells at an interface. The interface profoundly influences the character of the exciton dissociation, the decisive process for overall device performances.[19] Only in organic solar cells, this interface corresponds to an organic::organic interface. While bulk material design has considerably advanced in recent years, the understanding of the energetics at organic::organic interfaces is still limited.[20] Computational chemistry, which has already proven invaluable to shed light on fundamental optoelectronic mechanisms,[1] provides tools and concepts to fill this gap.

The organic::organic interfaces in organic solar cells (and in other optoelectronic devices such as organic light-emitting diodes) are unique for a number of reasons. Firstly and most importantly, this results from the character of the composing, usually π-conjugated small organic molecules and/or polymers.[20] π-conjugation is known to account for distinct electronic and optical molecular properties, but also affects intermolecular interactions.[21] Interactions between the π-conjugated systems, and therefore also across the interface, are commonly considered to be weak.[20] Compared to interfaces

between inorganic solids, the discrete nature of the molecules/polymer segments in combination with their weak intermolecular interactions give rise to a special alignment of the energy levels at the interfaces.[22,23] Secondly, the dielectric shielding in organic materials is usually low.[19] This implies that charge carriers, generated after light absorption in organic solar cells, produce pronounced effects on the interfacial energy level alignment. Thirdly, whereas inorganic materials are often conceived as being periodic and well-ordered,[24] disorder fundamentally determines all transport phenomena in organic materials.[25] Since an interface generally constitutes a structural inhomogeneity,[26] the consideration of disorder is intimately linked to any analysis of organic::organic interfaces.

These particularities of organic::organic interfaces clearly underline that an understanding of all interfacial processes requires insight on several description levels, i.e., on a molecular, intermolecular, and supramolecular level.[27] Firstly, the nature of the individual molecules/oligomers/polymers is decisive. Secondly, both the weak intermolecular interactions between the conjugated π-systems and the unshielded Coulomb forces need to be taken into account. Thirdly, the structural heterogeneity at the interfaces, their disorder and mesoscale morphology[28] must be considered. Therefore, a detailed computational description of organic::organic interfaces on a molecular, intermolecular, and aggregate scale is necessary to fully understand their electronic structure and the optoelectronic processes that take place in their vicinity. **Such a multi-level description is the central objective of this thesis.**

From a computational point of view, this is challenging because different theoretical approaches must be used on a molecular, intermolecular, and aggregate level. From the perspective of material science, a multi-level description can elucidate the fundamental relationships between molecular, intermolecular, and aggregate properties. One aim of this thesis is thus to deliver insight into basic structure-property relationships of all optoelectronic processes at organic::organic interfaces in organic solar cells. Since small organic molecules have more clear-cut structure-property relationships compared with polymers,[29] this thesis is entirely dedicated to an analysis of interfaces constructed from molecules. Furthermore, using molecules instead of large oligomers/polymers allows for fully quantum-chemical calculations on the molecular level, which is computationally unaffordable for polymers.

All investigations in this thesis are of two-fold character. On the one hand, methodological aspects are addressed. On the other hand, special attention is always given to the microscopic understanding of all fundamental optoelectronic processes at organic::organic interfaces, and on the influence of molecular/intermolecular/aggregate properties on these processes. For instance, the electronic structure of many π-conjugated molecules employed in organic solar cells is complex, but needs to be considered to understand its influence on the interfacial optoelectronic processes (*molecular level*).

This requires a suitable quantum-chemical treatment. Thus a prerequisite for an understanding of organic::organic interfaces at the molecular level consists in the identification of accurate – and possibly low-cost – methods that properly describe the electronic states of the individual molecules. Intermolecular interactions determine aggregate morphologies and couplings, both of which affect interfacial charge generation in organic solar cells (*intermolecular level*).[19] Understanding the origin of the intermolecular interactions permits both to develop computational approaches to model them and to rationally design distinct intermolecular arrangements via molecular-structure modifications. Aggregate properties such as disorder are well-known to impact the mechanisms of optoelectronic processes,[19] but their computational description requires simplifying assumptions and the inclusion of the environment. Only a balance between a physically well-grounded and a computationally affordable theoretical model to describe aggregate processes allows for meaningful results (*aggregate level*).

Therefore, starting at the molecular level, a structurally and electronically diverse set of molecular p-type semiconductors is selected first. The performance of many *ab initio*, DFT, and semiempiric methods is comprehensively analyzed for ground-, excited- and charged-state properties of these molecules. Their intermolecular interactions are subsequently addressed. Both the physical origin of the intermolecular interactions and different modeling approaches are discussed. Then, aggregate morphologies for organic::organic interfaces composed of the p-type semiconductors and fullerene C_{60} are *in silico* generated. Thereupon, computational models are developed and used to calculate the energy profiles as well as the kinetics of the charge separation process at the *in silico* generated interfaces. In contrast to the majority of literature investigations using also experimental data as input, the calculations based only on computed input parameters provide a direct unbiased relationship between molecular properties and macroscopic transport parameters.[30] Finally, the influence of disorder is addressed in more detail in QM/MM calculations.

On the one hand, these investigations provide a fundamental understanding of the accuracy of many quantum-chemical methods for different electronic states, weak interactions, and transport processes. On the other hand, they deliver a molecular picture of the charge generation mechanisms in OSCs and of their molecular and intermolecular dependencies.

3 Theoretical Background

3.1 The quantum-chemical ground-state description

3.1.1 The Born-Oppenheimer approximation and the electronic Schrödinger equation[a]

The first quantum-mechanical postulate states that the wave function Ψ fully describes a quantum-mechanical system. The wave function can vary with both time and space, $\Psi(\vec{r}, t)$, and it is obtained as the solution of the general time-dependent Schrödinger equation.[31,32]

$$\widehat{H}(\vec{r}, t)\Psi(\vec{r}, t) = i\hbar\frac{\partial}{\partial t}\Psi(\vec{r}, t)$$

(1)

The Hamiltonian $\widehat{H}(\vec{r}, t)$ is composed of the kinetic energy operator $\widehat{T}(\vec{r})$ and the potential energy operator $\widehat{V}(\vec{r}, t)$. Evidently, as soon as the potential energy does not depend on time, which is the case for all systems that are not subject to a time-dependent external potential, the Hamiltonian becomes time-independent as well. Separating the variables in Eq. (1) yields the time-independent Schrödinger equation with the time-independent wave functions $\Psi(\vec{r})$ as its solution.[31]

$$\widehat{H}(\vec{r})\Psi(\vec{r}) = \left(\widehat{T}(\vec{r}) + \widehat{V}(\vec{r})\right)\Psi(\vec{r}) = E(\vec{r})\Psi(\vec{r})$$

(2)

For clarity, spin coordinates are omitted and will be neglected throughout the following outline.

Due to its complexity, directly solving Eq. (2) is not possible (even not for the simplest systems) so that further approximations are necessary. The Hamiltonian of any molecule can be expressed as the sum of the kinetic energies of the nuclei $\widehat{T}_N$, the kinetic energy of the electrons $\widehat{T}_e$, the nuclei-nuclei-repulsion $\widehat{V}_{NN}$, the electron-electron repulsion $\widehat{V}_{ee}$, and the electron-nuclei interaction $\widehat{V}_{Ne}$. The wave function of any molecule thus depends on both nuclear coordinates $\{\vec{R}_K\}$ and electron coordinates $\{\vec{r}_i\}$.[31]

$$\widehat{H}\Psi(\vec{R}_K, \vec{r}_i) = (\widehat{T}_N + \widehat{T}_e + \widehat{V}_{NN} + \widehat{V}_{Ne} + \widehat{V}_{ee})\Psi(\vec{R}_K, \vec{r}_i) = E(\vec{R}_K, \vec{r}_i)\Psi(\vec{R}_K, \vec{r}_i)$$

(3)

Since the nuclei are considerably heavier than the electrons, they move much more slowly, i.e., the electron motion is significantly faster. In the Born-Oppenheimer approximation,[33] fundamental to all quantum-chemical calculations, this fact is utilized to separate variables in the total molecular wave function $\Psi(\vec{R}_K, \vec{r}_i)$. $\Psi(\vec{R}_K, \vec{r}_i)$ is then expressed as the product of the nuclear wave function $\phi(\vec{R}_K)$ and an electronic wave function $\psi(\vec{R}_K, \vec{r}_i)$, which depends only parametrically on the nuclear coordinates. The underlying idea of the parametric dependence is that the fast moving electrons instantaneously adapt to changes of the nuclear geometry.

---

[a] The following outline can be found in standard textbooks such as [31].

$$\Psi(\vec{R}_K, \vec{r}_i) = \phi(\vec{R}_K)\psi(\vec{R}_K, \vec{r}_i) \tag{4}$$

The product ansatz for the total wave function (Eq. (4)) is then inserted into the total time-independent Schrödinger equation (Eq. (3)). Three terms arise if the nuclear kinetic energy operator $\hat{T}_N$ (defined in Eq. (5)) acts on the total molecular wave function (Eq. (4), (6)).[31]

$$\hat{T}_N = -\frac{1}{2} \sum_N^{\#\,nuclei} \frac{\nabla_N^2}{M_N} \tag{5}$$

$$\hat{T}_N \phi(\vec{R}_K)\psi(\vec{R}_K, \vec{r}_i)$$

$$= -\frac{1}{2} \sum_N^{\#\,nuclei} \frac{1}{M_N} \begin{pmatrix} \psi(\vec{R}_K, \vec{r}_i)\nabla_N^2\phi(\vec{R}_K) \\ +2\nabla_N\psi(\vec{R}_K, \vec{r}_i)\nabla_N\phi(\vec{R}_K) \\ +\phi(\vec{R}_K)\nabla_N^2\psi(\vec{R}_K, \vec{r}_i) \end{pmatrix} \tag{6}$$

Compared with the derivative of the nuclear wave function, $\nabla_N\phi(\vec{R}_K)$, the derivative of the electronic wave function with respect to the nuclear coordinates, $\nabla_N\psi(\vec{R}_K, \vec{r}_i)$, is most often considerably smaller. This results from the different extent of localization of nuclei and electrons, i.e., the heavier nuclei are more localized in space than the electrons.[34] Therefore the electron density varies only smoothly with the nuclear coordinates, and it usually does not depend on the nuclear kinetic energy. Consequently, the second and third term in Eq. (6), the so-called non-adiabatic coupling elements, are neglected in the Born-Oppenheimer approximation.[b] This is a very good approximation for most systems of interest to quantum chemistry.[31] However, as soon as the nonadiabatic coupling elements become significant, i.e., as soon as the electron density varies strongly with the nuclear positions, for example at avoided crossings or conical intersections,[35] the Born-Oppenheimer approximations breaks down.[31]

Inserting the product ansatz (Eq. (4)) into the time-independent Schrödinger equation (Eq. (3)) and neglecting the non-adiabatic coupling elements (used in the division by the product wave function in Eq. (7)) yields two separate equations, the electronic (Eq. (8)) and the nuclear Schrödinger equation (Eq. (9)). Mathematically, the electronic energy $E^{el}(\vec{R}_K, \vec{r}_i)$ corresponds to the separation constant in Eq. (7). It depends "parametrically" on the nuclear coordinates $\{\vec{R}_K\}$.[31]

$$\frac{(\hat{T}_e + \hat{V}_{Ne} + \hat{V}_{ee} + \hat{V}_{NN})\psi(\vec{R}_K, \vec{r}_i)}{\psi(\vec{R}_K, \vec{r}_i)} = E(\vec{R}_K, \vec{r}_i) - \frac{\hat{T}_N\phi(\vec{R}_K)}{\phi(\vec{R}_K)} \tag{7}$$

---

[b] It should be noted that the diagonal correction is most often also neglected in quantum-chemical calculations.[31,1008]

$$\left(\hat{T}_e + \hat{V}_{Ne} + \hat{V}_{ee} + \hat{V}_{NN}\right)\psi(\vec{R}_K, \vec{r}_i) = E^{el}(\vec{R}_K, \vec{r}_i)\psi(\vec{R}_K, \vec{r}_i) \tag{8}$$

$$\left(\hat{T}_N + E^{el}(\vec{R}_K, \vec{r}_i)\right)\phi(\vec{R}_K) = E(\vec{R}_K, \vec{r}_i)\phi(\vec{R}_K) \tag{9}$$

Eq. (8), the electronic Schrödinger equation, is the relevant equation for all quantum-chemical methods. Its eigenvalues, the electronic energies $E^{el}(\vec{R}_K, \vec{r}_i)$, represent the potential energy surfaces (PESs) on which the slow nuclei move "adiabatically". The underlying Born-Oppenheimer approximation is therefore sometimes also called the "adiabatic approximation". The chemical concept of potential energy surfaces and molecular structures with well-defined nuclear geometries is thus entirely based on the Born-Oppenheimer approximation. It should be furthermore noted that due to the Hermitian character of the electronic Hamiltonian, solving Eq. (8) yields a complete set of eigenvectors $\{\psi_i(\vec{R}_K, \vec{r}_i)\}$ and eigenvalues $\{E_i{}^{el}(\vec{R}_K, \vec{r}_i)\}$.[31]

$$\left(\hat{T}_e + \hat{V}_{Ne} + \hat{V}_{ee} + \hat{V}_{NN}\right)\psi_i(\vec{R}_K, \vec{r}_i) = E_i{}^{el}(\vec{R}_K, \vec{r}_i)\psi_i(\vec{R}_K, \vec{r}_i) \tag{10}$$

The eigenvalues $\{E_i{}^{el}(\vec{R}_K, \vec{r}_i)\}$ are the electronic states of a molecule. To obtain a nuclear wave function, for example molecular vibrations, the electronic energies are calculated (either including its derivatives with respect to the nuclear coordinates in the harmonic approximation or for several nuclear points of the nuclear geometry) and subsequently inserted into the nuclear equation (Eq. (9)), which is then solved for nuclear energies and wave functions, again obtained as a complete set.

Solving Eq. (10) that still cannot be directly solved is the underlying objective of all quantum-chemical methods. The methods differ in the approximations that they introduce. Some of these approximations will be outlined in the following sections. For clarity, the operator superscript "^" is often omitted. Moreover, the symbol Ψ is used in the following for the electronic part of the wave function.

3.1.2 The Hartree-Fock method and the Roothaan-Hall equations[c]

A simple ansatz for the many-electron wave function of a molecule, the Hartree-Fock method, is to represent the wave function as an antisymmetrized product, i.e., as a single Slater determinant $\Phi(\vec{R}_K, \vec{r}_i)$, of single-particle wave functions, the spin orbitals $\{\chi_a\}$. Following the notation of Szabo and Ostlund,[36] only the trace of the determinant is given. Furthermore, the bracket-notation is adopted. σ corresponds to the spin coordinate, x will be employed for the combination of spin and spatial coordinates. The molecule contains N electrons.[36]

---

[c] The derivation can be found in standard textbooks such as [31,36,32].

$$\Psi(\vec{R}_K, \vec{r}_i) \approx \Phi(\vec{R}_K, \vec{r}_i, \sigma_i) = |\chi_1(x_1)\chi_2(x_2)\chi_3(x_3)\ldots\chi_N(x_N)| \tag{11}$$

The Hartree-Fock method consists in finding the determinant that provides the best description of the electron density of the system. Due to the variational principle, this amounts to identifying the determinant that yields the lowest electronic energy. The expectation value for the electronic energy of a Slater determinant $\langle E \rangle$ can be represented as sums of one-electron matrix elements h_i (Eq. (13)) containing the one-electron kinetic energy and the potential interaction energy of one electron with the nuclei and as sums of two-electron terms $\langle ab|ab \rangle$ and $\langle ab|ba \rangle$ (Eq. (12)). The spin orbitals χ_a and χ_b are abbreviated by a and b. The two-electron matrix elements are considered as Coulomb integrals J_{ab} (Eq. (14)) and exchange integrals K_{ab} (Eq. (15)). The integrals can also be expressed in terms of matrix elements of the Coulomb and the exchange operators $\hat{J}_b$ and $\hat{K}_b$. M designates the nuclei and Z_M their charge, the respective sum runs over all nuclei.[36]

$$\langle E \rangle = \langle \Phi|\hat{H}_{el}|\Phi\rangle = \sum_{a=1}^{N} h_a + \frac{1}{2}\sum_{a=1}^{N}\sum_{b=1}^{N}(\langle ab|ab\rangle - \langle ab|ba\rangle) \tag{12}$$

$$h_a = \left\langle \chi_a\left|-\frac{1}{2}\Delta - \Sigma\frac{Z_M}{r_{1M}}\right|\chi_a\right\rangle = \langle \chi_a|h|\chi_a\rangle \tag{13}$$

$$J_{ab} = \langle ab|ab\rangle = \left\langle ab\left|\frac{1}{r_{12}}\right|ab\right\rangle = \langle a|\hat{J}_b|a\rangle \tag{14}$$

$$K_{ab} = \langle ab|ab\rangle = \left\langle ab\left|\frac{1}{r_{12}}\right|ba\right\rangle = \langle a|\hat{K}_b|a\rangle \tag{15}$$

To obtain the lowest-energy determinant, the energy expectation value (Eq. (12)) is minimized by varying the underlying spin orbitals with the additional constraint that they are orthonormal (Eq. (16)). δ_{ab} corresponds to the Kronecker delta.[36]

$$\langle a|b\rangle = \delta_{ab} \tag{16}$$

For the constrained minimization, the Lagrangian $\mathcal{L}$ is constructed with the Lagrangian multipliers $\{\varepsilon_{ba}\}$.[36]

$$\mathcal{L}[\{\chi_a\}] = E[\{\chi_a\}] - \sum_{a,b}^{N} \varepsilon_{ba}(\langle a|b\rangle - \delta_{ab}) \tag{17}$$

Minimizing the energy expectation value of the Slater determinant subject to the constraint of orthonormal spin orbitals requires that the variation of the Lagrangian $\delta\mathcal{L}[\{\chi_a\}]$ vanishes. CC denotes the complex conjugate.[36]

$$\delta\mathcal{L}[\{\chi_a\}] = \sum_{a=1}^{N} \langle \delta\chi_a|h|\chi_a\rangle + \sum_{a,b}^{N} \langle \delta\chi_a\chi_b|\chi_a\chi_b\rangle - \langle \delta\chi_a\chi_b|\chi_b\chi_a\rangle \tag{18}$$

$$- \sum_{a,b}^{N} \varepsilon_{ba}\langle \delta\chi_a|\chi_b\rangle + CC = 0$$

For Eq. (18) to hold for any arbitrary variations $\delta\chi_a$, the remaining parts should be zero. This results in Eq. (19). The operator in the brackets of Eq. (19) is the Fock operator. A unitary transformation of Eq. (19) that diagonalizes the matrix of Lagrangian multipliers ε_{ba} and leaves the Fock operator unchanged leads to the standard Fock eigenvalue equation, Eq. (20). Its eigenvectors are the canonical Hartree-Fock orbitals. The orbitals in Eq. (20) are equivalent, but not equal to the orbitals in Eq. (19). The Lagrangian multipliers correspond to the orbital energies. According to Koopmans' theorem, the HOMO energy reflects the ionization potential of the molecule whereas the LUMO energy relates to its electron affinity *if orbital relaxation effects are ignored*. This can be easily shown by taking corresponding energy differences. For later-on purposes, it is important to point out that therefore, the HF HOMO-LUMO gap represents approximately the fundamental gap[d] of a molecule, albeit without taking relaxation effects into account.[36]

$$\left[h(x_1) + \sum_{b=1}^{N}\left(\hat{J}_b(x_1) - \hat{K}_b(x_1)\right)\right]\chi_a(x_1) = \sum_{b=1}^{N}\varepsilon_{ba}\chi_a(x_1) \tag{19}$$

$$\left[h(x_1) + \sum_{b=1}^{N}\left(\hat{J}_b(x_1) - \hat{K}_b(x_1)\right)\right]\chi_a(x_1) = \varepsilon_a\chi_a(x_1) \tag{20}$$

Solving the Fock eigenvalue equation (Eq. (20)) for the optimal spin orbitals of the energetically lowest Hartree-Fock (HF) determinant necessarily means that the off-diagonal elements of the Fock matrix are 0. This has another important implication, the so-called Brillouin theorem. Since an off-diagonal element of the Fock operator, which is zero, corresponds to a Hamiltonian matrix element between the ground-state determinant and a singly-excited determinant, singly-excited determinants do not mix with the HF ground state.[36]

In order to actually calculate the orbitals, the Fock eigenvalue problem is expanded into a usually atom-centered basis set $\{\varphi_i\}$. The procedure is demonstrated for a closed-shell system in the following. Assuming this and integrating over the spin in Eq. (20), the Fock eigenvalue problem for closed-shell systems is obtained (Eq. (21)), with $\psi_a(\vec{r})$ being the spatial part of an orbital.[36]

---

[d] The fundamental gap is defined as the difference between the ionization potential and the electron affinity of a molecule. It is thus considered as a counterpart to the optical gap of a molecule, i.e., its "bandgap".[160]

$$f(\vec{r})\psi_a(\vec{r}) = \left[h(\vec{r}) + \sum_{b=1}^{N/2} \left(2\hat{J}_b(\vec{r}) - \hat{K}_b(\vec{r}) \right) \right] \psi_a(\vec{r}) = \varepsilon_a \psi_a(\vec{r}) \tag{21}$$

$\psi_a(\vec{r})$ is expanded into the finite basis composed of K basis functions $\{\varphi_i\}$.[36]

$$\psi_a(\vec{r}) = \sum_{i=1}^{K} c_{ia}\varphi_i(\vec{r}) \tag{22}$$

c_{ia} are the expansion coefficients of the molecular orbital a in the basis set. The Roothaan-Hall equations are a compact way of representing the Fock equations for spatial orbitals as matrix equations in this basis set, containing the overlap matrix S, the Fock matrix F, the matrix of orbital energies ε, and the matrix of expansion coefficients C.[36]

$$FC = SC\varepsilon \tag{23}$$

Since the Fock matrix F depends on the expansion coefficients (in the Coulomb and the exchange operator), the Roothaan-Hall equations must be solved iteratively until a self-consistent solution is obtained. This defines the SCF procedure (self-consistent field). The basis set is orthogonalized to transform Eq. (23) into a standard eigenvalue equation. Several procedures exist to orthogonalize the basis set that differ in terms of their efficiency or numerical stability, for instance in case of linear dependencies.[36]

The spin integration leading to Eq. (21) assumed doubly-occupied spatial orbitals, i.e, it requires equal spatial orbitals for different spins. Due to this restriction, the resulting formalism is also designated as the restricted HF and Roothaan-Hall formalism. The so-called unrestricted HF/Roothaan-Hall formalism, i.e., different spatial orbitals for different spin states, is usually employed to describe open-shell systems with an otherwise unaltered procedure. It is important to note that due the different spatial orbitals, unrestricted HF solutions are not eigenvalues of the S²-operator (S-squared). They can, however, be expressed as sums over pure spin states of higher multiplicities. These "contaminating" higher-spin states induce an erroneously[e] increased $\langle S^2 \rangle_{UHF}$ expectation value of the unrestricted HF solution, which is obtained from the spatial overlap between the unrestricted spatial orbitals $S_{ij}^{\alpha\beta}$, the exact value $\langle S^2 \rangle_{exact}$, and the number of β-electrons N^β (assuming that there are more α-electrons).[36]

$$\langle S^2 \rangle_{UHF} = \langle S^2 \rangle_{exact} + N^\beta - \sum_{i}^{N} \sum_{j}^{N} \left| S_{ij}^{\alpha\beta} \right|^2 \tag{24}$$

---

[e] The S²-operator commutes with the electronic Hamiltonian so that the exact electronic solutions are necessarily pure spin states.

3.1.3 Single-reference correlated *ab initio* methods

The HF method is most often employed to calculate the HF reference for higher-level *ab initio* methods since it lacks electron correlation and does not provide sufficiently accurate results in itself. These higher-level *ab initio* methods retrieve electron correlation by additionally including excited determinants $|\Phi_i\rangle$, equally constructed from HF orbitals. Thus the total electronic wave function $|\Psi\rangle$ corresponds to a sum of determinants.[31,36]

$$|\Psi\rangle = C_0|\Phi_0\rangle + \sum_i C_i|\Phi_i\rangle \qquad (25)$$

The HF determinant is considered as the reference wave function, and all excited determinants are therefore classified according to the number of one-electron excitations with respect to this reference HF determinant.[36] Using a single HF determinant as the reference defines single-reference *ab initio* methods. The single-reference *ab initio* methods differ only in the way how they select the excited determinants and determine their expansion coefficients $\{C_i\}$. The CI approach (configuration interaction)[31,36] constitutes probably conceptually the most straightforward correlated method because the wave function is simply expressed as a linear combination of singly, doubly, triply, etc. excited determinants.[31] The expansion coefficients of the determinants $C_a = a$ and the CI state energies E are obtained from diagonalizing the CI matrix H, i.e., by solving the CI secular equations $Ha = Ea$. Full-CI calculations are in principle exact within the basis set, but quickly become computationally infeasible due to the size of the CI matrix. A number of truncated CI methods exist, most notably CIS (including only singly excited determinants) and CISD (including singly and doubly excited determinants). In contrast to the double excitations, which account for large parts of electron correlation, the single excitations do not directly contribute to the ground-state CI energy due to Brillouin's theorem. They are nonetheless important because as off-diagonal elements of the Fock operator, they are responsible for orbital relaxation in response calculations of excitation energies or first-order properties.[f] They constitute furthermore first approximations for excited states (see below). The lowest (or a few low) CISD eigenvalues are usually determined from the secular equation by an iterative procedure, i.a., an initial guess for the expansion coefficients is successively refined. The Davidson algorithm[37] is the most prominent example for such iterative CI solutions. Furthermore, in the usually employed so-called direct CI methods,[38] the CI matrix is not explicitly calculated. Only the two-electron integrals corresponding to the CI matrix elements directly needed for the multiplication

---

[f] The system is subject to an external perturbation in response calculations. Ground-state HF orbitals are no longer optimal so that the energy gradients with respect to orbital variations, i.e., the off-diagonal elements of the Fock operator, become non-zero and thus decisive.[31]

with the expansion coefficients are stored (or calculated).[31] Truncating the full-CI expansion in CISD comes, however, at the expense of size consistency[g].[31,36]

In contrast to the linear expansion of the wave function into excited determinants in CI, coupled cluster (CC) wave functions[31,39] are based on an exponential expansion in the basis of excited Slater determinants (see for instance [31,39] for details). This can be most easily expressed in terms of the excitation operator T, with T_i generating all i-fold excited determinants with respective amplitudes t. N is the number of electrons in the system.[31]

$$\mathrm{T} = T_1 + T_2 + T_3 + \cdots + T_N \tag{26}$$

$$T_1|\Phi_0\rangle = \sum_{i=1}^{N} \sum_{a}^{virt} t_i^a |\Phi_i^a\rangle \tag{27}$$

$$|\Psi_{CC}\rangle = e^T|\Phi_0\rangle = \left(\sum_{n=0}^{\infty} \frac{T^n}{n!}\right)|\Phi_0\rangle \tag{28}$$

Due to the exponential expansion in determinants (Eq. (28)), both connected excited determinants (generated by applying a certain T_i once) and disconnected excited determinants (generated for instance by applying $T_{i/2}$ twice) are included in the total coupled-cluster wave function. The disconnected excitations ensure the size consistency of coupled cluster approaches also in truncated versions, most notably in CCSD (Coupled Cluster Singles Doubles).[31] Coupled-cluster energies (Eq. (29)) and amplitudes (Eq. (30)) are usually obtained upon iteratively solving the coupled non-linear matrix equations obtained from a similarity transformed Hamiltonian.[31]

$$E_{CC} = \langle\Phi_0|e^{-T}He^T|\Phi_0\rangle \tag{29}$$

$$\langle\Phi_i^a|e^{-T}He^T|\Phi_0\rangle = 0 \tag{30}$$

$$\langle\Phi_{ij}^{ab}|e^{-T}He^T|\Phi_0\rangle = 0$$

A third way of determining the expansion coefficients in Eq. (25) is Møller-Plesset perturbation theory.[40] Perturbation theory in general divides the Hamiltonian of a system $H = H_0 + \lambda V$ into a zeroth-order part H_0 with known eigenvalues and eigenvectors and a perturbation V, with λ being a parameter. When applied in the form of the Rayleigh-Schrödiger perturbation theory to many-body problems, the final eigenvalues (Eq. (31)) and eigenvectors (Eq. (32)) of the real many-body system are expressed as Taylor series of the parameter λ.[31]

---

[g] Size consistency means that the calculated energies scale linearly with the system size. For instance, the energy of a non-interacting dimer is twice the energy of the composing monomers.[31]

$$E = E_i^{(0)} + \lambda E_i^{(1)} + \lambda^2 E_i^{(2)} + \cdots \tag{31}$$

$$\Psi = \Psi_i^{(0)} + \lambda \Psi_i^{(1)} + \lambda^2 \Psi_i^{(2)} + \cdots \tag{32}$$

All eigenvalues and eigenvectors to the n-th order are then expressed in terms of the zeroth-order eigenvalues and of matrix elements of the zeroth-order eigenvectors with the perturbation operator. The expressions are obtained by inserting the equations for E and Ψ into the full Hamiltonian and recollecting terms of equal power of λ in separate equations.[31,36]

In Møller-Plesset perturbation theory,[40] the zeroth-order Hamiltonian is defined as the sum of the one-electron Fock operators. The perturbation operator corresponds to the difference between this sum and the true electronic Hamiltonian.[31,36] V is also often designated as the fluctuation potential.[31,36]

$$H = H_0 + \lambda V = \sum_{i=1}^{N} f(\vec{r}_i) + \lambda \left(\sum_{i,j>i}^{N} \frac{1}{r_{ij}} - \sum_{j}^{N} \left(J_j(\vec{r}_i) - K_j(\vec{r}_i) \right) \right) \tag{33}$$

Zeroth-order energies of Møller-Plesset perturbation theory are thus sums of orbital energies. First-order Møller-Plesset perturbation theory recovers the HF ground-state energy. Second-order Møller-Plesset perturbation theory (MP2) is the commonly employed form of perturbation theory, providing a second-order correction to the energy and a first-order correction to the wave function. The second-order energy correction $E_0^{(2)}$ corresponds to sums over two-electron integrals.[31,36]

$$E_0^{(2)} = \sum_{i<j,a<b} \frac{|\langle ij \parallel ab \rangle|^2}{\varepsilon_i + \varepsilon_j - \varepsilon_a - \varepsilon_b} \tag{34}$$

Similarly, the first-order the wave-function $\Psi_0^{(1)}$ is written as[31,36]

$$\Psi_0^{(1)} = \sum_{i<j,a<b} \frac{\langle ij \parallel ab \rangle}{\varepsilon_i + \varepsilon_j - \varepsilon_a - \varepsilon_b} \Phi_{ij}^{ab} \tag{35}$$

In contrast to CC and CI-based methods, MP2 (like MPN in general) calculations are non-iterative. As stated by the so-called linked-cluster theorem,[41] MP2 is size-consistent. It is, however, non-variational.[31,36]

MP2-based methods are very popular, in particular because of their computationally efficient implementation compared with other wave-function based methods.[31] Procedures such as the so-

called RI approximation,[42] faster convergence in R12-MP2, and local MP2 methods[43] contribute to this efficiency by speeding up the calculation of the two-electron four-index integrals:[h]

$$\langle ab|rs \rangle = (ar|bs) = \sum_{m,n,p,q} c_{am}^* c_{bn}^* c_{pr} c_{sq} \langle \varphi_m \varphi_n | \varphi_p \varphi_q \rangle \tag{36}$$

RI-MP2 achieves the speedup by decreasing the individual calculation times (Eq. (36)). It should be noted that the RI approximation, also called the density fitting procedure,[44] is similarly used in DFT (density functional theory) calculations with pure functionals[31]. The RI approximation, which was first employed by Feyereisen et al.,[45] relies on an expansion of the product density of two atomic orbitals $|\varphi_m \varphi_p)$ in an auxiliary basis set $\{\theta_i\}$:[44]

$$|\varphi_m \varphi_p) = \sum_i^\infty |\theta_i\rangle \langle \theta_i | \varphi_m \varphi_p) = \sum_i^\infty |\theta_i\rangle C_{mp}^i \tag{37}$$

Although Eq. (37) is in principle exact, the approximation results from the (in practice) finite size of the auxiliary basis set $\{\theta_1, \theta_2, \dots \theta_M\}$. Nevertheless, according to Hättig and coworkers, the error introduced by the finite auxiliary basis set is about two orders of magnitude smaller than the usual basis set error of MP2.[46] With the RI approximation, the two-electron four-index integrals (Eq. (36)) can be transformed into two three-index integrals and one two-index integral:

$$(\varphi_n \varphi_q | \varphi_m \varphi_p) = \sum_{ij}^M \langle \varphi_n \varphi_q | \theta_j \rangle \langle \theta_j | \theta_i \rangle \langle \theta_i | \varphi_m \varphi_p \rangle = \sum_{ij}^M C_{nq}^j \langle \theta_j | \theta_i \rangle C_{mp}^i \tag{38}$$

This leads to a reduction of CPU times of up to two orders of magnitude. The reduction is basis set-dependent and becomes more significant for calculations with larger atomic basis sets $\{\varphi_i\}$.[46]

In contrast to the RI approximation, which aims at reducing the computation times for the two-center four-index integrals (Eq. (36)), local MP2 methods (LMP2) and R12-MP2 seek to decrease their number.

In fact, following the reasoning of Pulay,[47] using canonical molecular orbitals in the two-electron integrals (Eq. (36)) is somewhat inefficient because in contrast to the rather local dynamic correlation, canonical molecular orbitals are delocalized over many atoms. Whenever calculating dynamic

---

[h] It should be kept in mind that for a system with N basis functions, computing two-electron integrals, which is the bottleneck of any correlated *ab initio* calculation, in a procedure similar to Eq. (36) formally scales as N^8. N^4 integrals in the atomic orbital basis set need to be calculated and are subsequently multiplied with N^4 expansion coefficients of the molecular orbitals in the atomic basis set. However, the transformation from atomic to molecular orbitals is performed for one index at a time.[31] It corresponds therefore to a series of calculations scaling with N^5, i.e., the underlying N^4 two-electron integrals in an atomic orbital basis are sequentially multiplied with N expansion coefficients. The AO-to-MO transformation of the two-electron integrals determines the minimal scaling of all correlated wave functions. In contrast, since HF can be directly formulated in an atomic orbital basis, it formally scales only as N^4.[31,32]

correlation, many canonical delocalized molecular orbitals need to be included, i.e., according to Werner, the latter "destroy the local character of dynamic correlation".[48] The key idea of all local correlated methods is to use localized molecular orbitals or intrinsically local atomic orbitals instead of canonical molecular orbitals. At a given point of any molecule, only a small number of localized orbitals, which does not depend on the overall system size, will contribute to the dynamic correlation. Hence, in principle, this allows for linear-scaling correlated MP2 methods.[48,49] However, matrix equations in terms of the non-orthogonal local orbitals, which do not transform as the irreducible representations of the molecular point group symmetry, are more involved. Numerous approaches, for instance by Werner and coworker[50,51], Schütz and coworkers,[52] or by Head-Gordon and coworkers,[53,54] exist to circumvent these problems. Notably, a variety of local coupled-cluster methods was developed as well for example by Neese and coworkers.[55,56] They pointed out that apart from the implementation, a further general challenge for local correlated methods is the compulsory introduction of threshold values for the correlation treatment:[57] to fully benefit from the reduced scaling of local methods, not all two-electron integrals in the local basis are included, but only those contributing more than a predefined energy threshold. Introducing threshold values can generally produce a number of problems, such as discontinuities in the course of geometry optimizations.[31]

Compared with these local approaches, R12 methods intent to improve the basis set convergence of correlated wave functions. Due to the singularity of the electron-electron repulsion operator $1/r_{12}$ at $r_{12} = 0$, the total wave function possesses a correlation cusp at this point,[58] a consequence of the more general Kato theorem.[59] Wave functions constructed from determinants composed of one-electron wave functions describe these Kato cusps rather poorly. It can indeed be shown that the overall MP2 energy converges approximately with $(L + 1)^{-3}$, with L being the highest angular momentum comprised in the basis set.[58] Thus large basis sets are required to obtain converged energies with correlated methods, and a significant number of two-electron integrals must be calculated. It follows from Kato's theorem that for short interelectronic distances r_{12}, the exact wave function depends linearly on r_{12}. To improve the convergence behavior of correlated wave functions, the interelectronic distance r_{12} is explicitly included in the wave function Ψ.[31]

$$\Psi = \Phi_0 + \sum_{a,b,r,s} c_{ab}^{rs} \, \Phi_{ab}^{rs} + \sum_{a,b} c'_{ab} r_{ab} \, \Phi_0 \tag{39}$$

Please note that in the more general case, r_{12} is replaced by a general function of r_{12} often denoted as f_{12}.[60] R12 methods are therefore also designated as F12 methods. In combination with density fitting procedures, such R12-MP2 approaches become computationally feasible.[61] The convergence of the wave function with the basis set size reduces to $(L + 1)^{-7}$ so that fewer two-electron integrals need to be calculated.[58] A number of recent investigations, for example of Wang and Hättig et al.[62,63,60],

Hirata and coworker,[64] or of Klopper and coworker,[65] demonstrate the interest in the subject. There are naturally equivalent R12 extensions of coupled cluster theory, for instance of Hättig, Tew, and Köhn,[66] of Noga and Tenno and coworkers,[67] and of Werner and coworkers.[68,69]

Yet another important extension of MP2, which improves its performance without increasing the computational cost, is spin-component scaling[70] (SCS). The MP2 correlation energy E_{corr} (Eq. (34)) can be separated into contributions from same-spin electrons E_{corr}^{ss} and from opposite-spin electrons E_{corr}^{os}:[70]

$$E_{corr} = E_{corr}^{ss} + E_{corr}^{os} \tag{40}$$

$$E_{corr}^{ss} = \sum_{a<b,r<s} \frac{|\langle ab \parallel rs \rangle|^2}{\varepsilon_a + \varepsilon_b - \varepsilon_s - \varepsilon_r} + \sum_{\bar{a}<\bar{b},\bar{r}<\bar{s}} \frac{\left|\langle \bar{a}\bar{b} \parallel \bar{r}\bar{s} \rangle\right|^2}{\varepsilon_a + \varepsilon_b - \varepsilon_s - \varepsilon_r} \tag{41}$$

$$E_{corr}^{os} = \sum_{a,\bar{b},r,\bar{s}} \frac{\left|\langle a\bar{b}|r\bar{s} \rangle\right|^2}{\varepsilon_a + \varepsilon_b - \varepsilon_s - \varepsilon_r} \tag{42}$$

The MP2 correlation between same-spin and between opposite-spin electrons fundamentally differs. This results from differences between the same-spin and the opposite-spin correlation in the zeroth-order wave function, i.e., in the HF determinant. The biased description of correlation phenomena in the HF determinant can be only incompletely compensated in the subsequent perturbation treatment. Same-spin electrons are - due to the inclusion of the Pauli repulsion in a Slater determinant - already correlated in HF. Average distances between same-spin electrons are thus large. Therefore the electrons interact mainly via static (long-range) correlation. In contrast, opposite-spin electrons are not correlated on the HF level of theory. Their average interelectronic distances are thus smaller and can become zero. As a consequence, they interact mainly via short-range (dynamic) correlation, which is, due to the biased HF determinant, also underestimated in the subsequent MP2 treatment.[70] Grimme et al. were indeed able to demonstrate the correspondence of same-spin/static correlation and of opposite-spin/dynamic correlation by comparing the ratio $E_{corr}^{os}\big/E_{corr}^{ss}$ on the one hand to the D1-diagnostic in CCSD and on the other hand to the contribution of the triples correction in CCSD(T).[43] The key idea of SCS is thus to correct the imbalanced correlation treatment in MP2 by scaling up the opposite-spin and scaling down the same-spin correlation (empirical parameters: $c_{os} = 6/5, c_{ss} = 1/3$):[70]

$$E_{corr} = c_{ss}E_{corr}^{ss} + c_{os}E_{corr}^{os} \tag{43}$$

The SCS correction was shown to significantly improve the MP2 prediction of reaction energies,[70] geometries,[71] and non-covalent interactions[72].[43] The latter observation has furthermore channeled the

development of several SCS parameterizations specific for non-covalent interactions.[73,74,75,76] However, it is important to note that the good performance of the different SCS-MP2 variants for weak intermolecular interactions, most notably for dispersion, relies on an advantageous error compensation.[43] Head-Gordon and coworkers pointed out that for large distances between non-covalently bound subsystems, the spin dependence of the correlation vanishes, and both coefficients must add up to 2 ($c_{ss} + c_{os} = 2$). This is not the case for the standard parameters, which corresponds to a first error of SCS-MP2. Head-Gordon and coworkers enforced the condition $c_{ss} + c_{os} = 2$ by scaling the coefficients with a standard range-separation operator.[77] They obtained, however, deteriorated results for non-covalent interactions. In fact, eliminating the error of the scaling coefficients sheds light on the intrinsic incapability of MP2 to correctly describe dispersion, the second important error of SCS-MP2. According to an analysis of Cybulski and coworker, the so-called uncoupled HF dispersion energy including effects like charge penetration and higher-rank polarizabilities explains why MP2 usually overshoots for dispersion energies.[78]

Head-Gordon and coworkers proposed a simplified version of SCS, called spin-opposite scaling (SOS). It corresponds to considering only the opposite-spin correlation, i.e., the coefficient of the same-spin correlation is set to zero. This can be justified by the fact that the same-spin correlation, anyway considerably smaller than the opposite-spin correlation, is further downscaled in an SCS treatment. Neglecting it completely constitutes only a minor further approximation, which is also reflected in the satisfying accuracy of SOS-MP2.[79] More importantly, however, neglecting the same-spin correlation results in entirely local correlation (Eq. (34)), i.e., the MP2 correlation consists of local Coulomb integrals only. SOS-MP2 scales thus as N^4. It is therefore, as stated by Head-Gordon, "an economical electronic structure method".[79]

3.1.4   Multi-reference correlated *ab initio* methods[31]

Especially MP2 and coupled-cluster approaches yield very accurate results as long as the underlying reference HF determinant provides an adequate first-order description of a system's electronic structure. Only then, converged values for the correlation energy in a subsequent perturbation/cluster expansion can be obtained.[80] However, a single HF determinant is not always a good first-order approximation, e.g., the description becomes unsuitable for near-degeneracies.[31] Such systems, where a single Slater determinant composed of one-electron wave functions is a poor approximation, are also designated as strongly-correlated systems[81,82] or as systems with multireference character.[31] The latter term already implies that a single HF reference cannot capture the electronic character of the systems in a qualitatively correct way. Instead, the first-order wave function of such systems can be either expressed as a single Slater determinant constructed from two-electron wave functions (Cooper pairs[83] or geminals)[82] or as a linear combination of multiple Slater determinants constructed from one-

electron wave functions (orbitals). In view of the simplicity of a single-determinant wave function, the former has recently attracted some research interest.[82,84,80] Nevertheless, the second orbital-based approach is much more common and well-established. Instead of a single HF determinant, a linear combination of determinants is employed as the reference. The most straightforward way to select these determinants is to define a certain number of "active orbitals" among which all possible configuration state functions are created (CSFs).[85] This corresponds to the CASSCF method (complete active space self-consistent field). The linear combination of the CSFs forms the reference wave function. Both the orbitals, i.e, the coefficients of the molecular orbitals in the atomic orbital basis, and the coefficients of the determinants are optimized in the SCF procedure. This explains the significant computational effort involved in CASSCF calculations.[31] It limits the size of the active space to 14 to 16 orbitals and has led to the development of a number of algorithms such as the super-CI approach[86] to compute CASSCF wave functions as efficiently as possible.[87] RASSCF (restricted active space self-consistent field), an extension of CASSCF, allows for larger active spaces by introducing a division of the active space into three subspaces. While all possible CSFs are created in the center subspace, only CSFs with a predefined maximum number of electrons in the upper subspace and a given maximal amount of holes in the lower subspace are included in the ansatz of the RASSCF wave function.[88] Similar to CI calculations, CASSCF/RASSCF wave functions are obtained as the lowest roots of the CI matrix using a procedure analogous to the Davidson algorithm. If several roots are calculated, for instance to calculate excitation energies, state-averaged calculations are often performed, i.e., the same set of orbitals is used in all roots.[89] The orbitals are constructed by averaging the density matrix of the single CASSCF wave functions.[90] State-averaging has the advantage that resulting CASSCF states are orthogonal. Similar to the single HF determinant, the multi-determinant CASSCF wave function is the starting point, i.e., the reference, to subsequently take into account dynamic correlation by including some of its excited states. Although MRCI (multireference CI) is perhaps the most obvious choice, the selection of the excited CASSCF configurations for the CI treatment is not straightforward, and it is subject to severe computational limits. Meanwhile, a perturbative inclusion of dynamic correlation in CASSCF wave functions has become common practice. The main problem of the perturbative approach consists in its practical implementation. By reformulating the definition of the zeroth-order Møller-Plesset perturbation operator, Roos and coworkers[91,92] established the CASPT2 method that adds a perturbation correction to the CASSCF wave function. Some problems of CASPT2 are known, most notably valence-Rydberg mixing and the failure of CASPT2 for the vicinity of avoided crossings. To eliminate this deficiency, Roos and coworkers furthermore developed the multistate (MS) CASPT2 approaches. An effective Hamiltonian is perturbatively calculated from the state-averaged CASSCF wave functions and diagonalized to obtain final MS-CASPT2 energies.[93] Further modifications of the original CASPT2 method comprise the IPEA shift, which shifts all active orbitals by a slightly modified

zeroth-order Hamiltonian,[94] and a shift in the energy denominator of the perturbatively included excited states. This shift essentially removes the intruder states' problem of CASPT2.[95,96]

3.1.5 Ground-State Density Functional Theory (DFT)[97]
3.1.5.1   The Hohenberg-Kohn theorem and the Kohn-Sham formalism
The Hohenberg-Kohn theorem

In contrast to wave-function based approaches, density functional theory (DFT)[98] uses the only three-dimensional electron density instead of a multidimensional wave function to describe a molecule's electronic structure. Using only the density is possible due to the first Hohenberg-Kohn theorem,[98] which states that the ground-state energy E_0 (like any other ground-state property) is a unique functional of the ground-state density ρ_0. In other words, since the ground-state energy is defined by the Hamiltonian of the system (Eq. (10)) that contains the external potential $\hat{V}_{Ne}$ as the only system-specific part, there is a one-to-one correspondence between the external potential and the electronic ground-state density.[97]

$$\rho_0(\vec{r}) \leftrightarrow \Psi_0(\{\vec{r}_i\}) \leftrightarrow E_0[\rho_0(\vec{r})] \leftrightarrow \hat{V}_{Ne}(\vec{r}) \tag{44}$$

The theorem is based on a proof via *reductio ad absurdum*.[i] In this form (Eq. (44)), the first Hohenberg-Kohn theorem is often considered as a sheer "existence theorem",[32] i.e., it proves only the existence of an energy density functional $E_0[\rho_0(\vec{r})]$ without further specifications about the calculation of the density. However, it implicitly contains more information. The ground-state wave function $\Psi_0(\{\vec{r}_i\})$ does not only correspond the ground-state density $\rho_0(\vec{r})$, but according to the variational principle, it directly relates $\rho_0(\vec{r})$ also to the minimal ground-state energy $E_0[\rho_0(\vec{r})]$.[97]

$$E_0[\rho_0(\vec{r})] = \min_{\Psi \to \rho_0} \langle \Psi | \hat{H} | \Psi \rangle \tag{45}$$

This follows from Eq. (44) because if ρ in the more general Eq. (46) is not the ground-state density ρ_0, the resulting wave function Ψ differs from Ψ_0 due to the one-to-one correspondence between the density and the wave function (Eq. (44)). The energy of Ψ is consequently not the minimal ground-state energy E_0.[99]

$$E[\rho(\vec{r})] = \min_{\Psi \to \rho} \langle \Psi | \hat{H} | \Psi \rangle \tag{46}$$

This outlines what is often called the second Hohenberg-Kohn theorem: the ground-state density minimizes the energy functional according to the variational principle.[32]

---

[i] It is assumed in a first step that two different Hamiltonians H and H' yield the same density. However, since different wave functions Ψ and Ψ' are obtained from different Hamiltonians, this results in a contradiction.[31]

$$E[\rho(\vec{r})] \geq E_0[\rho_0(\vec{r})] \tag{47}$$

Equivalently, in a two-step procedure proposed by Levy[100] and summarized by Burke and coworker,[101] the ground-state energy of a system E_0 is calculated by minimizing a universal functional $F[\rho]$ over all wave functions with a given density (Eq. (48)) and subsequently minimizing over all densities (Eq. (49)):

$$F[\rho] = \min_{\Psi \to \rho} \langle \Psi | \hat{T} + \hat{V}_{ee} | \Psi \rangle \tag{48}$$

$$E_0[\rho_0] = \min_{\rho \to \rho_0} \left\{ F[\rho] + \int d\vec{r} \hat{V}_{Ne}(\vec{r}) \rho(\vec{r}) \right\} \tag{49}$$

Thus, according to the Hohenberg-Kohn theorem, (1) the energy is a unique functional of the density (Eq. (49), equivalent to Eq. (44)), (2) $F[\rho]$ is a universal functional (i.e., only the external potential is non-universal[99]), and (3) the ground-state density ρ_0 satisfies (equivalent to Eq. (47))[101]

$$\frac{\partial F[\rho]}{\partial \rho_0(\vec{r})} = -\hat{V}_{Ne}(\vec{r}) \tag{50}$$

It should be noted that while the proof of the Hohenberg-Kohn theorem via *reductio ad absurdum* excludes that *two* different external potentials yield the same density, it does not consider the case that *no* external potential exists to generate a given density. This problem is called the v-representability. Similarly, the Hohenberg-Kohn theorem presupposes that any density can be expressed as a wave function, i.e, it assumes N-representability.[99] While the latter seems to be guaranteed,[102,103] the question of the v-representability is more involved.[99,104] However, Levy[100] and Lieb[105] independently outlined a constrained-search proof of the Hohenberg-Kohn theorem without presupposing v-representability.

The exchange-correlation energy

The universal functional $F[\rho]$ is often represented as a sum of three terms, the kinetic energy functional $T[\rho]$, the Coulomb repulsion energy $J[\rho]$, and the exchange-correlation energy $E_{xc}^{(c)}[\rho]$.[106]

$$F[\rho] = T[\rho] + J[\rho] + E_{xc}^{(c)}[\rho] \tag{51}$$

The functional form of $J[\rho]$ is known (Eq. (52)), and $E_{xc}^{(c)}[\rho]$ absorbs the remaining parts of the electron-electron interaction, i.e., exchange and correlation. Scuseria et al. designate $E_{xc}^{(c)}[\rho]$ as the "conventional" exchange-correlation energy because it is similarly defined to exchange and correlation in wave-function based methods.[106]

$$J[\rho] = \frac{1}{2} \int \frac{\rho(\vec{r})\rho(\vec{r}')}{|\vec{r} - \vec{r}'|} \tag{52}$$

The universal functional $F[\rho]$ (Eq. (48), (49), (51)) is complicated and not known (except for $J[\rho]$, Eq. (52)).[j,31] It is therefore advantageous to reintroduce orbitals, as suggested by Kohn and Sham in 1965.[107] They imagined a fictitious reference system of non-interacting electrons having the same density as the real system. This can be expressed by introducing a parameter λ into Eq. (48) that continuously increases its value from $\lambda = 0$, the non-interacting reference system, to $\lambda = 1$, the real system.[106]

$$F_\lambda[\rho] = \min_{\Psi \to \rho} \langle \Psi^\lambda | \hat{T} + \lambda \hat{V}_{ee} | \Psi^\lambda \rangle \tag{53}$$

For all values of λ, the external potential $\hat{V}_{Ne}(\vec{r})$ is adapted so that the density is constant, i.e., $\hat{V}_{Ne}(\vec{r})(\lambda)$. This implies that the external potential of the non-interacting reference system $v_S(\vec{r})$ ($\lambda = 0$) is not equal to the $\hat{V}_{Ne}(\vec{r})$ of the true, interacting system ($\lambda = 1$).[31] The *exact* wave function of the non-interacting reference system ($\lambda = 0$) would be a Slater determinant Φ_S with the kinetic energy T_S calculated from the orbitals (see Eq. (13)). It follows furthermore from Eq. (53) that the universal functional of the non-interacting reference system $F_S[\rho]$ consists only of this orbital-kinetic energy term ($\lambda = 0$).[106]

In the Kohn-Sham approach, the kinetic energy of the non-interacting reference system T_S is used to calculate the universal functional of the real system $F[\rho]$. $F[\rho]$ is thus expressed as the sum of the orbital-kinetic energy $T_S[\rho]$, the Coulomb repulsion energy $J[\rho]$, and the DFT exchange-correlation energy $E_{xc}[\rho]$.[106,101]

$$F[\rho] = T_S[\rho] + J[\rho] + E_{xc}[\rho] \tag{54}$$

Compared with Eq. (51), an expression for $T_S[\rho]$, a large part of the universal function (Eq. (54)), is available (as a function of the orbitals). Eq. (54) defines the DFT exchange-correlation energy (see also Eq. (51)), which can be expressed as[106,101]

$$E_{xc}[\rho] = T[\rho] - T_S[\rho] + E_{xc}^{(c)}[\rho] \tag{55}$$

Thus the DFT exchange-correlation energy contains in addition to the contributions of the "conventional exchange-correlation energy" a kinetic-energy correction.[31]

It follows from Eq. (54) that the Kohn-Sham energy is calculated from the kinetic energy $T_S[\rho]$, the nuclei-electron $V_{Ne}[\rho]$ and the classical electron-electron interaction/Coulomb repulsion energy $J[\rho]$,

---

[j] Additionally, orbital-free approximations to the kinetic energy functional based on the Thomas-Fermi[1009,1010] model yield very poor results.

all of which can be exactly calculated for a Slater determinant, and the introduced DFT exchange-correlation energy $E_{xc}[\rho]$.[101]

$$E_0[\rho] = T_S[\rho] + V_{Ne}[\rho] + J[\rho] + E_{xc}[\rho] \tag{56}$$

A more intuitive expression for the exchange-correlation energy (than Eq. (55)) can be derived from Eq. (53)[106] and the Hellmann-Feynman theorem.[31]

$$\frac{\partial F_\lambda[\rho]}{\partial \lambda} = \langle \Psi^\lambda | \hat{V}_{ee} | \Psi^\lambda \rangle \tag{57}$$

"Adiabatic integration" of Eq. (57) yields the adiabatic connection formula (Eq. (59)).[108,109,110]

$$\int_{\lambda=0}^{\lambda=1} d\lambda \frac{\partial F_\lambda[\rho]}{\partial \lambda} = F[\rho] - F_S[\rho] = J[\rho] + E_{xc}[\rho] \tag{58}$$

$$E_{xc}[\rho] = \int_{\lambda=0}^{\lambda=1} d\lambda \langle \Psi^\lambda | \hat{V}_{ee} | \Psi^\lambda \rangle - J[\rho] \tag{59}$$

The adiabatic connection formula is commonly expressed as a function of the exchange-correlation hole $h_{xc}(\vec{r}_1, \vec{r}_2)$.[31] The exchange-correlation hole, also written as the sum of an exchange $h_x(\vec{r}_1, \vec{r}_2)$ and a correlation hole $h_c(\vec{r}_1, \vec{r}_2)$, is the decrease of the probability to find electron 2 at $\vec{r}_2$ if electron 1 is at $\vec{r}_1$, i.e., it corresponds to the (normalized) reduction of the pair density $\rho(\vec{r}_1, \vec{r}_2)$ compared with the uncorrelated product density $\rho(\vec{r}_1)\rho(\vec{r}_2)$.

$$h_{xc}(\vec{r}_1, \vec{r}_2) = \frac{\rho(\vec{r}_1, \vec{r}_2)}{\rho(\vec{r}_1)} - \rho(\vec{r}_2) \tag{60}$$

Thus it follows from Eq. (59)

$$E_{xc}[\rho] = \int_{\lambda=0}^{\lambda=1} d\lambda \int\int d\vec{r}_1 d\vec{r}_2 \frac{\rho^\lambda(\vec{r}_1, \vec{r}_2)}{r_{12}} - \frac{1}{2}\int\int d\vec{r}_1 d\vec{r}_2 \frac{\rho(\vec{r}_1)\rho(\vec{r}_2)}{r_{12}} \tag{61}$$

$$E_{xc}[\rho] = \frac{1}{2}\int_{\lambda=0}^{\lambda=1} d\lambda \int\int d\vec{r}_1 d\vec{r}_2 \frac{\rho(\vec{r}_1) h^\lambda{}_{xc}(\vec{r}_1, \vec{r}_2)}{r_{12}} \tag{62}$$

Along the adiabatic integration, the density $\rho(\vec{r}_1)$ is constant, thus it does not depend on λ.[106] Eq. (62) is a starting point for many derivations of exchange-correlation functionals.[106]

To arrive at the working equations of Kohn-Sham DFT (KS-DFT), the exchange-correlation potential $v_{xc}(\vec{r})$ as the functional derivative of the exchange-correlation energy with respect to the density is defined.

$$v_{xc}(\vec{r}) = \frac{\delta E_{xc}[\rho]}{\delta \rho(\vec{r})} \tag{63}$$

With this exchange-correlation potential (Eq. (63)), the external potential of a single electron $v_{Ne}(\vec{r})$ (Eq. (65)) and the Hartree potential $v_{ee}(\vec{r})$ (Eq. (66)), an effective one-particle equation is obtained (in a procedure similar to HF, i.e., by minimizing the expectation value of the energy functional, Eq. (56), as a function of orbital variations) to calculate the Kohn-Sham orbitals $\{\chi_i(\vec{r})\}$ that minimize the energy expectation value of Eq. (56), i.e., that define the Kohn-Sham determinant Φ_{KS} with the lowest energy.[k,106]

$$\left(-\frac{1}{2}\Delta + v_{xc}(\vec{r}) + v_{Ne}(\vec{r}) + v_{ee}(\vec{r})\right)\chi_i(\vec{r}) = \varepsilon_i \chi_i(\vec{r}) \tag{64}$$

$$v_{Ne}(\vec{r}) = -\sum_{A=1}^{nuclei} \frac{Z_A}{|\vec{R}_A - \vec{r}|} \tag{65}$$

$$v_{ee}(\vec{r}) = \int d\vec{r}' \frac{\rho(\vec{r}')}{|\vec{r}' - \vec{r}|} \tag{66}$$

Since the density and the orbitals of the true and the reference system are equal, Eq. (64) defines the external potential of the non-interacting reference system as $v_S = v_{xc}(\vec{r}) + v_{Ne}(\vec{r}) + v_{ee}(\vec{r})$. This potential of the non-interacting reference system in conventional Kohn-Sham was originally entirely *local*. The ansatz for the calculation of the density in Eq. (64) is in principle exact. However, the exact form of the exchange-correlation functional (Eq. (55)) is not known, and it must be approximated.[101] Developing improved approximations is the key challenge of KS-DFT. As stated by Cohen, "all of the complexity [of DFT] is hidden in one term, the exchange-correlation functional. This term holds the key to the success or failure of DFT".[111] In fact, already rather simple approximate versions for the exchange-correlation functional perform quite well.[111] This results from the fact that the corrections subsumed in the exchange-correlation energy (Eq. (55)) are small – as mentioned, they consist in the conventional exchange-correlation energy $E_{xc}^{(c)}[\rho]$ and an additional correlation correction of the kinetic energy $T - T_S$.[106]

To derive functional forms for $E_{xc}[\rho]$, it is common practice to divide the exchange-correlation functional $E_{xc}[\rho]$ into an exchange $E_x[\rho]$ and a correlation part $E_c[\rho]$.[31]

$$E_{xc}[\rho] = E_x[\rho] + E_c[\rho] \tag{67}$$

---

[k] All DFT equations are usually formulated for spin densities. For clarity, the spin suffixes are neglected in this section.

It follows from Eq. (59) that the sum of these parts corresponds to the difference between the exact electron-electron interaction $\langle\Psi_0|\hat{V}_{ee}|\Psi_0\rangle$ and the Coulomb repulsion energy $J[\rho]$. Formally, this difference can be further subdivided because the exchange energy is defined as the energy difference[106]

$$E_x[\rho] = \langle\Phi_{KS}|\hat{V}_{ee}|\Phi_{KS}\rangle - J[\rho] \tag{68}$$

As a consequence, the remaining energy difference to the exact electron-electron interaction is considered as the correlation energy[l].[106]

$$E_c[\rho] = \langle\Psi_0|\hat{V}_{ee}|\Psi_0\rangle - \langle\Phi_{KS}|\hat{V}_{ee}|\Phi_{KS}\rangle \tag{69}$$

Whereas Eq. (68) looks equivalent to the definition of the (exact) HF exchange, it should be kept in mind that KS and HF orbitals are not equal. In fact, Baerends and coworkers could show for diatomic molecules that using KS instead of HF orbitals produces pronounced differences in the individual energy contributions to the determinantal energy expectation value.[112] Hence, generally $E_x^{exact}[\rho] \neq E_x^{HF}[\rho]$.[106] This results also from the different characters of the underlying holes. Since the exchange hole in HF is highly nonlocal, the correlation hole, nonlocal as well, needs to compensate to a large extent this nonlocal character. In contrast, DFT exchange and correlation holes can be in principle local because KS-DFT only aims at reproducing the sum of the exchange and correlation energy correctly.[31,97]

Although the exact exchange-correlation functional is not known, a number of properties exist that it should fulfill.[113] Many of them are intimately related to the exchange-correlation hole,[31] and it was shown that their importance differs.[114] Most notably, the exact exchange-correlation functional must be self-interaction free. This requires for the exchange and the correlation energy of a one-electron system[106]

$$E_c[\rho] = 0 \tag{70}$$

$$E_x[\rho] + J[\rho] = 0 \tag{71}$$

While the formulation of equivalent conditions for many-electron systems is more involved, analogies exist.[111,115,116] In Hartree-Fock, the exchange interaction in a one-electron system elegantly cancels the non-physical Coulomb self-repulsion of the single electron (Eq. (71)).[31]

Furthermore, upper and lower bounds exist for the exchange-correlation energies, for instance the Lieb-Oxford condition[117].[31,106] Levy et al. derived numerous conditions on coordinate scaling

---

[l] The additional correction for the kinetic energy is then included in the correlation energy.

transformations of the density.[118,119,120,121,122,123,124] Upon coordinate transformation with a linear scaling parameter γ, the density expands or contracts while preserving its normalization.[106]

$$\rho(\vec{r}) = \gamma^3 \rho(\gamma\vec{r}) \tag{72}$$

From this so-called uniform scaling of the density (Eq. (72)), some restrictions for the scaling behavior of the exchange and correlation energy result.[106] For instance, the exchange energy depends linearly on the scaling parameter (Eq. (73)) whereas the correlation energy must be finite also for infinitely contracted densities, i.e., for infinite scaling parameters (Eq. (74)).[31]

$$E_x[\rho_\gamma] = \gamma E_x[\rho] \tag{73}$$

$$\lim_{\gamma\to\infty} E_c[\rho_\gamma] > -\infty \tag{74}$$

Yet another group of restrictions concerns the limiting case of the uniform electron gas. For uniform electron densities, the exchange-correlation functional should reduce to the expression for the uniform electron gas, i.e., the local density approximation (LDA).[106]

$$E_{xc}[\rho] = E_{xc}{}^{LDA}[\rho] \tag{75}$$

Functional development: models for the exchange-correlation energy

Among others with regard to these constraints, Scuseria et al. outlined in a recent review six different strategies frequently employed to design density functional approximations (DFAs), i.e. to devise improved exchange-correlation functionals.[106] Some of them are derived from expressions used to describe the inhomogeneous electron gas.[31] The classification was in fact readily adopted also by Truhlar et al.[125] Namely, the strategies of Scuseria et al.[106] include (1) the LDA, (2) the density-gradient expansion, (3) constraint satisfaction, (4) modeling the exchange-correlation hole, (5) empirical fits and (6) mixing exact and approximate exchange. Most functionals are constructed employing a combination of these strategies.[106]

In contrast to wave-function based methods, a systematic improvement of DFT results, for example via the inclusion of more higher-order excitations, is not possible. However, the plethora of exchange-correlation functionals developed with the strategies of Scuseria et al. differ in terms of the quantities used to calculate the exchange-correlation energy.[106] This results in Perdew's famous "Jacob's ladder" of DFAs.[126] Usually, results of a lower-rung functional improve if a higher-rung functional is used. The rungs of the Jacob's ladder are (1) LDA functionals, (2), GGA (generalized gradient approximation) functionals, (3) meta-GGA functionals (additionally including the second derivative of the density $\nabla^2\rho$

or the Weizsäcker kinetic energy τ_W),[31] (4) hybrid functionals[m] (including exact exchange), and (5) double-hybrid functionals, including exact exchange and MP2-type correlation. Particularly the hybrid functionals can be further differentiated. "Conventional" hybrid functionals with a fixed amount of exact exchange are also called global hybrids.[127] If the fraction of exact exchange $a_{x,HF}(\vec{r})$ comprised in a hybrid functional is position-dependent, so-called „local hybrids" result.[128] Long-range corrected functionals form another subgroup of hybrids.[129] Instead of a position-dependent Hartree-Fock coefficient, a range-separated Coulomb operator r_{12}^{-1} including a range separation parameter ω is used for the calculation of exchange[130], i.e., the amount of exact exchange is not determined by the position, but by the interelectronic distance.

$$\frac{1}{r_{12}} = \frac{1 - erf(\omega r_{12})}{r_{12}} + \frac{erf(\omega r_{12})}{r_{12}} \tag{76}$$

The range separation of the Coulomb operator was originally proposed by Savin et al.[131] for the purpose of combining long-range configuration interaction with short-range DFT. Hirao and coworkers adapted it to a GGA functional in order to obtain a range-separated exchange energy with short-range DFT exchange and long-range exact exchange.[132] A more general expression was introduced by Yanai et al.[133] where a fixed amount α of exact exchange is also included in the short-range limit. The amount of HF exchange rises to $\alpha + \beta$ in the long-range limit. This defines so called range-separated hybrids. For $\alpha = 0, \beta = 1$, standard long-range corrected functionals result.

$$\frac{1}{r_{12}} = \frac{1 - [\alpha + \beta \cdot erf(\omega r_{12})]}{r_{12}} + \frac{\alpha + \beta \cdot erf(\omega r_{12})}{r_{12}} \tag{77}$$

Double-hybrid functionals are not included among the strategies of Scuseria et al. They are rather recent, although modern double hybrids are based on the Görling-Levy perturbation theory (GLPT),[134,135] an extension of DFT that basically converges with wave-function type perturbation theory. In contrast to GLPT, however, KS orbitals of modern double-hybrid functionals are self-consistently solved only for the underlying hybrid functional. In a non-iterative subsequent step, MP2-type correlation is calculated and replaces some of the underlying GGA correlation. The KS orbitals do not depend on the MP2 correlation.[136] This considerably increases the accuracy and computational efficiency of the approach.[136,137] Double-hybrid functionals are motivated by the idea that not only the exchange energy is non-local, a fact recognized when designing hybrid functionals where the exchange hole acquires non-local character, but also the correlation energy includes non-local components (static correlation,[136] medium- to long-range correlation).[138]

---

[m] For a conceptual discussion of hybrids see below. Hybrid functionals result in non-local Kohn-Sham potentials because they include a fraction of exact exchange.

3.1.5.2 Dispersion in DFT

Long-range correlation phenomena are also important to correctly assess dispersion interactions (see MP2 discussion above). Although an improved description of dispersion by double hybrid functionals could be expected,[136] dispersion interactions are usually already incorporated via damped interatomic potentials of type $C_6 R^{-6}$ into DFAs, yielding very accurate results.[139] The currently most popular dispersion correction is Grimme's D3 correction,[140] replacing the former D1[141] and D2[142] versions. The dispersion energy E^{disp} is calculated between all atom pairs A, B using pairwise dispersion coefficients C_n^{AB} (Eq. (78)) and cutoff distances R_0^{AB} (Eq. (79)).[140]

$$E^{disp} = \sum_{AB} \sum_{n=6,8} s_n \frac{C_n^{AB}}{r_{AB}^n} f_{d,n}(r_{AB}) \tag{78}$$

r_{AB}^n is the distance between the atoms. s_n is a scaling coefficient that is set to 1 for $n = 6$ for all functionals except for the double-hybrid functionals, which already include a part of the long-range correlation needed to describe dispersion. The R^{-8}-term is short-range, lying on the same scale as the medium-range correlation of the functionals. To avoid double-counting the medium-range correlation, s_8 is individually adjusted for all functionals. $f_{d,n}(r_{AB})$ is a damping function proposed by Head-Gordon and Chai[143] that prevents singularities of the dispersion energy expression for short interatomic distances.

$$f_{d,n}(r_{AB}) = \frac{1}{1 + 6 \left(r_{AB}/(s_{r,n} R_0^{AB}) \right)^{-\alpha_n}} \tag{79}$$

$s_{r,n}$ is an order-dependent scaling factor that is computed for each functional for $n = 6$, while left unscaled for $n = 8$. α_n determines the "steepness"[140] of the damping; it is adjusted manually.[140] In contrast to the earlier versions, the D3 version relies on parameters mostly obtained from *first principle* calculations. Moreover, dispersion coefficients are specifically adapted to the coordination number of an atom.[140] However, as equally outlined by Grimme et al., a major disadvantage of a dispersion correction like Eq. (78) is that it does not depend on the electron density, ultimately limiting the highest achievable accuracy.[140] Nevertheless, the error of the underlying DFT calculation should be certainly larger.[140]

3.1.5.3 Deficiencies of Ground-State DFT

Indeed, despite its success, ground-state DFT calculations suffer from a number of known deficiencies.[144] This includes particularly underestimated reaction barriers, overestimated binding energies for charge-transfer complexes, wrong ionization potentials and electron affinities, and a poor description of the breaking of chemical bonds and of strongly correlated systems.[111] All of these errors result from two recurrent errors of the approximate exchange-correlation functionals: the

delocalization error and the static correlation error.[111] While the first arises from the Coulomb repulsion energy that separates electrons too much, the second corresponds to the difficulty of describing degenerate states with the electron density. The delocalization and static correlation errors can be understood in terms of fractional charges and fractional spins, respectively.[111]

Compared with the delocalization error, the static correlation error is less known although static correlation is omnipresent. It relies on another constraint that the exact functional must satisfy, the so-called constancy condition. In strongly-correlated systems, such as a dissociating hydrogen molecule, fractional spin states arise in closed-shell DFT calculations[145] (such as half a hydrogen molecule, the hydrogen atom, with half a spin-up electron and half a spin-down electron[111]). These fractional spin states should be isoenergetic with the regular ground state with normal spin (two hydrogen atoms). While the energy of the exact functional for the fractional spin states is a constant and equal to the energy of the degenerate ground state (two hydrogen atoms at the dissociation limit of the hydrogen molecule), energies of approximate functionals do not fulfill this constancy condition.[145] This corresponds to the static correlation error.[111]

The delocalization error of DFT, i.e., the artificial spreading of electron density due to the self-interaction error,[111] is more frequently addressed and becomes evident from a DFT treatment including fractional charges. Perdew and coworkers extended the Hohenberg-Kohn theorem to partial charges by considering statistical averages of systems with different numbers of electrons. They outlined that the energy of the exact functional as a function of the (continuous) electronic charge must correspond to a series of straight lines with slope discontinuities at each integer.[146] For an N-electron system, the segments (N-1, N) and (N, N+1) have by definition slopes of EA (electron affinity) and IP (ionization potential). The discontinuities are thus physically reasonable because the ionization potential and electron affinity are not equal.[147] Moreover, from the asymptotic decay of the densities of finite systems, Almbladh and Barth were able to prove a version of Koopman's theorem for DFT.[n] It associates the HOMO energy ε_{HOMO} with the ionization potential.[148]

$$\varepsilon_{HOMO} = -IP \tag{80}$$

As a consequence, the slope of the (N-1,N) segment corresponds to the HOMO energy. Thus, Janak's theorem is fulfilled "when approaching the integer from below"[o].[147] In fact, Janak's theorem[149] states

---

[n] It should be noted that as demonstrated by Baerends and coworkers, the slopes of all straight-line segments, the orbital energies, can be interpreted as approximate ionization potentials.[1011]

[o] As outlined by Kronik et al.,[147] this is automatically ensured by the choice of the reference point for the Kohn-Sham potential.

that the eigenvalues of occupied Kohn-Sham orbitals $\{\varepsilon_i\}$ are obtained as the derivatives of the total energy with respect to the occupation numbers n_i.

$$\frac{\partial E}{\partial n_i} = \varepsilon_i \tag{81}$$

Yet, Janak's theorem holds only for occupied orbitals, and the discontinuity at the integer N has important implications for the interpretation of the LUMO energy, a virtual orbital, and it is related to the delocalization error. It follows from the KS energy expression (Eq. (56)) that the discontinuity can only arise from either the kinetic energy or the exchange-correlation energy since the Coulomb energy and the external potential energy vary continuously with the density. As outlined by Kronik et al.,[147] a discontinuous exchange-correlation energy implies that a discontinuity Δ_{xc} exists for the exchange-correlation potential, usually called the derivative discontinuity. Indeed, exchange-correlation holes and potentials obtained from high-level *ab initio* calculations[150,151] indicated that values of Δ_{xc} can be quite significant.

Applying Eq. (80) to the N+1 system, neglecting nuclear relaxation effects for the electron affinity and recognizing $HOMO(N + \delta) = LUMO(N - \delta)$, the slope of the (N,N+1) segment corresponds to[147]

$$\varepsilon_{HOMO}(N + 1 - \delta) = -A = \varepsilon_{HOMO}(N + \delta) = \varepsilon_{LUMO}(N - \delta) + \Delta_{xc} \tag{82}$$

The exact exchange-correlation functional satisfies Eq. (80) and (82). This necessarily implies that if the HOMO energy corresponds to the ionization potential, the LUMO does cot correspond to the electron affinity due to the derivative discontinuity *even in exact KS-DFT*.[147] Moreover, as only the (continuous) density and its derivative are used to compute the exchange-correlation energy in LDA and GGA functionals, they intrinsically cannot reproduce the derivative discontinuity (unless the discontinuity is completely absorbed into the kinetic energy term, which is not the case).[147] Their energy as a functional of fractional charges is thus not a series of straight lines and slope discontinuities, but rather takes on a convex curvature.[111] The curvature results because LDA or GGA functionals average over the derivative discontinuity. Consequently, as stated by Kronik et al., ionization potentials resulting from the orbital energies are underestimated by about $\sim {\Delta_{xc}}/{2}$, while electron affinities are overestimated by approximately the same amount.[147] In general, a convex curvature of the energy dependence on the fractional-particle number is equivalent to the delocalization error of DFT.[111,152]

3.1.5.4 The Generalized Kohn-Sham Formalism

In this context, the concepts of the generalized Kohn-Sham theory (GKS) should be briefly mentioned. Although GKS is mostly dedicated to calculate accurate quasiparticle energies with DFT, i.e., to associate the HOMO and the LUMO energy with the ionization potential and the electron affinity, its

concepts are nevertheless intimately related to the delocalization error of DFT: it follows from Eq. (82) that the HOMO and the LUMO energy only correspond to the ionization potential and the electron affinity if the derivative discontinuity of the exchange-correlation potential vanishes. Similarly, if Δ_{xc} is zero and the complete discontinuity is absorbed in the orbitals defined by the universal functional F_S, the curvature of the energy curve would not necessarily exist. The delocalization error of the HOMO and the LUMO is then unnoticeable.

As demonstrated in a seminal work by Seidl et al.,[153] the Kohn-Sham ansatz, i.e., the mapping of the density of the real system to a *non-interacting* reference system with the same density, which is exactly described by a single Slater determinant with orbitals obtained from a *local* potential, is only a limiting case of generalized Kohn-Sham theory (GKS). In fact, the density of the true system can in principle be mapped to the density of any reference system that can be exactly represented by a single Slater determinant. In contrast to conventional Kohn-Sham, however, another reference system - an *interacting* one - does not necessarily result in a strictly local[p] Kohn-Sham potential.[147] The energy of the true system is then expressed as the sum of the energy functional of this Slater determinant $F_S[\rho]$,[q] the external potential $V_{Ne}[\rho]$, and a remaining term, the general correlation energy $E_c^{GKS}[\rho]$ (in the general case different from the exchange-correlation energy in standard Kohn-Sham DFT).[144]

$$E_0[\rho] = \min_{\rho}\left[\min_{\Phi \to \rho}\langle\Phi|F_S|\Phi\rangle + V_{Ne}[\rho] + E_c^{GKS}[\rho]\right] \tag{83}$$

Compared with the original Kohn-Sham ansatz, a different reference system changes the definition of F_S, the universal functional of the reference system. While F_S includes only the kinetic energy of non-interacting electrons in conventional KS-DFT ($\lambda = 0$) ($F_S = \langle\Phi|T|\Phi\rangle$), it might just as well absorb also the electron-electron interaction ($F_S = \langle\Phi|\hat{T} + \hat{V}_{ee}|\Phi\rangle$). As outlined by Kronik et al.,[147] this universal functional corresponds to a reference system where the electrons interact only via their mean field. Therefore, the electronic structure of the reference system can be exactly described by a single Slater determinant in the framework of Hartree-Fock. The remaining part, the dynamic correlation not included in Hartree-Fock, forms the "exchange-correlation energy" in such a "Hartree-Fock-Kohn-Sham" case.[147] Thus, the HF formalism forms a complementary limiting case of GKS to conventional pure functionals. Between these two limiting cases, hybrid functionals arise in a natural way in the GKS scheme. Instead of including no or the full electron-electron interaction, a fraction of $\hat{V}_{ee}$ is included in the functional F_S. This implies that a fraction of the Hartree-Fock potential $v^{HF} = \sum_{b=1}^{N}\left(\hat{J}_b(x_1) - \right.$

---

[p] In fact, when using hybrids or long-range corrected functionals (as outlined above), the non-local exchange operator is part of the Kohn-Sham potential.
[q] Since the Slater determinant is constructed from orbitals (one-electron wave functions), the energy functional $F_S[\rho]$ is defined in terms of the orbitals.

$\hat{K}_b(x_1)$) (Eq. (20)) is taken into account in the calculation of the KS orbitals of the "partially interacting" reference system. The remainder of the classical Coulomb interaction $\sum_{b=1}^{N} \hat{J}_b(x_1)$, the remaining exchange, and the complete correlation are incorporated into a remainder potential $v_c^{GKS}[\rho]$ instead of the original exchange-correlation potential.[147]

This perspective on hybrid functionals is certainly equivalent to what is commonly outlined as the key idea of hybrid functionals: as originally suggested by Becke,[154] hybrid functionals are supposed to combine advantages of both HF and DFT. However, hybrid functionals in the GKS scheme are defined in a formally exact way.[153]

Moreover, in view of the delocalization error, it can be readily understood in the framework of GKS that a part of the non-local exact exchange is included in the functional $F_S[\rho]$, i.e., in the orbitals (via the *non-local* potential v_S that defines them), and not in the correlation functional anymore $E_c^{GKS}[\rho]$. In other words, some of the derivative discontinuity might already be included in the Fock operator for the KS orbitals of the reference system. In the same manner, the discontinuity of the general correlation potential $v_c^{GKS}[\rho]$ decreases. Therefore, hybrid functionals offer the possibility to reduce the derivative discontinuity of their exchange-correlation potential to some extent. Similarly, the convex curvature of a fractional-particle energy analysis becomes less severe for hybrid functionals.[111] Moreover, with regard to the quasiparticle energies, the HOMO and the LUMO orbital energies provide improved estimates for the ionization potential and the electron affinity of the system compared with LDA or GGAs. However, accurate quasiparticle energies are still not obtained since not the complete derivative discontinuity is absorbed into the universal function $F_S[\rho]$.[147] Equivalently, excessive charge smearing, i.e., the influence of the delocalization error, is still observed.[r]

In view of the still not accurate quasiparticle energies, Kronik et al. reasoned that an additional degree of freedom compared with global hybrids is required to fully eliminate the excessive charge delocalization and the correspondingly underestimated fundamental gap.[147] The range separation parameter ω (Eq. (76)) constitutes such an additional degree of freedom. According to Kronik, the Hamiltonian of the reference system in the GKS framework is composed of the kinetic energy operator and the long-range component of the Coulomb operator.[147] Consistently, the remainder potential $v_c^{GKS}[\rho]$ includes the short-range Coulomb and exchange operator in addition to the correlation potential. It should be kept in mind that range separation does not affect the Coulomb energy, i.e., as outlined above, range separation is only applied to exchange. In most range-separated hybrids, the range separation parameter is a universal constant,[132,133,143,155,156] and its value is often fitted.[132,133,143]

---

[r] In the words of the traditional Kohn-Sham scheme (in contrast to GKS), only a fraction of exact exchange is included in hybrids that compensates the self-interaction error only to some extent and not completely.

However, Livshits and Baer[157] carefully analyzed that the range separation parameter depends on the density, i.e. $\omega = \omega[\rho]$. Furthermore, Baer and coworkers[158] showed that ω is not constant and highly system-specific. Since the exact functional must satisfy Koopmans' theorem,[148] Baer et al.[157,159] proposed to enforce Koopmans' theorem by tuning the range separation parameter ω. This implies that ω is obtained by minimizing the function $J(\omega)$[159]

$$J(\omega) = |-\varepsilon_{HOMO}(\omega) + \{E(N, \omega) - E(N - 1, \omega)\}| \tag{84}$$

By additionally requiring that Koopmans' theorem is also satisfied for the (N+1)-electron system, a slightly modified target function is obtained if relaxation effects are neglected.[147,159,160]

$$J^2(\omega) = \sum_{i=N,N+1} \left|-\varepsilon^i{}_{HOMO}(\omega) + \{E^i(N, \omega) - E^i(N - 1, \omega)\}\right|^2 \tag{85}$$

The derivative discontinuity of an optimally tuned long-range corrected functional can be estimated from the difference between Eq. (85) and an equivalent expression where the HOMO of the (N+1)-electron system is replaced by the LUMO of the N-electron system. Doing this for molecules and nanosized objects, Livshits and Baer[157] showed that for an optimally tuned long-range corrected functional, the derivative discontinuity of the exchange-correlation potential becomes negligible. The HOMO and the LUMO energies correspond almost exactly with the ionization potential and the electron affinity. This goes along with a straight-line behavior of the energy curve of optimally tuned hybrids as a function of the fractional charge.[147] Thus the delocalization error vanishes. Indeed, Baer, Livshits, and Salzner observed that range-separation parameters ω obtained by either enforcing a straight-line behavior of the energy or by imposing Koopmans' theorem (Eq. (84)) are almost identical.[144] In fact, it was already demonstrated by Yang and coworkers,[152] Perdew et al.[161] and Hirao and coworkers[162] that long-range corrected functionals in general yield much straighter line segments in the energy-versus-fractional-charge plot than global hybrids. It should be noted that despite their potential to eliminate a central deficiency of DFT – the delocalization error – optimally tuned long-range corrected functionals lack size consistency (due to the system specificity of ω).[144]

3.1.5.5 Constrained DFT (c-DFT)

Constrained DFT (c-DFT)[163] results from a special modification of the ground-state DFT equations. The concept of c-DFT is briefly outlined because it has proven to be an invaluable tool for the calculation of diabatic states and couplings, such as charge-transfer states and recombination couplings.[164,165]

The minimum principle of DFT (Eq. (49)) permits to calculate the ground-state density only. The key idea of c-DFT is to calculate non-equilibrium states (charge-transfer states, spin-localized states, etc.) as the ground states of another system which is characterized by a different external potential.[163] In some manner, the charges/spins in the non-equilibrium system are constrained. The different external

potential can then be readily identified when constructing the Lagrangian. For instance, as outlined by Wu and Van Voorhis, a possible constraint would be to require that a certain number of electrons N_C are localized somewhere in the system. By means of a weighting function $w_C(\vec{r})$, this can be converted into a condition for the density $\rho(\vec{r})$:[163]

$$\int d\vec{r} w_C(\vec{r})\rho(\vec{r}) = N_C \tag{86}$$

With the Lagrangian multiplier V_C, a new density functional $W[\rho]$ is constructed from the energy functional $E_0[\rho]$ (Eq. (56)).[163]

$$W[\rho] = E_0[\rho] + V_C\left(\int d\vec{r} w_C(\vec{r})\rho(\vec{r}) - N_C\right) \tag{87}$$

This results in a modified one-electron Kohn-Sham equation (Eq. (64)). It differs from the conventional form by the constraint potential $V_C w_C(\vec{r})$.

$$\left(-\frac{1}{2}\Delta + v_{xc}(\vec{r}) + v_{Ne}(\vec{r}) + v_{ee}(\vec{r}) + V_C w_C(\vec{r})\right)\chi_i(\vec{r}) = \varepsilon_i \chi_i(\vec{r}) \tag{88}$$

While $w_C(\vec{r})$ is predefined (Eq. (86)), the Lagrangian multiplier V_C needs to be calculated. Since the derivatives of $W[\rho]$ with respect to V_C are well defined, it can be shown[163] that $W[\rho]$ has only one stationary point (a maximum) with respect to V_C. Therefore, the optimization of V_C is integrated into each self-consistent iteration of Eq. (93).[163] Finally, the internal energy E of the system as well as the additional energy arising from the constraint $V_C N_C$ are computed.[163]

The formalism can be extended to deliver diabatic couplings that are comparable for example to Generalized Mulliken Hush theory (GMH).[164] These couplings are defined as the off-diagonal elements of the Hamiltonian matrix between orthogonal diabatic states.[166] By means of c-DFT, the initial and final states $\Psi_D[\rho_D]$ and $\Psi_A[\rho_A]$ of an electron-transfer reaction between a donor and an acceptor can be computed. As outlined by Wu and Van Voorhis,[164] they are not orthogonal because they correspond to different constraint potentials (i.e., equal weighting functions, but different multipliers V_C). The off-diagonal elements of the Hamiltonian between these states can be simplified as[164]

$$H_{AB} = \langle\Psi_D|H|\Psi_A\rangle = \langle\Psi_D|H + V_c^A w_c - V_c^A w_c|\Psi_A\rangle \tag{89}$$

$$\approx (E_A + V_c^A N_c)\langle\Psi_D|\Psi_A\rangle - V_c^A\langle\Psi_D|w_c|\Psi_A\rangle$$

The Hamiltonian in the constrained (non-orthogonal) basis thus becomes

$$H = \begin{pmatrix} E_D & H_{DA} \\ H_{AD} & E_A \end{pmatrix} \qquad (90)$$

The average of the off-diagonal elements is used, which differ due the constraint potentials in Eq. (89). The eigenvectors C of the w_c matrix are finally employed to obtain an orthogonalized diabatic basis. The transformed Hamiltonian $H' = C^\dagger H C$ then provides the transfer couplings as the off-diagonal elements that compare well with GMH couplings.[164]

3.1.6   Stability of HF- and KS-SCF-orbitals[s]

The energy expectation value of a Slater determinant is invariant (to first order) with respect to functional variations of the underlying HF/KS spin orbitals. This defines the HF/KS orbitals. However, a number of restrictions exist for their functional variations. As outlined by Pople and coworker,[167] spin orbitals are represented as products of spatial orbitals and a spin function, they are assumed to be real, some spin orbitals must have equal spatial orbitals, and a finite basis set is used. This ultimately leads to the Roothaan-Hall equations (Eq. (23)). Iteratively solving them in a self-consistent manner yields orbitals $\{\chi_i\}$ optimized in a constrained subspace. The corresponding determinant has a certain energy expectation value $E[\{\chi_i\}]$. Upon removing the constraints, i.e., in a larger space, the energy expectation value $E[\{\chi_i\}]$ (1) can still be a minimum, (2) can be stationary, but not a minimum, (3) can be not stationary with respect to functional variations of the orbitals.[167] The latter case constitutes a second-order external instability.[t] In order to identify unstable SCF solutions, Paldus and Čížek derived a matrix expression for the second-order correction to the energy $\Delta E^{(2)}[\{\chi_i\}]$ both for closed-shell[168] and simple open-shell[169] systems (from the ensemble of excited determinants). It is closely related to Casida's equation (see below for a detailed definition of the A- and B-matrix).[167]

$$\Delta E^{(2)}[\{\chi_i\}] = \frac{1}{2}\begin{pmatrix} D \\ D^* \end{pmatrix}^\dagger \begin{pmatrix} A & B \\ B^* & A^* \end{pmatrix} \begin{pmatrix} D \\ D^* \end{pmatrix} \qquad (91)$$

Depending on the constrained subspace and the type of constraint (e.g., coincident spatial orbitals, real orbitals,…), different conditions for the A- and B-matrix result as a necessary condition for a stationary, self-consistent HF solution.[167]

For instance, the most prominent instabilities, the singlet and triplet instabilities, result from the constraint of coincident spatial orbitals (RHF).[168] $A + B$ needs to be positive definite to preclude such singlet and triplet instabilities (only in this case, the HF determinant is stationary). A further differentiation into the spin components is possible: upon allowing different orbitals for different spins,

---

[s] It should be noted that the following considerations were deduced exclusively for HF. However, they similarly apply to KS-orbitals as shown by Ahlrichs and coworker.[170]
[t] If second-order functional variation within the subspace results in lower energy expectation values, the solution is internally unstable.

four excitations between a single original pair of closed-shell orbitals arise, one singlet and three triplet excitations. Singlet instabilities can be identified from negative eigenvalues of $^1A + {}^1B$ (including only singlet excitations) while $^3A + {}^3B$ (including only triplet excitations) must be positive definite[167] to rule out triplet instabilities.[167] The first eigenvalue of the corresponding matrixes are often indicated as an instability measure.[170] An additional feature of singlet instabilities is that a lower-energy singlet UHF solution exists, i.e., a single Slater determinant is a poor description of any system subject to a singlet instability.[168]

3.2   The quantum-chemical excited-state description

3.2.1   CIS-based approaches

CIS calculations of excitation energies and excited-state properties is conceptually one of the most straightforward excited-state approaches.[31]

As outlined by Pople et al.,[171] an excited-state wave function could in principle be obtained simply by replacing any occupied orbital $\{\chi_i\}$ in the HF determinant by a virtual orbital $\{\chi_a\}$.

$$\Phi_{ia} = |\chi_1\chi_2\chi_3\chi_4 \cdots \chi_a \cdots \chi_N| \tag{92}$$

However, Pople et al. concurrently pointed out that this has the drawback that (1) the resulting wave function is not an eigenfunction to the S²-operator, (2) orbital relaxation is not included, i.e., the wave function corresponds to an ionization rather than an excitation, (3) excitations from or to degenerate orbitals cannot be described in a single-determinant approach.[171] Representing the wave function as a linear combination of singly-excited determinants $\{\Phi_i^a\}$ with coefficients $\{a_{ia}\}$ compensates these deficiencies to some extent.

$$\Psi_{CIS} = \sum_{i,a} a_{ia}\,\Phi_i^a \tag{93}$$

The coefficients are obtained from diagonalizing the CIS matrix with elements H_{ij}^{ab}[31]

$$H_{ij}^{ab} = \langle\Phi_i^a|\widehat{H}|\Phi_j^b\rangle = (E_{HF} + \varepsilon_a - \varepsilon_i)\delta_{ij}\delta_{ab} + (ia \parallel jb) \tag{94}$$

In line with Pople et al., it should be emphasized that the resulting CIS excited-state wave function (1) is orthogonal to the ground state, (2) includes orbital relaxation, (3) allows to compute pure-spin states and excitations between degenerate orbitals, (4) is size-consistent, (5) is variational and (6) differentiable so that excited-state properties are readily accessible.[171] In fact, properties other than the energy are often obtained as derivatives of the energy.[31] For instance, the excited-state dipole moment μ is obtained as the first derivative of the energy $\langle E\rangle_{CIS}$ with respect to the electric field strength $\vec{E}$.[31]

$$\mu = \left(\frac{\partial \langle E \rangle_{CIS}}{\partial \vec{E}} \right)_{E=0} \tag{95}$$

Despite these advantages, any CIS description completely lacks dynamic correlation.[172] Head-Gordon et al. proposed an extension of CIS called CIS(D)[u],[173] a size-consistent follow-up version of CIS-MP2.[171] The key idea of both methods is that double excitations with respect to the CIS wave function provide the main contribution to dynamic correlation.[173] CIS-MP2 is a direct excited-state equivalent of ground-state MP2. The MP2 correction to the total CIS energy $E^{CIS-MP2}$ is composed of contributions from singly-excited states of CIS (double excitations of the ground state; no Brillouin theorem for singly excited states) and of contributions from doubly-excited states of CIS (triple excitations of the ground state).[173]

$$E^{CIS-MP2} = \langle \Psi_{CIS} | \hat{V} | U_2 \Phi_{HF} \rangle + \langle \Psi_{CIS} | \hat{V} | U_3 \Phi_{HF} \rangle \tag{96}$$

The excitation operators U_2 and U_3 generate doubly and triply excited states with respect to the ground state. Yet, they directly include the amplitudes for the energy correction *of the excited state* (and not the ground state). This similarly implies that U_3 includes all possible doubly-excited determinants with respect to the CIS wave function. When expressed in terms of spin orbitals, the first- and second-order corrections are equivalent to the ground-state MP2 expressions.[173]

$$\langle \Psi_{CIS} | \hat{V} | U_2 \Phi_{HF} \rangle = -\frac{1}{4} \sum_{ijab} \frac{\left| \langle \Psi_{CIS} | \hat{V} | \Phi_{ij}^{ab} \rangle \right|^2}{\varepsilon_a + \varepsilon_b - \varepsilon_i - \varepsilon_j - E_{CIS}} \tag{97}$$

$$\langle \Psi_{CIS} | \hat{V} | U_3 \Phi_{HF} \rangle = -\frac{1}{36} \sum_{ijkabc} \frac{\left| \langle \Psi_{CIS} | \hat{V} | \Phi_{ijk}^{abc} \rangle \right|^2}{\varepsilon_a + \varepsilon_b + \varepsilon_c - \varepsilon_i - \varepsilon_j - \varepsilon_k - E_{CIS}} \tag{98}$$

Head-Gordon et al.[173] could show that the triples correction (Eq. (98)) is responsible for the observed size-inconsistency of CIS-MP2. They reasoned that the triple excitations from the ground-state wave function are composed of two parts. This becomes evident from an analysis how the triple excitations are produced. In a first step, single excitations lead to the CIS wave function, i.e., the CIS determinants in the CIS wave function arise from a single orbital substitution in the underlying HF determinant. This can be expressed in terms of the single excitation operator U_1 that generates the CIS wave function as a linear combination of singly-excited determinants with suitable amplitudes (defined by the CIS secular determinant) from the ground-state HF determinant.

---

[u] The notation of the doubles in brackets follows similar designations for triple corrections to the ground state in CISD and CCSD.[1012]

$$\Psi_{CIS} = U_1\Phi_{HF} \tag{99}$$

Any double substitution in the CIS wave function leads then to the triply excited states generated by U_3:

- On the one hand, this subsequent double substitution of a CIS determinant can involve only orbitals that did not take part in the single substitution.[173] These orbitals are to a first approximation "spectators" to the electronic excitation, i.e., they are left unchanged. Therefore, Head-Gordon suggested to use the ground-state MP2 excitation operator (denoted as T_2) defined by the amplitudes in Eq. (35) for this type of double excitations. U_3 is then approximated by T_2U_1.

- On the other hand, a double substitution of a CIS determinant can include an orbital that was promoted beforehand, i.e., an orbital involved in the underlying single substitution. The net result is only a double excitation with respect to the HF ground state. Such double excitations are already included in the double correction $\langle\Psi_{CIS}|\hat{V}|U_2\Phi_{HF}\rangle$ (Eq. (96)).

Thus, Head-Gordon et al.[173] proposed to approximate the triples correction as

$$E^{CIS(D)} = \langle\Psi_{CIS}|\hat{V}|U_2\Phi_{HF}\rangle + \langle\Psi_{CIS}|\hat{V}|T_2U_1\Phi_{HF}\rangle \tag{100}$$

The first term in Eq. (100) is called the "direct term" while the second term is designated as the "indirect term". Evidently, only the "spectator"-type triple excitations are included.[174]

MP2-type corrections to excited states suffer from the same deficiencies as MP2 ground-state corrections. Most importantly, this concerns near-degeneracies of excited states. As also outlined by Thiel (see below),[175] near-degeneracies are more frequently encountered in excited states than in the ground state. The original CIS(D) formalism breaks down for nearly degenerate excited states (in underlying CIS). In order to obtain accurate transition energies also for nearly degenerate excited states, Head-Gordon proposed a near-degenerate extension of the original CIS(D) method leading to the family of CIS(D_n) methods.[176] The methods consist in rediagonalizing the CIS matrix to second order in the fluctuation potential $\hat{V}$. Depending on how accurately the doubles-doubles block in this rediagonalization is taken into account, different CIS(D_n) methods are defined. The rediagonalizing permits a remixing of nearly degenerate states via second-order correlation effects. The breakdown of the subsequent MP2-type correction is thus avoided. While CIS(D_0) and CIS(D_1) are equivalent to the original non-iterative CIS(D) method, the doubles-doubles block in CIS(D_∞) is iteratively included.[176]

Excitation energies calculated with CIS(D) were shown to be quite accurate.[173] Nevertheless, further improvement can be obtained by introducing spin-component scaling (see also above). Grimme and

coworker originally suggested in a first version of SCS-CIS(D) to scale only the direct term $\{c_T^{OS}, c_T^{SS}\}$ using ground-state MP2 parameters.[177] Head-Gordon et al. extended the scaling to the indirect term $\{c_{T'}^{OS}, c_{T'}^{SS}\}$ and additionally introduced a damping parameter λ into the excitation amplitudes (Eq. (102)) that was shown to improve the results, especially for $\lambda = 0$.[178]

$$E^{CIS(D)} = \langle \Psi_{CIS} | \hat{V} | (c_T^{OS} T_2^{OS} + c_T^{SS} T_2^{SS}) \Phi_{HF} \rangle \tag{101}$$

$$+ \langle \Psi_{CIS} | \hat{V} | (c_{T'}^{OS} T'^{OS}_2 + c_{T'}^{SS} T'^{SS}_2) U_1 \Phi_{HF} \rangle$$

$$T_2^{OS} \Phi_{HF} = - \sum_{\bar{\imath} < j, \bar{a} < b} \frac{\langle \Psi_{CIS} | \hat{V} | \Phi_{\bar{\imath}j}^{\bar{a}b} \rangle}{\varepsilon_{\bar{a}} + \varepsilon_b - \varepsilon_{\bar{\imath}} - \varepsilon_j - \lambda E_{CIS}} \Phi_{\bar{\imath}j}^{\bar{a}b} \tag{102}$$

By including only the opposite-spin excitation operators in Eq. (101), Head-Gordon et al. obtained furthermore a SOS-version of CIS(D). Hättig et al. implemented SCS-CIS(D) and SOS-CIS(D) into the Turbomole program package,[179] using the SCS[140]-/SOS[79]-MP2 ground-state parameters for both direct and indirect terms.[180] In a comprehensive benchmark dedicated to various spin-scaled variants, Goerigk and Grimme[174] concluded that parameters specifically adapted to excited states are necessary to obtain improved performances compared with conventional CIS(D).

Notably, a CIS(D)-like procedure was adopted by Grimme and Neese[181] to enable excited-state calculations with double-hybrid functionals. In complete analogy to CIS(D), single excitation amplitudes (from a previous TDA/TD-DFT calculation with the underlying hybrid) are employed to compute an energy correction (Eq. (101)) that is subsequently scaled (like in double-hybrid ground-state calculations) and added to the final transition energy, delivering very accurate results.[174]

3.2.2 Addendum: Semiempiric methods in excited-state calculations[31,32]

The *general* basics of semiempiric methods are briefly outlined. They are *not* specific for semiempiric excited-state calculations. However, semiempirics is here discussed in the framework of excited-state calculations because it was mostly employed in this area in this work (see Results and Discussion).

For the following discussion, the Fock matrix $F_{\mu\nu}$ (see also Eq. (23)) in an atomic orbital basis set $\{\mu, \nu, \dots\}$ is given using the core Hamiltonian $H_{\mu\nu}^{core} = \langle \mu | h | \nu \rangle$ and the density matrix $P_{\lambda\sigma}$.[36]

$$F_{\mu\nu} = H_{\mu\nu}^{core} + \sum_{\lambda\sigma} P_{\lambda\sigma} \left[(\mu\nu|\sigma\lambda) - \frac{1}{2}(\mu\lambda|\sigma\nu) \right] \tag{103}$$

$$P_{\lambda\sigma} = 2 \sum_a^{N/2} c_{\sigma a}^* c_{\lambda a} \tag{104}$$

Semiempiric methods aim generally at reducing the computational cost of the SCF procedure by (1) including valence electrons only, (2) employing a minimal basis set, and (3) reducing the number of the two-electron integrals.[31] The latter reduction results from the central so-called *Zero Differential Overlap* (ZDO) approximation of most semiempiric methods. It consists in setting the product between basis functions $\{\mu, \nu, \lambda, \dots\}$ located on different atoms $\{A, B, \dots\}$ to zero $\mu_A \lambda_B = 0$.[31] The overlap matrix (Eq. (23)) thus reduces to the unit matrix, the amount of two-center one-electron integrals decreases, three-center one-electron integrals are neglected, and all three- and four-center two-electron integrals in the Fock matrix are 0. All remaining integrals are parameterized by fitting results to experimental data.[31] The fitting procedure allows to fold errors due to the small basis set and the lack of correlation into the parameters.[182] Without any further approximations, this defines the NDDO set of semiempiric methods, relying on the *neglect of diatomic differential overlap* approximation. In terms of Fock matrix elements (Eq. (103)), this implies for diagonal elements of the basis function μ located at atom A:[183]

$$F_{\mu\mu} = H_{\mu\mu}^A + \sum_B V_{\mu\mu}^B + \sum_\nu^A P_{\nu\nu}\left[(\mu\mu|\nu\nu) - \frac{1}{2}(\mu\nu|\nu\mu)\right] + \sum_B^B \sum_{\lambda\sigma} P_{\lambda\sigma}[(\mu\mu|\sigma\lambda)] \tag{105}$$

It should be noted that the core Hamiltonian[v] has been further divided:[31]

$$H_{\mu\mu}^{core} = \left\langle\mu\left|-\frac{1}{2}\Delta - \frac{Z_A'}{|R_A - r|}\right|\mu\right\rangle + \left\langle\mu\left|\Sigma_B \frac{Z_B'}{|R_B - r|}\right|\mu\right\rangle = H_{\mu\mu}^A + \sum_B V_{\mu\mu}^B \tag{106}$$

Furthermore, the NDDO model implies for Fock matrix elements $F_{\mu\nu}$ of different basis functions $\{\mu_A, \nu_A\}$ located on the same atom A:[31]

$$F_{\mu\nu} = \sum_B V_{\mu\nu}^B + \frac{1}{2}P_{\mu\nu}[3(\mu\nu|\mu\nu) - (\mu\mu|\nu\nu)] + \sum_B^B \sum_{\lambda\sigma} P_{\lambda\sigma}[(\mu\nu|\sigma\lambda)] \tag{107}$$

It implies thirdly for Fock matrix elements $F_{\mu\lambda}$ of different basis functions $\{\mu_A, \lambda_B\}$ located on different atoms A and B:[183]

$$F_{\mu\lambda} = H_{\mu\lambda}^{core} - \frac{1}{2}\sum_\nu^A \sum_\sigma^B P_{\nu\lambda}(\mu\nu|\sigma\lambda) \tag{108}$$

In contrast, INDO (*intermediate neglect of differential overlap*) additionally neglects all two-center two-electron exchange integrals (second term in Eq. (108)). Moreover, only symmetric one- and two-

---

[v] The nuclear charges are reduced since only valence electrons are included.[31]

electron integrals[w] of type $V_{\mu\mu}^B$ and $(\mu_A\mu_A|\lambda_B\lambda_B)$ are included (see Eq. (107)).[31,182] The one- and two-center Coulomb integrals are parameterized as[31]

$$(\mu_A\mu_A|\lambda_B\lambda_B) = \gamma_{AB} \tag{109}$$

$$(\mu_A\mu_A|\nu_A\nu_A) = \gamma_{AA} \tag{110}$$

While INDO still takes into account one-center four-electron integrals of type $\langle\mu_A\nu_A|\kappa_A\lambda_A\rangle$ (Eq. (110)), CNDO methods (*complete neglect of different overlap*) neglect them as well. The Pariser-Pople-Parr model[184,185,186] is essentially a CNDO-based method applied exclusively to π-electrons.[31,32]

Although NDDO should be most accurate among the semiempiric first-generation models, it did initially not improve INDO results due to its deficient parameterization[182] and lack of rotational invariance[187]. In 1975, however, Dewar and Thiel[183] introduced the MNDO method (*modified neglect of diatomic overlap*), which corresponds essentially to a new approach of parameterizing NDDO integrals. A key ingredient of the method is to employ a multipole expansion instead of a single parameter for all two-center two-electron integrals like in INDO (Eq. (109)). This speeds up the calculations compared with the original NDDO methods while still including the electronic asymmetry.[183] Moreover, the two-center one-electron integrals $H_{\mu\lambda}^{core}$ (Eq. (108)) are approximated by the average of two atomic "resonance" parameters β_μ, β_λ and the overlap $S_{\mu\lambda}$ between the basis functions.[31]

$$H_{\mu\lambda}^{core} = \frac{1}{2}S_{\mu\lambda}\left(\beta_\mu + \beta_\lambda\right) \tag{111}$$

The fact that the overlap $S_{\mu\lambda}$ is explicitly calculated between the Slater-type basis functions (Eq. (111)) explains the name of the methods (*modified* neglect of diatomic overlap). In fact, including the overlap in the two-center one-electron integrals was already introduced in a slightly earlier INDO-based version, MINDO/3,[188] which requires, however, extensive parameterization because it relies on bond-specific parameters β_{AB} rather than on the atomic parameters in MNDO. One-center one-electron integrals $H_{\mu\nu}^{core}$ are expressed as a sum[31]

$$H_{\mu\nu}^{core} = H_{\mu\mu}^A\delta_{\mu\nu} - \sum_B Z'_B(\mu\mu|\nu\nu) \tag{112}$$

Z'_B is the reduced nuclear charge.[x] Parameters are employed for the two-electron integral $(\mu\nu|\mu\nu)$ (Eq. (112)), similar to all one-center two-electron integrals. A crucial point of all MNDO methods is the

---

[w] This implies that the ZDO approximation in INDO-based methods is also applied different basis functions on the same atom.
[x] The nuclear charge is reduced as the core electrons are not included.

core-core repulsion. Due to the approximated two-electron integrals, a balanced description between repulsive and attractive forces requires to include such two-electron integrals in the calculation of the core-core repulsion as well.[182] The original MNDO[183] method as well as its most prominent[182] modifications, AM1[189] and PM3[190], differ in their functional form only in the way how they compute the core-core repulsion V_{NN} (naturally, their parameters differ as well).[31]

- MNDO methods calculate V_{NN} from a two-electron two-center integral and a correction term f_{AB} including atomic fit parameters α_A, α_B.[182,183]

$$V_{NN}^{MNDO} = \sum_{A>B} Z'_A Z'_B (s_A s_A | s_B s_B) + f_{AB} \tag{113}$$

$$f_{AB} = Z'_A Z'_B (s_A s_A | s_B s_B)(e^{-\alpha_A R_{AB}} + e^{-\alpha_B R_{AB}}) \tag{114}$$

- To improve the overestimated MNDO core-core repulsion, another correction term f'_{AB} is included in the AM1[189] model.

$$V_{NN}^{AM1} = V_{NN}^{MNDO} + \frac{Z'_A Z'_B}{R_{AB}} \sum_k \left(a_{kA} e^{-b_{kA}(R_{AB} - c_{kA})^2} + a_{kB} e^{-b_{kB}(R_{AB} - c_{kB})^2} \right) \tag{115}$$

- The PM3[190] method relies on a similar expression for the core-core repulsion (Eq. (115)). However, PM3 accuracies are often superior compared with AM1 because Stewart implemented and conducted a comprehensive parallel optimization of all parameters.[190]

Due to their well-known deficiencies (limited applicability in terms of elements, intermolecular interactions, barriers, overestimated stabilities of small rings, erroneous relative stabilities of hydrocarbon conformations, etc.),[31] all three approaches were continuously improved. Thiel and coworker extended the MNDO approach to a broader range of elements, called MNDO/d,[191,192] by additionally including d-functions. This necessarily multiplies the number of required parameters.

Furthermore, Kolb and Thiel derived the OMx approach (*orthogonalization model*) from the underlying MNDO methods.[193] Via additional orthogonalization corrections, effective core potentials and penetration integrals, the one-center one-electron integrals are differently calculated and parameterized in OMx-based methods. In fact, Kolb and Thiel[193] reasoned that the approximations underlying semiempirical NDDO methods can be evaluated by comparison to the matrix elements of a Löwdin[194] orthogonalized Fock matrix. *Ab initio* methods solve the Roothaan-Hall equations in an orthogonalized basis set $\{\varphi'_i\}$ (Eq. (23)).

$$F'C' = C'E \tag{116}$$

$$F' = S^{-1/2} F S^{1/2} \tag{117}$$

Due to the ZDO approximation, semiempiric methods solve directly equations like Eq. (120) as well so that no orthogonalization is performed. Therefore, as outlined by Kolb and Thiel,[193] their integrals can be compared to *ab initio* calculated integrals in an orthogonalized basis set. This comparison led them to the conclusion that especially the one-electron one-center elements of the Fock matrix $H_{\mu\nu}^{core}$ change significantly in the basis set transformation (Eq. (117)), and that they are thus incompletely described by Eq. (112). To improve their description, they employed a power series expansion $H^{core,\prime}$ in terms of $S^{-1/2}$. The most important terms $\left\{ \Delta_{\mu\nu,B}^{(S)}, R_{\mu\nu,B}^{(S)} \right\}$ of this power series expansion are subsequently used as an orthogonalization correction $\sum_B V_{\mu\nu,B}^{ort}$ in the one-center one-electron matrix elements, which uses two additional atomic parameters $\{\gamma_1^A, \gamma_2^A\}$ and resonance integrals $\{\beta_{\lambda\nu}\}^y$.[193] The orthogonalization correction, which includes three-center terms especially in more recent OMx versions, results in stereodiscriminating properties.[195]

$$H_{\mu\nu}^{core,\prime} = H_{\mu\nu}^{core} + \sum_B V_{\mu\nu,B}^{ort} \tag{118}$$

$$V_{\mu\nu,B}^{ort} = \gamma_1^A \Delta_{\mu\nu,B}^{(S)} + \gamma_2^A R_{\mu\nu,B}^{(S)} \tag{119}$$

$$\Delta_{\mu\nu,B}^{(S)} = -\frac{1}{2} \sum_{\lambda_B} \left(S_{\mu\lambda} \beta_{\lambda\nu} + \beta_{\mu\lambda} S_{\lambda\nu} \right) \tag{120}$$

$$R_{\mu\nu,B}^{(S)} = \frac{1}{8} \sum_{\lambda_B} S_{\mu\lambda} S_{\lambda\nu} \left(H_{\mu\mu}^{AB} + H_{\nu\nu}^{AB} - 2H_{\lambda\lambda}^{AB} \right) \tag{121}$$

According to Kolb and Thiel,[193] the orthogonalization correction contains some of the repulsive contributions to the one-center one-electron integrals that were neglected beforehand (Eq. (112)). To preserve the balance between repulsive and attractive forces, OMx-based methods take into account the attractive terms of type $V_{\mu\nu}^B$ (Eq. (106), Eq. (107)) in the one-center one-electron integrals instead of approximating them (Eq. (112)). Furthermore, the core-core repulsion is explicitly included as well. As the third major modification in OMx-based methods, the repulsion between the core and the valence electrons is incorporated via effective core potentials (ECPs).[193] Apart from the original OM1[193] method, more recent parameterizations with slightly modified correction terms designated as OM2[195]

---

y It should be noted that the resonance integral $\beta_{\lambda\nu}$ in OMx-based methods differs from its original version. The original parameters cannot be used because due to the empirical fitting procedure to molecular properties, effects owing to the inexistent orthogonalization correction in MNDO-based methods are indirectly incorporated into the value of $\beta_{\lambda\nu}$. Kolb and Thiel outlined that a variety of fitting functions for the OMx resonance integral provide accurate results.

and OM3[196] exist. While OM1 includes the orthogonalization correction as outlined only in the one-center one-electron integrals, OM2[195] adds similar corrections to the two-center one-electron integrals. OM3[196] is a somewhat simplified version of OM2.

As a further addendum to the underlying MNDO approach and in view of the growing interest in semiempiric calculations on large biochemical systems,[182] Tuttle and Thiel[197] adopted Grimme's dispersion correction DFT-D[141] to the OMx-based methods. They simply fitted the scaling coefficient α and the s_6 parameter and added the resulting dispersion energy.[197] In fact, this approach can be considered as a complementary follow-up version of AM1-D and PM3-D suggested slightly earlier by Hillier and coworker.[198] Based on the same version of Grimme's dispersion correction, they adapted the semiempiric parameter and left the dispersion correction unchanged.

Except for dispersion, semiempiric methods describe also hydrogen bonding poorly, which seriously limits their applicability to biochemical problems as outlined by Hobza and coworkers[z].[199,200] However, as also pointed out by Clark and coworkers,[201] this seems to be related to the parameters rather than to an intrinsic inability of semiempiric methods to describe hydrogen bonds. The broaden the scope of semiempiric applications to biochemistry, Hobza et al. developed a combined correction called "DH" and "DH2" to integrate hydrogen bonding and dispersion into semiempiric methods.[199,200] A DFT-D approach of Jurečka et al.[202] much alike to the Grimme's dispersion correction[141] was adopted to model dispersion. The energies of hydrogen bonds E_{H-bond} is calculated in a purely electrostatic way. It is added as a summand to the final semiempiric energy. The DH energy is calculated from the charges q_A, q_H on the atoms, the bond angle θ, and three parameters a, b, c.[199]

$$E_{H-bond} = a \left[\frac{q_A q_H}{R_{AH}^2} \cdot \cos \theta + b \cdot c^{-R_{AH}} \right] \tag{122}$$

In order to account for the full three-dimensional arrangement of a hydrogen bond, the single bond angle θ was replaced by a term containing all three spatial angles θ, ϑ, ϕ in the later-on published DHs correction.[200]

The so-called *Pairwise Distance Directed Gaussian* (PDDG) modification proposed by Jorgensen and coworkers[203] is another correction adapted to both MNDO (PDDG/MNDO) and PM3 (PDDG/PM3) (in a similar way as dispersion). Based on the success of the Bond and Group Equivalents Scheme (BGE),[204] it aims at incorporating some functional group and fragment information into MNDO-derived methods that rely entirely on only atomic parameters. According to Jorgensen and coworkers, this can be

---

[z] Due to its high accuracy and broad applicability, Hobza and coworkers adapted their corrections for intermolecular interactions to PM6.[199,200]

achieved by modifying the core-core repulsion of either MNDO or PM3 with a correction term $PDDG(A, B)$ containing pairwise sums over all atoms of the molecule.[203]

$$PDDG(A,B) = \sum_{A,B>A} \frac{1}{n_A + n_B} \left[\sum_{i,j}^{2} \left(n_A P_{A_i} + n_B P_{B_j} \right) e^{\left(-10\text{Å}^2 \left(R_{AB} - D_{A_i} - D_{B_j} \right)^2 \right)} \right] \tag{123}$$

n_A, n_B are the number of valence electrons located at atoms A, B. D_{A_i}, P_{A_i} are atomic parameters. As the exponential term in Eq. (123) depends on the interatomic distance as well as on the atomic distance parameters D_{A_i}, the PDDG correction includes some fragment information while still keeping the number of required parameters limited.[203] The underlying MNDO and PM3 integrals were reparameterized. According to Jorgensen, improvements for resulting PDDG/PM3 and PDDG/MNDO methods were especially observed for small rings, hydrocarbon isomers, and systems with multiple heteroatoms.[203]

Among others, Stewart continuously improved PM3-based methods. By optimizing the reference data and the fitting procedure and additionally introducing a slightly modified scaling factor f_{AB} in the core-core repulsion term (Eq. (113)), he developed PM6 (*parameterization model 6*), which was shown to provide very accurate energies and geometries.[205] Further re-optimizations of the parameters, fitting procedures, and another modification of the core-core repulsion resulted in PM7, the most recent semiempiric method. DFT-like accuracies were found for example for PM7 reaction barriers.[206] In a similar way, Simas et al.[207] reparameterized AM1, giving rise to the recent RM1 model (*Recife Model 1*).

In contrast to the original NDDO-based approaches, which are rarely used themselves - being only employed in their modified MNDO versions – INDO as a representative of the original ZDO methods is still used.[31,182] Especially its version specifically parameterized for spectroscopic problems, called INDO/S, has become very popular.[32,208] ZINDO/S,[209,210] often denoted simply as ZINDO,[aa] is similar to INDO/S. While the applicability of the original version INDO/S remained initially limited to organic compounds as well as boron-containing substances, ZINDO/S includes more elements and could also calculate excited states for instance of transition metal complexes.[32] From the point of view of the parameterization, transition metals are challenging because they require a large number of additional parameters due to the variety of metals.[211] Moreover, Zerner and coworkers outlined that d-orbital specific parameters are required for the calculation of both one- and two-electron integrals (Eq. (109) and (111)).[211] One-electron core integrals in INDO are obtained from ionization potentials.[212]

[aa] It should be noted that ZINDO was a computer program package developed by the group of Michael C. Zerner. To his honor, his group renamed the reparameterized version of INDO/S to ZINDO/S.[32,182]

A particular feature of INDO/S or ZINDO/S excited-state calculations results from the fact that excitation energies are usually obtained via CIS (configuration interaction singles). This is consistent with the intrinsic approximations of all INDO-based methods (for the two-electron integrals).[175] Compared with the CISDTQ-calculations often used to calculate OMx transition energies,[bb] the CIS calcuations allow for a significant speedup of the calculation.[213] In a conventional semiempiric SCF calculation, the ground state is computed. Single-orbital replacements are subsequently used to construct excited configurations.[212] Transition energies and oscillator strengths are obtained from the final CIS treatment.[211] This CIS formalism restricts the scope of applicability of ZINDO/S to excited states that are qualitatively correctly described by a single excited-state determinant.[175] Due to the well-known deficiencies of ZINDO/S or INDO/S calculations for open-shell systems, Voityuk[213] developed recently an extension of INDO/S for triplet states, the so-called INDO/X method.

As outlined by Thiel and coworker,[175] ZINDO/S is a method dedicated rather to spectroscopy than to photochemistry. This results from erroneous ZINDO/S geometries. Indeed, calculating geometries and excitation energies with the *same* set of INDO parameters remains to be problematic since ZINDO and INDO/S geometries computed with spectroscopically derived parameters are rather poor.[214] Although a new INDO/1 approach developed in 2001 aims at removing this deficiency,[214] ZINDO and INDO/S are still rarely used to calculate geometries.

The orthogonalization correction in OMx approaches, originally also developed to improve ground-state results, is particularly beneficial in excited-state calculations.[175] In contrast to the CIS excited-state calculations with ZINDO, a larger number of excited determinants are usually included in excited-state calculations with MNDO-based methods to retrieve effects from correlation as completely as possible.[175] In fact, dynamic ground-state correlation is implicitly included in the MNDO parameters. However, due to rather common near-degeneracies in excited-state calculations and the resulting importance of static correlation, Thiel and coworker reasoned that the inclusion of many excited determinants in a suitable active space seems to be necessary.[175] Although a full-CI (FCI) treatment would therefore certainly be desirable, it becomes quickly computationally unaffordable with increasing system size also with semiempiric approaches.[175] Comparing semiempiric excitation energies of linear polyenes obtained with FCI and CISDTQ using the GUGA-CI (graphical unitary group approach) formalism implemented by Koslowski et al.[215] in a rather small active space demonstrated, however, that CISDTQ delivers excitation energies of almost comparable accuracy to FCI[cc] while

---

[bb] It should be noted that a CIS-OMx treatment is naturally also possible. However, results improve when using a CISDTQ framework.[175]

[cc] It should be noted that MR-CISD is computationally even less demanding than CISDTQ. It was still shown to provide excitation energies of reasonable accuracy.[175]

keeping the computational cost limited.[175] Thus OMx-CISDTQ is currently considered as one of the best performing semiempiric methods for both spectroscopic and photochemical problems.[216]

3.2.3   Addendum: Tight-Binding DFT (DFTB)

It should be briefly mentioned that tight-binding density functional theory (DFTB),[217] a variant of the tight-binding (TB) method dating back to the seminal paper of Slater and Koster,[218] and especially its SCC-DFTB version (self-consistent charge density DFTB) can be considered as a DFT counterpart of semiempiric methods.[219] The key idea of DFTB is shortly addressed because it has become increasingly important also for biological applications[219] and transport[220] and excited-state[221] calculations[217] although it is not employed in this thesis.

In the DFTB formalism, a reference density $\rho_0 = \sum_a \rho_a$ is defined that is the sum of the atomic charge densities ρ_a as if the system consisted of independent atoms.[222] The Kohn-Sham energy is then expanded in a series of density fluctuations with respect to the reference density $\delta\rho = \rho - \rho_0$.[223] The first-order terms in $\delta\rho$ vanish so that only second-order terms remain in a second-order expansion.[222]

$$E_{KS}[\delta\rho] = E_{KS}[\rho_0] + \frac{1}{2} \int \int \left(\frac{\delta^2 E_{XC}}{\delta\rho\delta\rho'} + \frac{1}{|\vec{r} - \vec{r}'|} \right) \delta\rho\delta\rho' \tag{124}$$

$$- \frac{1}{2} \int \int \frac{\rho_0(\vec{r})\rho_0'(\vec{r}')}{|\vec{r} - \vec{r}'|} + E_{xc}[\rho_0] + V_{NN} - \int V_{xc}[\rho_0]\rho_0(\vec{r})$$

The first term in Eq. (124), $E_{KS}[\rho_0]$, corresponds to the Kohn-Sham energy of the reference density, i.e., of the free atoms. The next two (second-order) terms arise from charge fluctuations (Coulomb energy, some exchange-correlation) denoted as E^{2nd}. The second line in Eq. (124) is often subsumed as the repulsive part E_{rep}.[222]

Then, three approximations are introduced that allow for a fast computation of Eq. (124).[219] Firstly, the repulsive energy is represented as the sum of atom-specific two-body potentials $U_{AB}(R)$.[222]

$$E_{rep} = \sum_{A<B} U_{AB}(R) \tag{125}$$

Secondly, the second order term is simplified. Since the reference state consists of free atoms, the density change $\delta\rho$ can be divided into atomic contributions $\delta\rho_a$, which are approximated by atomic charge fluctuations Δq_a. In the SCC-formalism, this is accomplished via a Mulliken population analysis (see Eq. (129)).[219] The second derivative $\delta^2 E_{XC}$ and the Coulomb operator are incorporated into an atom-specific function γ_{AB} that depends, among others, on the chemical hardness.[219,222]

$$E^{2nd} = \frac{1}{2} \sum_{AB} \gamma_{AB} \Delta q_A \Delta q_B \tag{126}$$

Thirdly – the actual tight-binding approximation – the orbitals employed to calculate the Kohn-Sham energy $E_{KS}[\rho_0]$ are assumed to be tightly bound. Thus expanding (only the valence) orbitals ψ_a into a minimal basis set $\{\varphi_\mu\}$ is assumed to be sufficiently accurate $\psi_a = \sum_\mu c_\mu^a \, \varphi_\mu$.[222] The Kohn-Sham energy $E_{KS}[\rho_0]$ can then be expressed as a sum over the matrix elements of the Hamiltonian $\{H_{\mu\nu}^0 = \langle\varphi_\mu|H[\rho_0]|\varphi_\nu\rangle\}$ in the atomic orbital basis set.[dd]

$$E_{KS}[\rho_0] = \sum_a \sum_{\mu\nu} c_\nu^{a*} c_\mu^a H_{\mu\nu}^0 \tag{127}$$

The matrix elements $\{H_{\mu\nu}^0\}$ as well as the overlap integrals between the basis functions $S_{\mu\nu} = \langle\varphi_\mu|\varphi_\nu\rangle$ are tabulated. Using the definition of Mulliken charges to represent Δq_a in the atomic orbital basis, the resulting eigenvalue problem to obtain the DFTB energy and the coefficients $\{c_\mu^a\}$ can be written as[219,222]

$$\sum_\nu c_\nu^a \big(H_{\mu\nu} - \varepsilon_a S_{\mu\nu}\big) = 0 \tag{128}$$

$$H_{\mu\nu} = H_{\mu\nu}^0 + \frac{1}{2} S_{\mu\nu} \sum_I (\gamma_{AI} + \gamma_{BI}) \Delta q_I \qquad \mu \in A \quad \nu \in B \tag{129}$$

As pointed out by Elstner et al.,[219] the solution of the eigenvalue problem for the self-consistent charge (SCC) Hamiltonian determines the computational cost of the method (and not the evaluation of the integrals). Despite the apparent similarity to semiempirics, a few conceptual differences of DFTB exist: no orthogonal basis is used, and empirical fitting of the parameters is not necessary as all parameters can be obtained from DFT calculations.[219,224,225] A plethora of applications of DFTB are available.[226] For instance, Grimme and coworker recently employed SCC-DFTB and an added dispersion correction to determine crystal structures of organic compounds.[223] Elstner and Cui and coworkers studied hydrolysis reactions by SCC-DFTB.[227] Elstner et al. employed DFT also to determine temperature-dependent transport parameters.[228]

3.2.4 Response functions and propagator methods[229]

In contrast to CIS calculations where the wave function is directly accessible, excitation energies and transition dipole moments with other methods are often obtained via response functions without explicitly calculating the excited-state wave function. As defined by Oddershede, a response function

---

[dd] It should be mentioned that further approximations such as the neglect of crystal field effects or three-center terms are introduced.[219]

describes the reaction of a system to an external perturbation.[230] The external perturbation can be expressed as a power series. Then, the response of the system corresponds to the sum of a linear, quadratic, … response function.[230] Not only the excitation energies but also a number of other observables can be obtained from response functions.[230]

Response functions are intimately related to propagator approaches.[231] In fact, response functions are sometimes called "polarization propagators".[230] It is, however, important to note that the term "propagator method" is not well-defined. "Propagators" are not used synonymously in the literature, and they often refer to different kinds of propagators.[230] To address the issue, a very short perspective on Green's functions is given first. In a second step, the linear response of a system is analyzed and related to the so-called time-retarded propagator. In a subsequent third step, a spectral representation of this propagator is derived, which illustrates its properties and the information that it contains. In a fourth step, an equation of motion to compute such propagators is determined. The outline follows Oddershede et al.[229]

Green's Functions[36]

In a certain way, quantum-mechanical propagators can be considered as a particular subgroup of Green's functions. Green's functions are employed to solve inhomogeneous differential equations.[36] For instance, H_0 is the Hamiltonian operator with known eigenfunctions $\{\psi_a\}$ and eigenvalues $\{E_a\}$, E is a parameter, and $\Phi_0(x)$ is an arbitrary function. The following inhomogeneous equation should be solved for $\Phi_F(x)$.[36]

$$(E - H_0)\Phi_F(x) = \Phi_0(x) \tag{130}$$

By means of basis set expansions, it is straightforward to show that the $\Phi_F(x)$ can be expressed via the *integration* of the product of $\Phi_0(x')$ and a Green's function $G_0(x, x', E)$.[36]

$$\Phi_F(x) = \int dx' \left[\sum_a \frac{\psi_a(x)\psi_a^*(x')}{E - E_a}\right] \Phi_0(x') = \int dx' G_0(x, x', E)\, \Phi_0(x') \tag{131}$$

A Green's function can in general be associated with each operator. The differential equation relating the Green's function and its operator can be for example derived from Eq. (130) and (131) for $\Phi_0(x') = \delta(x - x')$.[36]

$$(E - H_0)G_0(x, x', E) = \delta(x - x') \tag{132}$$

Notably, the poles of the Green's function $E = E_a$ correspond to the eigenvalues of the operator H_0. This implies that the eigenvalues obtained as the poles via complex function analysis[231] are accessible

from the Green's function. The numerator of a Green's function (in its spectral representation) contains its so-called residues.[36]

If the system is subject to a perturbation V, a different Green's function $G(x, x', E)$ corresponds to the resulting operator $H = H_0 + V$. It is related to $G_0(x, x', E)$ via integration.

$$G(x, x', E) = G_0(x, x', E) + \int dx'' G_0(x, x'', E) V(x'') G(x'', x', E) \tag{133}$$

The problem of solving the inhomogeneous differential equation of H for the eigenvalues is thus transformed into an integral equation of $G(x, x', E)$ whose poles are the eigenvalues of H. An example for a Green's function with an additional particularity is the Dyson equation[232].

$$G(x, x', E) = G_0(x, x', E) + \int dx'' G_0(x, x'', E) \Sigma(x'', E) G(x'', x', E) \tag{134}$$

The Dyson equation (Eq. (134)) differs from Eq. (133) by the so-called self-energy $\Sigma(x'', E)$ that is itself *energy-dependent*.[ee] If H_0 is the sum of the one-electron Fock operators F, $G_0(x, x', E)$ is the Hartree-Fock Green's function, the one-body Green's function that is associated with the F.[36]

$$G_0(x, x', E) = \sum_i \frac{\chi_i(x) \chi_i^*(x')}{E - \varepsilon_i} \tag{135}$$

Its poles, the HF orbital energies, are approximations to the electron affinity and the ionization potential of the system. The energy-dependent self-energy corresponds thus to the perturbation in Eq. (133) that corrects for orbital relaxation and differential correlation. Solving the Dyson equation and determining the poles of $G(x, x', E)$, a many-body Green's function, yields the electron affinity and the ionization potential of the system. Thus, the poles of $G(x, x', E)$ correspond to the quasiparticle energies discussed above in the GKS framework.

The Dyson equation is formally exact and preserves the one-particle HF picture in the calculation of properties of the N-particle system (i.e., the quasiparticle concept).[36,160] The Dyson equation is often represented as a matrix equation.[36]

$$G(E) = G_0(E) + G_0(E) \Sigma(E) G(E) = \left(\left(G_0(E) \right)^{-1} - \Sigma(E) \right)^{-1} \tag{136}$$

A particular advantage of all Green's function approaches is that the size of all matrices (Eq. (136)) is equal to the (rather limited) particle number.[36]

---

ee The self-energy is often approximated by a perturbation expansion.[36]

Propagators $G(x, x', t)$ can be considered as particular Green's functions that are time-dependent, i.e., a Fourier transformation[230] relates propagators in their spectral representation to particle-hole Green's functions that propagate the system in time[ff].[231] Consistently, a propagator is associated with a time-dependent perturbation $V(t)$ and the corresponding time-dependent Schrödinger equation.[36]

The Linear Response of a System to an External Perturbation and its Relationship to Propagators[229]

Propagator approaches are closely related to linear-response theory. To elucidate the exact relationship, the linear response of a system is computed in the first place. The system in the initial state Φ_0 with $H_0|\Phi_0\rangle = E_0|\Phi_0\rangle$ is subject to a time-dependent perturbation energy $V_t(\vec{r})$ (ϵ is infinitesimally positive).[229]

$$V_t(\vec{r}) = \int_{-\infty}^{\infty} d\omega V_\omega(\vec{r}) e^{-i\omega t + \epsilon t} \tag{137}$$

The exact state of the perturbed system is designated with $|\psi\rangle$ ($\hbar = 1$ in the following):[229]

$$i\frac{\partial}{\partial t}|\psi\rangle = (H_0 + V_t(\vec{r}))|\psi\rangle = E(t)|\psi\rangle \tag{138}$$

The time evolution of the density operator $|\psi\rangle\langle\psi|$ for state $|\psi\rangle$ in the interaction representation $\rho_I = e^{iH_0 t}|\psi\rangle\langle\psi|e^{-iH_0 t}$ is given by (using Eq.(138)):[gg]

$$i\frac{\partial}{\partial t}\rho_I = [V_t(t), \rho_I(t)] \tag{139}$$

$$V_{t'}(t) = e^{iH_0 t}V_{t'}e^{-iH_0 t} \tag{140}$$

Using the initial condition $\lim_{t\to-\infty}|\psi\rangle\langle\psi| = |\Phi_0\rangle\langle\Phi_0| = \rho_0 = e^{iH_0 t}|\Phi_0\rangle\langle\Phi_0|e^{-iH_0 t} = \lim_{t\to-\infty}\rho_I$, the integration of Eq. (139) yields[229]

$$\rho_I(t) = \rho_0 - i\int_{-\infty}^{t} [V_{t'}(t'), \rho_I(t')]dt' \tag{141}$$

[ff] It can be shown, however, that polarization propagators and particle-hole Green's function have the same poles, but not the same residues.

[gg] It should be noted that the prime (t') in Eq. (140) refers to the time dependence of the time-dependent interaction operator V, while t refers to the time dependence of the transformation into the interaction representation.

For small perturbations, Eq. (141) can be solved iteratively using to a first approximation an unperturbed density $\rho_I(t') \approx \rho_0$. In combination with Eq. (140), the *linear response* of the density operator $\rho(t) = |\psi\rangle\langle\psi|$ is given in the Schrödinger picture by[229]

$$\rho(t) = \rho_0 - i \int\limits_{-\infty}^{t} [V_{t'}(t' - t), \rho_0] dt' \tag{142}$$

The time-dependent expectation value of an operator A can be expressed in terms of a complete set of eigenfunctions $\{\phi_i\}$ and the density operator.[229]

$$\langle\psi|A|\psi\rangle = \sum_i \langle\psi|\phi_i\rangle\langle\phi_i|A|\psi\rangle = \sum_i \langle\phi_i|A|\psi\rangle\langle\psi|\phi_i\rangle = \sum_i \langle\phi_i|A\rho|\phi_i\rangle \approx \langle\phi_0|A\rho|\phi_0\rangle \tag{143}$$

Using the time evolution of the density operator (Eq. (142)) provides the time dependence of $\langle A\rangle$.[229]

$$\langle\psi|A|\psi\rangle = \langle\Phi_0|A|\Phi_0\rangle - i \int\limits_{-\infty}^{\infty} \Theta(t - t')\langle\phi_0|[A, V_{t'}(t' - t)]|\phi_0\rangle dt' \tag{144}$$

In Eq. (144), $\Theta(t - t')$ is the Heaviside step function that is 0 for $t < t'$.

$$\langle\langle A; V_{t'}(t' - t)\rangle\rangle^r = -i\Theta(t - t')\langle\phi_0|[A, V_{t'}(t' - t)]|\phi_0\rangle \tag{145}$$

The integrand in Eq. (144) is a two-time Green's function (Eq. (145)), i.e., a two-time retarded Green's function, which is often designated as a propagator (see above): the expectation value of the observable corresponding to A is the sum of the initial value and the propagation in time.[229]

$$V_\omega(t' - t) = e^{iH_0(t'-t)} V_\omega e^{-iH_0(t'-t)} \tag{146}$$

Using the Fourier transform[hh] of $V_{t'}(t' - t)$ (Eq. (137)) in Eq. (144) yields the well-known Kubo relation.[233] Since $V_{t'}(t' - t)$ is periodic in the frequency domain, the linear response of the system depends only on $t' - t$.[229]

$$\langle\psi|A|\psi\rangle = \langle\Phi_0|A|\Phi_0\rangle + \int\limits_{-\infty}^{\infty} d\omega \int\limits_{-\infty}^{\infty} dt' \langle\langle A, V_\omega(t' - t)\rangle\rangle^r e^{-(\epsilon-i\omega)t'} \tag{147}$$

[hh] In the Fourier transform of $V_t(t)$, an infinitesimal positive number ϵ is included to ensure that the reference state of the system for $t = -\infty$ is unperturbed: $V_t(-\infty) = 0$.

For the special case of an external electric field, the operators A and $V_\omega(t'-t)$ in Eq. (147) correspond to the dipole moment operator (the response property, an induced dipole moment) (Eq. (148)) and the interaction with the electric field (Eq. (149)) $\vec{E}$, respectively.[ii]

$$A = \vec{\mu} = \vec{r} \tag{148}$$

$$V_\omega(t'-t) = -\vec{r}(t'-t)\vec{E}_\omega \tag{149}$$

Components of the molecular dipole moment are designated with a while b refers to the components of the perturbation. Eq. (149) gives the interaction energy corresponding to the perturbation operator V. Inserting Eq. (148) and (149) into Eq. (147) yields[229]

$$\mu_a(t) = \mu_a(0) - \int\limits_{-\infty}^{\infty} d\omega \sum_b \int\limits_{-\infty}^{\infty} dt' \langle\langle\hat{r}_a;\hat{r}_b(t'-t)\rangle\rangle^r E_{\omega b} e^{(\epsilon-i\omega)t'} \tag{150}$$

Substituting variables in the central integrand $t'-t \to s$ yields an expression including the frequency-dependent polarizability $\alpha(\omega)$.[229]

$$\mu_a(t) = \mu_a(0) - \int\limits_{-\infty}^{\infty} d\omega \sum_b \left\{ \int\limits_{-\infty}^{\infty} ds \langle\langle\hat{r}_a(0);\hat{r}_b(s)\rangle\rangle^r e^{(\epsilon-i\omega)s} \right\} E_{\omega b} e^{(\epsilon-i\omega)t} \tag{151}$$

$$\alpha(\omega) = - \int\limits_{-\infty}^{\infty} dt \langle\langle\hat{r}_a(0);\hat{r}_b(t)\rangle\rangle^r e^{(\epsilon-i\omega)t} \tag{152}$$

Thus the second term in Eq. (151) corresponds to the induced dipole moment.

It follows from Eq. (151) and (152) that the Fourier transform of the propagator $\langle\langle\hat{r}_a(0),r_b(t)\rangle\rangle^r$ is the dynamic polarizability.[229] Moreover, the quantity in brackets (Eq. (150)) is a number-conserving propagator, hence a so-called *polarization propagator*.[229] In its general form, a polarization propagator can be expressed in terms of the number-conserving operators $A(t) = P(t) = \sum_{ij} P_{ij}a_i^+(t)a_j(t)$ and $V(t') = Q(t') = \sum_{ij} Q_{ij}a_i^+(t')a_j(t')$ (neglecting the superscript).[229]

$$\langle\langle P(t);Q(t')\rangle\rangle = -i\Theta(-t')\langle\phi_0|[P(t),Q(t')]|\phi_0\rangle \tag{153}$$

The propagator for the dynamic polarizability is thus a special case of Eq. (153).[229] $[P(t),Q(t')]$ is a correlation function because it correlates the evolution of two variables that both depend on time. If P,Q are different variables, $[P(t),Q(t')]$ is also referred to as a cross-correlation function. In contrast,

---

[ii] It should be kept in mind that atomic units are used. Moreover, indices are employed to distinguish the two non-equivalent position operators.

if P, Q correspond to the same variable (Eq. (152)), the resulting quantity is called an autocorrelation function.[229]

Expanding Eq. (153) in the complete set of basis functions $\{\phi_n\}$ of H_0 yields

$$\langle\langle P; Q(t)\rangle\rangle = -i\Theta(-t)\sum_n\{\langle\phi_0|P|\phi_n\rangle\langle\phi_n|e^{iH_0t}Qe^{-iH_0t}|\phi_0\rangle - \langle\phi_0|e^{iH_0t}Qe^{-iH_0t}|\phi_n\rangle\langle\phi_n|P|\phi_0\rangle\} \quad (154)$$

$$\langle\langle P; Q(t)\rangle\rangle = -i\Theta(-t)\sum_n\{\langle\phi_0|P|\phi_n\rangle\langle\phi_n|Q|\phi_0\rangle e^{i(E_n-E_0)t} - \langle\phi_0|Q|\phi_n\rangle\langle\phi_n|P|\phi_0\rangle e^{-i(E_n-E_0)t}\} \quad (155)$$

The spectral representation of the propagator[229]

Oddershede et al. outlined that the energy representation, i.e., the Fourier transform, of any polarization propagator provides more physical insight.[229]

$$\langle\langle P, Q\rangle\rangle_E = \lim_{\epsilon\to0^+}\int_{-\infty}^{\infty}\langle\langle P; Q(t)\rangle\rangle e^{\epsilon t - iEt}dt \quad (156)$$

Using Eq. (155) for the Fourier transformation yields the spectral representation of the operator. It is sometimes also designated as the Lehmann representation of the retarded operator.[229,234]

$$\langle\langle P, Q\rangle\rangle_{E+i\epsilon} = \lim_{\epsilon\to0^+}\sum_{n,n\neq0}\left\{\frac{\langle\phi_0|P|\phi_n\rangle\langle\phi_n|Q|\phi_0\rangle}{E - E_n + E_0 + i\epsilon} - \frac{\langle\phi_0|Q|\phi_n\rangle\langle\phi_n|P|\phi_0\rangle}{E + E_n - E_0 + i\epsilon}\right\} \quad (157)$$

Considering only the real part, the dynamic polarizability can be obtained from the propagator containing the autocorrelation function of the dipole vector (Eq. (151)):[229]

$$Re(\langle\langle r; r\rangle\rangle_E) = Re(\alpha_{ab}(\omega)) = 2\sum_{n\neq0}\frac{\langle\phi_0|r_a|\phi_n\rangle\langle\phi_n|r_b|\phi_0\rangle}{(E_n - E_0)^2 - E^2}(E_n - E_0) \quad (158)$$

Eq. (158) corresponds to the conventional representation of the dynamic polarizability in a sum-over-states representation.[31] Hence, the real part of the polarization propagator defined for the linear response to the perturbation of an electric field corresponds to the dynamic polarizability tensor. Its poles are the excitation energies, and its residues $\{\langle\phi_0|r_a|\phi_n\rangle, \langle\phi_n|r_b|\phi_0\rangle\}$ are the transition dipole moments.[231,229] Therefore, as summarized by Oddershede,[229] the properties of the polarization propagator in the energy representation (Eq. (158)) underline that this form is most suitable for extracting the quantities of interest. Thus it would be desirable to be able to directly calculate polarization propagators in the energy representation. An equation of motion for this purpose is derived.

Equation of motion for the spectral representation of a propagator[229]

To calculate the energy-dependent polarization propagator for the two time-dependent operators $[P(t), Q(t')]$, an equation of motion is derived. The Hamiltonian equation of motion in the Heisenberg picture can be expressed in terms of the commutator with the time-independent Hamiltonian H_0.[229]

$$i\frac{dP(t)}{dt} = [P(t), H_0] \tag{159}$$

For the (time-dependent) polarization propagator, this yields

$$i\frac{d\langle\langle P, Q(t')\rangle\rangle}{dt'} = \delta(-t')\langle\phi_0|[P,Q]|\phi_0\rangle + \langle\phi_0|P;[Q(t'),H_0]|\phi_0\rangle \tag{160}$$

Inserting the Fourier transform of $\langle\langle P(t), Q(t')\rangle\rangle$ into Eq. (160) delivers an expression for the propagator in the energy representation.[229]

$$-E\langle\langle P;Q\rangle\rangle_E = -\langle\phi_0|[P;Q]|\phi_0\rangle - \langle\langle P;[H_0,Q]\rangle\rangle_E \tag{161}$$

The propagator (Eq. (161)) is calculated as the sum of a commutator and another propagator $\langle\langle P;[H_0,Q]\rangle\rangle_E$. An equivalent situation to Eq. (133) is obtained. Consecutive higher-order expressions for $\langle\langle P;[H_0,Q]\rangle\rangle_E$ can be iteratively obtained.[31,229]

$$-E\langle\langle P;[H_0,Q]\rangle\rangle_E = -\langle\phi_0|[P,[H_0,Q]]|\phi_0\rangle - \langle\langle P;[H_0,[H_0,Q]]\rangle\rangle_E \tag{162}$$

$$-E\langle\langle P;[H_0,[H_0,Q]]\rangle\rangle_E = -\langle\phi_0|[P,[H_0,[H_0,Q]]]|\phi_0\rangle - \langle\langle P;[H_0,[H_0,[H_0,Q]]]\rangle\rangle_E \tag{163}$$

Thus it follows from Eq. (162) and (163) that the polarization propagator in the energy representation $\langle\langle P;Q\rangle\rangle_E$ corresponds to the sum of expectation values of commutators over the reference state ϕ_0.[31] The infinite expansion series (Eq. (164)) is also called the moment expansion of the propagator.[229]

$$\langle\langle P;Q\rangle\rangle_E = E^{-1}\langle\phi_0|[P,Q]|\phi_0\rangle + E^{-2}\langle\phi_0|[P,[H_0,Q]]|\phi_0\rangle + E^{-3}\langle\phi_0|[P,[H_0,[H_0,Q]]]|\phi_0\rangle + \cdots \tag{164}$$

To simplify the expression (Eq. (164)), the superoperator space[235] is introduced. Matrix elements of commutators are abbreviated.[31,229]

$$(P|Q) = \langle\phi_0|[P;Q]|\phi_0\rangle \tag{165}$$

Superoperators $\hat{H}^n$ are employed to shorten the commutator expressions. In contrast to "conventional" operators, superoperators act on operators.[31,229]

$$\hat{H}P = [H,P] \tag{166}$$

Using Eq. (165) and (166), the expansion of the polarization propagator is represented with $\hat{I}Q = Q$ by

$$\langle\langle P; Q\rangle\rangle_E = E^{-1}(P|\hat{I}Q) + E^{-2}(P|\hat{H}_0 Q) + E^{-3}(P|\hat{H}_0^2 Q) + \cdots = \frac{1}{E}\left(P\left|\hat{I} + \sum_{n=1}^{}\left(\frac{\hat{H}_0}{E}\right)^n\right|Q\right) \tag{167}$$

The series expansion of the superoperator in Eq. (167), $\frac{1}{E}\left[\hat{I} + \sum_{n=1}^{}\left(\frac{\hat{H}_0}{E}\right)^n\right]$, can be written as an inverse matrix.[229]

$$\frac{1}{E}\left[\hat{I} + \sum_{n=1}^{}\left(\frac{\hat{H}_0}{E}\right)^n\right] = \left(E\hat{I} - \hat{H}_0\right)^{-1} \tag{168}$$

To arrive at the final working form of the equation of motion, the so-called inner projection of the inverse (Eq. (168)) superoperator is used.[236] This means that it is projected on a complete set of operators $\{h\}$. Projecting a superoperator, which acts on operators, on a complete set of operators is similar to projecting a "conventional" operator, which acts on states, on a complete set of basis functions.[31]

$$\langle\langle P; Q\rangle\rangle_E = (P|h)\left(h|E\hat{I} - \hat{H}|h\right)^{-1}(h|Q) \tag{169}$$

The complete set of operators $\{h\}$ is only complete if all possible states are generated from the reference ϕ_0. If the reference is the ground-state Slater determinant, $\{h\}$ generates all excited determinants $\{h\} = \{h_2, h_4, h_6, \dots\}$. It can be subdivided into operators generating all single (de)excitations (h_2), double (de)excitations (h_4), etc.[31,229] It should be noted that reformulating $E\hat{I} - \hat{H}$ to $E\hat{I} - \hat{H} = E\hat{I} - \hat{F} - \hat{\Sigma} = \hat{H}_0 - \hat{\Sigma}$ leads to the Dyson equation (Eq. (135)).[229]

The equation of motion (EOM) (Eq. (169)) to calculate the polarization propagator[jj] and, with this, response properties, poles and residues, is exact. Approximate propagators are obtained by truncating $\{h\}$.[31] Additional approximations arise from the reference function, which can be for example a HF determinant, an MP2 wave function, or a CC2 wave function.

Linear-response approaches to calculate excitation energies can be subdivided as a function of these approximations used to construct the polarization propagator from Eq. (169).

Random Phase Approximation (RPA)[229]

If the reference wave function is a Hartree-Fock determinant, and only single (de)excitations are included, an approximate polarization propagator results. This defines the Random Phase Approximation (RPA) (for the polarization propagator).[229]

[jj] It should be noted that the derivation remains the same for other two-time operators.

The single (de)excitation operator is conventionally divided into an excitation and a deexcitation part $h_2 = \{e, d\}$ defined in terms of creation α^+ and annihilation α_i operators. $\{i, j, \dots\}$ refer to occupied orbitals while $\{a, b, \dots\}$ designate virtual orbitals. Since Eq. (170) and (171) create all possible excited determinants, $h_2 = \{e, d\}$ provides a complete manifold of excited determinants. There exist, however, other definitions for h_2.[229]

$$e = \sum_{a,i} \alpha_a^+ \alpha_i \tag{170}$$

$$d = \sum_{a,i} \alpha_i^+ \alpha_a \tag{171}$$

Assuming real orbitals, this results with the equation of motion (Eq. (169)) in

$$\langle\langle P; Q \rangle\rangle_E = \left((P|e) \quad (P|d) \right) \begin{pmatrix} (e|E\hat{I} - \hat{H}|e) & (e|E\hat{I} - \hat{H}|d) \\ (d|E\hat{I} - \hat{H}|e) & (d|E\hat{I} - \hat{H}|d) \end{pmatrix}^{-1} \begin{pmatrix} (e|Q) \\ (d|Q) \end{pmatrix} \tag{172}$$

Eq. (172) can be simplified by introducing matrices and vectors. The operators defining the propagator are assumed to be real and symmetric (Eq. (174) and (176)).[229]

$$P_{ai} = (P|e)_{ai} = \langle \phi_0|[P, \alpha_a^+ \alpha_i]|\phi_0\rangle = \langle \phi_0|P\alpha_a^+\alpha_i - \alpha_a^+\alpha_i P|\phi_0\rangle = \langle \phi_0|P\alpha_a^+\alpha_i|\phi_0\rangle = \langle \phi_0|P|\phi_i^a\rangle \tag{173}$$

$$P_{ia} = (P|d)_{ia} = \langle \phi_0|[P, \alpha_i^+ \alpha_a]|\phi_0\rangle = \langle \phi_0|-\alpha_i^+\alpha_a P|\phi_0\rangle = -\langle \phi_i^a|P|\phi_0\rangle = -P_{ai} \tag{174}$$

$$Q_{ai} = (e|Q)_{ai} = \langle \phi_0|[\alpha_i^+ \alpha_a, Q]|\phi_0\rangle = \langle \phi_0|\alpha_i^+\alpha_a, Q|\phi_0\rangle = \langle \phi_i^a|Q|\phi_0\rangle \tag{175}$$

$$Q_{ia} = (d|Q)_{ia} = \langle \phi_0|[\alpha_a^+ \alpha_i, Q]|\phi_0\rangle = \langle \phi_0|-Q\alpha_a^+\alpha_i|\phi_0\rangle = -\langle \phi_0|Q|\phi_i^a\rangle = -Q_{ai} \tag{176}$$

$$(e|\hat{I}|e) = \langle \phi_0|[\alpha_j^+ \alpha_b, \alpha_a^+ \alpha_i]|\phi_0\rangle = \delta_{ab}\delta_{ij} \tag{177}$$

$$(d|\hat{I}|e) = \langle \phi_0|[\alpha_b^+ \alpha_j, \alpha_a^+ \alpha_i]|\phi_0\rangle = 0 \tag{178}$$

$$(e|\hat{H}|e) = \langle \phi_0|[\alpha_j^+ \alpha_b, H, \alpha_a^+ \alpha_i]|\phi_0\rangle = \langle \phi_0|[\alpha_j^+ \alpha_b, H]|\phi_i^a\rangle - \langle \phi_0|[\alpha_j^+ \alpha_b, \alpha_a^+ \alpha_i], H|\phi_0\rangle \tag{179}$$

$$= \langle \phi_j^b|H|\phi_i^a\rangle - \delta_{ij}\delta_{ab}\langle \phi_0|H|\phi_0\rangle = A_{ij}^{ab}$$

$$(e|\hat{H}|d) = \langle \phi_0|[\alpha_j^+ \alpha_b, H, \alpha_i^+ \alpha_a]|\phi_0\rangle = \langle \phi_j^b|[H, \alpha_i^+ \alpha_a]|\phi_0\rangle - \langle \phi_0|H, [\alpha_j^+ \alpha_b, \alpha_i^+ \alpha_a]|\phi_0\rangle \tag{180}$$

$$= -\langle \phi_{ij}^{ab}|H|\phi_0\rangle = -B_{ij}^{ab}$$

$$(d|\hat{H}|e) = \langle \phi_0|[\alpha_b^+ \alpha_j, H, \alpha_a^+ \alpha_i]|\phi_0\rangle = -\langle \phi_0|H[\alpha_b^+ \alpha_j, \alpha_a^+ \alpha_i]|\phi_0\rangle \tag{181}$$

$$= -\langle \phi_0 | H | \phi_{ij}^{ab} \rangle = -B_{ij}^{ab}$$

The matrix elements $\{A_{ij}^{ab}\}$ (Eq. (179)) and $\{B_{ij}^{ab}\}$ (Eq. (180) and (181)) are traditionally expressed in terms of Mulliken two-electron integrals.

$$A_{ij}^{ab} = \delta_{ij}\delta_{ab}(\varepsilon_a - \varepsilon_i) + (ia|jb) - (ij|ab) \tag{182}$$

$$B_{ij}^{ab} = (ia|bj) - (ib|aj) \tag{183}$$

Inserting Eq. (173) to (181) into the equation of motion in a singly-excited subspace (Eq. (172)) yields the polarization propagator with the unit matrix $\overline{1}$[229]

$$\langle\langle P; Q \rangle\rangle_E = (P \quad -P) \begin{pmatrix} E\overline{1} - A & -B \\ -B & -E\overline{1} - A \end{pmatrix}^{-1} \begin{pmatrix} Q \\ -Q \end{pmatrix} \tag{184}$$

The excitation energies correspond to the poles of the propagator $\langle\langle P; Q \rangle\rangle_E$ (Eq. (184)). At these poles, the inverse matrix $\begin{pmatrix} E\overline{1} - A & -B \\ -B & -E\overline{1} - A \end{pmatrix}^{-1}$ does not exist because its determinant is 0.[229]

$$det \begin{pmatrix} \omega\overline{1} - A & -B \\ -B & -\omega\overline{1} - A \end{pmatrix} \overset{!}{=} 0 \tag{185}$$

This results in an eigenvalue problem (substituting E with ω) with eigenvectors $\begin{pmatrix} X \\ Y \end{pmatrix}_n$

$$\begin{pmatrix} A & B \\ B & A \end{pmatrix} \begin{pmatrix} X \\ Y \end{pmatrix}_n = \omega_n \begin{pmatrix} \overline{1} & 0 \\ 0 & -\overline{1} \end{pmatrix} \begin{pmatrix} X \\ Y \end{pmatrix}_n \tag{186}$$

The eigenvalues (= excitation energies) are obtained from the determinant

$$det \left| \begin{pmatrix} A & B \\ B & A \end{pmatrix} - \omega \begin{pmatrix} \overline{1} & 0 \\ 0 & -\overline{1} \end{pmatrix} \right| \tag{187}$$

To obtain the transition moments, the inverse matrix (Eq. (184)) is usually not explicitly calculated. Instead, the approximate propagator within the RPA framework, equivalently to the exact polarization propagator (Eq. (157)), can be expressed in terms of the eigenvectors X, Y of the determinant (Eq. (185)) and the matrix representation of the two vectors $(P|h)$ and $(h|Q)$ in the equation of motion (Eq. (169)).[229]

To derive the expression, at first a diagonal form of the inverse matrix in Eq. (184) is obtained with the eigenvectors $\left\{ \begin{pmatrix} X \\ Y \end{pmatrix}_n \right\}$. The derivation starts with recognizing that only pairwise eigenvectors result.[229]

$$\begin{pmatrix} A & B \\ B & A \end{pmatrix}\begin{pmatrix} Y \\ X \end{pmatrix}_{-n} = -\omega_n \begin{pmatrix} \overline{1} & 0 \\ 0 & -\overline{1} \end{pmatrix}\begin{pmatrix} Y \\ X \end{pmatrix}_{-n} \tag{188}$$

Eq. (186) and (188) can be summarized as

$$\begin{pmatrix} A & B \\ B & A \end{pmatrix}\begin{pmatrix} X & Y \\ Y & X \end{pmatrix} = \begin{pmatrix} \overline{1} & 0 \\ 0 & -\overline{1} \end{pmatrix}\begin{pmatrix} X & Y \\ Y & X \end{pmatrix}\begin{pmatrix} \omega & 0 \\ 0 & -\omega \end{pmatrix} \tag{189}$$

The eigenvectors $\left\{ \begin{pmatrix} X \\ Y \end{pmatrix}_n \right\}$ are normalized.

$$\begin{pmatrix} X \\ Y \end{pmatrix}^\dagger \begin{pmatrix} \overline{1} & 0 \\ 0 & -\overline{1} \end{pmatrix}\begin{pmatrix} X \\ Y \end{pmatrix} = 1 \tag{190}$$

$$\begin{pmatrix} Y \\ X \end{pmatrix}^\dagger \begin{pmatrix} \overline{1} & 0 \\ 0 & -\overline{1} \end{pmatrix}\begin{pmatrix} Y \\ X \end{pmatrix} = -1 \tag{191}$$

This can be summarized in the matrix

$$\begin{pmatrix} X & Y \\ Y & X \end{pmatrix}^\dagger \begin{pmatrix} \overline{1} & 0 \\ 0 & -\overline{1} \end{pmatrix}\begin{pmatrix} X & Y \\ Y & X \end{pmatrix} = \begin{pmatrix} 1 & 0 \\ 0 & -1 \end{pmatrix} \tag{192}$$

An energy-dependent term is added to Eq. (189).[229]

$$\begin{pmatrix} A - E\overline{1} & B \\ B & A + E\overline{1} \end{pmatrix}\begin{pmatrix} X & Y \\ Y & X \end{pmatrix} = \begin{pmatrix} \overline{1} & 0 \\ 0 & -\overline{1} \end{pmatrix}\begin{pmatrix} X & Y \\ Y & X \end{pmatrix}\begin{pmatrix} \omega - E\overline{1} & 0 \\ 0 & -\omega - E\overline{1} \end{pmatrix} \tag{193}$$

The inverse of Eq. (193) reads

$$\begin{pmatrix} X & Y \\ Y & X \end{pmatrix}^{-1}\begin{pmatrix} A - E\overline{1} & B \\ B & A + E\overline{1} \end{pmatrix}^{-1} = \begin{pmatrix} \omega - E\overline{1} & 0 \\ 0 & -\omega - E\overline{1} \end{pmatrix}^{-1}\begin{pmatrix} X & Y \\ Y & X \end{pmatrix}^{-1}\begin{pmatrix} \overline{1} & 0 \\ 0 & -\overline{1} \end{pmatrix} \tag{194}$$

Multiplying with $\begin{pmatrix} X & Y \\ Y & X \end{pmatrix}$ from the left yields

$$\begin{pmatrix} A - E\overline{1} & B \\ B & A + E\overline{1} \end{pmatrix}^{-1} = \begin{pmatrix} X & Y \\ Y & X \end{pmatrix}\begin{pmatrix} \omega - E\overline{1} & 0 \\ 0 & -\omega - E\overline{1} \end{pmatrix}^{-1}\begin{pmatrix} \overline{1} & 0 \\ 0 & -\overline{1} \end{pmatrix}\begin{pmatrix} X & Y \\ Y & X \end{pmatrix}^{-1} \tag{195}$$

Using Eq. (192) delivers

$$\begin{pmatrix} A - E\overline{1} & B \\ B & A + E\overline{1} \end{pmatrix}^{-1} = \begin{pmatrix} X & Y \\ Y & X \end{pmatrix}\begin{pmatrix} \omega - E\overline{1} & 0 \\ 0 & -\omega - E\overline{1} \end{pmatrix}^{-1}\begin{pmatrix} \overline{1} & 0 \\ 0 & -\overline{1} \end{pmatrix}\begin{pmatrix} X & Y \\ Y & X \end{pmatrix}^\dagger \tag{196}$$

$$\begin{pmatrix} A - E\overline{1} & B \\ B & A + E\overline{1} \end{pmatrix}^{-1} = \begin{pmatrix} X & Y \\ Y & X \end{pmatrix}\begin{pmatrix} \omega - E\overline{1} & 0 \\ 0 & -\omega - E\overline{1} \end{pmatrix}^{-1}\begin{pmatrix} X & Y \\ -Y & -X \end{pmatrix}^\dagger \tag{197}$$

Inserting Eq. (197) into the total propagator (Eq. (184)) yields

$$\langle\langle P; Q\rangle\rangle_E = (P \quad -P)\begin{pmatrix} X & Y \\ Y & X \end{pmatrix}\begin{pmatrix} E\bar{1} - \omega & 0 \\ 0 & \omega + E\bar{1} \end{pmatrix}^{-1}\begin{pmatrix} X & Y \\ -Y & -X \end{pmatrix}^{\dagger}\begin{pmatrix} Q \\ -Q \end{pmatrix} \tag{198}$$

Multiplying the matrixes delivers the propagator.

$$\langle\langle P; Q\rangle\rangle_E = (P \quad -P)\begin{pmatrix} X & Y \\ Y & X \end{pmatrix}\begin{pmatrix} E\bar{1} - \omega & 0 \\ 0 & \omega + E\bar{1} \end{pmatrix}^{-1}\begin{pmatrix} X & Y \\ -Y & -X \end{pmatrix}^{\dagger}\begin{pmatrix} Q \\ -Q \end{pmatrix} \tag{199}$$

Reformulating the equation yields

$$\langle\langle P; Q\rangle\rangle_E = P(X + Y)(E\bar{1} - \omega)^{-1}(X + Y)^{\dagger}Q + P(X + Y)(E\bar{1} + \omega)^{-1}(X + Y)^{\dagger}Q \tag{200}$$

In order to explicitly represent the poles and residues of the operator, Eq. (200) can be expressed as a sum of the poles.[237]

$$\alpha(\omega) = \langle\langle P; Q\rangle\rangle_E = \sum_n \frac{P(X_n + Y_n)(X_n + Y_n)^T Q}{\omega - \omega_n} - \frac{P(X_n + Y_n)(X_n + Y_n)^T Q}{\omega + \omega_n} \tag{201}$$

The residues can be then represented as a simple product.

$$res = \sum_{i,a} P_{ia}(X_{ia,n} + Y_{ai,n})(X_{ia,n} + Y_{ai,n})^T Q_{ai} \tag{202}$$

Since $\{Y_{ai,n}\}$ is associated with the deexcitations $\{Q_{ai}\}$, it summarizes the deexcitation amplitudes. Consistently, $\{X_{ia,n}\}$ refers to the excitations. Transition dipole moments are computed from the trace of the excitation and deexcitation vectors for a given excited state n with one-electron operators.[179] The three components μ_q of the transition dipole vector $\vec{r} = (x, y, z)$, which are included in the P- and Q matrices, are accessible from the vectors.

$$\mu_{q,n} = \sum_{ia}(X_{ia,n} + Y_{ai,n})^T \langle\Phi_i^a|\mu_q|\Phi_0\rangle \tag{203}$$

For the oscillator strengths f_n, this implies

$$f_n = \frac{2}{3}\omega_n \sum_q \left(\sum_{ia}(X_{ia,n} + Y_{ai,n})^T \langle\Phi_i^a|\mu_q|\Phi_0\rangle\right)^2 \tag{204}$$

It should be noted that the Thomas-Reiche-Kuhn sum rule is obeyed in an RPA formalism. It was shown above that the A-matrix corresponds to matrix elements between singly-excited determinants while the B-matrix contains double excitations with respect to the reference. It thus takes into account correlation both for the ground state and the excited states (no Brillouin's theorem for singly-excited states, see above). When neglecting the B-matrix, RPA becomes equivalent to CIS. Only the X-vectors

are included. These vectors contribute also most to the RPA excitation energies, with the double excitations constituting only a minor part.[229]

A number of equivalent derivations for RPA exist; and its name comes from the original derivation in terms of a diagrammatic construction.[238] RPA and TD-HF are often used interchangeably[31] although RPA is strictly speaking a linearized version of TD-HF, i.e., TD-HF in the limit of "small-amplitude deviations".[238] In the above equation-of-motion formalism, this is exploited by limiting the manifold of excitation operators $\{h\}$ to single excitations. The MCRPA (multiconfigurational random phase approximation) extends the RPA formalism to multiconfigurational reference wave functions[229] although it is only rarely employed, being mostly replaced with the CASSCF/CASPT2 formalism.

As outlined by Oddershede et al. and to summarize RPA for the subsequent section,[229] it follows from the equation of motion that the polarization propagator is the product of a vector multiplied with an inverse matrix and another vector (Eq. (169)). The polarization propagator (Eq.(184)) is therefore commonly rewritten as

$$\langle\langle P; Q \rangle\rangle_E = x\left(\omega - E\overline{1}\right)^{-1}x \tag{205}$$

x are the transition amplitudes.[239]

Algebraic Diagrammatic Construction (ADC)[240] Scheme for the Polarization Propagator[229,239]

The ADC family of methods calculates transition energies from approximating the polarization propagator as well. Similar to RPA, its poles and residues are computed in the spectral representation from the equation of motion.[239] The underlying kea idea is to obtain a certain polarization propagator with its poles and its residues that are correct to a predefined order of perturbation.

To derive the ADC approximations, the matrix of the propagator, $\left(\omega - E\overline{1}\right)^{-1}$ (Eq. (205)), is rewritten in a non-orthogonal basis. E is not a diagonal matrix anymore, but rather a matrix representation M of some effective Hamiltonian, with f being the corresponding effective transition amplitudes.[239]

$$\langle\langle P; Q \rangle\rangle_E = f(\omega - M)^{-1}f \tag{206}$$

Both the transition amplitudes and the effective Hamiltonian are expanded as a perturbation series in terms of the perturbation, i.e., the fluctuation potential V (see MP2 section).

$$M = M^{(0)} + M^{(1)} + M^{(2)} \dots \tag{207}$$

$$f = f^{(0)} + f^{(1)} + f^{(2)} \dots \tag{208}$$

An analysis of the expansion of $\langle\langle P; Q\rangle\rangle_E$ (Eq. (206)) provides explicit expressions for $M_{\mu\nu}^{(n)}$ and $f_\mu^{(n)}$. μ, ν refer to excitation types (single, double, etc. excitations). The order n of an ADC(n) method designates the highest order included in the calculation of M and f for $\langle\langle P; Q\rangle\rangle_E$ (Eq. (207), (208)).[239] M is then calculated and diagonalized, yielding the poles of the polarization propagator and the excitation energies of the system. Transforming f with the eigenvectors y of M permits to calculate transition dipole moments.[239]

The expressions for M and f are more easily derived by means of the intermediate state representation.[239] This is equivalent to choosing a different reference wave function and complete operator manifold for Eq. (169) than in RPA. In ADC(2), the reference wave function corresponds to a ground-state MP2 function ψ_0. In extension of the above model, it can be, on a more general level, represented as the sum of the SCF energy $|SCF\rangle$ and higher-order corrections $|0^{(n)}\rangle$.

$$\psi_0 = C\left(|SCF\rangle + |0^{(1)}\rangle + |0^{(2)}\rangle + \cdots\right) \tag{209}$$

A complete excited-state basis $\{\psi_J\}$ is obtained by acting with all types of excitation operators (i.e., a full manifold) on the MP2 function. Orthogonalizing these wave functions $\{\tilde{\psi}_J\}$ yields the intermediate state representation. The M matrix and the f vector can then be explicitly defined.[239]

$$M_{IJ} = \langle\tilde{\psi}_I|\hat{H} - E_N|\tilde{\psi}_J\rangle \tag{210}$$

$$f_{I,pq} = \langle\tilde{\psi}_I|\alpha_p^+\alpha_q|\psi_0\rangle \tag{211}$$

Inserting Eq. (210) and (211) into Eq. (206) yields an equation that can be compared to Eq. (169).

$$\langle\langle P; Q\rangle\rangle_E = \left((P|h_2), (P|h_4), \ldots\right) \begin{pmatrix} M_{22}(E) & M_{24}(E) & \ldots \\ M_{42}(E) & M_{44}(E) & \ldots \\ \vdots & \vdots & \ddots \end{pmatrix}^{-1} \begin{pmatrix} (h_2|Q) \\ (h_4|Q) \\ \vdots \end{pmatrix} \tag{212}$$

$$M_{22} = \langle h_2|\hat{H}_0 + V - E_N|h_2\rangle \tag{213}$$

Both the perturbation (fluctuation potential) V included in the M-matrix and the order of perturbation in the reference wave function contribute to the order n of the ADC-scheme for Eq. (207) and (208).[229] For the $(P|h_i)$ vector, this implies

$$(P|h_i) = C^2\langle SCF + 0^{(1)} + 0^{(2)} \ldots |[P, h_i]|SCF + 0^{(1)} + 0^{(2)} \ldots\rangle \tag{214}$$

Only single excitations contribute to the zeroth-order of $f = (P|h_i)$. Double and triple excitations enter into the first-order correction.

$$(P|h_2)_0 = C^2 \langle SCF|[P, h_2]|SCF \rangle \tag{215}$$

$$(P|h_i)_1 = C^2 \big(\langle SCF|[P, h_i]|0^{(1)} \rangle + \langle 0^{(1)}|[P, h_i]|SCF \rangle \big) \qquad i \in \{4,6\} \tag{216}$$

It follows for the zeroth-order polarization propagator.

$$\langle\langle P; Q \rangle\rangle_E^{(0)} = (P|h_2)_0 M_{22}^{(0)} (h_2|Q)_0 \tag{217}$$

$$M_{22}^{(0)} = \langle SCF|[h_2, [E - F, h_2]]|SCF \rangle \tag{218}$$

From Eq. (218), it is evident that the poles of the zeroth-order polarization propagator (Eq. (217)) are the orbital energies.[229]

The first-order polarization propagator is similarly calculated from the first-order $M_{22}^{(1)}$ (the perturbation/fluctuation potential) and contains no contributions from the excitation vectors.[kk][229]

$$\langle\langle P; Q \rangle\rangle_E^{(1)} = (P|h_2)_0 M_{22}^{(1)} (h_2|Q)_0 \tag{219}$$

Since the matrix $M_{22}^{(1)}$ is equivalent to the sum of the zeroth-order Hamiltonian and the perturbing fluctuation potential, Eq. (219) is equal to the polarization propagator in RPA, Eq. (172). Thus, a hypothetical "ADC(1)" is equivalent to RPA. Similarly, as stated by Oddershede, CIS somewhat corresponds to a mixture between the polarization propagator of zeroth- and of first-order. The zeroth-order polarization propagator computes excitation energies as orbital energy differences, i.a., in a frozen-orbital approximation (see CIS above).[229]

It can be shown that the influence of the triple excitations to the second-order contribution of M diminish if h_2 and h_6 are linearly independent. The inverse matrix (Eq. (212)) then becomes

$$M^{-1} = \begin{pmatrix} M_{22} & M_{24} \\ M_{42} & M_{44} \end{pmatrix}^{-1} = \begin{pmatrix} P^{-1} & -P^{-1}M_{24}M_{44}^{-1} \\ -M_{44}^{-1}M_{42}P^{-1} & M_{44}^{-1}+M_{44}^{-1}M_{42}P^{-1}M_{24}M_{44}^{-1} \end{pmatrix} \tag{220}$$

$$P(E) = M_{22} - M_{24}M_{44}^{-1}M_{42} \tag{221}$$

Inserting Eq. (220) into the equation for the propagator in the intermediate-state representation (Eq. (212)) yields the polarization propagator to second order.[229]

$$\langle\langle P; Q \rangle\rangle_E^{(2)} = T(P,E)P(E)^{-1}T(Q,E) + (P|h_4)M_{44}^{-1}(h_4|Q) = W_2(E) + W_4(E) \tag{222}$$

The transition matrices $T(P,E)$ are defined as

[kk] It should be noted that the rank of the single-excitation vector is 1. However, the first-order correction in the MP2 wave function is of rank 2.[229]

$$T(P, E) = (P|h_2) - (P|h_4)M_{44}{}^{-1}M_{42} \tag{223}$$

They provide the transition moments.[229] The eigenvalues of $P(E)$ correspond to the transition energies. $W_4(E)$ does not affect transition moments or energies.[229]

To obtain an explicit expression of the polarization propagator to second order, the excitation operators for h_2, h_4 are explicitly inserted in Eq. (220) and (222). As outlined by Oddershede, the M_{22} matrix can be represented in terms of A- and B-matrixes (comparable to RPA).[229]

$$M_{22} = \begin{pmatrix} ES - A & -B \\ -B & -ES - A \end{pmatrix} \tag{224}$$

However, the reference state is not a HF determinant, but a correlated ground-state function. Moreover, second-order terms arise in the A- and B-matrices that are neglected in first-order RPA.[229]

$$A(2) = \langle 0^{(1)}|[q,[V,q^+]]|SCF\rangle + \langle SCF|[q,[V,q^+]]|0^{(1)}\rangle + \langle 0^{(1)}|[q,[F,q^+]]|0^{(1)}\rangle \tag{225}$$

Similar terms are included in the B-matrix. In addition to the unit matrix, S incorporates some second-order contributions as well.[229]

$$S(2) = \langle 0^{(1)}|[q,q^+]|0^{(1)}\rangle \tag{226}$$

Thus, Eq. (221) becomes

$$P(E) = \begin{pmatrix} ES(0,2) - A(0,1,2) - C^{\ddagger}(1)\left(E - D(0)\right)^{-1}C(1) & -B(1,2) \\ -B(1,2) & -ES(0,2) - A(0,1,2) - C^{\ddagger}(1)\left(-E - D(0)\right)^{-1}C(1) \end{pmatrix} \tag{227}$$

$$C(1) = \left(q^+q^+|\hat{V}|q\right) \tag{228}$$

$$D(0) = \left(q^+q^+|\hat{F}|qq\right) \tag{229}$$

$C(1)$ and $D(0)$ act on the SCF reference state.[229] They correspond to two-particle-two-hole excitations. From Eq. (227), it is evident that they lower the excitation energies.[229] Including these excitations (i.e, the $C(1)\left(E - D(0)\right)^{-1}C(1)$ matrices) corresponds to the second-order polarization propagator approximation (SOPPA).[31,229]

In contrast to SOPPA, which is correct through second order, in ADC-based approaches, some terms in the matrices (Eq. (227) to (229)) are neglected. Wormit and Dreuw illustrate this by means of the structure of the ADC(2) matrix. In principle, the matrix includes all single (particle-hole) and double (two-particle-two-hole) excitations with respect to an MP2 ground state. Hence its size is identical to the CISD matrix of the system. It is well-known that the CISD matrix is composed of blocks between the ground-state and all single- and double-excited determinants. Furthermore, from the

diagrammatic construction outlined above (Eq. (227)), the matrix elements contain zeroth-, first- and second-order contributions. Including all matrix elements between the excitations to the second order corresponds to SOPPA. In the ADC(2) variants, several blocks of the ADC matrix are not fully included to second order. The strict ADC(2)-s scheme includes the (p-h)-block to second order, the (p-h,2p-2h) and (2p-2h,p-h) blocks to first order, and the (2p-2h,2p-2h) block to zeroth order. In comparison, including the (2p-2h,2p-2h)-block to first order defines the extended ADC(2)-x scheme. As could be expected from Eq. (227), ADC(2)-x excitation energies are usually lower than their ADC(2)-s counterparts. While this usually deteriorates the performance, Dreuw and Wormit[239] suggest employing ADC(2)-x to identify excited states with double-excitation character.[241,242]

According to Wormit and Dreuw, simplifications to the ADC(2) scheme exist as well. Starting from an SOS-MP2 ground state and including only opposite-spin excitations also in the (2p-2h) blocks corresponds to the SOS-ADC(2) approach. Compared with conventional ADC(2), it is more efficient.[239] Even more speedup can be achieved by starting from block-diagonalized ADC matrices. For instance, it has been suggested to neglect valence-core couplings to compute computationally challenging core excitations.[239,243,244,245] As pointed out by Wormit and Dreuw, it is evident from Eq. (210) and (211) that in contrast to most other excited-state methods, ADC(2) excited-state properties are directly accessible from the intermediate state representation, which provides the excited-state amplitudes $f_{I,pq}$.[239] This implies that whenever excited-state properties are required, ADC(2) constitutes a computationally efficient approach.

Finally, it should be noted that the MP2 ground state, the basis of ADC(2), can be problematic due to the well-known deficiencies of MP2 (see above).[239] In contrast, CC-based approaches rely on a more robust ground-state description. They are presented in the following sections.

Approximate Coupled Cluster to Second Order (CC2) in a Linear Response Formalism[246]

CC-based excitation energies obtained in a linear-response formalism or in an equation-of-motion approach are identical[247] but transition moments and properties might differ. CC2 excitation energies are conventionally obtained in a linear-response formalism. Therefore, the linear-response equations are given in the following.[246,248] As outlined by Christiansen et al.,[246] CC2 is an approximation of CCSD. As stated above, CCSD includes single and double excitations with respect to the reference wave function to an infinite order. CC2 still fully incorporates single excitations because they are decisive for orbital relaxation (see above). The double excitations are, however, approximated. They are correct to first order in the perturbation. Christiansen et al. pointed out that the original CIS(D) formalism of Head-Gordon et al.[173] (see above) can be considered as a non-iterative version of CC2.[246]

CC2 is particularly used for excited-state calculations, and it computes excitation energies and transition moments as the poles and residues of the linear-response function of a CC2 ground state. In CCSD, the CC excitation operator e^T involves only single and double excitations $e^{T_1+T_2}$. Eq. (29) and (30) for the amplitudes of the CCSD ground-state wave function thus become[246]

$$\langle\Phi_i^a|e^{-T_1-T_2}He^{T_1+T_2}|\Phi_0\rangle = 0 \tag{230}$$

$$\langle\Phi_{ij}^{ab}|e^{-T_1-T_2}He^{T_1+T_2}|\Phi_0\rangle = 0$$

With the transformed total Hamiltonian $\hat{H} = e^{-T_1}He^{T_1} = e^{-T_1}(F+V)e^{T_1}$, these equations yield[246]

$$\langle\Phi_i^a|\hat{H} + [\hat{H},T_2]|\Phi_0\rangle = 0 \tag{231}$$

$$\left\langle\Phi_{ij}^{ab}\left|\hat{H} + [\hat{H},T_2] + \frac{1}{2}\left[[\hat{H},T_2],T_2\right]\right|\Phi_0\right\rangle = 0$$

In CC2, the single equation is left as is since the singles respond to external perturbations to zeroth-order[246] in V.[ll] The doubles are correct only through first order. The singles are used as zeroth-order parameters, and they enter the final equations for the CC2 amplitudes (Eq. (232)) via the transformed Hamiltonian.[246]

$$\langle\Phi_i^a|\hat{H} + [\hat{H},T_2]|\Phi_0\rangle = 0 \tag{232}$$

$$\langle\Phi_{ij}^{ab}|\hat{H} + [F,T_2]|\Phi_0\rangle = 0$$

The final CC2 energy expression is closely related to the MP2-one ($\langle\Phi_{ij}^{ab}|H - H_0|\Phi_0\rangle = 0$), but integrals are transformed due the single-excitation operator. This does not affect the energy but ensures that properties from response functions can be more accurately computed. To derive the CC2 response function, a time-dependent perturbation V^t is added. However, F remains the zeroth-order reference so that the singles are still zeroth-order in V and first-order in V^t. This yields, via the time-dependent Schrödinger equation, the equations for the time-dependent amplitudes[mm] of CC2.[246]

$$\langle\Phi_i^a|\hat{H} + [\hat{H},T_2]|\Phi_0\rangle = i\frac{\partial t_1}{\partial t} \tag{233}$$

$$\langle\Phi_{ij}^{ab}|\hat{H} + [F+\hat{V},T_2]|\Phi_0\rangle = i\frac{\partial t_2}{\partial t}$$

[ll] This can be explained by the fact that the singles in MP2 enter only in second order if optimized Hartree-Fock orbitals are used. Otherwise, i.e., for non-optimized orbitals, they enter in zeroth-order.[246]
[mm] It should be noted that the similarity-transformed Hamiltonian in Eq. (233) differs by the time-dependent external potential from the Hamiltonian in Eq. (232) although the same symbols are employed.

With these amplitudes, a linear-response function of CC2, a "CC2 propagator" $\langle\langle P, Q\rangle\rangle_E$ can be defined, and with this an equation to compute its poles. A variety of methods exist to derive the CC2 response function.[249] Jørgensen et al. proposed a Lagrangian of the CC quasi-energy.[248]

The poles of the CC2 response function can be determined as the eigenvalues of the so-called CC2 Jacobian.[249] The cluster notation is employed for the excitation operators T, which are divided into the amplitudes t and corresponding excitation operators τ. $\{\mu_i\}$ designate excitations of a given type.[248]

$$T = t\tau = \sum_\mu t_\mu \tau_\mu \tag{234}$$

The CC2 Jacobian A is defined as

$$A_{\mu_i \nu_j} = \begin{pmatrix} \left\langle \mu_1 \left| [\hat{H}, \tau_{\nu_1}] e^{-T_2^{(0)}} \right| HF \right\rangle & \left\langle \mu_1 \left| [\hat{H}, \tau_{\nu_2}] \right| HF \right\rangle \\ \left\langle \mu_2 \left| [\hat{H}, \tau_{\nu_1}] \right| HF \right\rangle & \delta_{\mu\nu} \omega_{\mu_2} \end{pmatrix} \tag{235}$$

Its eigenvalues $\{\omega_k\}$ are the excitation energies.

$$A S_k = \omega_k S_k \tag{236}$$

The transition moments can be obtained from the residues of the response function.[246] Wormit and Dreuw[239] emphasized that in contrast to ADC-based approaches, approximate CC-matrices are not Hermitian. Therefore, CC calculations require in fact two calculations (except for computations of energy values only, i.e., of the poles), yielding left and right eigenvectors that form a biorthonormal set. Similarly, other properties of CC wave functions are not directly accessible, as it is the case for ADC(n). Although formalisms exist to calculate orbital-relaxed properties of the CC wave function from the left and right eigenvectors of the CC-matrices, such computations are computationally more demanding than comparable ADC-based calculations.[239]

Christiansen et al.[246] outlined that the CC2 model is intermediate between CCS and CCSD. In the same way, CC3 is intermediate between CCSD and CCSDT. They furthermore emphasized that CCn approximates the n-tuple excitations to order n-1. The singles take into account orbital relaxation due to the fluctuation potential and the external perturbation. The relationship to CIS(D) becomes evident from Eq. (233). Only disconnected triple excitations T_1, T_2 are included in the doubles. This is equivalent to the "spectator orbital"-type rationalization of Head-Gordon (see above).[173] Moreover, by neglecting the single contributions (the similarity-transformed Hamiltonian), the CC2 Jacobian can be transformed to the CIS(D∞)-Jacobian (A matrix). Symmetrizing it yields the M-matrix of ADC(2).[239]

Wormit and Dreuw noted that CC2 and ADC(2) should provide excitation energies of comparable accuracy. However, since ADC(2) excitation energies are obtained as the eigenvalues of a Hermitian

matrix, they potentially provide a more accurate description of conical intersections.[239] Apart from that, CC2 and ADC(2) differ mostly in their ground-state description.[239,246] While the CC2 ground state incorporates the single excitations to infinite order,[246] they are not included in MP2 (Brillouin's theorem).[239]

The linear-response formalism to obtain CC excitation energies was first suggested by Monkhorst.[250,251] The equation-of-motion formalism, which yields equivalent results, is presented in the following subsection although it is not directly a response/propagator approach.

Equation-of-Motion Approach to Coupled-Cluster Excitation Energies[252]

Sekino and Bartlett[253] demonstrated that an equation-of-motion (EOM) approach constitutes an alternative yet equivalent route to the expression of the CC linear response of a system (Eq. (235) and (236)). An excitation operator Ω_k acts on the CC ground state Ψ_{CC} and generates the k-th excited state Ψ_{CC}^k.

$$\Omega_k \Psi_{CC} = \Psi_{CC}^k \tag{237}$$

The states have energies E_0 and E_k, respectively.

$$H\Psi_{CC} = E_0 \Psi_{CC} \tag{238}$$

$$H\Psi_{CC}^k = E_k \Psi_{CC}^k \tag{239}$$

The transition energy ω_k is obtained as[253]

$$\omega_k \Omega_k \Psi_{CC} = [H\Omega_k - \Omega_k H]\Psi_{CC} = [H, \Omega_k]\Psi_{CC} \tag{240}$$

The ground state coupled-cluster wave function is defined as[254] (Eq. (28))

$$\Psi_{CC} = e^T \Phi_0 \tag{241}$$

Since the excitation operators commute, inserting Eq. (241) into Eq. (239) yields an expression including the excited-state energies.[254]

$$(He^T - E_k e^T)\Omega_k \Phi_0 = 0 \tag{242}$$

Excited-state energies can thus be obtained as the eigenvalues of a similarity-transformed Hamiltonian $\overline{H} = e^{-T} He^T$.[254,255]

$$|\overline{H} - E\overline{1}| = 0 \tag{243}$$

The similarity transformation of the Hamiltonian is not unitary. Therefore, each eigenvalue E is associated with a pair of eigenvectors.[254] This is conventionally expressed in a pair of coupled equations for the left and the right eigenvectors with $L = \widetilde{\Omega}_k$ and $R = \Omega_k$, respectively.[255]

$$L\bar{H} = EL \tag{244}$$

$$\bar{H}R = ER \tag{245}$$

L is thus a deexcitation operator. Equivalent expressions to this "bra state" are in fact used to compute linear-response CC2 properties as well as CC2 gradients.[254,256]

$$\widetilde{\Psi}_{CC}^k = \widetilde{\Psi}_{CC}L \tag{246}$$

Due to the non-Hermitian character of the EOM expressions, the right and the left eigenvectors are not Hermitian conjugates. They form a biorthogonal set and are often additionally chosen to be normalized. Due to the intermediate normalization, left and right eigenvectors are not Hermitian conjugates even for systems like the dihydrogen molecule where EOM-CCSD is exact.[254]

$$\left\langle \widetilde{\Psi}_{CC}^{(i)} \middle| \Psi_{CC}^{(j)} \right\rangle = \delta_{ij} \tag{247}$$

It should be stressed that the equations for the most common EOM-based approach, EOM-CCSD, have a form similar to the CI matrix equations (Eq. (243)). However, because of the similarity transformation, correlation effects are included in EOM-CCSD, and the approach is furthermore size-consistent[nn].[255,252]

In its so-called EOM-EE (excitation energy), EOM-CCSD is employed to calculate excitation energies. The general excitation operator Ω_k is then a spin-adapted linear combination of hole-particle and two-hole-two-particle operators.[255] As emphasized by Krylov,[255] this shape of the excitation operator and of its matrix representation, which is comparable to CI, results in good EOM performances for nearly degenerate excited states or for excitations subject to pronounced valence-Rydberg mixing. The SF-EOM methods (spin flip) provide access to accurate energies of biradicals and bond breaking processes. The excitation operator is not spin-conserving, and it changes the spin of a high-spin reference, which treats all involved (nearly degenerate) orbitals on an equal footing.[255,252] In contrast, IP-EOM (ionization potential) and EA-EOM (electron affinity), which yield accurate ionization potentials or electron affinities, rely on excitation operators that do not conserve the number of electrons comprised in the system.[257] The reference can still be a closed-shell determinant. The excitation operator Ω_k in IP-EOM is composed of particle, two-particle-hole-operators etc. This approach has the advantage that error-prone open-shell calculations are circumvented.

[nn] To guarantee size consistency, the excitation operator T must be truncated at a high level compared with R.[255]

The calculation of response properties with time-dependent DFT (TD-DFT) is discussed next. Whereas TD-DFT is certainly a linear-response approach, it is addressed in the next section (not as a subsection). This is justified by the fact that several additional considerations about the density are required before the above-discussed linear-response equations can be readily transferred to DFT. This yields then the so-called Casida equation. In fact, Casida's equation can equally be derived in a linear-response or in an equation-of-motion formalism.[258]

3.2.5   Time-Dependent Density Functional Theory (TD-DFT)[259]

TD-DFT relies on the Runge-Gross theorem,[260] the time-dependent extension of the Hohenberg-Kohn theorem (Eq. (44), (45)). It states that an exact correspondence between the time-dependent external potential $v_{ext}(\vec{r}, t)$ and the time-dependent density $\rho(\vec{r}, t)$ up to a mere phase factor exists.

$$\rho(\vec{r}, t) \leftrightarrow v_{ext}(\vec{r}, t) \tag{248}$$

Similar to the Hohenberg-Kohn theorem, it follows from the Runge-Gross theorem that (if the initial state $\Psi(\vec{r}, 0)$ is defined) the time-dependent density $\rho(\vec{r}, t)$ contains all the information about the system: due to the one-to-one-correspondence to the external potential, the density defines the Hamiltonian of the system.[261] The excited-state analog of the second Hohenberg-Kohn theorem (Eq. (45)) is the quantum-mechanical action integral.[259] Due to the Runge-Gross theorem (Eq. (248)), a one-to-one-correspondence between a time-dependent density $\rho(\vec{r}, t)$ and a time-dependent wave function $\Psi(\vec{r}, t)$ exists. The time evolution of wave functions $\Psi(\vec{r}, t)$ is in general described by stationary points of the action integral.[259]

$$A[\Psi(\vec{r}, t)] = \int_{t_0}^{t_1} dt \left\langle \Psi(\vec{r}, t) \middle| i\hbar \frac{\partial}{\partial t} - H(\vec{r}, t) \middle| \Psi(\vec{r}, t) \right\rangle \tag{249}$$

As $\Psi(\vec{r}, t) = \Psi(\vec{r}, t)[\rho(\vec{r}, t)]$ and hence $A[\Psi(\vec{r}, t)] = A[\rho(\vec{r}, t)]$, the time evolution of the density can be computed by minimizing the action integral.[259]

$$\frac{\delta A[\rho]}{\delta \rho} = 0 \tag{250}$$

It should be noted that Eq. (250) holds only for appropriate boundary conditions.[261]

Since the exact functional $E[\rho(\vec{r}, t)]$ is not known, a non-interacting reference system is again used. The external potential $v_S(\vec{r}, t)$ of the non-interacting reference system is adjusted so that its density is equal to the density of the true interacting system.[oo] The initial state of the non-interacting reference

---

[oo] As emphasized and discussed by Maitra,[261] this requires "non-interacting v-representability". For more information and references, the reader is referred to [261].

system $\Phi_0(\vec{r}, 0)$ is usually a Slater determinant composed of orbitals $\{\phi_i(\vec{r}, 0)\}$.[261] Their time evolution is described by the one-particle time-dependent Schrödinger equation ($\hbar = 1$).[259]

$$\left(-\frac{1}{2}\Delta + v_S(\vec{r}, t)\right)\phi_i(\vec{r}, t) = i\frac{\partial\phi_i(\vec{r}, t)}{\partial t} \tag{251}$$

Similar to above, the external potential of the non-interacting[pp] reference system is given by[261]

$$v_S(\vec{r}, t) = v_{ext}(\vec{r}, t) + v_H[\rho](\vec{r}, t) + v_{XC}[\rho, \Phi_0](\vec{r}, t) \tag{252}$$

In TD-DFT, similar to all other excited-state calculations, the approximate DFT ground state Φ_0, which is usually assumed as the initial state, accounts for the first approximations in the TD-DFT excitation energies. Furthermore, as outlined above and emphasized by Maitra,[261] the dependence of the one-to-one correspondence in Eq. (248) on the initial conditions and the mapping to the non-interacting reference system introduces a dependence of the exchange-correlation functional on this initial state $v_{XC} = v_{XC}[\Phi_0]$ (Eq. (252)). It was additionally discussed[262] that the exchange-correlation potential $v_{XC}[\rho, \Phi_0](\vec{r}, t)$ is not only time-dependent, but also depends on earlier times $t_i < t$.[263] This phenomenon is called memory dependence.[261]

As already mentioned, TD-DFT excitation energies are obtained in a linear-response formalism, i.e., the response function of the system is calculated. Due to the Runge-Gross theorem (Eq. (248)), the response function of the Kohn-Sham system is equal to the exact response function of the true interacting system.[261] The response function $\alpha_S(\omega)$ of the non-interacting reference system, where the electron-electron interaction is absorbed into a modified external potential ($v_S(\vec{r}, t)$), has a similar shape like the Hartree-Fock Green's function (Eq. (135)). In the spectral (Lehmann,) representation of the polarization propagator (see above, Eq. (157)), it is equivalent to the zeroth-order polarization propagator.

$$\alpha_S(\omega) = \sum_{ia}\frac{\psi_i(r)\psi_a(r)\psi_i(r')\psi_a(r')}{\omega - (\varepsilon_a - \varepsilon_i)} + \sum_{ia}\frac{\psi_i(r)\psi_a(r)\psi_i(r')\psi_a(r')}{-\omega - (\varepsilon_a - \varepsilon_i)} \tag{253}$$

However, in contrast to the zeroth-order polarization propagator, Eq. (253) is in principle exact for the non-interacting system. The response $\alpha_S(\omega)$ of the reference system is then mapped to the response $\alpha(\omega)$ of the interacting system. To do so, the definitions of the response functions $\alpha_S(\omega)$ and $\alpha(\omega)$ in terms of the density should be kept in mind.[264]

[pp] Although the mapping to general interacting systems subject to any non-local potential has not been established, an excited-state extension of GKS including non-local exchange exists.[147]

$$\alpha(\vec{r}, t, \vec{r}', t') = \left. \frac{\delta\rho(\vec{r}, t)}{\delta v_{ext}(\vec{r}', t')} \right|_{v_{ext}[\rho_0]} \tag{254}$$

$$\alpha_S(\vec{r}, t, \vec{r}', t') = \left. \frac{\delta\rho(\vec{r}, t)}{\delta v_S(\vec{r}', t')} \right|_{v_S[\rho_0]} \tag{255}$$

It follows from Eq. (254) and (255) that[264]

$$\alpha(\vec{r}, t, \vec{r}', t') = \int d\vec{r}'' \int dt'' \left. \frac{\delta\rho(\vec{r}, t)}{\delta v_S(\vec{r}'', t'')} \frac{\delta v_S(\vec{r}'', t'')}{\delta v_{ext}(\vec{r}', t')} \right|_{v_{ext}[\rho_0]} \tag{256}$$

$$v_S(\vec{r}, t) = v_{ext}(\vec{r}, t) + v_H(\vec{r}, t) + v_{XC}(\vec{r}, t) \tag{257}$$

The so-called time-dependent exchange-correlation kernel $f_{XC}(\vec{r}, t, \vec{r}', t')$ is defined as

$$f_{XC}(\vec{r}, t, \vec{r}', t') = \frac{\delta v_{XC}(\vec{r}, t)}{\delta\rho(\vec{r}', t')} \tag{258}$$

Therefore, the derivative on the right-hand side in Eq. (256) can be rewritten as

$$\frac{\delta v_S(\vec{r}'', t'')}{\delta v_{ext}(\vec{r}', t')} = \frac{\delta v_{ext}(\vec{r}'', t'')}{\delta v_{ext}(\vec{r}', t')} + \left. \left(\frac{\delta(t'' - t''')}{|\vec{r}'' - \vec{r}'''|} + f_{XC}(\vec{r}'', t'', \vec{r}''', t''') \right) \frac{\delta\rho(\vec{r}''', t''')}{\delta v_{ext}(\vec{r}', t')} \right|_{v_{ext}[\rho_0]} \tag{259}$$

Inserting Eq. (254) and (255) yields then a Dyson-type equation of TD-DFT.[264]

$$\alpha(\vec{r}, t, \vec{r}', t') = \alpha_S(\vec{r}, t, \vec{r}', t') \tag{260}$$

$$+ \int d\vec{r}'' \int dt'' \int d\vec{r}''' \int dt''' \, \alpha_S(\vec{r}, t, \vec{r}'', t'') \left(\begin{array}{c} \dfrac{\delta(t'' - t''')}{|\vec{r}'' - \vec{r}'''|} \\ + f_{XC}(\vec{r}'', t'', \vec{r}''', t''') \end{array} \right) \alpha(\vec{r}''', t''', \vec{r}', t')$$

A Fourier transformation of Eq. (260) provides the energy representation.

$$\alpha(\vec{r}, \vec{r}', \omega) = \alpha_S(\vec{r}, \vec{r}', \omega) + \int d\vec{r}'' \int d\vec{r}''' \, \alpha_S(\vec{r}, \vec{r}'', \omega) \left(\begin{array}{c} f_{XC}(\vec{r}'', \vec{r}''', \omega) \\ + \dfrac{1}{|\vec{r}'' - \vec{r}'''|} \end{array} \right) \alpha(\vec{r}''', \vec{r}', \omega) \tag{261}$$

It should be stressed that in contrast to the wave-function based methods, Eq. (260) and (261) are in principle exact. If the exact ground-state functional and the exact time-dependent exchange-correlation kernel were known, exact polarizabilities and, via the poles and residues, exact transition energies and moments, could be calculated. However, in a first and very fundamental approximation of TD-DFT (except for the approximate ground-state determinant, see above), the exchange-correlation potential $v_{XC}[\rho, \Phi_0](\vec{r}, t)$ is usually replaced with a ground-state potential that depends only on the density at time t.

$$v_{XC}{}^A[\rho, \Phi_0](\vec{r}, t) = v_{XC}{}^{gs}[\rho(t)](\vec{r}) \tag{262}$$

Eq. (262) corresponds to the adiabatic approximation.[259] As outlined by Maitra, the adiabatic approximation consists actually of two approximations. Firstly, the time and memory dependence of the exchange-correlation potential is neglected.[qq] Secondly, a ground-state functional is employed to describe excited-state correlation and exchange.[261] In the adiabatic approximation, the exchange-correlation kernel in Eq. (261) becomes frequency-independent. The time-dependent response of the density is thus determined by the response of the non-interacting reference system $\alpha_S(\vec{r}, \vec{r}', \omega)$, which is subsequently mapped by the exchange-correlation kernel to the response of the interacting system. This exchange-correlation kernel introduces so-called "dynamical effects".[261] Since the exchange-correlation is assumed to be time-independent in the adiabatic approximation, Eq. (261) takes on the shape of the Dyson equation of RPA, Eq. (169). This leads to a completely equivalent propagator-like expression (Eq. (184)). The poles (= excitation energies) are given by the Casida equation,[265] the analog of Eq. (187).

$$\begin{pmatrix} A & B \\ B^* & A^* \end{pmatrix} \begin{pmatrix} X \\ Y \end{pmatrix} = \omega \begin{pmatrix} 1 & 0 \\ 0 & -1 \end{pmatrix} \begin{pmatrix} X \\ Y \end{pmatrix} \tag{263}$$

The matrix elements are defined in terms of Kohn-Sham orbitals.

$$A_{ij}^{ab} = \delta_{ij}\delta_{ab}(\varepsilon_a - \varepsilon_i) + (ia|jb) + (ia|f_{XC}|jb) \tag{264}$$

$$B_{ij}^{ab} = (ia|bj) + (ia|f_{XC}|bj) \tag{265}$$

The inability of TD-DFT to describe charge-transfer states becomes evident from Eq. (264) and (265). The previously occupied and virtual orbitals barely overlap in charge-transfer states ($ai \approx 0, jb \approx 0$). This means that the TD-DFT excitation energy is dominated by the leading term ($\varepsilon_a - \varepsilon_i$). The other contributions to the A- and B-matrix vanish. This implies that the excitation energy does not include any distance-dependent terms that are, however, necessary to encompass the R^{-1}-dependence of the charge-transfer energy (R being the separation of the electron and the hole). The exchange-type integral in the RPA A-matrix (Eq. (182)) retrieves this dependence. This is the underlying reason why hybrids and especially range-separated hybrids are mandatory to correctly describe charge-transfer states.[259] Similar considerations hold for Rydberg excitations.[261]

A considerable part of the above section on ground-state DFT was dedicated to optimally tuned hybrid functionals. They are designed to fulfill certain criteria of the exact *ground-state functional*, such as the correct asymptotic decay of the exchange-correlation potential and the related correspondence of HOMO energy and ionization potential (Eq. (80)). However, range-separated hybrid functionals are

---

[qq] It should be noted that functionals containing exact exchange include some memory dependence.[261]

perhaps most useful in excited-state calculations. When employed adiabatically (Eq. (262)), they are responsible for an improved description of charge transfer[266] and account for more accurate quasiparticle energies,[158] i.e., they provide a more suitable description of the fundamental gap of compounds since the leading term $(\varepsilon_a - \varepsilon_i)$ in the A-matrix is more accurate. Nevertheless, they remain ground-state functionals developed in an attempt of constraint satisfaction, one of the strategies discussed by Scuseria[106] (see above).

In addition to these constraints for ground-state functionals, according to Maitra,[261] several constraints specific for TD-DFT exist as well. The so-called "resonance condition" proposed by Fuks et al.,[267] which states that if the external field is turned off, TD-DFT transition energies should be independent of the time when the perturbation is turned off, is violated by most functionals. It thus limits considerably the applicability of TD-DFT to problems of time-resolved spectroscopy.[261] Apart from that, it has generally often been outlined that TD-DFT is unsuitable for the description of non-adiabatic dynamics, for instance around conical intersections.[268] Indeed, the topology of conical intersections to the ground state is poorly described with TD-DFT because the branching space is only one-dimensional.[268] This results because couplings between the excited state and the reference are 0.[269] Nevertheless, this failure is not due to excited-state specific errors of the exchange-correlation functionals, but rather from the intrinsic inability of DFT to accurately describe static correlation. SF-TD-DFT approach uses a high-spin reference and provides a more suitable description of conical intersection.[270]

In addition to these problems (charge-transfer and Rydberg excitations, non-linear responses, conical intersections), TD-DFT provides also a poor description of double excitations.[261] In the non-interacting reference system, double excitations naturally require two photons (i.e., two non-interacting electrons are separately excited). This implies that double excitations are in principle not included in the linear response $\alpha_S(\vec{r}, t, \vec{r}', t')$. However, it has been shown for simple model systems that the exchange-correlation kernel strongly depends on the frequency for states with double-excitation character.[271] Therefore, if a time-dependent kernel was used instead of standard ground-state functionals, double excitations may still be accurately described with Eq. (261). Consistently, albeit not responsible for most TD-DFT failures, the adiabatic approximation of TD-DFT is in fact responsible for its incapability of describing double excitations.[261]

A simplification of TD-DFT, the so-called Tamm-Dancoff approximation (TDA), was proposed by Hirata and Head-Gordon.[272] It consists in neglecting the B-matrix in Casida's equation (Eq. (263)). This yields a CIS-like expression for the TDA excitation energies.

$$AX = \omega X \tag{266}$$

The errors introducing by this approximation are usually small, and the computational cost is roughly divided by two because the B-matrix is not calculated anymore. Furthermore, TDA, in contrast to conventional TD-DFT, does not suffer from triplet instabilities.[272] Casida et al. could show that the B-matrix is responsible for the triplet instabilities.[273]

It should be finally noted that equivalent equations to the Casida equation (Eq. (263)) and the Tamm-Dancoff approximation (Eq. (266)) can be derived in a constricted variational approach proposed by Ziegler et al.[274] The idea of constricted-variational DFT (CV(n)-DFT) is briefly outlined. It consists essentially in directly constructing an excited-state Kohn-Sham determinant $\Phi_{ES}^{KS} = |\phi_1'\phi_2'\phi_3' \dots \phi_N'|$. The orbitals $\{\phi_i'\}$ of the excited Kohn-Sham determinant are determined from the ground-state Kohn-Sham orbitals $\{\phi_i\}$ by a unitary transformation that is carried out to order n.

$$e^U \begin{pmatrix} \phi_{occ} \\ \phi_{virt} \end{pmatrix} = \left(\sum_m^n \frac{U^m}{m!} \right) \begin{pmatrix} \phi_{occ} \\ \phi_{virt} \end{pmatrix} = \begin{pmatrix} \phi_{occ}' \\ \phi_{virt}' \end{pmatrix} \tag{267}$$

The energy of the excited-state determinant Φ_{ES}^{KS} is expressed in terms of the elements of the transformation matrix $\{U_{ia}\}$. Usually, the transformation matrix is expanded to the second order, defining CV(2)-DFT. The energy $E[\Phi_{ES}^{KS}]$ is minimized by variation of the transformation matrix elements *subject to the constraint* that exactly one electron moves from the subspace spanned by the occupied ground-state orbitals $\{\phi_{occ}\}$ to the space spanned by the virtual orbitals of the Kohn-Sham ground state $\{\phi_{virt}\}$. This is reflected in the constraint[275]

$$\sum_{ia} U_{ia}^* U_{ia} = 1 \tag{268}$$

A constrained optimization using the Lagrangian and subsequent use of the Tamm-Dancoff approximation yields an equation identical to Eq. (266).[275]

$$AU = \lambda U \tag{269}$$

The transformation matrix U to the second order from Eq. (269), yielding CV(2)-DFT excitation energies, can then be used to carry out the transformation (Eq. (267)) to infinite order. This provides access to CV(∞)-DFT excitation energies.[276] If the transformation matrix is additionally optimized for each excited state[rr] in a self-consistent way, SCF-CV(∞)-DFT energies are obtained.[275,276,277] The SCF-CV(∞)-DFT scheme is based on expressions involving natural transition orbitals (NTOs) $\{\phi_i^o, \phi_i^v\}$.[278] The final occupied excited-state orbitals (to infinite order) are represented as sums of natural transition orbitals.[277]

[rr] The transformation matrix is always variationally optimized to the second order (Eq. (269)).

$$\phi_i' = \cos(\eta\gamma_i)\,\phi_i^o + \sin(\eta\gamma_i)\,\phi_i^v \tag{270}$$

The eigenvalues $\{\gamma_i\}$ are obtained from the transformation matrix.[277]

$$V^\dagger U W = \gamma 1 \tag{271}$$

The NTOs are obtained from the matrices V and W.

$$\phi_i^o = \sum_j W_{ji}\phi_j \tag{272}$$

$$\phi_i^v = \sum_a V_{ai}\phi_a \tag{273}$$

U to infinite order is varied subject to the constraint[275]

$$\sum_i \sin(\eta\gamma_i)^2 = 1 \tag{274}$$

Finally, SCF-CV(∞)-DFT excitation energies are obtained. Since CV(2)-DFT is comparable to linear-response TD-DFT/TDA, some improvement compared with TD-DFT can be expected already for CV(∞)-DFT.[277] It was indeed shown that higher-order terms of the transformation matrix U can be important especially for charge-transfer and Rydberg excitations.[279]

The NTOs were in fact first proposed by Martin.[278] They provide a very compact description of an electronic excitation in a molecule in terms of single particle-hole amplitudes. The importance of the individual particle-hole excitations i for the overall transition is given by a parameter λ_i. These parameters λ are obtained as the diagonal elements of the transition density matrix T, a diagonal matrix in the basis of the NTOs. The NTOs are obtained by a unitary transformation of the ground-state orbitals (Eq. (272) and (273)). Transformation matrices are in turn obtained as the eigenvectors of $TT^\dagger$ and $T^\dagger T$.[278] Therefore, natural transition orbitals are an equivalent to natural orbitals,[31] which diagonalize the ground-state density matrix.

In the framework of excited-state calculations with DFT, the GW approximation[280] in combination with the Bethe-Salpeter equation[281] (GW-BSE) should be briefly mentioned because such computations on molecules are usually based on the DFT single-particle states, i.e., the Kohn-Sham orbitals. GW calculations for molecules are difficult[160] but in view of the computational and methodological progress, calculating GW-BSE transition energies becomes increasingly feasible.[282] Such calculations can be conceptually divided into (1) determining quasiparticle energies (electron and hole energies) with GW and (2) taking into account the electron-hole interaction via Bethe-Salpeter.[283]

The GW approximation consists in an approximation of the self-energy Σ in the Dyson equation (Eq. (134)). It was already mentioned that the generally non-local energy-dependent self-energy is usually expanded in a perturbation series. In the GW approximation, the series is truncated after the first-order term, i.e., the many-particle self-energy is computed as the product of the single-particle Green's function G_0 and the screened Coulomb interaction W.[283]

$$\Sigma = iG_0 W \tag{275}$$

With the single-particle Green's function G_0 readily available from the orbitals of the KS determinant (Eq. 125)), the many-body Green's function can in principle be obtained (see above). Similarly, the poles of the many-body Green's function – the quasiparticle energies E_{QP} – can then be expressed as sums of the single-particle (zeroth-order) quasiparticle energies – the Kohn-Sham energies – and the self-energy.[283] Kohn-Sham orbital energies are used because they provide the best "zeroth-order guess".[284]

$$E_{QP,i} = \varepsilon_i + \langle \phi_i | \Sigma(E_{QP,i}) - v_{XC} | \phi_i \rangle \tag{276}$$

Using LDA orbitals and subsequently adding the correction (Eq. (276)) to the "frozen orbitals"[283] corresponds to the G_0W_0 scheme. This is standard for solids.[285] Usually, such an LDA@G_0W_0 yields unsatisfying results for molecules.[283,286] Resulting quasiparticle energies can be significantly improved by employing either hybrids/range-separated hybrids instead of LDA or by conducting the calculation in a self-consistent way.[283] For instance, Blase et al.[287] were able to compute very accurate ionization potentials and fundamental gaps of molecules with photovoltaic applications using GW and HF-like orbitals.

The four-point function $L(1,2,3,4) = \frac{\partial G(1,2)}{\partial v^{ext}(3,4)}$ is the key ingredient of the Bethe-Salpeter equation,[283] which introduces the coupling between the GW quasiparticle excitations.[288]

$$L(1,2,3,4) = L_0(1,2,3,4) + \int d(5,6,7,8) L_0(1,2,5,6) K(5,6,7,8) L(7,8,3,4) \tag{277}$$

As outlined by Blase, the four-point function $L(1,2,3,4)$ can be considered as a generalization of the two-point TD-DFT polarizability.[283,284] In fact, the two-point polarizability $\alpha(1,2)$ is equal to a diagonal element of L, $L(1,2,1,2)$. In the GW approximation for the self-energy, the Bathe-Salpeter kernel $K(5,6,7,8)$ is given by[284]

$$K(5,6,7,8) = v(5,7)\delta(5,6)\delta(7,8) + \frac{\partial \Sigma(5,6)}{\partial G(7,8)} \tag{278}$$

$$\approx v(5,7)\delta(5,6)\delta(7,8) - W(5,6)\delta(5,7)\delta(6,8)$$

$v(5,7)$ corresponds to the Coulomb potential. Similar to the adiabatic approximation in linear-response TD-DFT (Eq. (262)), the Bethe-Salpeter kernel is assumed to be time/frequency-independent.[283] $L_0(1,2,3,4)$, the initially uncoupled quasiparticles, can be consistently written as an uncorrelated product.

$$L_0(1,2,3,4) = iG(1,3)G(2,4) \tag{279}$$

The similarity of Eq. (277) to Eq. (260), the fundamental TD-DFT Dyson-like equation, is evident. Using matrices, this becomes evident from a direct comparison.

$$L = L_0 + L_0 K L \tag{280}$$

$$\alpha = \alpha_S + \alpha_S f_{HXC} \alpha \tag{281}$$

Therefore, upon expanding L in an electron-hole basis $\{[\phi_a(\vec{r}_e)\phi_i(\vec{r}_h)]\}$,[283,286] a Casida-like matrix expression (see Eq. (263)) is obtained for the Bethe-Salpeter equation.[284]

$$\begin{pmatrix} R & C \\ -C^* & -R^* \end{pmatrix} \begin{pmatrix} [\phi_a(\vec{r}_e)\phi_i(\vec{r}_h)] \\ [\phi_i(\vec{r}_e)\phi_a(\vec{r}_h)] \end{pmatrix} = \begin{pmatrix} \lambda_{ai} \\ \mu_{ia} \end{pmatrix} \begin{pmatrix} [\phi_a(\vec{r}_e)\phi_i(\vec{r}_h)] \\ [\phi_i(\vec{r}_e)\phi_a(\vec{r}_h)] \end{pmatrix} \tag{282}$$

The matrix R describes the resonant coupling between quasi-electrons and -holes. Its matrix elements are defined as[283]

$$R_{ij}^{ab} = \delta_{ij}\delta_{ab}(E_{QP,a} - E_{QP,i}) + 2(ia|jb) - (ab|W|ji) \tag{283}$$

As pointed out by Blase, the most important difference between the Bethe-Salpeter transition energies (Eq. (283)) and the Casida equation (Eq. (264)) is the leading term. While it corresponds to Kohn-Sham orbital energies in TD-DFT, it is the difference between GW quasiparticle energies in GW-BSE. Since the quasiparticle energies usually describe the fundamental gap of molecules more accurately (except for optimally tuned hybrids[158]), the Bethe-Salpeter transition energies (Eq. (283)) are more intuitive: the interaction between the quasiparticles stabilizes the excitation.[284] Especially self-consistent GW-BSE calculations, which are independent of the starting functional, were shown to provide very accurate transition energies also for challenging cases such as charge-transfer excitations or transitions to state with multiexcitation character.[283]

It should be noted that a plethora of further methods exist to compute quantum-chemical molecular ground and excited states, for instance approaches related to the DMRG (density matrix renormalization group) algorithm. DMRG approaches constitute a completely different route to construct the wave function than the above outlined methods. Without explicitly calculating basis functions and matrix elements, the DMRG algorithm relies on the density matrix and divides the Hilbert space into subblocks that contain important/negligible many-electron basis functions.[289,290]

However, presenting all methods in detail is beyond the scope of this work. The presented selection is necessarily an arbitrary one, and it is motivated by those methods employed in this work (see section "Results and Discussion").

3.3 The quantum-chemical decomposition of intermolecular interactions

A number of energy decomposition analyses (EDAs) of intermolecular interactions have been proposed although the concept of analyzing the intermolecular interaction energy in terms of its electrostatic, dispersion, charge-transfer, etc. contributions is still rather recent.[291] As outlined by Skylaris and coworkers,[291] the existing analyses of intermolecular interactions can be divided into two groups, depending on the underlying theory. On the one hand, the interaction energy is decomposed, which defines the *variational* analysis schemes. On the other hand, the interaction is considered as a perturbation of the non-interacting individual molecules. This corresponds to methods based on *perturbation* theory.[291] Whereas the Morokuma EDA[292] introduced for the interaction via hydrogen bonds is fundamental to most modern variational EDAs,[291] the EDA of Su et al. is presented in the following because it can be applied to DFT interaction energies as well.[293] The presentation focusses on the original version while a more recent adaption of this EDA[294] to the GKS formalism (see above) exists. This modern version improves the analysis of exchange and correlation contributions. SAPT(DFT)[295,296,297,298] is discussed as an example for a perturbative analysis of intermolecular interactions.

3.3.1 The energy decomposition analysis (EDA) of Su et al.[293]

According to Skylaris and coworkers, any variational EDA constructs a number of "intermediate wave functions" that correspond to certain states of the system (for example, one intermediate state includes electrostatics but not dispersion while a second includes both etc.). The energy differences between these intermediate state wave functions directly yield the energy contribution of a given type of interaction (for instance dispersion). As outlined by Skylaris, one of the main differences between the different EDA schemes results from the definition of the intermediate wave functions.[291]

The LMO-EDA (localized molecular orbital) of Su et al.[293] decomposes the intermolecular KS energy into contributions from electrostatics, exchange, repulsion, polarization, and dispersion. It provides a similar decomposition for HF interaction energies but the dispersion component is obtained from correlated *ab initio* calculations. The following outline follows Su et al.[293] The HF expressions are presented first because they are required for the subsequent presentation of the KS contributions.

In an orthogonal basis, the Hartree-Fock energy can be written as

$$E_{HF} = \sum_i^{\alpha\beta} h_{ii} + \frac{1}{2}\sum_{ij}^{\alpha\beta}(ii|jj) - \frac{1}{2}\sum_{ij}^{\alpha}(ij|ij) - \frac{1}{2}\sum_{ij}^{\beta}(ij|ij) + V_{NN}$$

(284)

The Hartree-Fock energy E_{HF} can be equally expressed in a non-orthogonal basis.

$$E_{HF} = \sum_{ij}^{\alpha\beta}\frac{h_{ij}}{S_{ij}} + \frac{1}{2}\sum_{ijkl}^{\alpha\beta}\frac{(ij|kl)}{S_{ij}S_{kl}} - \frac{1}{2}\sum_{ijkl}^{\alpha}\frac{(ik|jl)}{S_{ij}S_{kl}} - \frac{1}{2}\sum_{ijkl}^{\beta}\frac{(ik|jl)}{S_{ij}S_{kl}} + V_{NN}$$

(285)

The intermolecular Hartree-Fock energy ΔE_{HF} is defined as the difference between the HF energy $E_{HF}(X)$ of the supermolecule X and the HF energies $E_{HF}(A)$ of the individual monomers A.

$$\Delta E_{HF} = E_{HF}(X) - \sum_A E_{HF}(A) = \langle\Phi_X|H|\Phi_X\rangle - \sum_A \langle\Phi_A|H|\Phi_A\rangle$$

(286)

As mentioned, the intermolecular energy is decomposed as follows

$$\Delta E_{HF} = \Delta E_{elec} + \Delta E_{ex} + \Delta E_{rep} + \Delta E_{pol}$$

(287)

The non-orthogonal orbitals $\{ij\dots\}$ optimized for the monomer HF determinants $\{\Phi_A\}$ (right-hand term in Eq. (286)) are used in a first, abridged expression for the energy $E_{HF}(X)^{(1)}$ of the supermolecule. (1) It does not include exchange integrals involving orbitals localized on different monomers, and (2) it does not take into account the non-orthogonality of the monomer-derived orbitals. These effects are stepwise included when defining $E_{HF}(X)^{(2)}$ and $E_{HF}(X)^{(3)}$.

$$E_{HF}(X)^{(1)} = \sum_i^{\alpha\beta} h_{ii} + \frac{1}{2}\sum_{ij}^{\alpha\beta}(ii|jj) - \sum_A\left(\frac{1}{2}\sum_{ij\in A}^{\alpha}(ij|ij) + \frac{1}{2}\sum_{ij\in A}^{\beta}(ij|ij)\right) + V_{NN,X}$$

(288)

$$E_{HF}(X)^{(2)} = \sum_i^{\alpha\beta} h_{ii} + \frac{1}{2}\sum_{ij\in X}^{\alpha\beta}(ii|jj) - \frac{1}{2}\sum_{ij\in X}^{\alpha}(ij|ij) - \frac{1}{2}\sum_{ij\in X}^{\beta}(ij|ij) + V_{NN,X}$$

(289)

$$E_{HF}(X)^{(3)} = \sum_{ij}^{\alpha\beta}\frac{h_{ij}}{S_{ij}} + \frac{1}{2}\sum_{ijkl\in X}^{\alpha\beta}\frac{(ij|kl)}{S_{ij}S_{kl}} - \frac{1}{2}\sum_{ijkl\in X}^{\alpha}\frac{(ik|jl)}{S_{ij}S_{kl}} - \frac{1}{2}\sum_{ijkl\in X}^{\beta}\frac{(ik|jl)}{S_{ij}S_{kl}} + V_{NN}$$

(290)

To calculate the approximate energy expressions (Eq. (288) to (290)), all orbitals are ascribed to a monomer. The energy contributions (Eq. (287)) to the total interaction energy are then defined as

$$\Delta E_{elec} = E_{HF}(X)^{(1)} - \sum_A E_{HF}(A)$$

(291)

$$\Delta E_{ex} = E_{HF}(X)^{(2)} - E_{HF}(X)^{(1)}$$

(292)

$$\Delta E_{rep} = E_{HF}(X)^{(3)} - E_{HF}(X)^{(2)} \tag{293}$$

$$\Delta E_{pol} = E_{HF}(X) - E_{HF}(X)^{(3)} \tag{294}$$

Finally, the dispersion component, which is not covered by HF, is obtained as the difference between the HF intermolecular energy and the intermolecular energy obtained with a correlated method (CCSD(T)).

$$\Delta E_{disp} = \Delta E_{CCSD(T)}(X) - \Delta E_{HF}(X) \tag{295}$$

The series of "intermediate wave functions" as outlined by Skylaris and coworkers,[291] which is used to compute the individual energy contributions, becomes evident from Eq. (291) to (295). It follows from Eq. (294) that the polarization energy in the LMO-EDA of Su is defined as the orbital relaxation energy since monomer orbitals are used to compute $E_{HF}(X)^{(3)}$ while supermolecule orbitals are used for the calculation of $E_{HF}(X)$.

The HF formalism can be readily extended to KS-DFT. For that purpose, the Kohn-Sham energy of a system is given for orthogonal orbitals

$$E_{KS} = \sum_{i}^{\alpha\beta} h_{ii} + \frac{1}{2}\sum_{ij}^{\alpha\beta} (ii|jj) + E_c[\rho] + E_x[\rho] + V_{NN} \tag{296}$$

The density ρ in terms of non-orthogonal monomer orbitals $\{\phi_i\}$ is given by (leaving aside the spin)

$$\rho = \sum_{ij} \frac{\phi_i \phi_j}{S_{ij}} \tag{297}$$

Using this definition of the density, the Kohn-Sham energy in a basis of non-orthogonal orbitals can then be represented as

$$E_{KS} = \sum_{ij}^{\alpha\beta} \frac{h_{ij}}{S_{ij}} + \frac{1}{2}\sum_{ijkl}^{\alpha\beta} \frac{(ij|kl)}{S_{ij}S_{kl}} + E_c[\rho] + E_x[\rho] + V_{NN} \tag{298}$$

The Kohn-Sham interaction energy is equivalently to Eq. (286) defined and can be decomposed (Eq. (287)).

$$\Delta E_{KS} = E_{KS}(X) - \sum_{A} E_{KS}(A) = \Delta E_{elec} + \Delta E_{ex} + \Delta E_{rep} + \Delta E_{pol} + \Delta E_{disp} \tag{299}$$

In a similar manner to above, the energy of the Kohn-Sham supermolecule is represented as several successive approximate energy expressions (Eq. (300) to (303)). ρ_X^* is the density calculated with Eq.

(297) and orthonormal monomer orbitals. It should be noted that $\rho_X^* \neq \sum_a \rho_A$ since the overlap matrix is not a unit matrix.

$$E_{KS}(X)^{(1)} = \sum_i^{\alpha\beta} h_{ii} + \frac{1}{2}\sum_{ij}^{\alpha\beta} (ii|jj) + \sum_A (E_c[\rho_A] + E_x[\rho_A]) + V_{NN,X} \tag{300}$$

$$E_{KS}(X)^{(2)} = \sum_i^{\alpha\beta} h_{ii} + \frac{1}{2}\sum_{ij}^{\alpha\beta} (ii|jj) + \sum_A E_c[\rho_A] + E_x\left[\sum_A \rho_A\right] + V_{NN,X} \tag{301}$$

$$E_{KS}(X)^{(3)} = \sum_{ij}^{\alpha\beta} \frac{h_{ij}}{S_{ij}} + \frac{1}{2}\sum_{ijkl}^{\alpha\beta} \frac{(ij|kl)}{S_{ij}S_{kl}} + \sum_A E_c[\rho_A] + E_x[\rho_X^*] + V_{NN} \tag{302}$$

$$E_{KS}(X)^{(4)} = \sum_i^{\alpha\beta} h_{ii} + \frac{1}{2}\sum_{ij}^{\alpha\beta} (ii|jj) + \sum_A E_c[\rho_A] + E_x[\rho] + V_{NN} \tag{303}$$

Orthonormal supermolecule orbitals are employed for the calculation of $E_{KS}(X)^{(4)}$ (Eq. (303)). The contributions to the Kohn-Sham interaction energy are defined as

$$\Delta E_{elec} = E_{KS}(X)^{(1)} - \sum_A E_{KS}(A) \tag{304}$$

$$\Delta E_{ex} = E_{KS}(X)^{(2)} - E_{KS}(X)^{(1)} \tag{305}$$

$$\Delta E_{rep} = E_{KS}(X)^{(3)} - E_{KS}(X)^{(2)} \tag{306}$$

$$\Delta E_{pol} = E_{KS}(X)^{(4)} - E_{KS}(X)^{(3)} \tag{307}$$

$$\Delta E_{disp} = E_{KS}(X) - E_{KS}(X)^{(4)} \tag{308}$$

As outlined by Su, exchange and dispersion in the KS-formalism are defined by changes in the exchange and correlation functionals when changing from the monomer to the supermolecule density. In contrast to many other variational EDAs, exchange and repulsion are separated. Furthermore, as emphasized by Su, since no charge-transfer contributions are included, the EDA is basis-set insensitive. Moreover, calculations with counterpoise corrected monomer orbitals (i.e., using the basis set of the supermolecule) are also available.[293]

The variational LMO-EDA can be compared to an analysis based on SAPT (symmetry-adapted perturbation theory), a perturbational approach presented in the next section. It should be stressed that SAPT(DFT) closely follows the underlying SAPT[299] approach based on MP2 (or CCSD), which is addressed first. In contrast to LMO-EDA, which relies on supermolecule calculations and determines

the interaction energy as the difference to monomer energies (Eq. (286), (299)), SAPT directly calculates the interaction energy.[300]

3.3.2 Symmetry Adapted Perturbation Theory (SAPT) and SAPT with DFT[295,296,297,298]

SAPT-MP2 is not only employed to analyze intermolecular interactions,[299] but it constitutes also a viable route to obtain accurate interaction potentials of CCSD(T)-like quality.[298] As outlined by Jeziorski et al.,[299] the conceptually simplest perturbation treatment of intermolecular interactions is polarization theory: Rayleigh-Schrödinger perturbation theory, the starting point for Møller-Plesset perturbation theory as well, is adapted to intermolecular interactions. The zeroth-order Hamiltonian H_0 is defined as the sum of the monomer Hamiltonians H_A, H_B (Eq. (309)). Consistently, the zeroth-order energy $\mathrm{E}^{(0)}$ is the sum of the monomer energies E_A, E_B, with the zeroth-order wave function $\Psi^{(0)}$ arising as the product of the monomer wave functions.

$$H = H_0 + \lambda V = (H_A + H_B) + \lambda V \tag{309}$$

$$\Psi^{(0)} = \Psi_A \Psi_B \tag{310}$$

$$\mathrm{E}^{(0)} = E_A + E_B \tag{311}$$

The perturbation operator V is the sum of all Coulomb interactions between electrons and nuclei. According to Jeziorski et al.,[299] it is often designated as the intermolecular interaction operator. Higher-order terms of the energy and the wave function are obtained from the series expansions in λ (Eq. (31) and (32)). These series expansions are often called polarization expansions and polarization energies.[301] It follows from the basics of Rayleigh-Schrödinger perturbation theory[36] that in intermediate normalization (Eq. (313), Ψ is the final wave function), the n-th order energy can be expressed as a function of the (n-1)th-order wave function.

$$\mathrm{E}^{(n)} = \left\langle \Psi^{(0)} \middle| V \middle| \Psi^{(n-1)} \right\rangle \tag{312}$$

$$\left\langle \Psi^{(0)} \middle| \Psi \right\rangle = 1 \tag{313}$$

Similarly, by means of a recurrence formula, the Bloch form,[302] the n-th order wave function can be derived from the (n-1)th-order wave function.[300]

$$\Psi^{(n)} = \Psi^{(0)} + R_0 \left(\mathrm{E}^{(n)} - V \right) \Psi^{(n-1)} \tag{314}$$

$$R_0 = \frac{1 - \left| \Psi^{(0)} \right\rangle \left\langle \Psi^{(0)} \right|}{H_0 - E_0 + \left| \Psi^{(0)} \right\rangle \left\langle \Psi^{(0)} \right|} \tag{315}$$

The first-order polarization energy can then be written as

$$\mathrm{E}^{(1)} = \left\langle \Psi^{(0)} \middle| V \middle| \Psi^{(0)} \right\rangle = \int \int d\vec{r}_A d\vec{r}_B \frac{|\Psi_A|^2 |\Psi_B|^2}{|\vec{r}_A - \vec{r}_B|} = E_{elec} \tag{316}$$

Since it corresponds to the Coulomb interaction between the charge densities associated with monomers A and B, the first-order polarization energy $\mathrm{E}^{(1)}$ can be considered as the electrostatic interaction energy E_{elec}.[299]

The second-order polarization energy is given by an MP2-like expression. $\{\Psi_m\}$ designates the ensemble of excited states of $\Psi^{(0)} = \Psi_A \Psi_B$.

$$\mathrm{E}^{(2)} = -\left\langle \Psi^{(0)} \middle| V \middle| \Psi^{(1)} \right\rangle = -\sum_{m \neq 0} \frac{\left| \left\langle \Psi^{(0)} \middle| V \middle| \Psi_m \right\rangle \right|^2}{E_m - E_0} \tag{317}$$

The basis of excited states $\{\Psi_m\}$ is further subdivided. On the one hand, the excitations in $\{\Psi_m\}$ can be localized on a single monomer, i.e., if the involved excitations belong to the same monomer $\left\{ \Psi_m^{A \to A}_{B \to B} \right\}$. On the other hand, the excitations can include intermonomer excitations $\left\{ \Psi_m^{A \to B}_{B \to A} \right\}$.

The states $\left\{ \Psi_m^{A \to A}_{B \to B} \right\}$ correspond to an excited molecule next to a ground-state molecule. As comprehensively discussed above and outlined by Szalewizc,[303] such a molecular excitation can be interpreted as the response of the molecule to the static external charge distribution of the second molecule. Thus this part of the second-order polarization energy is defined as the induction (polarization) energy.[299]

$$E_{ind}^{(2)} = -\sum_{m \neq 0} \frac{\left| \left\langle \Psi^{(0)} \middle| V \middle| \Psi_m^{A \to A}_{B \to B} \right\rangle \right|^2}{E_m - E_0} \tag{318}$$

The corresponding expression with intermonomer excitations, i.e, the difference between the total second-order polarization energy and the induction energy, is associated with the dispersion energy.

$$E_{disp}^{(2)} = \mathrm{E}^{(2)} - E_{ind}^{(2)} = -\sum_{m \neq 0} \frac{\left| \left\langle \Psi^{(0)} \middle| V \middle| \Psi_m^{A \to B}_{B \to A} \right\rangle \right|^2}{E_m - E_0} \tag{319}$$

As a purely quantum-mechanical effect, the dispersion does not have a classical interpretation. It results from correlated density fluctuations in the monomers.[303,296]

In a similar way, the third-order polarization energy can be subdivided into a third-order induction, a third-order dispersion, and a coupled induction-dispersion term, depending on where the excitations are localized.[299]

$$\mathrm{E}^{(3)} = E_{ind}^{(3)} + \left(\mathrm{E}^{(3)} - E_{ind}^{(3)} \right) = E_{ind}^{(3)} + E_{disp}^{(3)} + E_{ind-disp}^{(3)} \tag{320}$$

Thus, up to the third order, the polarization energies have a physical interpretation and can be related to monomer properties.[299] However, among others, Adams outlined that the polarization perturbation expansion converges slowly and diverges for systems with more than two electrons.[304] Most importantly, this results from the definition of the zeroth-order Hamiltonian $H_A + H_B$. It ascribes the electrons to one of the monomers and thus violates their indistinguishability.[299] Consequently, the zeroth-order wave function is a poor starting point to describe exchange interactions and resonance coupling between the monomers,[305,306] which are therefore only retrieved at very high orders of the perturbation expansion.[299] As a consequence, polarization theory is for instance incapable of describing van-der-Waals minima.[303]

To eliminate this deficiency, the antisymmetrized zeroth-order wave function $\Psi^{(0)} = \mathcal{A}(\Psi_A \Psi_B)$ is a better starting point (with $\mathcal{A}$ being the antisymmetrization operator). With this modified zeroth-order wave function, the Rayleigh-Schrödinger perturbation formalism can no longer be employed if the zeroth-order Hamiltonian $H_0 = H_A + H_B$ is maintained, which is indeed the case. This results because $\mathcal{A}(\Psi_A \Psi_B)$ is not an eigenfunction to H_0.[299] A number of symmetry-adapted perturbation theories exist.[299] They are now summarized under the common name of SAPT.[300] In most SAPT calculations, one uses[303] usually the conceptually and computationally rather simple symmetrized Rayleigh-Schrödinger perturbation theory (SRS).[307] It is based on the standard Rayleigh-Schrödinger (RS) expressions for the wave function (Eq. (32)). However, when calculating the energies (Eq. (30)), the antisymmetrization operator is inserted.[307,308] With Eq. (312), (314) and (315), this yields the following general energy expression for the n-th order energy

$$E^{(n)} = \frac{1}{\langle \Psi^{(0)} | \mathcal{A} \Psi^{(0)} \rangle} \left[\langle \Psi^{(0)} | V | \mathcal{A} \Psi_{RS}^{(n-1)} \rangle - \sum_{k=1}^{n-1} E^{(k)} \langle \Psi^{(0)} | \mathcal{A} \Psi_{RS}^{(n-k)} \rangle \right] \tag{321}$$

The SAPT exchange energy $E_{ex}^{(n)}$ is then defined at each order of perturbation n as the difference between the SRS and the RS energies.[307]

$$E_{ex}^{(n)} = E^{(n)} - E_{RS}^{(n)} \tag{322}$$

The discussion up to this point has assumed that the exact monomer energies are available, which is not the case for many-electron systems. Furthermore, it has already been noted that before SAPT with DFT came to use, SAPT was most often used in combination with MP2 calculations on the monomers. Due to the MP2 partitioning of the monomer Hamiltonians H_A, H_B into the Fock operators F_A, F_B and the fluctuation potential, in the following called W, the ultimate zeroth-order Hamiltonian of SAPT-MP2 corresponds to the sum of the Fock operators.

$$H = H_0 + W + V = (F_A + F_B) + (W_A + W_B) + V \tag{323}$$

It is evident from Eq. (323) that two perturbation operators exist so that, as stated by Szalewizc,[307] SAPT is a "double perturbation theory". This is reflected in the fact that the energy contributions $E^{(ij)}$ to the total intermolecular energy E_{int} have two different orders i, j in V, W, respectively. Due to Eq. (322), the sum can be further divided into contributions from RS theory and exchange interactions.[300]

$$E_{int} = \sum_{i=1} \sum_j E^{(ij)} = \sum_{i=1} \sum_j \left(E_{RS}^{(ij)} + E_{ex}^{(ij)} \right) \tag{324}$$

In view of the interpretation of the polarization energies (Eq. (316), (318)-(320)), the energy corrections of order i in Eq. (324) can be ascribed to the different interaction types from polarization theory. Therefore, the exchange energy (Eq. (322)) can be equally related to an energy component. According to Szalewicz, the energy components are defined in terms of the SAPT terms as follows:[300]

$$E_{elec} = E_{elec}^{(10)} + E_{elec,resp}^{(12)} + E_{elec,resp}^{(13)} \tag{325}$$

$$E_{ind} = E_{ind,resp}^{(20)} + {}^tE_{ind,resp}^{(22)} \tag{326}$$

$$E_{disp} = E_{disp}^{(20)} + E_{disp}^{(21)} + E_{disp}^{(22)} \tag{327}$$

$$E_{ex} = E_{ex}^{(10)} + \epsilon_{ex}^{(1)}(MP2) + E_{ex-ind,resp}^{(20)} + {}^tE_{ex-ind}^{(22)} + E_{ex-disp}^{(20)} \tag{328}$$

$resp$ indicates that the calculations are performed with monomer orbitals distorted in the field of the second monomer ($\approx$ responding orbitals, coupled HF contributions are included[303]). ${}^tE_{ind,resp}^{(22)}, {}^tE_{ex-ind}^{(22)}$ recollect all (exchange)-induction components that are not included in the calculations with distorted orbitals. $\epsilon_{ex}^{(1)}(MP2)$ provides the contribution of the intramonomer correlation to the total exchange interaction.[300] An exemplary calculation can be found in [309]. Third-order expressions for SAPT were also developed.[310]

As outlined by Szalewizc,[303] the different SAPT terms in Eq. (325) to (328) can also be related to the intermolecular interaction energy obtained in a supermolecular approach, for example at the MP2 level.[311] Hence, the HF and MP2 interaction energies ΔE_{HF} and ΔE_{MP2} in terms of the above lowest-order SAPT-MP2 components are given by

$$\Delta E_{HF} \approx E_{elec}^{(10)} + E_{ex}^{(10)} + E_{ind,resp}^{(20)} + E_{ex-ind,resp}^{(20)} + \cdots \tag{329}$$

$$\Delta E_{MP2} \approx E_{disp}^{(20)} + E_{ex-disp}^{(20)} + E_{elec,resp}^{(12)} + \epsilon_{ex}^{(1)}(MP2) + \cdots \tag{330}$$

In fact, Eq. (329) is often rearranged, defining the quantity δE_{int}^{HF}.

$$\delta E_{int}^{HF} = \Delta E_{HF} - \left(E_{elec}^{(10)} + E_{ex}^{(10)} + E_{ind,resp}^{(20)} + E_{ex-ind,resp}^{(20)} \right) \tag{331}$$

This quantity recollects all higher-order induction and exchange terms and should be small. It is added to the sum of the other SAPT expressions ((325) to (328)). However, as emphasized by Szalewicz et al., this is an approximation because no direct, theoretically grounded relationship between SAPT interaction energies and supermolecular interaction energies exists. It was indeed shown that δE_{int}^{HF} improves interaction energies only for intermolecular potentials between polar or polarizable substances.[300]

It is important to point out that in contrast to variational EDA approaches and the supermolecule interactions in Eq. (329) and (330), SAPT, which relies entirely on monomer calculations, is free of the basis set superposition error (BSSE). SAPT computations were indeed employed to validate the quality of counterpoise corrections (CPs).[307] However, the very high accuracy of SAPT-MP2, which is comparable to CCSD(T),[303,312,313] comes at the expense of an equivalent CCSD(T)-like scaling behavior as N^7. Especially the treatment of the intramonomer MP2 correlation is computationally demanding in SAPT-MP2.[298] Moreover, it is well-known[31] that increasing the accuracy is a two-dimensional process. Correlated methods, such as MP2, require therefore large basis sets,[307] making the computations even more demanding.

Since correlation is in principle included in DFT, SAPT(DFT), or DFT-SAPT,[ss] is computationally more efficient than SAPT-MP2.[303] Chabalowski and coworker[314] suggested to replace the HF orbitals in Eq. (325) to (328) with Kohn-Sham orbitals. The SAPT interaction energy can then be obtained to second order as[300]

$$E \approx E_{elec}^{(10)} + E_{ex}^{(10)} + E_{ind}^{(20)} + E_{ex-ind}^{(20)} + E_{disp}^{(20)} + E_{ex-disp}^{(20)} \tag{332}$$

The double-perturbation treatment thus reduces to a single perturbative step; only the intermolecular interaction operator V needs to be considered while the zeroth-order Hamiltonian corresponds to the sum of the molecular Kohn-Sham operators. This decreases the number of terms required to obtain E and considerably improves the scaling behavior of SAPT(DFT)/DFT-SAPT approaches, which amounts to N^5 if density fitting is employed (equivalent to the RI approximation).[298,303]

The initial results of Chabalowski and coworker[314] were rather poor. However, Misquitta et al.[315] demonstrated that the failure was related to the wrong asymptotic behavior of the exchange-correlation potential. Therefore, if the monomer exchange-correlation potentials are corrected, for

---

[ss] It should be noted that a number of different implementations exist that combine SAPT with DFT. Although they are not completely equivalent, their results are almost equal.[303]

instance via IP-tuning of the underlying hybrid functional, very accurate electrostatic, induction, and exchange contributions compared with regular SAPT are obtained.[300] Different approaches were suggested to incorporate dispersion interactions, which are a priori not covered by DFT, into SAPT with DFT.[300] Misquitta et al. proposed to compute the DFT dispersion energies via the frequency-dependent polarizabilities (see above) obtained from TD-DFT calculations.[295] Dispersive interactions can readily be calculated from polarizabilities.[316] This defines the SAPT(DFT) procedure.[300] A similar procedure was developed by Heßelmann and Jansen.[297]

As outlined by Heßelmann, Jansen and Schütz, the components of the SAPT(DFT) energy (Eq. (332)) can be directly expressed as a function of the monomer Kohn-Sham determinants (zeroth-order wave functions) $\{\Phi_0^A, \Phi_0^B\}$. Orbitals are often obtained in a dimer-based basis.[298] The antisymmetrizer $\mathcal{A}$ is rewritten in terms of the permutation operator $\mathcal{P} = \mathcal{A} - 1$ that permutes all electrons, electron pairs, etc. m, n designate the excited states on monomers A, B. i, a are occupied and virtual orbitals localized on A with j, b being the counterparts for B. Some exchange integrals are approximated via the square of the overlap S^2 (Eq. (336)).[298]

$$E_{elec}^{(1)} = \left\langle \Phi_0^A \Phi_0^B \middle| V \middle| \Phi_0^A \Phi_0^B \right\rangle \tag{333}$$

$$E_{ex}^{(1)} = \frac{\left\langle \Phi_0^A \Phi_0^B \middle| \left(V - E_{RS}^{(1)} \right) \mathcal{P} \middle| \Phi_0^A \Phi_0^B \right\rangle}{\left\langle \Phi_0^A \Phi_0^B \middle| 1 + \mathcal{P} \middle| \Phi_0^A \Phi_0^B \right\rangle} \tag{334}$$

$$E_{ind}^{(2)} = -\sum_{m \neq 0} \frac{\left| \left\langle \Phi_0^A \Phi_0^B \middle| V \middle| \Phi_m^A \Phi_0^B \right\rangle \right|^2}{E_m^A - E_0^A} - \sum_{n \neq 0} \frac{\left| \left\langle \Phi_0^A \Phi_0^B \middle| V \middle| \Phi_0^A \Phi_n^B \right\rangle \right|^2}{E_n^B - E_0^B} \tag{335}$$

$$E_{ex-ind}^{(2)}(S^2) = \left\langle \Phi_0^A \Phi_0^B \middle| \left(V - E_{RS}^{(1)} \right) (\mathcal{P} - S^2) \middle| \Phi_{ind}^{(1)} \right\rangle \tag{336}$$

$$E_{disp}^{(2)} = \left\langle \Phi_0^A \Phi_0^B \middle| V \middle| \Phi_{disp}^{(1)} \right\rangle = 4 \sum_{ia,jb} T_{ia,jb}(ia|jb) \tag{337}$$

$$E_{ex-disp}^{(2)}(S^2) = \left\langle \Phi_0^A \Phi_0^B \middle| \left(V - E_{RS}^{(1)} \right) (\mathcal{P} - S^2) \middle| \Phi_{disp}^{(1)} \right\rangle \tag{338}$$

$\Phi_{ind}^{(1)}$ (Eq. (336)) is defined by $E_{ind}^{(2)}$. The amplitudes $\{T_{ia,jb}\}$ can be obtained from the frequency-dependent polarizabilities, i.e, the linear-response function. As emphasized by Szalewicz, according to Eq. (337), also higher-order multipoles and short-range dispersion effects are included in the dispersion component compared with the conventional R^{-6}-type interaction that relies exclusively on induced dipoles.[300] Heßelmann et al. similarly point out that the influence of higher-order terms at the uncorrelated level can be estimated from δE_{int}^{HF} (Eq. (331)) (similar to SAPT-MP2, see above).[298]

SAPT(DFT) provides a very efficient and accurate route to calculate intermolecular energies. Due to its favorable cost-accuracy ratio, it can be applied to dimers composed of up to 100 atoms.[303]

3.4 Continuum Solvation Models in Quantum-Chemical Calculations

Depending on whether solvation effects on a ground-state molecule or on an electronic excitation are computed, different variants of continuum solvation models can be distinguished that are presented in the following.

3.4.1 Equilibrium solvation in the ground state

Tomasi et al. define continuum solvation models as models in which a distribution function is employed to describe a large number of the degrees of freedom of the composing particles of a system.[317] Continuum solvation models are based on a decomposition of the system into two parts:[31] a core part, the solute, which is in the focus of the investigation,[317] and the environment, the solvent. As outlined by Tomasi et al.,[317] the Hamiltonian $H_{tot}(\vec{R}_{core}, \vec{R}_{env})$ can thus be written as the sum of the Hamiltonian of the core subsystem $H_{core}(\vec{R}_{core})$, the Hamiltonian of the environment $H_{env}(\vec{R}_{env})$, and the Hamiltonian for the interaction between the two systems $H_{int}(\vec{R}_{core}, \vec{R}_{env})$. $\vec{R}_{core}$ recollects all degrees of freedom of the core system while $\vec{R}_{env}$ includes the degrees of freedom of the environment.

$$H_{tot}(\vec{R}_{core}, \vec{R}_{env}) = H_{core}(\vec{R}_{core}) + H_{env}(\vec{R}_{env}) + H_{int}(\vec{R}_{core}, \vec{R}_{env}) \tag{339}$$

In order to reduce the number of degrees of freedom in the system, an effective Hamiltonian is defined from Eq. (339). Firstly, the Hamiltonian for the environment $H_{env}(\vec{R}_{env})$ is neglected. Thus the environment itself is not explicitly considered. Secondly, the degrees of freedom of the environment are eliminated from the interaction Hamiltonian. This is achieved by introducing a continuous solvent response function $Q(\vec{r}, \vec{r}')$ that depends only on a pair of position vectors $\vec{r}$ and $\vec{r}'$.

$$H_{eff}(\vec{R}_{core}, \{\vec{r}, \vec{r}'\}) = H_{core}(\vec{R}_{core}) + H_{int}\left(\vec{R}_{core}, Q(\vec{r}, \vec{r}')\right) \tag{340}$$

To specify the response function and thus $H_{int}\left(\vec{R}_{core}, Q(\vec{r}, \vec{r}')\right)$, the decomposition of the system requires a more detailed consideration. A key quantity in all continuum solvation approaches is the so-called cavity. The solute is placed into a "hole",[31] the cavity, in the solvent environment, which is assumed to be isotropic.[317,318] As emphasized by Tomasi et al.,[317] the cavity should include the solute as completely as possible[tt] to avoid unbalanced results for the interactions with the solvent. Therefore

---

[tt] It should be noted that due to the exponential decay of the electronic density of a molecule, it is never completely included in the cavity. The remaining parts of the density outside of the cavity are referred to as the "outlying charge".[317,1013,1014]

using spherical or ellipsoidal cavities is strongly discouraged although solute-solvent interactions can be analytically calculated for such symmetric cavity shapes. Instead, due to its favorable cost-accuracy ratio, a van-der-Waals surface of the solute is most often used in practice to define the cavity.[31] Van-der-Waals surfaces of the solute are obtained by interlocking atomic spheres (placed on all atoms of the solute) with radii defined by tabulated van-der-Waals radii. Different tabulations exist, for instance by Bondi.[319] Nevertheless, as pointed out by Jensen[31] and by Tomasi et al.,[317] the van-der-Waals surface might still contain small "pockets" that are inaccessible to solvent molecules. Thus the concepts of the solvent accessible surface (SAS)[320] and of the solvent excluded surface (SES)[321] were developed that slightly modify the van-der-Waals surface.[317] To derive these surfaces, a spherical probe that represents a solvent molecule rolls on the van-der-Waals surface. The positions of its center of mass define the SAS. If the positions of closest contact to the solute are used instead, the SES is obtained.[317] An alternative intuitive approach to model the cavity, proposed by Frisch and Wiberg and coworkers, is the isodensity surface: the cavity boundary corresponds to a certain isovalue of the electronic density.[322]

If the cavity is defined, the interaction Hamiltonian $H_{int}\left(\vec{R}_{core}, Q(\vec{r}, \vec{r}')\right)$ can in principle be defined. To do this, the free energy of solvation ΔG_{solv} is considered. It should be noted that the initial state in continuum solvation models is the pure liquid phase. To arrive at the final system, a cavity is created, and the solute is placed in the cavity. The "driving force" for this process, i.e., the free energy of solvation ΔG_{solv},[uu] is usually represented as a sum of four terms: an electrostatic term ΔG_{elec} (including polarization/induction, see above), a dispersion and a repulsion term $\Delta G_{disp}, \Delta G_{rep}$, and the free energy required to create the cavity, a cavity formation term ΔG_{cav}.[31]

$$\Delta G_{solv} = \Delta G_{elec} + \Delta G_{disp} + \Delta G_{rep} + \Delta G_{cav} \tag{341}$$

The individual contributions to ΔG_{solv} can either explicitly depend on the electronic structure of the solute, or they can be expressed as empirical/classical formulas containing fit parameters. In the latter case, they enter the effective Hamiltonian (Eq. (340)) only parametrically. They are thus simply added to the total self-consistent QM energy.[317] In the former case, however, they must be included in the self-consistent iteration.

[uu] It should be noted that due to the thermodynamic definition of the free energy, a term for the work $p\Delta V$ should be actually included in the definition for the ΔG_{solv} (Eq. (341)). When using continuum solvation models with *ab initio* methods, the work is, however, not included. Moreover, the *ab initio* calculations are usually based on the Born-Oppenheimer approximation (Eq. (4)-(6)). In the solvated state, the nuclear degrees of freedom of the solute are thus eliminated. However, they are explicitly considered in the reference state (an ideal state composed of the pure liquid and the non-interacting electrons and nuclei). This results in an additional contribution to ΔG_{solv} (Eq. (341)).[317]

Most continuum solvation methods differ mainly in the way they include the electrostatic contribution ΔG_{elec} in the effective Hamiltonian.[31] This is to some extent due to historical reasons: in the well-known Born model based on classical electrostatics, the solvation process is described only with electrostatics.[323] Several approaches to model ΔG_{elec} will be presented below. In contrast, the remaining contributions $\Delta G_{disp} + \Delta G_{rep} + \Delta G_{cav}$ are most often either neglected or calculated in a semiclassical/empirical manner.

Approaches to calculate the cavity formation energy ΔG_{cav} were comprehensively reviewed by Tomasi and Persico.[318] Meanwhile, computer simulations have proven to be an invaluable tool to get accurate reference values for cavity formation energies.[317] Cavity formation energies are usually evaluated either by statistical mechanics or from the solute surface exposed to the solvent by means of the surface tension.[324] In fact, since the evaluation of real liquid properties by hard sphere fluids in statistical mechanics was problematic, the so-called scaled-particle theory based on statistical mechanics is employed to derive ΔG_{cav} values.[325,326] It relies only on atomic radii and number densities of the solvent.

Although quantum-mechanical expressions for the repulsion term were proposed for example by Amovilli and Mennucci,[327] thus enabling an inclusion of the repulsion in the effective Hamiltonian (Eq. (340)), the repulsion is treated classically in most continuum solvation models. It is usually computed from the SAS and empirically fitted parameters.[328] Furthermore, the dispersion contribution ΔG_{disp} is commonly combined with the repulsion in a similar classical expression, yielding a combined dispersion-repulsion contribution. As outlined by Tomasi et al.,[317] this procedure is approximate especially in view of the different ranges of action of repulsion and dispersion. In order to include the dispersion in the quantum-mechanical treatment, it must be expressed as a function of the electronic structure of the solute. Based on the above mentioned relationship between dispersion and polarizability, several expressions were derived.[328] Nevertheless, due to the significantly increased computational cost, most implementations of continuum solvation approaches resort to empirical expressions of the dispersion interactions.[317,329]

Thus, in most applications of continuum solvation models, the combined effect of $\Delta G_{disp} + \Delta G_{rep} + \Delta G_{cav}$ can be directly – or indirectly via sums over atomic-specific parameters – computed from the SAS (β, γ are fit parameters).[31]

$$\Delta G_{disp} + \Delta G_{rep} + \Delta G_{cav} = \gamma SAS + \beta \qquad (342)$$

As already mentioned, the sum is added as a parameter to the QM energy. In contrast, the electrostatic component ΔG_{elec} (Eq. (341)) is treated differently, which is discussed in more detail in the following.

In fact, the charge density of the solute, $\rho_S(\vec{r})$, polarizes the surrounding solvent, which results in turn in back polarization of the solute.[317] Thus, the electrostatic component ΔG_{elec} gives rise to an additional term in the effective interaction Hamiltonian (Eq. (340)), an electric potential of the surrounding that depends on the charge density of the solute $V_R(\vec{r})$.[317] Due to the relation to the traditional Onsager's theory,[330] this potential is often designated as the "solvent reaction field".[317] A non-linear problem results because the equation – via $V_R(\vec{r}) = V_R[\rho_S(\vec{r})](\vec{r})$ – depends on its solution $\rho_S(\vec{r})$. It must be hence solved iteratively.[317]

The Poisson equation relates the electric potential $V(\vec{r})$ to the charge distribution $\rho_S(\vec{r})$ and the dielectric constant $\varepsilon(\vec{r})$. If the dielectric constant $\varepsilon(\vec{r})$ does not depend on the position, the Poisson equation is given, for all positions $\{\vec{r}\}$ inside the cavity, by[31,317]

$$\nabla^2 V(\vec{r}) = \nabla^2\big(V_S(\vec{r}) + V_R(\vec{r})\big) = -4\pi\rho_S(\vec{r}) \tag{343}$$

Outside the cavity, no charge density exists.[317]

$$-\varepsilon\nabla^2 V(\vec{r}) = -\varepsilon\nabla^2\big(V_S(\vec{r}) + V_R(\vec{r})\big) = 0 \tag{344}$$

The electric potential in Eq. (343) is composed of the potential created by the molecular charge density $V_S(\vec{r})$ and the reaction potential $V_R(\vec{r})$.[317] Several boundary conditions exist for the potential $V(\vec{r})$, i.e., the solution of Eq. (343), most notably the continuous progression of $V(\vec{r})$ and its first derivative, the electric field, across the cavity surface Γ.[317] Therefore, Tomasi et al.[317] designate them as "jump conditions".

$$[V] = V_{in} - V_{out} = 0 \qquad\qquad on\ \Gamma \tag{345}$$

$$[\partial V] = \left(\frac{\partial V}{\partial\vec{n}}\right)_{in} - \varepsilon\left(\frac{\partial V}{\partial\vec{n}}\right)_{out} = 0 \qquad on\ \Gamma \tag{346}$$

The dielectric constant ε inside the cavity is assumed to be 1. $\vec{n}$ is the cavity surface vector pointing outward.

From $V_R(\vec{r})$ and $\rho_S(\vec{r})$, the electrostatic component of the free energy of solvation and the effective interaction Hamiltonian of the solute are readily accessible.

$$\Delta G_{elec} = \frac{1}{2}\int d\vec{r}\,\rho_S(\vec{r})V_R(\vec{r}) \tag{347}$$

Tomasi and Persico proposed a classification of continuum solvation models depending on the way they proceed in solving Eq. (343) or Eq. (347).[318] As also emphasized by Tomasi et al. in a later review[317], the models can be subdivided into six categories: (1) the apparent surface charges models (ASC), (2) the multipole expansion methods (MPE), (3) the generalized Born approximation (GBA), (4) the image

charge methods (IMC), (5) the finite element methods (FEM), and (6) the finite difference methods (FDM). As only ASC-type models were employed in this thesis, only the first group is presented in more detail. It is, however, important to keep in mind that several further *conceptually different* approaches exist to model continuum solvation.

ASC methods considerably simplify the computation of the three-dimensional reaction field $V_R(\vec{r}) = V_R[\rho_S(\vec{r})](\vec{r})$. Firstly it is reduced to a two-dimensional problem that is secondly, via discretization, converted into a summation. This is achieved, as already indicated by the name, by means of the key ingredient of ASC models, an apparent surface charge on the cavity surface $\sigma(\vec{s}), \vec{s} \in \Gamma$. It follows that the potential created by the surface charge $V_\sigma(\vec{r})$, which corresponds to the reaction potential $V_R(\vec{r})$, can be computed as[317]

$$V_\sigma(\vec{r}) = V_R(\vec{r}) = \int_\Gamma d^2\vec{s}\, \frac{\sigma(\vec{s})}{|\vec{s} - \vec{r}|} \tag{348}$$

The cavity surface is then subdivided into small finite elements, called tesserae, with surfaces $\{A_k\}$. The surface charges on these tesserae $\{\sigma_k\}$ are then approximately constant so that the reaction field potential can be rewritten as[317]

$$V_\sigma(\vec{r}) = V_R(\vec{r}) \cong \sum_k \frac{\sigma_k(\vec{s}_k)A_k}{|\vec{s}_k - \vec{r}|} = \sum_k \frac{q_k}{|\vec{s}_k - \vec{r}|} \tag{349}$$

It is evident from Eq. (349) that the reaction field $V_\sigma(\vec{r})$ is accessible if the surface charge distribution is available. Eq. (349) is the common ingredient in all ASC methods.[317] They differ, however, in terms of their expressions for $\sigma(\vec{s})$.

The oldest ASC method is PCM, the polarizable continuum model.[331] Its original version is nowadays called D-PCM (dielectric). The most important follow-up versions are designated as C-PCM[332,333] (conductor) and IEFPCM[334] (integral equation formalism), the latter of which is formulated in terms of Green's functions.[317] Furthermore, an IPCM exists as well that relies on cavities defined from isosurfaces.[322]

In order to obtain the fundamental equation of PCM models, it follows from Gauss's law (i.e., the first Maxwell equation $\nabla(\varepsilon_0 \vec{E} + \vec{P}) = \nabla \varepsilon_0 \vec{E} = 4\pi\rho$) and the boundary condition of the Poisson equation (Eq. (346)) that a surface charge $\sigma(\vec{s})$ between two media i, j is given by the difference of the polarization vectors P_i, P_j. $\vec{n}_{ij}$ is a unit vector from medium i to medium j.

$$\sigma(\vec{s}) = -(\vec{P}_j - \vec{P}_i)\vec{n}_{ij} \tag{350}$$

The polarization can readily be expressed in terms of the gradient of the potential $\nabla V(\vec{r})$, the electric field strength.

$$\vec{P}_j = \frac{\varepsilon_j - 1}{4\pi} \vec{\nabla} V(\vec{r}) \tag{351}$$

Furthermore, the dielectric constant ε_j of the cavity is assumed to be 1. Thus no polarization exists within the cavity (Eq. (351)). Thus, the surface charge is given by

$$\sigma(\vec{s}) = \frac{(\varepsilon_j - 1)}{4\pi} \frac{\partial V(\vec{r})}{\partial \vec{n}} = \frac{(\varepsilon_j - 1)}{4\pi} \frac{\partial (V_S(\vec{r}) + V_R(\vec{r}))}{\partial \vec{n}} \tag{352}$$

For PCM, Eq. (348), (349) and (352) form a pair of coupled equations that can be solved iteratively. As pointed out by Tomasi and Persico, an initial guess is created for the surface charge distribution from Eq. (352) (assuming for instance $V_R(\vec{r}) \approx 0$). Then, the reaction potential is calculated, which is reinserted to obtain revised surface charges.[318] According to Tomasi and Persico, a few iterations are usually sufficient, hence limiting the computational cost.[318] The final self-consistent reaction field $V_R(\vec{r})$ is then used to define the effective Hamiltonian (Eq. (340)). Since the charge density of the solute, $\rho_S(\vec{r})$, must be also self-consistent with the reaction field, this version of PCM is sometimes considered as a double-iterative procedure.[335]

Due to the coupled nature of the equations, an effective surface charge $\sigma'(\vec{s})$ that is ultimately determined by the molecular charge density $\rho_S(\vec{r})$, can similarly be expressed in terms of the solvent response function $Q(\varepsilon, s, s')$.[336,337,338]

$$\sigma'(\vec{s}) = \int d\vec{s}' \, Q(\varepsilon, \vec{s}, \vec{s}') V_S(\vec{s}') \tag{353}$$

Klamt and Schüürmann proposed an alternative approach to compute the reaction potential, the so-called conductor-like screening model (COSMO).[335] Their key idea is to exploit the simplicity of all electrostatic expressions if conductors are considered. Therefore, the dielectric constant of the solvent is changed from ε to ∞. This implies that the potential at the cavity surface cancels (Gauss's law applied to conductors).[317] The surface charges $\sigma^*(\vec{s})$ are thus directly accessible from the potential of the molecular charge distribution $V_S(\vec{r})$ (for example Eq. (352)). To take into account the finite size of the actual solvent permittivity ε, the surface charges are subsequently scaled with a function $f(\varepsilon)$.[317] k is an empirical constant fitted to experimental reference data.[335]

$$\sigma(\vec{s}) = f(\varepsilon)\sigma^*(\vec{s}) = \frac{\varepsilon - 1}{\varepsilon + k} \sigma^*(\vec{s}) \tag{354}$$

The scaling function is motivated by classical electrostatics where the dielectric screening in media is obtained from similar expressions.[339,340] It is evident from this outline that the calculation of the surface

charges in COSMO is non-iterative. As pointed out by Barone et al. for the related C-PCM model,[vv] COSMO yields equivalent results to the traditional dielectric PCM approaches although it might be less intuitive.[333]

As already indicated, since the reaction field potential is accessible from either COSMO or PCM, the effective Hamiltonian is defined. The electronic-structure problem of the embedded QM system is solved by diagonalizing the effective Hamiltonian. To do this, electronic and nuclear degrees of freedom of the solute are usually decoupled. This is achieved by dividing the charge density of the solute into an electronic and a nuclear component, each inducing a reaction field. The interaction Hamiltonian consists of four different terms (two different reaction potentials interacting with two different charge distributions). Since the nuclear degrees of freedom are treated parametrically, the electronic equations obtain a more compact form. Then, as outlined, the problem is iterated until self-consistency. This explains the notion of SCRF (self-consistent reaction field).[317,318]

3.4.2 Linear response solvation for the excited state

The presented PCM and COSMO approaches are based on equilibrium conditions between the solute and its solvent environment. For electronic excitations, this is not the case anymore.[317] Instead, the electronic properties of the solute change with time. Consistently, the solute-solvent interactions (Eq. (341)) become time-dependent as well. Usually, only the time dependence of the electrostatic solute-solvent interaction is taken into account.[ww] [317]

It is well-known that the polarization $\vec{P}(\omega)$ of a medium like a solvent by a time-dependent electric field $\vec{E}(\omega)$ (such as an electronically excited dipole moment) is described by its complex dielectric constant $\varepsilon_r(\omega)$.[317]

$$\vec{P}(\omega) = \frac{(\varepsilon_r(\omega) - 1)}{4\pi} \vec{E}(\omega) \tag{355}$$

The complex dielectric constant $\varepsilon_r(\omega)$ is represented as the sum of a real part $\varepsilon_r'(\omega)$, which accounts for the in-phase polarization and corresponds to the static dielectric constant for the limiting case of low frequencies, and a complex part $\varepsilon_r''(\omega)$.[317]

$$\varepsilon_r(\omega) = \varepsilon_r'(\omega) + i\varepsilon_r''(\omega) \tag{356}$$

It is furthermore well-known that $\varepsilon_r(\omega)$ decreases with increasing frequencies. While some polarization processes are fast and immediately respond to a changing electric field $\vec{E}(\omega)$, others are

---

[vv] It should be noted that C-PCM and COSMO differ, apart from different implementations, only by their constant $f(\varepsilon)$, namely by the fit parameter k.
[ww] It should be noted that the time dependence of all other contributions to ΔG is usually neglected. Ground-state expressions are employed.

inertial (such as the orientational polarization of the solvent, i.e., the solvent relaxation, for vertical electronic excitations). This implies that given a certain timescale of a process or of $\vec{E}(\omega)$, the polarization (Eq. (355)) is composed of a contribution in equilibrium with the solute, the dynamic polarization, and a frozen contribution. For instance, it can be assumed that for optical excitations, only the electronic polarization of the solvent is in equilibrium with the solute. It is represented by the dielectric constant $\varepsilon_r'(\omega) = \varepsilon_{opt}'(\omega) = n^2$ with n being the refractive index.[336] The remaining degrees of freedom of the solvent are frozen and not in equilibrium. Thus, the polarization (Eq. (355)) as well as the effective surface charges can be decomposed into two parts.[336]

$$\vec{P}(\omega) = \vec{P}_{fast}(\omega) + \vec{P}_{slow}(\omega) \tag{357}$$

$$\sigma'(\omega) = \sigma'_{fast}(\omega) + \sigma'_{slow}(\omega) = \frac{\varepsilon_{opt}' - 1}{\varepsilon - 1}\sigma'(\omega) + \frac{\varepsilon - \varepsilon_{opt}'}{\varepsilon - 1}\sigma'(\omega) \tag{358}$$

Only the fast polarization contributes to the reaction potential. This is reflected in a reduced surface charge (only the first term on the right-hand side of Eq. (358)). In order to actually calculate the transition energies, the effective Hamiltonian, which defines the response function, contains only a fraction of the reaction potential in equilibrium. From a technical point of view, this is most easily represented in terms of the solvent response functions (Eq. (353)). The surface charge $\sigma_{fast}(\omega)$ is thus calculated as[336]

$$\sigma'_{fast}(\vec{s}) = \int_\Gamma d\vec{s}' \, Q(\varepsilon_{opt}, \vec{s}, \vec{s}') V_S(\vec{s}') \tag{359}$$

The electrostatic contribution to the free energy of solution ΔG_{elec} and the electrostatic interaction energy (Eq. (347)) are directly related to the surface charges.[336]

$$\Delta G_{elec} = \frac{1}{2}E_{int,el} = \frac{1}{2}\int_\Gamma \sigma'_{fast}(\vec{s})V_S(\vec{s})d\vec{s} = \frac{1}{2}\int_\Gamma \int_\Gamma V_S(\vec{s})Q(\varepsilon_{opt}, \vec{s}, \vec{s}')V_S(\vec{s}')d\vec{s}'d\vec{s} \tag{360}$$

It has been already mentioned that the solute potential is usually divided into its electronic and nuclear contributions.

$$V_S(\vec{s}) = \int d\vec{r} \frac{\rho^{el}(\vec{r})}{|\vec{r} - \vec{s}|} + \sum_n^{nuclei} \frac{Z_n}{|\vec{s} - \vec{R}_n|} \tag{361}$$

The equations for the linear-response solvation in the calculation of transition energies will be exemplified in the following for the TD-DFT formalism[xx].[336] Therefore, the electrostatic interaction energy is written as a functional of the solute electronic density.

$$E_{int,el}[\rho^{el}(\vec{r})] = \int\limits_{\Gamma} \int\limits_{\Gamma} V_S(\vec{s}) Q(\varepsilon_{opt}, \vec{s}, \vec{s}') V_S[\rho^{el}(\vec{r})](\vec{s}') d\vec{s}' d\vec{s} \tag{362}$$

In the Kohn-Sham operator, this results in an additional contribution, the PCM potential/operator $v_{PCM}(\vec{r})$.[336]

$$v_{PCM}(\vec{r}) = \int\limits_{\Gamma} \int\limits_{\Gamma} V_S(\vec{s}) Q(\varepsilon_{opt}, \vec{s}, \vec{s}') \frac{\partial V_S}{\partial \rho^{el}(\vec{r})}(\vec{s}') d\vec{s}' d\vec{s} = \int\limits_{\Gamma} \int\limits_{\Gamma} d\vec{s}' d\vec{s} \, V_S(\vec{s}) Q(\varepsilon, \vec{s}, \vec{s}') \frac{1}{|\vec{s}' - \vec{r}|} \tag{363}$$

Due to the discretization of the surface charges into tesserae, it can be represented as a sum where the continuous cavity surface is discretized into a finite amount of segments I with positions $\{\vec{s}_I\}$.[336]

$$v_{PCM}(\vec{r}) = \sum_I \sum_J V_S(\vec{s}_I) Q(\varepsilon_{opt}, \vec{s}_I, \vec{s}'_J) \frac{1}{|\vec{s}'_J - \vec{r}|} \tag{364}$$

For the dynamic response of a vertical transition, the solvent response $Q(\varepsilon, \vec{s}_I, \vec{s}'_J)$ (Eq. (364)) contains only the optical permittivity $\varepsilon'_{opt}(\omega)$. The PCM potential results in an additional term in the Casida equation. Diagonalizing them yields the transition energies in solution.[336] An extension of the linear-response theory for excited states to properties and gradients in solution has also been implemented.[341]

It should be stressed that in the linear-response formalism, excitation energies and excited-state properties are determined from ground-state properties, and no iterative procedure is needed to obtain a self-consistent reaction field for the excitation energies. In other words, since the excited wave function is not explicitly calculated, no self-consistent reaction field specific for the excited-state density is necessary (in contrast to the ground-state case above[317]). Only the ground-state reaction field is iteratively optimized in the underlying ground-state calculation. Hence solvent effects on the excitation energies are included via (1) polarized ground-state orbitals and via (2) the equilibrium non-iterative PCM potential (determined from ε_{opt}) in the Casida equation that includes only the optical permittivity.

The inclusion of solvent effects is fundamentally different for excitation energies calculated in the so-called state-specific approach, i.e., in those cases where the excited-state wave function is explicitly

---

[xx] It should be noted that TDHF/CIS/semiempirical calculations can be considered as a limiting case of TD-DFT for functionals containing only exact exchange. Expressions are thus equivalent.

calculated.[317] Then the optical solvent reaction field is self-consistent with the excited-state density, i.e., it is variationally optimized in an SCF procedure using ε_{opt}. Additionally, ground-state energies are obtained with a self-consistent reaction field based on ε. Excitation energies are obtained as the differences between these iteratively determined absolute state energies.

It is well-known that excitation energies calculated for gas-phase molecules in a linear-response formalism and in a state-specific framework (for instance TDA-TDHF vs. CIS) are equivalent.[317] However, Cammi et al.[342] and Corni et al.[343] demonstrated that this is not the case if continuum solvation models are employed in the calculation of the transition energies.[317] Further evidence was provided that the linear-response and the state-specific solvation differ mostly in terms of the non-equilibrium solvation energy or, otherwise stated, in terms of the energy difference between the equilibrium (calculated from the static permittivity ε) and the non-equilibrium free energy of solvation (determined with the optical permittivity ε_{opt} (Eq. (341)).[344] Improta et al. proposed a state-specific solvation approach for TD-DFT excited states that corrects this difference. The equilibrium excited-state solvation free energy $\Delta G_{elec,eq}$ is thus calculated by explicitly calculating the solute potential $V_{S,\rho}^{ex}(\vec{s})$ and the surface charges $\sigma^{ex}(\vec{s})$ with the excited state density (comparison with Eq. (360)).[344]

$$\Delta G_{elec,eq} = \frac{1}{2}\int_{\Gamma} \sigma^{ex}(\vec{s})V_{S,\rho}^{ex}(\vec{s})d\vec{s} = \frac{1}{2}\int_{\Gamma} \sigma_{fast}^{ex}(\vec{s})V_{S,\rho}^{ex}(\vec{s})d\vec{s} + \frac{1}{2}\int_{\Gamma} \sigma_{slow}^{ex}(\vec{s})V_{S,\rho}^{ex}(\vec{s})d\vec{s} \tag{365}$$

The non-equilibrium free energy $\Delta G_{elec,non-eq}$ of the excited state is then calculated by taking into account the ground-state density via its potential $V_{S,\rho}^{gs}(\vec{s})$ as well.[344]

$$\Delta G_{elec,non-eq} = \frac{1}{2}\int_{\Gamma} \sigma_{fast}^{ex}(\vec{s})V_{S,\rho}^{ex}(\vec{s})d\vec{s} \tag{366}$$

$$+ \int_{\Gamma} \sigma_{slow}^{gs}(\vec{s})V_{S,\rho}^{ex}(\vec{s})d\vec{s} - \frac{1}{2}\int_{\Gamma} \sigma_{slow}^{gs}(\vec{s})V_{S,\rho}^{gs}(\vec{s})d\vec{s}$$

$$+ \frac{1}{2}\left(\int_{\Gamma} \sigma_{slow}^{gs}(\vec{s})V_{S,f}^{ex}(\vec{s})d\vec{s} - \int_{\Gamma} \sigma_{slow}^{gs}(\vec{s})V_{S,f}^{gs}(\vec{s})d\vec{s}\right)$$

$V_{S,\rho}^{ex}(\vec{s})$ and $V_{S,\rho}^{gs}(\vec{s})$ are calculated from the densities of the solute (Eq. (361)) in the ground/excited state. In contrast, $V_{S,f}^{ex}(\vec{s})$ and $V_{S,f}^{gs}(\vec{s})$ are the potentials corresponding to the fast solvent polarization. $\sigma_{fast}^{gs}(\vec{s}), \sigma_{fast}^{ex}(\vec{s})$ are the corresponding surface charges, with $\sigma_{slow}^{gs}(\vec{s}), \sigma_{slow}^{ex}(\vec{s})$ being the counterparts for the slow solvent degrees of freedom. In state-specific TD-DFT calculations, an iterative procedure is proposed similar to ground-state calculations. From the initial gas-phase excited-state density, the state-specific reaction potential is estimated. The excited-state density is updated. The

procedure is iterated until convergence of the excited-state reaction potential is reached.[344] As pointed out by Improta et al., the state-specific approach seems to be especially important for polar solvents while in most apolar solutions, linear-response and state-specific solvation provide very similar results with TD-DFT.[344]

It should be noted that several state-specific solvation methods exist. For instance, a different approach for state-specific solvation was proposed by Mennucci and coworkers based on the excited-state reduced density matrix. A state-specific solvent response Q is computed and used to correct the linear-response excitation energies, which yields accurate results.[345]

3.5 Molecular Mechanics (MM)

3.5.1 The description of the electronic energy with force fields

The following outline closely follows Jensen.[31] In contrast to the quantum-chemical picture, molecules are described in a simple "ball-and-spring"-model in force fields, the defining feature of molecular mechanics.

Instead of explicitly solving the electronic Schrödinger equation to obtain the electronic energy E_{tot}, force fields express the electronic energy as a parameteric function of nuclear coordinates $\{\vec{R}\}$.[31]

$$E_{tot} = E_{stretch} + E_{bend} + E_{torsion} + E_{vdW} + E_{elec} + E_{cross} \tag{367}$$

$E_{stretch}$ is a function of the bond lengths, E_{bend} depends on bond angles, $E_{torsion}$ is obtained from torsional angles around a bond, E_{vdW} designates the van-der-Waals energy and E_{elec} the electrostatic intermolecular energy. A force field description of a molecule does not rely on its nuclei and electrons like in QM (Eq. (3)). It rather resorts to atom types as the basic building blocks that compose a molecule. This is justified by the observation that distinct structural entities (like C-H bonds, H-O-bonds etc.) behave similarly in different molecules. Therefore, the force field approach can be considered as being closely related to the notion of functional groups fundamental to organic chemistry.[31]

The energy terms of bond stretching and bending, $E_{stretch}$ and E_{bend}, can be expanded in a Taylor series. Usually, only the harmonic term is used. Yet, results usually improve if higher-order terms are included as well (more fit parameters). It should be kept in mind that a Taylor series of the bond stretching energy is unable to reproduce the dissociation limit. Thus, force fields are in general only reliable for geometries somewhat related to the minimum geometries defined by the zeroth-order bond lengths $\{R_0^{AB}\}$ and bond angles θ_0^{ABC} between atoms A and B and atoms A, B and C. Although these zeroth-order parameters define the energetic minimum conformation, they do not necessarily correspond to the equilibrium bond lengths.[31]

By introducing two force constants k^{AB} and k^{ABC} for the bond stretching and angle bending energies, respectively, these energy contributions can be written for bond lengths R^{AB} and angles θ^{ABC} as

$$E_{stretch} = k^{AB}\left(R^{AB} - R_0^{AB}\right)^2 \tag{368}$$

$$E_{bend} = k^{ABC}\left(\theta^{ABC} - \theta_0^{ABC}\right)^2 \tag{369}$$

For systems with unusual equilibrium values for the bond lengths and angles, such as small rings, special atom types are defined.[31] It is evident from Eq. (368) and (369) that two stretching and bending parameters have to be defined for each distinct bond/angle type ("distinct" refers in this context to the combination of atom types): a zeroth-order parameter R_0^{AB} (θ_0^{ABC}) and a force constant k^{AB} (k^{ABC}).[31]

In contrast to the stretching and bending motions, torsions are periodic. They are thus written as a Fourier series of the torsional/dihedral angle ω^{ABCD}, i.e., the angle between the bond vector between atoms A and B and the bond vector between atoms C and D. The energetic profile of the rotation around an sp³-hybridized carbon atom has three minima (for ethane they are isoenergetic). Thus the energetic profile is periodic in dihedral angles of 120°. This implies that the Fourier series for sp³-hybridized carbon atoms must contain at least a term corresponding to $\cos 3\omega$. Indeed, most force fields describe torsions by introducing three potential energy terms V_1^{ABCD}, V_2^{ABCD}, and V_3^{ABCD}.[31]

$$E_{torsion} = \frac{1}{2}V_1^{ABCD}[1 + \cos \omega^{ABCD}] + \frac{1}{2}V_2^{ABCD}[1 - \cos 2\omega^{ABCD}] \tag{370}$$

$$+ \frac{1}{2}V_3^{ABCD}[1 + \cos 3\omega^{ABCD}]$$

If for instance rotation around carbon-carbon double bonds are considered (B, C = sp²-hybridized carbon), V_3^{ABCD} vanishes. It follows from Eq. (370) that for a combination of four atoms A, B, C, D, three parameters $\{V_n^{ABCD}\}$ are required.[31]

Out-of-plane bending, for instance the pyramidalization of an sp²-hybridized carbon, deserves a special treatment in force fields. This results because upon pyramidalization, bond angles and torsions change only negligibly. Therefore, the energetic penalty for out-of-plane bending would be significantly too small to ensure the planarity of conjugated moieties unless bond angle force constants k^{ABC} are very large. In order to prevent this unbalanced treatment leading to too stiff bending potentials, two alternative possibilities exist to take into account out-of-plane bending. On the one hand, the out-of-plane angle of a central pyramidalized atom B can be described in terms of its distance d to the plane spanned by its substituents A, C, D. Again, the potential is assumed to be harmonic (k^B force constant).[31]

$$E_{out-of-plane} = k^B d^2 \tag{371}$$

On the other hand, out-of-plane bending can be described by defining an "improper" torsion potential for the entity $ABCD$. It is called "improper" because the torsional potential takes on a shape as if there were a bond between atoms C and D (although both atoms are bonded to atom A).[31]

A number of different expressions exist for the van-der-Waals energy. While its attractive term, the attraction between spontaneous induced dipoles, can be classically treated and has an R^{-6}-distance (R is the interatomic distance), no rigorously derived classical expression for the repulsive component exists. Maybe the most popular empirical van-der-Waals potential is the Lennard-Jones potential ($\{C_n\}$ are constants).[31]

$$E_{vdW,LJ}(R^{AB}) = \frac{C_1}{(R^{AB})^{12}} - \frac{C_2}{(R^{AB})^6} = \varepsilon\left[\left(\frac{R_0}{R^{AB}}\right)^{12} - 2\left(\frac{R_0}{R^{AB}}\right)^6\right] \tag{372}$$

The Lennard-Jones potential is often rewritten in terms of the minimum energy distance R_0 and the depth of the potential minimum ε. A related expression for the van-der-Waals energy, the so-called buffered 14-7 potential $E_{vdW,14-7}$,[346] is employed in the Merck Molecular Force Field (MMFF)[347] as well as in AMOEBA[348] (atomic multipole optimized energetics for biomolecular applications).[31]

$$E_{vdW,14-7}(R) = \varepsilon\left(\frac{1.07R_0}{R + 0.07R_0}\right)^7\left(\frac{1.12R_0{}^7}{R^7 + 0.12R_0{}^7} - 2\right) \tag{373}$$

The van-der-Waals distances R_0 and the energies ε are defined for atom pairs A, B. Many different approaches exist to derive these pair-specific values from atomic parameters, such as the one proposed by Halgren.[346] The van-der-Waals distance R_0^{AB} is often determined from the sum of the van-der-Waals radii of the atoms, R_0^A and R_0^B. However, this depends on the force field. For instance, it follows from the form of the Lennard-Jones-like potential (Eq. (372)) that the R_0^{AB} distances is rather calculated as the geometric mean.[349] The energies ε^{AB} are usually estimated from the geometrical means of the atomic parameters $\varepsilon^A, \varepsilon^B$.[31]

The Lennard-Jones potential (Eq. (372)) and the closely related buffered 14-7 potential (Eq. (373)) are most often employed because they are computationally very efficient. However, an exponential repulsive function would represent the physical repulsive forces more accurately because it reflects the exponential decay of the electronic density with increasing distance. This has motivated the utilization of a Buckingham-type potential $E_{vdW,Buck}$ (Eq. (374), A, B, C are constants) and a Morse potential[350] $E_{vdW,Morse}$ (Eq. (375), D is the dissociation energy, α depends on the force constant and can be considered as the compressability of the bond).[31]

$$E_{vdW,Buck}(R) = Ae^{-BR} - \frac{C}{R^6} = \varepsilon \left[\frac{6}{\alpha - 6} e^{\alpha(1 - R/R_0)} - \frac{\alpha}{\alpha - 6} \left(\frac{R_0}{R} \right)^6 \right] \tag{374}$$

$$E_{vdW,Morse}(R) = D\left(1 - e^{-\alpha(R - R_0)} \right)^2 \tag{375}$$

A problem of the Buckingham potential (Eq. (374)) arises from the fact that it becomes attractive for very short intermolecular distances. The Morse potential is best at reproducing the dissociation profile of a molecule.[350] It should be noted that it does not feature any attractive R^{-6}-distance dependence. This results because the exponential functional includes also higher-order attractive terms. Some phenomena might require separately adjusted van-der-Waals expressions, most notably hydrogen bonds and lone pairs. Some force fields scale the position of a hydrogen atom along a bond to an electronegative atom to reflect the anisotropy of the hydrogen electronic density. Sometimes, the Lennard-Jones potential (Eq. (372)) is modified to take into account the stronger binding energy of hydrogen bonds compared with standard van-der-Waals interactions. Moreover, orientational terms similar to the DH2 correction for semiempiric methods (Eq. (122)) are employed. Nevertheless, for the purpose of computational simplicity and generality of their parameters, most force fields provide a purely electrostatic description of hydrogen bonds. Lone pairs can be for instance included via dummy atoms, which are still often neglected.[31]

The electrostatic interaction energy can be included either by assigning partial charges to all atom types or by employing bond dipoles. This implies that a bond dipole moment is ascribed to all distinct bonds between atom types A and B. Then, the Coulomb interaction is calculated between the atomic charges or bond dipoles. Usually, both approaches yield rather equivalent results. Nevertheless, as outlined for example by Stone et al. for water clusters, many-body terms such as higher-order induction terms ($E_{ind}^{(2)}$, see Eq. (326)) are important to obtain accurate intermolecular potentials and geometries.[351] Intermolecular electrostatic potentials can be improved by either including non-atom-centered (= "off-center")) charges as proposed by Dixon et al.[352] or higher multipole moments. Stone developed an analysis to decompose the electrostatic potential created by a quantum-mechanically obtained electron density into atomic multipole moments. It relies on a decomposition of the electronic density in terms of products of Gaussian basis functions, which have distinct symmetries. For instance, while the products of s-orbitals correspond to pure isotropic charges, products of s- and p-orbitals represent – for symmetry reasons – a charge and a dipole. The procedure is designated as the Distributed Multipole Analysis (DMA). The resulting atomic multipole moments were shown to accurately reproduce the molecular electrostatic potential.[353]

To avoid double-counting of intramolecular interactions in the stretching/bending terms and in the van-der-Waals/electrostatic interactions, the van-der-Waals energy and the electrostatic energy

E_{vdW}, E_{elec} (Eq. (367)) are only calculated for atom pairs that are separated by at least three bonds. It follows that these energy contributions influence torsional potentials, in contrast to bond stretching and bending.[31] Therefore, an interdependence between the molecular geometry and the electrostatic/van-der-Waals energy contributions exists. This is problematic for two reasons. (1) In many force fields, the charges/bond dipoles and higher-order multipoles are derived from the molecular electrostatic potential, i.e., they aspire to reproduce intermolecular electrostatic interactions correctly. Because of their derivation, they are less accurate for intramolecular phenomena. Consistently, force-field intramolecular geometries of polar molecules are less reliable, especially compared with their apolar counterparts. An unbalanced treatment of different molecules results. (2) It is well-known that partial charges depend on the geometry. Due to their interdependence with the torsional parameters $\{V_n^{ABCD}\}$, this questions the generarility of these parameters that are derived from a (necessarily limited) training set/set of reference data.[31] This holds in principle equally for the van-der-Waals parameters. However, due to their short-range nature, they are, given a certain pair of bonds $A - B - C - D$ and its torsion $\omega(AB - CD)$, approximately constant in different molecules, in contrast to the electrostatic contribution.[31]

It would thus be desirable to include a coupling between the force-field partial charges and the molecular geometry. This can be achieved by including polarization.[354] In the lowest order, polarization is included via induced dipole moments $\vec{\mu}_{ind}$. To calculate an atom-centered induced dipole moment, the electrostatic potential $\phi(\vec{r})$ of the environment is computed from the summation of all surrounding charges and higher-order multipole moments. The resulting electric field together with the polarizability tensor of the atom α yields an induced dipole.

$$\vec{\mu}_{ind} = \alpha \vec{\nabla} \phi(\vec{r}) \tag{376}$$

Since all induced dipoles contribute themselves to the electrostatic potential, they must be calculated iteratively to self-consistency.[31]

Similar to atomic multipole moments, atomic polarizability tensors α can in principle be deduced from quantum-chemical calculations of the molecular electronic structure. Yet, this involves the challenge of separating permanent and induced atomic multipole moments obtained from the quantum-chemical calculation. Ren and Ponder proposed a scheme to accomplish that. It is based on an analytic formula derived from Thole's polarizability model[355] to eliminate effects from intramolecular polarization on atomic multipoles.[356]

Since the neglect of polarization and higher-order multipoles appeared to be a major bottleneck for more accurate force fields, Ren and Ponder developed the so-called AMOEBA force field (atomic multipole optimized energetics for biomolecular applications) for water that combines the DMA

analysis of Stone[353] with atomic polarizabilities. The buffered 14-7 potential from the MMFF force field is employed for the van-der-Waals energy.[348] Later-on, Ren, Ponder, and coworkers readily broadened the scope of applicability of the AMOEBA force field to a wide variety of small organic molecules.[357]

As the AMOEBA force field provides very accurate results due to the inclusion of higher-order multipoles and polarization, it is sometimes considered as a class III type force field,[358] similar to other polarizable force fields such as the Drude[359] polarizable force field. In contrast, conceptually simple force fields like OPLS[349]-AA[360] (optimized potentials for liquid simulations – All-Atom) belong to the class I force fields. For instance, OPLS-AA, originally parameterized to simulate proteins in their native (aqueous/liquid) environment (OPLS) and later generalized to all small organic molecules (-AA), relies on a simple expression for the electrostatic energy calculated from partial charges and a Lennard-Jones potential (Eq. (372)). The OPLS-AA electronic energy (similar to the electronic energy of the parent AMBER[361,362] force field) is calculated as the sum of the independent stretching/bending/torsional/van-der-Waals and electrostatic contributions, i.e., the cross term E_{cross} (Eq. (367)) is neglected. This differentiates class I from the more advanced class II force fields, for example the MM3[363,364,365] force field. They include cross-couplings between the individual degrees of freedom. Such energy contributions, for instance for the coupling $E_{str/str}$ between bonds $A-B$ and $B-C$, take on shapes such as[31]

$$E_{str/str} = k^{ABC}\left(R^{AB} - R_0^{AB}\right)\left(R^{BC} - R_0^{BC}\right) \tag{377}$$

The parameters $\{k^{ABC}\}$ (and related ones for different cross-couplings) do not necessarily depend on all three involved atoms A, B, C. They may equally be assumed to be specific for the central atom B or even overall constant. Furthermore, the class II-type MM3 force field can for example also account for changes in the zeroth-order bond length R_0^{AB} due to the presence of an electronegative atom.[366] In an extension of the MM3 force field, MM4, the effects of hyperconjugation on equilibrium bond lengths are incorporated in a similar manner.[367] The cross-coupling terms might also be important in small rings and conjugated systems unless additional atom types were defined for these structurally and electronically distinct moieties.[31]

In order to improve the force field description of conjugated systems without requiring additional atom types or a number of cross coupling terms, Allinger and coworkers[368] proposed an extension of the MM2[369] force field to adapt the equilibrium bond lengths, angles and dihedrals in conjugated systems in a system-specific way. It is based on a simple Pariser-Pople-Parr calculation (CNDO only for π-electrons, see above) that is conducted to estimate the π-bond order. Based on this bond order, revised equilibrium parameters are obtained from linear extrapolation formulas. In geometry

optimizations, this necessitates, however, two iteration cycles because the bond order strongly depends on the (initially non-optimized) geometry.[31]

Simulation Techniques with Molecular Mechanics

Before beginning this outline of simulation techniques, it should be noted that simulations are definitely not limited to force-field energies and gradients. In fact, both semiclassical and quantum-mechanical simulation techniques exist.[31] However, in view of the later-on results presented in this thesis, this outline will mostly refer to simulations based on force-field energies. Nevertheless, some other examples will be briefly addressed.

In general, simulations aim at sampling the conformational space of a system (for example the solvation shell in solvents and fluids). From the sampling, they generate ensembles, i.e., the entity of relevant conformations that describe the thermodynamic equilibrium of the system.[yy] Two very important simulation techniques are commonly employed in computational chemistry. On the one hand, in Monte Carlo (MC) techniques, a new system conformation is randomly produced, for instance by a random displacement of any of its atoms. Its energy is calculated. A Boltzmann criterion (metropolis sampling) based on this energy is used to decide whether the randomly generated conformation is kept or not. Ensemble properties are computed as the average values over all selected conformations.[31]

Most importantly, as pointed out for example by Nosé,[370] MC techniques, which are easily implemented and require only the calculation of energy changes, are entirely static, i.e., they are unable to describe time-dependent phenomena. This is fundamentally different for the second important subgroup of simulation techniques, the molecular dynamic (MD) simulations where dynamic quantities are accessible.[370] In MD simulations, a set of nuclear coordinates is propagated in time by solving their equation of motion.[371] MD simulations thus yield trajectories, "series of time-correlated points in phase space".[31] Average ensemble properties are obtained from these trajectories based on the ergodic hypothesis, i.e., they are calculated as time averages.[372] However, as MD simulations are not static,[370] they can be similarly employed to model dynamic processes such as protein motions or aggregation phenomena.[373,374,375]

To solve the equations of motion for the nuclear coordinates of a system, a set of initial coordinates $\{\vec{r}^A\}$ and velocities $\{\vec{v}^A\}$ is needed.[31] The propagation is governed by the forces accelerating the nuclei that correspond to the derivatives of the intermolecular potential energy $\partial V(\{\vec{r}^A\})/\partial \vec{r}^A$ of the system (with respect to the nuclear coordinates).[31] With these quantities, the equations of motion of the

---

[yy] It should be noted that other definitions of simulation techniques exist.

systems are defined. Solving them provides the time propagation of the nuclei. To do so, a short time increment Δt_i is chosen. Forces are assumed to be constant during this interval.[31] MD results can thus always be improved by decreasing[zz] the predefined time increment Δt_i. However, the total MD simulation time should at least correspond to the time scale of the process that is simulated (a certain total simulation time is equally required for time averaging of ensemble properties to ensure a sufficient sampling of the conformational space). Therefore, choosing a shorter time increment multiplies the number of required MD steps and the computational demand.[31] Nevertheless, to obtain reliable results, the maximum time increment must be approximately one order of magnitude smaller than the fastest process in the system, usually stretching vibrations including hydrogen. Thus the total simulation time is intrinsically limited. Algorithms to freeze the bond lengths involving hydrogen atoms were developed, for example the RATTLE[376] and the SHAKE[377,378] algorithm.

A variety of standard MD algorithms solve the Newton's equation of motion. m_a is the mass of particle a.

$$-\frac{\partial V(\{\vec{r}^A\})}{\partial \vec{r}^A} = m_a \frac{d^2 \vec{r}^A}{dt^2} \tag{378}$$

The Verlet algorithm[379] solves Newton's equation (Eq. (378)) numerically. The position $\vec{r}_{i+1}^a$ of a particle a at a later time $t_{i+1} = t_i + \Delta t_i$ is obtained from the position $\vec{r}_i^a$ and the acceleration $\vec{a}_i^a$ at time t_i and additionally the position $\vec{r}_{i-1}^a$ at time $i - 1$.[31]

$$\vec{r}_{i+1}^a = (2\vec{r}_i^a - \vec{r}_{i-1}^a) + \vec{a}_i^a \Delta t_i^2 = (2\vec{r}_i^a - \vec{r}_{i-1}^a) - \frac{1}{m_a}\frac{\partial V(\{\vec{r}^A\})}{\partial \vec{r}^A}\Delta t_i^2 \tag{379}$$

The Verlet algorithm is correct to third-order of the Taylor expansion of $\{\vec{r}^A\}$ in t. However, the Verlet algorithm can be numerically unstable: a small number proportional to Δt_i^2 is added to a large number $(2\vec{r}_i^a - \vec{r}_{i-1}^a)$. It is furthermore evident from Eq. (379) that the velocities $\{\vec{v}_i^a\}$ are not explicitly taken into account, which is a disadvantage (see below).[31]

The leap-frog algorithm, a standard algorithm to numerically solve differential equations, removes these deficiencies by including the velocities and eliminating the Δt_i^2-term.[31] This improves the numerical accuracy.[380]

$$\vec{r}_{i+1}^a = \vec{r}_i^a + \vec{v}_{i+\frac{1}{2}}^a \Delta t_i \tag{380}$$

[zz] Since it is based on a Taylor expansion, results obtained with the Verlet algorithm are exact in the limiting case of a time step of 0. Nevertheless, the accuracy of the MD predictions is then intrinsically limited by the numerical error of the calculations.[31]

$$\vec{v}^a_{i+\frac{1}{2}} = \vec{v}^a_{i-\frac{1}{2}} - \frac{1}{m_a}\frac{\partial V(\{\vec{r}^A\})}{\partial \vec{r}^A}\Delta t_i \tag{381}$$

The explicit calculation of the velocities comes, however, at the expense of introducing half times at times $i + \frac{1}{2}$ and $i - \frac{1}{2}$ so that positions and velocities are never determined at the same time.[31]

Employing more general equations of motions than Newton's equation (Eq. (378)), namely the Lagrangian L (Eq. (384)) and the Hamiltonian H (Eq. (386)), Andersen et al.[381] derived a set of equations also called the velocity Verlet algorithm because it utilizes simultaneous positions and velocities.

$$\vec{r}^a_{i+1} = \vec{r}^a_i + \vec{v}^a_i \Delta t_i - \frac{1}{2}\frac{1}{m_a}\frac{\partial V(\{\vec{r}^a_i\})}{\partial \vec{r}^a_i}{\Delta t_i}^2 \tag{382}$$

$$\vec{v}^a_{i+1} = \vec{v}^a_i - \frac{1}{2m_a}\left\{\frac{\partial V(\{\vec{r}^a_i\})}{\partial \vec{r}^a_i} + \frac{\partial V(\{\vec{r}^a_{i+1}\})}{\partial \vec{r}^a_{i+1}}\right\}\Delta t_i \tag{383}$$

The Lagrangian L (and the Hamiltonian H) can be written as a minimum principle determining the time evolution of a system. Compared with Newton's equation of motion (which requires necessarily spatial coordinates), the Lagrangian allows for an easier and more general formulation with regard to the coordinates,[31] for instance in terms of scaled coordinates. The Lagrange equation of motions can be expressed via such a generalized coordinate $\vec{q}$ and the corresponding momentum $\vec{p} = m\,{\partial \vec{q}}/{\partial t}$. The time derivative describes the time evolution of a system.[382]

$$L = T - V \tag{384}$$

$$\frac{d}{dt}\frac{\partial L}{\partial \vec{p}} - \frac{\partial L}{\partial \vec{q}} = 0 \tag{385}$$

Similar considerations apply to the Hamiltonian, which is a reformulation of the Lagrangian.

$$H = T + V \tag{386}$$

$$\frac{\partial H}{\partial \vec{q}} + \frac{\partial \vec{p}}{\partial t} = 0 \qquad\qquad \frac{\partial H}{\partial \vec{q}} - \frac{\partial \vec{p}}{\partial t} = 0 \tag{387}$$

Defined values for the positions and the velocities at the same time i can be significant because standard MD simulations give rise to averages of so-called microcanonical ensembles or, equivalently, to processes occurring at a constant energy E, a constant volume V, and a constant particle number N. Microcanonical ensembles are therefore also designated as NVE-ensembles. It is well-known from statistical thermodynamics that further important ensembles exist, most notably the canonical ensemble (NVT-ensemble) and the isothermal-isobaric ensemble (NPT-ensemble).[31] Since the fluctuations of thermodynamic properties differ in different ensembles, it would be desirable to

generate also NVT- and NPT-ensembles in MD simulations, especially because in all experiments and processes, *the temperature instead of the energy is constant*.[31] A number of techniques (velocity scaling, Andersen thermostat, Nosé-Hoover thermostat, Berendsen thermostat) are available. Their key concepts are briefly outlined in the following.

A constant temperature or pressure of the ensemble can be achieved by introducing a scaling step, i.e., scaling all position vectors by a quotient of the pressure $\left(P_{actual}/P_{desired}\right)^{1/3}$ or all velocity vectors by a quotient of the temperature $\left(T_{desired}/T_{actual}\right)^{1/2}$.[aaa] As noted by DiNola et al.,[383] such a velocity scaling has been common practice to eliminate the thermal drift (fluctuating temperature) in MD simulations for canonical ensemble values. For instance, velocity scaling was applied by Schneider and Stoll[384] to solid-state phase transitions and also by Evans[385] who further emphasized the inutility of the Verlet algorithm for canonical ensembles (because as mentioned above, the velocities are included only implicitly). Although the velocity rescaling seems to provide generally rather reliable results, it introduces discontinuities in the dynamics, as outlined by Broughton et al.[386]

Andersen outlined a first procedure (for periodic systems) that includes the environment to maintain a constant temperature.[387] Stochastic collisions with the surrounding constantly redistribute the kinetic energy. Due to this stochastic element, the approach mixes aspects of MD and MC. In a related expression, the pressure is kept constant by introducing a variable volume in the equation of motion that is determined from the internal system-specific and a predefined external pressure. The resulting constant temperature and constant pressure MD is considered as a significant breakthrough by Nosé.[370] The so-called Andersen thermostat is still implemented in current program packages, for instance in Tinker.[388] A plethora of extensions to it were proposed that consist all in modifying the Lagrangian/Hamiltonian.[383]

However, one of the two most prominent approaches for constant temperature MDs is the so-called Nosé-Hoover[389,390] thermostat, i.e., an extended system method, which permits to directly calculate canonical ensemble values. The key idea is to include the environment, i.e., the heat reservoir, into the system. In the original formulation of Nosé, this is accomplished by introducing an additional variable $\tilde{s}$ and its time derivative $d\tilde{s}/dt$ that represents the external system, the reservoir.[370] The variable $\tilde{s}$ is associated with a fictitious mass Q that determines the coupling between the reservoir and the system. The interaction between the two systems is expressed in terms of velocity scaling: the variable $\tilde{s}$ scales

---

[aaa] This is based on the fundamental relationship between the pressure and the volume for a constant number of particles. Therefore $\vec{r} \sim \sqrt[3]{V} \sim \left(\sqrt[3]{P}\right)^{-1}$ holds. Furthermore, it follows from statistical thermodynamics that the kinetic energy $E_{kin} = \frac{3}{2}RT$. It follows that $v \sim \sqrt{T}$.

the velocities of the particles to $\tilde{v}_i$ compared to their real velocities v_i. As stated by Nosé, this interdependence of the velocities can be conceived as an exchange of heat.[370]

$$v_i = \tilde{s}\tilde{v}_i \tag{388}$$

The extended Lagrangian is constructed (simplified in the following for one particle). The potential energy $gk_BTln\tilde{s}$ of the external system is chosen in a way that the ensemble averages of a canonical ensemble are later-on recovered.[370] g is the number of independent degrees of freedom of the external system.

$$L = \frac{1}{2}m(\tilde{s}\tilde{v}_i)^2 - V + \frac{1}{2}Q\left(\frac{d\tilde{s}}{dt}\right)^2 - gk_BTln\tilde{s} \tag{389}$$

Solving the extended Lagrangian (Eq. (389)) yields the Nosé[bbb] equations of motion.[389] Moreover, as shown by Hoover,[390] a transformation of the coordinates eliminates the fictitious variable $\tilde{s}$, and a non-Newtonian equation of motion is obtained.

$$\vec{a} = -\frac{1}{m}\frac{\partial V}{\partial \vec{r}} - \gamma\vec{v} \tag{390}$$

The derivative of the "thermodynamic friction"[390] coefficient (which is time-dependent) γ is proportional to the kinetic energy.

$$\frac{d\gamma}{dt} = \frac{1}{Q}\left(mv_i^2 - gk_BT\right) \tag{391}$$

It is evident from Eq. (391) that the coupling is smaller for large masses, but the relaxation becomes very slow.[390] The mass Q should be therefore carefully chosen. By analyzing the partition function of the ensemble defined by the Lagrangian (Eq. (389)), Nosé could show that the Nosé-Hoover thermostat generates correct canonical ensembles.[370]

The second popular thermostat in MD simulations is the so-called Berendsen thermostat.[383] In fact, in contrast to all approaches based on a modified Lagrangian, DiNola et al. introduced the concept of weak coupling to an external bath.[383] Based on a Langevin-type equation with additional stochastic terms, the heat transfer rate from the thermostat to the system is derived (α is a damping constant).

$$\frac{dT}{dt} = 2\alpha\left(T_0 - T(t)\right) = \frac{1}{\tau}\left(T_0 - T(t)\right) \tag{392}$$

The resulting equation of motion is then written as

[bbb] It can be furthermore demonstrated that the artificial variable can be interpreted as a time scaling coordinate between the real and the virtual system.

$$\vec{a} = -\frac{1}{m}\frac{\partial V}{\partial \vec{r}} - \gamma\vec{v} \qquad (393)$$

$$\gamma = \alpha\left(\frac{T_0}{T} - 1\right) \qquad (394)$$

It should be noted that the friction coefficient (and not its derivative) is proportional to the kinetic energy (Eq. (394)). The Berendsen thermostat is more strongly damped than the Nosé-Hoover thermostat. It is often employed for a first equilibration in MD simulations. In fact, the concept of the Berendsen thermostat can be considered as a damped version of the velocity rescaling, i.e. the scaling factor λ of the velocities is controlled. This follows from Eq. (392) for the temperature change ΔT during a finite time increment Δt.

$$\lambda = \sqrt{1 + \frac{\Delta t}{\tau}\left(\frac{T_0}{T} - 1\right)} \qquad (395)$$

It is very important to stress that similar to other velocity rescaling schemes, the Berendsen thermostat does not generate a correct canonical ensemble. It provides accurate average values but the fluctuations are incorrectly reproduced.[31]

Albeit being maybe less important, completely analogous procedures exist to generate isobaric ensembles, namely the isothermic-isobaric ensemble. An equivalent Berendsen barostat[383] and a Nosé-Hoover[389,390] barostat are defined. While the Nosé-Hoover barostat produces correct ensembles, ensembles obtained with the Berendsen barostat are again not totally correct although accurate average values are obtained.[31]

Periodic boundary conditions permit to conduct simulations also for extended systems such as crystals or liquids. Whereas most features of MD simulations can be directly transferred to periodic systems, electrostatic interactions, which are of long-range character and thus largely exceed the defined boundaries, require a special treatment.[31] Simply truncating them results in discontinuities in the potential energy surface. Conceptually simple switching functions,[391] which reduce the Coulomb interaction gradually to zero starting at a threshold distance, or shifting functions, which dampen the whole electrostatic interaction, can be employed. Of particular importance are methods based on Ewald sums.[392,393,394] By introducing opposite charges with Gaussian profiles around each charge that consequently screen their interactions, the electrostatic interactions are divided into a near-field and a far-field contribution. The near-field contribution corresponds to the interaction between the charge and its Gaussian "well".[31] The far-field contribution is, due to the screening, of short-range character. It can be directly computed. The effects of the introducing Gaussian profiles need to be finally subtracted, which can be very efficiently done in reciprocal space, i.e., by Fourier transformation.[31]

This efficiency is responsible for the reduced scaling of such Ewald methods. A subdivision of electrostatic interactions into near- and far-field contributions forms also the basis for the so-called Fast Multipole Moment method (FMM).[395] While near-field interactions are explicitly calculated, far-field interactions are approximated by interactions between electric multipoles. The three-dimensional space is represented by a sum of boxes, and the electrostatic potential of each box is folded into a multipole expansion. An extension of the FMM method, the very Fast Multipole Moment method (vFMM), adjusts the size of the multipole expansion to the distance between interacting boxes. [31,396]

Although this section is entirely dedicated to molecular dynamic simulations based on classical force fields, a short perspective on MD simulations with electronic structure methods is presented, especially because of the similarity of the mathematical formulation. The subject is usually denoted as *ab initio* molecular dynamics (AIMD).[397] In their seminal analysis, Car and Parrinello[398] provided very important theoretical foundations in the area by proposing a methodology designated as Car-Parrinello MD. As outlined by Hutter,[397] such simulations were especially until the mid 90's so popular that the notion of Car-Parrinello MD was used synonymously to AIMD. Car and Parrinello recognized that the variational principle for electronic-structure problems can be equivalently formulated by treating the parameters in the electronic wave function as dynamic variables.[399] Using a steepest descent approach for Newton's equation of motion, the electronic-structure problem can be solved. Furthermore, Car and Parrinello realized that a fictitious electron mass μ_i can be introduced that couples the electron dynamics to the nuclei (comparable to Q in the Nosé-Hoover thermostat). This results in an extended Lagrangian (similar to the Nosé-Hoover thermostat, Eq. (389)) that includes the Kohn-Sham/Hartree-Fock orbitals[ccc] $\{\psi_i\}$.[399]

$$L = \sum_i \frac{1}{2} \mu_i \langle \dot{\psi}_i | \dot{\psi}_i \rangle + \sum_I \frac{1}{2} m_I v_I^2 - E(\Psi_0, \{\vec{r}^A\}) + constr. \tag{396}$$

The constraints ($constr.$) refer to the imposed orbital orthonormality. The equations of motions are then obtained as the Euler-Lagrange equations from the Lagrangian.[399]

$$m_I a_I(t) = -\frac{\partial}{\partial \vec{r}^I} \langle \Psi_0 | H_0 | \Psi_0 \rangle + \frac{\partial}{\partial \vec{r}^I} \{constr.\} \tag{397}$$

$$\mu_i \ddot{\psi}_i(t) = -\frac{\partial}{\partial \psi_i^*} \langle \Psi_0 | H_0 | \Psi_0 \rangle + \frac{\partial}{\partial \psi_i^*} \{constr.\} \tag{398}$$

[ccc] It should be noted that due to the basis set expansion of the orbitals, the time derivative of the Kohn-Sham orbitals is often represented as a time derivative of the orbital coefficients.[31]

The forces on the nuclei (Eq. (397)) are Hellmann-Feynman or Pulay-type forces calculated from the electronic density.[397] It is obvious from the equation of motion for the dynamic electronic parameters (Eq. (398)) that if the artificial orbital kinetic energy ($\mu_i \ddot{\psi}_i(t)$) is set to 0 and the nuclear positions are constant, the equation reduces to a simple electronic-structure problem.[31] This is done to determine the initial electronic wave function. In the subsequent dynamic simulations, however, both nuclei and electrons freely propagate. The electronic structure is not solved iteratively.[399] This implies in turn that the electronic wave function is not fully converged in orbital space so that the nuclear forces are not totally accurate.[31] From the fixed constant total energy of the system, i.e, the constant of motion E_{const}, it becomes apparent when the incomplete convergence of the electronic wave function in orbital space becomes problematic.[397]

$$E_{const} = \sum_i \frac{1}{2} \mu_i \langle \dot{\psi}_i | \dot{\psi}_i \rangle + \sum_I \frac{1}{2} m_I v_I{}^2 + E(\Psi_0, \{\vec{r}^A\}) = E_{tot} + \sum_i \frac{1}{2} \mu_i \langle \dot{\psi}_i | \dot{\psi}_i \rangle \tag{399}$$

The artificial orbital kinetic energy term $\sum_i \frac{1}{2} \mu_i \langle \dot{\psi}_i | \dot{\psi}_i \rangle$ (Eq. (396)) delivers an unphysical additional contribution to the total combined nuclear and electronic energy E_{tot}. Thus for physically meaningful results, the term should be kept small.[397] In fact the orbital kinetic energy is bound by constantly transferring kinetic energy from the orbital parameters to the nuclei.[31] The amount of this energy exchange, i.e., the coupling between the electronic and the nuclear degrees of freedom, is dominated by the fictitious electronic masses $\{\mu_i\}$. If the masses are sufficiently small, the coupling is weak. Correspondingly the orbital kinetic energy is small. The electrons then follow the nuclear motion adiabatically, and the system can be considered as two decoupled systems.[397] In such a case, thus for small masses and hence small kinetic orbital energies, the error introduced by the incomplete convergence of the electronic wave function is small.[399,400] Nevertheless, the fictitious masses must not be too small because the maximal time step of the simulation – and consequently its efficiency – is proportional to $\sqrt{\mu_i}$.[397,401] Finally, it should be noted that originally, a general mass parameter μ was defined.[398] More flexible MD versions with different mass parameters for different electronic variables $\{\mu_i\}$ (Eq. (396)) were only later-on proposed.[397,402]

Although Niklasson[403] recently proposed an extended formalism for a Born-Oppenheimer dynamics, Car-Parrinello techniques have significantly dominated the area of AIMD – in contrast to the Born-Oppenheimer dynamics[397] that would maybe constitute the more obvious choice. The Lagrangian for the nuclear motion in such a Born-Oppenheimer dynamics takes on a slightly modified shape compared with the Lagrangian of the Car-Parrinello-MD (Eq. (396)).[397]

$$L = \sum_I \frac{1}{2} m_I v_I{}^2 - E(\Psi_0, \{\vec{r}^A\}) \qquad (400)$$

The so-called Born-Oppenheimer forces on the nuclei are calculated from the self-consistent electronic ground-state energy.[404] To guarantee the stability of the simulation, a tight convergence criterion must be applied for the electronic SCF cycles, which makes the simulations computationally very demanding.[397] Otherwise, energies and forces would not be consistent, and the energy conservation of the dynamics would be violated.[397] This observation contrasts with the Car-Parrinello methodogy and explains its widespread use. Car-Parrinello MDs ensure energy conservation even for not converged electronic structure via the coupling between the systems, i.e., the reversible energy exchange (which is evident from the Lagrangian). They provide – for a suitable choice of the masses – only slightly less accurate energy values at a considerably lower computational cost.[31,397,405]

3.6   Hybrid Quantum Mechanics – Molecular Mechanics Approaches (QM/MM)

Since the QM/MM formalism[406] is still mostly applied to biochemical[407] and explicit solvent[408] problems and not to material science,[ddd] it is only briefly outlined in the following. The QM/MM scheme can be considered as an extension of the QM/PCM formalism because (usually due to computational limitations) only a small part of the system – the QM part – is quantum-chemically treated while molecular mechanics is employed to describe the remaining MM part. However, in contrast to QM/PCM, the MM part is not considered as a continuum, but it is rather atomistically taken into account. While Warshel and Levitt conceptually devised the methodology,[406] Karplus and coworkers presented a detailed technical survey on the QM/MM treatment.[409]

The QM/MM formalism is formally based on a partitioning of the Hamiltonian of the system $\hat{H}_{tot}$, analogously to Eq. (339), into a Hamiltonian of the QM system $\hat{H}_{QM}$, a Hamiltonian of the MM system $\hat{H}_{MM}$, and the Hamiltonian including the interaction.[410]

$$\hat{H}_{tot} = \hat{H}_{QM} + \hat{H}_{MM} + \hat{H}_{QM/MM} \qquad (401)$$

Eigenvalues of the QM- and the MM-Hamiltonian are obtained with any available quantum-mechanical and molecular-mechanical methods.[31] According to Rothlisberger and coworker,[411] almost all QM/MM approaches can be subdivided into two classes, depending on how the total QM/MM energy is obtained from $\hat{H}_{tot}$ and these QM and MM energies. In the so-called subtractive scheme, the coupling between the systems, via $\hat{H}_{QM/MM}$, is classically treated, which is a disadvantage. The total energy

---

[ddd] Among others, this results from the predominance of accurate force fields specific for biomolecules in the 80's and 90's.[407] However, due to the increase of computer power, the range of application of QM/MM has broadened, see for example [560].

$E_{QM/MM}^{sub}$ is thus obtained from the QM energy of the QM part $E_{QM}(QM)$ and the MM energy difference between the complete system and the MM part $\left(E_{MM}(QM/MM) - E_{MM}(QM)\right)$.

$$E_{QM/MM}^{sub} = E_{QM}(QM) + \left(E_{MM}(QM/MM) - E_{MM}(QM)\right) \tag{402}$$

It follows from Eq. (402) that an MM parameter set is needed for the QM part.[410] This can be problematic, for instance for excited states.[411] The implementation of subtractive QM/MM schemes is straightforward. The ONIOM approaches by Morokuma et al.[412,413] can be considered as a generalization of the subtractive QM/MM scheme to multiple layers.

In contrast, the coupling between the two parts is included on a quantum-mechanical level of description in an additive QM/MM scheme. The total energy is computed as the sum of the QM energy of the QM part, the MM energy of the MM part, and an explicit coupling term $E_{QM/MM}(I[QM/MM])$ for the interface $I[QM/MM]$.[410]

$$E_{QM/MM}^{add} = E_{QM}(QM) + E_{MM}(MM) + E_{QM/MM}(I[QM/MM]) \tag{403}$$

The key focus of all additive QM/MM schemes is to provide an adequate description for the interaction term $\hat{H}_{QM/MM}$. As outlined by Senn and Thiel, it is composed of van-der-Waals and electrostatic contributions. Moreover, if bonds are cut to define the QM system, additional bonding terms arise.[410] The actual QM/MM method is defined by the way the electrostatic coupling between the QM part and the MM part is included in $\hat{H}_{QM/MM}$. In the so-called mechanical embedding, the electrostatic interaction between the QM and the MM part is classically treated, i.e., completely alike to the van-der-Waals interaction, which is always described in a classical framework. An improved description of the interface between the QM and the MM part is achieved if the MM charges polarize the QM part, i.e., if the electrostatic potential created by their point charges is included in $\hat{H}_{QM}$ (Eq. (401)). The electrostatic interaction energy is thus treated quantum-mechanically. Although the use of force-field charges to describe the electrostatic potential of the environment could be problematic (because force-field parameters are only meaningful in their combination and do not have a direct interpretation), QM/MM approaches based on an electrostatic embedding procedure yield quite accurate results.[410] Even more precision is obtained when back-polarization of the MM charges by the charge density of the QM part is included. This defines the so-called polarized embedding. Depending on whether the back-polarization is included in a "single-shot" way or iteratively, Senn and Thiel further subdivide the polarized embedding schemes in two classes.[410]

Sometimes, covalent bonds need to be broken to separate the QM and the MM part. Link atoms, boundary atoms, or frozen-orbital approaches are employed to treat the QM/MM interface.[410] Especially in these cases, overpolarization of the QM system close to the boundary to the MM part

with the MM charges constitutes a major computational challenge. In view of this deficiency of the electrostatic embedding, Friesner and coworkers[414] reparameterized OPLS-AA Lennard-Jones parameter and specifically adapted them for the QM/MM interface so that the van-der-Waals interactions counterbalance the electrostatic overpolarization.

Effective fragment potential (EFP) approaches[415] are increasingly used so that they should be at least mentioned in this context. The effective fragment potentials are equivalent to a non-empirical polarizable force field (composed of multipoles and polarizabilities) that is derived from quantum-chemical calculations.[416] The EFPs consist of a set of one-electron terms for each surrounding molecule, for instance a solvent molecule, representing inductive, repulsive, and electrostatic interactions with the environment. They are subsequently included in the QM Hamiltonian. They are thus to some extent comparable to QM/MM interfaces based on frozen orbitals.[417]

4 Optoelectronic Processes at Organic::Organic Interfaces in Organic Solar Cells

4.1 Fundamentals of Organic Solar Cells (OSCs)

Solar cells, or equivalently photovoltaic devices, convert the energy of incident light into an electric current. OSC devices are usually constructed in a "sandwich-type" arrangement (Figure 1), i.e., the semiconducting layers are sandwiched between the anode and the cathode.[418]
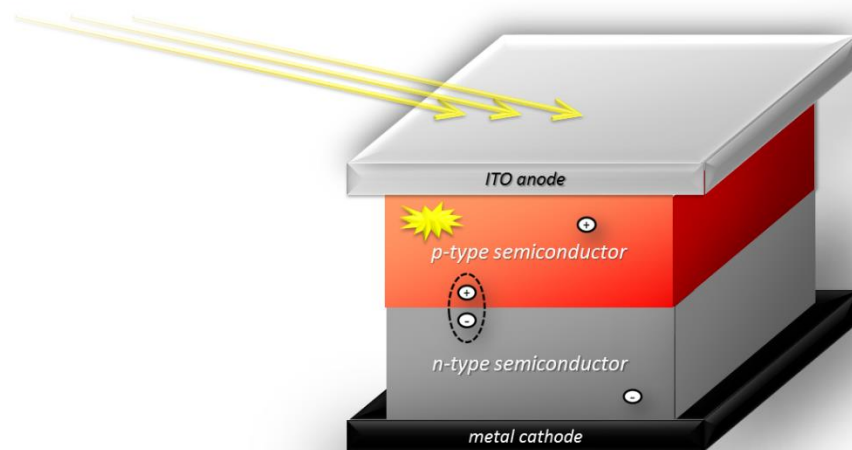
Figure 1: Schematic organic solar cell.

Compared with inorganic semiconductors, light absorption in the organic semiconducting layers does not immediately create free charge carriers. In contrast, due to the low dielectric constant in most organic materials, excitons – electron-hole pairs bound by the mutual Coulomb attraction – are generated. The excitonic character of light absorption profoundly influences all characteristics of OSCs:[19] since exciton binding energies in organic materials are considerable and reach values of several 100 meV,[419] exciton dissociation occurs mainly at the so-called donor-acceptor interface of OSCs where it is driven by the electrochemical gradient. The heterojunction is therefore the key ingredient of all OSCs, which are composed of a p-type (donor) and an n-type (acceptor) semiconducting layer in their simplest bilayer architecture.[418] In fact, Tang[420] obtained efficiencies around 1% with a first *planar* bilayer device composed of a donating phthalocyanine and an accepting perylene layer. However, the quite short lifetimes of excitons, combined with the required minimum thickness of OSC layers for sufficient light absorption, severely limit the efficiency of exciton dissociation in planar bilayer cells: due to their rather short diffusion lengths, most excitons do not reach the interface. In contrast, the *bulk heterojunction* (BHJ) architecture of OSCs,[421,422] where the donor and acceptor phases are intermixed, minimizes the required amount of exciton diffusion. More excitons can dissociate at some point of the very large interfacial area of the BHJ. The process of exciton dissociation is commonly

subdivided into two steps. At first, a so-called interfacial charge-transfer state is formed, meaning that the electron and the hole are located on adjacent molecules (an acceptor and a donor molecule, respectively). In a second follow-up step, the interfacial charge-transfer state breaks up, and a charge-separated state is formed.[19] In contrast to the first two steps of the light-to-energy conversion process in OSCs – the exciton formation and diffusion – the mechanism of exciton dissociation and charge separation is highly debated.[423] It will be addressed in more detail below. The separated charges migrate through the semiconducting layers and are eventually recollected at the electrodes.[19,424] Due to the comparably thin OSC layers compared with inorganic solar cells and the low dielectric screening, the built-in voltage (Figure 2) in OSCs results in a significant electric field.[425] Charge carrier migration in OSCs is thus mostly described by drift (and not diffusion), the more so as charge carrier densities in organic semiconductors are usually low.[418]
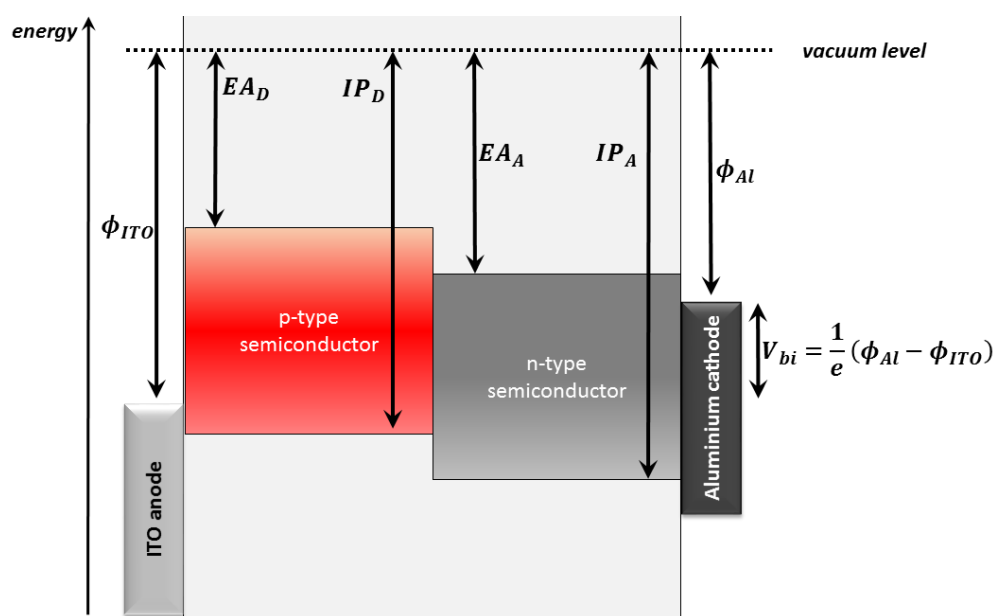
Figure 2: Energy alignment in an MIM model of an OSC under open-circuit conditions for a so-called type II heterojunction. For more information see text.[418]

The energy level alignment in OSCs can be described with a classical metal-insulator-metal model (MIM).[418] For open-circuit and short-circuit conditions, the energy levels are shown in Figure 2 and Figure 3, respectively. The built-in potential V_{bi} is defined as the difference of the work functions of the electrodes ϕ_{Al}, ϕ_{ITO}. IP_D (IP_A) and EA_D (EA_A) designate the ionization potential and electron affinity of the donor (acceptor). Under short-circuit conditions, the Fermi levels of the electrodes align by shifting charge from the cathode to the anode. This results in a vacuum level shift (Figure 3).[418] Furthermore, finite barriers for charge injection exist at both the anode and the cathode. If the electrodes provide an infinite reservoir of charge carriers, they are designated as Ohmic electrodes. Then, the electrode-semiconductor contacts form Schottky junctions, and OSC currents are space-charge limited.[418]

$$V_{bi} = \frac{1}{e}(\phi_{Al} - \phi_{ITO})$$
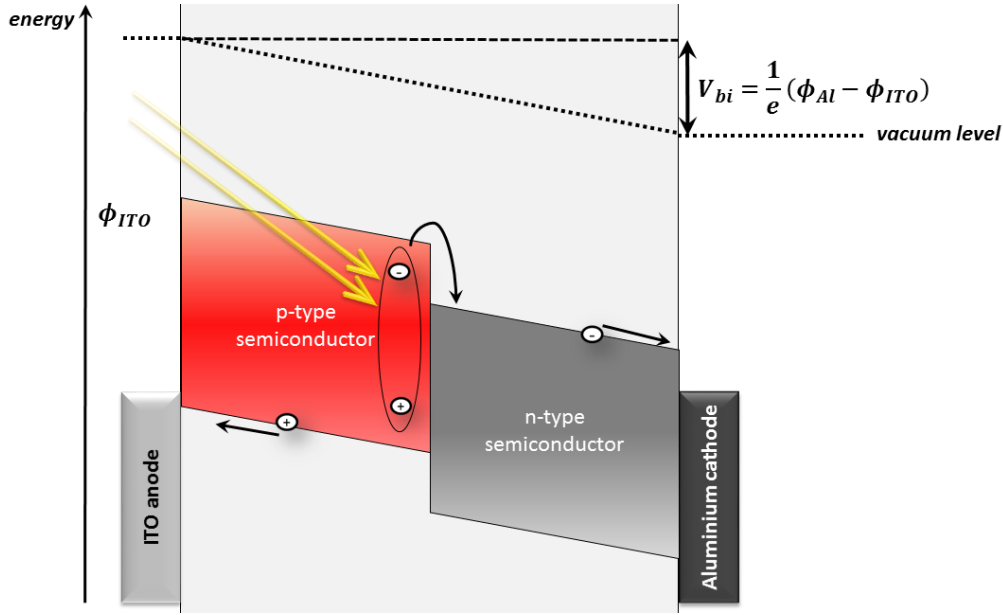
Figure 3: Energy alignment in an MIM model of an OSC under short-circuit conditions. For more information see text.[418]

Two important OSC characteristics, the external quantum efficiency (EQE) and the internal quantum efficiency (IQE), are measures for the quantum yield of the light-to-energy conversion process. The EQE corresponds to the number of recollected electrons referenced to the number of *incident* photons. It is obtained as the ratio of the short-circuit current density $J_{sc}(\lambda)$ and the intensity of the incoming light $I(\lambda)$.[418]

$$EQE(\lambda) = \frac{J_{SC}(\lambda)}{I(\lambda)} \frac{h\nu}{e} \tag{404}$$

In contrast, the IQE is defined as the ratio of the number of recollected electrons and the number of *absorbed* photons. It is thus calculated from the short-circuit current and the absorption spectrum of the cell.

Several additional figures of merit for the efficiency in OSCs exist that can be determined from the current-voltage characteristic of the cell obtained under illumination (Figure 4). Naturally, the current-voltage characteristic depends on the wavelength λ of the incident light. J_{sc} designates the short-circuit current, V_{oc} the open-circuit voltage. The maximal amount of power P_{max} that the device delivers is indicated by the yellow rectangle in Figure 4. The so-called fill factor FF corresponds to the ratio of the maximal power P_{max} and the product of the short-circuit current J_{sc} and the open-circuit voltage V_{oc} (Figure 4). The fill factor, which is easily identified from the current-voltage characteristic, is particularly useful to calculate the power conversion efficiency (PCE) η of the cell, thus the quotient of the maximum power of the OSC and the incident light intensity $I(\lambda)$.[418]

$$\eta(\lambda) = \frac{FF(\lambda) \cdot J_{sc}(\lambda) \cdot V_{oc}(\lambda)}{I(\lambda)} \tag{405}$$

Integration of Eq. (405) over all relevant wavelengths yields the PCE of the cell under sunlight illumination.[418] The efficiency depends on the short-circuit current, the open-circuit voltage, and the fill factor.
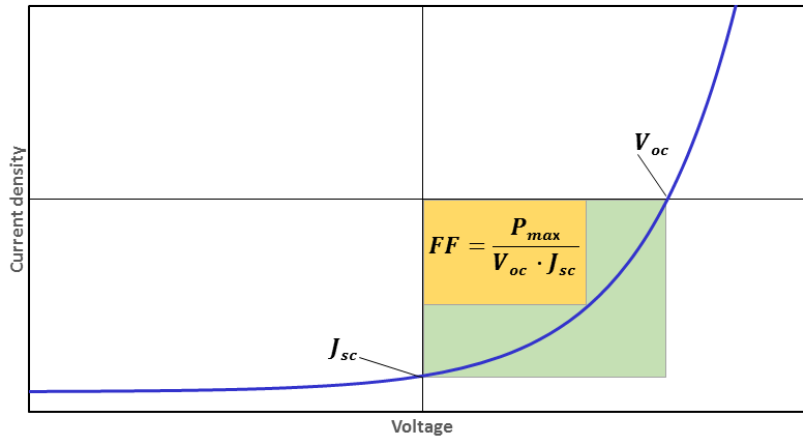
Figure 4: Current-voltage characteristic of an OSC measured under illumination. For more information see text.

The efficiency of the light-to-energy conversion process in solar cells is intrinsically limited and cannot exceed the so-called Shockley-Queisser limit.[426] Based on the principle of detailed balance, Shockley and Queisser derived an expression for the maximum efficiency of inorganic cells. Evidently, this efficiency depends on the optical gap of the cell, E_g.[418] Considering the sun as a black-body radiator, the efficiency of an ideal solar cell, which absorbs all incident photons with energies higher than $h\nu_g$, has an upper bound, the so-called ultimate efficiency[eee] $u(x_g)$, of 44% for an optimal energy gap of 1.1 eV.[426] Furthermore, Shockley and Queisser determined the steady-state current-voltage characteristic by taking into account five processes: the radiative generation of electron-hole pairs, the radiative recombination of electron-hole pairs, the non-radiative generation and recombination of electron-hole pairs, and the recollection of electrons and holes at the electrodes. According to the principle of detailed balance, the rate of photon absorption and the rate of radiative recombination are equal, as are the rates of non-radiative generation and recombination of electron-hole pairs. The electric current density $J(V)$ under steady-state conditions without illumination is then given by the Shockley equation[427] (see below).

$$J(V) = J_0 \left(e^{\left(\frac{qV}{kT}\right)} - 1 \right) = (J_{rad} + J_{non-rad}) \left(e^{\left(\frac{qV}{kT}\right)} - 1 \right) \tag{406}$$

[eee] This results because not all photons are absorbed. Furthermore, the excess energy of high-energy photons is "lost".[418]

$J(V)$ is the current at voltage V, and J_0, originally the sum of the saturation currents for electrons and holes at negative bias, corresponds to the sum of the radiative J_{rad} and the non-radiative recombination currents $J_{non-rad}$.[426]

From the current under illumination, obtained from Eq. (406) and the photocurrent, and the voltage, the maximum power of the cell can be derived. Referencing it to the power of the incident light, the maximal OSC efficiency η according to Shockley and Queisser depends on the ultimate efficiency and can be written as a function of four variables t_s, x_g, x_c, and f.

$$\eta(t_s, f, x_g, x_c) = t_s u(x_g) v(f, x_g, x_c) m\left(v^{x_g}/x_c\right) \tag{407}$$

t_s is the probability that an incident photon with an energy higher than the band gap is absorbed. x_g and x_c are ratios involving the temperature of the cell T_c, the temperature of the sun T_s, and the band gap of the cell E_g.

$$x_g = \frac{E_g}{kT_s} \tag{408}$$

$$x_c = \frac{T_c}{T_s} \tag{409}$$

f is a geometric parameter of the cell that actually subsumes a variety of phenomena. It is the product of f_c, the fraction of current generation and recombination that is radiative, a geometric parameter f_ω and of a transmission factor[fff] $t_s/2t_c$.[426]

$$f = \frac{f_c f_\omega t_s}{2t_c} \tag{410}$$

$v(f, x_g, x_c)$ corresponds to the ratio of the open-circuit voltage and the optical gap of the cell qV_{OC}/E_g. $m\left(v^{x_g}/x_c\right)$, designated as the "impedance matching factor" by Shockley and Queisser, is equal to the fill factor of a cell.[426] For optimal conditions ($t_s = 1$, $f \approx$ solid angle of a half sphere; $E_g = 1.34\ eV$, ambient and sun temperatures), the maximal achievable power conversion efficiency of an inorganic p-n-junction calculated from the Shockley-Queisser equation is 33.7 %.[418] The band gap results from the balance of optimizing the open-circuit voltage without sacrificing too much absorption in the NIR

[fff] In their derivation, Shockley and Queisser considered the thermal equilibrium for a cell surrounded by a black radiator with temperature T_c. The probability that a photon emitted by this radiator is absorbed is given by t_c.

region where the solar irradiation is maximal. It follows from the Shockley-Queisser equation that in an ideal solar cell, all existent recombination is radiative[428].[ggg]

Since the Shockley equation has already been mentioned (Eq. (406)), it should be noted that it was initially derived to describe the current-voltage characteristic of inorganic solar cells (and of any other p-n-junctions) in thermal equilibrium. Since charge carrier generation upon photon absorption is not field-assisted in inorganic solar cells, the photocurrent J_{Ph} can simply be added. A non-ideality factor of the diode η and the series and shunt (parallel) resistance R_s, R_p of the real solar cells are taken into account.[418]

$$J(V) = J_0(V) \left(e^{\left(\frac{q(V - JR_s)}{\eta kT} \right)} - 1 \right) + J_{Ph} + \frac{(V - JR_s)}{R_p} \tag{411}$$

Fitting experimental current-voltage characteristics also of OSCs to Eq. (30) (or simulating them with Eq. (30)) provides useful information (e.g., about the resistances) for further device optimization.[429,430,431]

In the Shockley-Queisser limit, i.e., for ideal *inorganic* solar cells, the open-circuit voltage can be directly expressed as a function of the bandgap of the material. At the open-circuit voltage, no net current flows so that the recombination current (for ideal cells entirely radiative) compensates the photocurrent.

$$v(f, x_g, x_c) = \frac{qV_{OC}}{E_g} \tag{412}$$

This contrasts with Scharber's seminal work[432] on the open-circuit voltage in *organic* solar cells. From a comprehensive analysis of literature data, an empirical relationship for the open-circuit voltage in OSCs was derived. In fact, V_{OC} is determined by the difference between the HOMO energy of the donor $\varepsilon_{HOMO}^{Donor}$ and the LUMO energy of the acceptor $\varepsilon_{LUMO}^{Acceptor}$. An additional constant of 0.3 eV was empirically found whose exact origin is still under debate. However, it may be interpreted as the minimal driving force for the charge-transfer step at the donor-acceptor heterointerface.[432]

$$V_{OC} = \frac{1}{e} \left(\left| \varepsilon_{HOMO}^{Donor} \right| - \left| \varepsilon_{LUMO}^{Acceptor} \right| \right) - 0.3 \, V \tag{413}$$

These findings already indicate that the excitonic character of OSCs and their heterojunction architecture require some modifications of the Shockley-Queisser limit. First of all, in OSCs, absorption does not take place into a continuum of states (like in inorganic semiconductors), but into a limited

---

[ggg] The radiative recombination results from the finite working temperature of the cell so that also the OSC must be considered as a black-body radiator.

number of well-separated electronic states. Absorption spectra are broadened by coupling to vibrations ("Franck-Condon envelope"), and emission is faster. For instance, for a molecule with one excited state in the relevant spectral region, it was shown that the maximum efficiency of OSCs reduces to 29% only due to this different excited-state landscape.[433,434] Moreover, the exciton binding energy of organic materials needs to be taken into account because Shockley and Queisser initially assumed that photon absorption immediately generates free charge carriers.[426] As outlined above, the considerable exciton binding energies in organic materials require heterojunction architectures, where absorption takes place in the donor (acceptor) phase while radiative recombination occurs rather from the only weakly-emitting interfacial charge-transfer states. A plethora of experimental evidence for such charge-transfer states exist, for instance by Veldman et al. [435,436]. Thus, in OSCs, absorption and emission occur at different energies which influences their maximum device efficiency. It implies furthermore that the interfacial charge-transfer energies need to be considered in some way to determine the ultimate efficiency of OSCs.

In a proof on the reciprocity between electroluminescence and external quantum efficiency of organic solar cells, Rau[437] and Kirchartz and Rau[438] related the photovoltaic efficiency (reverse bias) due to the low-energy charge-transfer absorption of a cell, $EQE_{PV}(E)$, to its electroluminescence efficiency (forward bias, i.e., the OSC acts an an OLED), $EQE_{EL}(E)$.

$$J_0 EQE_{EL}(E) = q EQE_{PV}(E) \phi_{BB}(E) \tag{414}$$

$\phi_{BB}(E)$ is the black-body radiation at energy E, and J_0 is the dark saturation current.

Using this theoretical framework of Rau, Vandewal et al.[439] provided extensive quantitative experimental evidence for the dependence of the open-circuit voltage on the charge-transfer state energies. On the one hand, they considered experimental values for the open-circuit voltage. On the other hand, they calculated values for V_{OC} from measured charge-transfer energies. In order to do so, Vandewal et al.[439] used the Shockley equation to express the injection current $J_{inj}(V)$ for the electroluminescence in an OSC.[439]

$$J_{inj}(V) = J_0 \left(e^{\left(\frac{qV}{kT}\right)} - 1 \right) \tag{415}$$

At the open-circuit voltage, the short-circuit current compensates the injection current. Hence reformulating the Shockley equation yields the open-circuit voltage as a function of the short-circuit current.[439]

$$V_{OC} = \frac{kT}{q} \ln\left(\frac{J_{SC}}{J_0} + 1\right) \tag{416}$$

Vandewal et al. furthermore recognized that the saturation current J_0 can be deduced from experimentally available quantum efficiencies (integrating Eq. (414)).[439]

$$J_0 = \frac{q}{EQE_{EL}} \int EQE_{PV}(E)\phi_{BB}(E)dE \qquad (417)$$

The comparison of calculated values to experimentally obtained values was excellent. With respect to the relationship between the open-circuit voltage and the charge-transfer states, they concluded that since the black-body radiation $\phi_{BB}(E)$ depends exponentially on the energy, a blue shift of the charge-transfer energy (via $EQE_{PV}(E)$) results in an exponential decrease of the saturation current. Correspondingly, due to the logarithmic dependence of the open-circuit voltage on the saturation current, V_{OC} rises linearly with the charge-transfer energy.[439] While Vandewal et al. employed polymer OSCs, Holmes and coworker recently found a similar dependence between the OSC open-circuit voltage and charge-transfer state energies for OSCs based on small organic molecules.[440]

Based on these considerations on the open-circuit voltage – and on the analytic formula for it, it is possible to determine the point of the J-V characteristic where the output power becomes maximal. To derive theoretical estimates for a "Shockley-Queisser limit" for OSCs, it is evident from Eq. (416) and (417) that some model for the external quantum efficiency, i.e., for the charge-transfer state absorption, is required. Kirchartz et al. employed a Gaussian absorption profile and calculated efficiencies around 23% for organic polymer::fullerene blends.[441] In a similar approach, Vandewal et al., based on their earlier investigations, derived a maximal efficiency of 28%, which already decreases to 16% only due to the low electroluminescence efficiencies.[442,443] Indeed, Vandewal et al. emphasize that the maximum efficiency is obtained only for an electroluminescence efficiency of 1 (Eq. (415)). However, values of $EQE_{EL} \approx 10^{-9} - 10^{-6}$ are commonly encountered for polymer-fullerene cells at room temperature.[439] Koster et al. modeled the EQE by a simplistic step function and obtained efficiency values around 30%, depending on the charge-transfer absorption and energy.[428] Finally, in an analysis entirely based on thermodynamic arguments (i.e., without requiring certain absorption/EQE profiles), Giebink et al. computed maximum efficiencies ranging from 27% to 22% that depend on the driving force of the electron transfer (0.3 − 0.5 eV).[444] Evidently, despite some differences, the Shockley-Queisser limit of OSCs, also called the radiation limit of OSCs, lies somewhere around 25%. In contrast, device efficiencies of single-junction OSCs[445,446] (and also of tandem cells[447,448]) have only recently reached the 10% landmark.

Therefore, Scharber and Sariciftci[443] stressed that the difference between the maximum efficiency of OSCs in the Shockley-Queisser limit and commonly encountered experimental efficiencies is significant. Indeed, Thompson and coworker emphasize that the presently limited device efficiencies result from a yet unoptimized balance between a "sufficient spectral coverage and augmented energy

122

level offsets".[449] Since solar irradiation is maximal in the infrared and near-infrared region, compounds with band gaps in this spectral range maximize light absorption. Yet, it follows from the relationship of Scharber et al. (Eq. (413)) that IR and NIR bandgaps inevitably come at the expense of sacrificing open-circuit voltage. Balancing these contrasting demands represents the fundamental task of solar cell optimization.

Moreover, due to the complex nature of the exciton dissociation and charge separation processes, it has been proposed, for instance by Okhita et al.,[450] that additional fundamental limits for a trade-off between the open-circuit voltage and the photocurrent exist. This requires a more detailed consideration of the exciton dissociation process. Investigations on the mechanism of exciton dissociation and charge separation are actually intimately related to the question what drives charge separation. In fact, the interfacial charge-transfer state consists of a geminate electron-hole pair with the charges separated by approximately 10 Å.[435] As a consequence, because of the low dielectric screening in organic materials,[19] the Coulomb binding energy between these charge carriers is significant (several 100 meV) and considerably exceeds the available thermal energy (25 meV at 298K).[435] Nevertheless, as thoroughly discussed by Clarke and Durrant in a comprehensive review,[423] the charge-separated state must be the energetically lowest state in functional OSCs. Therefore, a free energy gradient exists (at least in operable OPV devices) that drives the dissociation of the interfacial charge-transfer state and the subsequent charge separation. A variety of effects were shown to drive charge separation.[423,435] A detailed discussion of recent computational investigations is given below. While many of the effects contributing to the driving force are system-specific (the energy levels at the organic::organic donor-acceptor interface have to be carefully aligned[20]), others are of more general nature. Notably, entropy favors all exciton dissociation events because two separated charge carriers are entropically more favorable than a tightly bound interfacial charge-transfer state.[451] Deibel et al. subdivided contributions to the driving force into "static" and "dynamic" factors.[435] "Static" contributions directly affect the energy alignment at organic::organic interfaces, i.e., a gradient in the energy landscape exists that promotes charge separation. Apart from entropy, disorder,[26,452,453] electrostatic effects[454] such as interfacial dipole moments[455,456] or the dielectric screening of the medium,[428] the built-in field,[435] and morphological effects[457] can provide the required driving force for charge separation. In contrast, "dynamic" contributions refer essentially to the role of the excess energy of the dissociating exciton in driving charge separation. If the created interfacial charge-transfer state does not relax, i.e., if it possesses excess energy, it is considered as a "hot charge-transfer state".[435] Hot charge-transfer states were sometimes found to dissociate more easily and to result in higher quantum yields.[450,458,459] Fully relaxed (= thermalized) charge-transfer states are also designated as "cold charge-transfer states".[460]

As suggested by Okhita et al.,[450] it is the potential influence of the excess energy and of the hot exciton dissociation, i.e, the "dynamic" contributions,[435] that could additionally complicate the simultaneous optimization of the open-circuit voltage and the short-circuit current: since "hot" CT states were found to dissociate more easily, charge generation efficiencies could be improved when excess energy is available in the exciton dissociation process.[423,435] This would suggest to lower the charge-transfer state energies to increase the amount of available excess energy. Nevertheless, lower charge-transfer energies come at the expense of a reduced open-circuit voltage (Eq. (416)).[439] However, in a detailed discussion of existing literature findings, Deibel et al.[435] emphasized that from a mechanistic point of view, no fundamental limit for a simultaneous optimization of both the open-circuit voltage and the short-circuit current exists, particularly because other factors apart from the excess energy can provide sufficient driving force for charge separation.

Yet, the balance outlined for example by Thompson and coworker between the spectral coverage and the open-circuit voltage[449] remains to be optimized. Some optimization approaches are discussed in the next section.

4.2 Optimizing Efficiencies of Photovoltaic Devices

It follows from Eq. (405) that the OSC efficiency can be improved by increasing the fill factor, the short-circuit current or the open-circuit voltage (see also above).[418] From the outlined trade-off between V_{OC} and J_{SC}, it is evident that optimizing the power conversion efficiency is not trivial, as also noted for instance by Janssen.[461]

Optimizing the Fill Factor

It is evident from Figure 4 that a high fill factor is obtained if all steps of the light-to-energy conversion are field-independent. This concerns mostly the exciton dissociation as well as the charge separation and migration steps. Therefore, loosely bound geminate and non-geminate electron-hole pairs that already dissociate at the built-in voltage and high charge carrier mobilities are prerequisites for high fill factors.[418]

As underlined for example by Yu and coworkers[462] and by Blom and coworkers,[463] balanced electron and hole mobilities are especially important to avoid the accumulation of space charges. Since electron mobilities in fullerene acceptors are usually higher than hole mobilities in the donor phase, most efforts in optimizing mobilities focus on the donor phase. It is well-known that the largest charge carrier mobilities can be found in highly-ordered crystalline and pure materials,[464] which would suggest using aligned pure donor and acceptor layers in OSCs. As already mentioned above, this compromises, however, the exciton dissociation yield due to the limited exciton diffusion lengths. Forrest and coworkers proposed a hybrid planar-mixed heterojunction OSC that combines the advantages of

planar (high charge carrier mobilities) and mixed (high exciton dissociation yields) heterojunction architectures.[465] A number of other morphological modifications were introduced to ensure high charge carrier mobilities while maintaining the bulk heterojunction cell architecture. They involve particularly phase aggregation and crystallinity of the domains in the blend. Well-aggregated (crystalline) domains in the BHJ cell allow for tight interchain interactions, larger charge transport couplings, and high mobilities.[462] Domain aggregation can be for example influenced by side-chain modifications of both polymers and molecules.[466] For instance, Meager et al. systematically varied the branching point of branched alkyl side chains in polymeric diketopyrrolopyrrole donors. They found that the crystallinity in OFETs and OSC blends and the resulting charge-transport properties are a function of this branching point.[467] Another rather recent strategy is to employ fluorinated side chains, which often enhance aggregation and crystallinity.[462] Indeed, Yang et al. observed higher mobilities for different polymers if side chains were fluorinated.[468] Aggregation and crystallinity are also critically influenced by the fabrication conditions.[462] Carefully choosing the solvent for the spin-coating process and using supplementary solvent additives results in an improved aggregation behavior.[462] With X-Ray scattering techniques, Yu, Marks, Chen, and coworkers were able to elucidate the role of solvent additives. By selectively solubilizing the acceptor, they allow for a preformation of aggregated donor domains already during the spin-coating process.[469] For the same purpose, solvent mixtures (cosolvents) can be employed in the spin-coating process.[470,471] Moreover, thermal annealing[472,463] and solvent annealing[473] are known to significantly improve hole mobilities in polymers commonly employed in OSCs by increasing the fraction of well-ordered aggregates in the thin films.

Optimizing the Short-Circuit Current

Since the short-circuit current is at a constant intensity of the incident light only proportional to the EQE (Eq. (404)), increasing J_{sc} amounts essentially to optimizing the quantum efficiencies of the individual steps, i.e., of the exciton formation, diffusion, and dissociation, and of the charge separation, migration, and recollection.[418]

Optimizing Absorption

Exciton formation, or equivalently light absorption, is maximized if (1) the absorption spectrum of the OSC coincides with the emission spectrum of the sun and if (2) the absorption in this energy range is strong. To ensure sufficiently strong absorption (point (2)), OSC thin films should be as thick as possible without compromising exciton dissociation yields. This implies that thinner films can be employed with strongly absorbing molecules. A recent approach to further enhance absorption in OSCs with a given film thickness consists in the addition of noble-metal nanoparticles. Via localized surface plasmonic resonances, they largely increase the local electric field and, with it, light absorption.[464,474,475] The

amount of absorbed light is furthermore also influenced by the orientation of the molecules in the thin films of OSCs.[476,477] Solar concentrators were also found to increase OSC absorption.[478]

To maximize the overlap of the absorption with the solar spectrum (point (1)), especially the region around $\sim 750 - 850 \, nm$ is important.[479] Absorption at even higher wavelengths would deteriorate overall efficiencies because of too small open-circuit voltages.[464] In view of the discussed aggregation phenomena, it should be noted that as stressed by Heremans et al.,[479] absorption spectra of organic molecules strongly depend on the morphology and the environment. For instance, P3HT in regioregular aggregates is known to experience a significant red shift compared to its amorphous form.[480] Thus, tuning aggregation as outlined above constitutes a viable route to influence absorption properties as well. Designing compounds with strong absorption in the near-infrared (NIR) region to optimize OSC efficiencies has brought about a diversity of so-called low-band gap polymers and molecules.[481,482,483] A recurrent structural element in these low-band gap compounds is the donor-acceptor (D-A) structure that results in low-lying intramolecular charge-transfer states. A fine-tuning of the properties of D-A compounds becomes possible by independently varying the donating and the accepting moiety.[464] It was furthermore shown that strong absorption in the NIR region can also be obtained from compounds where quinoid resonance structures are important.[484,485] Nevertheless, as highlighted by Brabec et al.,[4] two major loss mechanisms in OSCs consist firstly in the sub-bandgap transmission, which is indeed diminished when using low-bandgap compounds, but secondly in the thermalization of hot charge carriers, which is larger when using low-bandgap compounds. Strategies were proposed to eliminate this deficiency of low-bandgap OSCs. Using ternary solar cells offers the possibility to include NIR absorption properties without sacrificing too much energy to thermalization losses.[464] Ameri et al. outline the possible mechanisms in ternary OSCs that result in increased device efficiencies, for instance cascade charge transfer, parallel charge transfer, or energy transfer.[486,487] Often, ternary blends are composed of a wide-band gap polymer, an acceptor, and a sensitizer that can be a low-bandgap molecule/polymer or a nanoparticle.[486] As outlined by You and coworkers,[487] the maximum OSC efficiency derived from the Shockley-Queisser limit[434] for single-junction cells could even be surpassed in such ternary blends by incorporating singlet fission/upconversion compounds as one of the components. A complementary approach to ternary blends is the so-called tandem cell, which also has a higher ultimate efficiency than conventional single-junction cells.[434] In tandem cells, two solar cells with complementary absorption profiles are combined.[488] As they are usually connected in series, an intermediate layer must be inserted that should allow for the alignment of the Fermi levels of the top donor and the bottom acceptor layer.[488]

Optimizing Exciton Diffusion

To obtain high short-circuit currents, exciton diffusion must be sufficiently fast so that the exciton reaches the interface within its limited lifetime. Akselrod et al.[489] were able to demonstrate in tetracene films that, similar to charge transport, exciton diffusion corresponds to a random walk, and that it is affected by disorder. Thus the same effects as discussed for optimal charge carrier mobilities should be equally advantageous for exciton diffusion. Due to the longer lifetime of triplet states, it was suggested to take advantage of triplet exciton diffusion instead of singlet exciton diffusion in OSCs.[490] Triplet exciton diffusion comes, however, at the expense of smaller couplings resulting in smaller exciton diffusion velocities. Nevertheless, the longer lifetimes seem to be decisive at least in some situations. For example, Heremans et al. demonstrated that the addition of a phosphorescent sensitizer, converting all singlet to triplet excitons, can increase the exciton diffusion lengths in polymers from 4 nm to 9 nm.[479] Podzorov and coworkers even observed triplet exciton diffusion lengths in the micrometer regime (2-8 μm) in highly ordered semiconductors.[491]

Optimizing Exciton Dissociation and Charge Separation

In addition to the driving force, the exciton dissociation and charge separation yield is also significantly influenced by the blend morphology.[418] As outlined by Yang and coworkers, percolation pathways must exist in the blend so that the electron and the hole formed upon exciton dissociation can rapidly migrate to the respective electrodes.[492] Indeed, it has been generally agreed that an intermixed phase-segregated morphology of the heterojunction with bicontinuous percolation pathways for the separating charges ensures optimal exciton dissociation efficiencies.[492] Janssen and coworkers were able to resolve such percolation pathways in a three-dimensional blend of a hybrid polymer solar cell.[493] According to Yang and coworkers, by carefully choosing the processing solvents, lateral phase separation during the fabrication process, which eventually leads to the interpenetrating network of percolation pathways, can often be triggered.[492] In some systems, vertical phase separation, induced by the different surface energies of the donor and the acceptor component, is additionally observed.[494] Therefore, the so-called inverted architecture was proposed (sometimes with the additional advantage of longer lifetimes). In inverted OSCs, ITO forms the cathode and accepts electrons from the fullerene layer.[492,494] The importance of percolation pathways was also highlighted for example by McGehee and coworkers[495] who stressed particularly the influence of the percolation pathways on bimolecular recombination. According to McGehee and coworkers,[495] bimolecular recombination can have an efficiency-limiting impact on OSC performances. It can be minimized by ensuring fast and directed charge transport of charge carriers produced upon exciton dissociation via the percolation pathways to the electrodes. McGehee and coworkers actually found a direct correlation between the recombination rates and the thin-film charge mobilities.[496] As a final example, in a recent analysis of

blend morphologies composed of diketopyrrolopyrrole polymers, Janssen and coworkers found a dependence of the short-circuit current on the width of the diketopyrrolopyrrole fibers in the blend, i.e., on the width of the percolation pathways for holes. They individually addressed the influence of the drying rate, the cosolvent type, the blend ratio, and additives on the fiber widths and came up with an empirical nucleation-and-growth model to rationalize the formation of the interpenetrating network.[497]

High charge carrier mobilities essential for high fill factors are naturally also prerequisites for high short-circuit currents (see previous section).[498]

Optimizing Charge Recollection at the Electrodes

Finally, the short-circuit current is also determined by the efficiency of charge extraction at the electrodes. The energy transport levels must be aligned with the work functions of the electrodes to produce Ohmic contacts.[418] Usually, this is achieved by inserting interfacial hole-selective and electron-selective layers. With the additional layers, so-called multilayer device architectures (in contrast to bilayer devices, see above) result.[418] The inserted interfacial layers contribute to the stability of the device, define its polarity, and minimize charge recombination at the electrodes.[464] PEDOT:PSS is most commonly used as the hole-selective layer.[464] Due to its acidic and hygroscopic nature and its structural inhomogeneity, however, it would be desirable to replace it.[499] Inorganic layers such as MoO_3[500] and organic compounds, for instance polyaniline,[501] have already been used as alternative hole-selective layers. The cathode is usually composed of aluminium, and Ca or LiF are used as the electron-selective layers.[464] Meanwhile, ZnO_x is also frequently employed.[502,503] Organic layers as electron-selective layers are rather uncommon. However, polyelectrolytes and self-assembled monolayers are sometimes inserted to improve the energy alignment of the cathode via the formation of dipole layers.[464,503] For instance, using such dipole layers in a tandem-cell device, Yang and coworkers fabricated an OSC based on small organic molecules with an efficiency exceeding 10%.[504]

Optimizing the Open-Circuit Voltage

With respect to the optimization of the open-circuit voltage (Eq. (405)), it follows from the relationship of Scharber et al.[432] (Eq. (413)) that a precise energy alignment of the electronic states of the donor and the acceptor is essential for high open-circuit voltages. The difference between the donor HOMO and the acceptor LUMO ($\approx$ the energy of the interfacial charge-transfer state) should be as large as possible while (1) retaining an optical gap (usually of the donor) in the relevant spectral region, (2) precluding ground-state electron transfer, and (3) still keeping the driving force for charge-transfer sufficiently large to enable exciton dissociation. Saunders and coworker[13] outline a number of design strategies how to tune the energy levels of the donor and the acceptor by structural modifications. For

instance, fluorination is not only a viable tool to improve film aggregation, but stabilizes the HOMO energies of donors as well, which has resulted in larger open-circuit voltages.[4] Donor-acceptor compounds were also widely utilized to optimize open-circuit voltages. Since the HOMO and the LUMO of these compounds are largely localized on the individual donor and acceptor moieties,[464] separate tuning of the energy levels becomes feasible.[4] In a combined experimental and theoretical approach, Leclerc and coworkers[505] were able to systematically vary the open-circuit voltage in a series of copolymers. The significance of such modular approaches to obtain high open-circuit voltages was also stressed by Li and Janssen and coworkers.[506]

Furthermore, the charge-transfer state energies, which are related to the open-circuit voltage as pointed out by Vandewal et al.[439] and by Deibel et al. (see above),[435] are not only influenced by the transport energies of the individual components, but also by their Coulomb binding energy. The Coulomb binding energy can be reduced by increasing the dielectric constant of the medium, which results in higher-lying and more loosely bound charge-transfer states.[428] Charge separation proceeds more easily from such loosely bound charge-transfer states. In a similar way, Havenith and coworkers[507] found that permanent dipole moments in the interfacial region can drive charge separation by increasing charge-transfer state energies: the additional electric fields arising from the permanent dipoles weaken the Coulomb binding energy. Inserting ultrathin ferroelectric layers in the interfacial region of OSCs[508] or employing ferroelectric donor polymers[509] equally reduces the Coulomb binding energies of charge-transfer states via additional electric fields.

It has been often pointed out that the open-circuit voltage is intimately related to the efficiency of recombination.[435] In fact, Vandewal et al.[439] recognized non-radiative recombination processes as a major efficiency-limiting factor in OSCs because they directly reduce the open-circuit voltage (Eq. (416)).[442,443] In the same sense and based on results of Veldman et al.[436] and of Vandewal et al.[510], Deibel et al. explain the difference between the interfacial charge-transfer energies and the measured open-circuit voltage with additional non-geminate (bimolecular) recombination losses. Recombination losses can be reduced by decreasing the coupling between the donor and the acceptor.[439,511] Moreover, recombination losses equally diminish when the Coulomb binding energies of electron-hole pairs decrease (the Coulomb capture radius increases, see below). Indeed, Clarke and Mozer and coworker were able to directly relate bimolecular recombination losses (and correspondingly decreased open-circuit voltages) to the dielectric constant of the medium.[512]

After this outline of device fabrication and optimization, the theoretical description of the microscopic molecular transfer processes is discussed in more detail in the next section. In a first step, exciton and charge transport are addressed. Subsequently, current microscopic models for charge separation are analyzed with a special focus on contributions from computational chemistry.

4.3 Exciton and Charge Transport in Organic Materials

As outlined by Jortner,[513] a close analogy exists between non-adiabatic electron transfer described by classical Marcus theory and the description of excitation energy transfer or small polaron motion. The basics of Marcus theory are therefore briefly presented. Subsequently, exciton and charge transport are individually addressed. While doing so, some computational investigations on exciton and charge transport in disordered organic materials are mentioned.

Marcus Theory[514] for Non-Adiabatic Electron Transfer

According to Jortner,[513] non-adiabatic electron transfer can be considered as a non-radiative decay process between two vibronic levels of a compound. From first-order perturbation theory (Fermi's Golden Rule), the rate k_{ET} is determined by the coupling between the electronic reactant and product states ψ_R, ψ_P, the overlap of the vibrational wave functions Φ_R, Φ_P, and the density of states ρ of product states at the energy difference E.[515] H is the Hamiltonian of the system.

$$k_{ET} = \frac{2\pi}{\hbar} |\langle\psi_R|H|\psi_P\rangle|^2 |\langle\Phi_R|\Phi_P\rangle|^2 \rho(E) \tag{418}$$

While the intermolecular vibrations are often classically treated, the intramolecular vibrations of the ground and the excited state are considered as (displaced) harmonic oscillators (force constant k). It is well-known that for a single vibration i excited at level m, the Franck-Condon factor $\left|\langle\Phi_{R,0}|\Phi_{P,m}\rangle\right|^2$, the square of the overlap between the two vibrational wave functions, can then be expressed in terms of the Huang-Rhys parameter S.[hhh]

$$\left|\langle\Phi_{R,0}|\Phi_{P,m}\rangle\right|^2 = \frac{S_i^m}{m_i!} e^{-S_i} \tag{419}$$

The Huang-Rhys parameter associates the change in the equilibrium coordinate ΔQ upon absorption with the vibrational frequency ω_i.[418] It thus describes the effective electron-phonon coupling.[435]

$$S_i = \frac{\frac{1}{2} k \Delta Q^2}{\hbar \omega_i} \tag{420}$$

The quantity $\frac{1}{2} k \Delta Q^2$ is defined as the relaxation energy λ and corresponds to half the reorganization energy of classical Marcus theory.[418,514] Using only a single effective vibrational mode ω, the final rate is then obtained as

---

[hhh] The Franck-Condon factor corresponds only to a Poisson distribution if the available thermal energy is small compared to the vibrational frequency ω_i.

$$k_{ET} = \frac{2\pi}{\hbar} |\langle \psi_R | H | \psi_P \rangle|^2 \left(\frac{1}{4\pi\lambda_0 kT} \right)^{1/2} \sum_{m=0}^{\infty} e^{-S} \frac{S^m}{m!} e^{\left(\frac{-(\lambda_0 + m\hbar\omega + E)^2}{4\lambda_0 kT} \right)} \qquad (421)$$

λ_0 is the reorganization energy of the medium. The second term $\left(\frac{1}{4\pi\lambda_0 kT} \right)^{1/2}$ describes the density of states of the classical medium modes.[435] The last exponential term refers to the population of molecules that have sufficient energy to undergo the electron transfer isoenergetically.[515] Eq. (421) corresponds to the semiclassical Marcus rate.[435] It is also designated as the Levich-Jortner rate.[513]

Classical Marcus theory naturally arises from the Levich-Jortner hopping rates in the high-temperature limit, i.e., if also intramolecular vibrations can be classically treated. The total reorganization energy λ, composed of the external (medium) and the internal reorganization energy, describes the density of states.[418,515]

$$k_{ET} = \frac{1}{\hbar} |\langle \psi_R | H | \psi_P \rangle|^2 \left(\frac{\pi}{\lambda kT} \right)^{1/2} e^{\left(\frac{-(\lambda + E)^2}{4\lambda kT} \right)} \qquad (422)$$

In the original derivation of Marcus on isoenthalpic electron transfer reactions in solution, an electron transfer activated[515] by thermal fluctuations is considered.[514] The reactant and product energies are expressed as harmonic functions of a joint solvent-and-solute coordinate. The transition state energy is determined from the crossing point of the two parabola and expressed as a function of the reorganization energy.[514]

The Marcus rate equation as a diabatic model for the weak-interaction limit has been widely used to analyze exciton and charge transport phenomena, the subjects of the next two subsections.

Excitons and Exciton Transport in Organic Materials

Transport phenomena in OSCs are ultimately determined by the interactions between the molecules/polymer segments in thin films. These interactions are most easily derived from effective Hamiltonians because the eigenvalues of these effective Hamiltonians correspond to the energy states of the assembled molecules.[516]

In a first step, a pair of identical molecules 1,2 is considered, which is excited into one of the excited dimer states $\Psi_{ex} = 1/\sqrt{2} \left(\Psi_1^* \Psi_2 \pm \Psi_1 \Psi_2^* \right)$.[iii] The Hamiltonian of the system H is defined by the Hamiltonians of the individual molecules H_1, H_2 and the interaction Hamiltonian V_{12}, $H = H_1 + H_2 + V_{12}$. The excited-state energies E are given by[418]

[iii] It should be noted that the overlap between the wave functions is neglected.

$$E = \frac{1}{2}\langle \Psi_1^*\Psi_2 \pm \Psi_1\Psi_2^* | H_1 + H_2 + V_{12} | \Psi_1^*\Psi_2 \pm \Psi_1\Psi_2^* \rangle \tag{423}$$

$$= E_1^* + E_2 + \langle \Psi_1^*\Psi_2 | V_{12} | \Psi_1^*\Psi_2 \rangle \pm \langle \Psi_1^*\Psi_2 | V_{12} | \Psi_1\Psi_2^* \rangle$$

While the third term in Eq. (423) is an induction/polarization term (see SAPT), the fourth term corresponds to the splitting of the excited states in a dimer, i.e., it is the coupling V between excitations localized on monomer 1 and monomer 2. The transition dipole moment from the ground state to Ψ_{ex}, $\vec{\mu}$, is simply the sum of the transition dipole moments of the individual monomers $\vec{\mu}_1, \vec{\mu}_2$.[418]

$$\vec{\mu} = \frac{1}{\sqrt{2}}(\vec{\mu}_1 \pm \vec{\mu}_2) \tag{424}$$

Depending on the couplings and transition dipole moments, two limiting cases for the excited-state splitting can be distinguished. For stacked dipole moments, the coupling is positive. The negative linear combination is the lower excited state, and the transition dipole moments mutually cancel. Only the higher-lying excited state of the dimer is bright. The coupled molecules form a so-called H-aggregate. For linearly aligned molecules, the coupling is negative. Hence, a net transition dipole moment results only for the lower excited state. Consistently, the second excited state is dark. The aggregate is designated as a J-aggregate.[418] Albeit being derived from a dimer Hamiltonian, the classification of J- and H-aggregates also holds for higher aggregates (composed of many molecules).

Yet, in a meaningful Hamiltonian H for exciton transport in such supramolecular aggregates, additional effects and more molecules than in Eq. (423) have to be included. A model Hamiltonian for exciton transport in an aggregate can for example be written (adapted from Troisi and coworkers[517]) assuming only one electronically excited state per site j.

$$H = \sum_j \left\{ (E_j + \Delta E_j) + \sum_k g_j^{(k)} q_j^{(k)} \right\} |j\rangle\langle j| \tag{425}$$

$$+ \sum_j \left\{ J_j + \Delta J_j + \sum_k a_j^{(k)} \left(q_j^{(k)} - q_{j+1}^{(k)} \right) \right\} |j\rangle\langle j+1| + CC$$

$$+ \sum_j \sum_k \left\{ \frac{1}{2} m^{(k)} \left(\dot{q}_j^{(k)} \right)^2 + \frac{1}{2} m^{(k)} \left(\omega^{(k)} q_j^{(k)} \right)^2 \right\}$$

Vibrations k are described by harmonic oscillators. They are defined in terms of their effective masses $m^{(k)}$, frequencies $\omega^{(k)}$ and nuclear coordinates $q_j^{(k)}$. J_j couples electronic excitations at sites j and $j + 1$. ΔE_j is the disorder of excitonic site energies (static diagonal disorder), ΔJ_j the disorder of electronic couplings (static off-diagonal disorder).[418] $g_j^{(k)}$ couples an electronic state and its vibrations at site j,

i.e., it is the local electron-phonon coupling (dynamic diagonal disorder). In contrast, $a_j^{(k)}$ modifies the coupling between sites j and $j + 1$, which varies due to intermolecular vibrations. Thus $a_j^{(k)}$ constitutes the non-local electron-phonon coupling (dynamic off-diagonal disorder).[517]

Depending on the relative orders of magnitudes of the couplings/disorder contributions in Eq. (425), two regimes of exciton transport can be distinguished. If the electronic coupling J_j is significantly larger than the static disorder $\Delta H_j, \Delta J_j$ and the dynamic disorder $g_j^{(k)}, a_j^{(k)}$, exciton transport is coherent. It is then described by band transport. In contrast, if any of the disorder contributions is larger than the electronic coupling, exciton transport becomes incoherent. Usually, either the static or the dynamic diagonal disorder are responsible for incoherent transport. In fact, Troisi and coworker outlined that the non-local electron phonon coupling (dynamic off-diagonal disorder) produces only pronounced effects on exciton transport if the latter is coherent.[518] Incoherent exciton transport is described in a hopping regime. Depending on the relative couplings, it may either be disorder-limited (static diagonal disorder dominates) or "reorganization-limited" (dynamic diagonal disorder dominates), or limited by a combination of both reorganization and disorder. Compared with coherent transport, incoherent random exciton diffusion in the hopping regime is observed in the vast majority of situations.[518] As already noted by Jortner, it can be described for example with Marcus hopping rates.[519]

A further, very common differentiation of incoherent exciton hopping processes is based on the dominant coupling mechanism. Using Fermi's Golden rule (weak coupling limit), the coupling of the excited states of a donor-acceptor system where the excitation migrates from the donor (Ψ_D) to the acceptor (Ψ_A) can be expressed as a matrix element of the perturbing Coulomb operator.

$$V' = \left\langle \mathcal{A}\Psi_D^*\Psi_A \left| \frac{1}{|r|} \right| \mathcal{A}\Psi_D\Psi_A^* \right\rangle \tag{426}$$

$$= \left\langle \Psi_D^*\Psi_A \left| \frac{1}{|r|} \right| \Psi_D\Psi_A^* \right\rangle - \left\langle \Psi_D^*\Psi_A \left| \frac{1}{|r|} \right| \Psi_A^*\Psi_D \right\rangle$$

$\mathcal{A}$ is the antisymmetrizing operator.

While the first term in the second line of Eq. (426) corresponds to a Coulomb-type coupling, the second term represents an exchange coupling. In the point-dipole approximation, the Coulomb coupling constant can be further simplified by introducing the transition dipole moments of the donor and the acceptor $\vec{\mu}_D, \vec{\mu}_A$. κ is an orientational factor. Transport mediated by such dipole-dipole couplings is designated as Förster energy transfer.[418]

$$V' \sim \frac{|\vec{\mu}_D||\vec{\mu}_A|}{R^3}\kappa \tag{427}$$

Since the transition dipole moments can be related to spectroscopically accessible quantities, this leads ultimately to the famous expression for the rate of excitation energy transfer derived by Förster. It includes the so-called Förster radius R_0, which depends on the spectral overlap between donor and acceptor, and the donor lifetime τ_0^D.[520]

$$k_{ET} = \frac{1}{\tau_0^D} \left(\frac{R_0}{R} \right)^6 \tag{428}$$

Although the Förster-type dipole-dipole coupling usually dominates the long-range behavior of the Coulomb coupling, the latter might deviate from the expected R^{-3}-dependence due to higher-order multipoles.[521]

In contrast, transport mediated by the exchange coupling (Eq. (426)) is called Dexter transfer.[522] Since the coupling corresponds essentially to an exchange of electrons, it depends on the wave function overlap and is strongly distance-dependent. Therefore, it is significant only at short intermolecular distances. Triplet exciton transport is mediated by Dexter-type couplings.[490]

It should be noted that the coupling calculated according to Eq. (426) is approximate. As outlined by Hsu,[166] there are additional contributions, namely an overlap-dependent term, which features an exponential dependence on the intermolecular overlap, similar to the exchange coupling of Dexter transfer. It results because in the derivation of Eq. (426), the finite overlap S_{if} between the initial and final diabatic states $\mathcal{A}\Psi_D^*\Psi_A$ and $\mathcal{A}\Psi_D\Psi_A^*$ was neglected. In general, the coupling (for electron or excitation energy transfer) between two diabatic states (initial and final energies E_i, E_f) is computed as the off-diagonal element of the Löwdin-diagonalized Hamiltonian.[166]

$$V = \frac{H_{if} - (E_i + E_f)S_{if}/2}{1 - S_{if}^2} \tag{429}$$

It could be shown that the overlap-dependent term plays a role that is at least as important as the Dexter-type coupling. In the short-range limit, it should therefore not be neglected.[523]

From a modeling perspective, incoherent exciton transport is often modeled with kinetic Monte Carlo (KMC) simulations[524,525,526,527] and Marcus-type rates in order to obtain macroscopic accessible diffusion lengths. For instance, Lu et al.[528] and Köse et al.[529,530] simulated exciton diffusion in P3HT, a system of particular interest for solar cells.[4] Beljonne et al. compared the temperature dependence of exciton transport rates in organic oligomers and observed a pronounced decrease of the spectral overlap with higher temperatures. As a consequence, diffusion rates obtained from the spectral overlap (Fermi's Golden Rule) decrease more than corresponding Marcus rates.[531] Nevertheless, a

good accordance between exciton diffusion lengths obtained with KMC and Marcus rates and experimental values was found for organic crystals.[532]

Before considering charge transport, some microscopic excitonic processes are briefly mentioned that change the number of excitons. During singlet fission, a singlet exciton splits into two triplet excitons.[533,534] This implies, among others, that the singlet excited state must be at least twice as high as the triplet excitation. A number of additional prerequisites exist for the couplings between these excited states.[535,536] Spectroscopic evidence provided by Musser et al. suggest that singlet fission is mediated by the same mechanisms as internal conversion, particularly by strong non-adiabatic coupling elements.[537] The reverse process of singlet fission, triplet-triplet annihilation, can decrease the quantum yield of OLEDs (organic light-emitting diodes) based on triplet emitters,[538] but is equally used to increase the luminescence efficiency[539] of OLEDs based on fluorescent dyes. It is actually a representative of the more general so-called upconversion processes.[434] In upconversion processes, lower-energy photons are converted into higher-energy photons.[434] Analogously to triplet-triplet annihilation, singlet-singlet annihilation is observed as well. Singlet-singlet annihilation can be used to convert low-energy excitons from the infrared part of the solar spectrum into higher-energy excitons.[540] More generally, different types of upconversion processes may be employed in OSCs, especially in order to obtain higher open-circuit voltages.[541]

Charge transport in Organic Materials

The Hamiltonian for charge transport in organic materials is completely equivalent to its counterpart for exciton transport (Eq. (425)).

$$H = \sum_j \left\{ (E_j + \Delta E_j) + \sum_k g_j^{(k)} q_j^{(k)} \right\} |j\rangle\langle j| \tag{430}$$

$$+ \sum_j \left\{ J_j + \Delta J_j + \sum_k a_j^{(k)} \left(q_j^{(k)} - q_{j+1}^{(k)} \right) \right\} |j\rangle\langle j+1| + CC$$

$$+ \sum_j \sum_k \left\{ \frac{1}{2} m^{(k)} \left(\dot{q}_j^{(k)} \right)^2 + \frac{1}{2} m^{(k)} \left(\omega^{(k)} q_j^{(k)} \right)^2 \right\}$$

E_j and J_j are the site energies for charge carriers and electronic couplings for charge transfer in a perfect crystal, respectively. ΔE_j and ΔJ_j are again the diagonal and off-diagonal static disorder at site j. $g_j^{(k)}$ is the local electron-phonon coupling (dynamic diagonal disorder), while $a_j^{(k)}$ is the non-local electron-phonon coupling (dynamic off-diagonal disorder).[418]

Similar to exciton transport, different regimes for charge transport may be differentiated, depending on which coupling element in the Hamiltonian is dominant. If the electronic coupling is significantly larger than all other contributions, band transport results. Band transport is particularly characterized by its marked temperature dependence of the mobility μ as $\mu \sim T^n, 0 < n < 3$.[418] However, even if band transport is the dominating transport regime, band widths in organic semiconductors are small, resulting from the rather small charge transport couplings due to the comparably weak intermolecular interactions.[418] Moreover, Troisi[464] pointed out that a very high purity of the semiconducting layers is an additional prerequisite for band transport because already the existence of some defects can convert a band transport into a hopping transport.

Similarly, if any of the disorder contributions becomes more important than the electron transfer coupling in the Hamiltonian, the hopping regime prevails as well. As outlined by Köhler and Bässler,[418] a further subdivision of the hopping transport of charges is possible: alike to exciton transport, the charge transport processes may either be limited disorder-limited or limited by coupling to phonons (or both).

Polaronic Transport

One usually refers to polaronic transport if dynamic disorder is dominant, i.e., if the coupling to phonons is strong. The combination of the charge carrier and its lattice deformation is then designated as a polaron. Furthermore, since the lattice deformation in organic materials is usually rather localized, the polaron is considered as a small polaron.[464] The transport of small polarons is often described in the diabatic limit, for instance with Marcus rates.[464] Small polaron theory was originally proposed by Holstein.[542,543] Compared with the Hamiltonian in Eq. (430), the Holstein Hamiltonian includes only disorder due to the local electron-phonon coupling. If the electronic coupling, which is assumed to be weak, is neglected in a first step, the site energies are given by[544]

$$\varepsilon_j = E_j - \frac{1}{2}\sum_k \hbar\omega_j^{(k)}\left|g_j^{(k)}\right|^2 + \sum_k \hbar\omega_j^{(k)}\left(n + \frac{1}{2}\right) \tag{431}$$

The second term in Eq. (431) is called the polaron binding energy E_{pol}; it corresponds to the intramolecular relaxation energy upon charge transport (see also Eq. (420)).[544] Evidently, its expression is based on an harmonic approximation for the site energy E_j as a function of the nuclear coordinates q. It can be shown that the activation energy for electron transfer corresponds to half the polaron binding energy.[jjj] Using these zero-order site energy, the Holstein charge transport rates are obtained

---

[jjj] Similarly, in Marcus theory, the activation energy corresponds to a quarter of the reorganization energy.

from first-order perturbation theory, which yields a Golden rule-like expression. If the vibrations are classically treated (high-temperature regime), the Holstein hopping rates are given by[418,544]

$$k_{ET} = \frac{V^2}{\hbar} \sqrt{\frac{\pi}{2E_{pol}kT}} e^{-\left(\frac{E_{pol}}{2kT}\right)} \tag{432}$$

For sufficiently strong electron-phonon couplings, the Holstein model predicts a characteristic temperature dependence of the charge carrier mobility. With the Einstein equation $\mu kT = eD$ and the dependence of the diffusion coefficient D on the transfer rate $D = (1/2\,n)k_{ET}a^2$ (n is the dimension of the system, a the intersite distance), it can be seen that the mobility increases for intermediate temperature, while it decreases again in the high-temperature limit.[544]

Disorder-Limited Transport

In the case of disorder-limited transport, variations of site energies ΔE_j and coupling values ΔJ_j are large compared to the electronic coupling J (Eq. (430)).[418] A conceptually simple and physically grounded model[425] to describe transport in disordered organic semiconductors is the Gaussian disorder model or, equivalently, the Bässler model.[25] The two key elements of the Bässler model are a Gaussian-shaped density of states (DOS) and asymmetric hopping rates.[425] The Gaussian shape of the DOS $g(E)$ is a consequence of the central limit theorem[545] because the energetic distribution of the sites arises from the combined effects of a large number of randomly distributed independent variables such as intersite distances, polarization energies, equilibrium couplings, etc.[418,425]

$$g(E) = \frac{1}{\sqrt{2\pi\sigma^2}} e^{-\left(\frac{E^2}{2\sigma^2}\right)} \tag{433}$$

The DOS is characterized by its width σ, the so-called disorder parameter.[418] It was observed[418] that σ is larger if static dipole moments are present in the environment.[546] σ characterizes the (static) diagonal disorder.[425]

Since site energies differ, hopping rates between forward and backward hops are asymmetric. Miller and Abrahams[547] included this asymmetry simply via a Boltzmann factor in the hopping rate v_{if} between an initial site i with energy E_i and a final site f with energy E_f. The rate v_{if} additionally contains a factor v_0, sometimes called the attempt-to-hop frequency,[418] and a coupling term. In the case of charge transport, the coupling depends on the wave function overlap. Therefore, the coupling term is usually approximated as an exponential function of the intermolecular distance. It contains the distance r_{if} between the initial and final sites i, f and a parameter γ. The Miller-Abrahams hopping rates are therefore defined as[418,425]

$$\nu_{if} = \nu_0 e^{-2\gamma r_{if}} \cdot \begin{cases} e^{-\frac{E_f - E_i}{kT}} & E_i < E_f \\ 1 & E_f < E_i \end{cases} \tag{434}$$

The off-diagonal disorder may additionally be included by using a Gaussian distribution for the coupling parameter, the exponential term $2\gamma r_{if}$, as well.[425] However, as pointed out by Hertel and Bässler,[548] a Gaussian distribution is physically not as well-grounded for the couplings as for the site energies. KMC simulations based on the Gaussian-shaped DOS and Miller-Abrahams hopping rates were widely employed to investigate the effects of disorder (especially, but not only of static disorder) on macroscopic transport parameters.[418,425]

An important conclusion from the Bässler model is a distinct time and temperature dependence of the charge carrier mobility in disordered semiconductors. In fact, after photoexcitation, charge carriers relax in the Gaussian DOS to thermal equilibrium following a logarithmic decay law. Due to this time-dependent energetic relaxation, the charge carrier mobility is initially time-dependent as well. This implies that transport is dispersive until thermal equilibrium is reached. Then, charge carrier mobilities are time-independent. The equilibrium energy E_{eq} of the charge carriers depends on the temperature and on the disorder and is given by[418,425]

$$E_{eq} = \lim_{t \to \infty} \langle E(t) \rangle = -\frac{\sigma^2}{kT} \tag{435}$$

Evidently, the equilibrium energy is below the center of the DOS so that charge transport processes are thermally activated. Moreover, since the equilibrium energy of charge carriers decreases with decreasing temperature, the temperature dependence of the charge transfer rates, and concomitantly of the mobility, should deviate from an Arrhenius-type law,[418,548] and therefore differs compared with polaronic transport (Eq. (432)). The temperature dependence of the mobility for disorder-limited transport is usually given by (C, μ_0 are constants) [418,425]

$$\mu = \mu_0 e^{-C\left(\frac{\sigma}{kT}\right)^2} \tag{436}$$

It should be furthermore noted that this holds only for low charge carrier densities.[544]

In disordered organic semiconductors, it is usually assumed that both disorder-related and polaronic effects are important for a complete description of charge transport.[418] Different models have been proposed to describe the combined effects. Furthermore, from a theoretical point of view and as outlined by Andrienko et al., a detailed understanding of the charge transport processes on a molecular level is only accessible from simulations with parameters obtained in *ab initio* calculations, i.e., without empirical parameters.[30] A variety of investigations based on first-principle calculations exist that

combine elements from polaron transport and disorder-limited transport. Usually, the disorder of electronic couplings is included as well. In fact, the influence of both types of static disorder was particularly addressed by Andrienko et al.[549,550,551] and by Gennett et al.[552] Furthermore, Li et al. calculated mobilities in disordered films of anthracene derivatives,[553] and Nelson et al. similarly computed electron mobilities in fullerene C_{60}-based transistors.[554] Transport parameters were also obtained from simulations of discotic mesophases such as phthalocyanines[555] and perylene derivatives.[556] Many investigations, for instance by Andrienko et al.,[557,558] by Nelson et al.,[559] and by Van Voorhis et al.,[560] focus on hole mobilities in tris(8-hydroxyquinolinato)aluminium, an important amorphous hole transporting material.

Since charge transport may be additionally affected by the non-local electron-phonon coupling (Eq. (430)), this last aspect will be addressed in the next subsection.

Transport Limited by Non-Local Electron-Phonon Coupling?

Generally, the non-local electron-phonon coupling (dynamic off-diagonal disorder) can also be important for charge transport in organic materials. As outlined by Coropceanu et al., this results because the charge transfer couplings strongly depend on small details of the intermolecular arrangements. A slight variation, for example of the intermolecular distance, can produce pronounced changes of the transfer coupling. Moreover, the (lattice) phonons are energetically low and thermally excited.[544] If the non-local electron-phonon coupling is dominant, Peierls-type models are employed.[544] For instance, soliton excitations in polyacetylene are described by a model Hamiltonian, the so-called Su-Schrieffer-Heeger-Hamiltonian, which includes only the diagonal site energies as well as the non-local electron-phonon coupling (in contrast to Eq. (430)).[561]

In most organic semiconductors, non-local electron-phonon coupling is usually not dominant, but certainly on the order of local electron-phonon coupling and of disorder contributions, both of which lead to charge carrier localization (see previous paragraphs).[544] Troisi and Orlandi analyzed the thermal fluctuations of charge transport couplings in crystalline organic semiconductors and found that these fluctuations are on the same order as the average coupling values. Therefore, they concluded that due to the effect of off-diagonal dynamic disorder alone, a description based on band transport is inappropriate for organic crystals.[562,563,564] With regard to fullerene systems, Brédas and coworkers came to similar conclusions.[565]

After this outline on theoretical concepts describing exciton and charge transport in bulk phases, the theoretical description of the key process in OSCs, the exciton dissociation, is discussed in the next section. While a number of established models for bulk transport phenomena exist, the understanding of the exciton dissociation and charge separation process is still not complete.[5]

4.4 Models for the Exciton Dissociation at the Donor-Acceptor Heterointerface

In spite of some observations of exciton bulk ionization, for instance in the fullerene layer,[566] exciton dissociation in OSCs is assumed to primarily occur at the donor-acceptor interface via an interfacial charge-transfer state.[567] As outlined above, the mechanism of exciton dissociation and charge generation is closely related to the question what drives charge separation. It should be noted that equivalent questions arise when considering molecular doping.[568,569]

According to Few and Nelson and coworkers, early models for exciton dissociation often rely on the Onsager-Braun concept.[567] Due to its historical significance, the key idea of Onsager and Braun is shortly outlined.

The Onsager-Braun Concept for Charge Separation

The Onsager-Braun concept is based on a classical picture of diffusing molecules and ions, and on the consideration of their electrostatic interactions.

In an earlier version of the model, Onsager assumed that optical excitation of a molecule in an electrolyte (permittivity ε_0) generates a pair of bound ions, a geminate pair. The Brownian motion of the electron and the hole is influenced by their mutual Coulomb binding energy, the thermal energy, and the external electric field. Without any external field, the dissociation yield p of the geminate electron-hole pair is a simple exponential function including the so-called Coulomb capture radius R_{AB} (Eq. (439)) and the initial electron-hole separation r_0.[570]

$$p = e^{-R_{AB}/r_0} \tag{437}$$

The Coulomb capture radius, sometimes also called the Langevin capture radius,[418] is the distance at which the thermal energy is equal to the electrostatic interaction energy of the electron-hole pair. It was initially defined to describe the rate constant γ of non-geminate[kkk] so-called Langevin-type (not trap-assisted) recombination of charge carriers in low-mobility media. With the Smoluchowski equation[571] for bimolecular reactions based on the diffusion coefficients D_A, D_B of the two charge carriers, the Coulomb capture radius (Eq. (439)), and the Einstein relation, Langevin derived an expression for γ (Eq. (440)).[418,572]

$$\gamma = 4\pi(D_A + D_B)R_{AB} \tag{438}$$

$$R_{AB} = \frac{e^2}{4\pi\varepsilon_0\varepsilon_r kT} \tag{439}$$

[kkk] While geminate recombination refers only to those processes where the electron and the hole emerge from the same exciton, the charge carriers have not the same precursor in non-geminate recombination.[418]

$$\gamma = \frac{e}{\varepsilon_0 \varepsilon_r}(\mu_+ + \mu_-) \qquad (440)$$

When the field dependence is additionally taken into account in the early Onsager concept (Eq. (437)) (see [418] for more details), a good agreement with experimentally found field dependences of the photoconductivity in single-component systems such as anthracene crystals was observed.[573] Yet, in single-component systems, bulk exciton ionization, instead of exciton dissociation at a donor::acceptor interface, leads to charge carrier generation.

In contrast, for donor-acceptor systems, one fundamental assumption of Onsager does not hold anymore. In fact, Onsager required that as soon as the electron and the hole collide, their recombination probability is 1. However, at donor-acceptor interfaces, a charge-transfer state is first formed. Due to its long-lived character, it may dissociate again in a field-assisted process.[418] Braun[574] included the non-negligible dissociation probability of the intermediate charge-transfer state into Onsager theory. By means of the joint Onsager-Braun concept, a number of experimental findings could be rationalized.[567]

Nevertheless, the Onsager-Braun model as well as all of its adaptions, also the recent ones, are entirely phenomenological, they provide no atomistic information and understanding about the molecular nature of exciton dissociation and charge separation.[567] *Ab initio* and first-principle QM calculations are necessary to gain insight into the influence of molecular properties on charge separation. Such theoretical investigations of the exciton dissociation and charge generation process, and the understanding that they offer, will be the subject of the next subsection.

First-principle Calculations on Exciton Dissociation and Charge Separation

Most theoretical investigations describe exciton dissociation and charge separation mainly by considering the energy landscapes around the organic::organic interfaces. Electronic-structure calculations provide the relevant excitonic/polaronic/charge-transfer states. From these energy landscapes and from the couplings between different states, information about the charge generation can be obtained. As outlined by Few, Nelson and coworker, many investigations use a single donor-acceptor pair or an oligomer. Calculated properties and energies are assumed to be representative for the whole interface.[567]

However, in a recent review, Beljonne et al.,[575] similar to Yost et al.,[26] point out that complete interfacial model systems with atomistic resolution can be used as a starting point for subsequent QM calculations as well. Their *in silico* generation of these interface models is usually based on molecular dynamic (MD) simulation techniques. MD is a valuable tool especially for systems composed of molecules (compared with polymer OSCs). This results because since the atomistic information in MDs

comes at a considerable computational cost, fully atomistic MD simulations are often inapplicable to the very large polymers.[575] In addition, Muccioli et al.[576] indicate the different time scales required for molecular compared with polymer rearrangements (see section on molecular dynamics). This implies that shorter simulation times are sufficient for molecular aggregates while longer time scales are needed to simulate polymer rearrangements.

A plethora of investigations based on MD simulations to generate disordered **bulk aggregate** structures exists. For more details and examples, the reader is referred to the reviews of Muccioli et al.[576] and of Beljonne et al.[575] Only some representative investigations are briefly addressed. For instance, in a combined theoretical and experimental investigation, Andrienko and coworkers[556] rationalized the packing motifs in perylene-based compounds. Using MD simulations, Martinelli et al. were able to assess the effects of lattice vibrations in anthracene and perfluoropentacene crystals.[577,578] As pointed out by Beljonne et al.,[575] compared to simulations of bulk phases, simulations on **organic::organic interface structures** are less abundant. Studies exist again from Martinelli et al., who investigated the packing motifs of pentacene on top of polymeric dielectric layers. They used the generated structures to determine hole mobilities in subsequent quantum-chemical calculations. Doing so, they were able to highlight the impact of electrostatic disorder created by the dielectric on charge carrier mobilities, a critical point in organic field-effect transistors (OFETs).[579] Brédas and coworkers studied the intermixing at pentacene-fullerene bilayer interfaces, probably the computationally most investigated interface, by means of MD simulations. Depending on the initial orientation of the pentacene layer, different degrees of disorder and intermixing were found when fullerenes were added.[580]

Quantum-mechanical calculations (QM) are subsequently employed to elucidate the electronic states at the interface, using either the representative heterodimer or a part of the previously generated interface. All investigations address at least to some extent the question why exciton dissociation is energetically feasible. Some of them focus additionally on kinetic effects. It was observed, among others, by Scholes and coworkers[581] that electron transfer in photovoltaic blends may be ultrafast. Theoretical models were proposed to explain this observation.

From a literature survey, existing investigations may be further subdivided into several groups depending on which effect is considered to primarily drive charge separation. (1) The main conclusion of a large number of investigations is that the **nature of the interfacial charge-transfer state**, which can be "hot", delocalized, vibrationally excited, etc., enables charge separation. (2) A considerable amount of other predictions emphasize the influence of **electrostatic effects** from the environment on interfacial energetics. Electrostatic interactions can lead to a favorable band bending at the interface so that no further driving force for charge separation is required.[26] (3) **Morphology** is predicted to be

of major importance as well. Distinct structural packing motifs at the interface and in its vicinity were found to facilitate/prohibit charge separation. Evidently, because of the interdependence of these effects, a clear differentiation is not always possible. However, several representative examples are discussed for each group in the following. **Many of them are in support or explain experimentally observed effects. Yet, in contrast to experiments, which are often interpreted based on postulations and simple models, the calculations provide a direct *molecular* understanding of the charge generation process.**

More examples can be found in reviews by Darling and coworker[5] and by Yost et al.[26]

The role of entropy in driving charge separation (see above), recently again outlined by Gulbinas and coworkers,[582] is not repeatedly discussed. It should be furthermore noted that some experimental investigations are cited in the following as well. The reader is referred to Deibel et al.[435] and the above discussion for more experimental investigations.

Charge Separation Via Hot/Delocalized Charge-Transfer States

A number of theoretical investigations predict that the nature of the interfacial charge-transfer state intrinsically allows further dissociation and charge separation. A further subdivision of these investigations is possible, depending on whether excess energy is involved (dissociation via hot CT states) or not (dissociation via cold CT states).

Exciton Dissociation via Cold CT States

The nature of the interfacial charge-transfer state was analyzed in a rather early[567] work of Kanai and Grossman for the P3HT::C_{60} system.[583] They proposed that exciton dissociation and charge separation are mediated by a so-called "bridging" interfacial charge-transfer state where charge density is smeared across the whole donor-acceptor pair. Due to the charge delocalization in this "bridging" charge-transfer state, no tightly bound geminate electron-hole pair is created, and charge separation becomes energetically feasible due to the reduced Coulomb binding energy. Although Kanai and Grossman used pure DFT to calculate the charge-transfer states,[583] which certainly introduces errors,[567] their concept of the "bridging" charge-transfer state was readily adopted in the literature.[567] For instance, Liu, Troisi and coworker[584] analyzed the influence of the P3HT conformation on the nature of such charge-transfer states and found two types of geminate pairs at the P3HT:: C_{60} system – a "bridging" and a "charge-separated" one. The amount of charge delocalization was observed to critically influence the rates of the photoinduced charge-transfer step. Few et al. studied the influence of chemical modifications at the donor on the nature of bridging charge-transfer states to fullerene C_{60}.[585] By means of ADC(2) calculations, also Borges and Lischka and coworkers observed delocalized

charge-transfer states for other donors and C_{60}.[424] They concluded that charge separation seems feasible from such delocalized charge-transfer states, which are directly accessible from an internal conversion process of bright interchain excitonic states.[424] It is important to stress that all of these studies consider *relaxed* charge-transfer states, i.e., cold exciton breakup is energetically possible due to the delocalization.

Many investigations address additionally the kinetics of such relaxed charge-transfer states. All of these investigations point out that even if the relaxed charge-transfer state is sufficiently high to allow for a cold exciton dissociation, the actual charge generation yield results from the competition between the charge separation and recombination dynamics of the charge-transfer state. This kinetic control of the charge generation process was also discussed by Thompson and coworker.[449] They particularly point out that it provides the charge generation yield with a noticeable temperature dependence. A few illustrative examples are mentioned. For instance, in a combined experimental and theoretical investigation, Baldo, Manca, and Van Voorhis were able to demonstrate for polymer-fullerene blends that charge separation occurs via relaxed charge-transfer states since excess energy did not affect the quantum yields.[586] Therefore, they explained existing differences in the quantum yields of the polymer-fullerene blends in terms of different (recombination) dynamics of these relaxed charge-transfer states.[586] In a very recent experimental study of Lu and coworkers,[587] the rate of non-radiative recombination at organic heterojunctions showed a Marcus-inverted behavior as a function of the charge-transfer state, which suggests that an energetically high-lying charge-transfer state simultaneously enables fast charge separation and disables recombination. Also Rumbles and coworkers found in an experimental investigation inverse trends of the separation and recombination rates as a function of the charge-transfer state energies. By systematically varying the driving force for the interfacial charge-transfer step, they observed that the charge generation yield has a maximum as a function of the driving force. With Marcus-type rates, they were able to rationalize that at this point, almost no activation energy is required for the photoinduced charge-transfer step (Eq. (422)). Recombination losses are in turn effectively suppressed in a kinetically controlled process. Lowering the charge-transfer states even more relative to the excitonic states (increasing the driving force) slows down the rate of exciton dissociation.[588] In addition, Lu and coworkers[587] furthermore emphasized the importance of small couplings between the relaxed charge-transfer states and the ground state. Reducing recombination couplings is also a key element of a cascade energy landscape proposed by Tajima and coworkers:[589] the energy cascade in the first monolayers around the interface serves to drive charges apart and prevents them from recombining.[589] Thus, all these investigations have the major conclusion in common that while the relaxed charge-transfer states might have sufficient energy to allow exciton dissociation, their couplings to other states must be controlled to drive charge separation in a kinetically controlled process.

In contrast to the above conclusions and from a combination of time-resolved spectroscopy and non-adiabatic dynamics, Rossky and Zhu and coworkers outlined that only excess energy of the interfacial charge-transfer state can channel charge separation. The excess energy contributes to the delocalization of the charge-transfer state, which subsequently dissociates. Thus the time scale of charge separation is ultimately determined by the cooling process of the charge-transfer state. Once it has cooled, the geminate electron-hole pair localizes and cannot escape from its Coulomb binding energy.[590] Similar conclusions were drawn by Bakulin et al.[591] in a joint computational and experimental study on a combination of polymer donors with fullerene derivatives. Bakulin et al.[591] showed that IR photons can excite bound charge-transfer states into a higher-lying band of delocalized charge-transfer states. This directly leads to charge separation.[591]

In a seminal experimental investigation on charge-transfer excitons at organic semiconductor surfaces and interfaces, Zhu et al. discussed two additional important effects related to hot charge-transfer states. Aside from their reduced binding energy, the DOS for higher-lying CT states is larger, and they couple more efficiently to the original excitonic states (because they are isoenergetic).[455] Both effects can assist in driving charge separation. Indeed, also Vázquez and Troisi pointed out that upon exciton dissociation, a partially delocalized charge-transfer state is always the first state to be populated because according to their calculations, only partially separated higher-lying CT states couple sufficiently with the initial bright excitonic state.[592] In a similar way, Beljonne and coworkers conducted comprehensive calculations on the CT DOS at the P3HT::PCBM interface, and equally came to the conclusion that the dark, higher-lying CT manifold is of major importance for the charge separation efficiency. Due to their strong coupling with singlet excitons, these higher-lying charge-transfer states can even be directly excited.[593] The so-called long-range exciton dissociation recently proposed by Caruso and Troisi can be considered as a limiting case of strong exciton coupling to delocalized charge-transfer states. In long-range exciton dissociation, the exciton actually never reaches the interface but dissociates, due to the pronounced coupling, directly into a delocalized charge-transfer state.[594] Ma and Troisi furthermore indicate, similar to Beljonne,[593] that while the absorption strength of such delocalized charge-transfer states is usually very low (yet increased due to the coupling to excitonic states), they might still contribute to the low-energy part of the OSC absorption due to their considerable DOS. Therefore, direct optical excitation of long-range charge-transfer states could be another pathway that leads, in addition to exciton dissociation, to charge separation.[595]

Finally, the role of both intrinsic charge delocalization in the relaxed charge-transfer state and vibronically excited states was emphasized by Tamura and Burghardt. They discussed in detail that only the combined effect of charge delocalization, which reduces the Coulomb binding energy, and

mediation via a vibronically excited charge-transfer state, enable an ultrafast charge-transfer process in the sub-picosecond regime at the P3HT/PCBM interface.[596]

Electrostatically Assisted Exciton Dissociation

It is well-known that the built-in voltage and further electric fields due to ferroelectric/dipolar additives assist in charge separation (see above). Yet, electrostatic fields facilitating exciton dissociation can also simply arise from the ground-state electronic structure at the interface.[567] A number of theoretical investigations analyze the influence of such local electric fields, an impact which is difficult to assess by experimental means.

Using the archetypical pentacene::fullerene heterojunction, Heremans and coworkers[597] could show with microelectrostatic calculations that the energy landscape at the interface is determined by the size and orientation of the molecular quadrupole moments of pentacene. In fact, electrostatic interactions of the quadrupole moments lead to band bending of the charge transport levels. This band bending is produced in a two-fold manner. On the one hand, the quadrupole moments directly interact with the generated geminate electron-hole pairs. On the other hand, the discontinuity of the electric field across the interface results in interfacial dipole moments that, depending on the orientation, can additionally promote/prohibit charge separation (by favorable/unfavorable band bending). Therefore, the authors conclude that the orientation of donors with quadrupole moments must be critically controlled to obtain efficient devices.[597,598] In a more detailed study on the origin of the ground-state interfacial dipole moments at the pentacene::fullerene interface, Castet et al. outline that ground-state charge transfer, compared with polarization due to the asymmetrically distributed quadrupole moments, is only of minor importance. More importantly, however, the size and even the orientation of these interfacial dipole moments is very sensitive to slight changes in the intermolecular arrangements and consistently subject to pronounced variations.[456] In fact, an experimental investigation highlighting the importance of interfacial dipole moments was provided by Akaike et al. for the copper phthalocyanine::fullerene interface. From UPS, X-Ray, and inverse photoemission experiments, they were able to deduce the energy band offset at the donor/acceptor phase induced by the interfacial dipole moments.[599] Beljonne and coworkers observed furthermore considerable substituent effects on the interfacial dipole moments and on the type of band bending when replacing pentacene with sexithiophene or with dicyanovinyl-substituted sexithiophene donors. While the band bending is similar to pentacene in the former case, using acceptor-substituted sexithiophenes inverses the bending. Interference effects influencing the transport levels were observed when a quadrupolar PTCDA acceptor instead of fullerene was employed.[600,601]

Turning to polymer OSCs, namely to the P3HT::PCBM interface, Castet et al. found that alike to pentacene, the quadrupole moments of P3HT contribute to the gradient in the energy landscape that drives charge separation. However, they additionally outlined that stabilizing polarization interactions of the charge carriers with their environment are larger for a separated electron-hole pair than for a geminate one. Polarization facilitates therefore charge separation.[602] Brédas already outlined the significance of polarization, owing to the nature of the polarizable conjugated systems, for charge-transport phenomena in all organic materials.[603]

The importance of electric fields created by ground-state multipole moments was also underlined by QM/MM calculations of Yost and Van Voorhis.[460] Using a variety of bilayer OSCs, they observed a considerable influence of these molecular multipole moments on the type of band bending, in line with Heremans[597,598]. Nevertheless, they additionally noted the influence of the bulk dielectric constant, which changes when going to the interfacial region. If it is lower, for instance due to lower packing densities,[26] charge carriers are destabilized at the interface.[26,460] Therefore, this issue is related to the strong variations of the polarization energy of charge carriers at organic::organic interfaces compared with the bulk phase, a phenomenon also addressed by Risko and Brédas and coworker for organic::vacuum interfaces.[604]

Influence of the Morphology on Charge Separation

From numerous computational investigations in the recent literature, it follows that different morphological effects may favor charge separation. Both morphological disorder and order can in principle facilitate the generation of free charges. Moreover, according to many investigations, the mutual molecular orientation at the interface plays a very fundamental role.

Charge Separation Favored by Disorder

Considering the P3HT::PCBM interface, Troisi and coworkers predicted that the larger amount of disorder at the interface has a favorable effect on the energetics of charge separation. In fact, due to the increased free volume at the interface, P3HT chains take on more disordered arrangements, which induces a blue shift of the absorption, i.e., the energy gap of P3HT increases. Correspondingly, the transport gap between the charge transport levels widens. As outlined by Troisi and coworkers, it follows that charge carriers are repelled from the interface, which increases the initial charge separation and suppresses geminate recombination.[457]

Charge Separation Favored by Order

In contrast, Akaike et al. addressed the influence of disorder on the energy alignment at organic donor-acceptor interfaces.[453] They concluded that the influence of disorder on the energy alignment is

complex, yet detrimental. Nayak and Cahen and coworker outlined similar effects in a recent perspective. They concentrated particularly on charge carrier mobilities, which must be high to ensure efficient charge separation. Disorder is known to deteriorate charge transport properties.[452] Similarly, Poelking and Andrienko highlighted the fundamental importance of long-range molecular order for high charge generation yields, albeit with a focus on electrostatics. Only if long-range mesoscale order exists, multipole moments can add up and produce homogeneous electric in-plane fields and inhomogeneous out-of-plane fields at the donor::acceptor interface. "Push-out forces" result from the out-of-plane fields for certain donor-acceptor mixing ratios and molecular orientations at the interface. These forces enable cold exciton dissociation.[605] In the same sense, Poelking and Andrienko emphasized in another investigation the profound influence of long-range electrostatic interactions induced by mesoscale disorder especially on the open-circuit voltage.[28] Long-range mesoscopic order and aggregation is also found to be of major importance by Chen, Marks, Ratner and coworkers.[606] In a combined experimental and theoretical investigation, they discussed that particularly fullerene cluster sizes and arrangements are decisive for charge separation. In large, well-aggregated fullerenes, a number of well-separated charge-transfer states exist that are almost isoenergetic to bright excitonic states. By directly coupling to these acceptor states, intermediate tightly bound interfacial charge-transfer states do not emerge. Yet, the existence of the acceptor states critically depends on fullerene crystallinity. The transfer mechanism explains furthermore the ultrafast timescale of exciton dissociation. In contrast to other investigations, Chen, Marks, Ratner and coworkers[606] concluded that exciton delocalization in the donor phase is not significant.[606] The profound influence of fullerene crystallinity was also stressed in a recent experimental investigation of Hsu et al. They systematically varied the fullerene (PC$_{71}$BM) concentration in P3HT-fullerene blends and observed the highest charge generation yields for intermediate fullerene concentrations. This led them to the conclusion that while exciton diffusion becomes rate-limiting at high fullerene concentrations (small donor-acceptor interface), fullerene crystallinity is compromised by too large donor concentrations. In accordance with Chen, Marks, Ratner and coworkers,[606] reducing fullerene crystallinity decreases charge delocalization, the charge-transfer state energies, and the charge separation yield.[607]

Charge Separation Favored by the Intermolecular Orientation

Rand and coworkers analyzed the influence of the molecular orientation on OSC performances in a joint experimental and computational investigation. They highlighted especially the role of the large charge-transfer coupling if phthalocyanine donors are orientated face-on on top of the fullerene layer. Following their reasoning, the larger charge-transfer couplings are responsible for the higher charge dissociation efficiencies encountered for the face-on morphology.[608] In addition to the orientation, Fréchet and coworkers[609] as well as D'Avino[610] and coworkers discussed the influence of the initial

electron-hole separation on the final charge generation (analogously to Onsager's theory). By introducing steric hindrance via bulky substituents at the donor or with a column mismatch in liquid crystals, respectively, initial electron-hole separations are larger. Geminate electron-hole pairs are less tightly bound and dissociate more easily. D'Avino et al. furthermore pointed out that a column mismatch is *a priori* unfavorable because couplings decrease, in line with Rand et al.[608] Nevertheless, the decrease in couplings is apparently overcompensated by the opportunity for isoenergetic charge separation due to larger initial electron-hole separations. Experiments in support of this conclusion were conducted for example by Holmes and coworker. By inserting an insulating layer at the organic::organic interface, they expanded the size of the charge-transfer state and observed via electroluminescence measurements a reduction of its binding energy.[440]

It follows from this literature perspective that calculations have further elucidated the microscopic charge generation mechanisms[567] of many of the "static" and "dynamic" effects of Deibel et al.[435] Yet, to finally extract the macroscopic device quantities from molecular calculations on charge separation, extensive KMC simulations on large model systems would be necessary, similar to the pure exciton/charge transport. A short outlook is given in the next subsection.

Outlook: First-Principle Simulations of Devices?

The holy grail of calculations on OSCs is certainly to obtain macroscopic device properties (J-V characteristics, quantum efficiencies, etc.) from KMC simulations using only *ab initio* calculated parameters. As outlined by Groves and Greenham in a review on OSC KMC simulations,[611] such calculations involve the microscopic simulation of the motions of excitons and charge carriers, the generation and recombination of charge-transfer states, and the interaction between pairs of diffusing charges as well as their recombination. Moreover, because of the difficulty of experimentally obtaining atomistically resolved interface morphologies, the *in silico* generation of suitable interface structures is an additional prerequisite.[611]

However, such KMC simulations based on *ab initio* input parameters are still limited to rather small and simple systems due to the large number of needed coupling parameters and site energies.[611] Therefore, only a few investigations using KMC simulations exist that describe the charge separation process. The exciton diffusion and dissociation process is usually not included, i.e, the simulations often start with a geminate electron-hole pair at the donor::acceptor interface that dissociates under the combined influence of the Coulomb binding energy and an electric field. For instance, Linares and Volpi et al. analyzed in a procedure based on Marcus hopping rates with *ab initio* parameters and artificially generated interface structures the field dependence of charge separation in different morphologies of the hypothetical anthracene::fullerene system.[612]

In contrast, most KMC simulations on OSCs introduce a number of simplifications. Two- or three-dimensional Cartesian grids are employed to model the cell. Such grids can be generated *in silico*. Hopping sites are often reduced to orbital energies that are sometimes obtained from experimental parameters. Time-independent couplings are usually used, which are commonly assumed to be isotropic. Values are obtained by fitting to experimental data. Also the disorder is obtained from experimental measurements, and the correlation of site-energy disorder[613] is often neglected. Although Marcus-type rates are sometimes used, the simpler[418] Miller-Abrahams and Förster transfer rates are frequently employed as well.[611] To cite only two examples for such investigations (because they further illustrate above-discussed effects), Walker and coworkers analyzed the influence of phase segregation on the IQE in the PFB/F8BT system, a system for which Westenhoff and Beljonne[614] and coworkers carefully investigated the energies of interfacial charge-transfer states. They concluded, in line with a number of above mentioned investigations, that the IQE has a maximum at intermediate phase separations (of about 20 nm).[615] In a similar procedure, albeit with Marcus rates, Marsh et al. used such simulations to investigate the influence of the morphology on the charge generation yield. Their results similarly underline the importance of phase segregation for high charge carrier mobilities and minimal bimolecular recombination.[616]

Evidently, as also pointed out by Groves and Greenham, these large and somewhat empirical KMC simulations are indeed especially suitable to study implications of such mesoscale morphological changes, and also of the dynamics of non-geminate recombination, of the confinement of charge carriers in strongly intermixed heterojunctions, and of space charge effect (included by taking state filling effects in the DOS[617]) on the device efficiency.[611] Nevertheless, it should be kept in mind that they provide no atomistic molecular-specific or mechanistic information. Therefore, simulating devices without empirical parameters remains a yet unreached landmark of modern material science.

5 Results and Discussion

5.1 The selection of the molecules

Since the photovoltaic effect was observed in anthracene single-layer solar cells,[618] the spectrum of molecules used in organic photovoltaics (OPVs) has enormously broadened.[29,619] Traditionally used acenes and phthalocyanine pigments like copper or zinc phthalocyanine still play an important role in the field,[620,621,622] but other compound classes, e.g., squaraine dye molecules[623] and, inspired by the high performances of polymer organic solar cells (OSCs),[462] star-shaped or three-dimensional oligomers,[624] have been successfully employed in OPVs as well. Fullerenes and functionalized derivatives[625,626] are the most common acceptors since Sariciftci's discovery of rapid luminescence quenching in organic polymers by fullerene C_{60},[627] and they are combined in OPVs with either molecular or polymer donors. Nevertheless, known deficiencies of fullerene acceptors like low open-circuit voltages[628] have recently brought about the development of non-fullerene acceptors.[629,630,631,632]

In view of this diversity of donor and acceptor molecules with OPV applications, any selection of molecules used in subsequent computational investigations will necessarily be an arbitrary one. The selection of molecules for this work (Figure 5) comprises a number of donor molecules and only one acceptor.

The predominance of fullerene acceptors[631] justifies the choice to always use fullerene C_{60} as the acceptor. Solubility distinguishes fullerene C_{60} from its most widely used derivative,[633] $PC_{61}BM$[634]. This is decisive for the fabrication process (evaporation vs. spin-coating)[418] and was shown to have morphological implications.[635] Due to the otherwise very similar optoelectronic properties,[636] conclusions from a computational chemistry study on fullerene C_{60} can, however, be readily transferred to PCBM. Similar considerations apply to the transferability of results for C_{60} to its less symmetric higher homologue, fullerene C_{70}, which differs mostly by its light absorption in the visible region from C_{60},[637] and to the $PC_{71}BM$ derivative of C_{70}, which usually leads to more disordered thin films apart from otherwise unchanged properties compared to C_{70} (similar to the C_{60}-$PC_{61}BM$ system).[565] Using only one acceptor combined with various donors has the additional advantage that observed differences in the computational investigations directly relate to the donor component, making the establishment of structure-property relationships more straightforward.

molecular semiconductors of low polarity

anthracene

rubrene

ACENES/ ALTERNANT HYDROCARBONS

diindenoperylene (DIP)

3,6-dimethylbenzo-[1,2-b:4,5-b']-dithiophene (dithiophene)

OLIGOTHIOPHENES & NONALTERNANT HYDROCARBONS
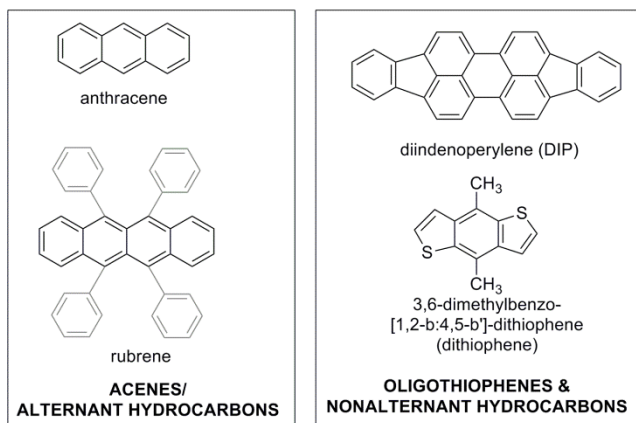
molecular semiconductors of intermediate polarity

diketopyrrolopyrrole

squaraine

DONOR-ACCEPTOR-DONOR COMPOUNDS

tri(biphenyl-4-yl)amine ("triamine")

donor-substitued triarylmine ("triamine-methoxy")

acceptor-substitued triarylmine ("triamine-aldehyde")
substitution: conjugated aldehyde - nitrile for CASPT2

TRIPHENYLAMINE-BASED COMPOUNDS
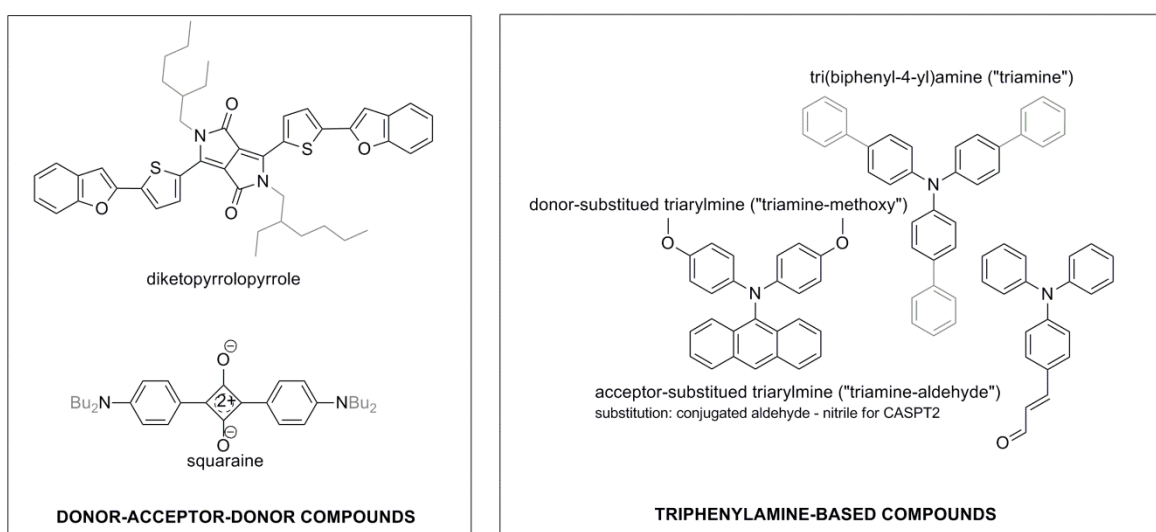
molecular semiconductors of high polarity

HB238

HB194

MD353

MEROCYANINES/DONOR-ACCEPTOR COMPOUNDS
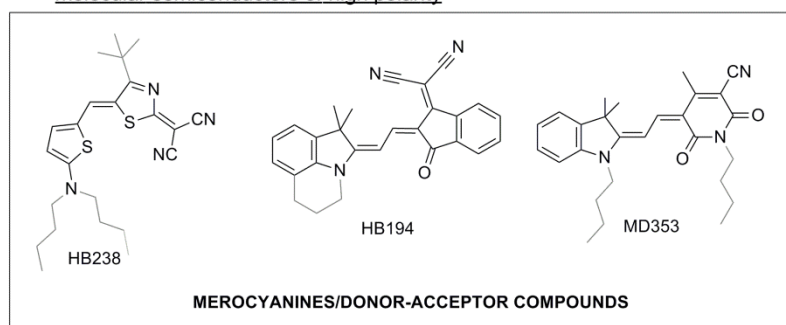
DONORS

ACCEPTOR

fullerene C_{60}

Figure 5: Employed donor molecules (above) and fullerene C_{60} as the only acceptor.

Donor molecules comprised in this work include compounds from various classes ranging from acenes and thiophenes over donor-acceptor-donor dyes like a squaraine and a diketopyrrolopyrrole and different three-dimensional triarylamines to highly dipolar merocyanines. References for all molecules are given in Table 1. See also [638] for a survey. The structural diversity of the selected donor molecules suggests regrouping them into classes of similar compounds to organize the following discussion and to systematize conclusions. This could help to reveal and establish structure-property relationships. In this context, it should be kept in mind that one of the key focuses of this work is to gain insight into fundamental relationships between *molecular* structures and resulting *thin-film* and aggregate properties, i.e., the relationship between atomistic and nanoscale properties. From numerous investigations on transport processes in organic semiconductors, Bässler et al. identified molecular polarity as one of the key *molecular* parameters significantly influencing *thin-film* properties.[25,546,548] The more polar the individual substances, the more vary polarization energies and resulting site energies due to position-dependent electrostatic interactions.[425] Site energy variations profoundly influence transport processes and nanoscale mobilities and diffusion lengths.[639] Würthner et al. outlined the important implications of the polarity of molecular organic semiconductors as well,[27] also in a historic sense because originally the findings of Bässler et al. fueled especially the development of apolar semiconductors.[640] More polar substances attracted more research attention only later-on, triggered by the success of compounds like merocyanines[641,27] or intramolecular charge-transfer (i.e., low bandgap) polymers[482,483]. Given this special significance of polarity in the field of organic optoelectronics, the donor molecules are organized according to their polarity.

In contrast to this polarity regrouping motivated by semiconductor physics, computational chemistry understands optoelectronic properties of molecular organic semiconductors rather in terms of the present chromophores, i.e., carbonyl chromophores or coumarin chromophores,[642,643,644] than as a result of more or less polar structures. From the point of view of a computational chemist, the discussion of the optoelectronic properties of different donor molecules would be best organized as a function of the composing chromophores, emphasizing their relationship (i.e., between electronic properties and individual chromophores). However, molecular polarity is intimately linked to and inseparable from the presence (or absence) of certain chromophores: apolar molecules with no overall dipole moment and no local dipole moments like alternating acenes or non-alternating hydrocarbons (diindenoperylene (DIP), 3,6-dimethylbenzo[1,2-b:4,5-b']dithiophene (BDT) donor moiety) contain usually only aromatic hydrocarbon or thiophene chromophores. As soon as electron-withdrawing carbonyl chromophores or donating electron-rich aromatic rings are introduced, local dipole moments arise. The group of intermediate polarity includes such molecules, which either have small overall dipole moments (the triphenylamine-based compounds) or large local dipole moments that mutually cancel due to symmetry (donor-acceptor-donor dyes). The merocyanines with a large overall dipole

moment, an originally unusual property in the field,[27] constitute the polar molecules. An equivalent classification of these merocyanine dyes within the chromophore framework is equally possible: the combination of several electron-withdrawing functional groups yields new accepting chromophore structures, which are strongly electron-deficient only via the synergistic combined effects of all composing functional groups.[645] Hence the polarity classification originated in the physics of organic semiconductors and the chromophore approach from computational chemistry are more or less equivalent for the given molecules and can be used interchangeably. In the following, however, the regrouping of the molecules (Figure 5) will always be referred to as the "polarity classification".

Table 1: Employed molecules and references for structure information. Please note that for some molecules, very short abbreviations had to be used in some of the figures in the following.

Molecule	Reference
anthracene	[646]
diindenoperylene (DIP)	[647]
3,6-dimethylbenzo[1,2-b:4,5-b']dithiophene (dithiophene)	[648]
rubrene	[649]
tri(biphenyl-4-yl)amine ("triamine", TBA)	[650]
9-(N,N-dianisylamino)anthracene ("triamine-methoxy", "trimet", TMA)	[651]
(E)-4-(diphenylamino)cinnamaldehyde ("triamine-aldehyde", "trial", TAA)	[652]
2,4-bis[4-(N,N-dibutylamino)phenyl]squaraine ("squaraine")	[653]
3,6-bis(5-(benzothiophene-2-yl)thiophen-2-yl)-2,5-bis(2-ethylhexyl)pyrrolo[3,4-c]pyrrole-1,4-dione ("diketopyrrolopyrrole", DPP)	[654]
HB194	[655]
HB238	[656]
MD353	[655]

In the following, the molecules (Figure 5) are presented in more detail. It should be emphasized that this outline parallels the discussion in [638]. Throughout the following discussion, the interfaces between

the organic donor and acceptor phases in OSCs will be designated as *donor*::*acceptor* interfaces, with the donor and acceptor component being further specified.

Although acenes are today rather used in OFETs (organic field-effect transistors) and OLEDs (organic light-emitting diodes)[621], anthracene is included among the model systems because, as mentioned above, it was among the first molecules where photoconductivity was observed.[618,657] Moreover, the anthracene chromophore is still widely used in organic polymers[484] and – in functionalized versions – as an organic molecular semiconductor[621,658,619,620,659] and also in dye-sensitized solar cells.[660] As a second representative of the acene group, rubrene, a substituted tetracene with very high observed hole mobilities[661] and bright yellow fluorescence exploited in OLEDS[662], is employed. The rubrene::fullerene (PCBM) heterostructure was also experimentally investigated.[663,511,664] While high charge carrier mobilities were observed for crystalline rubrene, which were also comprehensively investigated in calculations,[464,665,666] rubrene does not readily form crystalline films after evaporation, but leads to rather disordered, polymorphic thin films[667,668]. The DIP::fullerene heterojunction has been experimentally thoroughly investigated as well.[669,670] In contrast to rubrene, DIP thin films are usually crystalline with very favorable transport properties.[671] However, due to the perpendicular orientation of the transition dipole moments in deposited DIP films with respect to the thin-film surface,[672] the amount of light absorption is significantly reduced.[671] The introduction of substituents has been shown to shift the absorption maximum and to induce the formation of amorphous thin films,[673] which increases light absorption. DIP is comprised in the model set to analyze the energetics and kinetics at DIP::fullerene interfaces with different orientations of the DIP molecules with respect to the fullerenes.

Oligo- and polythiophenes with P3HT (poly(3-hexylthiophen-2,5-diyl)) as a particularly prominent representative constitute one of the most common classes of organic molecular and polymeric semiconductors.[674,619,675,676,677] A number of computational studies has already addressed their structures, excited-state properties, and charge generation mechanisms in photovoltaic devices with fullerene acceptors.[424,678,584,583] In contrast, this thesis comprises a small bridged dithiophene that is a very common donating moiety (BDT) in donor-acceptor polymers.[679,680] The small molecular size ensures short computation times. Furthermore, the HOMOs and LUMOs in donor-acceptor polymers are generally considered to be largely localized on the donating and accepting moieties, respectively.[484] Therefore, only a small error is introduced when hole transport levels are computed using only the donor structure instead of the complete donor-acceptor system. Naturally, absorption energies shift considerably when only the donating part of donor-acceptor polymers is taken into account. However, the resulting poor overlap of the absorption of the separate donor with the solar spectrum is not relevant for a computational chemistry case study while it renders an experimental investigation

impossible. The dithiophene is comprised in the set of molecules (Figure 5) as an example for a strong electron donor with very high excitation energies.

In contrast to two-dimensional acenes, oligothiophenes, and related aromatics that readily crystallize, three-dimensional triphenylamines are soluble[681] and form amorphous films with isotropic and homogeneous properties due to the absence of grain boundaries.[682,683] Triphenylamines are often used as hole-conducting materials (for example as amorphous resists and in conductive coatings) and in electroluminescent devices,[683,681] but they and their derivatives have only recently come to use in OPV as well. In fact, it was found that a finetuning of their properties is possible by means of small structural modifications.[683,684] The introduction of electron-withdrawing groups in particular shifts the absorption to longer wavelengths and ensures high oxidation potentials necessary for high OPV open-circuit voltages while simultaneously preserving the good hole-transport properties of triphenylamines.[685] Molecular donor-acceptor semiconductors with a triphenylamine donor were shown to be promising candidates for highly efficient OSCs, which results from their low band gap and concomitantly high absorption.[686] The inclusion of a triphenylamine[650] without electron-withdrawing substituents and of a triphenylamine with a cinnamaldehyde[652] accepting group in the set (Figure 5) permits to analyze the influence of electron-accepting groups on the optoelectronic properties. A third spectroscopically characterized triphenylamine-based dye is included, disposing a donor-acceptor structure with a dianisylamine donor and an anthracene acceptor. Upon electronic excitation of its lowest excited state, an intramolecular charge-transfer state, it undergoes a torsional movement resulting in intramolecular charge separation.[651] Its properties (absorption wave length, processing conditions, etc.) prohibited experimental photovoltaic testing.[651] However, in view of its interesting excited-state properties, it is ideally suited for a computational chemistry case study on its hypothetical optoelectronic behavior in OPVs.

Turning to the dye molecules, a rather small symmetric squaraine was included to keep the calculations computationally affordable (Figure 5).[653] In general, squaraine dyes have extremely high extinction coefficients in the visible and NIR (near infrared) region due to the high electron density in their central squaraic acid ring system.[623] Similar to other dyes, squaraine thin-film properties are largely determined by aggregation caused by strong intermolecular interactions. The aggregation properties depend especially on the squaraine substituents and the fabrication conditions.[687,688,623,689] Experimental investigations on the chosen symmetric squaraine revealed that the formation of J-aggregates favorably influences the photovoltaic performance of the squaraine's blends with fullerene acceptors.[623,690] J-aggregation is known to result in bathochromically shifted absorption spectra,[418] which improves the overlap of the squaraine absorption with the solar spectrum and thus increases the short-circuit current. Furthermore, larger hole mobilities are observed in squaraine J-aggregates

compared with other supramolecular arrangements, owing to larger couplings between the tightly packed adjacent squaraine molecules.[691] It is of interest to computationally investigate the experimentally demonstrated close relationship between the supramolecular structure of this symmetric squaraine and its optoelectronic performance and to analyze predicted energetics and kinetics of the squaraine::fullerene interface in terms of the aggregation properties.

Merocyanines are another important class of organic dyes with a pronounced tendency to form J- or H-aggregates.[29,688] Their high tinctorial strengths and favorable charge-transport properties[692,693] in combination with their structural diversity, which allows for a finetuning of the HOMO and LUMO levels and the absorption maxima,[694] form the basis for the experimentally observed high performances in all optoelectronic devices[692,641] and in OSCs in particular.[619] Due to this structural diversity and the overall unusual electronic structures of the compounds, three different dyes, HB238[656], HB194[656], and MD353[655], all with different donating and accepting moieties as well as with different experimental cell performances, are included (Figure 5).

Finally, a diketopyrrolopyrrole (DPP) is comprised (Figure 5),[654] representing a compound class that has been used for high-performant dyes and inks for several decades, but has come to use in OSCs only recently.[695] Due to its profitable optoelectronic properties, the diketopyrrolopyrrole entity is frequently employed in low-band-gap polymers as the electron-deficient component.[696,483] However, the number of advantageous properties equally found for molecular diketopyrrolopyrroles, namely their strongly absorbing core moiety, their high mechanical and photochemical stability[697] and the possibility to modify core substituents to tailor properties[698] and thin-film morphologies,[699,700] led to a variety of performant OPV devices based on molecular diketopyrrolopyrrole donors as well. From a theoretical point of view, the optoelectronic properties of diketopyrrolopyrroles are most interesting because they are significantly influenced by the bright intramolecular charge-transfer excitations found in all diketopyrrolopyrroles. These low-lying excitations result from the DPP donor-acceptor-donor structure[695] that simultaneously gives rise to distinct structural phenomena, for instance an intramolecular twisting in the electronic ground state and the formation of specific packing motifs in thin films and crystals.[506]

As stated in the Introduction (see above), a central objective of this work is to understand how molecular properties relate to aggregate morphology and thin-film features and to gain insight into nanoscale implications of variations in the molecular structures. This requires a multiscale description taking into account the molecular, intermolecular, and aggregate level.

To this end, the first step to begin with is an understanding of the electronic structures of the individual molecules. This occurs in a two-fold objective. (1) The electronic structures of the molecular

semiconductors are far from being trivial. Citing only two popular electronic-structure problems widely discussed for the compounds comprised in the model set (Figure 5), a correct and computationally affordable description of the closely-lying L_a/L_b excitations in anthracene continues to be a yet unreached landmark for excited-state methods.[701,172] Similarly, the delicate equilibrium between steric strain and electronic delocalization responsible for the twisting of the donating substituents around the central diketopyrrolopyrrole moiety in diketopyrrolopyrrole dyes remains to be understood and properly described.[506] Hence a first objective of this thesis is to understand the molecules' electronic structures. (2) Effectuating a multiscale description necessitates computational methods at hand that are applicable to large systems. This requires prior benchmark calculations. Thus the second objective is to identify methods that are *both efficient and accurate* to utilize them later-on in larger-scale calculations. The description of the individual molecules will be the focus of the next chapter.

On a molecular level, optoelectronic processes in OPV include different types of electronic states, i.e., ionized states, neutrally excited or charge-transfer states. The natural starting point for a discussion of the properties of the individual molecules is their respective ground-state description, which is comprehensively discussed in the next section. It should be noted that all benchmark calculations presented in the following were carried out only for the molecular donors in Figure 5.

5.2 Benchmarking ground-state geometries

The following data and a similar discussion can also be found in [702].

5.2.1 Outline of the computational approach

In this section, ground-state geometries of all molecules comprised in the model set are benchmarked. The reference geometries were optimized at the SCS[70]-MP2[703,704]/cc-pVTZ[705] level of theory. Spin-component scaling was shown to significantly improve MP2 geometries, especially for difficult cases where regular MP2 fails.[71] The SCS-MP2 method, as a combination of the improvements of spin-component scaling[43] and the usually robust performance of MP2 with triple-zeta basis sets for geometries of organic molecules[39], should provide sufficiently reliable ground-state reference geometries for all molecules at a reasonable computational cost. For well-converged orbitals, the convergence of the SCF cycles and the density convergence were set to $1 \cdot 10^{-7} \, a.u.$ During the optimizations, an energy threshold of $1 \cdot 10^{-6} \, a.u.$ and a gradient threshold of $1 \cdot 10^{-3} \, a.u.$ were used.

Geometries of DFT methods, *ab initio* and semiempiric methods were benchmarked. The cc-pVDZ basis sets[705] were employed. For a more thorough discussion of basis set effects, see the section "Benchmarking vertical excitation energies of molecular semiconductors". All methods comprised in the benchmark are summarized in Table 2.

Table 2: Wave-function based methods, DFT functionals and semiempiric methods employed to benchmark ground-state geometries of the p-type semiconductors.

method	References
wave-function based methods	
MP2	703,704
SCS-MP2	70,703,704
CC2	256
SCS-CC2	256,180
HF	706
density functional based approaches	
BLYP-D3	707,708,709,140
M06L(-D3)	710,140
APFD	711
B3LYP-D3	707,712,713,708,709,140
SOGGA11X	714
ωB97X-D	143

CAM-B3LYP-D3	[133,707,712,713,708,709,140]
B2PLYPD3	[137,715,716]
mPW2PLYPD	[137]
semiempiric methods	
orthogonalization model 1 (OM1)	[193,197]
orthogonalization model 2 (OM2) with dispersion correction (OM2-D3)	[197,195]
Modified Neglect of Diatomic Overlap (MDNO/H)	[183]
Austin Model 1 (AM1)	[189]
Recife Model 1 (RM1)	[207]
Parameterization Model 3 (PM3)	[717,190]
Parameterization Model 6 (PM6-D3/DH2)	[205]
Parameterization Model 7 (PM7)	[206]

In terms of wave-function based methods, MP2[703,704] and CC2[256,246] along with their spin-component scaled variants[70,180] were used. Geometry differences to the reference geometry arise also from the different employed basis sets (cc-pVDZ vs. cc-pVTZ; for SCS-MP2 geometries, geometry differences are exclusively due to basis set effects). HF is included as well (see Table 2).

To assess the reliability of DFT-based approaches, diverse functionals were selected. The set of functionals encompasses the long-range corrected functionals CAM-B3LYP[133,707,712,713,708,709] and ωB97X-D[143] and the hybrid functionals B3LYP[707,712,713,708,709], SOGGA11X[714] and APFD[711]. As pure functionals the local functional BLYP[707,708,709] and the meta-GGA Minnesota functional M06-L[710] were employed. As examples for the upper limit of the Jacob's ladder[126], two different double hybrid functionals (B2PLYPD3[137,715,716] and mPW2PLYPD3[137]) were used. The Grimme dispersion correction D3[140] was added to all functionals without any intrinsic dispersion correction. In all DFT calculations, the ultrafine (99,950) grid was used.

To investigate the accuracy of semiempirical methods, the benchmark encloses the OMx methods with and without dispersion correction.[197] Additionally, the performances of AM1, its reparametrized variant RM1[207], MNDO/H[183], an MDNO parameterization with a special focus on hydrogen bonding, and of PM6[205] and PM7[206] are analyzed. In the semiempirical calculations, the SCF convergence was set to $1 \cdot 10^{-6}$ eV and the optimization threshold to $1 kcal/mol$, the default values.

The crystal structure conformations (see Table 1) of the molecules were used as starting structures for the geometry optimizations. The Turbomole program package[179] was used for the computations with

all correlated wave-function based methods. All DFT and the HF calculations were conducted with the Gaussian program package.[718] The Mopac program package[719] was employed for the PM6 and PM7 optimizations while all other semiempirical calculations were performed with the MNDO program package[183].

A multitude of criteria exists to assess the quality of quantum-chemically optimized geometries, e.g., equilibrium bond lengths and frequencies,[70] isomerization and atomization energies,[720] or energy differences to a reference geometry calculated with a reference method[332,721,722]. In the following, the quality of optimized geometries is analyzed in a two-fold manner. (1) RMSD (root mean square deviation) values with respect to the reference geometry are calculated (see for example [723] for a literature example). In the RMSD calculations only the atoms within the rigid backbones of the semiconducting molecules are included. Flexible side chains are not included. Small conformational changes in the alkyl side chains would otherwise dominate the RMSD calculations, resulting in an imbalanced description of the performance of the methods. (2) MAE (mean absolute error) values are calculated for the deviations of distinct geometric parameters such as angles or bond length alternations (BLAs) from the benchmark geometry. As also utilized by Mennucci et al.[724] who used BLA values to evaluate excited-state geometries of conjugated molecules in solution, such geometric parameters summarize very effectively the electronic structure and character obtained with a certain method.

5.2.2   Benchmark Results for Ground-State Geometries

The performance of the different methods for geometries is first discussed by means of RMSD values of the geometries. The corresponding results for organic molecular semiconductors of high, intermediate, and low polarity as well as the average over all compounds are given in Figure 6. It is evident from these data that all methods perform rather well for apolar dyes, while significant deviations exist for the molecules of high and intermediate polarity. These deviations are especially pronounced for the semiempirical methods (MDNO/H) as well as for HF and BLYP.

In a first step, polar dyes are considered. Due to their generally large errors, semiempirical results are not specifically discussed for the individual molecular groups, but only later-on for their average.Compared to the SCS-MP2/cc-pVTZ reference geometry, the geometries of polar dyes are best described with the M06-L local functional (RMSD=0.024 Å) and the range-separated hybrid ωB97X-D (RMSD=0.025 Å). As already pointed out by Truhlar et al.,[725] M06-L-D3 overshoots for dispersion interactions so that M06-L performs better without the dispersion correction (RMSD(M06-L-D3)=0.035 Å). These deviations correspond approximately to half the deviation of SCS-MP2 (RMSD=0.046 Å), which results only from the basis set error. CC2 and SCS-CC2 show comparable deviations (0.053 Å and 0.049 Å, respectively).
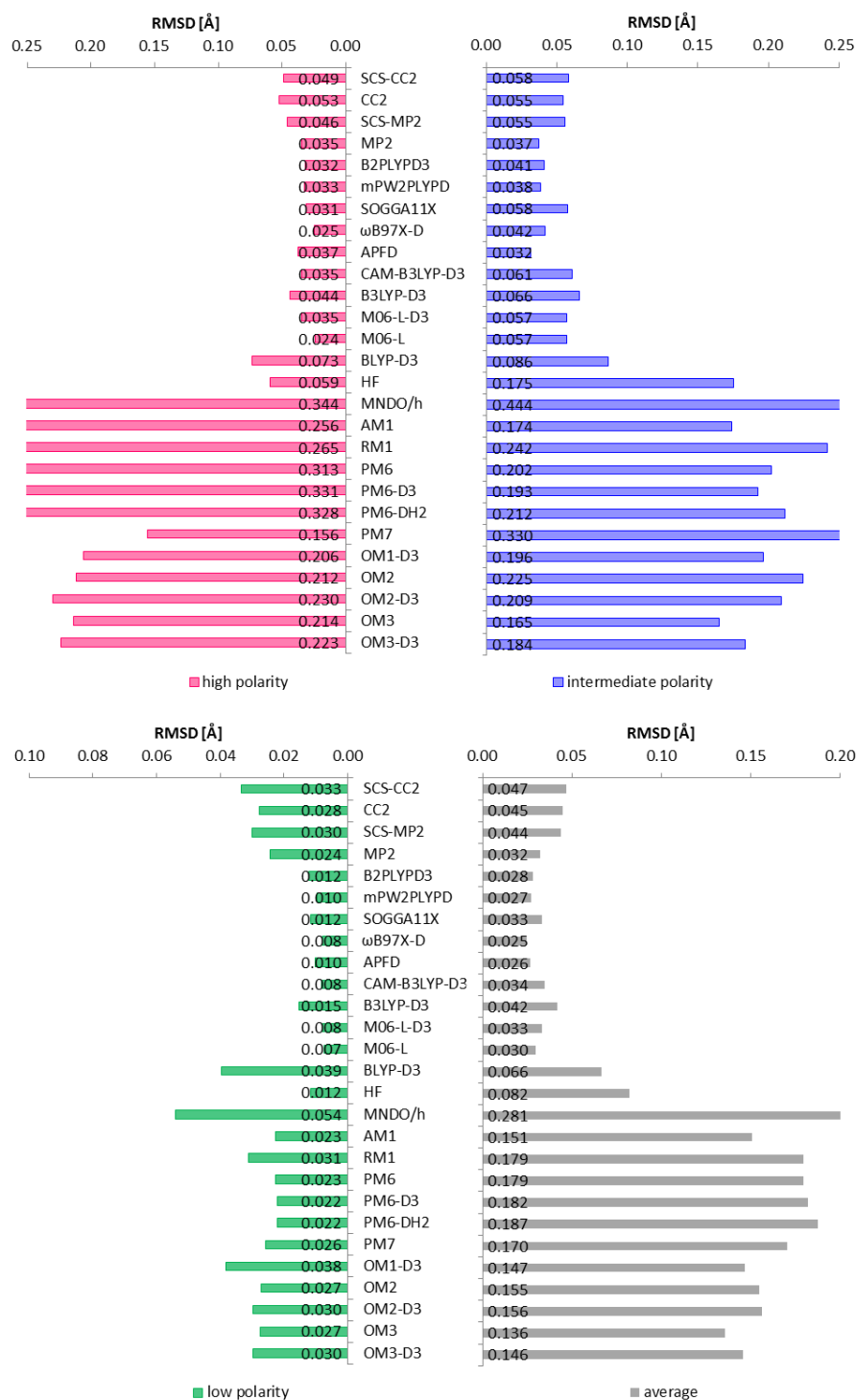
Figure 6: RMSD values for the molecules optimized with the different methods calculated with respect to the SCS-MP2/cc-pVTZ reference geometry. Adapted with permission from [702]. © 2015 American Chemical Society.

Using the smaller cc-pVDZ basis sets, MP2 performs best among the wave function-based methods (RMSD=0.035 Å). This holds for all compound classes and indicates an error compensation between the basis set error and the somewhat inaccurate ratio between the local same-spin and opposite-spin correlation in MP2, which is corrected in the SCS treatment. It becomes evident that compared with the wave-function based methods, density functionals apart from BLYP-D3 and HF perform better,

162

with smaller RMSD values ranging from 0.024 Å (M06-L) to 0.044 (B3LYP-D3). These smaller RMSD values and the underlying general performance differences between DFT and *ab initio* methods can be explained with basis set effects. The basis set dependence of the RMSD values of DFT optimized structures is shown in Figure 7. As no polarity/functional group dependence exists, the values were averaged for all molecules.
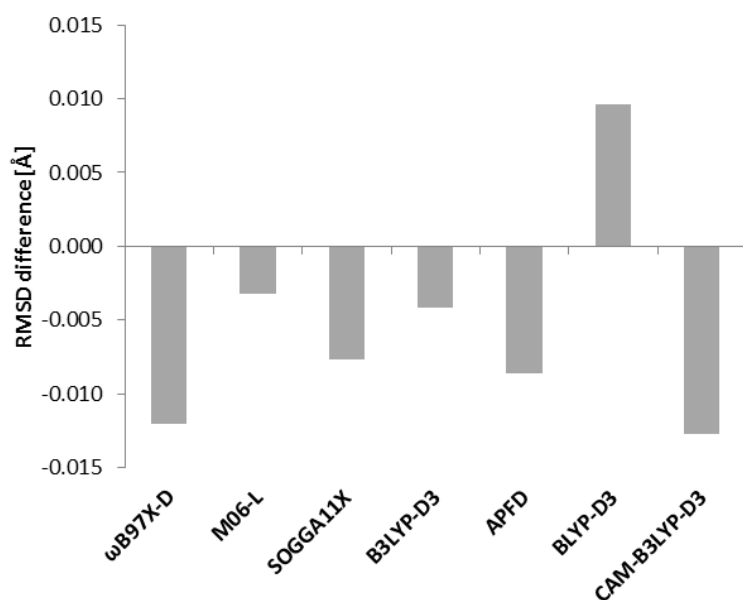
Figure 7: Change in the RMSD values upon enlarging the basis set, $\Delta RMSD = RMSD(cc-pVDZ) - RMSD(cc-pVTZ)$. Negative signs indicate that the basis set increase is detrimental. The RMSD values are averaged over all molecules. Adapted with permission from [702]. © 2015 American Chemical Society.

While the RMSD values for the SCS-MP2 geometries increase upon decreasing the basis set from cc-pVTZ to cc-pVDZ (average RMSD of SCS-MP2/cc-pVDZ: 0.044 Å, see Figure 6), the RMSD values for DFT geometries decrease by ~ 0.010 Å upon decreasing the size of the basis sets, i.e., DFT geometries optimized with smaller basis sets are more similar to the reference geometries. This means that due to an error compensation, most density functionals in Figure 7 yield more reliable geometries with smaller basis sets. Such a behavior has already been analyzed in more detail for the B3LYP/6-31G(+)-level of theory by Grimme et al.[726] Please note that in the case of BLYP-D3, a larger basis set leads to an improved (smaller) RMSD value. In general, however, these results suggest that for large systems where high-level *ab initio* methods with large basis sets are computationally too demanding, DFT combined with smaller basis sets provides a better description of molecular geometries than wave-function based methods employed with the same small basis sets.

Compared with the polar dyes, the RMSD values are generally higher for the molecules of intermediate polarity. In view of the well-known challenging electronic structure of cyanine dyes,[727] which is highly dependent on correlation effects,[728] this is *a priori* surprising. To some extent, the larger errors for the molecules of intermediate polarity might result from their larger size as well as from their enhanced

torsional flexibility. The structures of the three-dimensional triphenylamine-based compounds arise from a delicate balance between conjugation and steric strain, often leading to shallow torsional potentials as pointed out by Gierschner et al.[21] Indeed, the huge torsional flexibility of these molecules also frequently led to convergence problems in the geometry optimizations. In general, for the dyes of intermediate polarity, APFD, a modern functional with an intrinsic dispersion correction, performs best (RMSD=0.032 Å), maybe owing to the fact that this functional has been particularly optimized for weak interactions such as hydrogen bonding and van-der-Waals interactions in noble-gas clusters.[711] Hence this local DFT functional incorporates both elements correctly describing conjugation – its DFT correlation and exchange part – and steric strain and dispersion between polarizable groups – the dispersion correction optimal for noble-gas atoms. Apart from APFD, also ωB97X-D yields reliable geometries (RMSD=0.042 Å). The good performance of ωB97X-D is equally in line with the importance of a correct description of weak interactions between separate molecular moieties for accurate geometries of the dyes of intermediate polarity: it has recently been shown by Grimme et al. that ωB97X-D is very reliable for the calculation of host-guest interactions.[139] Moreover, for high as well as intermediate polarities, the double hybrids yield very accurate results. Grimme et al.[138] highlighted that double hybrids are constructed in a way to include all important regimes of electron correlation, the long-range dispersion, the medium-range correlation, and the short-range (repulsive) instantaneous electron-electron correlation. In view of the outlined particular importance of different correlation regimes (dispersion vs. conjugation) for the geometries of dyes of polar[729] and intermediate polarity, the good performance of the double hybrids seems to be consistent.

Geometries of apolar molecules optimized with different methods differ less than those of the more polar molecules, and corresponding RMSD values are small. This originates from the structural rigidity of the apolar scaffolds and from the simple electronic ground-state structures of these molecules.

Considering the mean RMSD values averaged over all molecules (Figure 5, grey bars, Figure 6), ωB97X-D, APFD, and the double hybrid functionals perform best. Please note that the APFD optimized geometries of polar dyes are not as reliable as those of the two less polar substance classes. The good performance of ωB97X-D is in line with similar findings in the literature about reliable ωB97X-D geometries of various systems with complicated electronic structures like transition metal complexes[730] or transition states[731]. Geometries optimized with semiempirical methods are significantly less accurate with RMSD values of approximately 0.150 Å. While these semiempirical methods perform satisfactorily for apolar dyes, RMSD errors increase for molecules of intermediate and high polarity that possess a more complex electronic structure.

Small RMSD values are one important criterion for the accuracy of a given geometry. Nevertheless, there are certain geometric parameters that reflect the electronic ground-state structure predicted by

a certain method in a very compact manner. This is most easily explained for the bond length alternation (BLA) in merocyanines being a very prominent structural parameter for conjugated systems in general.[21,732,127] Depending on the amount of (de)localization in the systems, the bond lengths indicated in Figure 8 for the merocyanines alternate to a variable extent, which is called the bond length alternation. It can be expressed as a single BLA parameter[645]:

$$BLA = \frac{0.5 \cdot (bond\ 3 + bond\ 1) - bond\ 2}{bond\ 2} \cdot 100 \tag{441}$$

The electronic structure of merocyanines in a VB approach is described in terms of the relative contributions of a neutral and a zwitterionic resonance structure.[645] If both contributions are identical, all bond lengths are ideally equal like in perfect small[III] cyanines,[728] and the BLA is 0. If the neutral resonance structure prevails in the electronic ground state, bond 2 as indicated in Figure 8 is elongated while bonds 1 and 3 acquire more double-bond character. The BLA becomes negative. Thus the BLA directly mirrors the nature of the electronic ground state. In comparison with RMSD values, this provides complementary information: if any method overestimated all bond lengths by a certain percentage, RMSD values of its optimized geometries would be large although the method describes the electronic character correctly – all bond lengths are equally overestimated. An analysis in terms of the BLA, on the other hand, would reveal this. The inverse is also true. Geometries with very accurate average bond lengths yield small RMSD values. The BLA and, correspondingly, the electronic character might still be flawed, which would be reflected in a too large/too small BLA value.
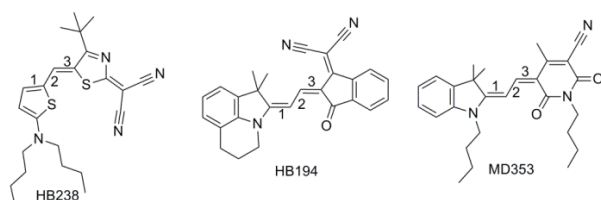
Figure 8: Designation of the carbon-carbon bonds of the bridge in merocyanines used to calculate the BLA.

For the merocyanines, MAE (mean average error) values of the BLAs obtained with all methods were calculated with regard to the BLA of the SCS-MP2/cc-pVTZ reference geometry. The favorable accuracy/cost ratio of the SCS-MP2 method for BLA values was pointed out by Jacquemin et al.[733], and it was also employed by Sancho-García et al. for a benchmark on BLA values in oligoacetylenes with increasing chain length.[734] Jacquemin et al. investigated systematic basis set effects on the BLA, albeit

---

[III] Please note that this is only valid for small cyanines since the Peierls distortion results in bond localization for larger cyanines above a certain number of polymethine moieties, also called the cyanine limit.[1015]

at the MP2 level, and found the cc-pVTZ basis sets to provide converged results.[735] All these findings support the reliability of the herein employed SCS-MP2/cc-pVTZ reference BLAs.
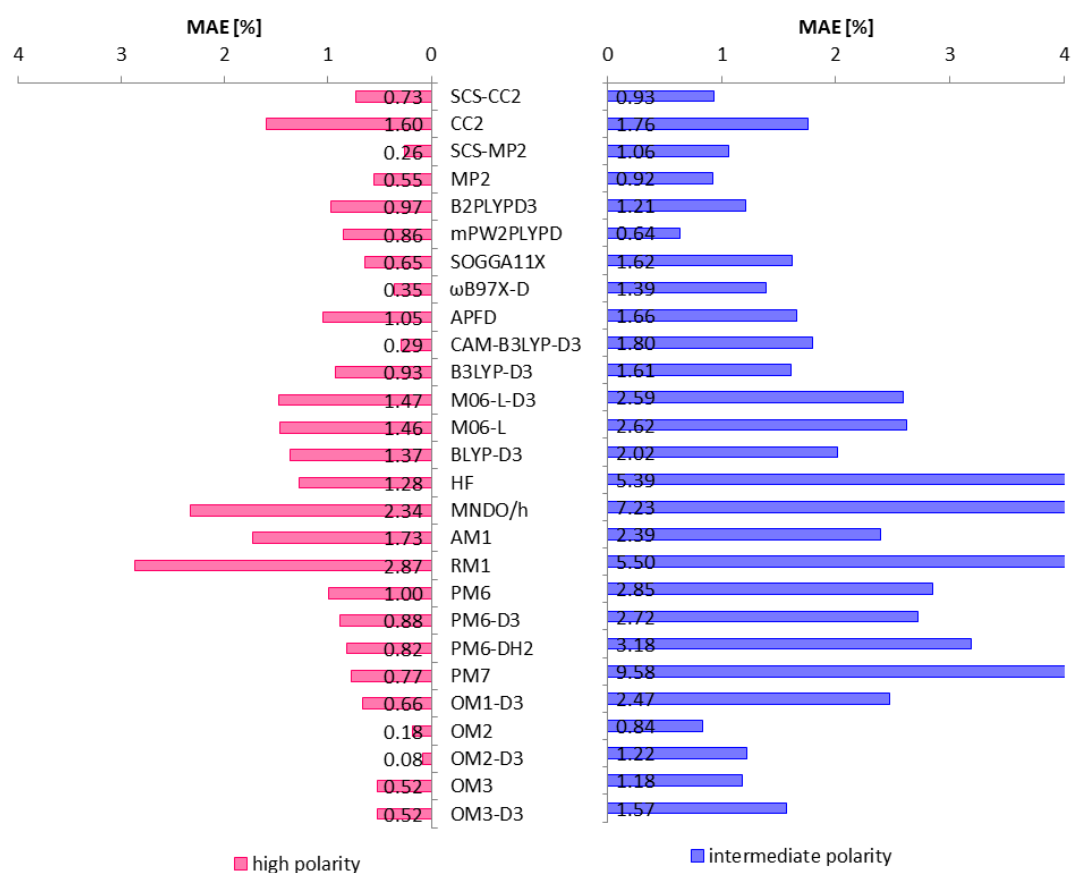
Figure 9: MAE values for BLA of merocyanines (left panel) and for different structural parameters of molecules of intermediate polarity (right panel). All MAE values were calculated from the optimized ground-state geometries using programs implemented in C++. Adapted with permission from [702]. © 2015 American Chemical Society.

All MAE values for the BLAs in merocyanines are displayed in Figure 9. The smallest MAE of only 26% is found for SCS-MP2 using the cc-pVDZ basis sets. This corresponds to the findings of Jacquemin et al. that in MP2 computations the 6-31G(d) basis provides qualitatively similar results to larger basis sets.[735] In contrast to the RMSD values, applying spin-component scaling or using CC2 instead of MP2 has pronounced effects on computed BLAs. Among the DFT functionals, CAM-B3LYP delivers the best BLAs with an average error of 29%. Also ωB97X-D performs rather well (MAE: 35%). The beneficial effects of a long-range correction for computed BLA values were equally analyzed by Jacquemin et al. who studied the efficiency of long-range corrected functionals for large organic compounds.[736] The accuracy improvement due to the long-range correction can be explained by means of the many-electron self-interaction error (MSIE). Brédas and Körzdörfer et al. outlined that the elimination of the MSIE via IP-tuning of long-range corrected functionals results in improved, yet not vanished BLA errors.[737] In line with this, the MAE errors in Figure 9 are also highly susceptible to the amount of HF

exchange included in the functionals. Both pure DFT functionals, i.e., BLYP-D3 (MAE: 137%) and M06-L (MAE: 147%), and HF (MAE: 128%) yield poor results. Hybrid functionals, especially with a significant amount of HF exchange like SOGGA11X, perform better (MAE: 65%). This suggests that adjusting the amount of HF exchange to minimize the MSIE ameliorates BLA results. In a similar way, a benchmark by Jacquemin et al. using different series of conjugated systems showed that hybrid functionals with equal amounts of HF exchange deliver very similar BLA values.[732] The double hybrids B2PLYP-D3 and mPW2PLYPD yield acceptable errors of 97% and 86%, respectively. However, this contrasts with results of Wykes et al. who found very good performances of double hybrids for BLAs, yet employing the cc-pVTZ basis sets.[738] This divergence is presumably due to the larger basis set dependence of the double hybrids compared to regular DFT functionals[138].

Hence, while the reduced MSIE owing to the long-range correction is usually exploited to improve excitation energies, the CAM-B3LYP and ωB97X-D functionals originally optimized for excited states perform best for the BLA (Figure 9). Surprisingly, the same is true for semiempiric methods (but certainly not for the same reason). In terms of BLA values, the OMx approaches yield the smallest errors among all methods. The very accurate BLA values could be due to the asymmetric HOMO-LUMO splitting in OMx-based methods that was shown to particularly improve excitation energies. Moreover, the asymmetric splitting could possibly ensure that the OMx methods describe the relative contributions of the neutral and the zwitterionic configurations to the merocyanines' ground state accurately because the HOMO-LUMO splitting could translate into a correct energetic separation between the configurations. As discussed, this results in reliable BLA values.

All other semiempirical methods are considerably worse, but stay within the error margin spanned by the DFT functionals. This highlights also the above-mentioned importance of consulting MAE in addition to RMSD values. Furthermore, it suggests doing a similar evaluation for the dyes of intermediate polarity.

For the molecules of intermediate polarity, a consistent evaluation is more difficult to achieve because due to the chemical diversity of these molecules, no single geometric parameter qualitatively reflecting their electronic character exists. In four molecules, twisting motions can be taken as parameters because, as mentioned above, they are indicative of the balance between steric strain and electron delocalization:

- In the substituted diketopyrrolopyrrole (DPP), the furane substituents twist with respect to the plane of the central DPP moiety. This twist is a key feature of the resulting DPPs: experimentally, the torsion angle of furane-substituted DPP polymers was shown to influence

optoelectronic properties such as absorption and charge transport.[739] At the SCS-MP2/cc-pVTZ level of theory, the averaged torsion angle equals 9°.

- In molecules possessing a three-coordinate nitrogen center, electron delocalization and resulting electronic properties are determined by the amount of torsion of the phenyl substituents around the central nitrogen.[21] Moreover, with regard to the relationship between molecular properties and aggregate features (see above), the three-dimensional molecular shape arising from the torsion has a significant impact on charge transport properties.[740] Please note that the emergence of dye-sensitized cells has additionally channeled structural investigations on triphenylamine-based dyes.[741,742] Therefore, the torsional angles between the planar substituents and the central nitrogen plane are used as structural parameters.

Apart from these twisting motions, the BLA of the electron-withdrawing cinnamaldehyde moiety in the aldehyde-substituted triphenylamine is employed. In the case of the completely planar squaraine, the ratio of the averaged C-C bond lengths in the central four-membered ring to the C-O bond lengths reflects the donating power of the substituents, the "aromatic" character of the central ring and thereby the zwitterionic character of the squaraine. This ratio is used for MAE evaluation of the optimized squaraine geometries. All structural parameters for the dyes of intermediate polarity are listed in Figure 10.
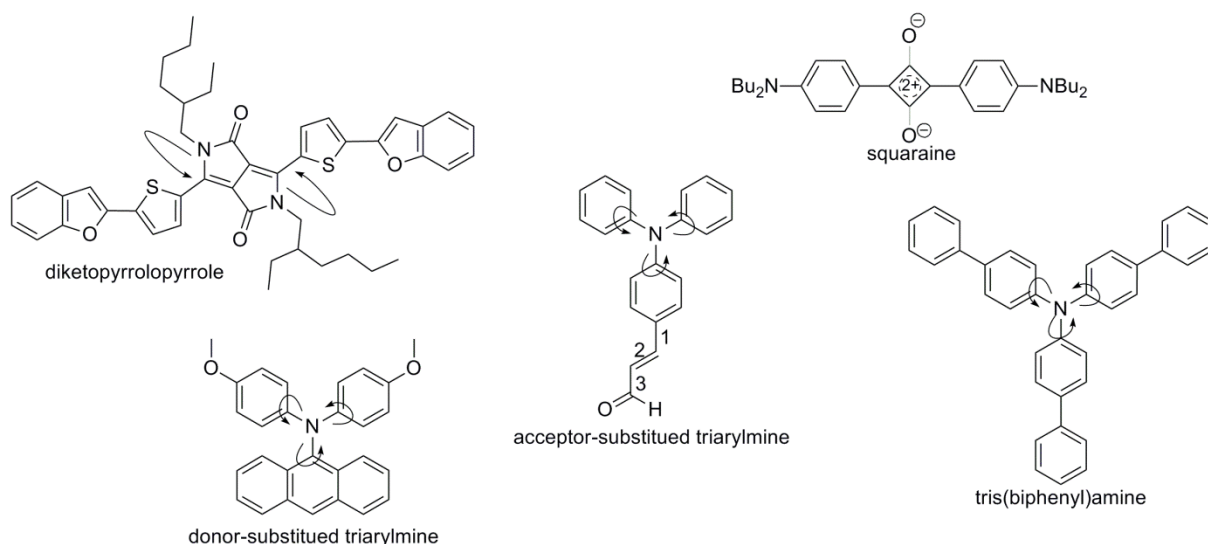
Figure 10: Structural parameters used for the dyes of intermediate polarity. Torsional angles between planes of different molecular entities are designated with bent arrows. Applied scaling factors different from 1: tris(biphenyl)amine: 10; squaraine: 100. Adapted with permission from [702]. © 2015 American Chemical Society.

Using several structural parameters for the dyes of intermediate polarity instead of a single one – the BLA – for the polar dyes has the drawback that resulting percentaged MAE values have different orders of magnitudes. For instance, bond lengths are significantly less flexible than torsional angles. Hence MAE values calculated from bond length deviations are much smaller than those from torsional angles.

The BLA as a scaled ratio of bond lengths defined in Eq. (1) varies most. This means that the average MAE value for the molecules of intermediate polarity would be entirely dominated by the MAEs of the BLA and certain torsional angles. In order to avoid this unbalanced treatment, scaling factors are applied to ensure that all MAE values have equal magnitudes (Figure 10). This makes averaging of the MAEs for all molecules in Figure 10 possible.

Resulting MAE values are shown in Figure 9. Wave-function based methods yield the best description although they are employed with smaller basis sets compared with the reference. As also found for the polar dyes, MP2-based methods (MAEs: MP2: 92%; SCS-MP2: 106%) are more accurate than CC2 methods (CC2: 179%; SCS-CC2: 93%).[mmm] Spin-component scaling has a pronounced effect, leading especially to considerably improved MAE values of SCS-CC2 (MAE of SCS-CC2: 93%) compared to CC2 (MAE of CC2: 179%). The improvement of SCS-MP2 compared to MP2 is less distinct (SCS-MP2: 106%; MP2: 92%). Also Hättig et al. outlined a stronger effect of SCS on CC2 than on MP2.[180] The significance of SCS for either method is in line with the above discussed importance of different correlation regimes. Due to the Pauli repulsion, the average distance between electrons with parallel spin is larger than between electrons with opposite spin. Thus dynamic correlation is very important for the interaction between electrons with opposite spin, while it is less important for electrons with parallel spin, where static correlation becomes an issue. The static correlation between same-spin electrons is usually overestimated in MP2 and CC2 because the biased HF reference overshoots for the static (=left-right) correlation and completely disregards dynamic correlation. Scaling both the same-spin and the opposite-spin correlation, i.e., spin-component scaling, essentially removes these deficiencies.[43] Therefore, a pronounced effect of spin-component scaling suggests a considerable importance of the relative contributions of dynamic (short-range) and static (long-range) correlation.

The double hybrid functional mPW2PLYPD provides the most accurate description among all methods (MAE: 64%). Surprisingly, the second double hybrid functional comprised in the benchmark – B2PLYPD3 – performs significantly worse with an almost doubled error of 121%. Similarly, comparably large differences are found for the MAE values of CAM-B3LYP (180%) compared to ωB97X-D (139%), the more so as rather similar values were obtained in the case of the polar dyes. HF and pure functionals perform particularly poorly with MAE values larger than 200%. As already found for the polar dyes, MAE values of the OMx methods are small, even smaller than 100% for OM2. Therefore,

---

[mmm] It should be kept in mind that a comparison between the performances of MP2- and CC2-based methods could be somewhat biased because SCS-MP2/cc-pVTZ is the reference method. However, similar to the results of RMSD values and in contrast to BLA errors, MP2 and not SCS-MP2 performs best in terms of MAE values of the dyes of intermediate polarity.

the MAE results for dyes of intermediate polarity mirror quite well their counterparts for polar molecules, albeit with more pronounced differences between the methods.

Since apolar dyes possess less complex electronic structures, MAE value analyses of apolar dyes turned out to provide no additional information compared to the RMSD evaluation.

With the objective of understanding the the properties of the individual molecules, this section focused on molecular ground states. All molecular semiconductors included in the benchmark possess extended π-systems so that their electronic ground-state structures often result from the combined effects of conjugation, (de)localization, and steric strain. Hence the simultaneous incorporation of different correlation regimes, i.e., dispersion, medium-range correlation and short-range repulsion[138], was shown to be of major importance to account for these effects. As a consequence, DFT functionals and semiempiric methods specifically optimized for correlated systems provide the most accurate description of the semiconductors' ground states. On the one hand, this involves functionals originally optimized for excited-state calculations, particularly ωB97X-D that was found to be very accurate. In a similar way, reliable BLA values can be obtained with the semiempiric OMx series, parameterized for the purpose of excited-state calculations as well. On the other hand, good performances were observed for functionals specifically developed to describe weak interactions, most prominently APFD, but also the local meta-GGA M06-L(-D3).

The next logic step to encompass molecular properties is the investigation of vertical excitation energies of the molecular p-type semiconductors.

5.3 Benchmarking vertical excitation energies of molecular semiconductors

A benchmark of vertical excitation energies of the comprised molecular semiconductors, which are medium- to large-size molecules, faces a number of problems:

1. Excited states are usually assumed to be more diffuse than the electronic ground state.[39] Thus for a balanced description of excitation energies, larger basis sets are in principle necessary. However, as specifically pointed out above for geometry optimizations, the basis set dependence differs for different methods in any kind of calculation so that unequal basis set dependencies are to be expected also for different excited-state methods. Given the intrinsically high cost of excited-state calculations, it would be thus desirable to identify those methods that provide the most accurate excitation energies when employed with a given rather small basis set. Such basis set related aspects of excited-state calculations are analyzed in the first part of this section.

2. Any benchmark requires accurate reference values for excitation energies. As outlined by Furche et al.[743] and discussed by Thiel et al.,[744] accurate reference values are not readily accessible even if experimental absorption spectra are available. A multitude of extrapolation schemes exist to determine vertical excitation energies from spectra.[174] Nevertheless, even with highly-resolved spectra at hand, some uncertainties still remain (e.g., energy shifts due to vibronic couplings, excited-state relaxations, etc.). Therefore, in line with the proceeding of Thiel et al.,[744] theoretical best estimates from MS-CASPT2 calculations are used to deduce reference values of excitation energies for subsequent benchmark calculations. The procedure to calculate these theoretical best estimates will be discussed in more detail in the second part of this section.

3. Low-lying excited valence states of organic molecular semiconductors comprise both neutral and charge-transfer excitations. While neutral excited states responsible for light absorption and the resulting photocurrent are of primary interest in OSCs,[479] their interplay with nearby charge-transfer states is nonetheless crucial for macroscopic device performances as well. To cite only two examples, charge-transfer states in molecular semiconductors were shown to act as doorway states for exciton trapping,[745] and they play a key role in modulating the rates of singlet fission.[536] Therefore, a comprehensive understanding of excitonic processes in organic thin films presupposes the knowledge of the positions of both types of molecular valence excited states. However, due to their different electronic character, a balanced description of both types of states might require the utilization of different methods for different states. For instance, it is well-known that the description of charge-transfer states particularly in a TD-DFT framework can be troublesome.[266,259,746] A discussion of high-performing methods as a function of the excitation type will be the subject of the third part of this section.

4. Both singlet and triplet excitons exist in OSCs. On the one hand, the generation of triplet excitons, possibly via fast intersystem crossing in C_{60},[479] has been considered as an OSC energy loss channel[423], particularly when triplet energies are lower than the interfacial charge-transfer states.[435] On the other hand, in view of the growing interest in singlet fission[533,534] and in potentially long triplet exciton diffusion lengths compared to their singlet counterparts,[479,490] research has recently also focused on exploiting benefits from triplet excitons. Therefore, profound knowledge of triplet states in molecular semiconductors and, concomitantly, of methods reliably predicting triplet excitation energies is mandatory. An evaluation of excitation energies for states of different spin multiplicity will be presented in the fourth part of this section.

In the following, the outlined points will be subsequently addressed.

5.3.1 Basis set dependencies of excited-state methods
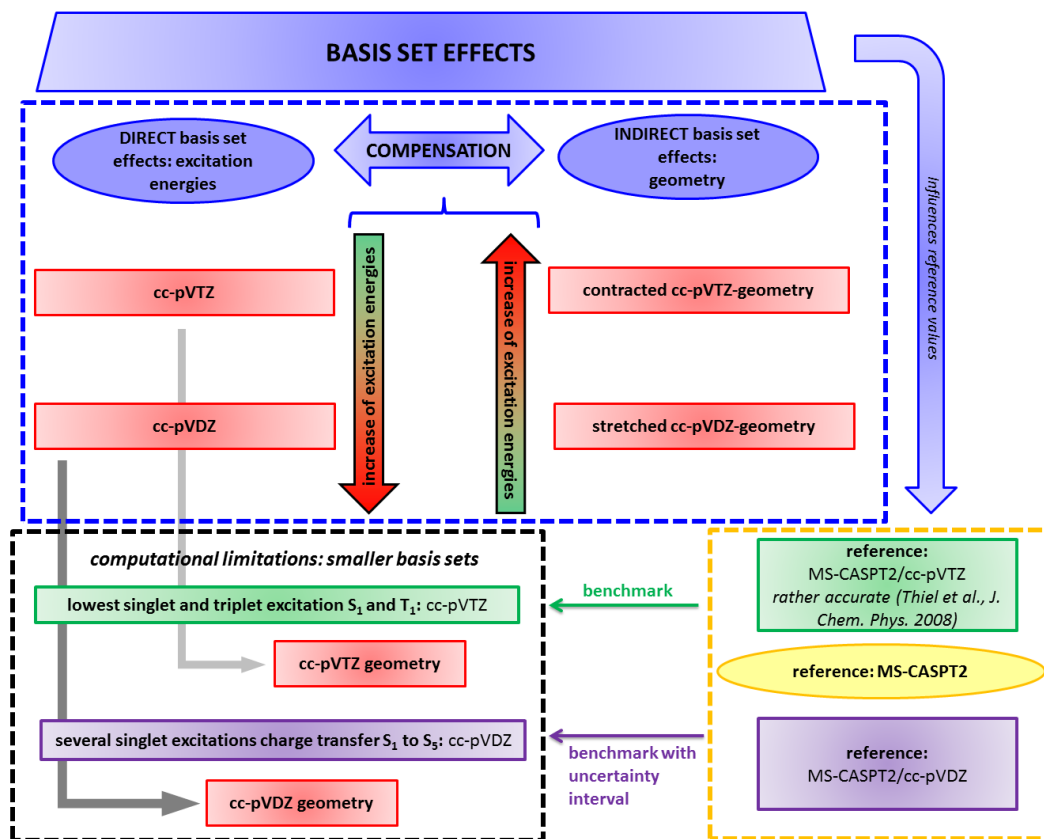
Figure 11: Outline of investigations on basis set effects and their influence on excitation energies.

The presented analysis of the basis set influence on calculated excitation energies is outlined in Figure 11 (uppermost panel, "Basis set effects"). It is discussed in detail in the following.

The basis set dependence of excitation energies has already been analyzed in numerous investigations. Triple-zeta basis sets were shown to provide converged TD-DFT excitation energies by Grimme,[174]

Furche,[743] and Jacquemin[747]. Thiel et al. demonstrated for coupled-cluster methods[744] as well as for MS-CASPT2[748] that the size of the TZVP basis[749], compared with its augmented counterpart, is already sufficient for low-lying valence excitation energies, resulting in a maximum systematic overestimation of excitation energies of approximately 0.1 eV. In line with these results, Jacquemin et al. found in a recent benchmark entirely dedicated to excited-state basis set effects only modest basis set dependencies for TD-DFT calculations and a slightly more pronounced basis set dependence of wave-function based methods, which is, however, very similar for all wave-function based methods.[750] This data suggests that the cc-pVTZ basis sets can be expected to provide valence excitation energies within an error range that results primarily from method deficiencies rather than from basis set limitations. Therefore, the cc-pVTZ basis sets will be employed in the following to evaluate method performances for the lowest singlet and triplet excitation energies of the molecular semiconductors (Figure 11, left green panel). Similarly, reference excitation energies for the lowest singlet and triplet states are obtained as theoretical best estimates from calculations on the MS-CASPT2/cc-pVTZ level of theory (Figure 11, right green panel).

Since both neutral and charge-transfer excitations are taken into consideration, a number of excited states have to be calculated for each molecule (6 to 8 states per molecule and method). In view of the molecular sizes, using the cc-pVTZ basis sets for all excitation energies exceeds computational feasibility. Moreover, it is one of the purposes of this section to identify efficient methods that can be subsequently used in a multiscale approach. This necessarily precludes using large basis sets because large-scale calculations in conjunction with cc-pVTZ or equally large basis sets are computationally definitely not affordable.[735] Furthermore, it has been already mentioned that different methods might perform better with small basis sets than with large basis sets (similar to the results of the geometry benchmark), i.e., that an error cancellation occurs. This in turn suggests choosing a specific rather small basis set as a tradeoff between accuracy and computational efficiency first. Then, excitation energies are benchmarked using always the predefined smaller basis. Due the possibly considerable basis set error of the smaller basis sets, high performances in the benchmark can only be attributed to the *combination* of the specific method and the predefined rather small basis set. The cc-pVDZ basis is chosen as the smaller basis. Excitation energies obtained with this basis for a number of states will be evaluated in the following sections (Figure 11, left purple panel).

Employing smaller basis sets raises particularly the question about the accuracy of the reference values (Figure 11, blue arrow to yellow oval and dashed yellow line). As outlined above, reference values for excitation energies are obtained from theoretical best estimates of MS-CASPT2 values. Being the most accurate method, MS-CASPT2 is also the computationally most demanding method so that MS-CASPT2 calculations employing cc-pVTZ basis sets are not feasible for a number of states per molecule and

symmetry. Consequently, smaller basis sets have to be also used when deducing CASPT2 reference values (Figure 11, right purple panel) although high-level *ab initio* methods such as MS-CASPT2 possess more pronounced basis set dependencies than for example TD-DFT[39,750]. Hence, resulting reference values are necessarily less accurate.[748] To account for the reduced accuracy of the reference values, errors of the benchmarked methods calculated for a number of excited states are not evaluated with respect to the MS-CASPT2 excitation energies themselves, but with respect to a certain interval around these excitation energies. This interval will be designated as the "uncertainty interval" in the following (green and purple arrows, Figure 11).

Before quantitatively estimating the uncertainty interval, please note that not only the basis sets employed in the actual excited-state calculations influence resulting vertical excitation energies, but also the basis sets (and the methods!) used to optimize the underlying geometries. Due to this two-fold basis set influence, basis set effects are subdivided into direct and indirect effects in Figure 11 (blue ovals). With regard to the underlying optimized geometries, it is common practice to benchmark excitation energies using ground-state geometries that were beforehand optimized with any reasonably accurate method.[751] In line with most investigations employing MP2 along with triple-zeta basis sets,[751] optimized SCS-MP2/cc-pVTZ geometries are employed in the following to benchmark excitation energies with cc-pVTZ basis sets (red panel in the black dashed panel, Figure 11).

However, it was found that the use of equal and rather small basis sets for the geometry optimization and the subsequent transition energy calculation leads to an error cancelation of direct and indirect basis set errors (center blue arrow, dashed blue panel, Figure 11). This error cancelation seems to be rather method-independent. It is demonstrated using the example of anthracene (Figure 12), which has two extremely close-lying excited states, the so-called L_a (B_{2u}) and L_b (B_{3u}) state, making it a difficult case and a highly sensitive test system (see below for a more detailed discussion of the L_a and L_b states). The sensitivity of the excited-state properties of anthracene is already reflected in the fact that SCS induces a reordering of the L_a and L_b states, i.e., while the L_b state (B_{3u}) is lowest at the SCS-CC2 level of theory (Figure 12), CC2 predicts the L_a (B_{2u}) excitation to be lower than its L_b counterpart. Similarly, a comparison of the L_a (blue lines) and L_b (pink lines) excitations for SCS-CC2 and ωB97X-D shows that their relative order is reversed.

Computing both the ground-state geometry and excitation energies with the cc-pVDZ basis sets (cc-pVDZ//cc-pVDZ), SCS-CC2 predicts vertical excitation energies of 3.81 eV ($^1B_{3u}$), 3.91 eV ($^1B_{2u}$), and 5.38 eV ($^1B_{1g}$). These values deviate by only 0.01 eV, 0.07 eV, and 0.03 eV, respectively, from the cc-pVTZ//cc-pVTZ-values, i.e., upon increasing the basis sets employed in both the geometry optimizations and the excited-state calculations, computed excitation energies barely change (red-to-green arrows, Figure 11).[174] If only the basis sets of the ground-state geometry optimizations are

174

increased (cc-pVDZ//cc-pVTZ, Figure 12), all states are shifted to higher energies by 0.08 eV, 0.05 eV, and 0.09 eV due to the more contracted ground-state geometry (red right panels, Figure 11).[39] Obviously, the effect is larger than the overall basis set effect observed when simultaneously increasing all basis sets (cc-pVTZ//cc-pVTZ, Figure 12). If, on the other hand, only the vertical excitation energies are computed with larger basis sets (cc-pVTZ//cc-pVDZ, Figure 12), all excited states are downshifted with respect to cc-pVDZ//cc-pVDZ by a similar amount. This downshift results because the electronic structures of the excited states are more diffuse than the ground state so that the excited states profit more from larger basis sets than the ground state (red left panels, Figure 11). This trend seems to be quite general for all methods because a similar proceeding with ωB97X-D yields equivalent results. Deviations for ωB97X-D transition energies and geometries are comparable, but slightly smaller. This can be expected since the basis set dependence of DFT methods like ωB97X-D/cc-pVDZ is usually smaller than the one of wave-function based approaches (see Figure 6).

The discussed error compensation of direct and indirect basis set effects is highlighted by dashed blue lines in Figure 11.
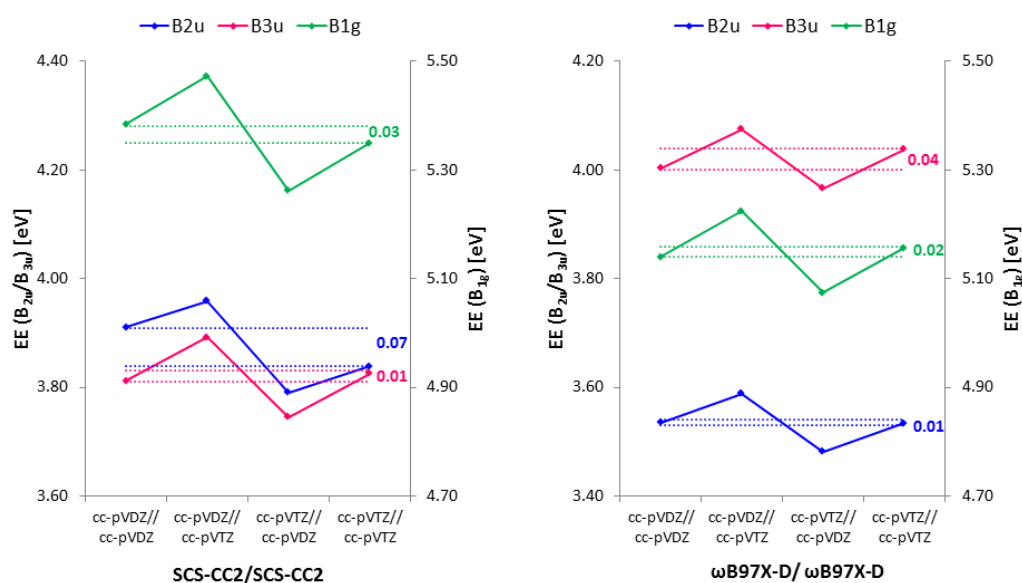
Figure 12: Basis set effects on the excitation energies of anthracene calculated with SCS-CC2 (left panel) and with ωB97X-D (right panel). Adapted with permission from [702]. © 2015 American Chemical Society.

Table 3: Basis set effects on the lowest excitation energies calculated at the MS-CASPT2 level of theory.

Molecule	State	MS-CASPT2/cc-pVDZ// SCS-CC2/cc-pVDZ [eV]	MS-CASPT2/cc-pVTZ// SCS-MP2/cc-pVTZ [eV]	Basis set error [eV]
anthracene	$1B_{2u}$	3.70		
	$1B_{3u}$	3.60	3.55	-0.05

	1B$_{1g}$	4.90		
rubrene	1A$_u$	2.70	2.65	-0.05
	1B$_u$	3.30		
	1A$_g$	3.80		
dithiophene	1A$_u$	4.00	4.10	+0.10
	2A$_u$	4.60		
	3A$_u$	5.40		
DIP	1B$_{3u}$	2.60	2.75	+0.15
	1B$_{1g}$	3.00		
	1B$_{2u}$	3.30		
squaraine	1B$_{3u}$	2.60	2.55	-0.05
	1B$_{3g}$	2.20		
	1A$_g$	3.60		
diketopyrrolo-pyrrole	1B$_u$	2.50	2.50	0.00
	1A$_g$	3.20		
	2A$_g$	3.70		
triarylamine	1E	4.25	4.10	-0.15
	1A	4.50		
methoxy-sub. triarylamine	1A	3.15	3.15	0.00
	2A	3.80		
	1B	4.00		
aldehyde-sub. triarylamine	1A	4.10	4.10	0.00
	1B	4.25		
HB194	1A$_g$	2.90	2.90	0.00
	1A$_u$	3.50		
	2A$_g$	3.50		
HB238	1A$_g$	2.80	3.00	+0.20
	2A$_g$	3.70		
	1A$_u$	4.40		
MD353	1A$_g$	3.15	3.10	-0.05
	2A$_g$	4.50		
	1A$_u$	4.30		
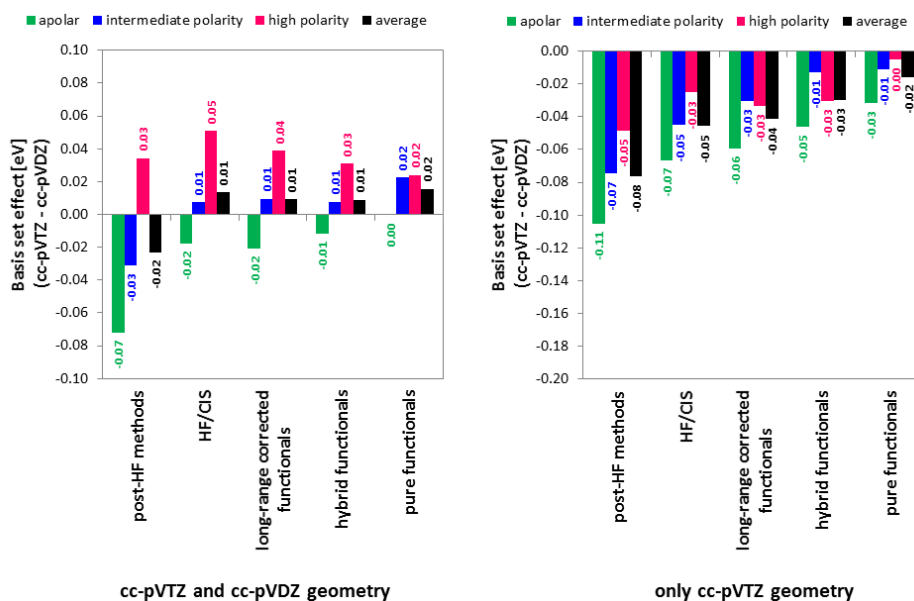
Figure 13: Left panel: Differences (= basis set effects) between excitation energies calculated with cc-pVTZ basis sets and SCS-MP2/cc-pVTZ optimized geometries and excitation energies calculated with cc-pVDZ basis sets and SCS-CC2/cc-pVDZ optimized geometries. Right panel: Basis set effects for excitation energies calculated with cc-pVTZ or cc-pVDZ basis sets using always the same SCS-MP2/cc-pVTZ optimized geometry.

The results in Figure 12 indeed indicate that accurate excitation energies are most likely obtained at the cc-pVDZ//cc-pVDZ level if the otherwise optimal cc-pVTZ//cc-pVTZ combination is computationally too demanding. To put this result about the relationship between direct and indirect basis set effects on a more quantitative footing, direct and indirect basis set effects are evaluated for the excitation energies of all molecules comprised in the benchmark (Figure 5). To be consistent with the above-stated discussion, results are arranged according to molecular polarity. As already mentioned, the basis set dependence of both excitation energies and geometries is a method-specific property, and it is usually larger for post-HF methods than for DFT or HF.[750] Thus, related methods are pooled into groups, and average results for basis set effects are presented for the respective groups, i.e., for post-HF methods, range-separated hybrids, global hybrids, pure functionals, and HF and CIS.

The right panel of Figure 13 displays basis set effects for excitation energies calculated with different basis sets (cc-pVTZ vs. cc-pVDZ basis) but always with the same geometry (SCS-MP2/cc-pVTZ). Thus the right panel shows only direct basis set effects. As discussed above for anthracene, all excitation energies decrease when the basis sets employed in the excited-state calculations increase (only negative values in the right panel, Figure 13; direct basis set effects, Figure 11). These effects are most pronounced for apolar dyes, which is due to the presence of very close-lying low valence excitations in anthracene, the dithiophene, and in DIP. This large basis set dependence of excitation energies of apolar dyes justifies the above evaluation of basis set effects on anthracene (Figure 12). However, it cannot necessarily be anticipated because donor-acceptor dyes are also known to have very

177

polarizable excited states.[752,753] Hence their excitation energies could significantly vary with small changes of the theoretical approach, which is however, as can be seen, not the case.

With respect to different methods (and not different compound classes), post-HF methods indeed depend more strongly on the basis sets (error: -0.08 eV) than HF (-0.05 eV) and hybrid functionals (-0.03 eV), with pure functionals showing the smallest basis set dependence (-0.02 eV). This is again found for all molecular groups and their average as well.

The observed basis set dependencies are compared to basis set effects on excitation energies calculated with different basis sets and different ground-state geometries. For this purpose, excitation energies with the cc-pVDZ basis sets are calculated for a number of methods using the optimized SCS-CC2[nnn]/cc-pVDZ ground-state geometry. Resulting values are compared to the above discussed excitation energies obtained employing the cc-pVTZ basis sets and the SCS-MP2/cc-pVTZ optimized geometry (left panel, Figure 13). The left panel of Figure 13 thus summarizes combined direct and indirect basis set effects. For apolar dyes, these combined basis set effects on excitation energies are very similar to purely direct basis set effects (right panel, Figure 13). Excitation energies always decrease when using larger basis sets, and they particularly do so for post-HF methods (error: -0.07 eV). Nevertheless, basis set errors are significantly smaller than those found when using the same geometry (-0.11 eV). Except for post-HF methods, the basis set errors of apolar molecules for all other methods do not fall below -0.02 eV, i.e., their absolute values are very small.

Compared with apolar dyes, positive deviations result for dyes of intermediate and high polarity as well as for the overall average. This indicates that the decrease of excitation energies due to the less contracted ground-state geometries overcompensates their increase induced by the smaller basis sets. The effect is especially pronounced for polar dyes where no systematic increase of the deviations from post-HF methods to pure functionals is observed. Nevertheless, average basis set errors stay within a range of -0.02 eV to 0.02 eV. This corresponds to a four-fold reduction of the basis set errors found when using the same geometries (right panel, Figure 13) and underlines the significant error compensation between direct and indirect basis set effects. Therefore, SCS-CC2/cc-pVDZ ground-state geometries are used whenever a number of excited states are calculated since the cost of calculating multiple excitation energies constrains the basis set size of the excited-state calculations to cc-pVDZ (see above). Then, errors arising from the limited basis set sizes in both calculations, i.e., direct and indirect basis set errors, partially cancel. As soon as only the lowest valence excitations are required, larger basis sets like cc-pVTZ become affordable also for the excited-state calculations. Ground-state

---

[nnn] Geometries are optimized with SCS-CC2 and not with SCS-MP2 because later-on, similar calculations will be performed for optimized excited-state geometries. Hence CC2-based methods have to be used.

geometries at the SCS-MP2/cc-pVTZ level are used in these cases. In view of the above discussed literature findings, resulting *method*/cc-pVTZ//SCS-MP2/cc-pVTZ excitation energies can assumed to be essentially converged in terms of basis set size (Figure 11, red panels).

The different underlying geometries are also used in the benchmark MS-CASPT2 calculations, and their effects are used to estimate the above introduced "uncertainty interval". The uncertainty interval, i.e., the basis set error of the MS-CASPT2/cc-pVDZ reference excitation energies, is estimated from a comparison of MS-CASPT2/cc-pVDZ//SCS-CC2/cc-pVDZ and MS-CASPT2/cc-pVTZ//SCS-MP2/cc-pVTZ excitation energies (Table 3). The maximal deviation in Table 3 amounts to 0.20 eV. Therefore, an uncertainty interval of ±0.20 eV will be used in the following whenever MS-CASPT2/cc-pVDZ excitation energies are used as the reference values.

Before turning to a description of the MS-CASPT2 calculations, one further phenomenon related to basis set effects is briefly addressed. Apart from the mere basis set size, i.e., the ζ-value, its composition, namely the inclusion of diffuse functions, may be influential. Although low-lying valence excitations are usually not diffuse[754], the necessity of augmented basis sets is analyzed for anthracene and the aldehyde-substituted triarylamine (Table 4). It should be mentioned that the first excitation energy (1EE) of the aldehyde-substituted triarylamine corresponds to a bright intramolecular charge-transfer excitation. The L_a excitation of anthracene corresponds in this case to the first excitation energy (1EE). It features local charge-transfer character as well (see below).

Table 4: Influence of augmented basis sets on excitation energies for two different compounds.

Molecule	Method	Basis set	1EE [eV]	2EE [eV]	3EE[eV]
anthracene	SCS-CC2	cc-pVDZ	3.91	3.81	5.38
		aug-cc-pVDZ	3.77	3.75	5.36
		difference	**0.14**	**0.06**	**0.02**
	ωB97X-D	cc-pVDZ	2.72	4.13	4.24
		aug-cc-pVDZ	2.67	4.09	4.26
		difference	**0.05**	**0.04**	**0.02**
aldehyde-substituted triarylamine	SCS-CC2	cc-pVDZ	3.72	3.92	4.13
		aug-cc-pVDZ	3.53	3.90	4.10
		difference	**0.19**	**0.02**	**0.03**
	ωB97X-D	cc-pVDZ	3.71	3.63	4.28
		aug-cc-pVDZ	3.60	3.69	4.11
		difference	**0.11**	**0.04**	**0.17**

It becomes evident from the results in Table 4 that augmented basis functions do not significantly influence excitation energies other than charge-transfer excitations, i.e., the first excitation energies (1EE) of both compounds. It should be kept in mind that Rydberg excitations are disregarded. The impact of diffuse functions on charge-transfer excitations is larger because these states with partially separated charges benefit more from the augmented basis than does the ground state. However, such diffuse charge-transfer states normally do neither exist in solution[755] nor in thin films where solvation effects much alike to those in liquids occur due to the comparably amorphous and dense molecular packing.[756] Instead of that, solvation effects considerably stabilize soluted charge-transfer states and lead to rather contracted electron densities because they enable the formation of tight solvation shells.[340] The pronounced basis set effects of the charge-transfer excitations (Table 4) can thus be considered as a gas-phase artifact. Therefore, the results in Table 4 permit to conclude that diffuse functions are not necessary for a proper description of the lowest excited valence states of the molecular organic semiconductors, which agrees well with other literature findings.[757,754]

Having dicussed this last aspect of basis set effects of excited-state calculations, the derivation of the MS-CASPT2 values is described in the next part of this section (green and purple boxes, Figure 11).

Theoretical best estimates for reference excitation energies from MS-CASPT2/cc-pVDZ and MS-CASPT2/cc-pVTZ calculations

As the accuracy of electronically excited states obtained at the MS-CASPT2 level of theory is well established,[744] MS-CASPT2[91,92] is ideally suited as a benchmark method for excitation energies. Yet, its applicability is limited by its high computational cost, and the molecules comprised in the benchmark set (Figure 5) are too large to be directly used in CASPT2 calculations, especially due to their bulky substituents. One could be tempted to assume that these bulky substituents (like the butyl side chains in the squaraine and in MD353; highlighted in grey in Figure 5) do not significantly influence excitation energies anyway. This brings up the questions (1) how much the excitation energies of the molecules with (black in Figure 5) and without substituents (grey in Figure 5) actually differ and (2) whether it is possible to use the MS-CASPT2 excitation energies of the abridged symmetric systems, for which the calculations would be computationally feasible, as reference values for the complete molecules. Indeed, test calculations indicated that excitation energies of the molecules with and without substituents are related by only small substituent shifts (Table 5, Table 6). Furthermore, the substituent-induced shifts were shown to be rather method-insensitive, i.e., all methods predict equal shifts for the excitation energies when substituents are added/subtracted (Table 5, Table 6). This implies that it should in fact be possible to employ MS-CASPT2 excitation energies obtained for the molecules without substituents as reference values for excitations of their completely substituted counterparts after adding an approximately method-independent substituent shift. However, an

additional problem arises because the subsitutent shifts depend on the type of excitation, i.e., whether the latter is neutral or of charge-transfer character. Hence the following approach is chosen[702]:

1. MS-CASPT2 calculations are performed on the π-conjugated cores of the molecules without substituents. These smaller systems devoid of non-conjugated substituents are highlighted in black in Figure 5. The substituents that are cut off are colored in grey.[ooo]

2. In order to estimate the influence of the substituents on the CASPT2 energies (method-independent!), the influence of the substituents is computed with various other methods (see below for a detailed discussion) that are computationally less demanding so that excited-state calculations on molecules both with and without substituents are possible. Resulting substituent shifts are averaged although they are almost constant (Table 5, Table 6).

3. The averaged substituent corrections are subtracted from the MS-CASPT2 reference values.

Table 5: Substituent shifts of the first three excited states in all molecules at the cc-pVDZ level of theory. The electron-withdrawing group in the aldehyde-substituted triphenylamine was replaced by a nitrile to be able to exploit symmetry. Thus, the charge-transfer excitation in this compound changes character. In the case of the squaraine, the S3 excitation mixes with a higher-lying excited state in the squaraine. Therefore, the corresponding CC2 shift was additionally computed (0.48 eV).

Molecule	Method	S_1 [eV]	S_2 [eV]	S_3 [eV]
rubrene	SCS-CC2	0.28	0.14	0.45
	CAM-B3LYP	0.23	0.14	0.29
	LC-ωPBE	0.26	0.14	0.25
	ωB97X-D	0.23	0.14	0.26
	average	0.25	0.15	0.35
squaraine	SCS-CC2	0.21	-0.04	0.40
	CAM-B3LYP	0.15	-0.02	
	LC-ωPBE	0.14	-0.02	
	ωB97X-D	0.15	-0.03	
	average	0.20	0.00	0.40
diketopyrrolopyrrole	SCS-CC2	0.12	0.38	0.17
	CAM-B3LYP	0.07	0.44	0.09
	LC-ωPBE	0.06	0.49	0.22
	ωB97X-D	0.06	0.50	0.09
	average	0.10	0.45	0.15

[ooo] All compounds without substituents were optimized both at the SCS-CC2/cc-pVDZ and at the SCS-MP2/cc-pVTZ levels of theory for subsequent excited-state calculations, similar to their substituted counterparts.

triarylamine	SCS-CC2	0.46	0.14	0.46
	CAM-B3LYP	0.39	0.13	0.39
	LC-ωPBE	0.43	0.14	0.43
	ωB97X-D	0.39	0.13	0.39
	average	0.40	0.10	0.40
aldehyde-substituted triarylamine	SCS-CC2	0.45		0.05
	CAM-B3LYP	0.49		0.06
	LC-ωPBE	0.43		0.06
	ωB97X-D	0.46		0.05
	average	0.45		0.05
HB194	SCS-CC2	0.11	0.13	0.00
	CAM-B3LYP	0.08	0.09	-0.01
	LC-ωPBE	0.09	0.10	-0.01
	ωB97X-D	0.06	0.05	0.01
	average	0.10	0.10	0.00
MD353	SCS-CC2	0.17	0.08	0.12
	CAM-B3LYP	0.11	-0.01	0.15
	LC-ωPBE	0.14	0.02	0.12
	ωB97X-D	0.12	0.00	0.16
	average	0.15	0.00	0.15
HB238	SCS-CC2	0.24	0.19	0.10
	CAM-B3LYP	0.14	0.11	-0.02
	LC-ωPBE	0.16	0.12	0.09
	ωB97X-D	0.14	0.11	0.01
	average	0.20	0.10	0.05
methoxy-substituted triarylamine	SCS-CC2	0.04	0.00	0.02
	CAM-B3LYP	0.02	0.02	-0.01
	LC-ωPBE	0.01	0.03	0.00
	ωB97X-D	0.02	0.02	0.00
	average	0.00	0.00	0.00

Table 6: Substituent shifts for the first singlet and triplet excited state in all molecules at the cc-pVTZ level of theory.

Molecule	Method	S_1	T_1
rubrene	SCS-CC2	-0.27	-0.15
	ADC(2)	-0.30	-0.15
	M06-2X	-0.23	-0.20
	SOGGA11X	-0.36	-0.19
	ωB97X-D	-0.36	-0.20
	average	-0.35	-0.20
squaraine	SCS-CC2	-0.22	-0.04
	ADC(2)	-0.27	-0.07
	M06-2X	-0.18	-0.04
	SOGGA11X	-0.17	-0.04
	ωB97X-D	-0.15	-0.03
	average	-0.25	-0.05
diketopyrrolopyrrole	SCS-CC2	-0.15	-0.09
	ADC(2)	-0.19	-0.11
	M06-2X	-0.10	-0.09
	SOGGA11X	-0.08	-0.08
	ωB97X-D	-0.09	-0.08
	average	-0.15	-0.10
triarylamine	SCS-CC2	-0.15	-0.34
	ADC(2)	-0.19	-0.37
	M06-2X	-0.24	-0.41
	SOGGA11X	-0.26	-0.41
	ωB97X-D	-0.19	-0.46
	average	-0.25	-0.40
aldehyde-substituted triarylamine	SCS-CC2	-0.47	-0.53
	ADC(2)	-0.52	-0.54
	M06-2X	-0.51	-0.58
	SOGGA11X	-0.57	-0.59
	ωB97X-D	-0.47	
	average	-0.55	-0.65

HB194	SCS-CC2	-0.11	-0.05
	ADC(2)	-0.13	-0.07
	M06-2X	-0.08	-0.03
	SOGGA11X	-0.08	-0.19
	ωB97X-D	-0.08	-0.04
	average	-0.10	-0.05
MD353	SCS-CC2	-0.16	-0.03
	ADC(2)	-0.19	-0.06
	M06-2X	-0.10	-0.03
	SOGGA11X	-0.09	-0.02
	ωB97X-D	-0.11	-0.02
	average	-0.20	-0.05
methoxy-sub. triarylamine	SCS-CC2	-0.06	-0.01
	ADC(2)	-0.06	-0.02
	M06-2X	-0.04	-0.01
	SOGGA11X	-0.04	-0.01
	ωB97X-D	-0.03	0.00
	average	-0.05	0.00

The procedure to perform CASPT2 calculations on smaller subsystems and correct for substituents afterwards is verified for the three lowest excited states of rubrene/tetracene. The system is chosen because due to the high symmetry of rubrene and its still manageable size, MS-CASPT2 calculations can be conducted on both rubrene and the underlying tetracene core. Furthermore, rubrene should be a very sensitive test system because its phenyl substituents, in contrast to non-conjugating alkyl chains, are partly involved in the excitations. Figure 14 shows the results. Vertical [14,14]-MS-CASPT2 excitation energies of rubrene amount to 2.7 eV (1^1A_u), 3.3 eV (1^1B_u), and 3.8 eV (1^1A_g), with slightly higher values for corresponding excitations in tetracene (3.0 eV, 3.4 eV, 4.1 eV). Computed substituent effects for the first excited state (1^1A_u) are 0.28 eV (SCS-CC2), 0.23 eV (CAM-B3LYP), 0.23 eV (ωB97X-D), and 0.26 eV (LC-ωPBE). Clearly, all predicted shifts are almost equal. Averaging them yields a shift of 0.25 eV for the first excited state (1^1A_u), compared to a difference of 0.3 eV between the CASPT2 excitation energies for rubrene and tetracene. For the second (1^1B_u) and third excited state (1^1A_g), the "direct" MS-CASPT2 excitation energies calculated on rubrene and the "indirect" excitation energies from MS-CASPT2 calculations on tetracene with subsequent substituent corrections differ by less than 0.05 eV. Thus the overall approach is rather accurate although the absolute substituent shifts are

different (0.15 eV for the second excited state and 0.35 for the third excited state). Therefore, excitation energies obtained from this composite MS-CASPT2-and-substituent-correction approach should be sufficiently reliable to be used as reference values in subsequent benchmark calculations.
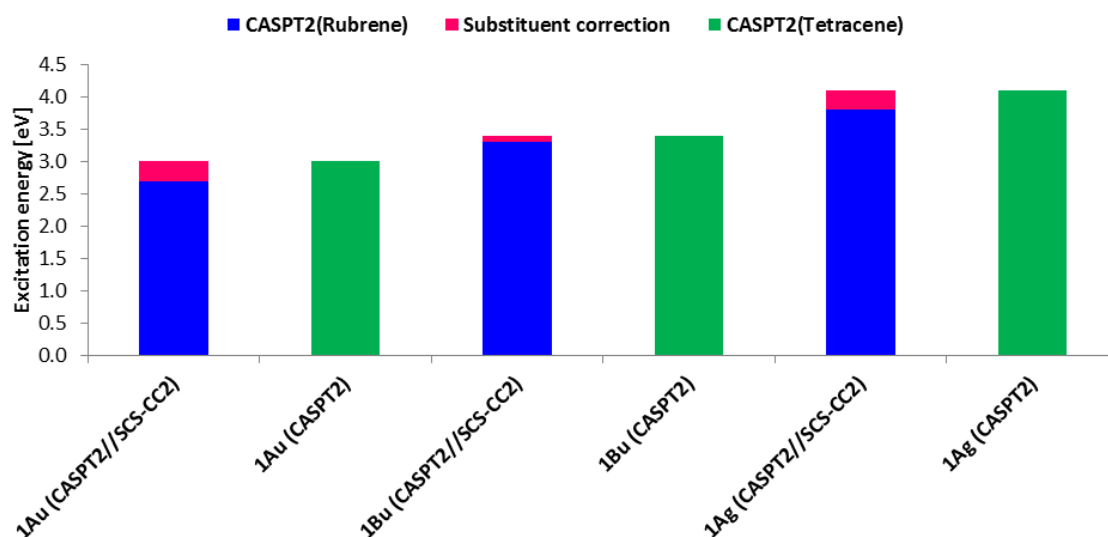

Figure 14: Evaluation of the approach which consists in conducting MS-CASPT2 calculations on smaller systems without substituents and successively including substituent effects obtained with other methods. CASPT2 results on tetracene are given in green. Blue values indicate CASPT2 results for rubrene. Pink bars correspond to the substituent corrections added to the rubrene values for a comparison with the tetracene excitation energies. Adapted with permission from [702]. © 2015 American Chemical Society.

MS-CASPT2 reference values (Table 3) were calculated with this procedure for all molecules. More details and CASPT2 triplet reference values can be found in [702] and [758]. The methods employed to calculate substituent effects are shown in Table 7. They differ depending on whether several excited states (left-hand side) or only the first excited singlet and triplet state (right-hand side) of the molecules are computed. Substituent shifts are given Table 5 in for the calculation of several excited states of all molecules.

Table 7: Methods employed to assess substituent effects on excitation energies. The cc-pVDZ basis sets are used if several (singlet) excited states are computed. If only the lowest (singlet and triplet) valence excitations are calculated, the cc-pVTZ basis sets are employed in line with the above discussion.

Calculation of S_1 to S_5		Calculation of S_1 and T_1	
Method	Reference	Method	Reference
SCS-CC2	256,180	SCS-CC2	256,180
CAM-B3LYP-D3	133,707,712,713,708,709,140	ADC(2)	240,759, 180,760,761,762,703
ωB97X-D	143	ωB97X-D	143
LC-ωPBE-D3	156,155,161,140	SOGGA11X	714
		M06-2X-D3	125,140

Different methods are used due to two reasons.

On the one hand, while the first excited state S_1 always corresponds to a bright neutral excitation in molecules employed in OPV, this is not the case for the first few excitations S_1 through S_5. At least one charge-transfer or charge-transfer like excitation is among the lowest three excited states for all molecules except for the dithiophene. Long-range corrected functionals are needed to properly describe charge-transfer excitations,[159] but they necessarily raise valence excitation energies.[165,763] Eriksson et al. showed that this can be troublesome for low-lying excitations, i.e., excitations above 600 nm.[764] These findings suggest that long-range corrected functionals deliver more accurate excitation energies for sure only if charge-transfer states are involved. Otherwise, (meta) hybrid functionals can also be very accurate.[765]

On the other hand, as pointed out by Jacquemin et al.,[766] the accuracy of DFT functionals for triplet excited states depends on the exact nature of the functional. Due to well-known triplet instabilities,[273] especially functionals with large HF amounts like long-range corrected functionals fail for triplet excitations.[767]

With regard to these two reasons, only long-range corrected functionals are used to assess substituent effects of excitation energies including charge-transfer states. CAM-B3LYP, LC-ωPBE, and ωB97X-D are utilized. Two hybrid functionals, the hybrid SOGGA11X and the meta hybrid M06-2X, and only one long-range corrected functional, ωB97X-D, which performed very well for low-lying valence states according to Eriksson,[764] are employed to estimate substituent effects on the S_1 and the T_1 (Table 7). SCS-CC2 substituent effects are additionally computed.

All MS-CASPT2 calculations were conducted using the Molcas program package.[768,769,770] Pyramidalized substituents were planarized to take advantage of symmetry. In all calculations, the IPEA[94] shift option (default value: 0.25) and multistate averaging were employed. At least one more state than subsequently used was included in the multistate averaging. In the case of intruder states in the perturbative treatment of the CASSCF wave function, a level shift of 0.2 was applied.[771] Except for anthracene and the dithiophene, all molecular π-systems are too large to include all π-electrons in the CASSCF computations. Hence series of MS-CASPT2 calculations were performed for all molecules where the sizes of the active spaces were stepwise enlarged from [4,4] to [14,14] ([16,16] for molecules with D_{2h} symmetry). All active spaces were symmetric. It was checked whether asymmetric spaces are required, but converged values in symmetric active spaces were obtained even for charge-transfer excitations from in-plane π-orbitals.

In order to check whether MS-CASPT2 excitation energies are sufficiently converged in a [14,14] active space, the changes in excitation energies upon increasing the active space from [12,12] to [14,14] are

analyzed. Table 8 displays the three lowest excitation energies for all compounds obtained at the MS-CASPT2/cc-pVDZ level in a [12,12]- and in a [14,14]-active space. The small changes in excitation energies upon increasing the active spaces for the molecules demonstrate that all excitation energy values are sufficiently converged in a [14,14] active space. As an additional criterion for the convergence of the CASSCF calculations, resulting excitation energies were compared to SCS-CC2 results.

Table 8: Dependency of MS-CASPT2/cc-pVDZ excitation energies on the size of the active space.

Molecule	State	[12,12]/cc-pVDZ	[14,14]/cc-pVDZ
anthracene	$1B_{2u}$	3.69	3.77
	$1B_{3u}$	3.53	3.61
	$1B_{1g}$	4.79	4.93
rubrene	$1A_u$	2.83	2.67
	$1B_u$	3.44	3.42
	$1A_g$	3.83	3.84
dithiophene	$1A_u$	3.69	3.98
	$2A_u$	4.60	4.61
	$3A_u$	5.35	5.38
DIP	$1B_{3u}$	2.59	2.55*
	$1B_{1g}$	2.95	2.97*
	$1B_{2u}$	3.22	3.30
squaraine	$1B_{3u}$	2.48	2.59
	$1B_{3g}$	2.24	2.27
	$1A_g$	3.64	3.64
diketopyrrolopyrrole	$1B_u$	2.53	2.55
	$1A_g$	3.17	3.11
	$2A_g$	3.69	3.75
triarylamine	1A	4.35	4.29
	1E	4.48	4.52
„triamine-methoxy"	1A	3.15	3.20
	2A	3.83	3.80
	1B	4.01	3.91
„triamine-aldehyde"	1A	4.13	4.07
	1B	4.31	4.37**

HB194	$1A_g$	2.86	2.93
	$1A_u$	3.43	3.44
	$2A_g$	3.51	3.56**
MD353	$1A_g$	3.12**	3.22
	$2A_g$	4.56**	4.42
	$1A_u$	4.35**	4.43
HB238	$1A_g$	2.92	2.78
	$2A_g$	3.66	3.85
	$1A_u$	4.44	4.45

*calculated in a [16,16] active space

**calculated in a [10,10] active space

It should be emphasized that the values in Table 8 refer to MS-CASPT2 reference values obtained with cc-pVDZ basis sets and geometries optimized at the SCS-CC2/cc-pVDZ level of theory. Nevertheless, [14,14]-MS-CASPT2/cc-pVTZ//SCS-MP2/cc-pVTZ values were found to be converged as well (Table 9).

Table 9: Dependency of MS-CASPT2/cc-pVTZ excitation energies on the size of the active space. For simplicity, the first singlet and triplet excited states are abbreviated by S_1 and T_1, disregarding symmetry.

Molecule	State	[12,12]/cc-pVTZ	[14,14]/cc-pVTZ
anthracene	S_1	3.73	3.63
	T_1	2.42	2.25
rubrene	S_1	3.02	2.96
	T_1	1.75	1.67
tetracene	S_1	3.02	2.96
	T_1	1.75	1.67
pentacene	S_1	2.39	2.41
	T_1	1.46	1.35
dithiophene	S_1	4.12	3.09
	T_1	4.10	3.06
DIP	S_1	2.72	2.71
	T_1	1.66	1.66
squaraine	S_1	2.60##	2.65
	T_1	1.54##	1.62
diketopyrrolopyrrole	S_1	2.48	2.34
	T_1	1.55	1.31
triarylamine	S_1	4.23	4.07

	T_1	3.81	3.66
„triamine-methoxy"	S_1	3.14[#]	3.14[#]
	T_1	2.36[#]	2.34[#] (2.30)
„triamine-aldehyde"	S_1	4.15[#]	4.13[#] (4.14)
	T_1	3.47[#]	3.40[#] (3.46)
HB194	S_1	2.84	2.90
	T_1	2.10	2.12[**]
MD353	S_1	3.09	3.10
	T_1	2.32	2.35

\# calculated with cc-pVDZ
() uppermost converged value with cc-pVTZ
** calculated in a [10,10]-active space
\#\# calculated in a [16,16]-active space

In the last two sections, the technical details, particularly basis set effects and the determination of reference excitation energies for the benchmark, were addressed in detail. It was found that basis set errors from the geometry optimization and the excited-state calculation, i.e., direct and indirect basis set effects, mutually cancel. MS-CASPT2 reference values are calculated for smaller subsystems without substituents. The substituent influence is accounted for by subsequently adding a "substituent shift" that is obtained as an average from a number of quantum-chemical calculations.

With this information at hand, benchmark calculations are presented in the following. In a first step, several singlet excitations per molecule are calculated and benchmarked. As outlined above, this is done using cc-pVDZ basis sets for geometry optimizations and excited-state calculations.

5.3.2   Benchmark of several singlet excitation energies per molecule

Singlet excitation energies obtained with wave-function based methods, DFT functionals, and semiempiric methods are benchmarked. All methods as well as their references are listed in Table 10.

Table 10: Methods employed in the benchmark of excitation energies.

method	References
wave-function based methods	
(SCS-)ADC(2)	240,759,180,760,761,762,703,46
SCS-CC2	256,180,760,761,762,703,46
(SCS-/SOS-)CIS(D)	173, 180,760,761,762,703,46
HF	706
CIS	760
density functional based approaches	

BLYP-D3	707,708,709,140
M06L(-D3)	710,140
APFD	711
B3LYP-D3	707,712,713,708,709,140
SOGGA11X	714
ωB97X-D	143
LC–ωPBE	156,155,161,140
CAM-B3LYP-D3	133,707,712,713,708,709,140
LC-BLYP-D3	707,708,709,140,132
LC-M06-L-D3	710,140 ,132
semiempiric methods	
orthogonalization model 1 (OM1)	193,197
orthogonalization model 2 (OM2)	197,195
orthogonalization model 3 (OM3)	196
Austin Model 1 (AM1)	189
Parameterization Model 3 (PM3)	717,190
ZINDO (Zerner's neglect of intermediate differential overlap)	209,210,772

The semiempiric methods comprised in the benchmark set can be divided into two groups, which has important implications for results of later-on excited-state calculations. AM1, PM3, and ZINDO correspond to different parameterizations of the MNDO (modified neglect of diatomic overlap) model. In contrast, the OMx methods aim to improve especially one underlying assumption of the MNDO model, i.e., they correct for the non-orthogonality of the atomic orbital basis, which is assumed to be orthogonal in MNDO.[773,774] In addition to the different underlying approximations, the employed formalism to calculate semiempiric excitation energies differs as well. Excitation energies with ZINDO are calculated in a CIS formalism, while GUGA-CI[775] calculations are employed in the following for the OMx methods as well as for AM1 and PM3. In these multiconfigurational calculations, all triple excitations in a [16,16] active space were included (indicated with "OMx-T" in Figure 15, Figure 17 and Figure 18).

All wave-function based calculations were conducted with the Turbomole program package.[179] All DFT and ZINDO calculations were performed with Gaussian[718] while MNDO[183] was used for all other semiempiric calculations.
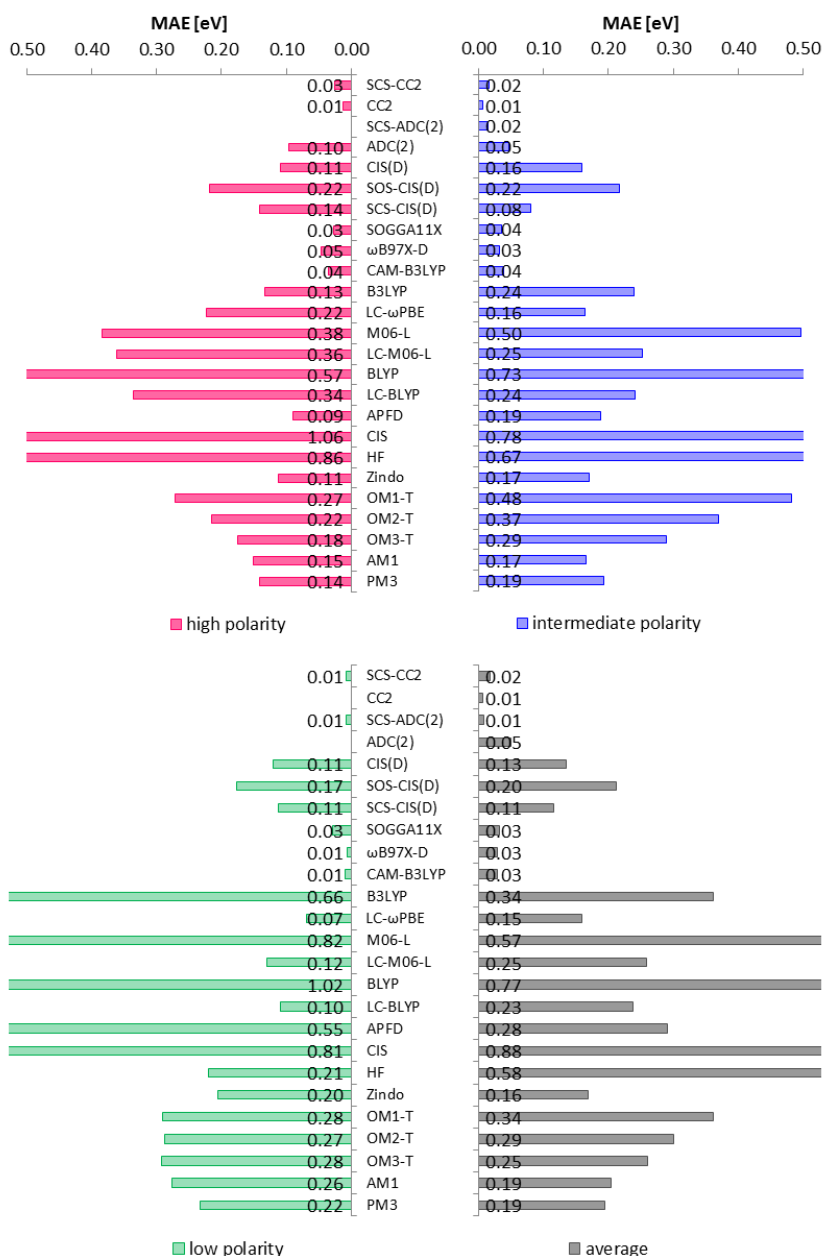
Figure 15: MAE (mean absolute error) values for the three lowest excitation energies of the molecules. Both bright and dark excitations are included. "OMx-T" indicates that all excitations up to triple excitations were included in the active space of the OMx GUGA-CI calculations. Adapted with permission from [702]. © 2015 American Chemical Society.

Mean average errors (MAE) were calculated for the three lowest excitation energies of all molecules (Figure 15). Please note that the excited-state order strongly depends on the method. Therefore, the three lowest excitation energies vary with the employed method. Hence, the three lowest excitation energies used to deduce the benchmark results were defined by the lowest excitation energies of the CASPT2 reference. As cc-pVDZ basis sets had to be used to keep the calculation of numerous excited states affordable, the above introduced uncertainty interval was included in the MAE calculation. In this way, calculated MAE values correspond to deviations from this interval. Apart from accounting for

the inaccuracy of the reference method, the benchmark against an uncertainty interval is also justified by the user's point of view that correct trends and a good qualitative agreement of excitation energies are more significant than quantitatively correct values. When using the uncertainty interval instead of the exact reference values, methods with a constant but rather small offset from the reference values would still perform very well. For instance, the errors of two methods that differ by 0.4 eV from each other and by 0.2 eV from the reference method would both be zero.

The performance of DFT approaches is discussed first (Figure 15). Excitation energies of SOGGA11X, CAM-B3LYP, and ωB97X-D agree very well with the reference values for all compound classes. Their MAE values never exceed 0.05 eV. This is a very small error, but combined with the uncertainty interval of ±0.20 eV, the total error amounts to 0.20 eV to 0.30 eV, which is in accordance with commonly cited errors of TD-DFT excitation energies (~ 0.20-0.50 eV).[751] The very good performance of CAM-B3LYP and ωB97X-D has already been outlined by Jacquemin and Adamo et al. who compared capabilities of hybrid and long-range corrected hybrid functionals for excitation energies of organic compounds in a recent benchmark.[763] The accuracy of SOGGA11X excitation energies coincides with findings of Truhlar et al.[714] Although SOGGA11X is not a long-range corrected functional as opposed to CAM-B3LYP and ωB97X-D, its good performance can be readily explained in terms of its considerable amount of exact exchange. With 41% of HF exchange, the SOGGA11X HF amount is very similar the one of CAM-B3LYP that varies between 19% and 65%.

In contrast to the polarity-independent performance of SOGGA11X, ωB97X-D, and CAM-B3LYP, the performance of Hirao's long-range correction with pure functionals, i.e., LC-BLYP and LC-M06-L, as well as the performance of LC-ωPBE strongly vary with molecular polarity. Very good results are obtained for apolar dyes. MAE values only amount to roughly 0.10 eV, and compared to the large errors of the underlying pure functionals, i.e., of BLYP (0.66 eV) and M06-L (0.82 eV), a significant improvement is found. This does not hold for polar dyes, however. With an error of 0.38 eV for M06-L and of 0.36 eV for LC-M06-L, the long-range correction does not ameliorate excitation energies anymore. The effects for BLYP/LC-BLYP are less pronounced, but qualitatively similar (BLYP: 0.57 eV; LC-BLYP: 0.34 eV). While pure functionals still underestimate excitation energies of polar dyes considerably (similar to apolar dyes), long-range corrected functionals with significant amounts of exact exchange overestimate them (in contrast to apolar dyes). Reference values are just midway. Also Jacquemin and Truhlar discussed for the related cyanine dyes that already hybrid functionals (instead of long-range corrected functionals) provide very accurate excitation energies.[776] This problem will be discussed in more detail below for valence excitations only. The improvements due to the long-range correction for the dyes of intermediate polarity are noticeable, but resulting excitation energies are already overestimated (similar to polar dyes): the errors of 0.25 eV for LC-M06-L and 0.24 eV for LC-BLYP are considerably

reduced with respect to the errors of the underlying pure functionals with 0.50 eV for M06-L and 0.73 eV for BLYP, but remain significant. In general, by means of the long-range correction, it can be seen that method performances systematically vary as a function of molecular polarity. This illustrates that the above discussed molecular groups are meaningful also for a computational analysis of molecular properties, i.e., it underlines the equivalence of the polarity and the chromophore classification.

In view of the fact that it is an old semiempiric method, ZINDO performs surprisingly well. The error for excitation energies of polar dyes amounts to only 0.11 eV. The good performance for polar dyes in particular is in line with earlier findings that hyperpolarizabilities of donor-acceptor dyes computed with ZINDO agree nicely with corresponding experimental values.[777,778] The overall average error of ZINDO is with 0.16 eV also very small, i.e., it is almost equal to the error of LC-ωPBE, a sophisticated functional especially optimized for excited states.[129] For the purpose of identifying methods applicable in a multiscale approach, the very favorable cost-accuracy ratio of ZINDO should be emphasized; it makes the method suitable for studying excitations in large molecules and molecular aggregates using geometries obtained with other methods. Please note that ZINDO also predicts the correct excited-state order, in contrast to PM3 and AM1, which – despite tolerable overall errors of 0.19 eV – do not provide an accurate description of the lowermost excitation energies of the molecules.

In this context, it should be pointed out that the picture of the low-lying molecular valence excitations delivered by the OMx methods is considerably more reliable than its counterpart obtained with AM1 and PM3 although the numerical OMx errors are somewhat larger. The OMx excited-state order of the lowest excitations mostly coincides with the order predicted by MS-CASPT2, whereas totally different states appear among the lowest excitations of AM1 and PM3. Both approaches significantly underestimate energies of doubly excited states and do not capture the interplay of neutral and charge-transfer valence excitations correctly. The underestimation of excited states with predominantly doubly-excited character in semiempiric excited-state GUGA-CI calculations was also outlined in more detail by Thiel and coworker. They analyzed performances of semiempiric methods for the ^1A_g states of linear polyenes,[175] the archetypal example where double excitations are important.[231] Thiel and coworker found significantly underestimated doubly-excited state energies for all semiempiric methods but INDO/S, which relies on CIS instead of GUGA-CI.[175] The CIS treatment, which precludes doubly excited states, is also used for the herein presented ZINDO calculations and is certainly partially responsible for the very good performance of ZINDO in contrast to other semiempiric methods. Moreover, albeit also relying on a GUGA-CI treatment, the OMx-based methods underestimate doubly-excited states less strongly than AM1 or PM3, an observation that might result from the nonorthogonality correction, i.e., from the specific inclusion of the Pauli repulsion in the OMx methods giving rise to an antisymmetric splitting of bonding and antibonding levels.[175]

To further illustrate this aspect, Figure 16 shows where the three lowest excited states of the merocyanine HB194 and the aldehyde-substituted triphenylamine as defined by MS-CASPT2 and SCS-CC2 are situated in a semiempiric treatment. It becomes evident that the excited-state order is correctly reproduced by OM2, albeit with overestimated excitation energies. In contrast, AM1 performs especially poor for charge-transfer excitations, which are significantly overestimated, and positions several double excitations in between the neutral and the charge-transfer singly excited states. Please note, however, that the first excitation energy is rather accurately predicted by all semiempiric methods. This is well in line with the investigation of Thiel and coworker. For instance, they found an average error of 0.40 eV for excitation energies computed with the OMx methods and a slight improvement from OM1 over OM2 to OM3.[175] Taking into account the uncertainty interval of ±0.20 eV, this error quantitatively agrees with the results of roughly 0.25 eV presented in Figure 15.
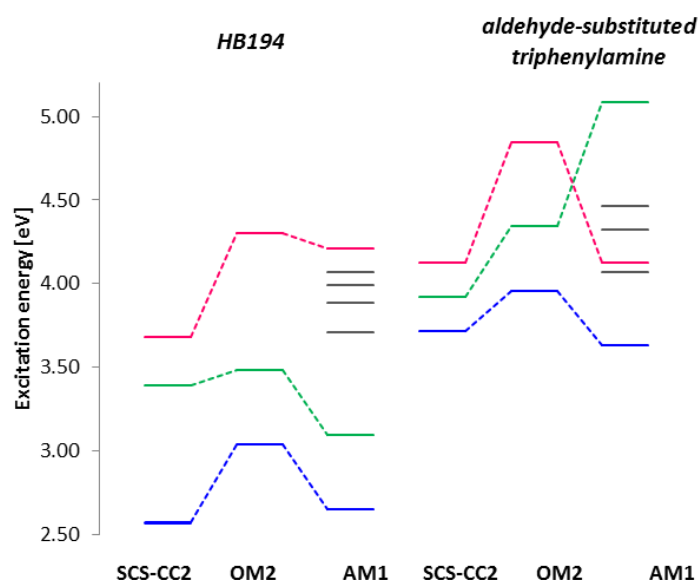

Figure 16: Correlation of the three lowest excitations (defined by the SCS-CC2 and MS-CASPT2 calculations) for two different semiempiric approaches. Please note that the third excited state of HB194 corresponds to a charge-transfer excitation, while the second excited state of the aldehyde-substituted triphenylamine is of charge-transfer character. The first excited state of the triphenylamine corresponds to a bright intramolecular charge-transfer like excitation that changed its character upon adding diffuse functions (see above). Adapted with permission from [702]. © 2015 American Chemical Society.

Figure 17 and Figure 18 show the MAE values for the bright neutral and dark excited-state energies of the molecules, respectively. Most but not all dark excitations correspond to charge-transfer excitations. This results because no clear charge-transfer excitations like n-π*-excitations exist for the dye molecules of low polarity. Therefore, for the apolar dyes, bright valence states with *ungerade*-symmetry are instead distinguished from the dark third excited state of A_g symmetry, existing at least in DIP, anthracene, and rubrene. No low-lying dark excitations exist in the dithiophene, which is therefore precluded from the analysis in Figure 18. The assignment of the charge-transfer character to

the excited states of the dyes of intermediate and high polarity is straightforward because the charge-transfer excitations present, i.e., n-π*-excitations, can easily be identified.

Bright neutral excitations are discussed first (Figure 17). As could be expected in view of the theoretically challenging description of charge-transfer states,[266,231] MAE errors decrease noticeably compared to the overall errors (Figure 15) as soon as only neutral excitations are included in the averaging. This effect is most pronounced for polar dyes since all wave-function based methods and numerous DFT functionals including several hybrids approach the reference values up to an energy difference smaller than the uncertainty interval. Among the DFT functionals, the long-range corrected functionals show the largest deviations, a point already addressed by Jacquemin et al.[763] and discussed in detail by Autschbach and coworkers[779] in the framework of charge-transfer and charge-transfer-like excitations. It was mentioned above that the charge-transfer correction introduced by the splitting of the Coulomb operator comes at the expense of systematically increasing all valence excitation energies. This can sometimes result in overestimated excitation energies, which is here obviously the case. In contrast, as outlined by Truhlar and Jacquemin and coworkers for cyanines, (meta) hybrid functionals are perfectly sufficient to describe bright valence excitations.[776] In a similar way a recent study by Zhang and coworkers benchmarked excitation energies of acridine derivatives by means of experimental values. In line with the data in Figure 17 and with Truhlar and Jacquemin, they also found that the hybrid functionals PBE0 and B3LYP perform better than M06-2X and notably CAM-B3LYP and ωB97X-D, which overestimated excitation energies.[780]

Evidently, the performance of hybrid functionals and range-separated hybrid functionals differs significantly between polar molecules and dyes of intermediate polarity (Figure 17). While hybrid functionals provide the most accurate excitation energies for the merocyanines, range-separated hybrids are considerably more precise for excitation energies of dyes of intermediate polarity. This can be understood in terms of the different charge-transfer character of the respective low-lying valence excitations. Despite the donor-acceptor structure, the valence π-π*-excitations in merocyanines are only of moderate charge-transfer character because the involved π- and π*-orbitals are completely delocalized and significantly overlap.[781] In contrast, the orbitals involved in the valence excitations of dyes of intermediate polarity barely overlap because they are localized on different spatially separate moieties. Therefore, all valence excitations in the dyes of intermediate polarity, particularly in triphenylamines, have a significant charge-transfer character. Hence the wrong asymptotic behavior of the exchange-correlation potential of hybrid functionals and the related spurious self-interaction error become an issue.[159] As a consequence, range-separated hybrids perform better.[782,144] This is in good accordance with numerous investigations on excitation energies of triphenylamine-based dyes that were found to be accurately predicted by long-range corrected functionals. Triphenylamine-based

dyes have recently attracted considerable research interest due to their use as photosensitizers in dye-sensitized solar cells (DSSC).[783,784,785]
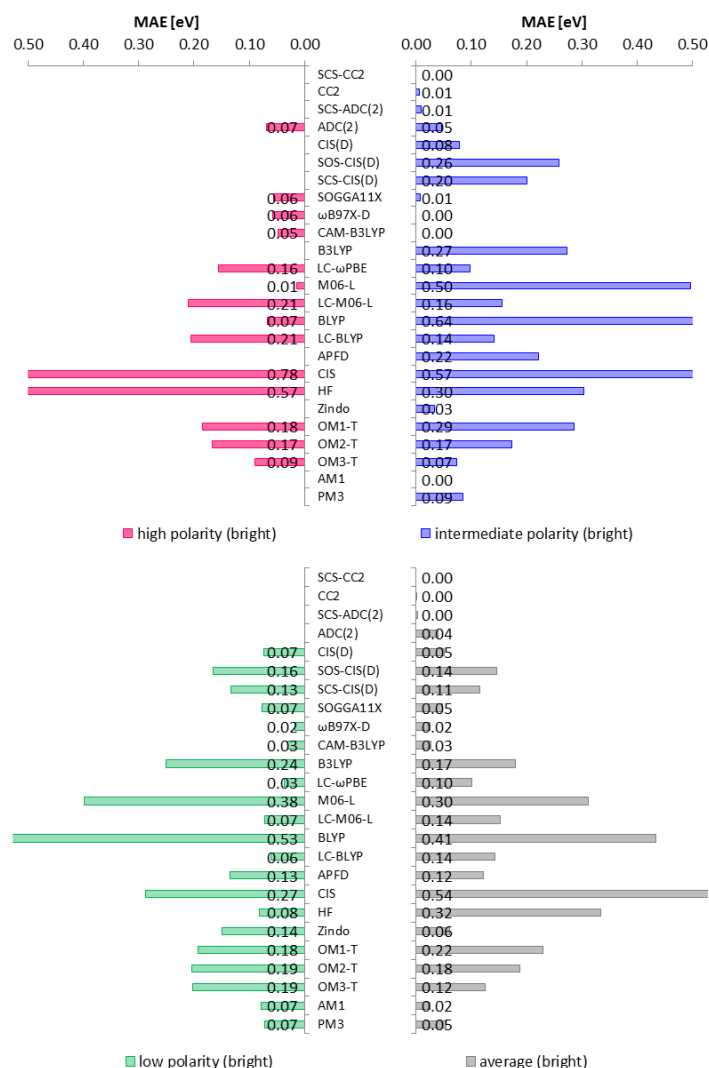

Figure 17: MAE (mean absolute error) values for the neutral excitations among three lowest excitation energies of the molecules. "OMx-T" indicates that all excitations up to triple excitations were included in the active space of the OMx GUGA-CI calculations. Adapted with permission from [702]. © 2015 American Chemical Society.

The errors of bright valence excitations are largest for apolar dyes (Figure 17). In view of the ongoing discussion[172] on the L_a and the L_b excitation in acenes and derivatives (i.e., anthracene, rubrene), this is not surprising. According to an analysis of excitation energies in acenes by Grimme and coworker[701], which he subsequently extended to polycyclic aromatic hydrocarbons in general,[786] the nature of the L_a and the L_b excitations differs. While the L_b excitation is a purely neutral transition, its L_a counterpart corresponds rather to a charge-transfer like excitation because local charge-transfer configurations were shown to possess a considerable weight in the VB description of the L_a excited state.[701] Due to the different charge-transfer character of the two excitations, no *single* existing functional provides accurate values for *both* excitations since the many-electron self-interaction error (MSIE) differs for

196

the two transitions. Thus different amounts of exact exchange would in principle be required to correct for it. It follows that some functionals comprised in the benchmark set provide accurate energies for either the L_a or the L_b excitation but never for both. For instance, LC-BLYP and LC-ωPBE perform very well for L_a excitation energies. For this reason, however, they are necessarily worse for the L_b excitation. The reverse is observed for hybrid functionals like B3LYP, which deliver reliable L_b transition energies but underestimate L_a excitations. This implies that with all functionals, considerable errors are obtained for at least one low-lying bright excitation of apolar dyes, explaining the large errors (Figure 17).

For all compounds, semiempirical methods yield bright excitation energies with rather satisfying accuracy but similar effects as found for the DFT functionals can be observed (Figure 17): errors of ZINDO, AM1 and PM3 in particular are negligible for dyes of high polarity and increase with decreasing polarity. In contrast, errors of the OMx methods are more uniformly distributed over the different molecular classes. In fact, OMx excitation energies are systematically overestimated. Therefore, it is certainly possible to deduce qualitatively correct trends from OMx calculations in a multiscale approach. The rather constant error of OMx based approaches is furthermore in line with findings of Thiel and coworker.[175]

Errors of charge-transfer and dark excitations are discussed next (Figure 18). Expectedly, average errors are larger. Except for the high-level *ab initio* methods (SCS-)CC2 and (SCS-)ADC(2), the long-range corrected functionals ωB97X-D (MAE: 0.05 eV) and CAM-B3LYP (0.06 eV) as well as the hybrid functional SOGGA11X (0.05 eV) perform best for all molecules. Surprisingly, B3LYP (0.08 eV) and APFD (0.07 eV) perform well for the charge-transfer excitations in dyes of intermediate polarity, i.e., for the squaraine and the diketopyrrolopyrrole, although they are not long-range corrected and do not contain a significant amount of exact exchange. Their surprisingly good performance highlights again the importance of the correct excited-state order for the overall accuracy of the results (see also Figure 16). In contrast to all other molecules comprised in the benchmark set (Figure 5), the charge-transfer excitation and the lowermost bright excitation in the squaraine and the diketopyrrolopyrrole are energetically very close-lying. Their relative order depends on the method, and it largely determines resulting excitation energies. If the charge-transfer state is lowest, the valence excitation experiences a blue shift, whereas it drops considerably when it lies below the charge-transfer state. In contrast to other methods (LC-M06-L, M06-L, LC-BLYP, BLYP, etc.), APFD and B3LYP reproduce the MS-CASPT2 excited-state order which positions the charge-transfer excitation above the bright excitation, in line with the experimental data.[653,654] The significance of the relative excited-state order has often been pointed out, and its importance has been thoroughly studied by both experimental and theoretical means for example for host materials of OLEDs.[787,788,789]

In comparison with the bright excitations (Figure 17), errors of semiempiric methods for charge-transfer states are generally larger (Figure 18). However, their errors (0.30 eV – 0.40 eV) are on the order of the errors of functionals with too much exact exchange such as LC-BLYP (0.33 eV) or LC-M06-L (0.36 eV). Pure functionals like BLYP (MAE: 0.89 eV) and M06-L (0.57 eV) yield larger errors. As discussed by Nelson and coworkers,[567] semiempiric methods like ZINDO show a correct asymptotic behavior for the Coulomb interaction between the electron and the hole in charge-transfer excitations, an aspect not included in pure DFT functionals. Therefore, according to Nelson,[567] semiempiric approaches should provide a more adequate description of charge-transfer excitations than pure DFT functionals in spite of their intrinsic neglect of overlap-dependent contributions. This agrees nicely with the findings in Figure 18.
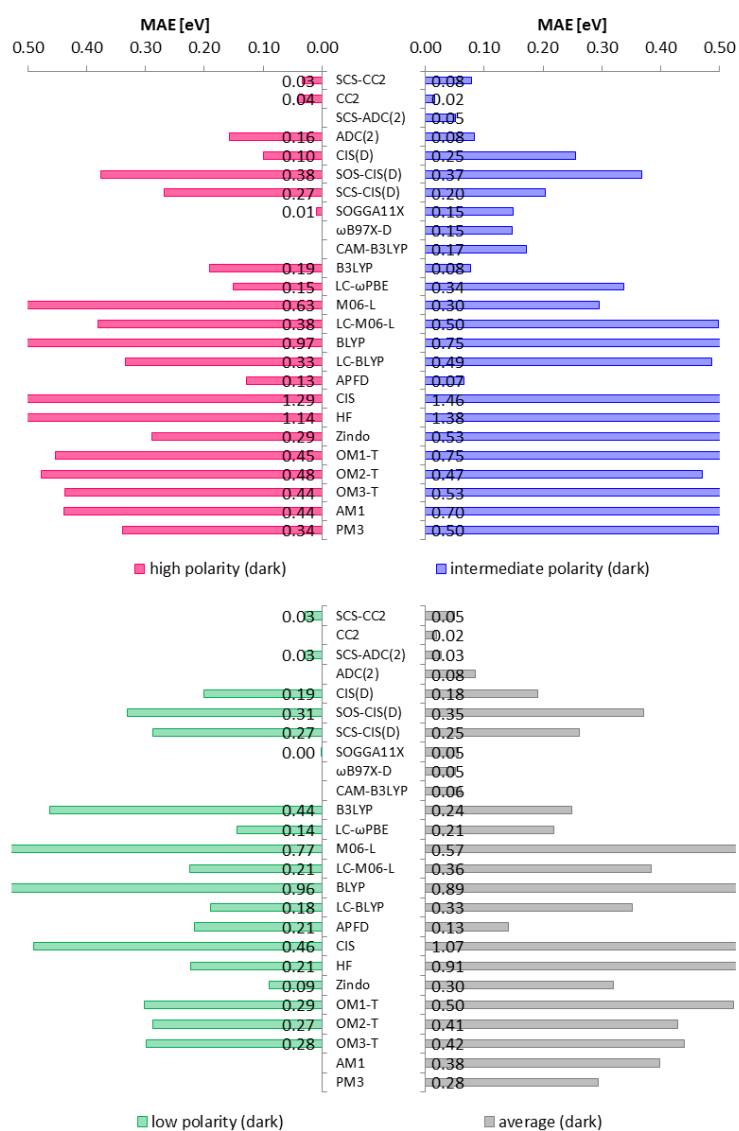

Figure 18: MAE (mean absolute error) values for the charge-transfer excitations among three lowest excitation energies of the molecules. "OMx-T" indicates that all excitations up to triple excitations were included in the active space of the OMx GUGA-CI calculations. Adapted with permission from [702]. © 2015 American Chemical Society.

Overall, Figure 15, Figure 17, and Figure 18 demonstrate that results from wave-function based approaches (CC2 and ADC(2)) agree very well with the MS-CASPT2 reference values. Their errors vary slightly as a function of the compound class, but never exceed 0.10 eV with respect to the uncertainty interval. For bright excitations, CIS(D) performs almost as well as CC2 and ADC(2), but its deviations are larger for charge-transfer excitations, especially in dyes of intermediate and low polarity. As can already be seen from the errors in Figure 15, Figure 17, and Figure 18, spin-component scaling produces pronounced changes in predicted excitation energies. While spin-component scaling is well-established for CC2, it has not been thoroughly evaluated for ADC(2). To analyze the influence of spin-component scaling in more detail, Figure 19 displays the improvement of the first excitation energies of all compound classes when SCS is added to CC2, ADC(2), and CIS(D). In order to visualize performance differences between the methods, the uncertainty interval is not included in this case. Errors are calculated with respect to the MS-CASPT2 reference values. With regard to the above-discussed reduced accuracy of MS-CASPT2/cc-pVDZ reference values, only the first excitation energy is used to analyze SCS effects since it is presumably most converged and least diffuse. Irrespective of the compound class, spin-component scaling induces a blue shift of excitation energies of approximately 0.15 eV (Figure 19). It depends on the underlying method and the compound class whether this blue shift increases or decreases the error. While spin-component scaling reduces the errors of CC2 excitation energies of compounds of high and intermediate polarity, excitation energies of apolar dyes are better reproduced without spin-component scaling. This is based on the fact that CC2 excitation energies of dyes of high and intermediate polarity are usually too low, while they coincide well with the CASPT2 reference values for apolar molecules. ADC(2) behaves exactly like CC2. This improved description of excitation energies upon spin-component scaling is well in line with results of Hättig and coworkers for CC2,[180] but contrasts with a recent benchmark of Jacquemin and coworkers[790] who found that the numerical accuracy of CC2 excitation energies is superior to the one of SCS-CC2. Furthermore, the findings of the effects of SCS on ADC(2) complement an analysis of SOS-ADC(2) by Dreuw and Wormit who concluded that SOS, similar to the outlined influence of SCS, leads to improved excitation energies.[239]
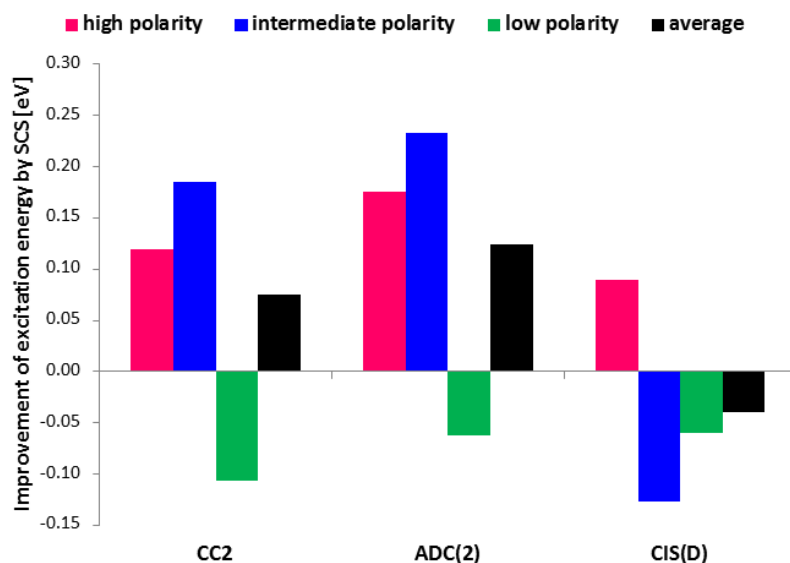
Figure 19: The differences of the errors of the different methods with respect to the CASPT2 results are calculated, i.e., error(CC2)-error(SCS-CC2). When spin-component scaling improves resulting excitation energies, the differences are positive. Adapted with permission from [702]. © 2015 American Chemical Society.

Compared with CC2 and ADC(2), Figure 19 provides evidence that CIS(D) behaves differently. The perturbative doubles in CIS(D) decrease underlying CIS excitation energies considerably due to the inclusion of dynamic correlation.[172] Yet, CIS(D) excitation energies are still too high. To some extent, this might result from the incomplete treatment of higher excitations in CIS(D) in contrast to CIS(D∞). Nevertheless, because of the already overestimated CIS(D) excitation energies, CIS(D) errors necessarily increase when additional blue shifts induced by spin-component scaling or spin-opposite scaling are introduced. Polar dyes are the only exception where spin-component scaling improves CIS(D) excitation energies. This may arise from the fact that correlation effects were shown to be especially important in cyanine dyes and derivatives, which is also reflected in the pronounced influence of spin-component scaling on cyanine ground-state properties (see above).[791] Grimme and coworker benchmarked CIS(D) and SCS-CIS(D) as well and found improved excitation energies.[174] This contrasts with the findings for the majority of the dyes in Figure 19. However, it is important to mention that the SCS and SOS parameters used throughout this work were optimized by Hättig and coworkers for CC2.[180] This possibly explains the differences found when compared to other benchmark calculations like the one of Grimme and coworker.[174] It should be noted that other SCS and SOS parameterizations specifically optimized for ADC(2) or CIS(D) are available such as the SOS parameters by Dreuw and coworkers for ADC(2).[792] In view of different parameterizations, Grimme and coworkers provided an overview over the influence of the spin-component parameters on resulting excitation energies, which was found to be nonetheless rather modest.[43]

The presented results on the lowest excited states in different molecular p-type semiconductors suggest that a plethora of methods deliver excitation energies with reasonable accuracy. Among the most efficient methods, an important aspect for later-on calculations on large systems, particularly ZINDO stands out. The most balanced description of all excitation energies and of all compound classes is provided by ωB97X-D, followed by CAM-B3LYP and SOGGA11X. Wave-function based approaches certainly yield results of remarkable numerical accuracy, albeit at the expense of a high computational effort rendering them unsuitable for large-scale applications.

The next part of this section gives a more detailed perspective on the lowermost valence excitations in p-type molecular semiconductors with a special focus on states with different multiplicities. The low valence excitations of these molecules are of special interest because they determine absorption properties of resulting OSC devices. As only one excitation energy is required, larger cc-pVTZ basis sets are used and the uncertainty interval can be discarded (see above).

5.3.3 Benchmark of the S_1 and the T_1 energies of the molecular p-type semiconductors

As outlined in detail by Clarke and Durrant, the light-to-energy conversion in OSCs is an energetic downhill process.[423] All states that are very low in energy, including triplet states,[435] constitute possible energy loss channels in OSC devices. Already this aspect emphasizes the importance of precisely knowing the lowest singlet and triplet excitation energies of any system employed in OSCs. Moreover, the growing interest in triplet excitations of organic semiconductors arises also from the possibility to potentially double IQE (internal quantum efficiency) values in singlet fission devices, which similarly requires the precise alignment of singlet and triplet excited states.[533,793] Therefore, singlet and triplet excited states are benchmarked in the following with a degree of accuracy that is computationally not affordable for several excited states (see previous sections). For further details, the reader is referred to [758].
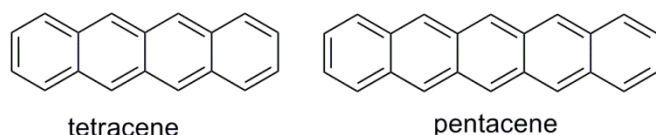

Figure 20: Structures of common singlet fission compounds tetracene (left-hand side) and pentacene (right-hand side).

Singlet fission is known to occur on very fast timescales and can compete with intramolecular relaxation.[794,795,796] Recent pump-probe-dump investigations by Musser et al. revealed that singlet fission is an ultrafast process, much alike internal conversion.[537] Therefore, adiabatic and vertical singlet and triplet excitation energies have to be taken into account. In the following, they are separately evaluated.

Moreover, as particularly pentacene and also tetracene are the most common systems to study the energetics and dynamics of singlet fission by experimental and computational means, they are included in this part of the benchmark and the thesis (Figure 20).[533,797,536,798,799] HB238 is not further analyzed because its optoelectronic behavior was found to be highly similar to MD353.

The functionals employed in the benchmark calculations for the lowest singlet and triplet excitations are listed in Table 11. For the following reasons, they slightly differ from above (Table 10). In a benchmark on TD-DFT singlet and triplet excitation energies, Jacquemin and coworkers found considerable performance differences between singlet and triplet excitation energies calculated with the same functional. They furthermore pointed out that especially the accuracy of predicted triplet states strongly depends on the exact form of the exchange-correlation kernel.[747] This suggests enlarging the scope of functionals employed in the benchmark compared to above (Table 10) in order to obtain a more comprehensive survey of singlet and triplet performances. Especially M06-2X and PBE0 are frequently used for triplet calculations in the literature so that these functionals are

additionally used.[723] Moreover, due to the observed very good performance of ωB97X-D in its standard version, an IP-tuned version of ωB97X-D individually adjusted for all molecules in a non-empirical tuning procedure is additionally included, denoted as ωB97X-D*. In the non-empirical tuning procedure, the range-separation parameter was varied in steps of 0.05 Bohr^{-1} until the ionization potential met the HOMO energy. Optimal values can be found in [758]. LC-M06-L is not employed anymore because the use of range-separated hybrids with large amounts of HF exchange, as ensured by Hirao's LC correction, was shown to be advantageous for singlet excitation energies (see also above),[129,160] but seems to be less promising for accurate triplet excitation energies as demonstrated by Brédas et al.[800]

Table 11: Methods employed to benchmark singlet and triplet excitation energies as well as singlet-triplet gaps of molecular p-type semiconductors. Their references are given as well.

method	References
wave-function based methods	
(SCS-)ADC(2)	240,759,180,760,761,762,703,46
SCS-CC2	256,180,760,761,762,703,46
(SCS-/SOS-)CIS(D)	173, 180,760,761,762,703,46
HF	706
CIS	760
density functional based approaches	
BLYP-D3	707,708,709,140
M06L(-D3)	710,140
PBE-D3	801,802,140
PBE0-D3	803,801,802,140
B3LYP-D3	707,712,713,708,709,140
BHLYP-D3	712, 140
M06-2X-D3	125,140
SOGGA11X	714
ωB97X-D	143
LC-ωPBE	156,155,161,140
CAM-B3LYP-D3	133,707,712,713,708,709,140
LC-BLYP-D3	707,708,709,140,132

In contrast to the previous section where only the adiabatic linear-response TD-DFT formalism was considered, several different TD-DFT formulations (i.e., Tamm-Dancoff, Δ-SCF) are employed in the following. This results mainly from the well-known triplet instabilities of TD-DFT calculations, leading to imaginary frequencies for triplet excitations.[170,167] Casida et al. concluded from calculations on a two-level model system that these instabilities and resulting imaginary TD-DFT frequencies originate from symmetry-breaking of the DFT ground state. A linearized[273] and thus Hermitian version of the TD-DFT Casida equations,[804] the Tamm-Dancoff approximation (TDA) in the TD-DFT framework proposed by Head-Gordon et al.,[272] constitutes a possible solution to the instability problem.[805] As the B-matrix of the original Casida equations is neglected, this comes with the additional advantage of reduced computation times.[272] Please note that the Tamm-Dancoff approximation of TD-DFT is abbreviated by TDA in the following, while "TD-DFT" will always still refer to the adiabatic linear-response TD-DFT formulation. Tozer et al. thoroughly demonstrated the usefulness of the TDA scheme for the calculation of triplet excitation energies.[806] They correlated the existence of triplet instabilities and negative triplet excitation energies with the amount of exact exchange of the DFT functionals[807] and with the charge-transfer character of the excitation[767]. This led them to the conclusion that the TDA scheme is especially important for neutral (in contrast to charge-transfer) triplet excitations, yielding very accurate results when used with range-separated hybrids. Apart from the TDA and the adiabatic linear-response scheme, the applicability of the Δ-SCF method for calculating triplet energies was also discussed by Casida et al.[273] Δ-SCF triplet excitation energies are computed as the excitation energy differences between the respective ground states. This approach yields values of acceptable accuracy for organic molecules according to Nguyen et al.[808] In view of this literature perspective, triplet excitation energies are in the following not only calculated in a "traditional" adiabatic linear-response TD-DFT approach, but also within the TDA approximation and as Δ-SCF excitation energies.

The same wave-function based methods are used as in Table 10. Semiempiric methods are not comprised in the benchmark (Table 11). Their rather weak performance for triplet excited states has been already pointed out.[175,213]

To avoid redundancies with the above given results for several excitations per molecule and to focus more on important trends, mean signed instead of mean absolute errors are used to evaluate singlet and triplet excitation energies. In a first step, singlet and triplet excitation energies are discussed for DFT and HF. Wave-function methods will be subsequently addressed. Results for the first singlet excitation energy are compared to the average values presented in the previous section.
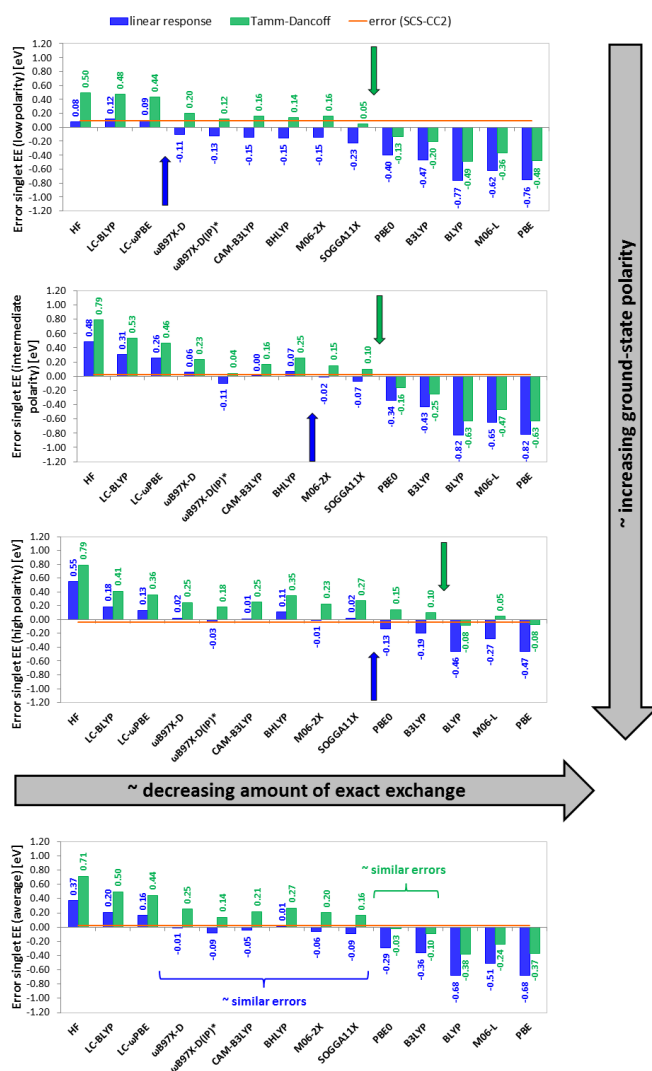
Figure 21: Mean signed errors for singlet excitation energies obtained with DFT functionals or HF employing the cc-pVTZ basis sets. Green (blue) arrows indicate the HF percentage that is optimal in the TDA (linear-response TD-DFT) approach. Reproduced with permission from [758]. © 2016 Elsevier B.V.

The mean signed errors with respect to MS-CASPT2/cc-pVTZ for the singlet excitation energies obtained with DFT functionals and HF and the cc-pVTZ basis are shown in Figure 21. Errors for each group of molecules (panel 1 – 3, Figure 21) and average errors (panel 4, Figure 21) are given. The error of SCS-CC2 indicated as an orange line allows for a comparison with the accuracy of wave-function based approaches. The functionals are roughly arranged according to their amount of HF exchange (x-axis). Evidently, excitation energies systematically decline upon reducing the amount of exact exchange in a functional. This dependency forms the basis for the IP-tuning procedure used to obtain more accurate fundamental and excitation gaps in organic compounds.[160] As already analyzed for different TD-DFT formulations by Truhlar et al.[809] and by Tozer et al.,[767] TDA singlet excitation energies are systematically blueshifted compared to standard adiabatic linear-response TD-DFT excitation energies. This systematic increase of TDA excitation energies gives rise to the observation that for a given molecule, optimal TDA excitation energies are obtained with functionals containing less exact

exchange than optimal adiabatic TD-DFT excitation energies. This is visualized by the green arrows (optimal TDA excitation energies) and the blue arrows (optimal adiabatic TD-DFT excitation energies) in Figure 21. The green arrows (optimal TDA excitation energies) always correspond to functionals containing a reduced amount of exact exchange.

A comparison between the three molecular groups shows a characteristic dependence of the optimal amount of exchange on the group, which coincides well with above discussed different performances of long-range corrected functionals for the individual compound classes. A comparably high amount of exact exchange is required for correct excitation energies of apolar molecules like the acenes, rubrene and DIP. Minimal signed errors in the adiabatic TD-DFT/HF formulation are found for HF (0.08 eV), LC-ωPBE (0.09 eV), and ωB97X-D (-0.12 eV) while SOGGA11X yields very accurate excitation energies with an error of only 0.05 eV in the TDA formulation. As already mentioned above, this observation of high HF amounts required for the ^1L_a states of linear acenes and other polycyclic hydrocarbons has been comprehensively studied by Grimme et al.[701,786] and also by Grimme and Ziegler et al. in the context of constricted variational DFT.[277] Valence-bond arguments highlighted the significant contributions of local charge-transfer configurations to the ^1L_a excited states of linear acenes (see previous section). This explains the necessity for considerable amounts of HF exchange.[701] In line with this, Wu et al. found a considerable improvement of ^1L_a excitation energies calculated with hybrid functionals employed in the TDA formulation instead of the adiabatic linear-response TD-DFT framework (see above).[810] These results specific for the charge-transfer like L_a excitation complement nicely above discussed average results for the combined errors of the L_a and the L_b excitations.

Compared with the apolar molecules, LC-BLYP and LC-ωPBE considerably overshoot for singlet excitation energies of triphenylamines and donor-acceptor-donor compounds. Their errors are around 0.50 eV. This performance deterioration is well in line with above findings (Figure 15) and contrasts with the improved performance of ωB97X-D, its IP-tuned version ωB97X-D*, CAM-B3LYP, M06-2X, and SOGGA11X that provide reliable values with errors smaller than ~0.10 eV in both the TDA and the linear-response TD-DFT scheme. The average MAE values (Figure 15) did not reveal this small, yet important trend of the errors of the long-range corrected functionals, also because slight error differences are masked by the above employed uncertainty interval. As pointed out by Autschbach et al., the amount of HF exchange required for accurate excitation energies correlates with the excited-state delocalization. The less HF exchange needed for reliable values, the more delocalized is the excited state.[782] Thus excited states of the compounds of intermediate polarity are presumably more delocalized than those of acenes. These more delocalized structures result in reduced self-interaction errors, requiring less correction via exact exchange. The effect becomes even more pronounced for

the group of merocyanines, i.e., donor-acceptor push-pull systems, as also found above.[ppp] While most DFT functionals yield too small excitation energies for apolar molecules, they tend to overestimate excitation energies of the merocyanines, especially in the TDA approach. The considerable overestimation of excitation energies in cyanines by TD-DFT is a well-known problem[727] and was attributed to a wrong description of the differential correlation between the ground and the first excited state.[782] As discussed by Autschbach et al., less overestimated excitation energies are to be expected as soon as some charge-transfer character is introduced into the first excited state of cyanine dyes. Then, an error cancelation between the underestimation of excitation energies due to the partial charge transfer and the overestimation typical for cyanines can take place, affording accurate excitation energies,[791] which is the case for the merocyanines where a number of range-separated and hybrid functionals (ωB97X-D, ωB97X-D*, CAM-B3LYP, SOGGA11X, M06-2X) yield very accurate excitation energies (Figure 21). This more detailed picture on well-performing methods for the first excitation energy in merocyanines is again in accordance with the above presented average results. Hence it refines the result from Figure 15 and Figure 17. Nevertheless, it also validates the underlying benchmark approach, which relies on considerable approximations with regard to basis set effects.

Since the amount of optimal HF exchange to be included in the DFT functionals depends on the compound class, averaging the signed errors over all compound classes yields a range of functionals with different amounts of HF exchange but with similar errors (panel 4, Figure 21).This explains why, in line with the previously presented absolute errors, very small signed errors of the first transition energy are found for ωB97X-D (-0.01 eV), CAM-B3LYP (-0.05 eV), BHLYP (0.01 eV) and M06-2X (-0.06 eV). Please note that IP-tuning of ωB97X-D does not result in an improvement for the excitation energies (TD-DFT error of ωB97X-D: -0.01 eV; TD-DFT error of ωB97X-D*: -0.09 eV), a phenomenon which is sometimes observed. Since the MSIE is minimal in the non-empirically tuned ωB97X-D* functional, one should, however, expect higher accuracies for ωB97X-D* excitation energies. As thoroughly discussed by Autschbach,[779] the fact that further optimizing the ωB97X-D functional via IP-tuning does not result in a better performance suggests that the original high accuracy of ωB97X-D is not necessarily based on a correct description of the physics of the system, for instance on a small MSIE. If this was the case, one would otherwise obtain even more accurate values after non-empirical IP-tuning. Thus the good performance of ωB97X-D arises rather from some kind of error compensation, i.e., ωB97X-D is "right for the wrong reason". The point that excitation energies with long-range corrected functionals are not always obtained "for the right reason" and hence that IP-tuning does not

---

[ppp] It should be noted that the different extent of excited-state delocalization is intimately related to the already addressed different charge-transfer character of the bright excitations in dyes of high and intermediate polarity: the more charge transfer between rather localized orbitals (such as lone pairs, etc.) on spatially separate moieties occurs, the more localized the corresponding excited state.

always lead to more accurate values has been already addressed by Autschbach et al. in terms of charge-transfer and charge-transfer like excitations.[779]
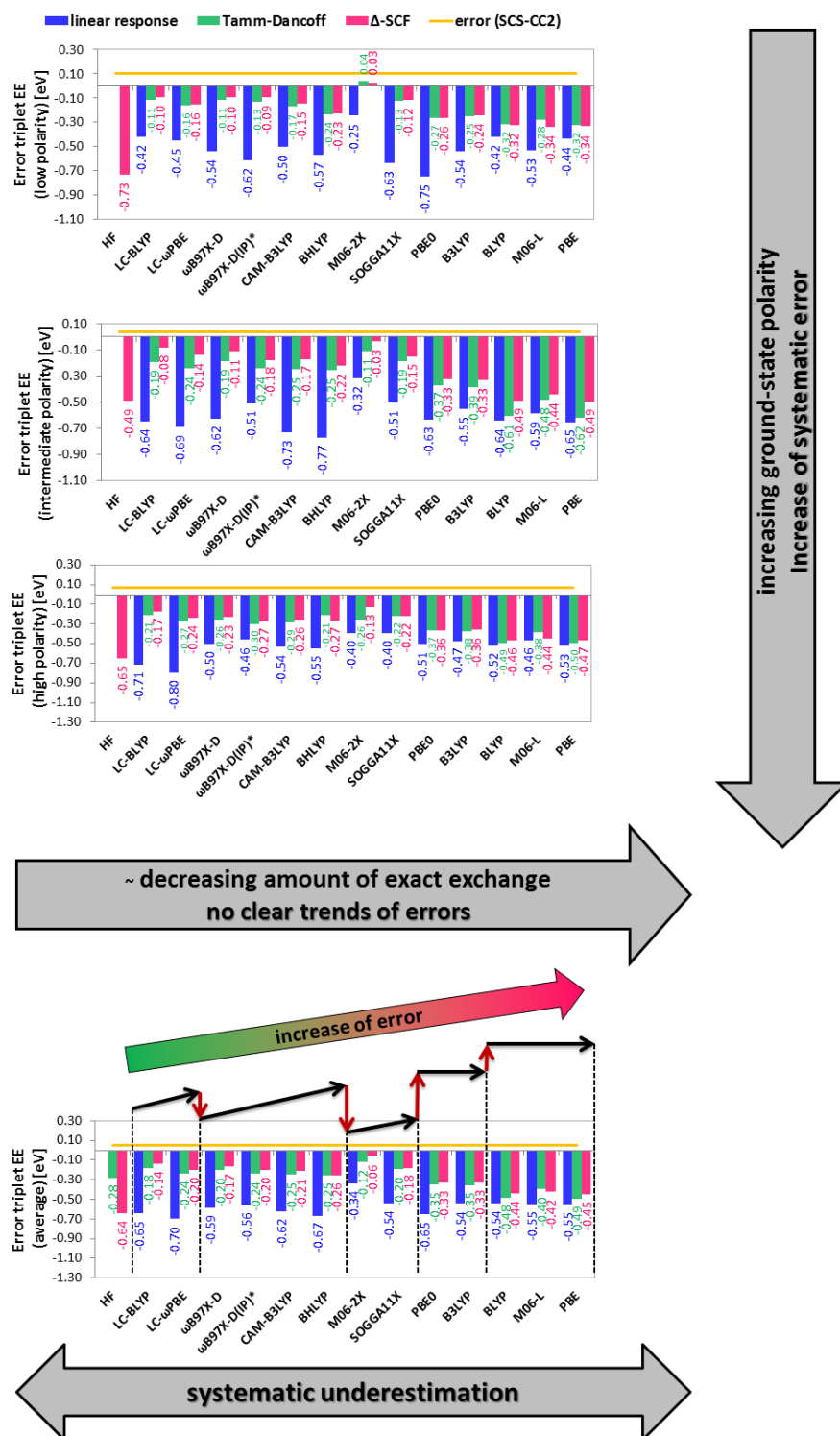

Figure 22: Mean signed errors for triplet excitation energies obtained with DFT functionals and HF employing the cc-pVTZ basis sets (cc-pVDZ basis sets for Tamm-Dancoff, which was shown to be sufficient). Reproduced with permission from [758]. © 2016 Elsevier B.V.

With regard to the performance of hybrid functionals, PBE0 has a very small average error of -0.03 eV in the TDA formulation (Figure 21). This is in part due to a cancellation of positive and negative deviations; the mean absolute error amounts to 0.22 eV. The very good average performance of the meta-hybrid functional M06-2X, the good averaged performance of the hybrid functional PBE0, and the fact that M06-L is the best pure functional are in accordance with findings of Gordon et al.[811]

The elucidated trends, most notably the dependence of the excitation energies on the amount of HF exchange, underline why mean signed errors of the first singlet excitation energies provide a more profound understanding than averaged mean absolute errors (Figure 17). However, it should be stressed that such mean signed deviations are only meaningful as long as only one excitation per molecule is included. Otherwise, signed errors of different excitations per molecule average and obscure any trends.

In a similar way, mean signed errors for triplet excitation energies are given in Figure 22. To avoid unbalanced average results, triplet instabilities were calculated for all compounds. Excitation energies of systems subject to triplet instabilities were discarded from the analysis. In accordance with the investigation of Tozer et al.,[806] negative triplet excitation energies due to triplet instabilities are especially found for HF and (range-separated) hybrids with significant amounts of HF exchange. Moreover, triplet instabilities and corresponding negative excitation energies were particularly frequent for apolar, highly symmetric molecules (pentacene, tetracene, etc). Consequently, HF, LC-BLYP and LC-ωPBE triplet excitation energies of these molecules had to be subsequently excluded. Therefore, the largest errors for TD-DFT triplet excitation energies of apolar molecules are not obtained for these methods, i.e., for HF, LC-BLYP and LC-ωPBE as it is the case for the dyes of intermediate and high polarity.

In general, pure functionals provide the most accurate triplet excitation energies for all molecules within the traditional adiabatic linear-response TD-DFT formalism whereas the best performing functional is M06-2X (blue bars, Figure 22). Although it contains 54% of HF exchange, it underestimates triplet excitation energies by an average value of only -0.34 eV. This contrasts with the performance of BHLYP that possesses a comparable amount of HF exchange, but an almost two-fold error of -0.67 eV. This agrees nicely with benchmark results of Jacquemin et al.[747] and underlines the above-stated point that the existence of triplet instabilities and correspondingly underestimated excitation energies critically depends on the exact nature of the functional, namely on the details of its exchange-correlation part, and not only on the amount of exact exchange.

With regard to all DFT formulations (adiabatic TD-DFT, TDA, Δ-SCF), the smallest errors are also obtained with M06-2X, yet not in the TD-DFT framework. Employing the functional within the TDA

formulation yields an average error of -0.12 eV, which further declines to -0.06 eV in the Δ-SCF method (Figure 22). Similar to the results for all other functionals, differences between the TDA scheme and the Δ-SCF method are rather small. In general, Δ-SCF triplet excitation energies are usually slightly higher, resulting in smaller mean signed errors as long as the spin contamination is low. As discussed by Van Voorhis et al. in the context of triplet states in TADF (thermally activated delayed fluorescence) compounds, the different performance of the Δ-SCF method and the TDA approximation could be due to differences in the orbitals. While Δ-SCF-orbitals are specifically optimized for triplet states, ground-state orbitals are the basis of the TDA framework.[812] The more specifically optimized Δ-SCF-orbitals could thus be responsible for the somewhat higher accuracy of the Δ-SCF method. Nevertheless, in systems with significant spin contamination, the performance of the Δ-SCF method deteriorates, and TDA triplet excitation energies are more reliable.

It follows from the calculations that the same methods that provide the most accurate singlet excitation energies also deliver reliable triplet excitation energies within the TDA/Δ-SCF method. Only the lowest triplet excited state was considered. Please keep in mind that in accordance with Jacquemin et al.,[766] this is not true for the adiabatic TD-DFT excitations. The smallest mean signed errors within the TDA/Δ-SCF method are obtained with LC-BLYP (-0.18 eV/-0.14 eV), ωB97X-D (-0.20 eV/-0.17 eV), CAM-B3LYP (-0.25 eV/-0.21 eV), M06-2X (-0.12 eV/-0.06 eV), and SOGGA11X (-0.20 eV/-0.18 eV). Despite these similarities, three major differences between the errors of singlet and triplet excitation energies exist:

1. Calculated triplet excitation energies are systematically too low.
2. There seems to be no clear dependence of triplet excitation energies on the amount of HF exchange.
3. While signed errors for singlet excitation energies are increasingly positive for molecules of increasing ground-state polarity, the opposite is true for triplet excitation energies. The more polar the ground state, i.e., the more delocalized the involved states (see above discussion), the more underestimated triplet excitation energies and the more negative corresponding signed errors. The underestimation of triplet excitation energies of cyanines was thoroughly discussed by Autschbach et al.[791] With regard to the herein discussed merocyanines, it was found that calculated singlet excitations are rather accurate, probably due to an error cancelation between the intrinsic overestimation of excitations and an additional underestimation due to the charge-transfer character. Apparently, no error cancelation occurs for triplet excitation energies since they are too low for both cyanines and merocyanines.

Adiabatic singlet and triplet excitation energies are shown in Figure 23. For excited-state optimizations, only cc-pVDZ basis sets were affordable. Since SCS-CC2 provides very accurate vertical excitation

energies (see below), adiabatic SCS-CC2/cc-pVDZ values were used as the reference. All trends discussed for vertical excitation energies are also reflected in the adiabatic excitations. Errors of both vertical and adiabatic triplet excitation energies differ less than corresponding singlet excitation energy errors. This could result from the more contracted nature of the triplet state,[813,490] which permits only small variations of the electron density as a function of the method. As it was the case for vertical singlet excitation energies, a linear dependence between adiabatic singlet excitation energies and the amount of exact exchange is found. Moreover, in a similar way to vertical excitations, deviations of adiabatic singlet excitations become increasingly negative with increasing ground-state polarity. In most cases, adiabatic TDA singlet excitation energies are larger than TD-DFT energies by approximately 0.20 eV. The smallest average errors in the TD-DFT/TDA framework are obtained with M06-2X (-0.12 eV/0.11 eV), ωB97X-D (-0.04 eV/-0.19 eV), CAM-B3LYP (-0.09 eV/0.14 eV), and SOGGA11X (-0.20 eV/0.00 eV). This agrees with Mennucci et al.[724] who found that M06-2X and CAM-B3LYP provide very accurate adiabatic excitation energies of solvated organic molecules. Minimal signed errors for triplet energies in the Δ-SCF/TDA framework are encountered with the same functionals, but much alike vertical triplet excitation energies, a systematic underestimation is found (M06-2X: -0.07 eV/-0.11 eV; ωB97X-D: -0.22 eV/-0.15 eV; CAM-B3LYP: -0.20 eV/-0.19 eV; SOGGA11X: -0.20 eV/-0.17 eV). Moreover, the systematic underestimation becomes more pronounced with increasing polarity of the systems so that the largest errors are found for the most polar molecules, i.e, for the merocyanines.

Jacquemin et al. also highlighted the systematically underestimated adiabatic triplet excitation energies of TD-PBE0 in a recent benchmark on triplet excited-state geometries.[723] In accordance with the results in Figure 23, they found that the underestimation was alleviated when using M06-2X instead of PBE0. Durbeej et al. raised the question whether errors for vertical singlet excitation energies significantly differ from their adiabatic analogs.[814] According to their benchmark results, this is not the case, which is also reflected in the findings for singlet excitations in Figure 23 and Figure 21: as already mentioned, vertical and adiabatic singlet excitation energies show similar trends and errors. Furthermore, the existence of only small differences between vertical and adiabatic excitation energies is equally found for triplet excitation energies (Figure 23, Figure 22).
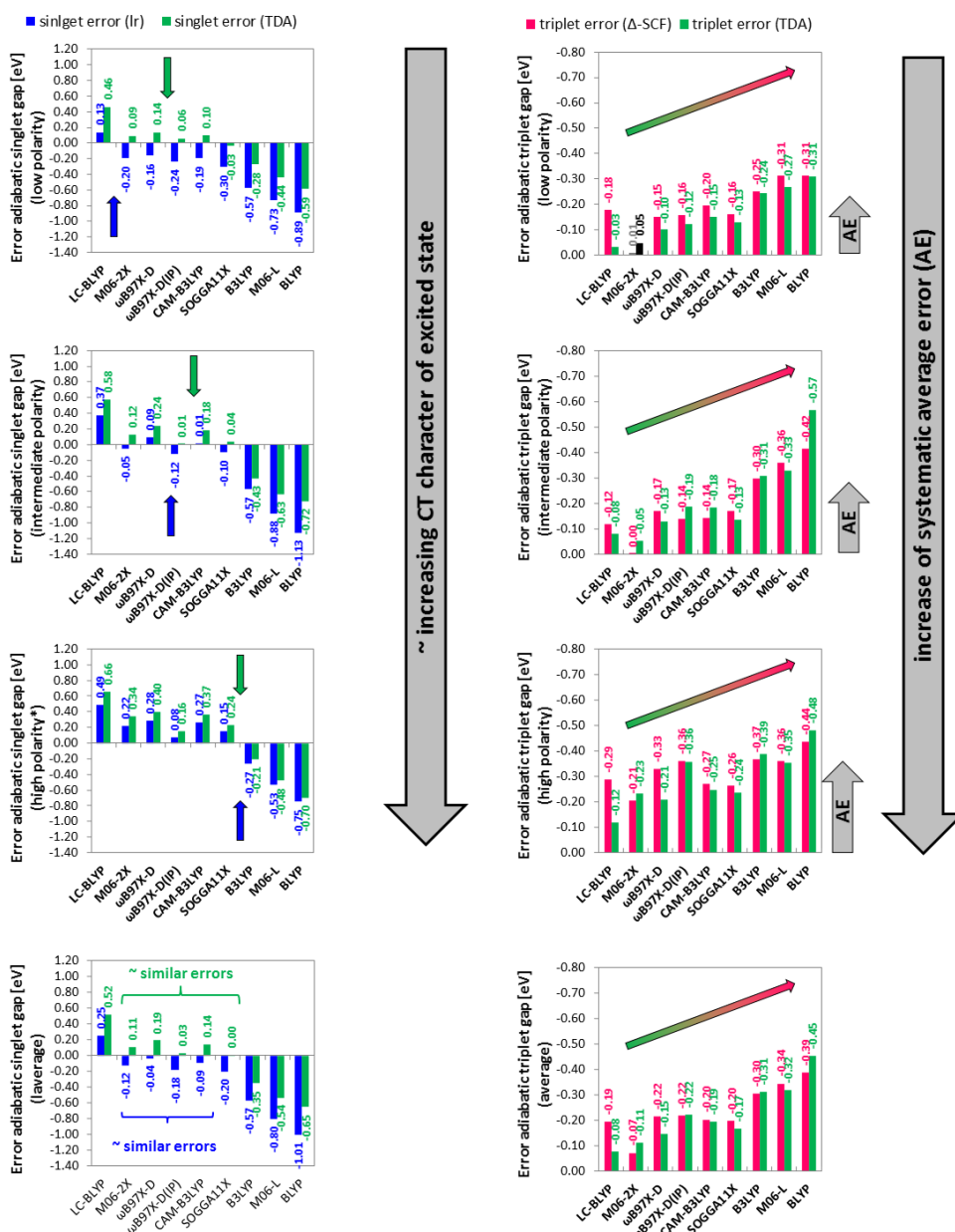
Figure 23: Mean signed errors for adiabatic singlet and triplet excitation energies obtained with DFT functionals/HF and cc-pVDZ basis sets. The black and grey deviations for M06-2X triplet excitations are positive. Reproduced with permission from [758]. © 2016 Elsevier B.V.

Since singlet fission is known to occur on an ultrafast timescale,[537] both vertical and adiabatic singlet-triplet gaps, i.e., the vertical and adiabatic S_1-T_1 energy difference, can influence its energetic feasibility: only if the singlet energy is at least twice as high as the triplet, singlet fission is possible.[533] A selection of promising candidates based on computations thus requires accurately predicted gaps.

Vertical singlet-triplet gaps are obtained from the calculated singlet and triplet excitation energies. They are discussed next (Figure 24). Because of the existence of several formulations (TD-DFT, Δ-SCF, TDA), different protocols are employed to compute vertical singlet-triplet gaps. Most obviously, singlet-triplet gaps can be calculated as difference between adiabatic linear-response TD-DFT

excitation energies. Results are indicated with "lr-lr" (=linear response) in Figure 24 (blue error bars). If TDA or Δ-SCF triplet excitation energies are employed instead of TD-DFT triplet excitations, resulting gaps are denoted either with "lr-TDA" (green error bars, Figure 24) or with "lr-gs" (gs: ground state; pink error bars, Figure 24). Finally, also TD-DFT singlet excitation energies can be replaced by their corresponding TDA values, yielding the "TDA-TDA" protocol for which TDA triplet excitation energies are used (black error bars, Figure 24). The performance of a variety of functionals with these different protocols has yet not been investigated.

As could be expected from the above discussed accuracies of singlet and triplet excitation energies, M06-2X, ωB97X-D, CAM-B3LYP, and SOGGA11X provide reliable singlet-triplet gaps when TD-DFT singlet excitation energies are used in conjunction with either TDA or Δ-SCF triplet energies (M06-2X: 0.19 eV/0.17 eV; ωB97X-D: 0.23 eV/0.21 eV; CAM-B3LYP: 0.25 eV/0.21 eV; SOGGA11X: 0.19 eV/0.19 eV). Since TDA singlet excitation energies become less accurate, i.e. more overestimated, with increasing ground-state polarity, the quality of "TDA-TDA" singlet-triplet gaps deteriorates in this direction. For the same reasons, the TDA-TDA protocal is rather reliable for singlet-triplet gaps of apolar substances as can be seen from "TDA-TDA" average errors that are generally smaller than 0.20 eV for all local and hybrid functionals, a point addressed to some extent by Wu et al. who calculated TDA singlet-triplet gaps of several hydrocarbons.[810] For all protocols, errors are largest for polar substances. This is to be expected from the above outlined particularly severe underestimation of triplet excitation energies for polar substances.

Error differences between different functionals are smaller for singlet-triplet gaps than for individual singlet/triplet excitation energies. For instance, the error for the singlet-triplet gap in the "lr-TDA" scheme of M06-2X amounts to 0.19 eV, whereas it is 0.28 eV for M06-L. However, the error of M06-2X triplet excitation energies in the TDA scheme is 0.16 eV, whith M06-L triplet excitation energies having an almost three-fold error of 0.40 eV. In a similar way, the errors of singlet excitation energies of M06-2X and M06-L are -0.06 eV and -0.51 eV, respectively.

These smaller performance differences of different functionals for singlet-triplet gaps arise from error cancelations if TD-DFT singlet excitation energies are combined with TDA or Δ-SCF triplet energies. Pure functionals with too small singlet excitation energies[259] usually underestimate triplet excitation energies as well. Therefore, the respective errors mutually cancel when taking differences, and mean singlet-triplet errors increase by only 0.10 eV when passing from hybrid to pure functionals. Furthermore, few differences exist among different hybrid functionals, which becomes evident from a comparison of PBE0 and B3LYP errors with results obtained with SOGGA11X (errors of the TDA/Δ-SCF protocol: PBE0: 0.20 eV/0.20 eV; B3LYP: 0.21 eV/ 0.23 eV; SOGGA11X: 0.19 eV/0.19 eV). The compensation of errors is even more pronounced for adiabatic singlet-triplet gaps. These findings

coincide well with the investigations of Nguyen et al. who simply used B3LYP to calculate singlet-triplet gaps of chromophores with nonlinear absorption properties and obtained values in good accordance with experimental data.[808]
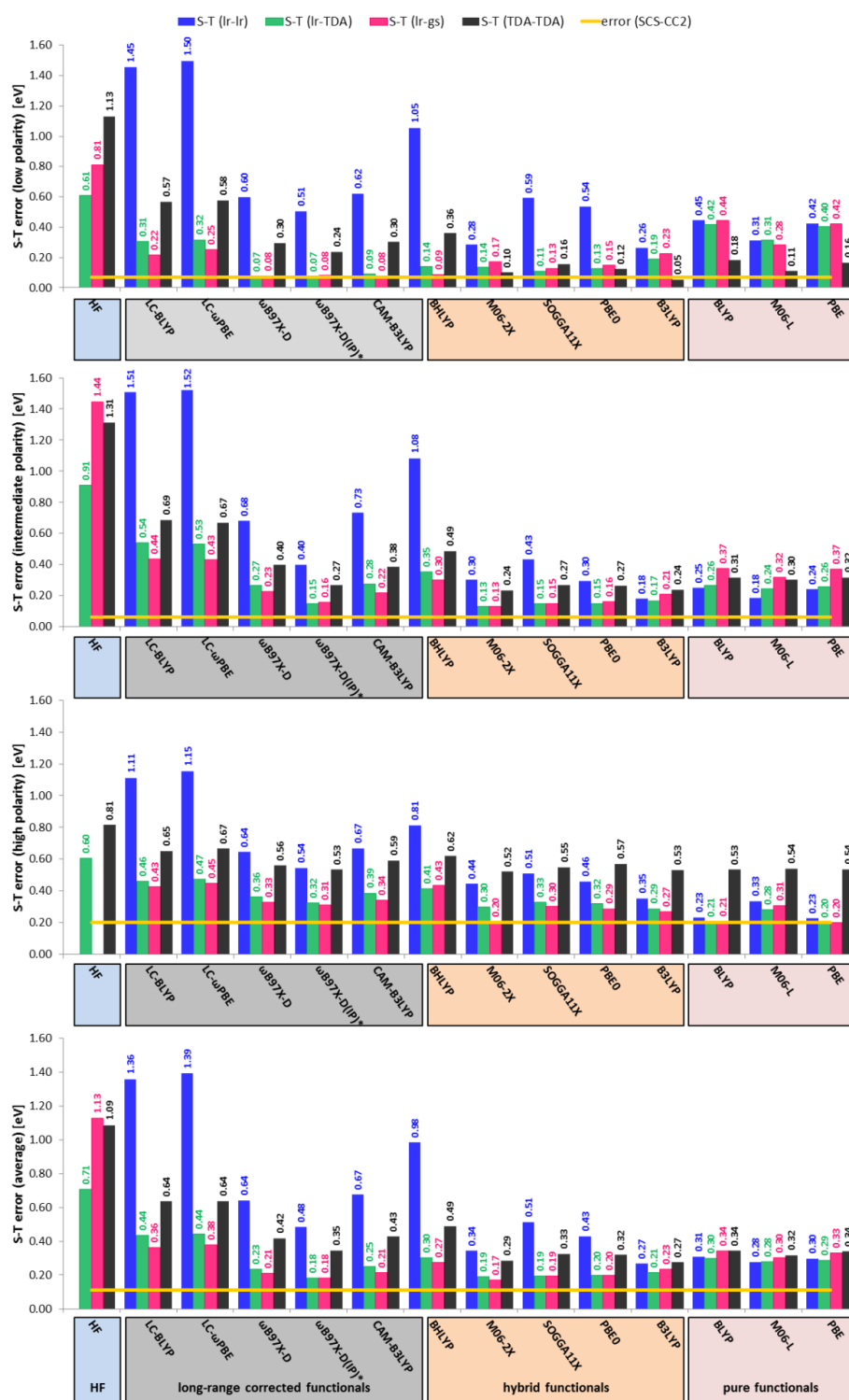

Figure 24: Mean absolute error for vertical singlet-triplet gaps obtained with DFT functionals/HF employing cc-pVTZ basis sets (TDA: cc-pVDZ). The "S-T error" refers to the averaged error for the singlet-triplet gap. Reproduced with permission from [758]. © 2016 Elsevier B.V.

Before analyzing the failure of DFT for triplet excitation energies and corresponding singlet-triplet gaps in more detail, a brief overview over results obtained with wave-function based approaches is given (Figure 25). Mean signed errors for vertical singlet and triplet energies are shown in the first and second panels, respectively. The third panels dispose signed errors for singlet-triplet gaps while absolute errors can be found in the fourth panels. An analysis specific for the compound classes is given on the left-hand side whereas average values are shown on the right. All values are obtained within the linear-response formalism.
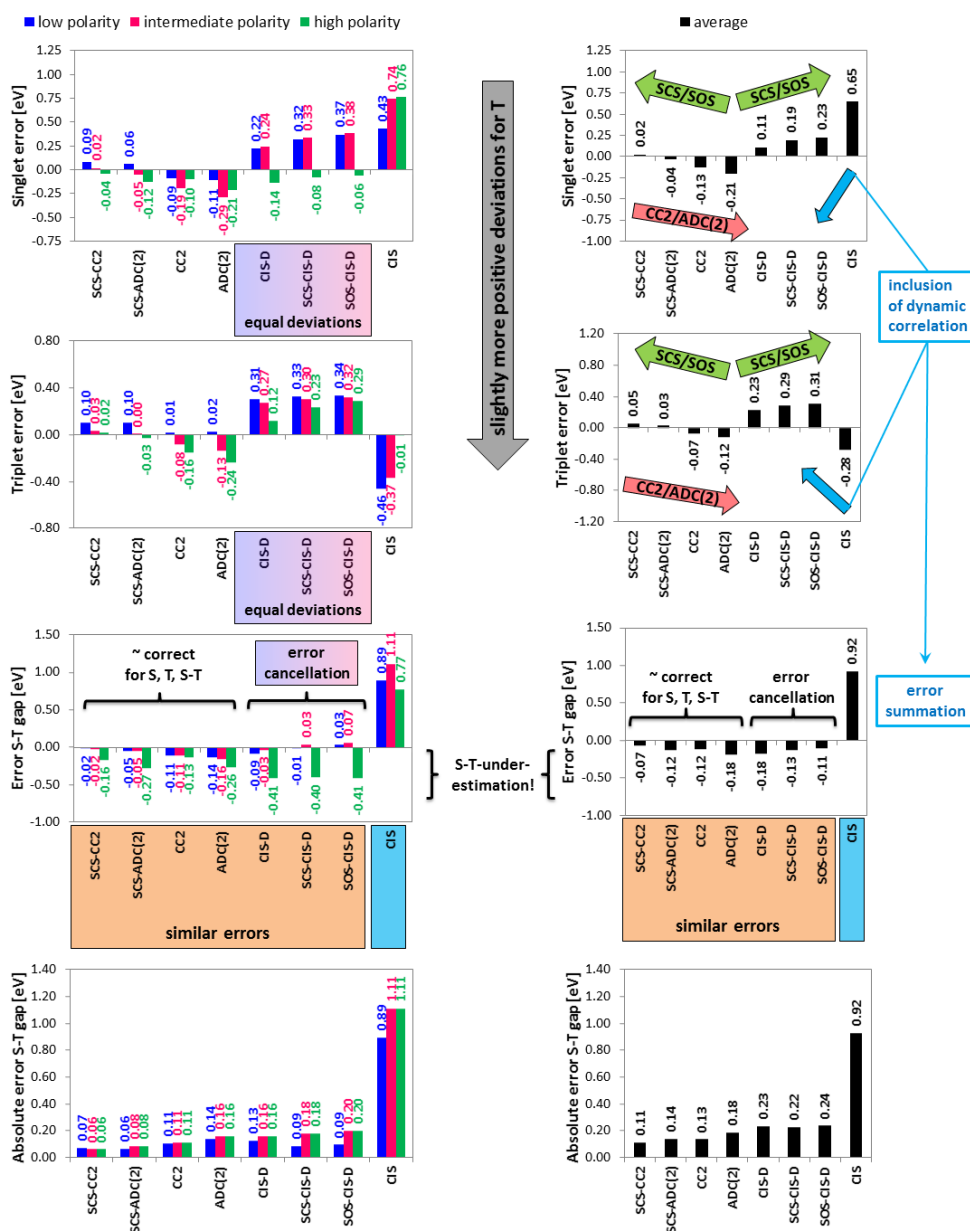
Figure 25: Mean signed errors of wave-function based methods for vertical singlet excitation energies (first panels), vertical triplet excitation energies (second panels), and vertical singlet-triplet gaps (third panel). Mean absolute errors for vertical singlet-triplet gaps are shown in the fourth panels. The cc-pVTZ basis sets were employed in all linear-response calculations. The error cancelation between singlet and triplet excitation energy errors is highlighted. To stress the fundamentally different behavior of CIS, its performance is colored in blue. Adapted with permission from [758]. © 2016 Elsevier B.V.

Equal trends are found for singlet and triplet excitation energies. In order to emphasize only these important trends, arrows were inserted into Figure 25. As discussed above,[702] spin-component scaling decreases the errors of CC2 and ADC(2) while it deteriorates results for CIS(D)-based methods. This applies also to the SOS treatment of CIS(D) excitation energies. This effect is indicated with green arrows for both singlet and triplet excitation energies (Figure 25). Furthermore, another point already addressed above recurs: singlet and triplet excitation energies computed with CC2 are larger than corresponding ADC(2) values, emphasized by red arrows in Figure 25. While CC2 and ADC(2) methods deliver rather accurate excitation energies, all values are blue-shifted in CIS(D). However, as CIS(D) errors for excitations with different multiplicity are almost equal, errors cancel for singlet-triplet gaps that are consequently very accurate. Purple boxes in Figure 25 underline this error compensation. ADC(2) and CC2 singlet-triplet gaps are also very accurate which is, however, not the result of a fortuitous error compensation but rather relies on correct individual singlet and triplet excitation energies. The fact that highly similar errors for singlet-triplet gaps are obtained with all wave-function based methods is marked with ocher boxes in Figure 25. Moreover, most notably and in contrast to DFT, errors of wave-function based methods for different compound classes are almost equal. This indicates that the wave-function based approaches provide a balanced and unbiased description of singlet-triplet gaps for all molecular classes. An essentially correct description of singlet-triplet gaps, yet only in cyanines, by wave-function based approaches was also found by Le Guennic and Jacquemin.[727]

It becomes most evident from the analysis of the results in Figure 25 that all wave-function methods behave very similarly with the exception of CIS. Large signed errors of 0.65 eV are obtained for CIS singlet excitation energies. In contrast, CIS triplet excitation energies are too low with a signed error of almost -0.30 eV, which gives rise to severely overestimated singlet-triplet gaps with an absolute average error of 0.92 eV.

In a recent investigation on low-lying π-π^* excitations in organic π-conjugated molecules, Corminbœuf and Jacquemin and coworkers suggested to use CIS and CIS(D) excitation energies to identify singlet excited states where differential correlation – included in CIS(D) via the perturbative doubles and left aside in CIS – is significant.[172] Assuming that this similarly applies to triplet states, a comparison of CIS and CIS(D) suggests that the implications of the inclusion of dynamic correlation qualitatively differ for excited states of different spin multiplicity. Whereas CIS and CIS(D) errors of singlet excitation energies have equal signs and are of the same order of magnitude at least for apolar substances (CIS(D): 0.21 eV; CIS: 0.43 eV), corresponding errors of triplet excitation energies are larger and of opposite sign (CIS(D): 0.31 eV; CIS: -0.46 eV). The concept that a correct description of the dynamic correlation is of major importance for accurate singlet-triplet gaps is further supported by the high accuracy of those

methods that are known to efficiently cover dynamic correlation phenomena,[172] i.e., by CC2 and ADC(2) methods.
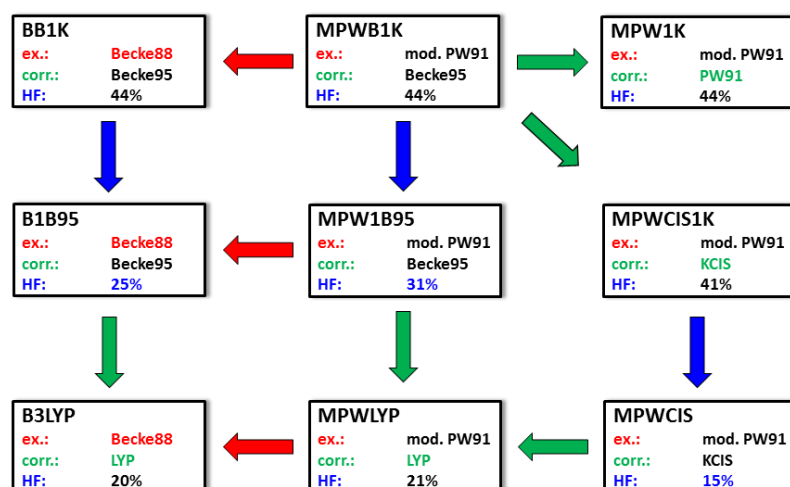

Figure 26: Hybrid and meta hybrid functionals constructed by Truhlar et al. and B3LYP. The DFT exchange (changes indicated with red arrows), correlation (changes indicated with green arrows) and the HF exchange (changes indicated with blue arrows) are varied in a systematic manner. Starting from MPWB1K (center top) the modified part is indicated in bold. For references see [815] for an overview and [707,712,816] (BB1K), [712,817,816] (MPWB1K), [817,818] (MPW1K), [707,712] (B1B95), [712,817,816] (MPW1B95), [712,819,820,821,822] (MPWCIS1K), [708,817,816] (MPWLYP), [712,819,820,821,822] (MPWCIS).

Keeping these conclusions from wave-function based approaches in mind, the erroneous singlet-triplet gaps of DFT are analyzed more in detail since the situation for DFT seems to be more complicated. As outlined above, exact exchange has clear-cut effects on singlet excitation energies, but triplet excitations vary unsystematically with the amount of exact exchange and are often underestimated. To gain more insight, singlet and triplet excitation energies are calculated for all molecules with a series of hybrid and meta hybrid functionals of Truhlar and coworker[815] where the amount of DFT and HF exchange and the DFT correlation is systematically varied (Figure 26). A color code is employed to underline this systematics, i.e., blue arrows and colors indicate modifications of the amount of exact exchange, red arrows and colors highlight changes of the DFT exchange functional, and green arrows and text stand for the replacement of the DFT correlation functional. See reference[815] for more information on the functionals.

The influence of the amount of exact exchange on singlet and triplet excitation energies is analyzed first. TDA singlet and triplet excitation energies calculated with all functionals from Figure 26 are correlated with the amount of exact exchange included in the respective functionals. The correlations are displayed for two representative compounds, anthracene and MD353, in Figure 27. All other correlations can be found in [758]. They dispose similar tendencies. It is evident from the plots that a linear dependence between the singlet excitation energies and the amount of exact exchange exists (blue lines, Figure 27). As stated above, this very clear-cut correlation between the HF amount of a

217

functional and its excitation energies is widely exploited in IP-tuning.[127,160] Moreover, it simultaneously implies that since singlet excitation energies depend linearly on the amount of exact exchange of functionals constructed from *different* exchange and correlation parts (coefficients of determination = R^2-value > 95%), they necessarily cannot significantly depend on the exact form of these exchange and correlation parts.
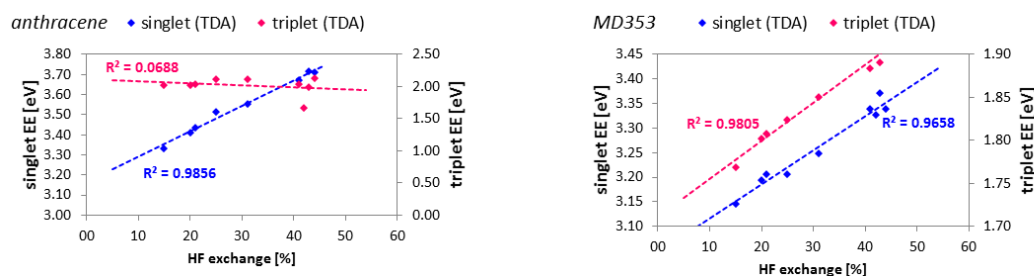

Figure 27: Correlation of singlet and triplet excitation energies with the amount of exact exchange (TDA formulation). The TDA formalism is used due to its computational efficiency. For a demonstration that the same correlations are found for TD-DFT, see Figure 28 and text. Reproduced with permission from [758]. © 2016 Elsevier B.V.

In contrast, the dependence of the triplet excitation energies on the amount of exact exchange differs as a function of the molecule (Figure 27): on the one hand, triplet excitation energies in anthracene do not systematically vary with the amount of exact exchange (pink line, left panel, Figure 27, R^2-value: 7%). On the other hand, a linear dependence on the amount of HF exchange is found for triplet excitation energies in MD353 (pink line, right panel, Figure 27; R^2-value: 98%), similar to the one observed for singlet excitation energies (blue line).

To further illustrate this point, the amount of exact exchange of a given functional is systematically varied (instead of employing different functionals to vary the amount of HF exchange). Using the B3LYP functional in a first step, Figure 28 displays the evolutions of singlet and triplet excitation energies with increasing HF exchange of anthracene (upper left panel), the diketopyrrolopyrrole (lower left panel), MD353 (upper right panel), and HB194 (lower right panel). Different DFT formalisms (TD-DFT, TDA, Δ-SCF) are used for anthracene. A comparison of resulting TDA and adiabatic linear-response TD-DFT singlet excitation energies (upper left panel, Figure 28) shows that the dependence on the amount of exact exchange does not differ for different DFT formulations. This similarly holds for triplet excitation energies, for which TDA and Δ-SCF results are given. Please keep in mind that adiabatic TD-DFT triplet excitation energies are negative for larger amounts of HF exchange due to the existing triplet instabilities.
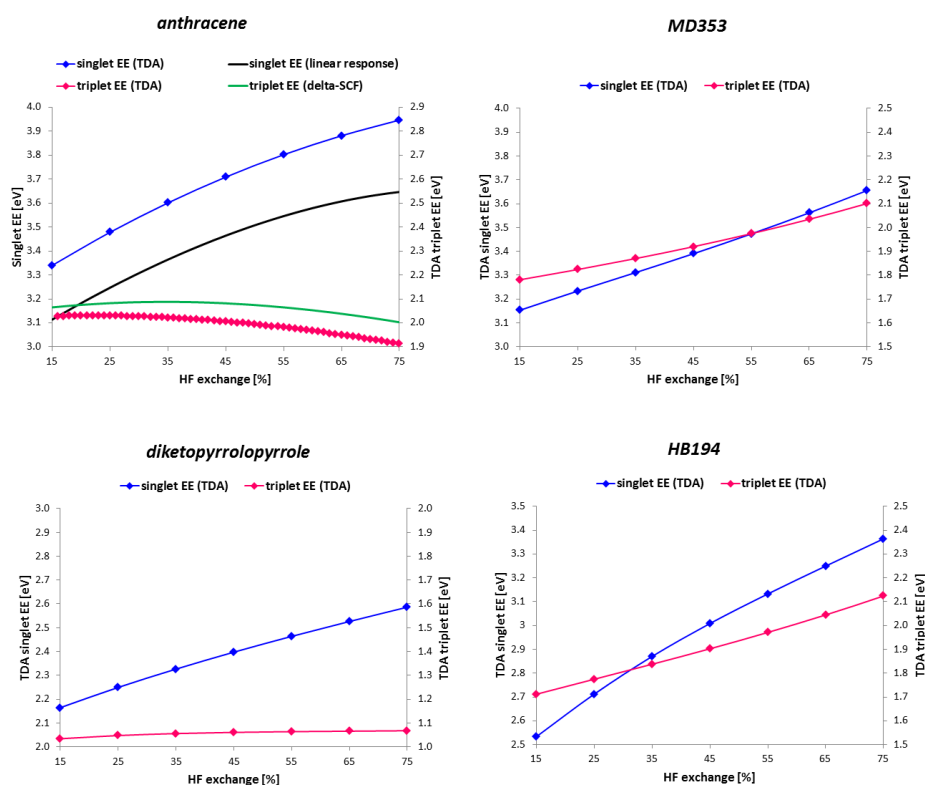
Figure 28: Correlation of singlet excitation energies (blue lines) and triplet excitation energies (pink lines) with the amount of exact exchange using functionals constructed from B3LYP for four different molecules. For additional comparison, the linear-response singlet and the Δ-SCF triplet excitation energies for anthracene are given, disposing equal tendencies.

With regard to the influence of the amount of exact exchange, similar effects to the Truhlar functionals in Figure 27 are observed:[qqq] singlet excitation energies linearly depend on the amount of exact exchange included in the underlying B3LYP-based functional. The extent of changes induced when increasing the exact exchange is molecule-specific. Increasing the amount of HF exchange by 60% increases the lowest π-π*-transition energy by 0.6 eV (anthracene), 0.4 eV (diketopyrrolopyrrole), 0.3 eV (MD353), and 0.8 eV (HB194). The merocyanines' triplet excitation energies equally depend in a linear way on the amount of exchange, albeit less strongly (smaller slopes of pink lines). In contrast, TDA triplet excitation energies for anthracene and the diketopyrrolopyrrole do not increase with more exact exchange included in the functional. The evolution of the pyrrole's triplet transition energy essentially corresponds to a flat line, while a slightly descending line is obtained for anthracene, which might, however, result from approaching triplet instabilities. Altogether, this perfectly mirrors the above observations for the Truhlar functionals (Figure 27).

[qqq] It is worth emphasizing that these findings are not completely equivalent because several parameters (HF exchange, DFT exchange, DFT correlation) are varied for the Truhlar functionals (Figure 27) whereas in Figure 28, only the HF amount of B3LYP is modified. The DFT exchange-correlation part remains the same.

Apart from directly changing the amount of exact exchange in conventional hybrid functionals, adjusting the range-separation parameter ω in range-separated hybrids constitutes another route to systematically vary the exact exchange comprised in functionals.[782,823] As outlined by Baer and coworkers, this strategy is of large utility to describe optoelectronic effects in a DFT framework.[160] In contrast to the amount of HF exchange of a hybrid that offers no direct interpretation, the range-separation parameter is, as already mentioned, intimately related to the delocalization of the electron density:[782] its reciprocal value can be interpreted as the length scale of the state's charge-transfer character. The progression of ωB97X-D singlet and triplet excitation energies with increasing range separation parameter (i.e., the charge-transfer length scale is shortened) is shown in Figure 29. Overall, effects are equivalent to those observed for hybrids with a variable amount of exact exchange (Figure 29 vs. Figure 27/Figure 28). Singlet excitation energies (blue lines) of the two molecules expose slightly different tendencies. Whereas a threshold value for the range separation parameter exists above which the singlet excitation energy of anthracene saturates, this is not the case for MD353. However, more importantly and in contrast to their triplet counterparts, the singlet excitation energies *for both molecules* experience a considerable blue shift for larger values of ω. The behavior of triplet excitation energies as a function of ω is again molecule-specific. While the triplet excitation energy of MD353 systematically increases with increasing ω, this is not the case for anthracene. Its triplet excitation energy barely changes, with a slight blue shift for small ω values followed by a red shift for larger ω values. With regard to the excited-state delocalization that is reflected in ω, the different dependence of triplet excitations on ω suggests that fundamental differences exist between the molecules' triplet excited-state (de)localization.
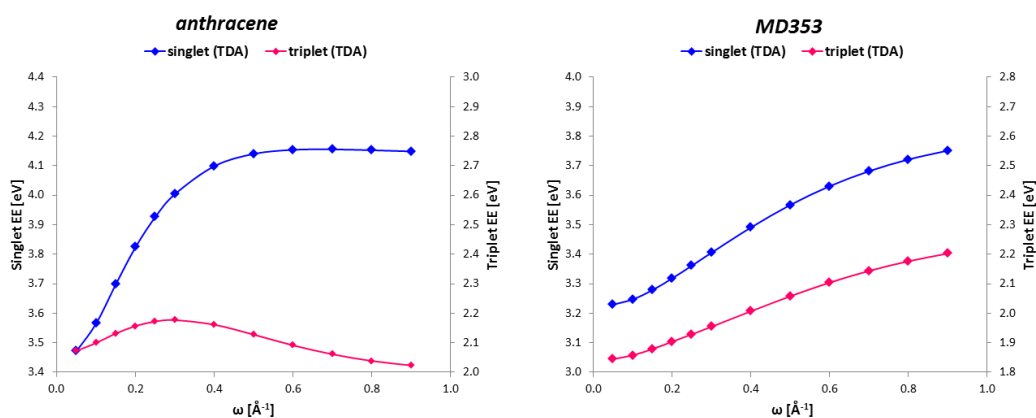

Figure 29: Correlation of singlet excitation energies (blue lines) and triplet excitation energies (pink lines) with the range-separation parameter of ωB97X-D for two different molecules.

Hence, two important conclusions can be drawn from the results presented in Figure 27 to Figure 29:

1. All singlet excitation energies rise if the amount of exact exchange of a functional increases. This applies both for different functionals differing *among other things* in their amount of exact exchange and for tuned functionals where *only* the percentage of exact exchange is varied.

2. Triplet energies show for some molecules a linear dependence on the amount of exact exchange of a functional as well. For others, they do not increase with the amount of exact exchange at all. Upon increasing the amount of exact exchange, they spread randomly for functionals with different exchange-correlation kernels, and they give rise to flat lines for a given exchange-correlation functional.

To further elucidate the molecule-specific behavior of triplet excitation energies, an electronic-structure parameter is identified on the basis of literature findings that is related to triplet energies and resulting singlet-triplet gaps. It will be used to organize the following discussion. According to Michl and coworker, the MO exchange integral between the HOMO and the LUMO of a system contributes most to the stabilization of a triplet state compared to the corresponding singlet state.[533] This exchange integral is large if the HOMO and LUMO densities are localized on the same atoms. Therefore, it increases whenever the product density between the HOMO and the LUMO increases. As a first approximation, this product density can be employed to estimate the stabilizing exchange interactions. The product density $S_{H \cdot L}$ can be expressed in terms of expansion coefficients $\{c_i\}$ of the molecular orbitals $\{\varphi_i\}$ in the atomic basis set and overlap integrals S_{ij} between two basis functions i and j:

$$S_{H \cdot L} = \int dr_1 \varphi_{H \cdot L}(r_1) \varphi_{H \cdot L}(r_1) = \sum_{i=1}^{N} \sum_{j=1}^{N} \left(c_i^{HOMO} c_i^{LUMO} \right) \left(c_j^{HOMO} c_j^{LUMO} \right) S_{ij} \tag{442}$$

Calculations of $S_{H \cdot L}$ were implemented with C++ using the ouput of Gaussian09[718].

The product density $S_{H \cdot L}$ will be used as the electronic-structure parameter to organize the following discussion. Since it quantifies the amount by which the HOMO and the LUMO charges overlap, it will be designated as the charge overlap density in the following. Although it will be used to analyze the molecule-dependent behavior of triplet energies, it is important to keep in mind that it was derived to estimate singlet-triplet gaps. In this context, it should be noted that other rationales for singlet-triplet gaps based on the absolute overlap[824] or on the overlap between natural transition orbitals[278,825] exist as well.
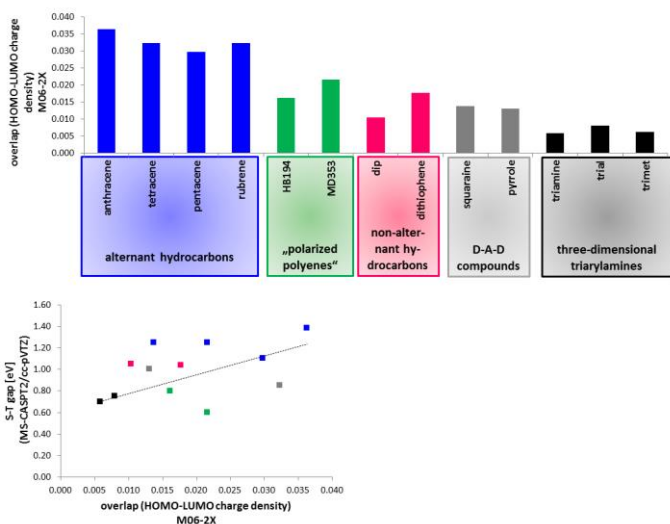
Figure 30: Calculated M06-2X charge overlap densities for all molecules arranged with decreasing size (upper panel) and correlation with the MS-CASPT2/cc-pVTZ singlet-triplet gaps (lower panel). Reproduced with permission from [758]. © 2016 Elsevier B.V.

Before continuing the analysis of triplet excitation energies, it should be verified whether the charge overlap densities indeed correlate with corresponding singlet-triplet gaps. For this purpose, charge overlap densities calculated for all molecules with M06-2X-D3/cc-pVDZ are given in Figure 30. To rule out any functional-specific influence, BLYP-D3/cc-pVDZ values for $S_{H \cdot L}$ were calculated for comparison (Table 12), but the influence of the functional turned out to be negligible.

Table 12: Comparison of BLYP-D3 and M06-2X charge overlap densities.

molecule	BLYP-D3/cc-pVDZ	M06-2X-D3/cc-pVDZ
anthracene	0.0364	0.0363
pyrrole	0.0140	0.0131
DIP	0.0112	0.0104
dithiophene	0.0177	0.0178
HB194	0.0166	0.0162
MD353	0.0232	0.0217
pentacene	0.0293	0.0298
rubrene	0.0305	0.0323
squaraine	0.0110	0.0137
tetracene	0.0322	0.0324
"triamine"	0.0060	0.0058
"trial"	0.0094	0.0080
"trimet"	0.0041	0.0063

222

Figure 30 shows that the charge overlap densities vary in a characteristic way as a function of the molecular structure, giving rise to a rearrangement of the employed compounds (Figure 5) into five different groups (colored boxes, first panel, Figure 30). Moreover, the correlation between the computed charge overlap densities and the MS-CASPT2 singlet-triplet gaps (second panel, Figure 30) demonstrates that the charge overlap densities are indeed related to the size of the singlet-triplet gaps. Alternant linear acenes possess the largest charge overlap densities, which are smaller for non-alternant hydrocarbons. Similarly, particularly large singlet-triplet gaps are obtained for acenes, while DIP and the dithiophene compound possess smaller gaps. Rather large charge overlap densities and, concomitantly, rather high singlet-triplet gaps are also obtained for the merocyanines, which could be considered as "polarized polyenes". In fact, some polyene-like structures are known to undergo singlet-fission, which requires large exchange interactions in the triplet excited state. Large singlet-triplet gaps are necessary to fulfill the most fundamental condition for singlet fission, i.e., $S_1 \geq 2T_1$.[826] The donor-acceptor-donor-type compounds have smaller, yet still noticeable charge overlap densities, while the latter almost completely diminish for triphenylamine-based compounds. This arises from the three-dimensional structure of the triphenylamine moiety, resulting in barely overlapping orbitals. This goes along with vanishing singlet-triplet gaps in triphenylamine-based molecules and slightly larger gaps in donor-acceptor-donor compounds (second panel, Figure 30). In addition to the charge overlap density, these five groups (highlighted in Figure 30) are used to organize the following discussion. It should be kept in mind that the regrouping is equivalent to the above introduced polarity classification (Figure 5), but further differentiates it.
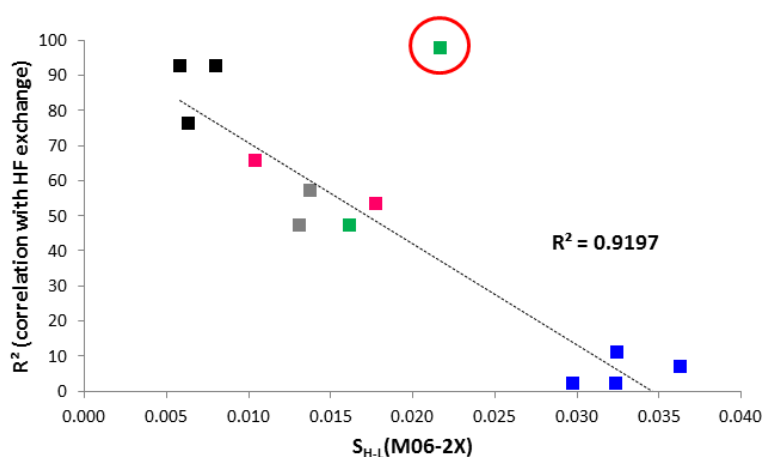
Figure 31: Correlation between the R^2 values from the relationship between triplet excitation energies and HF exchange for the series of functionals of Truhlar and coworker and the calculated charge overlap density. Reproduced with permission from [758]. © 2016 Elsevier B.V.

The molecule-dependent influence of the amount of exact exchange on the triplet excitation energies can be quantified by means of the coefficients of determination of the correlation, the R^2-value. These R^2-coefficients for the correlation between triplet excitation energies obtained with the Truhlar

functionals (similar to Figure 27) and the amount of exact exchange are calculated for all molecules and plotted versus the charge overlap density in Figure 31. It becomes evident (Figure 31) that the charge overlap density determines the influence of the amount of HF exchange on the triplet excitation energy. Whenever the HOMO and the LUMO barely overlap, i.e., if they localize on different molecular entities, the amount of HF exchange becomes decisive. Therefore, singlet-triplet gaps can be tuned by adjusting the amount of HF exchange/the range-separation parameter for the limiting case of small charge density overlaps. This result is in line with numerous investigations where IP-tuning was successfully employed to calculate singlet-triplet gaps of TADF compounds, for example by Brédas et al.[827], Adachi et al.[828] and Gierschner et al.[829] Small charge overlap densities are a common feature of all employed TADF compounds because a prerequisite for the occurrence of TADF is precisely a small spatial HOMO-LUMO overlap (although the decisive role of the small spatial HOMO-LUMO overlap for the applicability of IP-tuning was not pointed out in these investigations).[830]

In contrast, no clear-cut relationship between the amount of exact exchange and the triplet excitation energies is observed for all compounds with large charge overlap densities, i.e., for substances where the HOMO and the LUMO are predominantly situated on the same molecular entities. The R^2 coefficients are smaller than 50% especially for acenes, but also for non-alternating hydrocarbons and substances with a donor-acceptor-donor structure. This agrees nicely with an investigation of Niehaus et al.[831] who did not find a systematic improvement of triplet excitation energies with tuned functionals. They concluded from a detailed orbital analysis that different functionals result in different localization behaviors of the triplet states.[831] This conclusion parallels the results from Figure 29. Please note that in Figure 31, the merocyanine MD353 does not fit into the general trend, wherefore it is circled in red. This could be due to above-addressed intrinsic errors of DFT for cyanine dyes and related compounds.[791]

To further understand these molecule-specific effects of an increase in exact exchange, spin densities of the triplet states of all molecules are analyzed. They are calculated with HF and the pure BLYP functional, i.e., a functional without any exact exchange. Furthermore, difference densities (i.e., $\Delta \rho^{spin} = \rho^{spin}(HF) - \rho^{spin}(BLYP)$) are calculated. Results are shown in Figure 32.

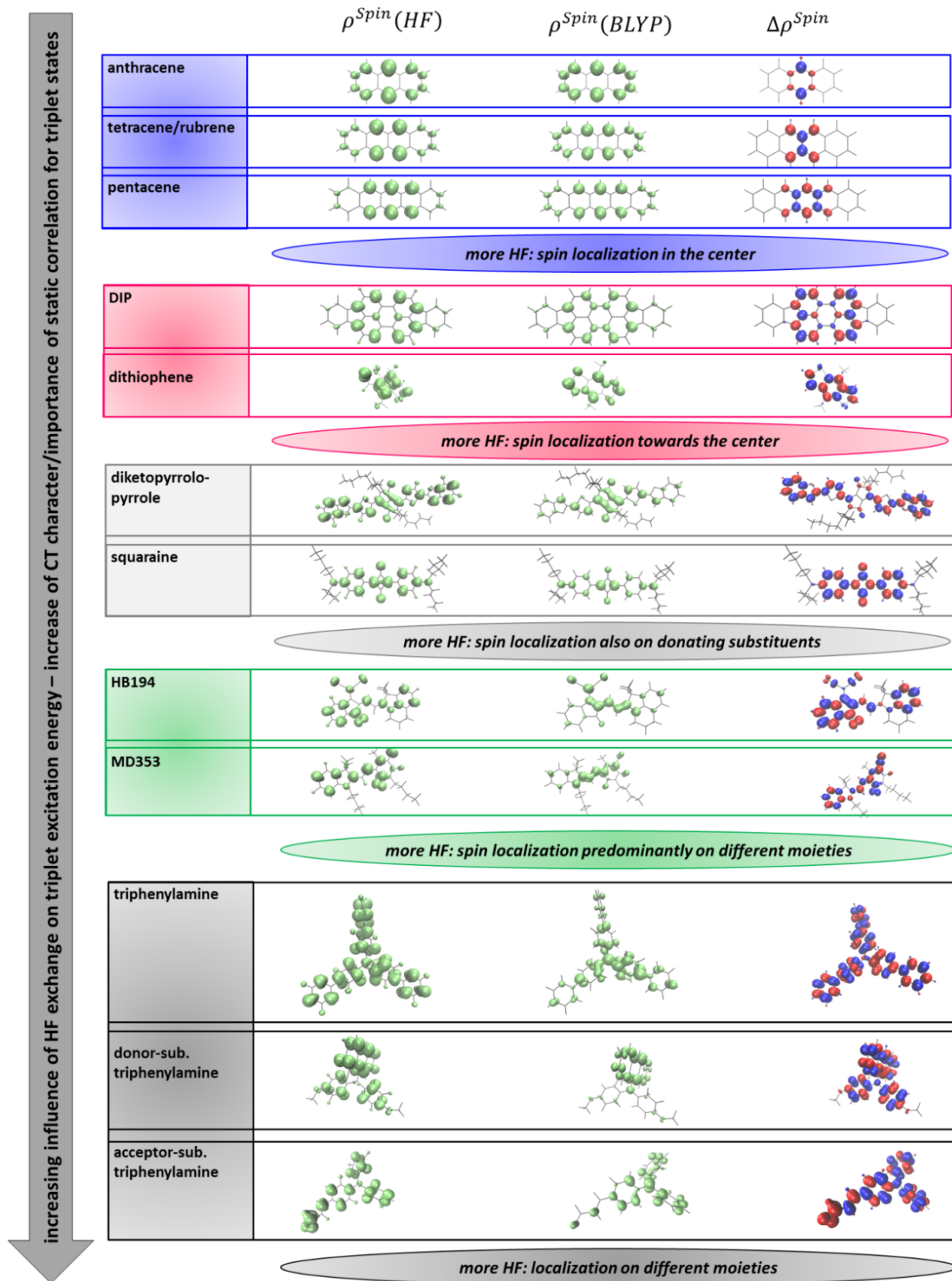Figure 32: HF spin densities (left), BLYP spin densities (center, and difference densities (right) for all molecules. Rubrene behaves identically to tetracene. Reproduced with permission from [758]. © 2016 Elsevier B.V.

The first three rows (Figure 32) illustrate HF and BLYP spin densities as well their difference density for

the acenes. Please note that rubrene behaves exactly like tetracene. While the BLYP spin densities are

225

more evenly spread across all atoms, HF tends to localize the total spin on the center atoms of the acenes (see the larger HF coefficients for anthracene, tetracene, and pentacene in the center rings compared to BLYP). Similarly, the difference density between the two spin densities is always located on these center atoms. This shows that an increase in exact exchange leads to a localization of the spins of the triplet states in the center regions of acenes. This triplet-state localization is in line with the above-observed saturation of triplet excitation energies when increasing the range-separation parameter ω (Figure 29). Upon reaching a certain threshold, a further localization of the triplet is not possible so that its density and energy cannot noticeably change anymore.

For non-alternant hydrocarbons, the situation is qualitatively similar. Peak HF spin densities in the dithiophene are found on the central benzene ring, while BLYP attributes slightly more spin density to the outer thiophene rings. Nevertheless, from the spin difference density of the DIP molecule, it can already be seen that HF tends to localize the spin more on the periphery of the perylene core. Since no spin density is found for either method on the outer rings (although the HOMO and LUMO of the neutral molecule are non-zero in this region), it can be concluded that HF tends to localize the spin in the center region of the molecules, albeit to a smaller extent than in the acenes.

This picture changes progressively when passing to donor-acceptor-donor molecules (the squaraine and the diketopyrrolopyrrole) and donor-acceptor molecules. Comparing the HF and BLYP spin densities of the diketopyrrolopyrrole, it is evident that HF predicts a significant amount of spin density on the outermost benzofurane moieties, while the spin is more or less delocalized across the central diketopyrrolopyrrole scaffold according to BLYP. Also in the squaraine, the HF spin density is significantly more pronounced on the outer aniline substituents. In line with this, the spin difference densities for the diketopyrrolopyrrole and the squaraine are spread over the complete molecules and possess pronounced peaks on the outer donating groups. The different localization behavior of the triplet states, also observed by Niehaus et al.,[832] can be rationalized in this case by the fact that due to the donor-acceptor-donor structure, the triplet states acquire local charge-transfer character. This means that the parallel spins are situated on different moieties of the molecules. Correspondingly, static correlation, i.e., left-right correlation, becomes an issue. Evidently, it is somewhat included in the unrestricted Kohn-Sham formalism. Moreover, it has been pointed out that DFT exchange – and not DFT correlation – is response for static correlation, and that a fraction of exact exchange is useful to accurately include static correlation.[112,833,834] As a pure functional with a completely local exchange hole, BLYP does not properly describe static correlation. Thus due to the absence of non-local exchange, it seems to be incapable of describing the distribution of the spin density over remote moieties. Consequently, it is found that for triplet states with charge-transfer character, HF possesses a more widely spread spin density while still localizing the individual spins to a larger extent

(contracting the density). An analysis of the spin densities of the merocyanines leads to the same conclusions. Differences become even more distinct. The BLYP spin density of HB194 is delocalized over the bridge between the donating and the accepting moiety. In contrast, most spin density is found for HF on both the donor and the acceptor, and no HF spin density smearing in the bridge occurs. Similar effects are observed for MD353. Hence functionals with more HF exchange describe the triplet states in merocyanines in terms of two separate barely interacting spins (except for static correlation). Considering only the spin separation, the HF triplet state is more delocalized.

Such delocalized HF triplet states are most pronounced for the triphenylamine-based compounds. While the BLYP spin density is centered on the central nitrogen atom and its vicinity, it spreads across all substituents for HF. No BLYP spin density is observed on the outer benzene rings of the biphenyl substituents in the triphenylamine, where the HF spin density reaches its maximum values. This applies also to the methoxy-substituted phenyl rings of the donor-substituted triphenylamine and to the conjugated-aldehyde moiety of the acceptor-substituted triphenylamine.

The presented analysis of the spin densities allows for the conclusion that the amount of exact exchange changes the triplet description in a way that depends on $S_{H \cdot L}$, i.e., on the spatial HOMO-LUMO overlap. If the latter is significant, HF describes the triplet states as being more localized in the center regions of the molecule than BLYP. With decreasing spatial HOMO-LUMO overlap, i.e., with increasing charge-transfer character, static correlation becomes an issue. It is well-known that DFT exchange, possibly with some amount of exact exchange,[112,833,834] accounts for static correlation.[97] Therefore, the individual spins separate more with an increasing amount of HF exchange, while they still tend to be localized in the same molecular regions in a BLYP treatment – albeit being smeared due to the intrinsic tendency of pure functionals to delocalize charges.

The observed different localization/delocalization behavior of the triplet states readily explains the different influence of exact exchange on their energies. As mentioned above, the energetic stabilization of triplet states arises predominantly from favorable exchange interactions between the parallel spins. On the one hand, if more HF exchange delocalizes the spins, i.e., positions them on different molecular entities as it is the case for molecules with small charge overlap densities, the exchange contribution to the triplet state diminishes. As a consequence, triplet energies rise. It is worth noting that additional destabilizing energy contributions result from the more contracted wave functions as described with HF.[835,836] On the other hand, with larger amounts of exact exchange, the parallel spins in acenes are increasingly situated within the same molecular regions. This increases stabilizing exchange interactions. However, destabilizing energy contributions from the more contracted wave function counterbalance the exchange stabilization, leading to more or less unchanged triplet energies.

After this analysis of exchange, the role of correlation is tackled next. A possible influence of dynamic correlation on triplet energies was already suggested above from the differences between CIS and CIS(D) singlet-triplet gaps. The influence of differential correlation on excited-state energies is a research area of ongoing discussions. As mentioned above, according to Autschbach,[782,791] underestimated triplet energies in cyanines result from a wrong treatment of the differential correlation combined with overshooting exchange interactions. In view of this deficiency, Grimme and Neese[136,181] outlined that the DFT description of differential correlation can be improved by including MP2-type correlation into double hybrid functionals. To test whether this different treatment of differential correlation influences triplet excitation energies, triplet excitation energies (Δ-SCF) were calculated with two double hybrids, B2PLYPD3[137,715,716] and mPW2PLYPD[137] in combination with the cc-pVTZ basis sets. Figure 33a shows the relationship between triplet excitation energies obtained with the double hybrid functionals and the MS-CASPT2 reference energies (upper plots). It becomes evident that these triplet excitation energies correlate very well with the reference values with coefficients of determination larger than 99% for most compounds summarized as "normal" compounds. The only exceptions are three push-pull systems (MD353, aldehyde- and methoxy-substituted triphenylamine), indicated as "charge-transfer compounds". As MD353 was already an outlier in previous discussions (Figure 31), the error might result from an intrinsically wrong DFT description of these compounds. Apart from that, the double hybrid functionals deliver very accurate triplet excitation energies for all other compounds rather than systematically underestimated values as found for other functionals.

To further illustrate this aspect, Figure 33b shows a comparison of B2PLYPD3 triplet excitation energies with values obtained with BHLYP. B2PLYPD3 triplet excitation energies are always considerably larger than their BHLYP counterparts (Figure 33b). Because of the very similar amounts of HF exchange (BHLYP: 50% vs. B2PLYPD3[136]: 53%) and the same DFT exchange part of the functionals, the differences in excitation energies necessarily result from differences in the differential correlation treatment. This suggests that many DFT functionals predict too low excitation energies because they provide an inadequate description of the differential correlation between the ground and the triplet excited states.
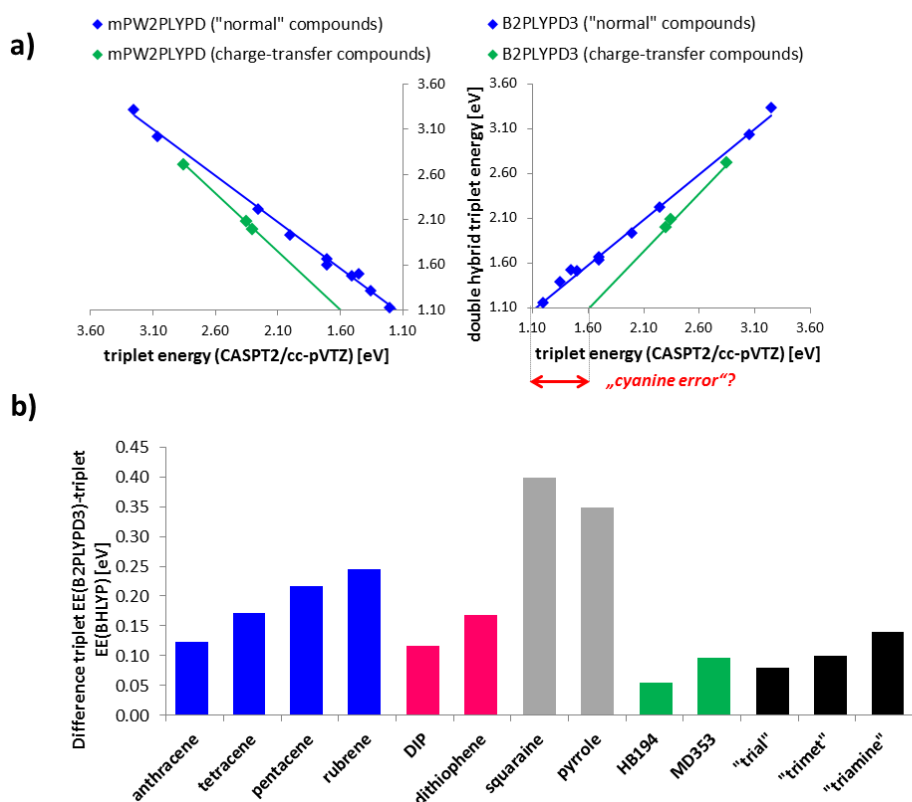
Figure 33: a) Comparison of triplet excitation energies with double hybrid functionals to MS-CASPT2 reference values. The offset for the charge-transfer compounds could be due to the intrinsic "cyanine error" of DFT. b) Assessing the contribution of the MP2 correlation energy to triplet excitation energies by comparing BHLYP and B2PLYPD3 Δ-SCF triplet energies. Reproduced with permission from [758]. © 2016 Elsevier B.V.

Local correlation in the correlation part of DFT functionals is usually included in a spin-dependent manner, and different functionals cover the same-spin and the opposite-spin correlation in different manners.[837,838,839] For instance, local same-spin correlation is ignored in the LYP correlation functional,[708] while the B95 correlation functional[712] accounts for both the same- and the opposite-spin correlation. Perdew and Burke outlined that the differences in the description of local same-spin and opposite-spin correlation have among others important implications for the description of spin polarization and localization.[840] Differences between the local same-spin and opposite-spin correlation are also introduced by the SCS correction in wave-function based methods that was shown to improve ADC(2) and CC2 results for triplet excitations (see above). [761,71] An equivalent of the SCS coefficients has recently been successfully incorporated into DFT functionals to improve the performance of double hybrid functionals.[43,841,842]

In a similar way and in view of the potential impact of differential correlation on triplet energies, it would be interesting to analyze how scaling the amount of same-spin and opposite-spin local correlation affects calculated singlet and triplet energies. As a first step, equal scaling coefficients for

both correlation effects are employed. This implies that the scaling coefficient of the total local correlation is increased.
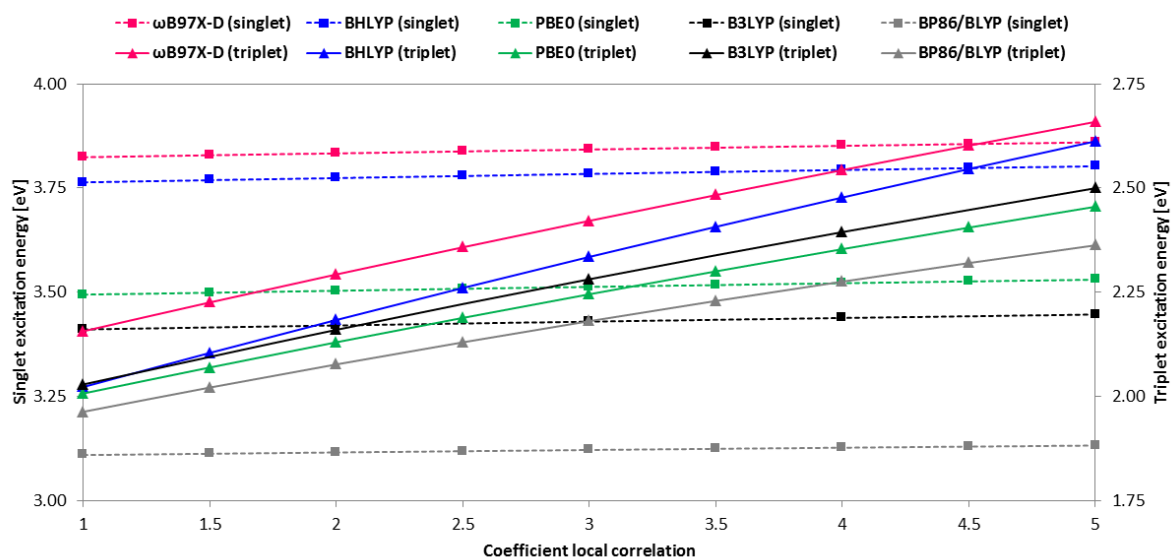

Figure 34: Dependence of the TDA singlet excitation energies (dashed lines and squares) and TDA triplet excitation energies (continuous lines and triangles) for anthracene on the local correlation coefficients. Reproduced with permission from [758]. © 2016 Elsevier B.V.

The data in Figure 34 reveal the general trend that increasing local correlation coefficients raises triplet energies and leaves singlet energies largely unchanged. On the one hand, this indicates that local correlation is similar between the ground state and singlet excited states, i.e., between states of the same multiplicity. On the other hand, local correlation obviously differs considerably between the singlet ground state and excited triplet states. This agrees well with the above-discussed results that the incomplete treatment of differential correlation between the singlet ground state and triplet excited states accounts for underestimated DFT and CIS triplet excitation energies. As soon as more local correlation is included, either via the inclusion of double excitations in double hybrids and CIS(D) or via an upscaling of the local correlation, triplet energies raise.

Finally, this raises the question whether it is possible to design functionals accurately describing both singlet *and* triplet excitation energies. In view of the observations that variations of the amount of local correlation influences triplet excitation energies while adjusting the amount of exact exchange primarily affects primarily singlet excitation energies, this seems feasible. Therefore, varying both parameters (i.e., the amount of HF exchange and the local correlation coefficient) independently can be expected to yield functionals reliably predicting singlet *and* triplet excitation energies and, with this, singlet-triplet gaps. To design such functionals, DFT excitation energies were fitted to the MS-CASPT2 benchmark values using the local correlation coefficient and amount of exact exchange/the range-separation parameter as the two fit parameters. In the fitting procedure, both fit parameters were

independently varied in steps of 0.5 (local correlation coefficient) or 2.5% (HF exchange)/0.025 Bohr^{-1} (range-separation parameter). Depending on the nature of the functional, i.e., on the nature of the correlation part, different scaling factors for the amount of local correlation were obtained (Table 13). As ωB97X-D and BHLYP provide rather accurate singlet excitation energies, the amount of HF exchange was left unchanged. The fit parameters, i.e., the local correlation coefficients and the amount of exact exchange, are shown in Table 13. Optimal values differ slightly for different molecules.

Table 13: Optimal fit parameters for the range separation parameter ω to obtain optimal singlet (S) and triplet (T) TDA excitation energies, for the HF amounts, and for the local correlation coefficients c(corr) as a function of the molecules. "ni" indicates that tuning the range-separation parameters or the amount of exact exchange does not improve ("ni" = "not improved") the corresponding excitation energies. The coefficient for the local correlation in standard functionals is 1. The reader is referred to [758] for more details.

	ωB97X-D			PBE0			B3LYP			BHLYP	BP86	BLYP
molecule	ω(S) [Bohr^{-1}]	ω(T) [Bohr^{-1}]	c(corr)	HF(S) [%]	HF(T) [%]	c(corr)	HF (S) [%]	HF (T) [%]	c(corr)	c(corr)	c(corr)	c(corr)
anthracene	0.125	ni	1.50	38	ni	3.00	35	ni	2.50	2.50	3.50	3.50
tetracene	0.125	ni	2.00	45	ni	4.00	45	ni	4.00	3.00	5.00	5.00
pentacene	0.125	ni	2.00	50	ni	4.00	45	ni	3.50	3.00	4.50	4.50
rubrene	0.100	ni	2.00	35	ni	3.50	35	ni	3.00	3.00	4.00	4.00
DIP	0.150	ni	1.50	55	ni	4.50	45	ni	5.00	2.50	7.50	8.00
thiophene	0.100	ni	2.00	33	ni	4.00	30	ni	3.00	2.50	6.50	6.50
HB194	0.150	0.500	3.00	43	65	7.00	35	65	8.00	2.50	ni	ni
MD353	ni	0.900	8.00	25	ni	10.00	ni	85	8.00	5.00	ni	ni
DPP	0.125	ni	2.50	40	ni	5.00	35	ni	4.50	3.00	7.50	7.50
squaraine	ni	ni	5.00	na	ni	5.00	ni	ni	5.00	3.50	6.50	7.00
„triamine"	0.125	0.200	1.00	40	67.5	4.50	35	ni	5.00	1.50	ni	ni
„triamine-methoxy"	0.200	ni	3.50	55	ni	6.00	50	ni	7.50	4.00	ni	ni
„triamine-aldehyde"	0.125	ni	2.75	38	ni	8.50	35	ni	10.00	3.25	ni	ni

Values are separately averaged for "normal" and "charge-transfer compounds" (ωB97X-D: "normal compounds": c(corr)=2.0; "charge-transfer compounds": c(corr)=3.0; BHLYP: c(corr)=3.5 for all compounds; B3LYP: "normal compounds": HF=20%, c(corr)=3.5; "charge-transfer compounds": HF=40%; c(corr)=7.0; PBE0: "normal compounds": HF=25%, c(corr)=4.5; "charge-transfer compounds": HF=35%; c(corr)=6.5). The adjusted functionals are used to compute singlet and triplet excitation energies. Resulting errors are compared to errors of the original functionals and to the best-performing standard functional, M06-2X (Figure 35).

From the data, a net improvement of the performance of all functionals becomes evident. The final error range of the fitted functionals is very small. Even more importantly, the remaining errors of the

fitted functionals are nearly independent from the exact nature of the functional and lie below the "chemical accuracy of excited states"[843] of 0.1 eV. Of course, due to the non-empirical tuning and fitting using the same set of molecules, errors naturally decline. Nevertheless, such a systematic decrease for all molecules and all functionals could not be expected *a priori*. Therefore, this allows for the conclusion that by scaling the same-spin/opposite-spin correlation and the amount of HF exchange, functionals efficiently predicting triplet excitation energies and singlet-triplet gaps with a very high accuracy can be obtained.
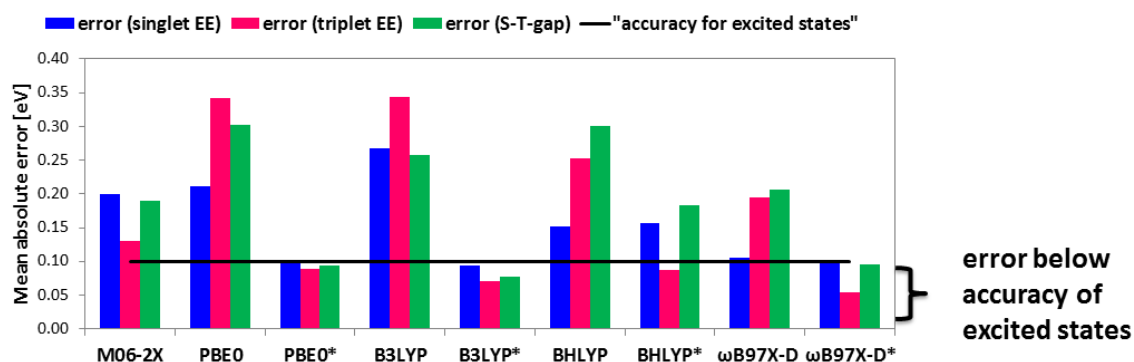

Figure 35: Mean absolute errors for singlet and triplet excitation energies and resulting singlet-triplet gaps of tuned functionals with an optimized amount of HF exchange and optimal local correlation coefficients. Linear-response adiabatic TD-DFT singlet excitation energies and TDA triplet energies were employed. The asterisk * refers to optimally fitted functionals, while standard functionals are indicated without an asterisk. Reproduced with permission from [758]. © 2016 Elsevier B.V.

To summarize the presented detailed analysis of different excitation energies of molecular p-type semiconductors, a few key conclusions can be drawn that complement existing literature data:

1. For large-scale excited-state calculations, the investigated basis set dependence is of major importance. An unprecedented error cancelation between the basis set error of the geometry optimization and of the excited-state calculation was found and rationalized. It can be utilized to keep high-level *ab initio* calculations of a number of excitations as well as excited-state optimizations computationally affordable.

2. The ADC(2) and CC2 methods were shown to provide reliable singlet excitation energies (irrespective of the amount of charge transfer) and triplet states (irrespective of the exact molecular structure). Spin-component scaling improves the accuracy of both methods for all states. In contrast to CC2 and ADC(2), the herein employed SCS parameters deteriorate the performance of CIS(D) approaches, which usually overestimate singlet and triplet excitation energies. The further blue shift induced by SCS increases average errors.

    The reliability of SCS-CC2 was already indirectly exploited when SCS-CC2 adiabatic excitation energies were employed as benchmark values for adiabatic singlet and triplet transitions.

Moreover, SCS-CC2 excited-state geometries should be reasonably accurate to be employed in multiscale approaches whenever excited-state monomer geometries are of interest.

3. Especially ωB97X-D, but also CAM-B3LYP and SOGGA11X provide very accurate singlet excitation energies. Moreover, when employed in conjunction with TDA, errors of resulting triplet excitation energies are also rather small. As a standalone functional, M06-2X performs best for triplet excitation energies, especially within a Δ-SCF treatment. M06-2X singlet excitation energies are also satisfyingly accurate although they tend to be too high due to the large amount of HF exchange.

   Singlet-triplet gaps are also most accurately predicted with M06-2X, using TD-DFT singlet excitation energies and Δ-SCF triplet energies. Yet, also ωB97X-D delivers very accurate gaps in a TD-DFT/TDA protocol for singlet/triplet energies.

4. ZINDO delivers very accurate neutral singlet excitation energies. This is very important because the very low computational effort could allow for a broad application of ZINDO excited-state calculations to large systems.

Ground-state geometries and excitation energies were benchmarked in the last two sections. In the next section, a different way of conceptualizing adiabatic transition energies, i.e. via exciton reorganization energies, is briefly addressed. Adiabatic excitation energies and exciton reorganization energies are in a certain sense equivalent because they both require excited-state optimizations. They thus depend both on the quality of the underlying excited-state gradients. However, while exciton reorganization energies are calculated as energy differences between optimized ground- and excited-state geometries both in either the ground or the excited state, adiabatic excitation energies correspond to energy differences between these geometries in different states.

5.4 Benchmarking exciton reorganization energies

Usually, in order to calculate macroscopic transport properties in a multiscale approach, several molecular quantities are required as input parameters, such as reorganization energies for exciton or charge transport.[844] While many investigations on charge reorganization energies exist (see also below),[666,845] exciton reorganization energies have hardly been directly addressed. While this represents certainly an important gap in the literature that should be filled, it could result to some extent from the fact that exciton reorganization energies correspond to energy differences between absorption and fluorescence energies, both of which have been comprehensively analyzed from a theoretical perspective.[844,724,846,847,848] In a similar way, an extensive investigation of vertical and also of adiabatic transition energies was presented in detail in the last section ("Benchmarking vertical excitation energies of molecular semiconductors").

Nevertheless, it is illustrative for a number of reasons to briefly reexamine some of the presented results from the point of view of exciton reorganization energies. (1) While adiabatic excitation energies take into account only the excited-state relaxation, exciton reorganization energies are composed of the excited-state and the ground-state relaxation that a migrating exciton induces.[rrr] In view of the rather complex electronic ground-state structures of many molecular semiconductors (see Section "Benchmarking ground-state geometries"), the additional description of the ground-state relaxation indirectly reflected in the exciton reorganization energies seems worth analyzing. (2) The dimensions of adiabatic excitation energies and exciton reorganization energies differ. Whereas adiabatic transition energies in most molecular semiconductors amount to several eV, typical values for exciton reorganization energies are around a few hundred meV.[532] This arises from the fact that exciton reorganization energies are calculated as differences between two electronic transition energies (absorption and fluorescence) while adiabatic excitation energies correspond to the difference between the large absorption energy and the comparably small excited-state relaxation. Additional factors might determine exciton reorganization energies, i.e., transition energy differences, compared with those decisive for transition energies themselves. The latter were found to essentially dominate adiabatic excitation energies (see Figure 23). (3) It should be always kept in mind that reorganization energies enter exponentially into the Marcus rate equation (see below, also for a discussion of the relevance of the Marcus equation for the hopping process). Therefore, slightly different reorganization energies produce pronounced differences in the corresponding hopping rates.

[rrr] Please note that the terms ground-/excited-state "relaxation" and ground-/excited-state "reorganization" are both used in the literature. "Relaxation" is certainly the more general notion as it does not only refer to the intramolecular electron/hole/excitation-"phonon" coupling, but rather includes a number of phenomena of nuclear relaxation upon a change in electronic structure. Nevertheless, the two terms will be used interchangeably in the following.

Exciton reorganization energies are discussed for selected functionals listed in Table 14. Because of the significant computational cost of excited-state optimizations, only methods with good performances for vertical and adiabatic singlet excitation energies were employed (see previous section). Therefore, the three best performing functionals for the computation of several excited states per molecule, i.e., SOGGA11X, CAM-B3LYP, and ωB97X-D, are used. Additionally, LC-BLYP and TD-HF are included (Table 14) since TD-HF in particular was shown to yield correct trends for excited-state properties.[849] From a user's point of view, correct trends are often even more important than numerical accuracy. The same is true for LC-BLYP, which, similar to TD-HF, reliably reproduces the excited-state order in spite of generally overestimated excitation energies (see previous section).[763]

As for the adiabatic excitation energies (Figure 23), SCS-CC2 is used to compute the benchmark values. The cc-pVDZ[705] basis was used for the SCS-CC2 and DFT calculations to keep them computationally feasible (see above). A dispersion correction was added to CAM-B3LYP and to LC-BLYP, using the S6 and S8 parameters for BLYP in the latter case. An ultrafine grid was employed, and all calculations were conducted in the gas phase. The Gaussian program was used for the DFT calculations.[718] Exciton reorganization energies for SCS-CC2 and HF were calculated with the Turbomole[179] program package.

Table 14: Methods employed to calculate exciton reorganization energies. Due to the good performance for vertical excitation energies, SCS-CC2 is employed as the benchmark method.

method	References
reference values	
SCS-CC2	256,180,760,761,762,703,46
benchmarked methods	
HF	706
SOGGA11X	714
ωB97X-D	143
CAM-B3LYP-D3	133,707,712,713,708,709,140
LC-BLYP-D3	707,708,709,140,132

Figure 36 shows the errors of computed exciton reorganization energies. Absolute percentaged errors (upper panel), signed percentaged errors (center panel), and signed errors in eV (lower panel) are compared. As always, average errors as well as errors for each compound class are given. Moreover, it has been investigated both theoretically[645,850] and experimentally[851,852] that merocyanines can undergo an excited-state torsional motion. Naturally, this excited-state torsion significantly increases total exciton reorganization energies, which consequently attain sizes of 1-2 eV. When calculating

average errors, either for polar dyes or for all compounds, these exciton reorganization energies would therefore dominate the averaging. In order to avoid this, only exciton reorganization energies of merocyanines that do not spontaneously twist in the excited state, i.e., of HB194, are included in the average over all compounds. Furthermore, errors of the exciton reorganization energies of all merocyanines and only of HB194 are separately indicated in Figure 36. Errors for HB194 are highlighted with an asterisk ("high polarity*"), in contrast to averages for all merocyanines denoted with "high polarity".
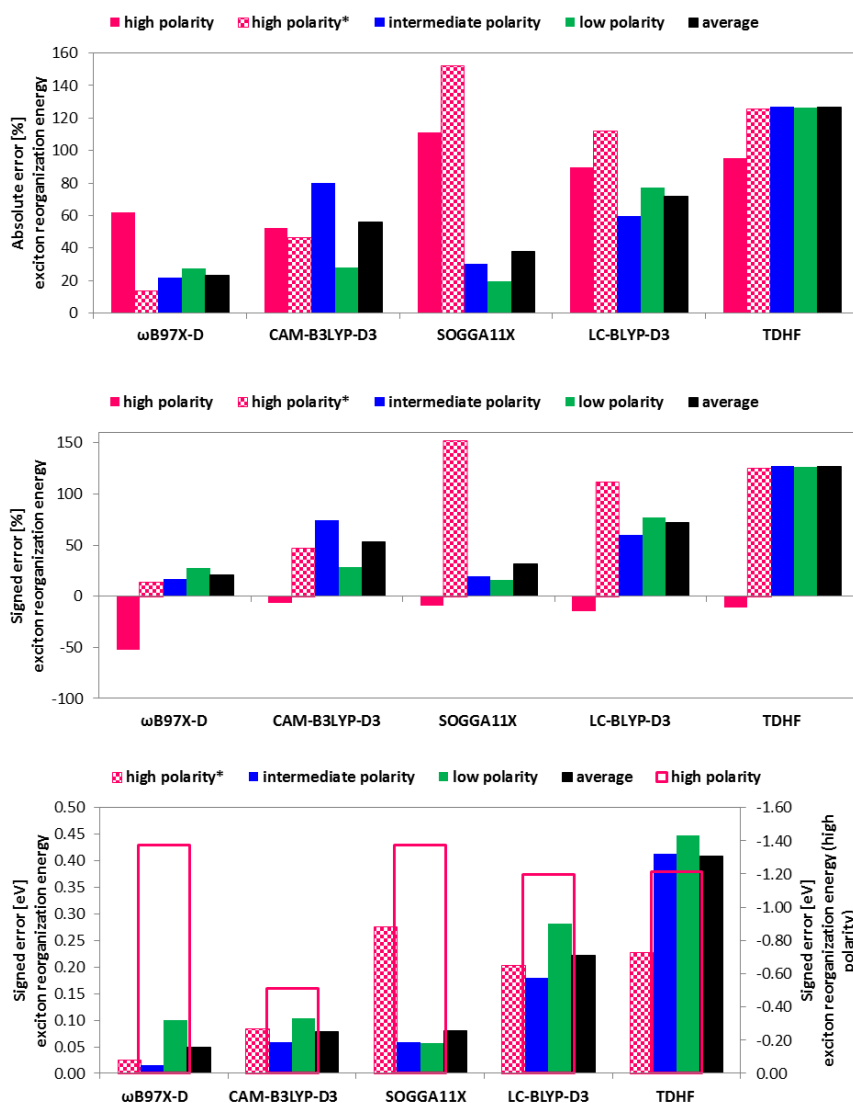
Figure 36: Errors of exciton reorganization energies. Please note that some merocyanines may undergo an excited-state torsion upon photoexcitation (see text), which is correctly reproduced in the SCS-CC2 calculations, but neither in all DFT functionals nor in TD-HF computations. The excited-state torsion results in both large exciton reorganization energies and large errors. HB194 does not twist upon electronic excitation so that its exciton reorganization energies and the deviations between different methods are smaller. In contrast to the other merocyanines, its errors are therefore on the same order as those for all other compounds. Hence, to avoid overemphasizing the impact of the excited-state torsion of the merocyanines on resulting error bars, the errors for exciton reorganization energies of HB194 only are additionally given and indicated as "high polarity*".

Figure 36 illustrates that especially ωB97X-D performs very well, having the smallest percentaged absolute errors (first panel), the smallest percentaged signed errors (second panel) as well as the smallest overall signed errors (third panel) among all functionals. In average, percentaged errors of ωB97X-D are below 20% for all compounds. Larger errors are found for LC-BLYP and particularly for TD-HF. Percentaged absolute and signed errors of LC-BLYP amount to 60%, with corresponding average errors attaining 100% for TD-HF (Figure 36). However, these errors are almost constant and uniformly distributed over all compound classes. Therefore, despite a reduced numerical accuracy, LC-BLYP and TD-HF provide a balanced description of the exciton reorganization energies of all compounds. This mirrors the literature findings.[849,532]

CAM-B3LYP and SOGGA11X yield errors of an intermediate size in between the errors of ωB97X-D and TD-HF/LC-BLYP. Especially the performance of SOGGA11X depends on the compound class. It provides accurate exciton reorganization energies of apolar semiconductors and of dyes of intermediate polarity. However, its description of the exciton reorganization energies in merocyanines is rather poor since it is incapable of assessing both the excited-state torsion and the inversion of the bond length alternation (BLA) pattern[sss] in the merocyanines' excited state.[645] The completely incorrect excited-state BLA explains furthermore why the SOGGA11X errors for exciton reorganization in HB194, which does not twist, are rather significant as well. These failures of SOGGA11X could resort from the missing long-range correction that, according to investigations of Jacquemin, is important to properly describe electron correlation and BLA values (see above).[732,736,733] In contrast, CAM-B3LYP performs reasonably well but its performance differs also for different types of compounds. On the one hand, it correctly predicts excited-state torsions in merocyanines. Concomitantly, it yields correct exciton reorganization energies for these molecules. On the other hand, as already discussed above, its performance is slightly weaker for the dyes of intermediate polarity, maybe because the different correlation regimes important for the dyes' geometries are somewhat incompletely included in CAM-B3LYP. This, in turn, would suggest that the slightly limited accuracy of CAM-B3LYP for exciton reorganization energies results mainly from errors already present in the ground-state description of the molecules. The interpretation that CAM-B3LYP actually performs well for excited states but suffers in some cases from an inaccurate ground-state treatment is supported by investigations of Mennucci and coworkers. In a benchmark on excited-state geometries of organic molecules in the gas phase and in solution, they found that CAM-B3LYP performs well for excited-state geometries while other functionals like B3LYP and PBE0 can be more accurate for ground-state structures.[724] A benchmark study of wave-function and TD-DFT approaches on the uranyl(IV) cation by Réal et al. led to equivalent conclusions.[853]

[sss] Please note that none of the employed functionals (Table 14) correctly captures the excited-state inversion of the bond length alternation in merocyanines. However, SOGGA11X performs particularly poorly.

The results in Figure 36 raise the question to what extent the presented analysis of exciton reorganization energies differs from the discussion of adiabatic transition energies, i.e., for which additional insight it allows. A few aspects are outlined. Since exciton reorganization energies have not been investigated, all of these conclusions are new.

1. The ωB97X-D functional performs very well for both adiabatic transition energies and exciton reorganization energies. These findings rely on the one hand on the very accurate ground-state geometries of ωB97X-D (see Section "Benchmarking ground-state geometries") and on the other hand on the reliable ωB97X-D vertical excitation energies (see Section "Benchmarking vertical excitation energies of molecular semiconductors"). Moreover, ωB97X-D excited-state gradients and structures have to be essentially correct because otherwise, no accurate exciton reorganization energies could be obtained. For later-on large-scale computations, the promising accuracy of ωB97X-D for diverse molecular properties suggests using this functional whenever computationally feasible.

2. Similar to their overestimation of transition energies, LC-BLYP and TD-HF overshoot for exciton reorganization energies. However, the size of the error of exciton reorganization energies does not depend on the compounds, in contrast to the systematically varying error of transition energies.

3. SOGGA11X was found to be quite accurate for excitation energies as well as for ground-state geometries (see previous sections). However, its performance deteriorates apparently as soon as excited-state gradients and excited-state structures are involved. This result becomes evident only from the analysis of exciton reorganization energies (Figure 36) and not from the results on adiabatic excitation energies (Figure 23). In the latter case, the SOGGA11X deficiency for excited-state gradients is presumably obscured by its rather accurate excitation energies. These accurately predicted excitation energies largely dominate adiabatic transition energies and contribute considerably more than the excited-state relaxation.

4. CAM-B3LYP yields reliable excitation energies. However, the reduced accuracy of CAM-B3LYP for ground-state geometries of the dyes of intermediate polarity is reflected in slightly less accurate exciton reorganization energies of these dyes. It is still rather accurate for exciton reorganization energies of merocyanines, which could be due to the long-range correction. In a previous section ("Benchmarking ground-state geometries"), the long-range correction was found to be important for correct structures and BLAs in merocyanines.

This summary illustrates that (1) accurate ground-state geometries (in contrast to CAM-B3LYP), (2) accurate excitation energies (in contrast to LC-BLYP and TD-HF) and (3) accurate excited-state gradients (in contrast to SOGGA11X) are needed to calculate exciton reorganization energies as

accurately as possible. All these conditions are only fulfilled by ωB97X-D. The presented analysis of exciton reorganization energies has especially clarified the importance of the first and the third condition, which were not evident from the discussion of adiabatic excitation energies.

After having discussed ground- and excited-state properties of molecules in the last sections, an analysis of cationic energies and structures of the molecular p-type semiconductors is the next consequential step. It should be kept in mind that fullerene C_{60} will always be employed as the electron acceptor. Furthermore, to fully assess molecular properties in preparation of multiscale calculations on aggregates, charge reorganization energies should be also analyzed in addition to exciton reorganization energies.

5.5 Benchmarking charge reorganization energies

The following discussion parallels [854].

Similar to exciton transport (see previous section), charge transport in amorphous organic thin films is usually assumed to proceed via a succession of random hopping processes between individual hopping sites. Rates for the hopping steps are calculated with the classical Marcus rate equation. While Marcus rates depend on the square of the electronic coupling between the initial and the final hopping sites, they are largely determined by the charge reorganization energy,[524,855] which enters exponentially. As already mentioned for exciton reorganization energies, the reorganization energy is a molecular property. It is used as an input parameter in multiscale computations of macroscopic quantities of organic materials. In order to accurately predict macroscopic charge-transport properties of these organic materials, using correct charge reorganization energies as input parameters is absolutely mandatory. Please note that charge reorganization energies are also experimentally investigated. They are thus furthermore of utility to understand experimentally observed charge-transport phenomena and to establish structure-property relationships.[856,857,858,859]

Like exciton reorganization energies, charge reorganization energies can be subdivided into an internal (intramolecular) and an external (intermolecular) contribution.[645] Liu and Troisi[860] as well as Solà and Voityuk[861] and coworker discussed effects and errors arising from the external contribution in more detail. Analogous investigations on DNA bases were conducted by Newton and Rösch.[862] They all pointed out that the predicted values for external reorganization energies are extremely method- and model-dependent. A combined experimental and theoretical study of Kocherzhenko et al. revealed in addition that among others, static disorder plays a major role in determining the size of the external charge reorganization energy.[863] The fact that static and dynamic disorder would have to be included further underlines the difficulty of correctly predicting external reorganization energies. However, as this section is entirely concerned with molecular quantities, only intramolecular charge reorganization energies are computed and discussed in the following. Moreover, they seem to be considerably more important because it was found for oligoacenes that the internal contribution to the total reorganization energy is much larger than the external one.[855,603,864]

From a computational perspective, the calculation of charge reorganization energies can be troublesome because it requires energy calculations and geometry optimizations of radical species. Although multi-reference methods are very accurate for radical species,[865] they cannot be employed for molecules as large as most molecular p-type semiconductors. High-level *ab initio* methods cannot be used either because they are based upon a HF reference wave function which usually suffers from spin contamination. Therefore, DFT is almost always employed in the literature to compute charge reorganization energies.[845,862,565,866] However, also DFT charge reorganization energies can be

erroneous since all DFT calculations are subject to the above-discussed MSIE (many-electron self-interaction error), which differs for states with different numbers of electrons. This might reduce the reliability of DFT charge reorganization energies, and underlines the need for a DFT benchmark of (internal) charge reorganization energies because no comprehensive benchmarks on the accuracy of different DFT functionals for charge reorganization energies exist in the literature. Therefore, to obtain as accurate values for them as possible for later-on multiscale applications, the ability of different DFT functionals to compute charge reorganization energies of molecular p-type semiconductors is carefully benchmarked in this section. The benchmarked functionals are given in Table 15. Two long-range corrected functionals, i.e, ωB97X-D and LC-BLYP, three hybrid functionals – B3LYP, SOGGA11X, and PBE0 – and three pure functionals – BLYP, PBE, and the meta-GGA M06-L – are included (Table 15). Apart from the functionals that were shown to provide were accurate ground-state geometries (ωB97X-D, SOGGA11X, M06-L, see Section "Benchmarking ground-state geometries"), this involves the standard functionals PBE0, PBE, B3LYP, and BLYP along with its long-range corrected counterpart LC-BLYP. It is worth noting that more exact exchange in DFT calculations on open-shell systems is necessarily accompanied by an increasing amount of spin contamination. However, S^2-values of the radical species evaluated in the following never exceed 0.80.

Table 15: Functionals employed in the benchmark of charge reorganization energies.

method	References
reference values	
IP-EOM-CCSD	255
benchmarked methods	
ωB97X-D	143
LC-BLYP-D3	707,708,709,140,132
B3LYP-D3	707,712,713,708,709,140
PBE0-D3	803,801,802,140
SOGGA11X	714
BLYP-D3	707,708,709,140
PBE-D3	801,802,140
M06-L-D3	710,140

The two long-range corrected functionals (ωB97X-D and LC-BLYP) are employed both in their standard version and in their empirically-tuned version, which is indicated as "(IP)". Empirical tuning instead of non-empirical tuning is used because it was found to yield very good results. In the empirical tuning

procedure, the range separation parameter in ωB97X-D and in LC-BLYP is adjusted (in steps of 0.02 Bohr[-1]) so that the molecular HOMO energy of each molecule corresponds to its ionization potential obtained in high-level *ab initio* IP-EOM-CCSD[255] calculations. IP-EOM-CCSD is known to deliver very accurate ionization potentials.[255] IP-EOM-CCSD calculations are based on a closed-shell reference and the coupled-cluster expansion to the second order. Due to their considerably computational demand, the molecules in Figure 5 have to be further reduced in size to allow for the IP-EOM-CCSD calculations. The abridged model systems in Figure 37 are created and used for the benchmark of DFT charge reorganization energies.
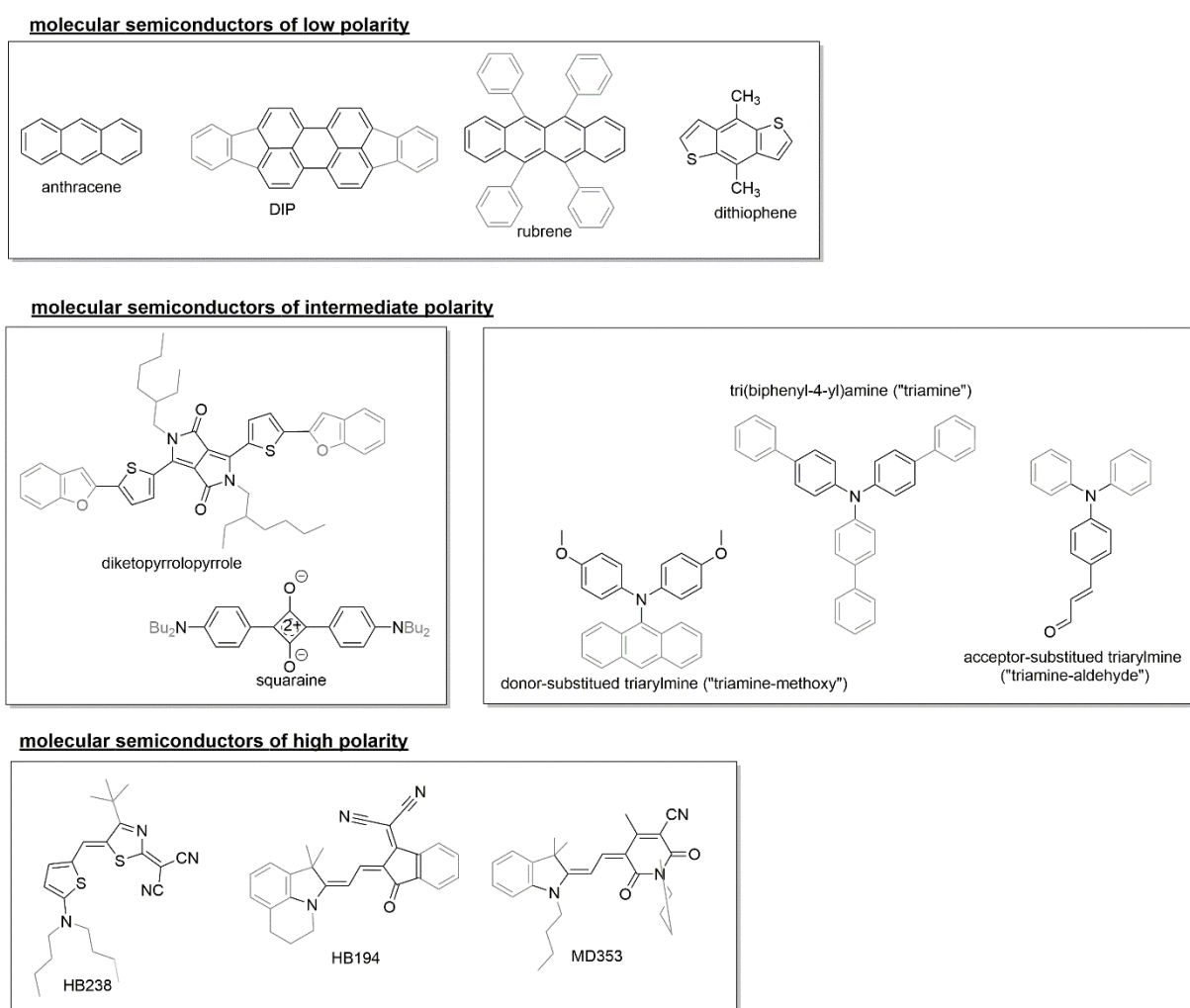

Figure 37: Molecules and abridged model systems for the IP-EOM-CCSD benchmark calculations. HB238 contains two polarizable aromatic ring systems including sulfur atoms. Since these polarizable aromatic moieties with no counterpart in MD353 or HB238 could affect charge reorganization energies, HB238 is again considered in this part of the benchmark section.

Table 16: Ionization potentials obtained for all molecules comprised in the test set (Figure 37) using the SCS-CC2/cc-pVDZ optimized geometry ("SCS-CC2") or the SCS-MP2/cc-pVTZ optimized geometry ("SCS-MP2").

Molecule	IP-EOM-CCSD [eV]	
	SCS-CC2	SCS-MP2
anthracene	7.02	7.00
diketopyrrolopyrrole	6.75	6.75
Dip	6.65	6.65
dithiophene	7.02	7.00
HB194	7.63	7.67
HB238	7.15	7.18
MD353	7.66	7.70
rubrene	6.59	6.59
squaraine	6.41	6.41
triamine	6.91	6.92
triamin-aldehyde	7.37	7.38
triamine-methoxy	6.49	6.48

Vertical IP-EOM-CCSD ionization potentials (IPs) calculated for the empirical tuning procedure are compared in Table 16 for two different geometries of the abridged model systems (Figure 37), namely for the SCS-CC2/cc-pVDZ[256,180] and the SCS-MP2/cc-pVTZ[70,703,704] optimized geometry. Table 16 demonstrates that the geometry influences resulting IPs only in a limited way. For the tuning, the average of the values in Table 16 is used together with the DFT-optimized geometry.

High-level *ab initio* IP-EOM-CCSD ionization potentials (instead of measured IPs) have to be used to tune ωB97X-D and LC-BLYP because experimental gas-phase values are not available for all molecules. Nevertheless, IP-EOM-CCSD ionization potentials compare well with experimental counterparts of those molecules with existing experimental data. To cite only two examples, the experimental ionization potential in Rydberg absorption measurements in anthracene was found to be 7.15 eV,[867] which is very close to the IP-EOM-CCSD value of 7.00 eV. Similarly, the predicted ionization potential of 6.91 eV for the diphenylamine fragment (Figure 37) agrees nicely with the experimentally determined value of 7.19 eV.[868] It should be furthermore emphasized that whenever several experimental values for the ionization potential of a given molecule exist, they tend to significantly

deviate from one another.[869] This underlines that using experimental reference values for the empirical tuning is somewhat problematic.

Grimme's dispersion correction[140] was added to the DFT functionals if available. All calculations were conducted in the gas phase with the Gaussian program package.[718] Similar to above, the cc-pVDZ basis sets are employed.[705] The NWChem program package is used for all IP-EOM-CCSD calculations.[870]

The limited range of methods applicable to open-shell calculations on the medium- to large-size molecules raises the question how to obtain accurate benchmark values for the charge reorganization energies. IP-EOM-CCSD,[255] already used in the IP-tuning procedure, was shown to provide accurate energies and geometries for charge-localized and delocalized radical species at a comparably moderate computational cost.[871,872] Yet, IP-EOM-CCSD geometry optimizations on the medium-size molecular organic semiconductors in Figure 37 still largely exceed computational feasibility although the abrdiged systems are already considerably smaller than the underlying complete systems (Figure 5). Therefore, geometries optimized with optimally-tuned long-range corrected functionals are used instead of geometries optimized at the IP-EOM-CCSD level of theory. IP-EOM-CCSD single-point calculations on these DFT-optimized structures are subsequently carried out to deduce benchmark values. The latter aspect, however, presupposes that geometries obtained with IP-tuned functionals are essentially correct. Otherwise, wrong DFT geometries could spoil the benchmark values.

A number of literature results indeed suggest that IP-tuned range-separated hybrids provide quite accurate geometries. Findings by Brédas and coworkers indicate that IP-tuned functionals deliver reliable geometries even for the limiting case of computationally very challenging mixed-valence compounds.[835] In line with this, Jacquemin and Autschbach also proposed that IP-tuned functionals offer an efficient way to obtain accurate excited-state geometries.[823,873] According to an investigation on the crystal structure of rubrene by Sherrill and Brédas and coworkers, IP-tuned functionals correctly predict the interplay between intra- and intermolecular interactions in crystalline rubrene. As a consequence, they yield very accurate rubrene conformations resulting from this interplay.[665]
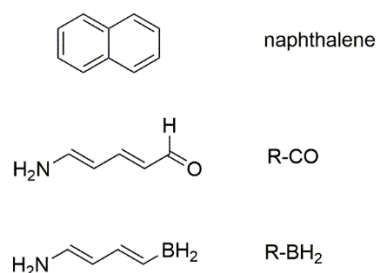

Figure 38: Small model systems used to compare geometries obtained from optimizations with IP-EOM-CCSD and with IP-tuned functionals.

244

Although these literature results imply that geometries optimized with optimally tuned hybrids can be very reliable, three small model systems are introduced (Figure 38) to evaluate the quality of the geometries obtained with the herein employed ωB97X-D(IP) functional specifically tuned for each molecule. The model systems are chosen so that geometry optimizations with IP-EOM-CCSD are computationally affordable. Hence IP-EOM-CCSD//IP-EOM-CCSD and IP-EOM-CCSD//DFT(IP) (and in addition DFT(IP)//DFT(IP)) charge reorganization energies can be compared, as shown in Table 17. Please note that only cc-pVDZ basis sets are affordable in combination with the demanding IP-EOM-CCSD calculations.

Table 17: Comparison of charge reorganization energies calculated for the three small model systems and IP-tuned functionals and/or IP-EOM-CCSD calculations.

model system	ωB97X-D(IP)// ωB97X-D(IP) [eV]	IP-EOM-CCSD// IP-EOM-CCSD [eV]	IP-EOM-CCSD// ωB97X-D(IP) [eV]
naphthalene	0.23	0.22	0.23
R_BH2	0.47	0.47	0.47
R_CO	0.47	0.48	0.47

Table 17 shows that charge reorganization energies obtained from IP-EOM-CCSD single-point calculations using geometries optimized at the same level of theory and from IP-EOM-CCSD single-point calculations and geometries optimized with IP-tuned functionals are equal up to 0.01 eV. This underlines the reliability of geometries obtained with IP-tuned functionals, in line with the outlined literature results. Furthermore, it justifies using charge reorganization energies obtained from IP-EOM-CCSD single-point calculations on DFT(IP)-optimized geometries as benchmark values in the following.

For a first overview, Figure 39 displays the charge reorganization energies of the complete molecules calculated with the functionals listed in Table 15. As in the last sections, the functionals are approximately arranged according their amount of exact exchange (see top row of Figure 39). For each molecule, computed charge reorganization energies vary in a characteristic way with the employed functionals. Functionals with large amounts of HF exchange yield large charge reorganization energies, while the smallest charge reorganization energies are obtained with pure GGAs. Differences in the charge reorganization energies often amount to 0.2-0.3 eV. Due to the exponential dependence of the charge transport rates on the charge reorganization energies, such deviations are quite significant because they can result in a ten-fold increase/decrease of corresponding hopping rates. Since the charge reorganization energies of all molecules depend in a similar manner on the amount of exact

exchange, predicted trends among the molecules remain the same for all functionals. For instance, irrespective of the exact functional, the diketopyrrolopyrrole always possesses a rather large charge reorganization energy. In contrast, charge reorganization energies of the triphenylamine-based compounds are somewhat smaller, in line with the expectations.[682,683] However, it is worth noting that the ratios of charge reorganization energies calculated with different functionals for a given molecule change when a different molecule is considered. In a similar way, ratios of charge reorganization energies for different molecules calculated with a given functional are not constant either when a different functional is employed in the calculation.
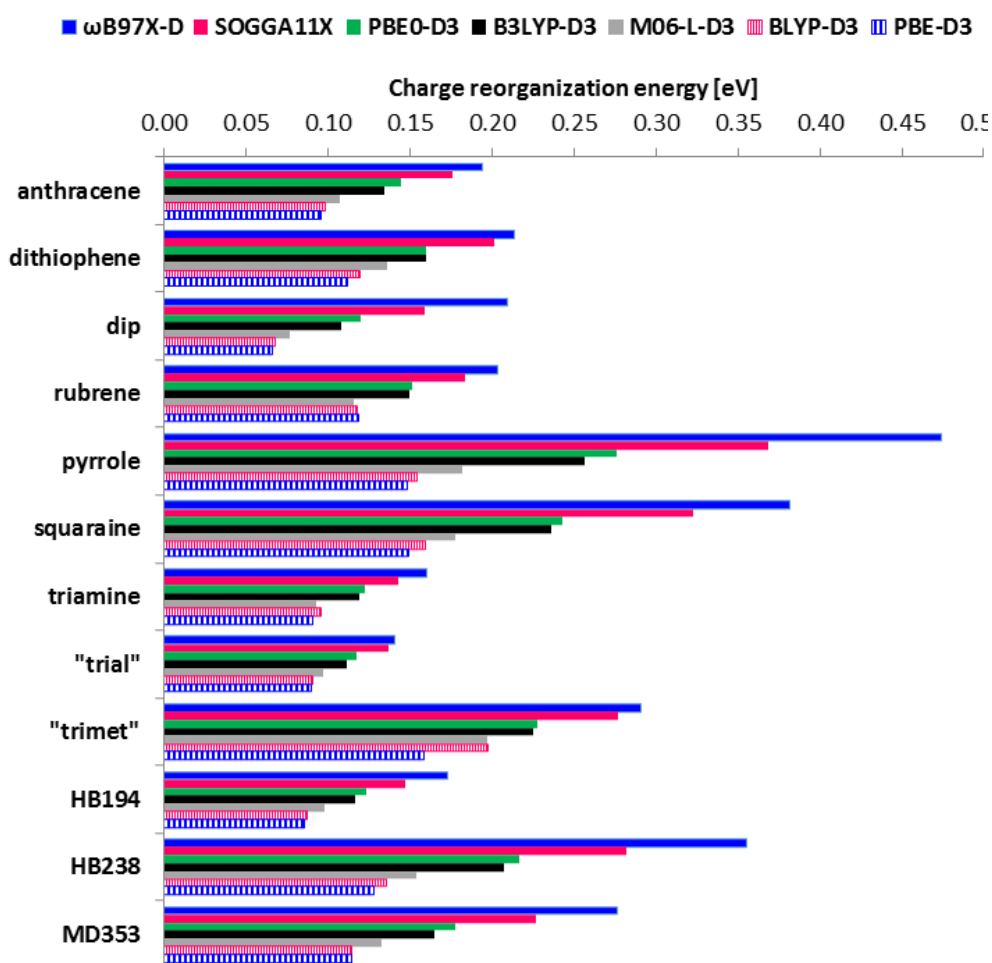

Figure 39: Charge reorganization energies in eV calculated with different functionals (no IP-tuning) for the molecular p-type semiconductors. The complete molecules (not abridged) are used. As already mentioned, since it contains sulfur, HB238 is again included in this part of the benchmark section.
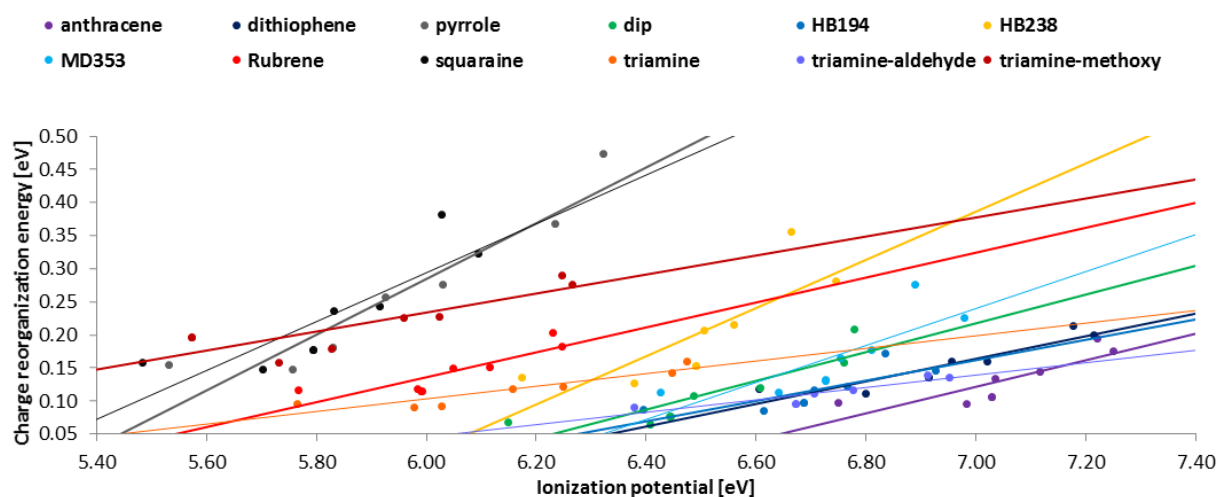
Figure 40: Correlation of charge reorganization energies with the ionization potentials for a given molecule. All reorganization energies and ionization potentials are calculated with the functionals in Table 15. The complete molecules (not abridged) are used. Adapted with permission from [854]. © 2016 Wiley Periodicals, Inc.

It is well-known in DFT that in any finite-sized object, the calculated fundamental gap[144,160] and with this the quasi-particle eigenvalues[160,874] such as the ionization potential depend on the amount of HF exchange in the employed functional. Please keep in mind that despite the nonconstant ratios, the charge reorganization energies in Figure 39 also depend in a qualitatively systematic manner on the amount of exact exchange. Therefore, since both the ionization potentials and the charge reorganization energies correlate with the exact exchange, they necessarily also mutually correlate (Figure 40). Pure functionals yield both small charge reorganization energies and ionization potentials, while considerably larger values are obtained with functionals with a significant amount of exact exchange (Figure 40). The correlation between charge reorganization energies and the amount of HF exchange arises from the changing description of the electron density with more exact exchange. The more HF exchange, the more localized the charges. A highly localized charge induces more structural reorganization when it is created via ionization than a smeared charge which – due to its delocalization and correspondingly small partial charges on individual atoms – barely affects molecular moieties.

As discussed in detail by Baer et al.,[160,147] the ionization potential is intimately linked to the MSIE of DFT. DFT ionization potentials are usually too low, which is more pronounced for GGAs compared to hybrid functionals. According to the rationalization of Baer et al., the underestimation of ionization potentials results from the spurious repulsion of an electron with itself, favoring charge extraction.[147] The self-interaction error can be systematically reduced and even eliminated via non-empirical IP-tuning.[782] Since the ionization potential of a molecule and its reorganization energy calculated with a given functional are obviously related (Figure 40), IP-tuned functionals could therefore possibly yield also more accurate charge reorganization energies. It is assumed that this holds to some extent for

empirical tuning as well (the HOMO energy is enforced to correspond to a very accurately determined ionization potential).

As described above, benchmark values for the charge reorganization energies are obtained from IP-EOM-CCSD single-point calculations using geometries optimized with empirically tuned functionals (LC-BLYP, ωB97X-D). To obtain these benchmark values, the geometry optimizations are performed in a first step, which directly yields charge reorganization energies calculated with IP-tuned functionals. Before conducting the IP-EOM-CCSD single-point calculations, the charge reorganization energies obtained with ωB97X-D(IP) and with LC-BLYP(IP) are compared to analyze to what extent they deviate from one another. Although the validity of geometries obtained with IP-tuned functionals was verified above (Table 17), strong differences between geometries optimized with different IP-tuned functionals and between resulting charge reorganization energies would make the choice of the suitable geometry for subsequent IP-EOM-CCSD calculations difficult. Deducing benchmark values for charge reorganization energies would be barely feasible. The chosen model would thus be questionable.

Figure 41 displays the charge reorganization energies for all molecules obtained with two different IP-tuned functionals, i.e., with LC-BLYP(IP) and with ωB97X-D(IP). Equal ionization potentials were enforced in the IP-tuning procedure. Please note that in all calculations for the benchmark values presented in the following, the abridged model systems were employed (Figure 37). It is evident from Figure 41 that charge reorganization energies calculated with different IP-tuned functionals are almost equal. They usually barely deviate with average differences of 0.01-0.02 eV. Larger differences of 0.05 eV are only found for the squaraine and the aldehyde-substituted triarylamine. The good coincidence of the charge reorganization energies suggests that underlying geometries are rather similar.

Moreover, to further analyze differences between these geometries optimized with different IP-tuned functionals, RMSD values were calculated. Resulting values averaged over both functionals between all neutral and all cationic geometries amount to only 0.020 Å and 0.016 Å, respectively. This corresponds to an approximate five-fold decrease of the RMSD values compared to the values between the standard ωB97X-D and LC-BLYP functionals. The decrease underlines the fact that the nice agreement between the charge reorganization energies (Figure 41) obtained with different tuned functionals is at least in parts due to highly similar geometries. This implies (1) that similar and probably reliable geometries can be obtained with tuned range-separated hybrids and (2) that furthermore IP-tuned functionals could constitute a general route to predict accurate charge reorganization energies (see below).
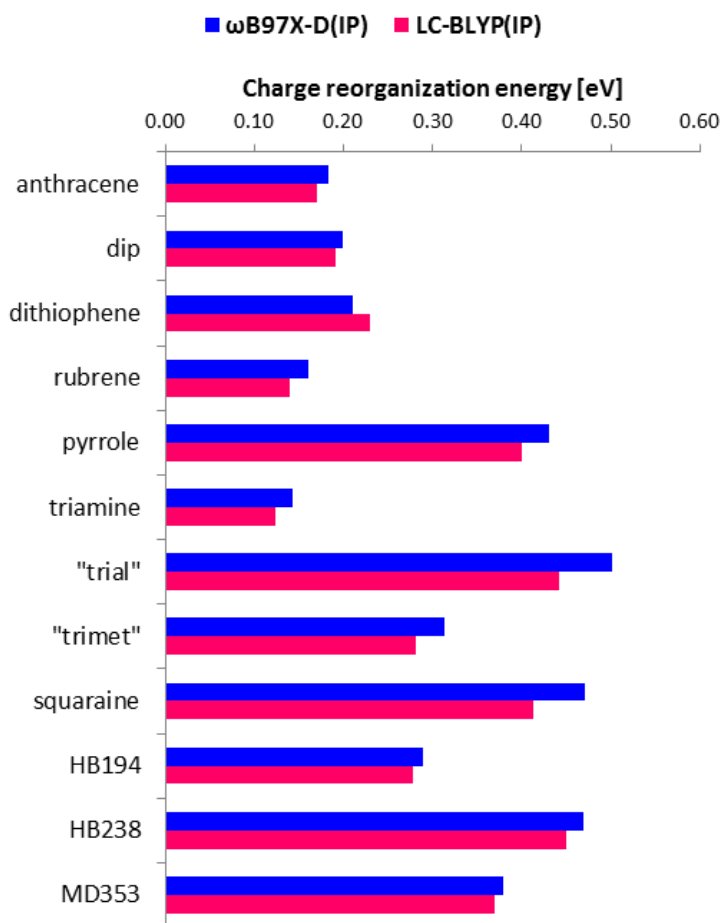
Figure 41: Charge reorganization energies obtained with an empirically tuned version of ωB97X-D ("ωB97X-D(IP)") and of LC-BLYP ("LC-BLYP(IP)"). It should be noted that the abridged model systems were employed (Figure 37). Adapted with permission from [854]. © 2016 Wiley Periodicals, Inc.

To obtain benchmark values of the charge reorganization energies, IP-EOM-CCSD single-point calculations are performed in a second step using the geometries obtained with the optimally tuned long-range corrected functionals. Figure 42 shows the results. Additionally, the deviations to the pure DFT(IP) charge reorganization energies (given in Figure 41) are displayed in Figure 42. It is evident that deviations between charge reorganization energies only obtained with IP-tuned functionals on the one hand and with IP-EOM-CCSD single-point calculations on DFT(IP)-optimized geometries on the other hand are very small (Figure 42, shaded bars). The maximal errors amount to 0.05 eV for MD353 and the aldehyde-substituted triarylamine ("trial"), which corresponds to a six-fold decrease compared to deviations among the standard functionals (in this case, ωB97X-D and PBE). The good coincidence between the DFT(IP) and IP-EOM-CCSD single-point calculations implies that not only geometries of IP-tuned functionals (see above), but also DFT(IP) energies of open-shell species are essentially correct. Therefore, the values in Figure 42 obtained with IP-EOM-CCSD single-point calculations and DFT(IP)-optimized geometries can be used as benchmark values to evaluate the quality of standard DFT functionals for the prediction of charge reorganization energies.
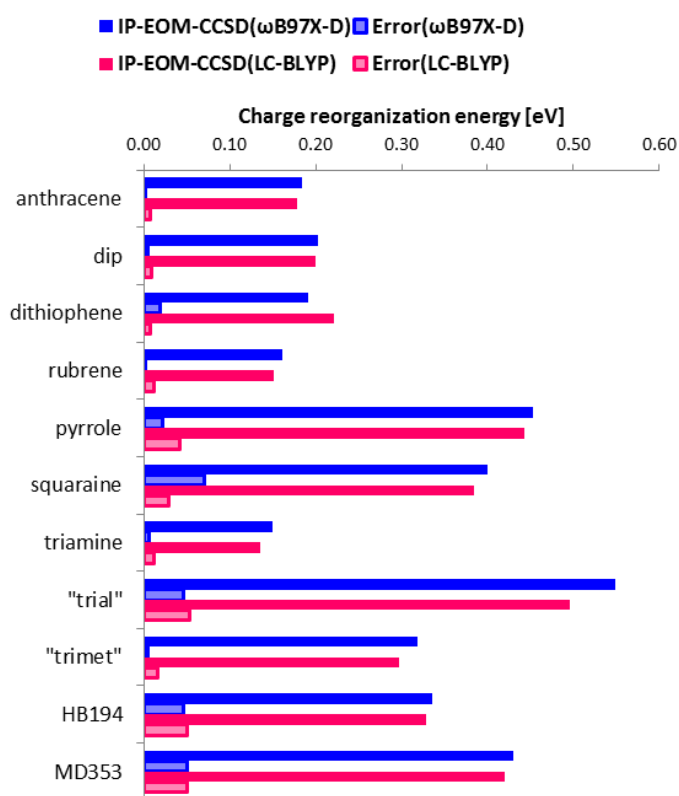
Figure 42: Charge reorganization energies from IP-EOM-CCSD single-point calculations using geometries optimized with IP-tuned long-range corrected functionals. Errors of the pure DFT(IP) charge reorganization energies are indicated with shaded bars. The IP-EOM-CCSD calculation for HB238 did not converge. It should be noted that the abridged model systems were employed (Figure 37). Adapted with permission from [854]. © 2016 Wiley Periodicals, Inc.

For the following statistical analysis of the errors of the charge reorganization energies, the average of the IP-EOM-CCSD values in Figure 42 is used as the reference. The MAE values of all default functionals (Table 15) compared to these average reference values are shown in Figure 43 as a function of polarity. Errors are given in percent to provide a balanced description of all molecules. As always, overall average values as well as polarity-specific deviations are indicated. Moreover, for comparison, the errors of the charge reorganization energies obtained with the IP-tuned functionals (Figure 41) with respect to the reference values, deduced from subsequent IP-EOM-CCSD single-point calculations using the same geometries (Figure 42), are given ("ωB97X-D(IP)", "LC-BLYP(IP)"). It is worth emphasizing that since geometries of the IP-tuned functionals were used to calculate the reference values, errors of the default functionals in Figure 43 are not directly comparable to the errors of their IP-tuned counterparts. Errors of the latter only arise from inaccuracies of the energy calculations whereas potentially erroneous geometries additionally contribute to the overall errors for all other functionals.
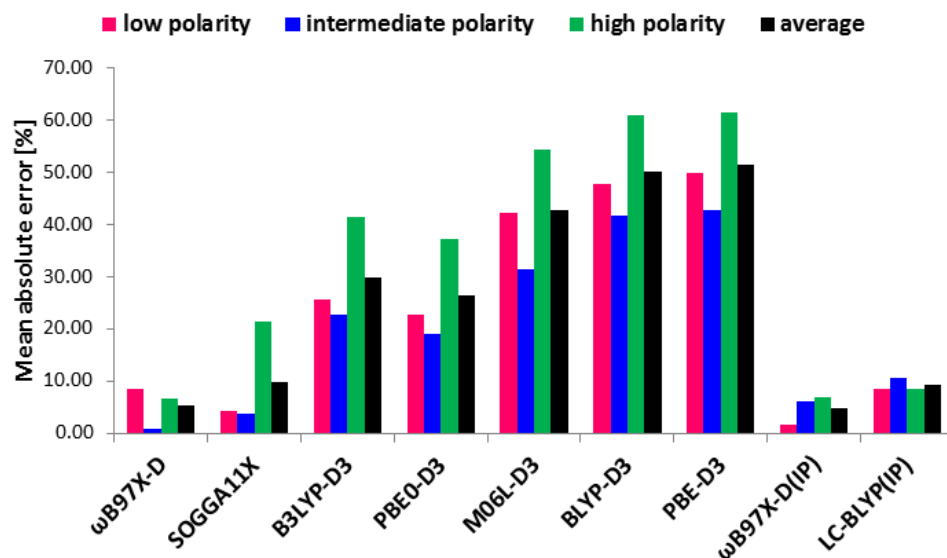
Figure 43: Mean absolute errors [%] of charge reorganization energies calculated with different default DFT functionals benchmarked against the average of IP-EOM-CCSD/cc-pVDZ//ωB97X-D(IP)/cc-pVDZ and IP-EOM-CCSD/cc-pVDZ//LC-BLYP(IP)/cc-pVDZ. It should be noted that the abridged model systems were employed (Figure 37). Adapted with permission from [854]. © 2016 Wiley Periodicals, Inc.

It is evident from the errors (Figure 43) that ωB97X-D, with the default range-separation parameter, and SOGGA11X provide the most accurate charge reorganization energies. ωB97X-D performs twice as well as SOGGA11X. Errors of the default ωB97X-D and the tuned ωB97X-D(IP) functional are very similar and both very small because the default range separation parameter amounts to 0.20 Bohr^{-1},[143] which is almost equal to tuned values ranging mostly between 0.16 Bohr^{-1} and 0.18 Bohr^{-1}. To complete the description of charge reorganization energies, absolute values in eV are given in Table 18.

Table 18: Absolute values of charge reorganization energies in eV calculated for the model systems in Figure 37 with diverse functionals.

Molecule	B3LYP	BLYP	M06-L	PBE	PBE0	SOGGA11X	ωB97X-D
anthracene	0.13	0.10	0.11	0.10	0.14	0.18	0.19
DPP	0.32	0.22	0.25	0.22	0.33	0.41	0.47
DIP	0.15	0.10	0.11	0.10	0.15	0.19	0.22
dithiophene	0.16	0.12	0.14	0.11	0.16	0.20	0.21
HB194	0.23	0.16	0.19	0.16	0.24	0.29	0.32
HB238	0.23	0.14	0.16	0.13	0.25	0.33	0.42
MD353	0.29	0.20	0.24	0.21	0.30	0.36	0.40
rubrene	0.11	0.08	0.08	0.07	0.12	0.15	0.17
squaraine	0.24	0.16	0.18	0.16	0.25	0.31	0.37

„triamine"	0.13	0.10	0.12	0.10	0.13	0.15	0.15
„trial"	0.40	0.30	0.43	0.29	0.42	0.54	0.52
„trimet"	0.27	0.22	0.24	0.21	0.28	0.32	0.32

It is worth emphasizing again that only small energetic differences in the charge reorganization energies result in significantly diverging rates (Table 18). For instance, the rate for charge transport in the diketopyrrolopyrrole as predicted by PBE-D3 is twenty times faster than the rate computed with ωB97X-D (assuming equal coupling constants). Figure 43 illustrates that all GGAs underestimate reorganization energies considerably with respect to the IP-EOM-CCSD reference, which could be due to some excessive charge smearing imposed by the GGA description.[737] The underestimation of approximately 60% gives rise to two- to six-fold overestimated hopping rates. It could furthermore partially account for the general overestimation of predicted charge carrier mobilities based on Marcus hopping rates.[855,532] As trends in charge reorganization energies of different molecules are rather similar for all functionals (Figure 39), this is also in line with the observation that despite a general overestimation of mobilities, trends predicted with Marcus theory are essentially correct.[855]

A comparison of the compound classes with different polarity in Figure 43 shows that all functionals except for the IP-tuned versions perform best for the dyes of intermediate polarity. The Minnesota hybrid functional SOGGA11X delivers the most accurate charge reorganization energies for dyes of low polarity but it is slightly outperformed by ωB97X-D for dyes of intermediate and high polarity. Consequently, ωB97X-D yields the most reliable average charge reorganization energies with a mean error of 5.3%. This perfectly agrees with the above findings for exciton reorganization energies, which were also most accurate when calculated with ωB97X-D.

As stated above, abridged model systems without substituents were used for the benchmark calculations presented in Figure 43 to render the calculations computationally feasible. This raises the question whether charge reorganization energies change significantly when going from the smaller model systems to the complete molecules. Deviations between the abridged and the complete molecules averaged over all functionals are given in Figure 44. Their generally very small sizes indicate that substituents do not significantly influence charge reorganization energies. Internal charge reorganization energies are largely determined by structural changes in the molecular cores and π-conjugated backbones. Therefore, it seems reasonable to assume that all above discussed findings for the smaller model systems can be readily transferred to the complete molecular semiconductors. Despite this general observation, Figure 44 shows that there exist significant deviations in charge reorganization energies for three different molecules, HB194, MD353, and the aldehyde-substituted

triarylamine. A comparison between the model systems and the complete molecules for these three systems suggests that this results from considerable changes in the electronic character when these three model systems are created from the complete underlying molecules (Figure 38, Figure 37). For instance, the complete aldehyde-substituted triarylamine is propeller-shaped, whereas its model system rather corresponds to a push-pull system. This naturally affects all electronic properties, i.e., also the charge reorganization energy. Similarly, the donating character of the nitrogen "push moiety" in MD353 and HB194 gains in strength as the aromatic indoline motif is removed upon creating the model systems. This is also reflected in the bond length alternations of HB194 and MD353 which are significantly larger in the model systems compared to the original molecules. Although this questions the transferability of the charge reorganization energies calculated for these specific model systems to the corresponding complete systems, it is not necessarily contrary to the conclusion that benchmark results for the smaller model systems are equally valid for complete molecules, the more so as the reorganization energies of all other compounds coincide, i.e., are transferable.
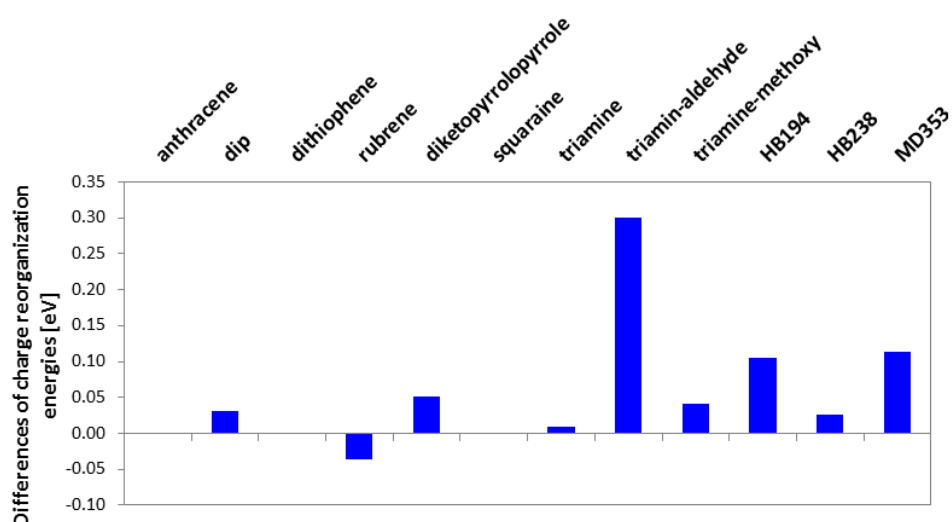
Figure 44: Differences in eV between charge reorganization energies of the abridged model systems and the complete molecules averaged over all functionals included in the benchmark set. Adapted with permission from [854]. © 2016 Wiley Periodicals, Inc.

To summarize the presented benchmark results, the need for a detailed analysis of DFT charge reorganization energies was underlined by considerable differences between calculated charge reorganization energies computed with different functionals. The observation that calculated charge reorganization energies correlate with computed ionization potentials suggests that the reorganization energies are somewhat related to the MSIE. Hence, optimally tuned hybrid functionals with range separation parameters designed to essentially eliminate the MSIE were employed. Benchmark calculations on small model systems indeed showed that charge reorganization energies with different IP-tuned functionals and with IP-EOM-CCSD calculations agree very well. Subsequent benchmark

calculations on model systems constructed from the molecular semiconductors furthermore demonstrated the usefulness of optimally-tuned range-separated hybrids to calculate accurate charge reorganization energies. Among default functionals, SOGGA11X and ωB97X-D with its standard range separation parameter yielded accurate charge reorganization energies. The reliability of the values depends only little on the compound class. Altogether, this suggests using ωB97X-D for the calculation of monomer charge reorganization energies in a later-on multiscale approach, also because its errors are most uniformly distributed among the compound classes.

Moreover, in a more general context, the results suggest that charge reorganization energies calculated with common GGAs and hybrid functionals like BLYP, PBE or B3LYP are usually too low. This offers a possible explanation why Marcus rates and derived transport parameters were found to be often overestimated for organic semiconductors while exposing correct trends.[855]

For the purpose of later-on use in a multiscale approach, the four last sections were entirely dedicated to a precise assessment of molecular properties, which include ground-state geometries, excitation energies, exciton reorganization energies and excited-state geometries, and charge reorganization energies and cationic-state geometries. It was outlined in line with Meerholz and Würthner[27] that an understanding of optoelectronic processes at the interfaces of organic solar cells involves insight at several levels, with the individual molecules being the most basic level. Starting from single molecules, the natural next higher level is the intermolecular level, i.e., an investigation of the intermolecular interactions between individual molecular semiconductors. This will be the subject of the next section.

5.6 Interactions between the π-systems of molecular organic semiconductors

The results presented in the following are also found in [875].

It is well-known that intermolecular interactions favor specific orientations of the molecular organic semiconductors relative to one another in organic thin-film devices such as OSCs.[876] A detailed understanding of these intermolecular interactions is particularly important because the resulting orientations between the semiconducting molecules critically determine the efficiencies of all optoelectronic processes in OSCs such as exciton and charge transport. For instance, Fink et al. highlighted the outstanding impact of changes in intermolecular configurations for the efficiency of exciton trapping in perylene-based dyes.[745,877,878]

With regard to this profound influence of intermolecular interactions, an analysis specific for molecular semiconductors is definitely necessary before proceeding with calculations on aggregates. Prior to turning to the results on intermolecular interactions, it is, however, worth discussing several literature findings since a considerable amount of scientific research has been dedicated to phenomena related to π-π-interactions and π-stacking. More detailed perspectives than the herein presented summary were provided by Iverson and coworkers[879] and by Diederich et al.[880] in a review article with a more biochemical focus.

Traditionally, in the very popular Hunter model, the interactions between π-conjugated molecules and between aromatic π-systems in particular were described as electrostatic interactions between the molecular quadrupole moments.[881] Since quadrupole moments are a special feature of organic π-systems – a consequence of their electronic anisotropy – the Hunter model suggests the existence of a special kind of interaction between π-systems, often denominated in the literature as "π-π-interactions" or "π-stacking".[879] However, modern SAPT (symmetry-adapted perturbation theory) calculations by Sherill and coworker[882] and CCSD(T) calculations by Lee et al.[883] attribute the energetically most important contributions to the total "π-π-interactions" to dispersion rather than to electrostatics, which can play a conformation-determining role only for conformations that are similarly favored by dispersion.[882] In this sense and in line with Iverson,[879] Grimme challenged the physical soundness of the frequently employed notion of "π-π-interactions" because albeit being strong, interactions between π-conjugated molecules are nevertheless equivalent to "standard" dispersion forces. According to Grimme, the dispersion forces between organic π-systems are certainly stronger than average dispersion forces between aliphatic counterparts. However, this strength results rather from the close intermolecular contacts between π-conjugated molecules enabled by their structural planarity than from some special nature of the forces.[884] Furthermore, Wheeler and Houk demonstrated in DFT-D calculations on substituted aromatic systems that electrostatics can be very important. Yet, substituents interact usually directly through space and not indirectly via inducing

changes in molecular quadrupole moments, which alters resulting quadrupole-quadrupole interactions.[885,886]

Although the conclusions might be transferable to molecular organic semiconductors, benzene and substituted derivatives were used in most investigations. In contrast, this investigation includes a number of compounds with polarized π-systems (Figure 5), i.e., compounds with large local dipole moments in the conjugated cores that result from the incorporation of heteroatoms and electron-withdrawing moieties in the systems. It is possible that the energy contributions of dispersion and electrostatics to the total intermolecular interaction energies change when molecules with these structural features are considered instead of substituted aromatics. This raises the question whether electrostatic interactions dominate intermolecular potentials between such polar organic π-systems and their resulting transport properties, as outlined by Würthner and Meerholz.[27]

Moreover, it should be noted that the global energy minimum is the main point of concern of most literature investigations.[879] In contrast, the global energy minimum is not of primary interest for thin-film structures because the static disorder[548,425] present in all amorphous thin films leads essentially to a distribution of conformations over many local energy minima.[552] Therefore, to gain insight into the number of local energy minima in the following, potential energy surfaces (PES) are calculated along different internal coordinates of dimers composed of organic semiconductors. To focus exclusively on interactions between the π-systems, non-conjugating three-dimensional substituents were cut off, and only two-dimensional planar molecules are employed. Thus some molecules from the original compound set had to be excluded. Furthermore, for an in-depth analysis of the Hunter model and the implications of electrostatics in general, it seems necessary to include some electron-poor aromatic systems, i.e., some n-type semiconductors. For this purpose, PBI and perfluorinated acenes (naphthalene and anthracene) are additionally taken into account. The slightly modified set of compounds employed for the calculation of intermolecular interactions is given in Figure 45.

PES scans were calculated with high-level SAPT calculations,[887,296,888] the local molecular orbital energy decomposition analysis (LMO-EDA) by Su et al.,[293] DFT-D surface scans, and different force-field approaches. SAPT(DFT) calculations were shown to be very accurate for intermolecular potentials,[889,890] but due to their considerable computational cost, they can be employed only for small systems. Therefore, computationally less sophisticated LMO-EDA analyses were additionally used. Force-field approaches play an important role in modern computational material sciences because they provide an efficient route to do calculations on large systems.[891] This makes them attractive for the targeted multiscale approach, but requires that their applicability is thoroughly evaluated beforehand. Except for these advantages from a user's point of view, modeling calculated

intermolecular interactions obtained with *ab initio* methods also provides insight and understanding of these interactions.

molecular semiconductors with non-polarized conjugated systems

anthracene

diindenoperylene (DIP)

perylene

dithiophene

fluorinated anthracene

fluorinated naphthalene

naphthalene

perylene bisimide (PBI)

molecular semiconductors with polarized conjugated systems

diketopyrrolopyrrole
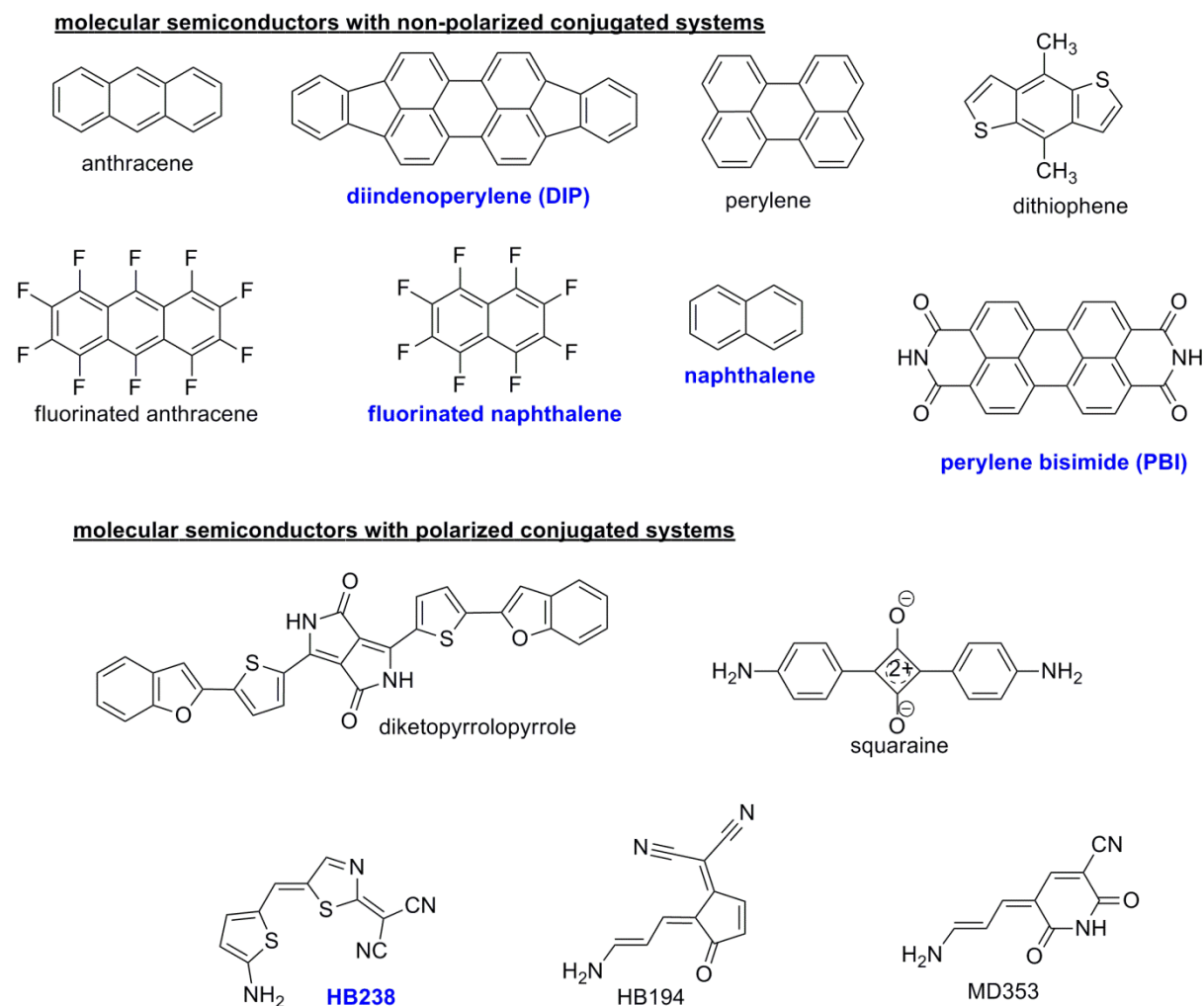
squaraine

HB238

HB194

MD353

Figure 45: Selection of molecular semiconductors with different degrees of polarization in the conjugated systems. Molecules with names in blue are analyzed in more detail. For more details on the fragments of HB238, HB194, and MD353, see Würthner et al.[656,655]

Like in all other benchmark calculations, optimized SCS-MP2/cc-pVTZ geometries obtained with the Turbomole program package[179] were employed for the molecules in Figure 45. Their ESP (electrostatic potential) charges using the Merz-Singh-Kollman scheme[892,893] were computed at the MP2/cc-pVTZ level of theory with Gaussian.[718] All SAPT calculations were performed with the tuned PBE0 functional[802,801] and the Molpro program package.[894,895] Augmented basis sets (aug-cc-pVDZ) were employed in the SAPT computations.[896,897] All LMO-EDA calculations were conducted with the GAMESS-US program package using ωB97X-D/6-31G[898] densities. LMO-EDA was shown to be basis set insensitive.[293] DFT-D surface scans were performed either with ωB97X-D/cc-pVDZ or with PW6B95-D3[815,140]/def-TZVP[749]. Sure and Grimme outlined in a recent benchmark that these two functionals provide reliable intermolecular potentials.[139] The MM3,[363,365,364] OPLS-AA,[360,349] and AMOEBA[388,356,348]

force fields were chosen for the calculations. These force fields were selected because they include electrostatic interactions in complementary ways: via bond dipoles (MM3), via atomic charges (OPLS-AA) or via distributed multipoles and induction (AMOEBA). Default parameters were used for MM3 and OPLS-AA while Stone's generalized multipole distribution analysis[353] (GDMA) was carried out to generate AMOEBA parameters using ωB97X-D densities. The Tinker program package[899] was employed for all force-field calculations.

All presented PES scans are referenced to their energetic minimum. They are performed either at the equilibrium distance of stacked monomers (vertical displacement between the π-systems, i.e., distance between the monomer planes: 3.3 Å) or in the slightly repulsive regime (vertical displacement between the π-systems: 3.0 Å). Investigations of energy decompositions in the slightly repulsive regime allow deducing more clear-cut trends because all energy contributions are larger. It was checked beforehand that the relative contributions hardly change when going from the equilibrium distance to the *slightly* repulsive regime. The potential energy scans can be subdivided into horizontal longitudinal (x-direction) and lateral (y-direction) scans (exemplified with naphthalene in Figure 46). Depending on the direction of the scan, one of the stacked monomers is displaced with respect to the other. In line with previous results, both coordinates were employed to analyze intermolecular PESs.[900,901]
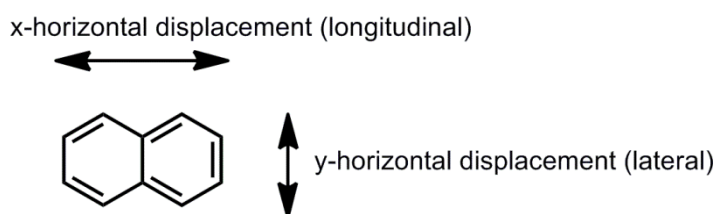

Figure 46: Illustration of the x-horizontal and the y-horizontal shift/scanning coordinate. Due to their positions with respect to the molecular axes, they are also called the longitudinal and lateral displacement.

5.6.1 Analysis of basis set effects and related phenomena on intermolecular potentials

In a first step, basis set effects on DFT-D surface scans are analyzed for both longitudinal and lateral displacements. The evolution of the surface scans upon increasing the basis set size from cc-pVDZ over aug-cc-pVDZ, cc-pVTZ, aug-cc-pVTZ to cc-pVQZ[705] is shown in Figure 47 for the naphthalene homodimer. It becomes evident that the increase of the basis sets does not change the characteristics of the intermolecular potential (Figure 47). However, for small vertical displacements (blue line), the basis set superposition error (BSSE) leads to too small values around the minimum x-/y-horizontal displacement of 0 Å. This corresponds to overestimated binding energies. The overbinding in dimers is a characteristic of the BSSE. Consistently, upon increasing the basis set and thereby decreasing the BSSE, larger intermolecular potential energies are obtained around 0 Å. Nevertheless, the BSSE varies only smoothly with the displacement. Therefore, it has no impact on the characteristic features of the potential. Local potential energy minima are thus left unchanged. The BSSE furthermore falls off

quickly with increasing vertical distance between the π-conjugated systems. In a certain way, it therefore compensates the errors introduced from scanning in the slightly repulsive regime, which artificially decreases the binding energy.
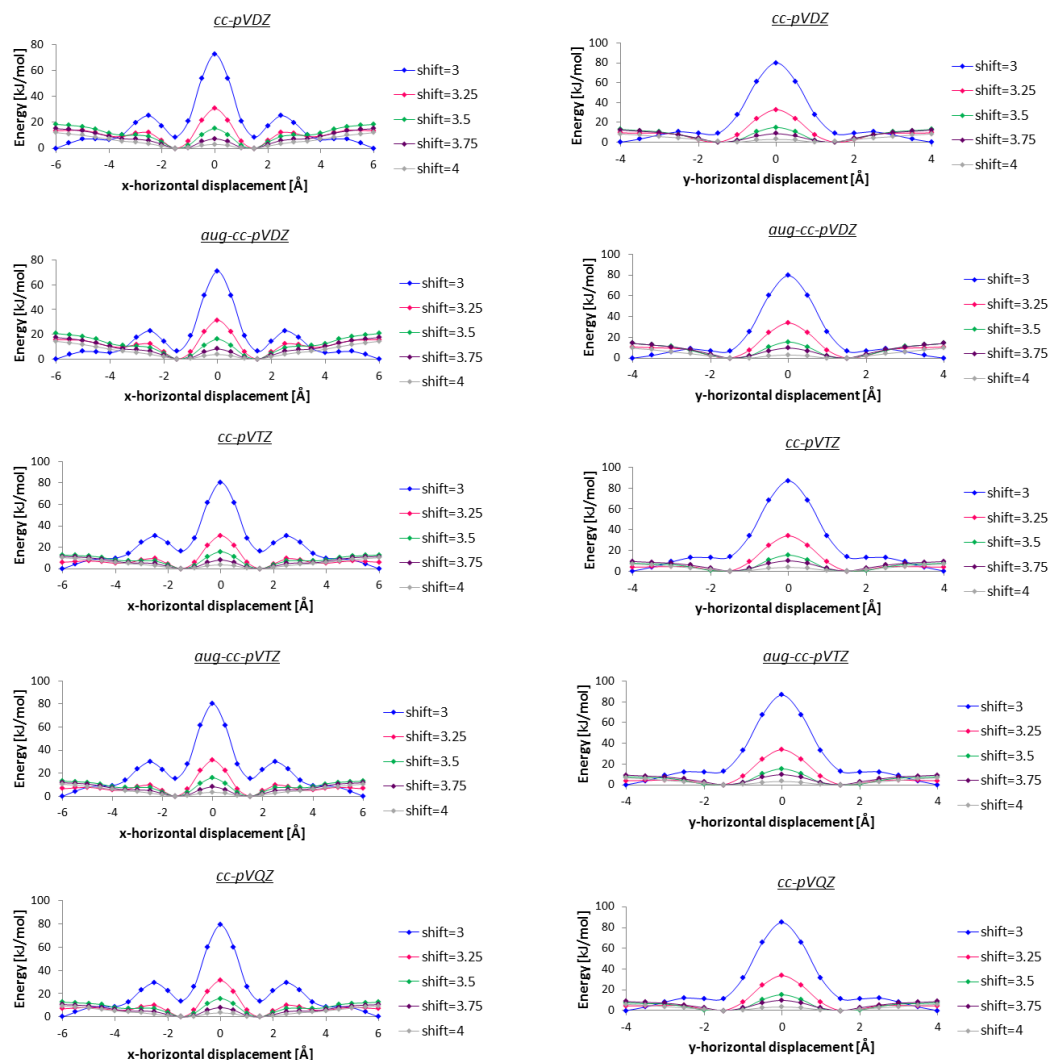
Figure 47: Basis set effects on horizontal displacements within a naphthalene dimer for different vertical displacements using ωB97X-D and various basis sets.

In addition to changes induced by systematically increasing the basis sets, the BSSE can also be assessed using counterpoise-corrected energies.[31] Results of counterpoise-corrected[902,903] ωB97X-D/cc-pVDZ calculations for the naphthalene homodimer and the perfluoronaphthalene homodimer are given in Figure 48 (left panels and right panels, respectively). From the energy difference of standard ωB97X-D/cc-pVDZ calculations, the BSSE can be directly computed. It is indicated with green lines in Figure 48.

As already discussed for the results in Figure 47, the BSSE values in Figure 48 clearly indicate that the BSSE is approximately constant along the longitudinal and lateral shift coordinates as well as for rotations of two monomers stacked on top of each other (i.e., on of the stacked monomers forming

the dimer is rotates while the position of the other is kept unchanged). Nevertheless, it is not small and amounts to ~ 10 kcal/mol for the naphthalene homodimer and even exceeds 20 kcal/mol for the dimer composed of two fluorinated naphthalene molecules. As could be expected, it smoothly falls off with increasing vertical displacement between the planar π-systems.

Altogether, the results in Figure 47 and Figure 48 underline that as long as absolute energy values are not interpreted, the BSSE does not change the characteristics of the intermolecular potentials. Hence using the cc-pVDZ basis with ωB97X-D or, in line with Sure and Grimme,[139] the def-TZVP with PW6B95-D3 should be completely sufficient to obtain a qualitatively correct overview over typical progressions of intermolecular PESs.
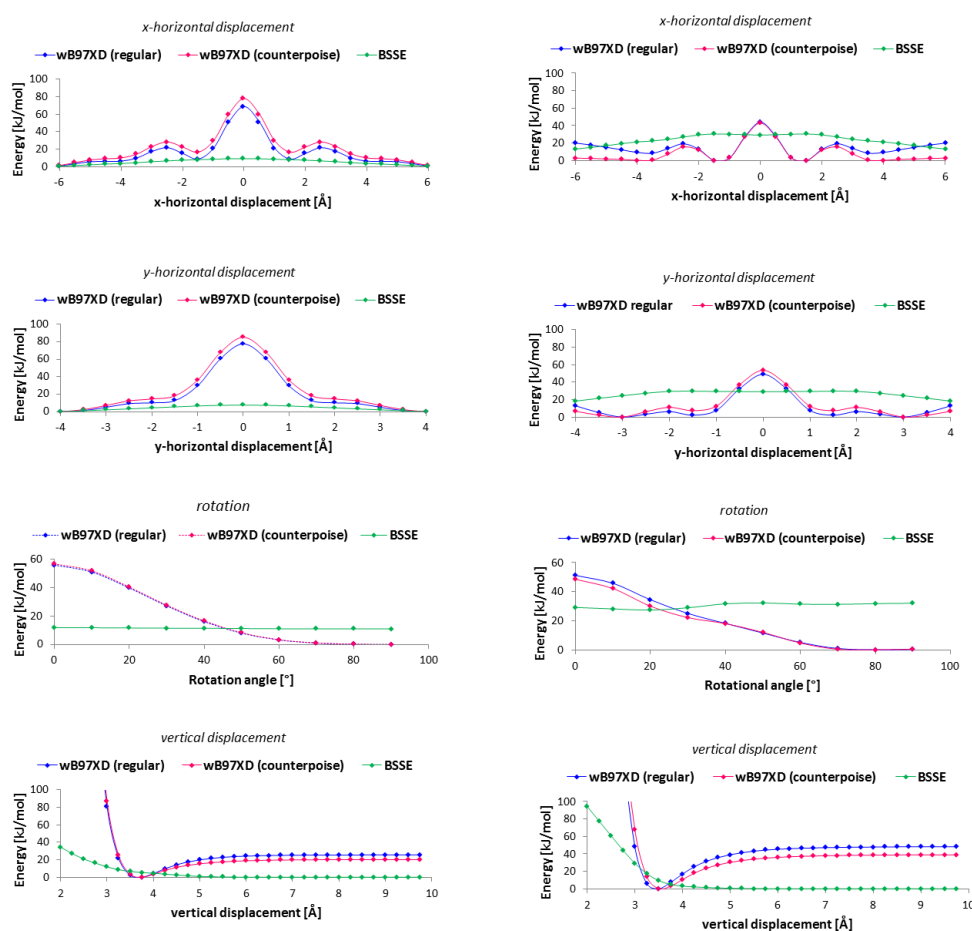
Figure 48: Results for different coordinates of the PES of the naphthalene homodimer (left panels) and the perfluoronaphthalene homodimer (right panels) calculated with ωB97X-D/cc-pVDZ and ωB97X-D/cc-pVDZ with counterpoise correction. The energy differences between both calculations yield the BSSE. In a rotation, on of the face-on stacked monomers is rotated while the position of the second is kept constant.

Given that the BSSE of DFT calculations is only of minor importance, the question arises how accurately DFT-D surface scans actually describe intermolecular potentials between molecular organic semiconductors. A comparison of the PESs calculated with SAPT(DFT), ωB97X-D and PW6B95-D3 is

given in Figure 49. While the right-hand side of the two graphs displays the actual energy curves, the left-hand side illustrates the differences between the DFT-D and the SAPT(DFT) values. The two PESs are calculated for a slightly repulsive vertical displacement of 3.0 Å; the equilibrium distance was determined to be 3.75 Å (Figure 48). Nevertheless, the characteristic features of the energy progressions remain the same for the repulsive regime compared with the equilibrium distance (see also Figure 47). Moreover, the slightly repulsive regime is still relevant in thin films where a distribution of conformations around the energy minimum is obtained.
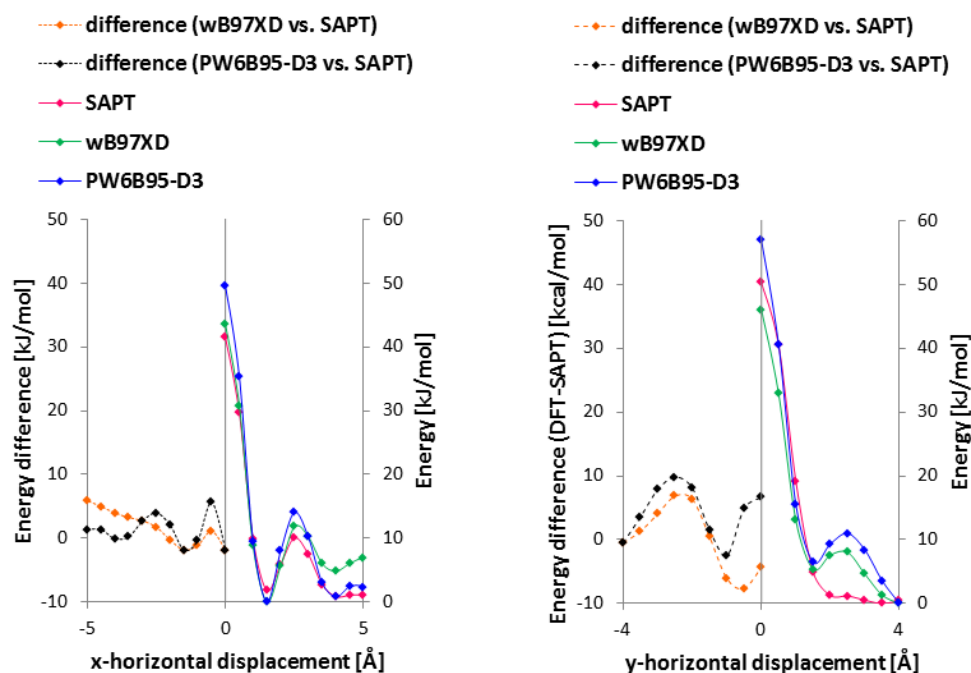

Figure 49: PESs for the x-horizontal and the y-horizontal displacements within a naphthalene homodimer. As discussed above, the scan was calculated for a slightly repulsive vertical displacement of 3.0 Å. It should be kept in mind that the potential energy of each scan was referenced to the minimal point of the respective scan. Reproduced with permission from [875]. © 2016 Wiley Periodicals, Inc.

The small energy differences between DFT-D and SAPT(DFT) and the good mutual coincidence of the two DFT-D curves clearly indicate that DFT-D curves provide reliable intermolecular potentials, as also outlined by Grimme and coworker.[139] According to all three methods, conformational energy minima exist for edge-on conformations (Figure 50) with x- and y-displacements of ±1.5 Å. Further energy minima are situated at larger displacements of ±4.0 Å. Similarly, the global maximum of all three methods is given by the face-on conformation. Additional local energy maxima can be found at x-/y- horizontal displacements of ±2.5 Å. Deviations from the SAPT reference values for ωB97X-D/cc-pVDZ energies in particular are most pronounced for large displacements. This arises from the BSSE that deteriorates the quality of the DFT-D values while SAPT results are counterpoise-corrected. The BSSE was found to be constant for the center regions of the scans, but alters relative energies between small and large displacements. This explains the good accordance between DFT-D and SAPT(DFT) for regions

with constant BSSEs and increasing deviations when comparing dimer geometries with different BSSEs. However, as outlined above, the BSSE does not change the characteristic features of the curves, which is again reflected in the PESs in Figure 49.

It should be noted that both PW6B95-D3/def-TZVP and ωB97X-D/cc-pVDZ energy profiles were calculated for all scans that will be presented in the following. They always agree very well as it was already the case in Figure 49. Therefore, only ωB97X-D/cc-pVDZ energy profiles are given.
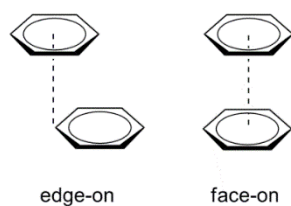
Figure 50: Face-on and edge-on conformation of stacked aromatic systems illustrated at the example of benzene.
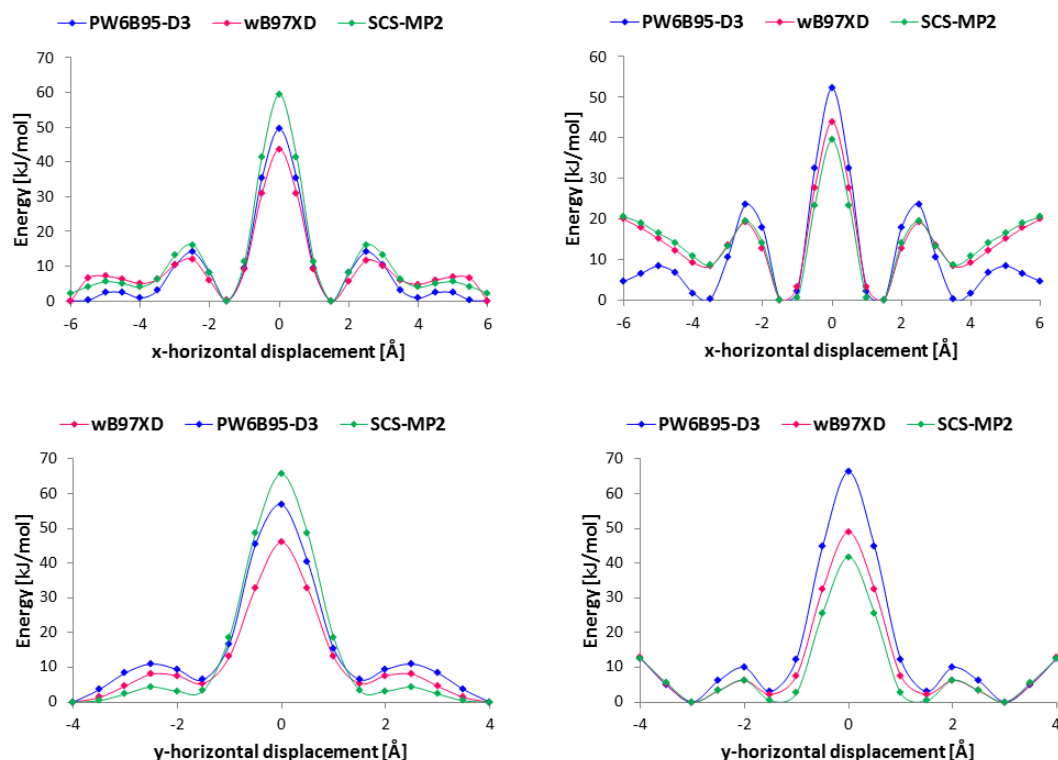
Figure 51: Comparison of DFT-D energy profiles and SCS-MP2 energy profiles for the naphthalene homodimer (left panels) and the dimer composed of two fluorinated naphthalene molecules (right panels). The distance between the π-system was set to 3.0 Å.

It is well-known in computational chemistry that MP2 cannot be used to properly describe intermolecular interactions other than hydrogen bonding,[76] as for example emphasized by Grimme and coworker.[139] Numerous studies exist that outline the characteristic overshooting of MP2 for dispersion-like interactions.[904,905,78] Nevertheless, it is instructive to compare SCS-MP2/cc-pVTZ intermolecular potentials to the DFT-D energy profiles (Figure 51). From the PESs given in Figure 51, it

can be seen that SCS-MP2 energy profiles show all characteristic features of the DFT-D curves and, with this, also of the SAPT reference values (Figure 49). Still, the characteristic overbinding becomes evident from the PESs of both dimers. For instance, the energetic minimum for the edge-on conformation of the naphthalene homodimer (upper left panel) is most pronounced for SCS-MP2. This indicates that the SCS-MP2 predicts the largest, i.e, an overestimated binding energy for the naphthalene homodimer, in line with the findings of Grimme and coworker.[139] Furthermore, SCS-MP2/cc-pVTZ PESs for the perfluoronaphthalene dimer resemble the ωB97X-D/cc-pVDZ profiles more than the PW6B95-D3/def-TZVP in spite of the contrary employed basis sets. Apparently, the overbinding of MP2-based methods produces artificial binding interactions similar to the BSSE.

5.6.2 Energy decomposition analyses of homo- and heterodimers composed of π-conjugated organic molecules

In a next step, results from SAPT(DFT) and from LMO-EDA are compared. For this purpose, Figure 52 displays SAPT(DFT) results for the energy decomposition of the intermolecular energy of the naphthalene homodimer and the corresponding LMO-EDA results. Before turning to a detailed interpretation of the presented energy decomposition, it should be discussed how to compare the individual energy contributions from SAPT(DFT) and LMO-EDA. SAPT(DFT) to the second order decomposes intermolecular interaction energies into contributions from electrostatics, exchange-repulsion, induction, and dispersion, leaving aside higher-order terms.[890] The LMO-EDA delivers contributions from electrostatic, polarization, exchange-repulsion, and dispersion. While an exact mapping of the SAPT and LMO-EDA contributions is not possible,[293] contributions arising from electrostatics, exchange-repulsion, and dispersion are directly comparable,[906,907] i.e., all terms except for the induction term from SAPT and the LMO-EDA polarization. A direct comparison between those two terms is not possible because LMO-EDA polarization includes induction and ground-state charge-transfer[906] whereas the SAPT induction evidently does not account for charge-transfer contributions.[293] Head-Gordon and coworkers proposed a slightly modified version of LMO-EDA, namely ALMO-EDA (absolutely localized molecular orbital EDA), where the more general LMO-EDA polarization is further subdivided into composing induction and charge-transfer contributions.[908]

Comparable energy contributions from SAPT and LMO-EDA are equally colored in Figure 52. While the exchange-repulsion is further subdivided for LMO-EDA, only the sum is given for SAPT. Albeit being non-equivalent, the LMO-EDA polarization and the SAPT induction are indicated with blue lines. From a comparison of the panels in Figure 52, it becomes evident that energy contributions from SAPT and LMO-EDA are very similar. Also the total energy (pink) is almost equal. The only difference remains the polarization/induction component where large deviations exist especially for large displacements. The LMO-EDA induction contribution is larger in terms of absolute values than SAPT polarization, but it

largely parallels the progression of the electrostatic energy. This is in line with the fact that charge-transfer contributions are included in the LMO-EDA induction so that it acquires some characteristics of the electrostatic stabilization. However, the generally equivalent results in Figure 52 are most important because this similarity allows using LMO-EDA also for larger systems where SAPT becomes inapplicable due to computer limitations.
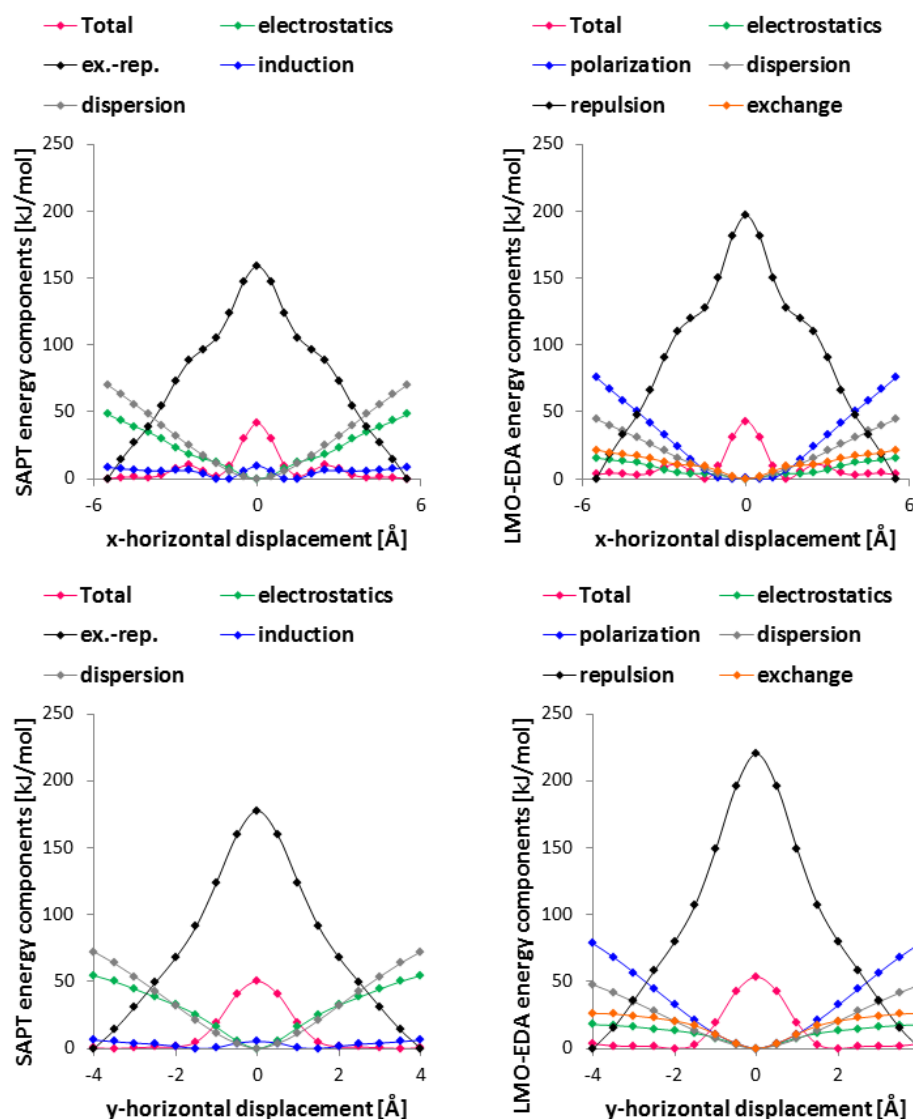
Figure 52: Comparison of SAPT (left) and of the LMO-energy decomposition (right) analysis for the x- and y-horizontal shift of two naphthalene monomers (vertical displacement of the molecules: 3.0 Å). Reproduced with permission from [875]. © 2016 Wiley Periodicals, Inc.

Since both energy decomposition schemes were shown to be equivalent, SAPT results for naphthalene are discussed more thoroughly in the next step. To do so, different sums of individual energy contributions are compared to the overall SAPT results in Figure 53. As already mentioned above, the x-horizontal displacement contains more distinct features. Therefore, it will be discussed in more detail in the following. Stabilizing contributions are indicated with dashed lines.

A comparison of the total energy (pink line, Figure 53) to the various energy contributions suggests that the characteristic progression of the intermolecular potential energy results mainly from variations in the exchange-repulsion component (black line, Figure 53).
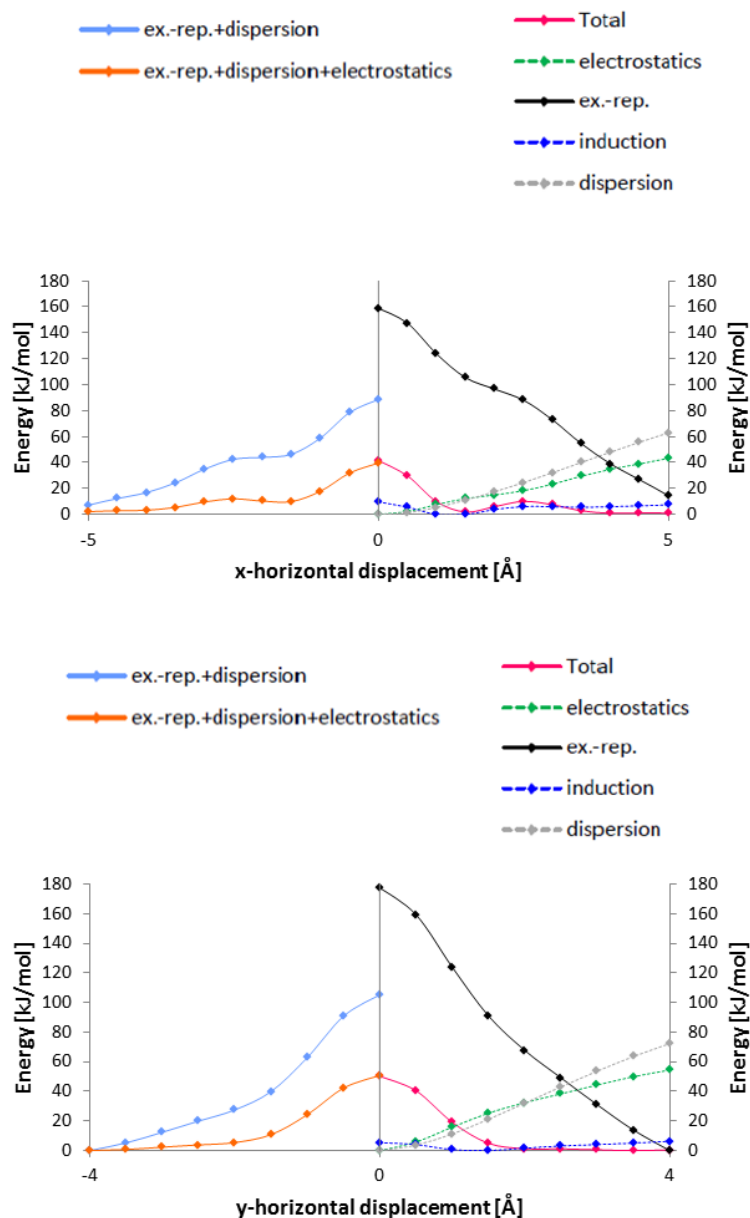
Figure 53: SAPT analyses for the x-horizontal (upper panel) and y-horizontal (lower panel) displacement within a naphthalene homodimer. Solid lines correspond to repulsive (positive) contributions while dashed lines correspond to attractive (negative) contributions. All energy contributions were referenced to zero. Reproduced with permission from [875]. © 2016 Wiley Periodicals, Inc.

Contrary to the exchange-repulsion, the induction is an attractive energy contribution (dashed line in Figure 53). Although it shows also some characteristic features along the displacement coordinate, its overall energy contribution is considerably too small to account for significant variations in the total intermolecular potential. Moreover, its progression does not parallel the evolution of the total

intermolecular energy, but rather opposes it, particularly around the global energy maximum (x-displacement: 0.0 Å). Both the total energy (pink line) and the induction component (blue dashed line) reach maximal values for this conformation. However, it is important to keep in mind that the induction is most stabilizing while the total energy is most repulsive for an x-horizontal displacement of 0.0 Å. This indicates that the energetic contribution from induction does not considerably influence the shape of the intermolecular PES. Moreover, a comparison of the total energy (pink line, Figure 53) with the sum of all energy contributions apart from the induction (orange line, Figure 53) indicates that the overall stabilizing contribution of induction is almost negligible.

In contrast, pronounced stabilization to the total intermolecular potential is contributed by the electrostatic and dispersion components. Yet, these energy contributions are rather unspecific and do not expose any characteristic features along the x-coordinate (Figure 53). Therefore, the existing specific features of the total intermolecular energy arise from the combined effects of an unspecific stabilization from dispersion and electrostatics and highly specific and localized destabilizing repulsion forces. The fact that these site-specific repulsion forces show a maximum for the symmetric face-on conformation is reflected in the maximum of the total intermolecular energy. Consequently, as outlined above, SAPT calculations predict the edge-on conformations to be most stable. Although this matches the predictions of the Hunter model, the results presented in Figure 53 suggest that the Hunter model is right for the wrong reason. Otherwise stated, according to the SAPT calculations, repulsion forces rather than unspecific long-range electrostatic interactions are responsible for the formation of distinct energetic minima along the PES.

So far, naphthalene was employed as an example to discuss intermolecular potentials of organic π-systems. In order to verify how general the above-stated conclusions are and whether they are transferable to larger molecular organic semiconductors, an LMO energy decomposition analysis is conducted for the x-horizontal displacement within the perylene dimer (Figure 54). It should be noted that SAPT calculations were computationally not feasible for the perylene dimer. Alike to the PES of the naphthalene dimer, the PES of the perylene dimer is equally characterized by a succession of numerous local energy maxima and minima. The features of the total intermolecular energy again coincide with features of the LMO-EDA exchange-repulsion term, indicating that the energy progression as well as local energetic minima and maxima are determined by the exchange-repulsion contributions. The total shape of the PES results when these localized repulsive forces are combined with the smoothly varying attraction arising from dispersion and electrostatics (light blue and orange lines in Figure 54).
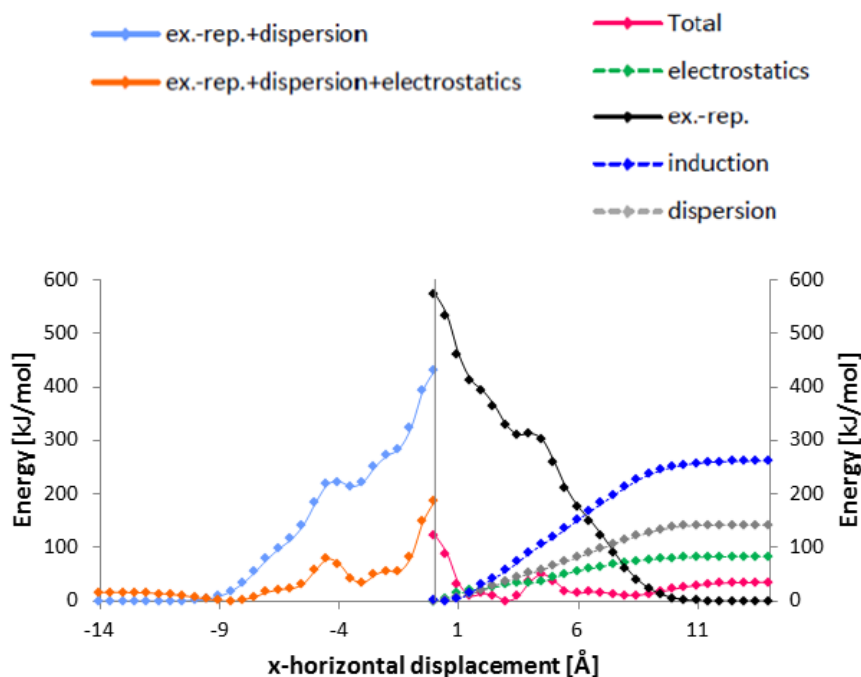
Figure 54: LMO-EDA of the intermolecular potential of a perylene dimer. Please note that the perylene dimer is the scaffold for many molecular semiconductors such as DIP, PBI, and PTCDA. The intermolecular distance between the π-systems was set to 3.0 Å. Extensive theoretical investigations on such perylene-based dimers were conducted by Settels et al. ([745] and references therein). Reproduced with permission from [875]. © 2016 Wiley Periodicals, Inc.

For the naphthalene and the perylene dimer, the edge-on conformations (Figure 50) are energetically lowest according to SAPT, which is in line with the Hunter model, albeit for the wrong reason. However, the Hunter model furthermore predicts that face-on conformations become energetically increasingly favorable when electron-rich and electron-poor aromatics are combined. This is again rationalized with electrostatic arguments. According to the Hunter model, the quadrupole moment is reversed in electron-poor aromatics. The electrostatically based model then predicts favorable quadrupole-quadrupole interactions for the face-on stacked dimers. To gain further insight into the relationship between above presented SAPT results and the electrostatic Hunter model, heterodimers composed of one "regular" and one fluorinated acene were analyzed.

In a first step, quadrupole moments were computed for acenes and fluorinated acenes, both at the SCS-MP2/cc-pVTZ and at the ωB97X-D level of theory (Table 19). The inversion of the quadrupole moments is reproduced for all molecules, with both methods yielding very similar results.

To verify whether underlying quadrupole-quadrupole interactions are important for the intermolecular potential of heterodimers, SAPT(DFT) and LMOEDA results for the naphthalene:: fluorinated naphthalene heterodimer are compared in Figure 55. As for the naphthalene homodimer, Figure 56 shows SAPT results and sums of specific energy contributions in more detail.

267

Table 19: Inversion of the quadrupole moments of acenes upon fluorination (quadrupole moments in Debye-Å).

molecule	ωB97X-D/cc-pVDZ			SCS-MP2/cc-pVTZ		
	Q(x,x)	Q(y,y)	Q(z,z)	Q(x,x)	Q(y,y)	Q(z,z)
anthracene	5.33	6.14	-11.48	7.07	6.68	-13.75
fluoroanthracene	-3.65	-6.35	10.00	-6.25	-8.94	15.19
naphthalene	4.30	3.96	-8.26	5.12	4.94	-10.06
fluoronaphthalene	-2.93	-4.43	7.36	-4.66	-6.30	10.96
tetracene	8.13	6.64	-14.78	9.15	8.37	-17.52
fluorotetracene	-4.81	-7.98	12.79	-8.53	-11.15	19.67
pentacene	10.29	7.88	-18.17	10.00	11.40	-21.39
fluoropentacene	-9.29	-6.55	15.83	-12.84	-11.74	24.58

The comparison of SAPT and LMO-EDA results in Figure 55 shows that both energy decompositions agree nicely also for the heterodimer, again with the exception of the induction/polarization component. The total energy of SAPT or LMO-EDA is rather similar and differs only for large displacements where the BSSE of ωB97X-D underlying the LMO-EDA calculations becomes noticeable. If electrostatic contributions were dominant as in the Hunter model, the inversed computed quadrupole moments (Table 19) in the heterodimer would result in a face-on type minimum-energy conformation. This contrasts with the energetic minima found for SAPT and LMO-EDA that still predict the edge-on conformation to constitute the global minimum structure (Figure 55, Figure 56). Comparing electrostatic contributions in the homodimer (Figure 53) and the heterodimer (Figure 56) certainly demonstrates the increased stabilization due to more favorable quadrupole-quadrupole interactions in the heterodimer – stabilizing electrostatic interactions rise from 60 kJ/mol to more than 80 kJ/mol for zero x-horizontal displacement (±0.0 Å). However, the electrostatic stabilization varies smoothly without any features and is not site-specific. In contrast, the evolution of the exchange-repulsion component shows pronounced variations along the displacement coordinate. Combining these features with the smoothly varying electrostatic contributions results in a minimum energy conformation that is still of edge-on character. Nevertheless, this edge-on conformation shifts to a smaller x-horizontal displacement (±1.0 Å instead of ±1.5 Å) because the unspecific stabilization arising from favorable quadrupole-quadrupole interactions is larger in the heterodimer (Figure 56) compared with the homodimer (Figure 53).
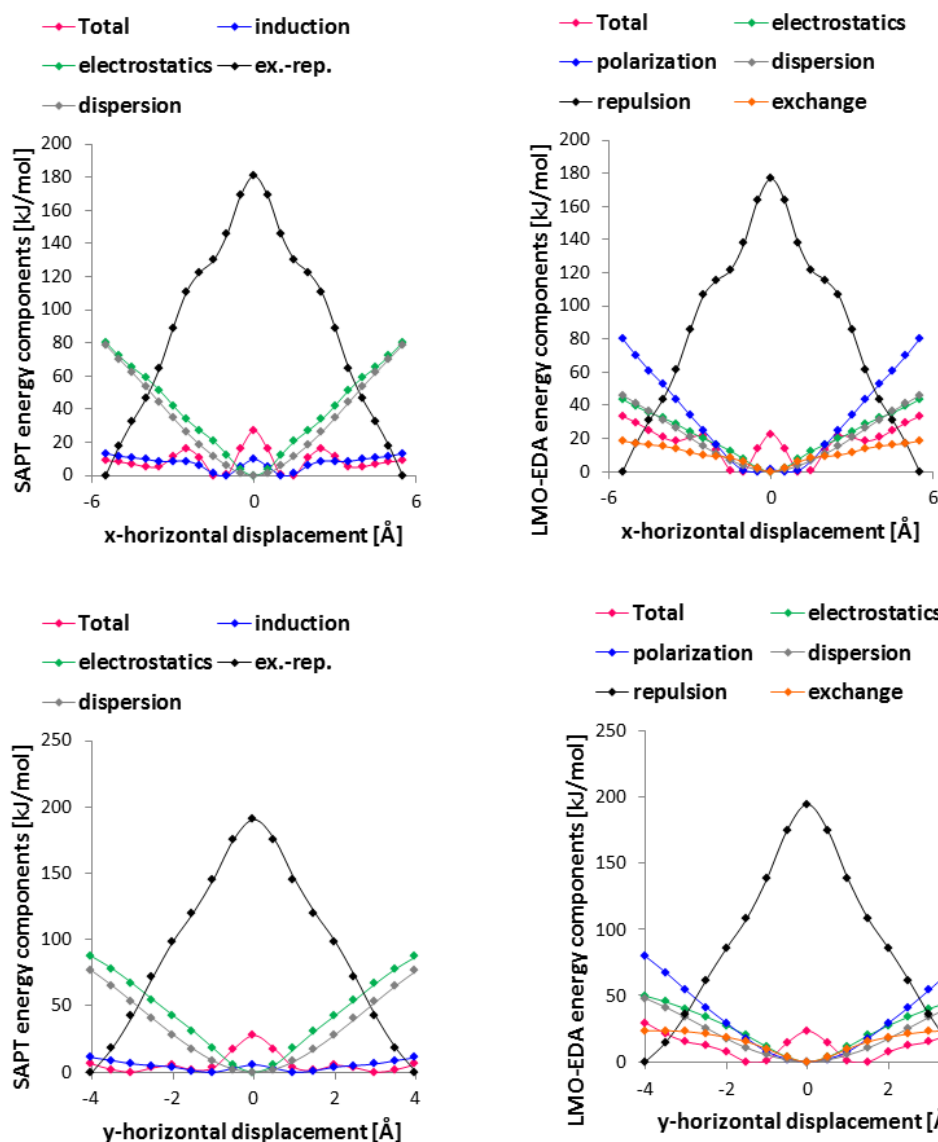
Figure 55: Comparison of SAPT (left) and LMO-energy decomposition (right) analysis for the x- and y-horizontal shift of a naphthalene molecule and a fluorinated naphthalene molecule (vertical displacement of the molecules: 3.0 Å). Reproduced with permission from [875]. © 2016 Wiley Periodicals, Inc.

Altogether, the presented SAPT and LMO-EDA analyses of intermolecular energies in naphthalene dimers as well as the LMO-EDA results for the perylene dimer indicate that localized strongly destabilizing energy contributions due to the exchange-repulsion are somewhat smoothened by unspecific stabilizing electrostatic and dispersion contributions. The relative sizes of these energy contributions determine to what extent the monomers are shifted with respect to each other in the edge-on minimum energy conformation. This naturally includes the face-on energetically minimal conformation as a limiting case for very large stabilizing energy contributions from dispersion and/or electrostatics.
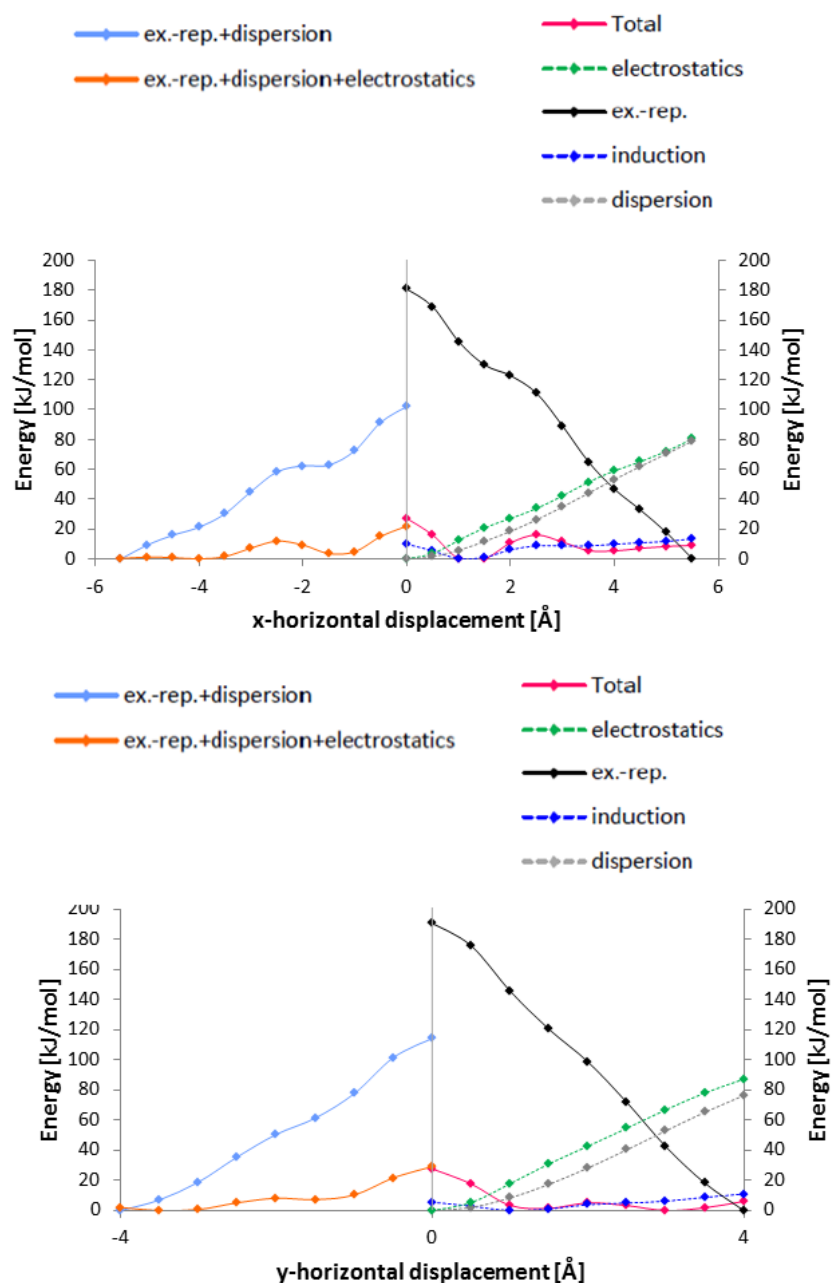
Figure 56: SAPT analyses for the x-horizontal (upper panel) and y-horizontal (lower panel) displacement within a naphthalene::perfluoronaphthalene heterodimer. Solid lines correspond to repulsive (positive) contributions while dashed lines correspond to attractive (negative) contributions. All energy contributions were referenced to their minimum. Reproduced with permission from [875]. © 2016 Wiley Periodicals, Inc.

To further illustrate this point, PESs are calculated for dimers of the next higher homologue of the acenes, i.e., for the homodimer and heterodimer of anthracene and its fluorinated counterpart using ωB97X-D/cc-pVDZ single-point calculations. In order to provide more insight, two-dimensional PESs are computed, i.e., the vertical separation between the anthracene molecules is varied in addition to their x-horizontal displacement. Figure 57 displays the results for the homodimer (upper panel) and the heterodimer (lower panel). It becomes evident that in accordance with the stated conclusion, the larger yet unspecific electrostatic stabilization in the heterodimer combined with more or less

270

unchanged destabilizing exchange-repulsion contributions lead to an energetically most favorable heterodimer conformation with a smaller x-displacement compared with the minimum energy conformation of the homodimer (compare center of pink circles in upper and lower panel in Figure 57). It follows that in contrast to the Hunter model, the type of conformation between stacked aromatic systems is not determined by quadrupole-quadrupole interactions.
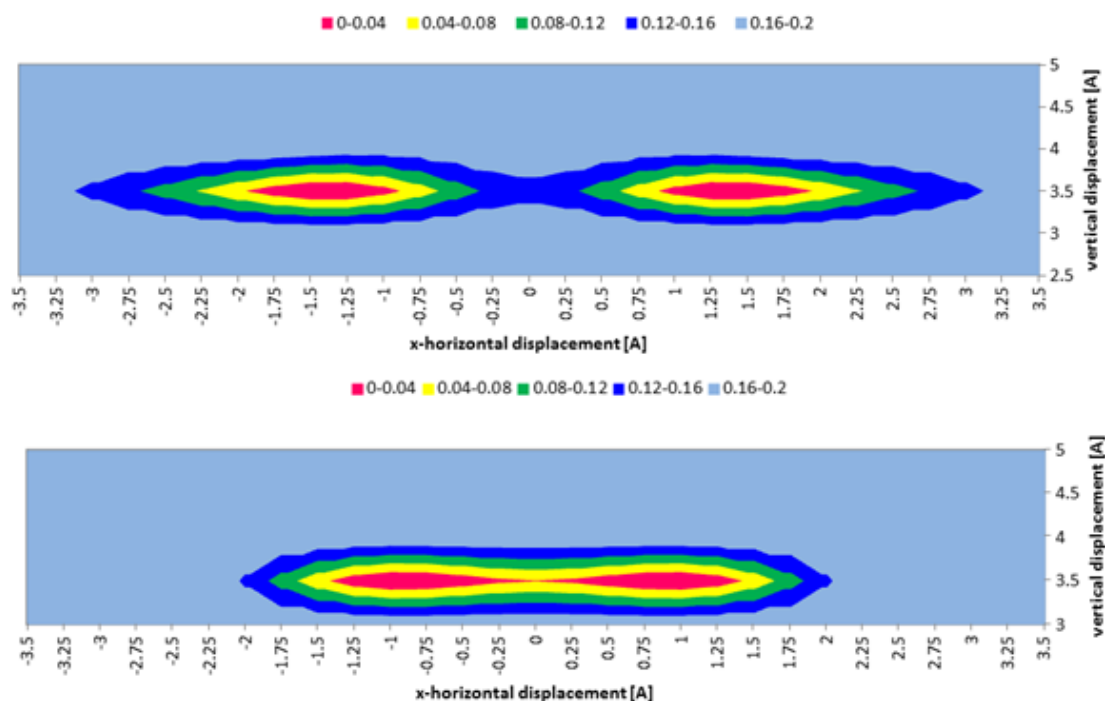
Figure 57: Potential energy surface scans for the anthracene homodimer (upper panel) and the anthracene::fluorinated anthracene heterodimer (lower panel) calculated with ωB97X-D single-point calculations. Reproduced with permission from [875]. © 2016 Wiley Periodicals, Inc.

One could assume that in contrast to the findings for apolar molecules like naphthalene or perylene, intermolecular interactions between strongly polarized π-systems, i.e., molecules like squaraines or cyanines, are still dominated by electrostatic contributions rather than by local repulsive forces. To analyze to what extent the importance of these local repulsive forces changes when considering strongly polarized instead of non-polarized π-systems, the intermolecular potential of a dimer composed of dipolar HB238 monomers (Figure 45) is investigated in more detail. This system is chosen because it contains on the one hand very polarizable sulfur atoms – allowing for pronounced dispersion and repulsion interactions – and on the other hand a very polarized push-pull π-system.[656] Therefore, the interplay between dispersion, repulsion, and electrostatics can be studied at this system. Electrostatic interactions between the polarized HB238 π-systems can be directly calculated as charge-charge interactions between the atomic charges generated in a ωB97X-D/cc-pVDZ ESP fit of the HB238 monomer. These charge-charge interactions do not include, however, polarization effects between the two HB238 molecules that change the atomic charge distributions within the monomers. In contrast,

using atomic charges generated in ωB97X-D/cc-pVDZ ESP fits of the HB238 dimer conformations instead of monomer ESP charges accounts for the additional changes of atomic charges induced by the intermolecular polarization. Charge-charge interactions from monomer ESP atomic charges ("charges", black line in Figure 58) and from polarized dimer charges ("polarized charges", green line in Figure 58), which were obtained with a C++-script using the output of the Gaussian program package, are compared to the total DFT-D energy line (Figure 58). In principle, electrostatic interactions between strongly dipolar[27,641,909] systems could also be calculated as dipole-dipole interactions between the molecular dipole moments. Such calculations were in effect conducted for the HB238 dimer but results are rather poor because the point dipole approximation is not valid for short intermolecular distances.[340]
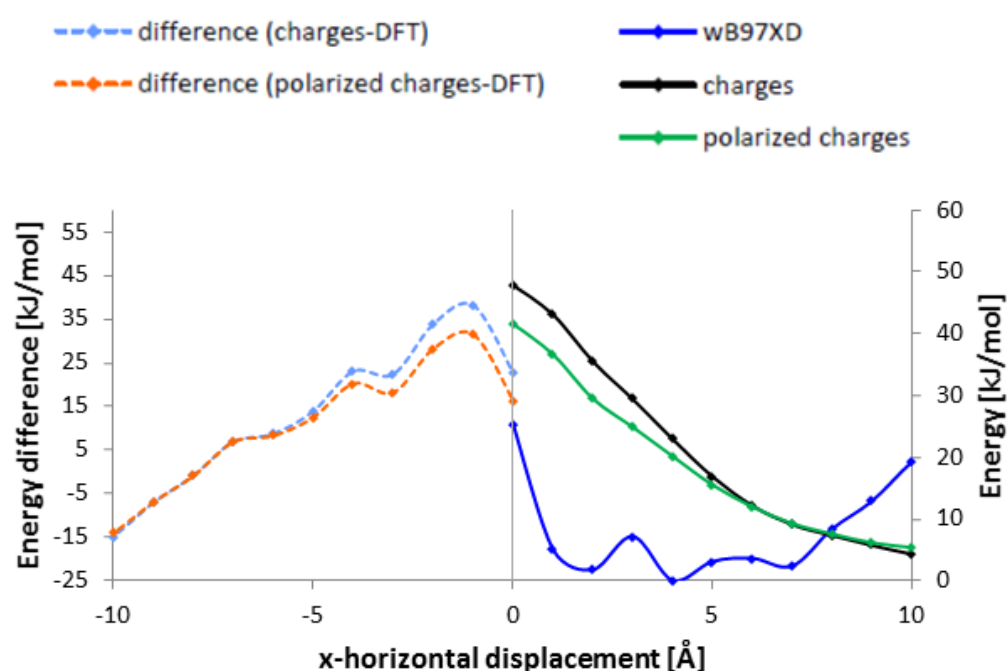
Figure 58: Intermolecular potential energies obtained for a parallel longitudinal shift of the HB238 monomers with respect to each other for a vertical distance of 3.5 Å between the planar π-systems. This distance corresponds approximately to the equilibrium distance, but is still in the slightly repulsive regime. It is larger than the above used distances because HB238 contains large polarizable sulfur atoms. Reproduced with permission from [875]. © 2016 Wiley Periodicals, Inc.

From the calculated charge-charge interactions between charges or polarized charges (Figure 58), it becomes evident that the electrostatic energy does not show any characteristic features, in contrast to the total intermolecular potential energy. Much alike to the above discussed results for naphthalene and perylene, the electrostatic component varies rather smoothly as a function of the nuclear coordinates. To gain more insight into the interferences between the different intermolecular energy contributions in the HB238 dimer, the SAPT decomposition is given in Figure 59. It is furthermore compared to LMO-EDA results. Again, it is found that SAPT and LMO-EDA coincide nicely also for interactions between rather polarized organic π-systems like dipolar merocyanines. Moreover, a

comparison between the exchange-repulsion (black line, Figure 59) and the total intermolecular energy (pink line, Figure 59) demonstrates that characteristic features of both curves coincide, indicating that the energy progression again results from pronounced variations of the exchange-repulsion. Similar to the electrostatic energy calculated from charge-charge interactions between atomic ESP charges (Figure 58), the SAPT electrostatic energy varies in an unspecific way and does not possess any features. This results from the long-range $\frac{1}{r}$-dependence of charge-charge interactions. As a consequence, charge-charge interactions vary only slowly with increasing distance, i.e., with the coordinate. Such slow energy variations do not favor specific dimer conformations, in contrast to exchange-repulsion forces, which, via sharp fluctuations, distinguish between slightly different conformations.
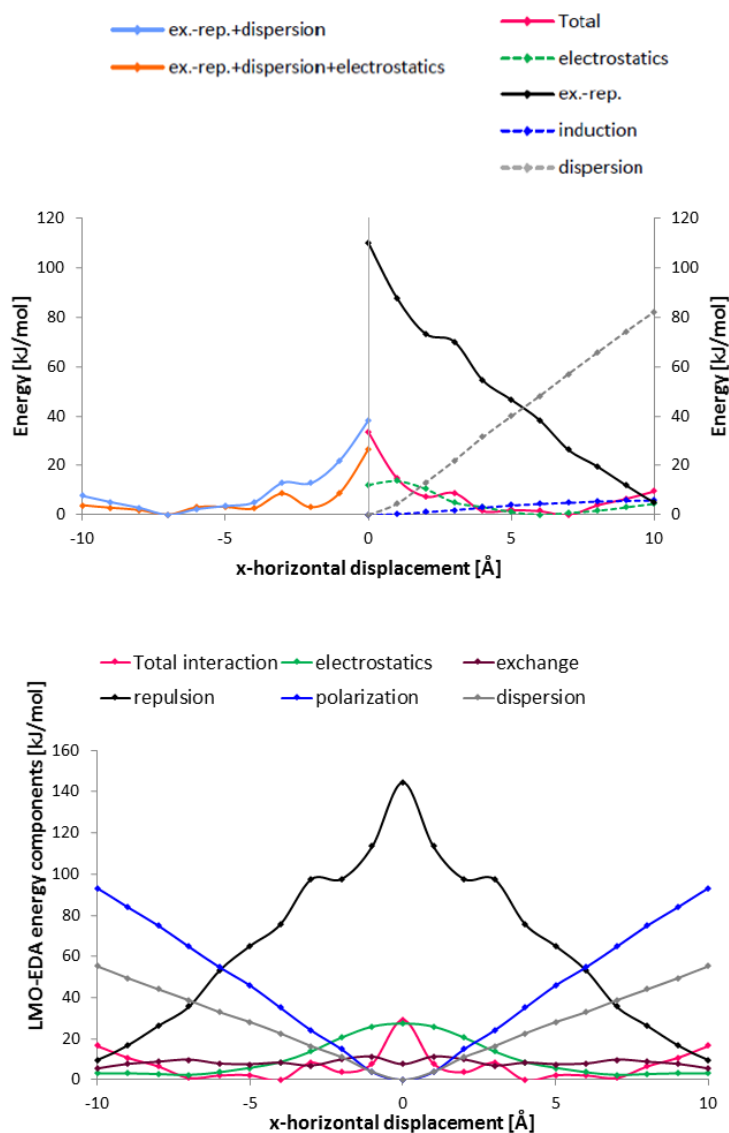
Figure 59: SAPT results (upper panel) and LMO-EDA results (lower panel) for the decomposition of the intermolecular energy in a HB238 dimer. The vertical distance between the π-systems was set to 3.5 Å. Reproduced with permission from [875]. © 2016 Wiley Periodicals, Inc.

Similar conclusions can be also drawn from the LMO-EDA analyses of homodimers composed of squaraine and diketopyrrolopyrrole molecules, i.e., of two organic π-systems with significant local dipole moments. Results are shown in Figure 60. Please keep in mind that the polarization component is differently interpreted in LMO-EDA. The polarization shows some features along the coordinates for both the squaraine and the diketopyrrolopyrrole, similar to the SAPT induction component in the naphthalene homodimer. Nevertheless, most variations arise from the exchange-repulsion component (Figure 60). Its pronounced features contrast with the continuous energy progressions of the dispersion and the electrostatic components. Hence the results clearly indicate that the exchange-repulsion component is decisive for the formation of local energy minima and maxima irrespective of the degree of polarization of the π-systems.
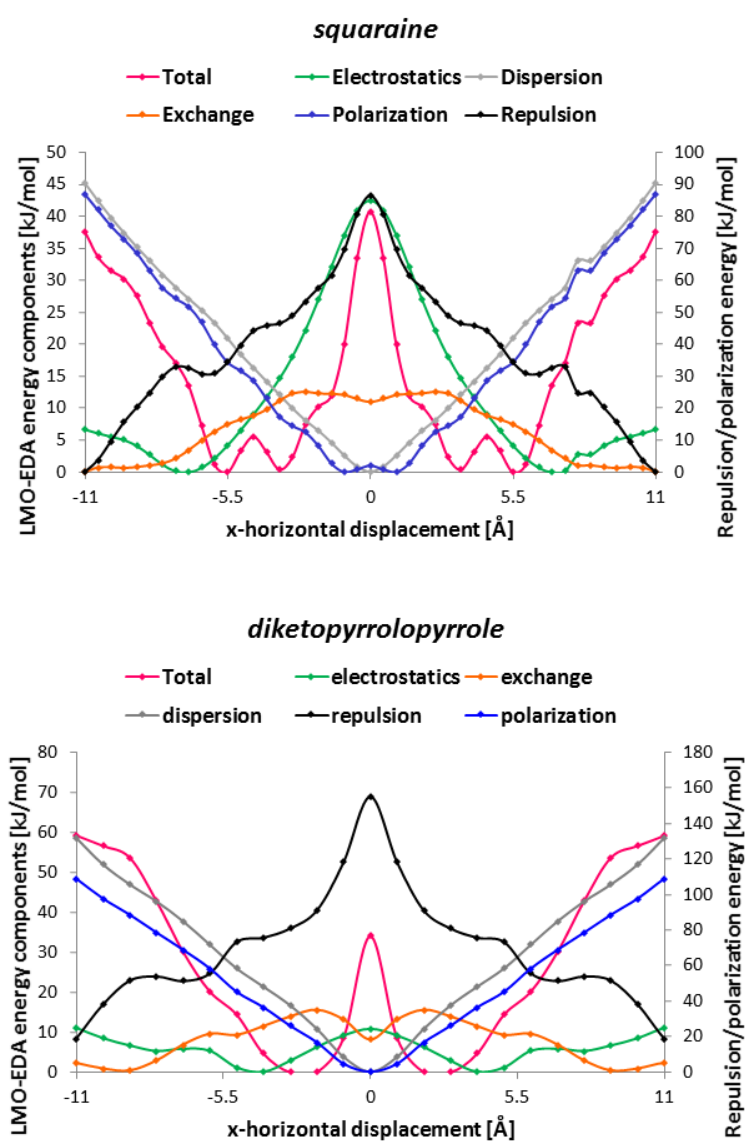
Figure 60: LMO-EDA for a dimer composed of squaraine molecules (upper panel) and of diketopyrrolopyrrole molecules (lower panel). It is worth noting that only the repulsion component varies in a pronounced way as a function of the nuclear coordinates. The vertical distance between the π-systems was set to 3.5 Å for both dimers. Reproduced with permission from [875]. © 2016 Wiley Periodicals, Inc.

This allows for the general conclusion that the positions of the local minima in the intermolecular PESs of organic π-systems result from a combination of dispersion and electrostatics providing the needed driving force and highly localized short-range repulsive forces that specifically favor distinct conformations while destabilizing others. This interpretation is in accordance with the investigations of Sherrill and coworkers[882] and Iverson et al.[879] However, they considered only much smaller and simpler model systems, notably substituted benzenes, and did not take into account the stacking behavior characteristic for molecular organic semiconductors. In a similar way, compared to the Hunter model, it has a different focus and does not attach much importance to electrostatics other than some unspecific energetic stabilization.

While insights into the physical origin of intermolecular interactions between molecular organic semiconductors are important to understand such π-π-interactions, modeling them accurately is even more essential from a user's point of view. DFT-D surface scans were shown to provide correct intermolecular potentials, but for the purpose of understanding optoelectronic processes near the organic::organic interfaces in OSCs, i.e., for multiscale approaches, even larger systems must be described. This can be achieved with force-field calculations that are widely used due to their computational efficiency.[910] Therefore, three different force fields are analyzed in the following with respect to their abilities to describe intermolecular interactions between organic π-systems.

5.6.3 Force-field description of interactions between organic π-systems

For a number of reasons, the intermolecular potential of the DIP dimer is used to investigate the outcome of force-field calculations. Firstly, DIP, a derivative of perylene, is one of the most common and most widely studied molecular organic semiconductors.[671,911,912,913,914] Secondly, due to its considerable size, the intermolecular potential of DIP dimers has many characteristic features. Thirdly, extensive data on force field calculations with DIP exist, and in a recent investigation, the crystal structure of DIP could not be reproduced with standard force fields.[745]

In order to deduce approaches to model intermolecular interactions, it is of particular interest to identify those force-field energy contributions that are responsible for the shape of the PES. It should be nevertheless kept in mind that force fields are developed so that only total force-field energies are physically meaningful.

The intermolecular potential calculated with ωB97X-D/cc-pVDZ possesses a global energy minimum at ±3.0 Å and two additional minimum energy conformations between ±3.0 Å and ±7.0 Å (blue line, Figure 61). Results for three different force fields, i.e., energies and energy decompositions for MM3, OPLS-AA, and AMOEBA, are given in Figure 62 for a vertical distance of 3.0 Å. A comparison to the force field decompositions for a larger vertical distance of 3.3 Å shown in Figure 63 demonstrates the advantages

of using the slightly repulsive regime for force-field scans: all features are more pronounced for shorter intermolecular distances. Moreover, numerous features even disappear for larger intermolecular distances, making a clear-cut interpretation of the force field energy decompositions impossible.
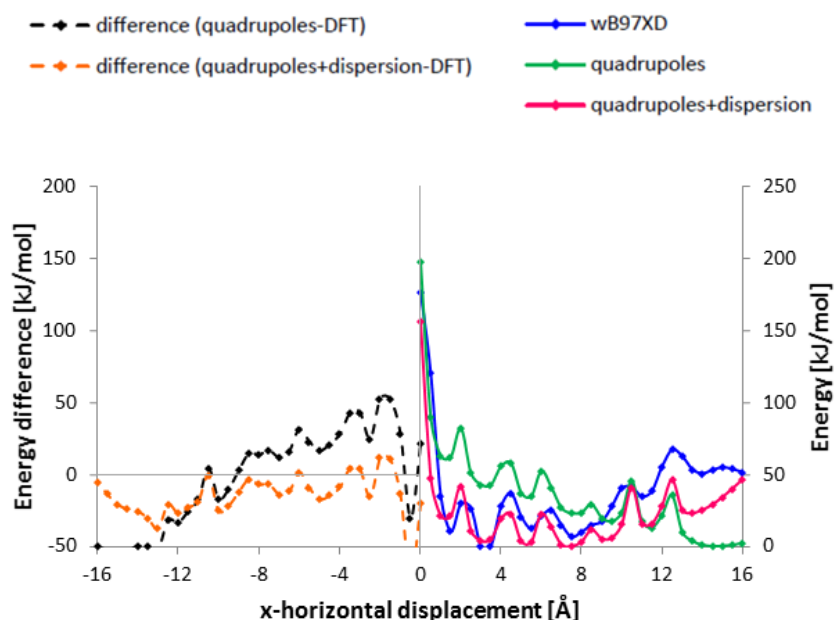
Figure 61: Intermolecular potential energy of the DIP dimer and the model potentials calculated with molecular quadrupoles. The vertical displacement between the molecules was set to 3.0 Å. Reproduced with permission from [875]. © 2016 Wiley Periodicals, Inc.
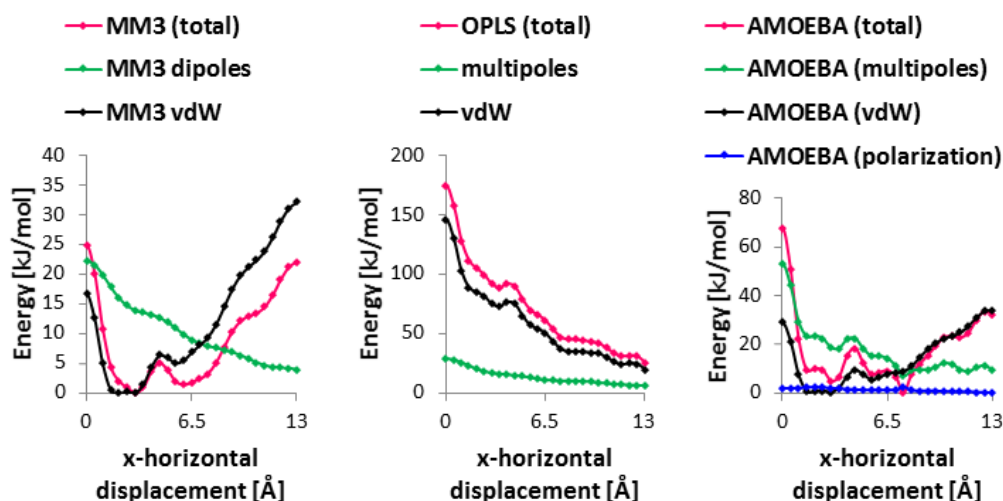
Figure 62: Energy decompositions of force field energies for the intermolecular potential of the DIP dimer. The vertical distance was set to 3.0 Å. Reproduced with permission from [875]. © 2016 Wiley Periodicals, Inc.

Comparing force field energies (Figure 62) to the DFT-D potential energy (Figure 61) reveals considerable deviations. The AMOEBA force field reproduces most features correctly but some local energy minima are still missing. Only two energy minima exist according to MM3, one of which actually

corresponds to the global DFT-D energy minimum. In contrast, no stable conformations are predicted by OPLS-AA. Still, some kinks and variations in the total intermolecular energy progression exist.
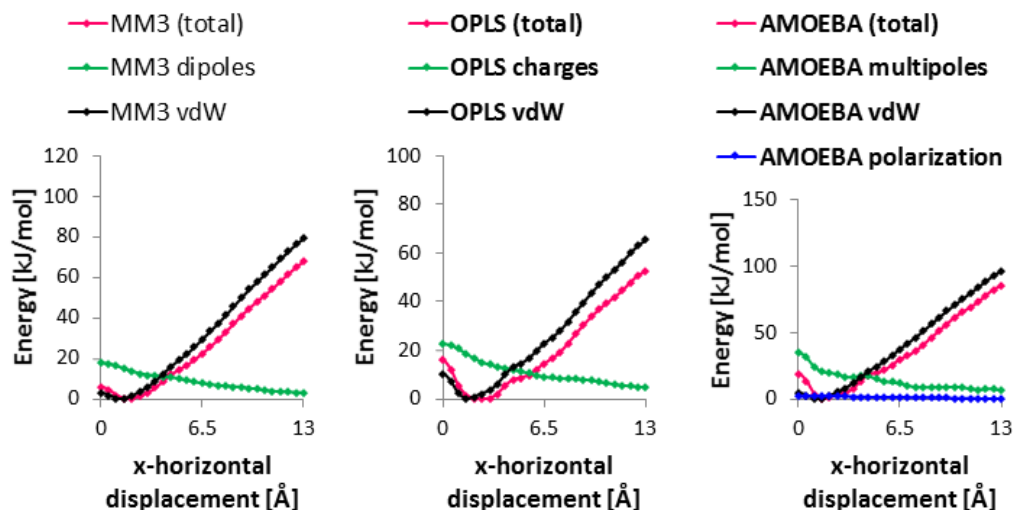
Figure 63: Energy decompositions of force field energies for the intermolecular potential of the DIP dimer. The vertical distance was set to 3.3 Å. While the minimum of the DFT-D curve is well reproduced, many of its kinks and characteristic features are still missing. Yet, the force-field description should be sufficient to describe qualitatively accurate aggregate interactions. Reproduced with permission from [875]. © 2016 Wiley Periodicals, Inc.

The force field energy decompositions permit to compare force field energy contributions responsible for the characteristic features of the intermolecular potential to the above discussed SAPT results that particularly highlighted the role of the exchange-repulsion. It is evident from Figure 62 that the force field energy contributions responsible for the shape of the total intermolecular energy depend on the force field. The MM3 van-der-Waals contribution roughly parallels the progression of the total intermolecular energy. The same holds for OPLS-AA. Corresponding features between the van-der-Waals term and the total energy exist also for AMOEBA but additional local variations in the electrostatic energy emerge. These fluctuations of the electrostatic interaction energy also coincide with the progression of the total energy. While the dominant influence of the van-der-Waals energy on the shape of the potential mirrors the importance of the exchange-repulsion predicted by SAPT, additional electrostatic contributions from atomic multipoles as found for AMOEBA are rather in line with the Hunter model.

Approaches to model intermolecular interactions between organic π-systems

In this sense, it is often stated that molecular quadrupole moments are required to correctly describe intermolecular energies between organic π-systems with force fields.[915] This contrasts with the SAPT

results that rather emphasize the significance of exchange and repulsion. As already outlined by Tafipolsky and Engels,[889] correct total force field energies do not necessarily rely on an accurate decomposition into correct individual energy contributions. In fact, the fitting process to generate force field parameters rather results in a somewhat arbitrary decomposition of the total force field energy into its individual energy components. These individual force field terms consequently depend on each other and are only physically meaningful in the sum. This is accepted because force field calculations are usually conducted to efficiently obtain energies and geometries where total energies are significantly more important than individual components. Nevertheless, the AMOEBA energy decomposition (Figure 62) suggests that characteristic features of intermolecular energies can *in principle* also be modeled with multipole-multipole interactions. Although this is not physically grounded according to the SAPT results, it is analyzed in the following whether quadrupole-quadrupole interactions actually predict correct intermolecular potentials, in line with common claims.[915] The DIP dimer is again used as an example. The Hunter model is transferred to the DIP molecule, and each aromatic ring is described in terms of a quadrupole moment (Figure 64). Please note that this contrasts with most force fields including higher-order electric moments because they rather utilize atom-centered multipole moments.[348]
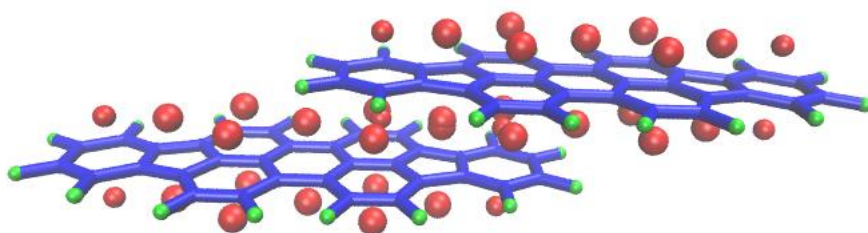
Figure 64: Quadrupole moments used to model intermolecular energies via quadrupole-quadrupole interactions. The DIP molecules are colored in blue. Positive charges are positioned in the elongation of the C-H-bonds and are colored in green. Negative charges corresponding to the π-electron densities are situated above and below the molecular planes and are colored in red. Reproduced with permission from [875]. © 2016 Wiley Periodicals, Inc.

To generate quadrupole moments for all aromatic rings, positive charges are positioned in the elongation of the C-H-σ-bonds in the plane of the aromatic system. Out-of-plane negative charges are placed above and below the center of each ring. By tuning their out-of-plane displacement, the anisotropy of the quadrupole moment can be modified. Values for the out-of-plane displacement of the negative charges, for the exact position of the positive in-plane charges, and for the sizes of negative and positive charges are obtained by minimizing the difference between the quadrupole-quadrupole interaction energy and the DFT-D energy. Quadrupole-quadrupole interactions were conducted using a C++-program. More information and values can be found in [875]. The resulting quadrupole-quadrupole interaction energy is shown in Figure 61 (green line, "quadrupoles").

Obviously, it is possible to reproduce all characteristic features of the intermolecular potential energy, which arise from exchange and repulsion, with quadrupole-quadrupole interactions. If one subsequently adds a smoothly varying and entirely stabilizing dispersion-type interaction to the quadrupole-quadrupole interaction, the resulting energy almost totally coincides with the DFT-D intermolecular potential (pink line, "quadrupoles+dispersion", Figure 61). Local minima in the PES are correctly reproduced. This suggests that as long as some kind of destabilizing short-range contribution is combined with a long-range stabilizing energy component, π-π-interactions can be correctly modeled. Nevertheless, this should not imply that a correct description of the underlying physics of the interactions is not important. To demonstrate this, the parameters fitted above for a vertical distance of 3.0 Å between the DIP molecules are employed to calculate the intermolecular potential energy for a larger vertical distance of 3.3 Å. Results are shown in Figure 65. They indicate that although the features are still correctly reproduced by means of quadrupole-quadrupole interactions, the agreement between the DFT-D and the quadrupole-quadrupole energies decreases. This is due to the different distance behavior of the exchange-repulsion on the one hand and of the quadrupole-quadrupole interactions on the other hand. In the following, it will be briefly discussed that the correct distance dependence represents a serious problem for a multitude of model potentials for intermolecular interaction energies.
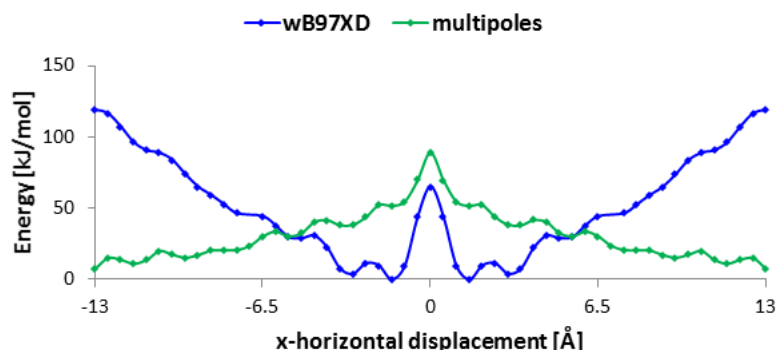
Figure 65: Comparison of ωB97X-D profile and quadrupole-quadrupole interaction energies for a larger vertical displacement of 3.3 Å in the DIP dimer.

According to SAPT, the intermolecular potential energy between organic π-systems results from a balance between stabilizing yet unspecific dispersion contributions and destabilizing and very specific repulsion interactions. Hence it could be similarly possible to use empirical van-der-Waals potentials like in force fields to model π-π-interactions, especially by tuning the repulsion term. The qualitatively satisfying performance of MM3 (Figure 62) demonstrates that such potentials should indeed be capable of reproducing the intermolecular DFT-D PESs.

To verify this assumption, a number of empirical potentials presented in the following were implemented in C++. More more information, the reader is referred to [875].

In the OPLS-AA force field, a traditional Lennard-Jones potential is used to obtain van-der-Waals interaction energies E_{vdw}, which are calculated from the distances R_{ij} between two atoms i and j and the corresponding van-der-Waals parameters folded into the coefficient C_{ij}:

$$E_{vdw} = \sum_{i=1}^{N} \sum_{j=1}^{N} \frac{C_{ij}}{R_{ij}^{12}} - a \cdot \frac{C_{ij}}{R_{ij}^{6}}$$

(443)

a is a constant that equals 1 in the regular Lennard-Jones potential.[340] Increasing its value, however, changes the ratio of stabilizing and destabilizing energy contributions in the total van-der-Waals energy. In view of the entirely repulsive Lennard-Jones energy in Figure 62, an upscaling of stabilizing contributions could improve the OPLS-AA performance. Setting a to 1.3 and scaling the complete van-der-Waals energy with a similar scaling factor of 1.3 yields the energy profile (green line) shown in Figure 66. Compared to the original OPLS-AA Lennard-Jones potential, it constitutes a significant improvement. Nevertheless, the fit parameters are distance-dependent, and the good agreement is not found for larger vertical displacement anymore (upper panel, Figure 67).

The buffered 14-7 potential used in the AMOEBA force field behaves similarly. The van-der-Waals energy is again expressed in terms of the interatomic distance R_{ij} and the van-der-Waals parameters $\varepsilon_{ij}, R_{ij}^0$:

$$E_{vdw} = \sum_{i=1}^{N} \sum_{j=1}^{N} \varepsilon_{ij} \left(\frac{1.07}{\rho_{ij} + 0.07} \right)^7 \left(\frac{1.12}{\rho_{ij}^7 + 0.12} - 2 \right)$$

(444)

ρ_{ij} is the quotient $\rho_{ij} = \frac{R_{ij}}{R_{ij}^0}$. Although the regular AMOEBA 14-7 van-der-Waals energy delivers the correct characteristics of the energy (Figure 62), differences between minima and maxima are not sufficiently pronounced. Using the numbers in the buffered 14-7 potential as parameters and minimizing the energy difference to the DFT-D potential (by separately varying the parameters[875]) yields a set of modified parameters and a potential energy with essentially correct features (green line, second panel, Figure 66; parameters: 1.07 → 1.12; 1.12 → 1.32; 0.12 → 0.08; 2 → 2.48).
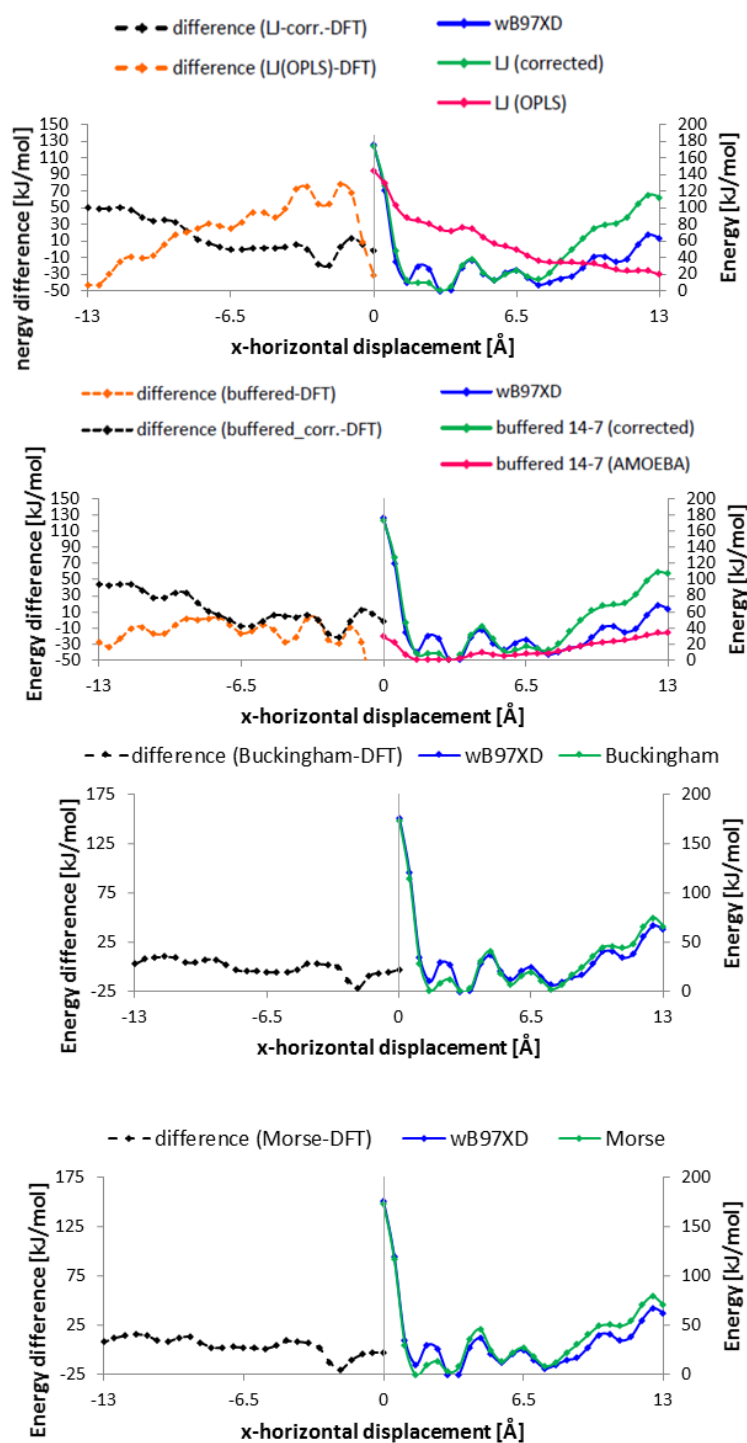
Figure 66: Different adapted van-der-Waals potentials to model the intermolecular potential of the DIP dimer. The ratio of attractive and repulsive forces is scaled in the OPLS-AA and the AMOEBA energy expressions (first and second panel). The Buckingham and the Morse potentials (third and fourth panel) are fitted to the DFT-D energy. The vertical displacement is set to 3.0 Å. Reproduced with permission from [875]. © 2016 Wiley Periodicals, Inc.
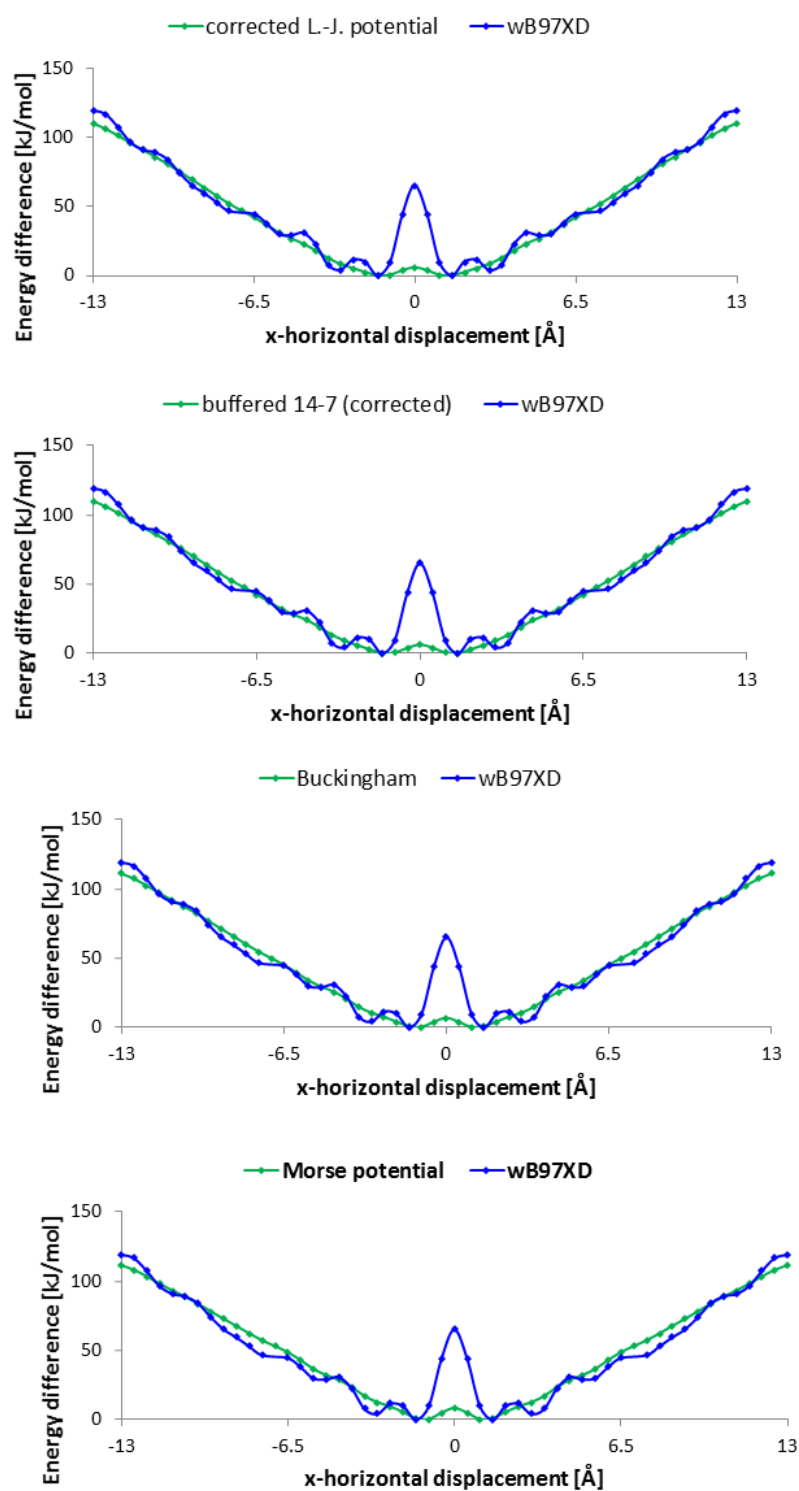
Figure 67: Using the fit parameters of the above given fits, intermolecular potentials are calculated for larger intermolecular distances of 3.3 Å. Reproduced with permission from [875]. © 2016 Wiley Periodicals, Inc.

Equivalent fitting procedures were applied to obtain Morse and Buckingham-type potentials[340] in good accordance with the DFT-D potential (second, third panel, Figure 66). The fitted Buckingham potential $E_{buckingham}$ is composed of a potential dispersion and an exponential repulsion contribution, and it depends on a polarizability-like parameter α:

$$E_{buckingham} = 0.07 \cdot \sum_{i=1}^{N} \sum_{j=1}^{N} \varepsilon_{ij} \cdot \frac{6}{6-\alpha} \left(e^{\alpha\left(1-\frac{R}{r_{ij}}\right)} - 1.95 \cdot \left(\frac{r_{ij}}{R}\right)^6 \right) \tag{445}$$

The parameters ε_{ij} and r_{ij} were obtained from the standard AMOEBA parameters as follows:

$$\varepsilon_{ij} = \sqrt{\varepsilon_i \cdot \varepsilon_j} \tag{446}$$

$$r_{ij} = \frac{1}{2}\left(r_i + r_j\right) \tag{447}$$

Similar parameters were also employed for the Morse potential E_{Morse}, which corresponds to using exponential functionals for both dispersion and repulsion. Fitting to the DFT-D PES yields the following potential:

$$E_{Morse} = 0.14 \cdot \sum_{i=1}^{N} \sum_{j=1}^{N} \varepsilon_{ij} \cdot \frac{6}{6-\alpha} \left(e^{\alpha\left(1-\frac{R}{r_{ij}}\right)} - 3.1 \cdot e^{\frac{\alpha}{1.85}\left(1-\frac{R}{r_{ij}}\right)} \right) \tag{448}$$

However, the problem that the parameters optimized for a certain vertical distance are not readily transferable to other distances (Figure 67) remains the same for all presented empirical van-der-Waals potentials, a fact already pointed out for the OPLS-AA Lennard-Jones potential. The potentials in conjunction with the fitted parameters (i.e., fitted for a given distance) do not satisfactorily reproduce the features of the intermolecular energy at other distances (Figure 67). This severely restricts the usefulness of these potentials. It should be furthermore noted that the fitting procedure becomes troublesome for molecules containing multiple different atom types such as squaraines or diketopyrrolopyrroles.

In view of the lack of generality of the empirical potentials and their parameters and the intrinsic technical problems of multiparameter fits, one would like to have a physically grounded model, which naturally results in a correct distant-dependent behavior as well as more generality. On the basis of fundamental investigations of Stone and others,[916,917,918] an approach based on the overlap of atomic p-orbitals that correctly captures the underlying physics was developed by Walter.[919] For more information see [875].

To summarize this section, a detailed analysis of intermolecular interactions between organic π-systems with a special focus on the underlying physics was presented. PESs of the intermolecular potentials between the molecular organic semiconductors calculated with DFT-D approaches are always characterized by a distinct succession of local energy minima and maxima. SAPT and LMO-EDA

analyses underlined the major importance of the exchange-repulsion interaction in determining these local energy minima and maxima while the overall binding energy is rather provided by contributions from dispersion and electrostatics. Empirical electrostatic and van-der-Waals approaches were employed to model the characteristics of the PESs. However, severe limits exist to the accuracy of such empirical approaches, most notably the lack of generality and a wrong distance dependence. Moreover, energy differences between different conformations are frequently underestimated.

In view of these findings, the question arises how to include intermolecular interactions in a multiscale approach as completely as possible. Since all force-field approaches are error-prone, they should be employed with care. This implies using DFT-D and other quantum-chemical based approaches instead of force fields as much as possible. Hence all details of the intermolecular potentials should be (if possible) included in subsequent QM single-point calculations using only parts of the MM generated geometries. Therefore, accurate equilibrium distances are the most important result from force-field calculations for multiscale approaches. Nevertheless, for equilibrium distances, force-field approaches differ only slightly (Figure 63). They generally underestimate these equilibrium distances but the effect is least pronounced for OPLS-AA (completely repulsive potential in Figure 62). Therefore, the repulsive character of OPLS-AA for short intermolecular distances and its accurate prediction of the equilibrium distance suggests using this force field in the following, the more so as it has been specifically optimized for fluids,[360,349] which are somewhat related to amorphous thin-film aggregates. Moreover, OPLS-AA calculations are efficient and low cost (type I force field), in contrast to AMOEBA (type III force field; and also to MM3, type II force field), which frequently encounters convergence problems[864] and comes at the additional expense of considerably higher calculation times due to the iterative inclusion of polarization.

Taking advantage of these key results on intermolecular interactions specifically analyzed for the π-systems of molecular organic semiconductors, the discussion continues with a description of aggregate morphologies and properties in the next section. It describes the generation of interfacial model structures for organic::organic interfaces in OSCs.

5.7 MM (Molecular Mechanics) Generation of Interface Structures

Some of the results discussed in the following can be also found in [638].

Understanding optoelectronic processes at organic::organic interfaces requires realistic model aggregates of the interfacial morphologies. In this section, the generation of interfacial model systems using molecular dynamic (MD) simulations and the OPLS-AA force field is described. In contrast to coarse-graining approaches, force fields like the herein employed OPLS-AA have the advantage of providing results with atomistic resolution.[575] Molecular dynamics (MD) in conjunction with force fields was shown to yield suitable interface model structures,[575,26] and numerous investigations on interfacial morphologies[920,580] and the resulting energy alignment[460,456] employing different variants of MDs exist. It is well-known that the MD starting structure plays a very important role[26] because a complete sampling of the conformational space of large systems is not possible.[921,922] Furthermore, large barriers cannot be overcome in MD simulations due to the limited available thermal energy.[31]

The aligned donor and acceptor crystal structures are often used as the starting structures for subsequent MD simulations where they are equilibrated.[26,923,457] This approach is also adopted for the herein generated interfacial model systems, and it is slightly adapted to mimic the experimental coevaporation/spin-coating process. This is achieved with a succession of MD simulations (Figure 68). The starting point is a single crystalline monolayer of the molecular p-type semiconductor. Vacancies are created (i.e., roughly a third of the molecules is removed) to enable some degree of structural rearrangement during the simulations. As it is the case in the experimental process, kinetic control is assumed so that the last frame of a subsequent short MD simulation (~100 ps) is used for further build-up of the interfacial structure (Figure 68, "starting point"). The last MD frame should in fact be rather disordered. Then, all coordinates are frozen. In the following step ("generation of disordered p-type semiconducting layer", Figure 68), a second crystalline slice composed of molecular p-type semiconductors with artificially created vacancies is placed several angstroms above the frozen and disordered first slice. In the subsequent MD simulation, a harmonic potential (force constant 2 kcal/Å starting at a threshold distance of 7 Å from the first slice; no potential acts below that threshold) is applied between the two slices that accelerates the molecules of the second crystal slice toward the disordered interface composed by the frozen first slice. This leads to the deposition of a second disordered layer of molecular p-type semiconductors. All coordinates are again frozen, and the next crystal slice is added. The whole cycle is repeated four to five times. A similar procedure is adopted for the fullerenes ("addition of fullerenes" in Figure 68) that are deposited on top of the disordered molecular p-type semiconductors. Single crystalline slice with created vacancies are placed above the disordered p-type semiconducting layer. The following MD step along with an applied harmonic potential simulates their deposition. The cycle is repeated several times for the fullerenes as well.

285
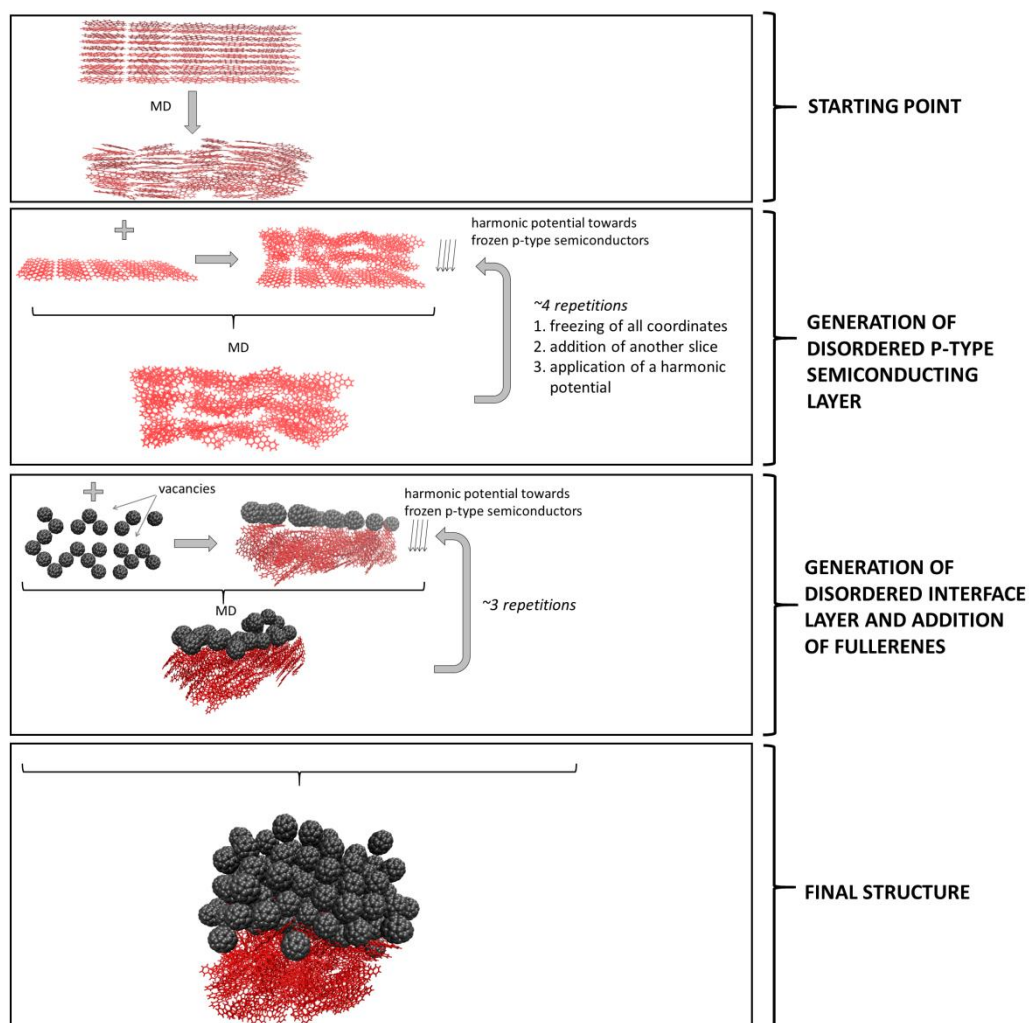
Figure 68: Illustration of the adopted method to generate disordered interfacial model systems. A single crystal slice is the starting point (top view in the first panel). Vacancies are subsequently created. A succession of MD simulations is used to stepwise construct the final interfacial structure.

In order to ascertain that the conformational space, which cannot be completely sampled (see above), is investigated at least at several complementary positions, the simulation described in Figure 68 is applied to crystalline slices taken from the three basis crystallographic planes, i.e., (001), (010), (100), of the crystal structures of the molecular p-type semiconductors. It should be noted that these planes are identical for the fullerene crystal structure because it is face-centered cubic (fcc).[924] Cleavage planes in face-centered cubic crystal structures usually correspond to the (111) crystal face and not to the crystallographic planes (001), (010), and (100).[925] However, diverse experimental investigations have shown that the crystallographic orientation of deposited fullerenes C_{60} critically depends on the substrate.[926,927] Therefore, in the MD simulations, the loosely added fullerenes should be able to freely rearrange to the correct orientation ("vacancies", Figure 68). Moreover, using the crystallographic planes instead of the cleavage planes has the additional advantage that the system is more flexible since the cleavage plane (111) in fcc structures corresponds to the crystal face with the densest packing and, correspondingly, the least spatial flexibility.

Hence, the different crystallographic planes of the crystalline molecular p-type semiconductors are aligned with the same crystalline slice of fullerene C_{60}. The dimensions of the aligned slices are determined by the least common multiple of the dimensions of the unit cell axes of the crystal structures of the molecular donors and of C_{60}. More details and values can be found in [638]. For each of these orientations, the procedure described in Figure 68 is repeated. Ultimately, this yields three different interfacial model systems per molecular p-type semiconductor. The generated structures are used for all later-on calculations of thermodynamic and kinetic data. Hence, they profoundly influence all final results.

The quality of these structures depends on the underlying force field (OPLS-AA, see above). Hence, a thorough investigation of the quality of the force-field parameters is required. It is well-known that molecules with complicated electronic structures cannot be suitably described by force fields if they are not included in the training set of the force field parameters. This presumably holds also for some of the herein included conjugated systems like squaraines, diketopyrrolopyrroles, and triphenylamines. To prevent an erroneous force-field description from spoiling morphologies and with this the results of later-on calculations, force-field monomer geometries are directly discarded. Instead, quantum-chemically optimized monomer geometries are superposed onto all force-field molecules. A three-point criterion is used for the superposition, i.e., the plane defined by three atoms in the molecular backbone is used to map high-quality QM geometries to the MM ones. A program implemented in C++ is used for the superposition. It is worth emphasizing that due to this procedure, all molecular geometries of resulting interfacial model systems are equal. Static disorder created by possibly position-dependent intramolecular relaxation processes and dynamic disorder arising from vibrations are not included in any of the later-on presented calculations. Nevertheless, replacing all MM geometries with optimized QM ones reduces the amount of required evaluation of the force-field parameters because all intramolecular force-field parameters, i.e., bond lengths and potentials, angles, torsions, and out-of-plane torsions, do not directly enter subsequent calculations. In view of the electronic complexity of the employed molecular semiconductors, it would be questionable anyway whether suitable parameters could be defined at all.[ttt] Therefore, only intermolecular force-field parameters, the atomic charges and the van-der-Waals parameters that determine the intermolecular arrangements in the interfacial model systems, remain to be evaluated.

In the previous section ("Interactions between the π-systems of molecular organic semiconductors"), standard van-der-Waals parameters of the OPLS-AA force field were used to calculate diverse

---

[ttt] Structural phenomena resulting from electron correlation, namely the bond length alternation, electron delocalization, or substituent-dependent distortions (in triphenylamines or diketopyrrolopyrroles), are difficult to incorporate into a classical MM treatment.

intermolecular potentials with an acceptable accuracy (see for instance Figure 63). The same van-der-Waals parameters were applied to atom types in different molecules. This suggests that, as commonly assumed when using force fields, van-der-Waals parameters are not molecule-specific. This assumption is quite general and fundamental to all MM calculations, and it was similarly utilized for MM3 and AMOEBA computations in the previous section. Therefore, the employed standard OPLS-AA van-der-Waals parameters will not be evaluated in detail in the following.

The use of atomic charges is, however, not as straightforward at least with the OPLS-AA force field[uuu] because overall charge neutrality of the molecules needs to be ensured. The following approach is chosen to deduce suitable atomic charges. Standard OPLS-AA parameters of distinct structural moieties (DNA bases, anthracene, naphthalene, benzamide, acetaladehyde, diphenylamine) were used to parameterize the molecules in a first step. In a second step, excess positive or negative charges were evenly redistributed so that the net molecular charge vanishes. This proceeding is certainly approximate and requires evaluation. To do so, the morphologies resulting from these charge parameters are compared to morphologies obtained with other charge parameters and otherwise unaltered simulation settings. For the comparison, three different molecules – DIP, MD353, and the squaraine – were used. Apart from the OPLS-AA charges, Mulliken, Hirshfeld,[928] CM5,[929] and ESP charges[892] obtained in B3LYP-D3/cc-pVDZ calculations were employed in separate MD simulations. Please note that in these separate simulations, each atom and not each atom type carries a different charge. The amount of disorder in resulting aggregates was analyzed because, as discussed above, MD simulations were only used to generate intermolecular disorder, with intramolecular effects being disregarded. Therefore, the intermolecular rearrangements are the only later-on used aspect where the force-field parameterization enters.

To put the analysis of disorder on a quantitative footing, a disorder parameter needs to be defined. The mutual orientations of the π-conjugated planes of the molecules are most decisive for subsequently calculated couplings, state energies, and rates.[745] These mutual orientations are reflected in the tilting angles of the planar molecular π-systems with respect to a reference plane (Figure 69; the tilting angles are defined as the angles between the normal vectors of the planar π-systems and the reference plane). The interfacial plane can be readily used as a reference plane in this case. The triphenylamine-based compounds do not have a clear-cut molecular plane so that the plane spanned by the three α-carbon atoms vicinal to the central nitrogen is used instead. In ordered crystalline systems, all molecules are equally oriented with respect to each other so that all tilting angles are exactly the same. No disorder exists, and the standard deviation of the distribution of tilting

---

[uuu] It should be noted that MM3 employs bond dipoles to describe electrostatic interactions between the molecules. This has the advantage that since only dipoles are employed, the overall charge is automatically 0.

angles is zero. In contrast, in amorphous systems tilting angles vary. Their distribution is marked by a non-zero standard deviation. The broader the spread in tilting angles, i.e., the more the orientations of individual π-conjugated molecules vary, the larger the standard deviation. Hence the standard deviation can be taken as a measure of the disorder present in any aggregate composed of π-conjugated molecules.
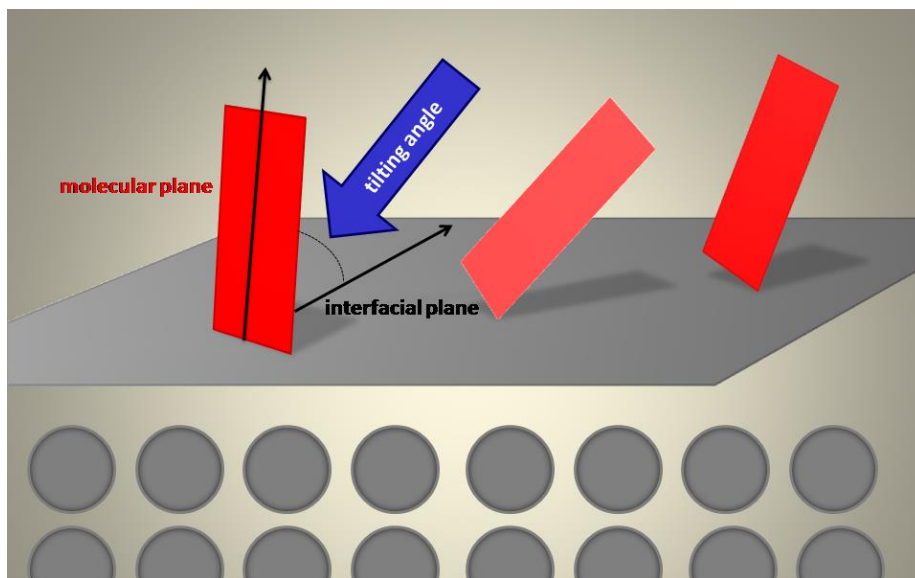
Figure 69: Illustration of the tilting angles (blue arrow) of the planar molecular π-systems (red rectangles) with respect to the interfacial plane (grey plane). Each tilting angle is defined as the angle between the normal vectors of the reference plane and the planar π-system. A C++-program was used to calculate and average all tilting angles.

The amount of disorder, i.e., the standard deviation of tilting angles, was calculated for aggregates obtained with the MD simulations using the different sets of charge parameters (standard OPLS-AA, Hirshfeld, CM5, ESP, Mulliken). It is nevertheless important to emphasize that the outcome of MD simulations does not only depend on the force-field parameters, but also on the trajectory itself. Although MD simulations are in principle deterministic, they are non-deterministic in practice especially for long simulation times due to the summation of the numerical error. Therefore, the disorder in aggregates generated with the same force-field parameters also varies because of the non-deterministic nature of the simulation. To differentiate both effects, two additional simulations with the original OPLS-AA were conducted. In the following tables (Table 20 to Table 22), the standard deviations of the tilting angles, i.e., the amount of disorder in the systems, are listed for DIP (Table 20), the squaraine (Table 21), and MD353 (Table 22). The first row of all tables indicates the methods employed to deduce the set of atomic charges. The three separate simulations conducted with the same OPLS-AA parameter set are indicated as "OPLS-1", "OPLS-2", and "OPLS-3". To rule out that the influence of the force-field charges depends on the crystallographic plane, the analyses were

performed for all crystallographic orientations, as indicated in the first columns of the tables (Table 20 to Table 22).

Table 20: Standard deviation of tilting angles, i.e., the amount of disorder, in DIP thin films generated in MD simulations using different sets of atomic charges (column 2 – column 6). The generated disorder due to the non-deterministic MD character is estimated from separate MD simulations employing the same parameters (column 6 – column 8).

charges	Mulliken	Hirshfeld	CM5	ESP	OPLS-1	OPLS-2	OPLS-3
a-b [°]	18	20	18	16	15	17	11
a-c [°]	38	52	29	36	33	37	40
b-c [°]	51	48	45	47	43	53	50
Mean [°]	**35**	**40**	**31**	**33**	**31**	**36**	**34**

Table 21: Standard deviation of tilting angles, i.e., the amount of disorder, in squaraine thin films generated in MD simulations using different sets of atomic charges (column 2 – column 6). The generated disorder due to the non-deterministic MD character is estimated from separate MD simulations employing the same parameters (column 6 – column 8).

charges	Mulliken	Hirshfeld	CM5	Esp	OPLS-1	OPLS-2	OPLS-3
a-b [°]	43	50	47	39	60	50	57
a-c [°]	40	41	33	28	31	30	41
b-c [°]	51	48	42	59	57	35	58
Mean [°]	**45**	**46**	**40**	**42**	**49**	**38**	**52**

Table 22: Standard deviation of tilting angles, i.e., the amount of disorder, in MD353 thin films generated in MD simulations using different sets of atomic charges (column 2 – column 6). The generated disorder due to the non-deterministic MD character is estimated from separate MD simulations employing the same parameters (column 6 – column 8).

charges	Mulliken	Hirshfeld	CM5	ESP	OPLS-1	OPLS-2	OPLS-3
a-b [°]	16	19	17	18	38	38	38
a-c [°]	27	28	29	29	28	38	22
b-c [°]	36	28	27	34	46	38	44
Mean [°]	**26**	**25**	**24**	**27**	**37**	**38**	**35**

It is evident from the standard deviations given in the Table 20 to Table 22 that morphology differences arising from the non-deterministic character of the MD simulations are nearly as large as those owing to the usage of different sets of atomic charges. For instance, the standard deviations for the

orientation of the squaraine molecular planes (Table 21) vary between 38° and 52° for different MD simulations with the *same* parameters. In contrast, variations range from 40° to 46° with *different* parameters. This clearly indicates that charge parameters are not necessarily decisive for the outcome of the simulations, i.e., for the final disorder. To conclude from the evaluation of the force-field parameters, the presented results suggest that in view of the inherent inaccuracies of the method and the limited influence of the parameters, resulting morphologies calculated with the OPLS-AA force field can be assumed to be sufficiently reliable, the more so as only the amount of intermolecular rearrangement and disorder will be subsequently used.

The Tinker program package[899] was used for all MD simulations. A time step of 1.0 fs and a total simulation time of 0.1 ns were employed. For the NPT-ensemble, a pressure of 1 bar was applied. The temperature was set to 500 K to facilitate sufficient intermolecular motion. To accelerate the dynamics, a cutoff of 12 Å for van-der-Waals-interactions and of 16 Å for electrostatic interactions was added.

Overall, this section presented an approximate scheme employed to obtain disordered organic::organic model interfaces. Inspired by the experimental manufacturing process, the scheme relies on force-field calculations. With regard to the difficulty of describing electronically complex molecular semiconductors with classical force fields, the influence of the force-field parameters is kept as small as possible. An evaluation in support of this was carried out.

A comparison of the resulting model systems reveals that few differences exist among the interfaces composed of different donors along with fullerene C_{60}. Tight stacks, which exist especially in the crystal structures of DIP, anthracene, rubrene, and of the diketopyrrolopyrrole, possess the most pronounced influence on the final morphology because they barely change during the MD simulations. Smaller molecules allow for a stronger intermixing of the donor phase with the fullerenes. Apart from the size, molecular properties did not show any significant influence on the interface morphology. This results probably from the fact that the apolar spherical fullerenes C_{60} undergo similarly weak interactions to all donors. Pictures of some of the model interfaces can be found in [930].

It should be always kept in mind that this thesis aims at describing optoelectronic processes at organic::organic interfaces in a multiscale approach. So far, molecular properties were comprehensively discussed on the one hand. On the other hand, intermolecular interactions and resulting aggregate morphologies were addressed. To finally accomplish the multiscale description, thermodynamic and kinetic properties of the organic::organic model interfaces are analyzed in the following.

5.8 Energetics of the exciton dissociation and charge separation processes in the vicinity of the organic::organic interfaces

To organize the discussion of the properties of the interfacial model systems, thermodynamic and kinetic aspects are separately treated. Moreover, for the purpose of improving OSC efficiencies, a special focus lies particularly on thermodynamic and kinetic loss mechanisms. In a first step, this section is entirely dedicated to the thermodynamics at organic::organic interfaces, i.e., to the energetics of the exciton dissociation and charge separation process. Similar information can be found in [638].

5.8.1 The importance of loss channels for OSC efficiencies

The light-to-energy conversion in OSCs can be subdivided into several steps.[931] In the first step, an exciton is created upon photon absorption (Step 1: light absorption).[424,5] It is usually assumed that light absorption takes place in the donor phase,[5] which is only a negligible approximation particularly with regard to the poor absorption of the herein employed C_{60} acceptors. The created exciton diffuses in a second step through the donor phase (Step 2: exciton diffusion). If it reaches the interface within its limited lifetime,[452] it can dissociate in a photoinduced charge-transfer step into an interfacial charge-transfer state (Step 3: exciton dissociation/breakup). Please note that the designation of this state is ambiguous in the literature, and various notions are frequently employed.[5] In the following, the term "charge-transfer state" refers to the interfacial geminate electron-hole pair that, depending on numerous environmental parameters, may or may not be bound. As soon as the electron and the hole escape from their mutual Coulomb attraction and move independently from one another, a charge-separated state is formed (Step 4: charge separation/transport). Finally, the electron and the hole may reach in successive charge transport steps the corresponding electrodes where they are recollected (Step 5: charge recollection).

For well-performing OSC devices, each step of the light-to-energy conversion should be as efficient as possible.[423,459] This requires a detailed atomistic understanding of all elementary processes. However, especially the exciton dissociation and charge separation mechanisms are still under debate,[423,586] and contrasting findings exist in the literature.[452] Furthermore, it has been pointed out[436] that energy dissipation channels (=energy loss channels) severely limit efficiencies of the individual processes, thereby restricting final device performances. As this thesis focusses entirely on processes in the vicinity of organic::organic interfaces, only Step 2 through Step 4 and corresponding energy dissipation channels are addressed in the following discussion. Nevertheless, these three steps are subject to a number of prominent loss mechanisms. Before presenting the results on interfacial energetics, these loss mechanisms are briefly outlined.

The BHJ cell architecture is conceived to shorten exciton diffusion lengths to increase the percentage of created excitons that actually dissociate.[462] Nevertheless, also in BHJ OSCs, excitons are quenched at impurities[493] or other quenching agents.[932] They may as well undergo exciton self-trapping.[745,877,878] Exciton trap states are energetically low-lying tail states in the excitonic DOS (density of states). If an exciton reaches such a tail state, its excess energy is dissipated into the environment, whereupon the exciton remains confined to the trap site because any further diffusion would be an energetic up-hill process. Thereby, exciton trapping reduces the OSC EQE (external quantum efficieny) and IQE (internal quantum efficiency) and, as a consequence, the short-circuit current[423,459] and the total PCE ot the device.

It is often outlined that in contrast to inorganic solar cells, the usually rather low dielectric constant in organic materials results in a significant Coulomb attraction within a geminately formed electron-hole pair.[26,452] Otherwise stated, the considerable Coulomb attraction in organic thin films gives rise to energetically very low-lying interfacial charge-transfer states. Once a dissociating exciton relaxes at the interface to such a low-lying charge-transfer state, i.e., once its excess energy is dissipated, the exciton cannot undergo charge separation anymore. EQE/IQE values decrease. Concomitantly, it was shown that the moderate addition of dopants at the donor-acceptor interface, which fill such low-lying interfacial charge-transfer states, i.e., tail states in the DOS, improves charge separation and IQE/EQE values.[933] Apart from limiting the quantum efficiencies, a number of spectroscopic investigations revealed furthermore that interfacial charge-transfer states are also intimately linked to the OSC open-circuit voltage.[439,934] Hence, these trap states deteriorate device performances in a two-fold manner by reducing both the short-circuit current and the open-circuit voltage.

Like in pristine organic semiconductors,[464] charge trapping occurs also in OSC devices. Tail states in the DOS of the charge transport levels result from oxidizing agents and disorder.[935,544] Similar to exciton trapping, once a charge has populated such a tail state, it stops migration and does not contribute to the current anymore. Organic semiconductors can be doped to increase charge carrier densities and resulting conductivies. Much alike to the effects of doping at interfaces, one of the beneficial side effects of doping in bulk phases is to fill these DOS tail states, i.e., to simultaneously improve charge carrier mobilities.[936]

To obtain a detailed understanding of many of these outlined loss mechanisms, the energetics of Step 2 through Step 4 is simulated in the following using the dimer method in combination with an effective epsilon and electric fields. Using dimers instead of monomers as the quantum-mechanical system has the advantage that the delocalization of excitons or charge carriers, which causes both a shift and a splitting of underlying monomer energies, is included. Moreover, the intermolecular interactions are quantum-mechanically treated.[745] In view of the results on intermolecular interaction energies (see

the section "Interactions between the π-systems of molecular organic semiconductors"), this can be expected to considerably improve the accuracy of the results. Employing the dimer method instead of monomer-based models contrasts with most literature investigations.[452] It would be certainly desirable to perform calculations on larger oligomers to study delocalization effects in even more detail.[536,567,575,26] However, such oligomer calculations are computationally not affordable. Moreover, in contrast to crystalline systems, the large amount of static disorder in amorphous thin films promotes exciton and charge localization so that delocalization across several monomers becomes less important for an accurate description of thin-film phenomena.

To capture the essential energetics of the interfaces, energetic profiles, i.e., diagrams with all relevant excitonic, charge-transfer, and charge carrier energies, are calculated. Please note that in the following, the terms "charge carrier" and "polaron" will be used interchangeably. By means of these diagrams, the energetic changes that an exciton undergoes on its way to a charge-separated state can be retraced. Since the interplay of the individual processes becomes evident from the diagrams, this allows for an identification of the most important efficiency-limiting loss processes. Moreover, structure-property relationships can be defined from a comparison of profiles of different molecular p-type semiconductors. Nevertheless, before addressing these aspects, the adopted theoretical approach is described in more detail.

5.8.2 Composite embedded dimer approach to calculate energetic profiles of organic::organic interfaces

Calculating the energy landscapes in the vicinity of organic::organic interfaces is computationally demanding because a large number of calculations is required. Additionally, environmental effects need to be included in the calculations since they are particularly decisive for energies of polaronic and charge-transfer states.[460,26] As already mentioned, keeping the calculations computationally manageable, quantum-mechanically treated dimers are embedded into an environment modeled with continuum solvation models and electric fields. Three types of dimers exist in the interfacial model systems (Figure 70). There are dimers composed of two molecular p-type semiconductors, dimers composed of two fullerene molecules, and dimers composed of one molecular donor and one fullerene C_{60}. Heterodimers are used to compute interfacial charge-transfer energies while the transport levels for charge carrier (polaron) transport and exciton diffusion are calculated using homodimers composed of either molecular p-type semiconductors or fullerenes C_{60}. Dimers are cut out from the interfacial model systems based on a distance criterion: all next-neighbor dimers where the distance between the centers of mass does not exceed a certain threshold value are used as QM systems in subsequent calculations.[vvv] All threshold values can be found in [638]. As described in the previous

---

[vvv] It should be noted that double-counting of dimers was avoided.

section, quantum-chemically optimized geometries are superimposed onto the dimers extracted from the MM aggregates. Using optimized ionized-state or excited-state geometries instead of ground-state geometries for the superpositions permits to estimate effects arising from intramolecular relaxation, i.e., to assess excitonic and polaronic effects. All energetic profiles are referenced to the neutral ground state of the system.
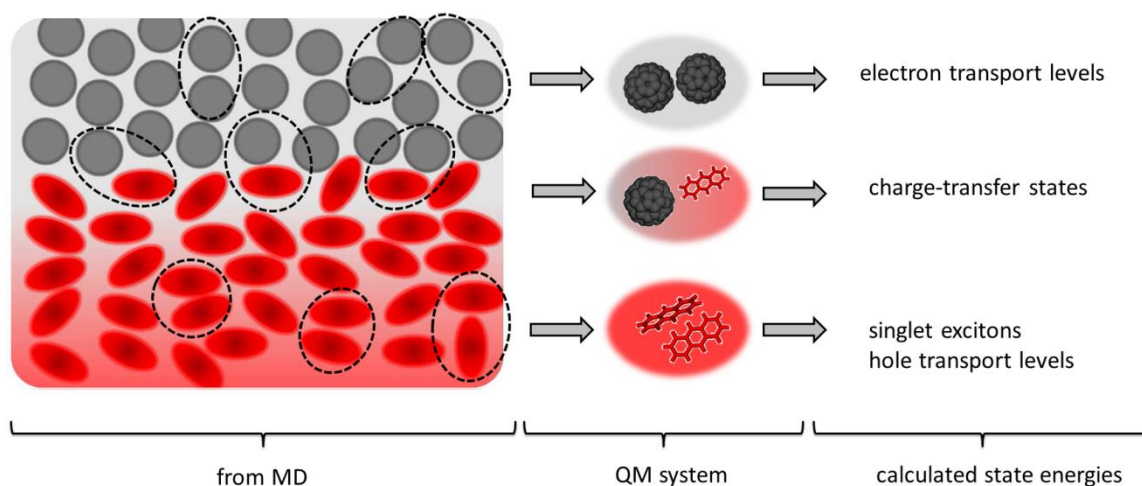
Figure 70: Possible QM dimer systems when the dimer method is applied to the interfacial model systems.

Calculations of excitons localized on dimers are straightforward since they are directly accessible from a dimer excited-state calculation. However, computing energies of both interfacial charge-transfer states (= geminate electron-hole pairs) formed upon exciton breakup at the interface and of charge-separated states is less clear-cut. It has been emphasized that the Coulomb binding energy between the geminately formed electron and hole profoundly influences the charge transport levels in the vicinity of organic::organic interfaces, underlining the necessity to incorporate it in the energy calculations.[423,5]

With regard to the computation of the charge transport levels, it is thus not sufficient to consider isolated embedded dimers. Instead, pairs of dimers are employed. This is illustrated in Figure 71 where the black circles highlight a given pair of dimers (left panel). In addition to the energies of the electron and the hole located on the respective dimers, their mutual Coulomb attraction needs to be taken into account. Therefore, the energy $E^{charge\ transport}$ for an electron-hole pair with the electron situated on a fullerene dimer and the hole located on a donor dimer is calculated as the difference between the ionization potential of the embedded donor dimer IP^{p-type} (the energy of the hole in the p-type semiconductor) and the electron affinity of the fullerene dimer EA^{n-type} (the energy of the electron in the fullerene phase) plus their Coulomb attraction $\frac{e^2}{4\pi\varepsilon_0\varepsilon|\vec{r}|}$. The electron-hole separation $|\vec{r}|$ needed

for the calculation of the Coulomb energy is estimated from the distance between the centers of mass of the corresponding dimers.

$$E^{charge\ transport} = IP^{p-type} - EA^{n-type} - \frac{e^2}{4\pi\varepsilon_0\varepsilon|\vec{r}|} \tag{449}$$

Selecting pairs of corresponding dimers in the donor and acceptor phase requires several further approximations, which are illustrated in Figure 71. First of all, only pairs of donor and acceptor dimers are used to calculate charge transport energies as in Eq. (449) if the distances between the donor or acceptor dimers and the original geminate electron-hole pair are approximately equal. The underlying physical assumption is that important charge-transfer/-separated states are symmetric with respect to the interfacial plane (blue distances in the left panel of Figure 71) because balanced electron and hole mobilities would be ideal for OSC efficiencies (see section on optoelectronic processes). Furthermore, for efficient charge separation, displacements of holes and electrons perpendicular to the interfacial plane are particularly decisive, i.e., motions away from the interface toward the electrodes. Therefore, only dimers are included to calculate energies of geminate electron-hole pairs (Eq. (449)) that are situated at similar perpendicular distances from the interfacial plane (red distances in the left panel of Figure 71). The right panel in Figure 71 contains two examples for pairs of dimers that would be selected to calculate energies of geminately formed and already partially separated electron-hole pairs. The interfacial plane is calculated as the middle plane between the centers of mass of all molecular p-type semiconductors and the centers of mass of all fullerenes. Its orientation is given by the underlying crystallographic faces (see previous section).

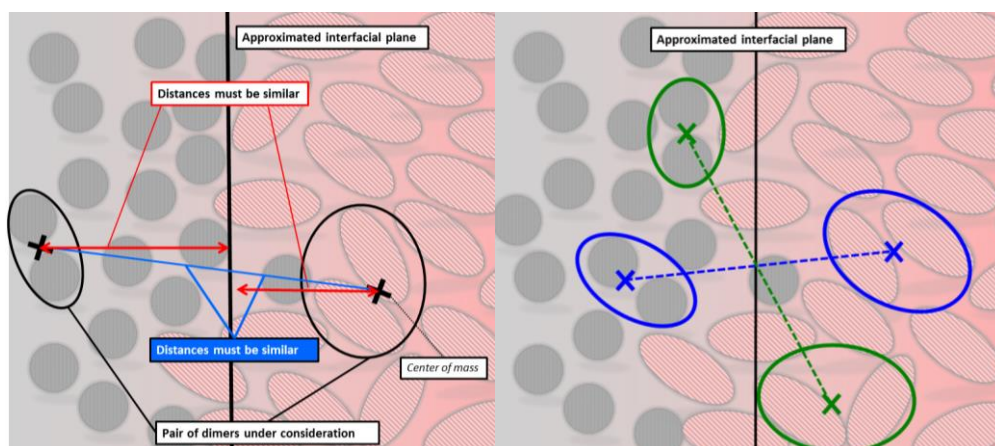Figure 71: Description how the dimers are selected for the calculation of the charge transport energies (left-hand side) and examples (right-hand side). Notably, the coordinates were rotated compared with Figure 70.

Please note that interfacial charge-transfer states are calculated in a completely equivalent procedure. Yet, individual heterodimers are used so that the ionization potential IP^{hetero} and the electron affinity

EA^{hetero} are calculated for the *same* heterodimer. The electron-hole separation $|\vec{r}|$ is approximated by the distance between the centers of mass of the monomers. With these modifications, the equation to calculate the interfacial charge-transfer states $E^{interfacial\ charge\ transfer}$ on heterodimers reads:

$$E^{interfacial\ charge\ transfer} = IP^{hetero} - EA^{hetero} - \frac{e^2}{4\pi\varepsilon_0\varepsilon|\vec{r}|} \tag{450}$$

This procedure to calculate the interfacial charge-transfer states might seem counterintuitive because the ionization potential and electron affinity of the *total* heterodimer are used in addition to the Coulomb binding energy between the *individual* monomers. Nevertheless, the soundness of the results from Eq. (450) was evaluated by comparing them to c-DFT calculations (constrained density functional theory) of charge-transfer energies at the anthracene::fullerene interface, which is the only interface where a large number of c-DFT calculations were computationally affordable due to the small size of the anthracene donor. Results can be found in [638]. Furthermore, it is well-known from the design of donor-acceptor polymers that the ionization potential is usually exclusively determined by the donating moiety (because the HOMO is localized on the donor) while the electron affinity and the corresponding LUMO are dominated by the acceptor.[462,484,13] This similarly holds for the donor-acceptor pairs at the interfaces, as further verified by visual inspection of the HOMOs and LUMOs of the heterodimers. It follows that the ionization potential (electron affinity) calculated for the total heterodimer corresponds essentially to an ionization (electron attachment) of the donor (acceptor). Additionally, some delocalization effects are taken into account.

It should be pointed out that the large number of dark states in fullerene C_{60} prohibits the direct calculation of the charge-transfer state energies as excitation energies. Nevertheless, excitonic states of the heterodimers, i.e., heterodimer excitations mostly localized on either the donor component or on the fullerene C_{60}, can be nonetheless obtained from excited-state calculations of the heterodimers. Resulting excited states correspond predominantly to an excited donor molecule next to a fullerene/to an excited fullerene next to a donor molecule. Computed excitation energies are influenced by the respective neighboring molecule. These excitation energies are designated as "interfacial excitations" in the following.

Modeling a complex anisotropic environment with a continuum solvation model, i.e., an effective epsilon, was shown to provide an acceptable description of intermolecular interactions even in polar bulk phases. [26,937,938,645] However, the environmental discontinuity present at the interface gives rise to regions with varying polarizabilities. This requires the usage of different effective epsilon values for at least three different regions: for the bulk phase of the molecular p-type semiconductor, for the bulk fullerene phase, and for the imminent vicinity of the interface. The measured permittivity of fullerene

C_{60} is used to describe the acceptor phase,[939] and, if experimental data are available, measured values for ε are used for the donor phase as well. Otherwise, ε values of structurally similar substances are used instead. Compared with the bulk phases, the presence of intermixed molecules with different polarizabilities[26] and the less dense packing around the interface[457] explain why an adequate description of the imminent interfacial vicinity with a single effective epsilon value cannot be physically grounded. It has been furthermore discussed that the energies of interfacial charge-transfer states critically depend on the choice of the epsilon value.[26,560] In order to describe the environment in the interfacial region as completely as possible while simultaneously maintaining computational efficiency, a two-fold procedure is adopted. It is illustrated in Figure 72.
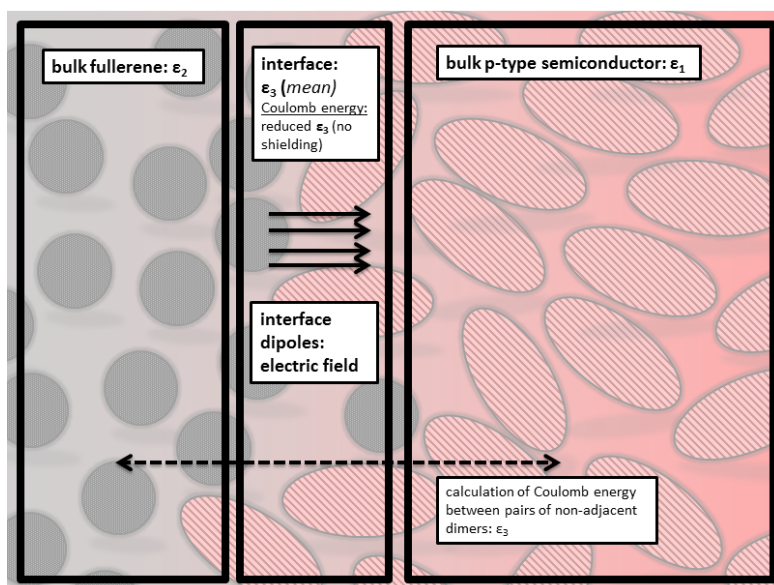
Figure 72: Illustration of the adopted approach to describe the environment in the vicinity of organic::organic interfaces. ε_1 was used for all interactions between homodimers composed of donor molecules. ε_2 was used for the fullerene phase. ε_3 was used for interactions across the interface between geminate pairs located on pairs of homodimers, i.e., between a hole on a donor homodimer and an electron on a fullerene dimer. If the Coulomb binding energy of the electron-hole pair situated on a single heterodimer was calculated, ε_3 was further reduced.

In a first step, the average value of the effective epsilons of the two adjacent bulk phases is used as an effective epsilon for interactions across the interface, i.e., between the geminate pairs (dashed arrow in Figure 72, Eq. (449)). The decrease (increase) of the epsilon at the interface compared to the bulk phase models the intermixing with molecules characterized by a smaller (larger) effective epsilon in their respective bulk phase. Please note, however, that whenever the electron and the hole are located on adjacent molecules, i.e., on a single heterodimer, this epsilon value is decreased because no shielding takes place. This is important for the calculation of interfacial charge-transfer states as in Eq. (450). All epsilon values can be found in [638].

In the calculation of the interfacial excitations, a mean electric field is applied perpendicular to the interfacial plane in a second step in addition to the polarizable continuum environment. Spectroscopic

investigations as well as computations revealed the existence of interfacial dipoles and local electric fields at organic::organic interfaces that can promote or impede charge generation (see also the Background Section).[454,455] Such local electric fields result from the combined effects of ground-state charge transfer, differing degrees of polarization in the adjacent phases,[26] and the anisotropic distribution of molecular multipole moments across the interface[456]. In the following, the locally varying electric fields and interfacial dipole moments are folded into a single average electric field. Its electric field strength is calculated as follows. From an electrostatic potential fit (ESP fit) of a gas-phase heterodimer situated at the interface and the centers of mass of its composing monomers, a dipole moment can be calculated. Since the dipole moment is obtained from a potential fit of the density, it contains all effects influencing the density such as ground-state charge transfer or polarization. Such a dipole moment can be attributed to each heterodimer located at the interface. Hence, the interface can be interpreted as an electrical double layer, in analogy to classical electrochemistry.[940] Alike to a plate condenser, the electric field inside a double layer is accessible via its capacitance, which can be computed from simple geometric quantities as well as from the dipole charges. Therefore, charges on each monomer of the heterodimer were summed to a total charge Q. As the dimer is neutral, the charges on the respective monomers are equal, but of opposite sign. This yields a surface charge distribution at both sides of the interface. According to classical electrostatics (see [940]), the electric field $\vec{E}$ resulting from a surface distribution of charges Q at both plates of a plate condenser is given by

$$\vec{E} = \frac{Q}{\varepsilon_0 \varepsilon_r \vec{A}} \tag{451}$$

$\vec{A}$ is the surface area occupied by one dipole moment. It is thus determined by the packing density. As the packing density is governed by the sterically demanding fullerene C_{60} molecules, the surface area for one dipole moment, i.e., one heterodimer, is estimated from the cross section of C_{60}. The length of the three crystallographic axes of the fullerene fcc crystal structure is $l = 14.04078$ Å.[924] Consequently, the surface area of charges can be approximated by:

$$|\vec{A}| = 15\text{Å} \cdot 15\text{Å} = 225 \cdot 10^{-20} m^2 \tag{452}$$

Similar to Castet et al.[456] who outlined that the individual dipole moments of the pairs vary considerably, significant differences between different heterodimers are found. It is, however, computationally not affordable to calculate all individual dipole moments. Therefore, performing this type of calculation for several heterodimers and averaging resulting electric field strengths yields a mean field strength associated with a specific interfacial structure. It was included in the QM Hamiltonian. The electric mean field strength completely ignores the considerable variations of the

interface dipoles, which were shown to sometimes inverse their directions,[456] but in combination with the averaged permittivity, the approach constitutes a computationally very efficient and intuitive route to model the influence of the changing environment at the interface.

Before stating actual results, the computational details are briefly described. Optimized SCS-CC2[256,180]/cc-pVDZ[705] ground- and excited-state[www] geometries and ωB97X-D[143]/cc-pVDZ[705] cationic and anionic geometries are used to replace the force-field geometries. The reliability of SCS-CC2 especially for excited-state geometries was addressed above in the framework of adiabatic excitation energies and exciton reorganization energies (section "Benchmarking vertical excitation energies of molecular semiconductors", "Benchmarking exciton reorganization energies"). In the benchmark of charge reorganization energies, ωB97X-D showed a remarkable performance (see section "Benchmarking charge reorganization energies"). In view of the favorable cost-accuracy ratio of ZINDO,[209,210,772] which was comprehensively outlined above for the individual monomers (section "Benchmarking vertical excitation energies of molecular semiconductors"), it was employed for all excited-state calculations, i.e., for the computation of all excitation energies of both homo- and heterodimers. Interfacial charge-transfer states and pairwise charge-transport levels of geminate electron-hole pairs were calculated at the RI[941,942]-BLYP[707,708,709]-D3[140]/cc-pVDZ[705] level of theory including the MARIJ[943] approximation. Using a pure GGA functional is advantageous since particularly calculations on the anionic species of fullerene C_{60} are prone to spin contamination because of the three-fold degenerate LUMO. For the ESP fits, the same level of theory was used. All SCS-CC2 and BLYP calculations were conducted with the Turbomole program package.[179] The Gaussian program package was used for all ZINDO and ωB97X-D calculations.[718] Depending on the program package, either COSMO[335] (Turbomole[179]) or IEFPCM[317] were used as a continuum solvation model (although its use would have been more consistent with COSMO, C-PCM was not employed instead of IEFPCM because initially, calculations were conducted with an anisotropic epsilon and IEFPCM). All state energies are referenced to the energy of the neutral ground-state system. A complete tabulated survey of the state-energy calculations can be found in the Supporting Information of [638]. C++ programs were employed to cut out the dimers from the interfacial model systems and to superpose quantum-chemically optimized geometries. Bash scripts were used to prepare and evaluate the large number of calculations (~ 50 000).

After the presentation of all computational details, the results are discussed. To do so, in a first step, differences between the dimer- and the monomer-based approach and the general features of the

---

[www] As discussed in a previous section ("Benchmarking exciton reorganization energies"), merocyanines undergo an excited-state torsion in the gas phase that is disabled by steric strain in the solid state. Therefore, instead of using the completely twisted excited-state structure of MD353, the same structure (i.e., with an inversed BLA) but without twisting was employed for the superposition to subsequently calculate relaxed excitonic energies.

energetics in the vicinity of interfaces are illustrated at the profile of the anthracene::fullerene interface. Then, various loss mechanisms are successively addressed. Starting with exciton trapping, charge traps as well as the influence of molecular orientation, molecular size, and polarity on interfacial charge-transfer states are subsequently discussed. Structure-property relationships are defined.

As described in the previous section on the MM generation of interfaces, all interfacial model systems exist in three different orientations resulting from the underlying orthogonal crystallographic faces. In the following, the crystallographic orientation is always indicated, and several orientations are only discussed if they are in some way influential.

5.8.3   General aspects of calculated energetic profiles: the anthracene::fullerene interface

The rather simple anthracene::fullerene interfacial system is discussed first. Its energetic profile, i.e., the relative energetic positions of excitonic, polaronic, and charge-transfer states, is given in Figure 73 for dimer calculations while Figure 74 shows corresponding results obtained with a monomer approach. The horizontal axes in Figure 73 and Figure 74 are orientated perpendicular to the interfacial plane that is located at approximately -7 Å. The origin (0 Å) corresponds to the surface of the first underlying p-type semiconducting crystalline layer. The overall size orthogonal to the interface amounts to roughly 50 Å, which is on the order of typical exciton diffusion lengths.[944] It can be thus expected that the system size is sufficient to incorporate most of the important processes in the vicinity of organic::organic interfaces. As outlined above, the horizontal dimensions of the cells are determined by the least common multiple of the unit cell dimensions of the underlying crystal structures, the fullerene C_{60} crystal structure and the donor crystal structure. Horizontal dimensions of the anthracene::fullerene-(b-c)-system (Figure 73 and Figure 74) are 45 Å times 45 Å. Energies are displayed in eV at the ordinate.
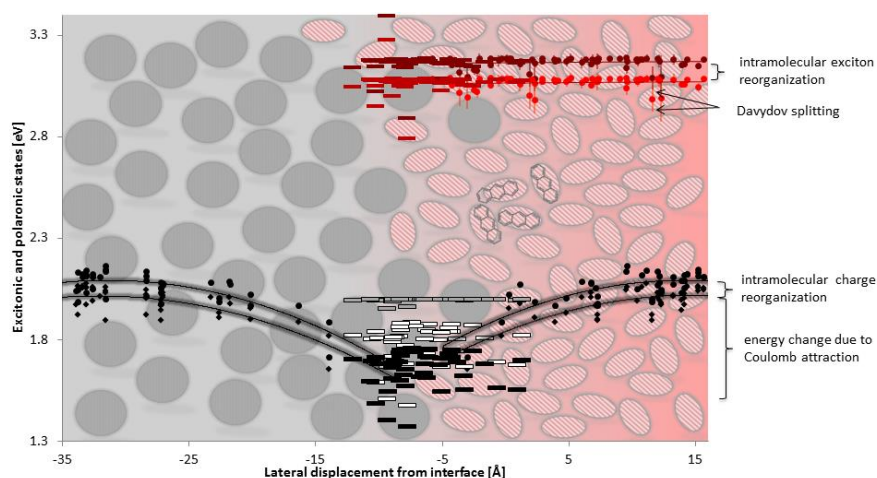
Figure 73: Anthracene::fullerene interface (b-c-plane) obtained with a dimer-based approach. Solid lines serve as a guide to the eye. The background is only a schematic representation of a general interface.
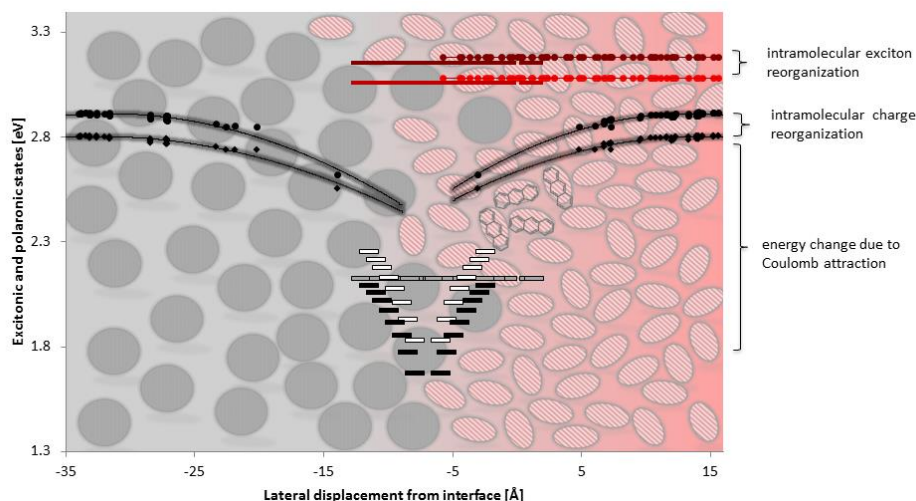
Figure 74: Anthracene::fullerene interface (b-c-plane) obtained with a monomer-based approach. Solid lines serve as a guide to the eye. The background is only a schematic representation of a general interface.

The employed symbols are clarified in Table 23. The computational approach employed to calculate the different states is repeated in curly brackets. Three different types of states are distinguished: excitons (= excitations), polarons (= charges), and charge-transfer states. Depending on its position, an excitation is further subdivided into a bulk excitation or an interfacial excitation (Table 23). An interfacial excitation is localized on a heterodimer. Moreover, vertical and relaxed states are obtained as a function of the underlying monomer geometry. Please note that both vertical and relaxed states are denoted as "excitons" or "polarons" although the lattice deformation accompanying excitations and charge carriers and resulting in the actual excitons and polarons is included only in relaxed states. In the following figures as well as in Figure 73 and in Figure 74, projections of the positions of all dimers onto the normal vector of the interfacial plane are used to indicate the position of the corresponding dimer energies (x-axis). It should be kept in mind that each symbol given in Table 23 refers to the center of mass of a dimer.

Table 23: Symbols used to designate different states in the following figures. If not stated otherwise, symbols refer to states in the donor phase, i.e., of the p-type semiconducting materials.

State	Symbol
bulk excitations	
bulk exciton (vertical) {ZINDO on homodimers with ground-state monomer geometries}	🔴
bulk exciton (relaxed)	🔴

{ZINDO on homodimers with excited-state monomer geometries}	
interfacial excitations	
interfacial exciton (vertical) {ZINDO on heterodimers with ground-state monomer geometries}	▬ (dark red)
interfacial exciton (=donor) (relaxed) {ZINDO on heterodimers with excited-state monomer geometries}	▬ (red)
interfacial excited fullerene {ZINDO on heterodimers with ground-state monomer geometries}	▭ (gray)
polarons	
polaron (vertical) {BLYP on pairs of homodimers with ground-state monomer geometries}	●
polaron (relaxed) {BLYP on pairs of homodimers with charged-state monomer geometries}	◆
interfacial charge transfer	
charge-transfer state (vertical) {BLYP on heterodimers with ground-state monomer geometries}	▭ (light gray)
charge-transfer state (relaxed) {BLYP on heterodimers with charged-state monomer geometries}	▬ (black)

Light absorption in the donor phase (right-hand side in Figure 73 and Figure 74) leads to the formation of excitons (light and dark red circles). Vertical singlet excitations are indicated with dark red circles ("bulk exciton (vertical))", Table 23). When dimers are employed as the quantum-mechanical systems, several relaxation mechanisms for a vertical exciton can be distinguished, in contrast to monomer-based approaches where only the following one exists:

1. The coupling of the excitation to intramolecular vibrations leads to intramolecular reorganization, resulting in an energetic relaxation of ~ 0.10 eV (light red circles, Figure 73, "bulk exciton (relaxed)", Table 23). As this coupling mechanism is confined to a single monomer, it is naturally also included in monomer-based approaches (Figure 74). It is evident from the Marcus rate equation that the amount of internal reorganization induced by a diffusing exciton profoundly impacts the diffusion rate.[532] This has been discussed in detail in the context of exciton reorganization energies (see section "Benchmarking exciton reorganization energies").

Additionally, in dimer-based approaches, underlying monomeric excitations split. This gives rise to two additional relaxation mechanisms that are not included in the monomer picture.

2. Especially in H-aggregates, the second (=bright) Frenkel state is excited. Upon exciton relaxation, the exciton may undergo internal conversion to the lowest Frenkel state (Kasha's rule).[418] This implies that the additional energetic relaxation due to the coupling of monomer excitations in a dimer is given by the Davydov splitting of dimer excitations. This Davydov splitting is displayed as vertical red bars on all excitonic state energies (Figure 73).

3. Moreover, it is evident from a comparison of Figure 73 and Figure 74 that the lowest dimer excitation energies spread energetically while excitation energies calculated with the monomer-based approach constitute flat lines. The variations of the first excitation energies of the dimers result from their different arrangements, i.e. from the structural disorder at the interface.[5] The disordered dimer states cover an energy interval of approximately 0.15 eV. In such a disordered excitonic DOS, spectral diffusion[548] occurs: excitons relax over time to dimers with particularly low energies. As discussed above, such low-lying excitonic states act as trap states because once an exciton has relaxed to these sites, its further diffusion is energetically hampered. Experimentally, the population of such trap states has been observed as a spectral shift of luminescence spectra.[548]

Exciton diffusion is influenced by all outlined relaxation mechanisms (intramolecular reorganization, H-aggregation, disorder). Nevertheless, an exciton diffusing through the donor bulk phase (right-hand side, Figure 73) may still reach the interface where it begins feeling the neighboring C_{60} molecules. Energies of interfacial excitons slightly shift compared with bulk excitons (red and dark red bars, Figure 73, "interfacial exciton (vertical)", "interfacial exciton (relaxed)", Table 23).[xxx] Furthermore, the energy range covered by excitonic states broadens, i.e., the energetic disorder increases. Tail states in the

---

[xxx] It is again noted that these interfacial excitons are calculated from ZINDO excited-state calculations on heterodimers.

excitonic DOS have energies around 2.80 eV, whereas the high-energy limit lies at 3.40 eV. Van Voorhis et al. discussed several types of band bending occurring at organic::organic interfaces, among others, a spread in energies due to the existence of vacancies and density variations.[26] In line with this reasoning, unsystematic changes of band energies are found for the anthracene::fullerene system, contrasting with other literature findings.[601] Band bending is not incorporated in monomer-based approaches. Excitons reaching the vicinity of the interfaces only feel changes in the electrostatic description of the environment (Figure 74). As can be seen from Figure 74, the environmental influence on excitonic energies is rather weak.

Once the exciton has reached the interface, a number of possible follow-up processes exist. First of all, Förster transfer of the excitation energy to a fullerene is possible, leading to an excited fullerene adjacent to a ground-state anthracene. This type of state is given as grey bars in Figure 73 ("excited interfacial fullerene", Table 23). In contrast, the exciton could also dissociate into a geminate electron-hole pair, i.e., an interfacial charge-transfer state composed of a hole located on an anthracene molecule and an electron situated on a neighboring fullerene ("charge-transfer state (vertical)", Table 23, white bars, Figure 73; calculated with Eq. (450)). Again, intramolecular reorganization – local electron-phonon[YYY] coupling – leads to corresponding relaxed states ("charge-transfer states (relaxed)", Table 23, black bars, Figure 73).

As stressed by Clarke and Durrant,[423] the light-to-energy conversion in OSCs is an energetic down-hill process. This means that the charge-separated state should be the energetic minimum of the system, and that no other thermodynamic sinks should exist that prevent the system from reaching this energetic minimum. In the anthracene::fullerene system, the interfacial charge-transfer states are energetically more stabilized than interfacial excitations on fullerene molecules (Figure 73). This is a prerequisite for efficient charge generation. Otherwise, excitation energy transfer from the donor to the fullerene, then the thermodynamically most favorable process, will rather occur than exciton dissociation. In this case, no significant charge generation takes place.[945] It should be furthermore emphasized that as long as the charge-transfer state is the energetically lowest-lying state at the interface, it constitutes the major thermodynamic sink even if excitation energy transfer is kinetically more favored. Under these conditions, the incoming exciton would probably first hop to a fullerene C_{60} molecule (= excitation energy transfer). In a subsequent step, however, it can still dissociate into an interfacial charge-transfer state via hole back transfer to the donor phase. Such a situation was

---

[YYY] Please note that by definition, a „phonon" as a lattice vibration cannot be local. However, the coupling to intramolecular vibrations leading to nuclear reorganization upon ionization/excitation is nonetheless often referred to as the "local electron-phonon coupling".[418]

investigated by Brédas, Beljonne, Janssen and coworkers for an oligophenylene-vinylene::fullerene derivative dyad.[946]

Charge-transfer states obtained with the monomer-based approach (Figure 74) can be compared to the discussed dimeric charge-transfer states (Figure 73). Monomeric charge-transfer states are computed from the ionization potential of anthracene, which is constant aside from an environmentally induced change in the direct vicinity of the interface, the fullerene electron affinity, which is also constant, and the mutual Coulomb attraction between the electron and the hole, featuring an r^{-1} dependence. The Coulomb attraction, the only position-dependent contribution to monomeric charge-transfer energies, results in an exact r^{-1} dependence of total charge-transfer energies (Figure 74). The markedly different and much more disordered behavior of dimer interfacial charge-transfer energies (black and white bars, Figure 74) underlines the importance of including delocalization effects.

After exciton dissociation, the generated geminate electron-hole pair breaks up and the electron and the hole begin to separate. The charge transport (= polaron) levels describe the energetics of the charge separation process. Vertical polaron states are indicated with black circles in Figure 73 ("polaron (vertical)", Table 23). Including intramolecular relaxation yields the relaxed polaron states (black diamonds, "polaron (relaxed)", Table 23). The amount of reorganization in the ionized states corresponds to the difference between vertical and relaxed polaron states. Close to the interface, the Coulomb attraction between the dissociating electron and the hole is still considerable. Its decrease with increasing charge separation results in an r^{-1} dependence of the polaron transport levels. The Coulomb attraction is somewhat reduced by the dielectric screening in the environment (Figure 72). Polaron transport levels become a flat line only for larger distances from the interface. These distances are above the Coulomb capture radius from classical Onsager theory.[5] At the Coulomb capture radius, the Coulomb attraction drops below the available thermal energy so that the charges are not bound anymore. Then, they represent independent, freely migrating charges that may or may not be eventually recollected at the electrodes. As already observed for exciton diffusion, monomer-based approaches (Figure 74) do not capture local disorder in the polaron transport levels, which are consequently entirely determined by the Coulomb attraction between the oppositely charged polarons. It is well-known that disorder significantly affects charge transport properties in organic thin films.[418]

It has been outlined above that tail states in the DOS of excitons, polarons, and charge-transfer states induce trapping and limit OSC quantum efficiencies as well as device performances. Nevertheless, it becomes evident from Figure 73 that there are barely any systematic trap states in the anthracene::fullerene system. All state energies are located within rather small energy ranges. Other

problems of this donor::acceptor combination are responsible for its inexistence in optoelectronic devices. These include notably the poor overlap of the anthracene absorption with the solar spectrum and the high tendency of photoexcited anthracene molecules to undergo cycloaddition reactions.[947] Moreover, two further *general* aspects might additionally account for the absence of the anthracene::C_{60} OSCs, namely a potentially disadvantageous mechanism of charge generation imposed by the interfacial energetics and energy-dissipating triplet states in the fullerene layer. These two aspects are briefly discussed before turning to other employed systems and their energy loss channels.

As already mentioned above, the mechanisms for charge generation in OSCs is a research area of intense debate. One differentiates between the cold and the hot exciton breakup, depending on whether excess energy plays an important role or not. In hot exciton breakup, an exciton dissociates at the interface into higher-lying "hot" charge-transfer states that are electronically/vibrationally excited and more delocalized. The excess energy and excited-state delocalization assist in driving charge separation. In contrast, according to the cold mechanism, a fully relaxed charge-transfer state undergoes further dissociation and final charge separation.[26] The driving force is provided by other existing gradients in the free energy landscapes, for instance entropy.[451] A plethora of both experimental and computational investigations is dedicated to the further elucidation of the mechanism of charge generation in OSCs.[590,591,455,586] As kinetic aspects are disregarded in this section of the thesis, the energetic profiles focusing exclusively on thermodynamic data only allow for a statement whether cold exciton breakup is *in principle* feasible, not whether it actually takes place. It can be seen from Figure 73 that rather low-lying relaxed interfacial charge-transfer states exist in the anthracene::fullerene system (black bars). On the one hand, they arise from the low dielectric constant of the medium that shields charge-charge interactions only to a minor extent. On the other hand, the small size of the anthracene molecule is also to some extent responsible because it enables close contacts between geminately formed electron-hole pairs and gives rise to very short initial charge separations: in average, the electron and the hole are separated by only 7 Å in the interfacial charge-transfer states, a value that compares well with experimental ones ranging from 5 Å to 10 Å.[423] The decisive influence of the initial charge separation for the outcome of the charge generation process is already included in the classical Onsager theory.[5] Because of the low-lying interfacial charge-transfer states at the anthracene::fullerene interface, the charge-separated states (black circles and squares, Figure 73) are *significantly* higher in energy by about 0.20 eV to 0.50 eV, which considerably exceeds the available thermal energy. These findings suggest that in hypothetical anthracene::fullerene OPV, only hot exciton breakup would be possible.

Turning to the triplet states in the anthracene::fullerene system, it should be kept in mind that the charge generation process in OSCs must be energetically down-hill.[423] So far, only singlet states were

considered but it has been already mentioned (see section "Benchmarking vertical excitation energies of molecular semiconductors") that the energetic positions of triplet states are also fundamental to functional OSCs.[423] Triplet states can act as traps, effectively quenching especially polarons.[948,949] Furthermore, depending on their energies, they might be thermodynamic sinks in the system, leading to energy dissipation. The energy of the lowest fullerene C_{60} triplet state has been experimentally determined to be 1.6 eV.[950] As a result of the high ionization potential of anthracene,[621] the energies of charge-separated states in the anthracene::fullerene system considerably exceed this value. Therefore, the energetically lowest state of the system does not correspond to the targeted charge-separated state, but to a fullerene triplet state, which thereby constitutes a potentially significant energy loss channel.
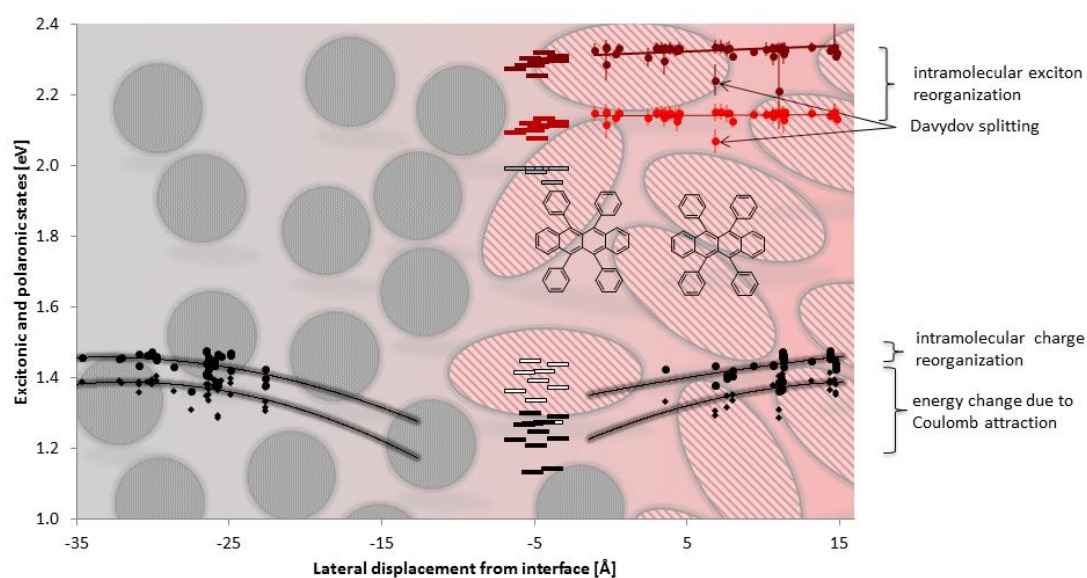
Figure 75: Energetic profile along the rubrene::fullerene interface (a-b-crystallographic plane). For an explanation of the symbols see Table 23.

Altogether, a number of reasons for the inexistence of operative anthracene::fullerene systems were outlined, i.e., the poor overlap of the anthracene absorption with the solar spectrum, the susceptibility of photoexcited anthracene to cycloadditions, energetically low-lying interfacial charge-transfer states at the anthracene::fullerene interface, and the possibility of triplet quenching. With these at the back of one's mind, the rubrene::fullerene system is considered next (Figure 75). In contrast to the anthracene::fullerene system, resulting OSCs based on rubrene are quite well-performing.[511] First of all, the larger overlap of the rubrene absorption with the solar spectrum certainly contributes to this improved photovoltaic performance. Moreover, photoinduced cycloadditions of rubrene are not a problem either. Nevertheless, two additional aspects might be also significant:

1. The charge-separated states indeed constitute energetically very low-lying states of the fullerene::rubrene system (Figure 75). In contrast to their counterparts in the anthracene::fullerene system, the charge-separated states are furthermore lower in energy than all fullerene triplet states. This results mainly from the lower ionization potential of rubrene compared with anthracene. Charge generation is thus thermodynamically favorable.

2. The larger size of rubrene together with its bulky phenyl substituents account for larger initial electron-hole separations in the interfacial charge-transfer states. This raises corresponding charge-transfer energies because the Coulomb binding energy between the geminate electron and hole decreases. No interfacial charge-transfer trap states exist at the rubrene::fullerene interface anymore, and the open-circuit voltage should be higher. In fact, You and coworkers[951] experimentally measured side-chain effects on the open-circuit voltage in polymer::fullerene OSCs. They found a pronounced influence of polymer side chains, which could be possibly explained by side-chain induced shifts of the interfacial charge-transfer states. Apart from the higher open-circuit voltage, the energetically less stable interfacial charge-transfer states in the rubrene::fullerene system suggest furthermore that cold exciton breakup should be feasible.

After this analysis of general aspects of the interfacial energetics and a brief discussion of the rubrene::fullerene system, energy loss mechanisms are discussed for a number of systems in the following. The discussion begins with exciton trapping in DIP::fullerene OSCs.

5.8.4 Exciton traps in the p-type semiconducting layer

Due to the distinct tendency of DIP to crystallize, crystalline DIP aggregates exist in thin-films OSCs, as demonstrated by X-ray diffraction measurements.[671] Therefore, similar to the pure DIP crystals where exciton diffusion lengths sometimes exceed 60-70 nm,[952] favorable exciton and charge transport properties[671] result for the DIP::fullerene OSCs, also explaining their usually high device efficiencies.[671] In contrast to the very effective exciton diffusion in DIP, exciton diffusion lengths are considerably shorter (22 nm)[745] in crystals of the structurally and electronically related PTCDA compound. The divergence was explained by the existence of an exciton self-trapping mechanism via an intermolecular rearrangement within a PTCDA/DIP dimer[745] that is possible in PTCDA crystals, but disabled by steric strain in DIP crystals. The intermolecular rearrangement results in a specific PTCDA dimer conformation with a very low exciton energy. From Figure 76, it can be seen that in amorphous DIP::fullerene systems, equivalent DIP dimer conformations with very low exciton energies exist. Such DIP conformations constitute deep tail states in the excitonic DOS and certainly cause exciton trapping. Moreover, in contrast to PTCDA crystals, no further intermolecular rearrangement is necessary for exciton trapping to occur in amorphous DIP phases. Apparently, already the structural diversity of

309

existing DIP dimer conformations results in a broad distribution of excitonic energies. Among the existing dimer conformations, the conformation corresponding to a self-trapped exciton is included. It can be seen from Figure 76 that tail states in the excitonic DOS lie by up to 0.30 eV in energy below the average exciton transport levels. This largely exceeds the available thermal energy so that any exciton relaxing on such sites is trapped (deep red circles, Figure 76). The trapping enabled by the amorphous DIP environment explains the experimentally observed shorter exciton diffusion lengths in amorphous DIP films and the reduced device performances of OSCs based on amorphous DIP derivatives.[671]
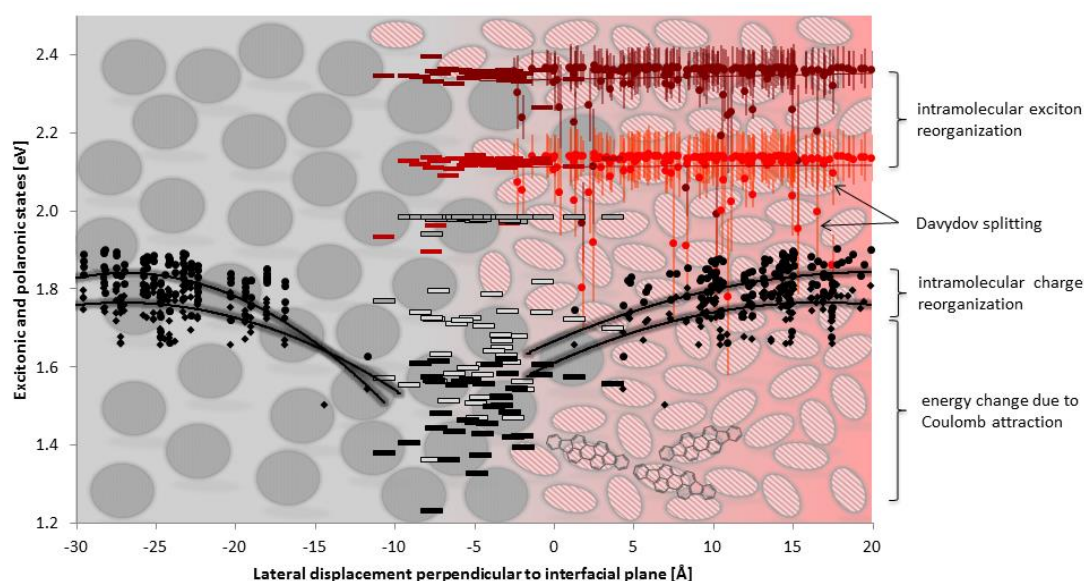
Figure 76: Energetic profile along the DIP::fullerene interface (a-c-crystallographic face). The DIP molecules are orientated almost flat and face-on on top of the fullerene phase – a lying conformation. Please note that the Davydov splitting is depicted as small bars. For an explanation of the symbols see Table 23.

Figure 77: "Triamine-methoxy"::fullerene system (a-b-crystallographic plane). It is worth emphasizing that some energetically low-lying relaxed singlet excitons exist. For an explanation of the symbols see Table 23.

A different mechanism for exciton trapping can be found in the bulk phases of the triphenylamine-based compounds. To illustrate this, Figure 77 displays the energetic profile of the "triamine-methoxy"::fullerene system, while Figure 78 shows the corresponding profile for the "triamine"::fullerene system. Evidently (Figure 77), there exist tail states in the excitonic DOS of the bulk phase of "triamine-methoxy". Analyzing these low-energy excitations reveals that they possess the characteristics of excimers, i.e., of intermolecular charge-transfer complexes. The methoxy-substituted triphenylamine-based compound features an intramolecular charge-transfer excitation. Such an excitation is quite typical for the underlying donor-acceptor structure where a considerable molecular backbone or scaffold separates the donating from the accepting moiety. If such a donor-acceptor compound forms a thin film, it can happen that donating and accepting moieties belonging to different molecules are in closer contact than the corresponding moieties within a single molecule. In this case, charge separation in an intermolecular charge-transfer process is smaller than in the intramolecular one so that the former becomes energetically favorable. An excimer results. Since such excimers are energetically very stable, they often constitute exciton traps. Generally, the intimate relationship between intra- and intermolecular charge-transfer states in donor-aceptor compounds similar to the "triamine-methoxy" compound has already been experimentally addressed.[953,954] Furthermore, as described above, a particularity of the methoxy-substituted triphenylamine is the excited-state torsion that it undergoes upon photoexcitation. It is evident from Figure 77 that more exciton trap states exist for the relaxed excited-state geometry. This implies that the excited-state torsion in the methoxy-substituted triphenylamine contributes to the trapping and promotes excimer formation.
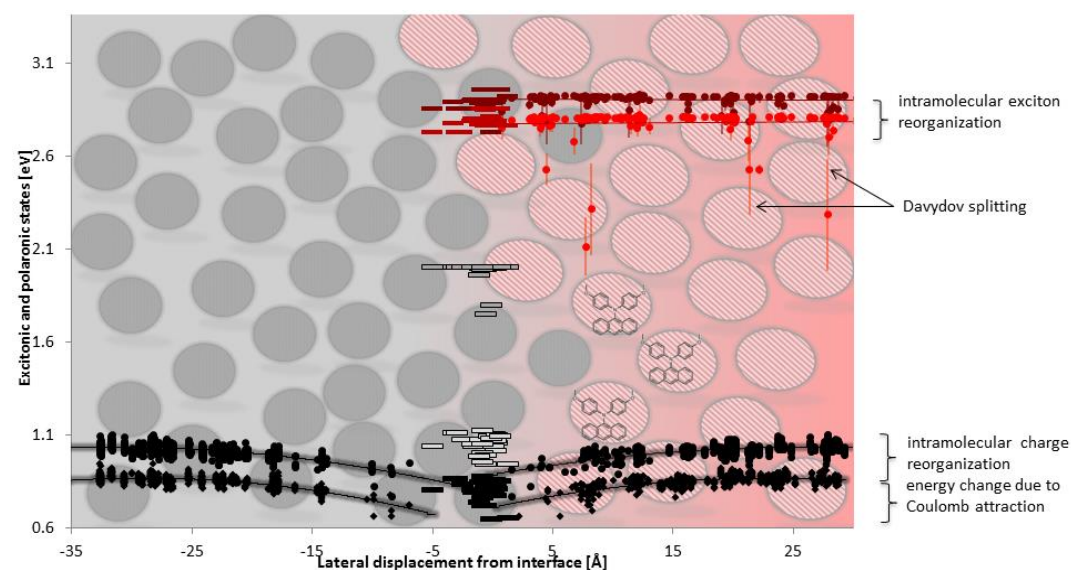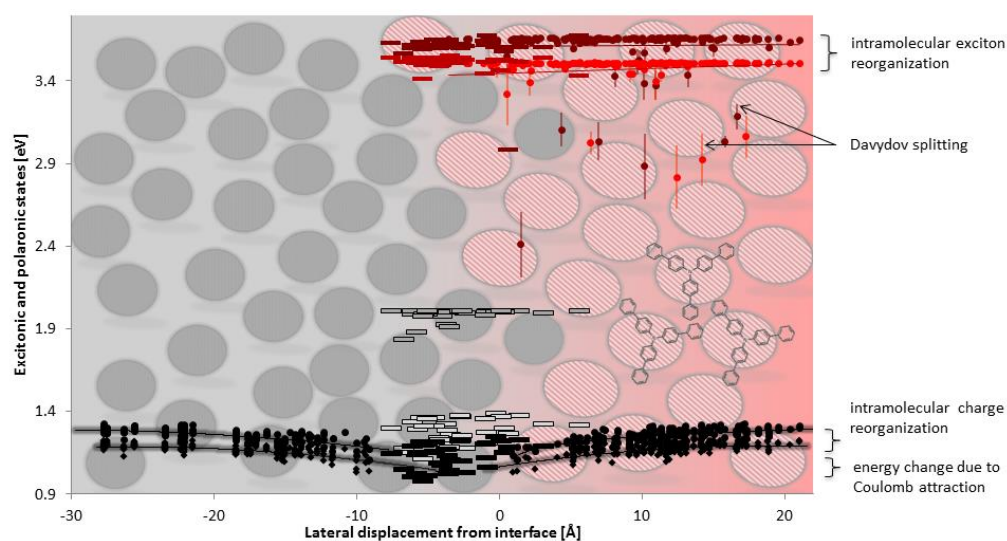

Figure 78: "Triamine"::fullerene system (a-b-crystallographic plane). It is worth emphasizing that some energetically low-lying relaxed singlet excitons exist. In contrast, charge transport levels are very narrow. For an explanation of the symbols see Table 23.

A comparison of the polaronic states in the bulk phase of "triamine-methoxy" (Figure 77) with the DIP results (Figure 76) reveals that the polaronic states in "triamine-methoxy" dispose a rather narrow energetic distribution. The energy range covered by polaronic states in the "triamine" compound (Figure 78) is even narrower. This suggests that charge transport is efficient because it is subject to an only small amount of static disorder. Yet, similar to the "triamine-methoxy" compound, exciton traps also exist in the "triamine" bulk phase (red circles, Figure 78), thereby limiting exciton diffusion. These results for triphenylamines, i.e., efficient charge and poor exciton transport, mirror the fact that few functional OSC devices based on triphenylamine derivatives exist[685] although the latter are widely employed as hole conductors.[682,683] Moreover, as triphenylamines have approximatively spherical three-dimensional shapes, their properties can be expected to be rather isotropic. In line with this expectation, all discussed findings (Figure 77, Figure 78) were shown to be independent of the crystallographic orientation. The reader is referred to the Supporting Information of [638] for a comparison of the energetic profiles in different crystallographic orientations. Diverse experimental results were already explained with the isotropic and homogeneous properties[682,683] of triphenylamines. Properties and energetic profiles of other molecules such as DIP depend significantly on the morphology, as discussed below.

Other than the poor overlap between the solar spectrum and the absorption of many triphenylamine derivatives,[zzz] the rather low-lying interfacial charge-transfer states at the interfaces of triphenylamines with fullerene C_{60} are incompatible with good device performances because they lead to low open-circuit voltages.[440,439] The calculated interfacial charge-transfer state energies of around 1 eV at the interface between the "triamine-methoxy" (Figure 77) or the "triamine" (Figure 78) compound to fullerene C_{60} are certainly very low-lying. Low ionization potentials of most triphenylamines are one of the underlying reasons for such energetically deep interfacial charge-transfer states. It was shown that the drawbacks of triphenylamines - high excitation energies and low ionization potentials - can be eliminated to some extent by attaching conjugating electron-withdrawing groups to the triphenylamine-based scaffolds.[624] Resulting donor-acceptor compounds feature red-shifted intramolecular charge-transfer absorption bands as well as higher ionization potentials. A comparison of the energetic profiles of the "triamine" and the "triamine-methoxy" compound to the corresponding profile of an aldehyde-substituted triphenylamine (Figure 79) supports these general findings, particularly with regard to the charge-transfer states. Relaxed interfacial charge-transfer states at the "triamine-aldehyde"::fullerene interface (black bars) are about 0.50 eV higher in energy than corresponding states in the other two systems. Notably, since the aldehyde-substituted

---

[zzz] In line with Figure 77 and Figure 78, absorption energies of triphenylamine-based compounds are too high compared with the solar spectrum.

triphenylamine system is smallest, shorter electron-hole separations and thus increased Coulomb binding energies of geminate electron-hole pairs result at first. However (Figure 79), this increase in stabilization of the charge-transfer states is apparently overcompensated by the higher ionization potential of the underlying "triamine-aldehyde", which destabilizes them. Leaving aside the interfacial charge-transfer states, all remaining energetic aspects of the "triamine-aldehyde"::fullerene system, i.e., charge transport levels and the excitonic DOS, are quite similar to those already discussed for its larger relatives, the "triamine" and the "triamine-methoxy" compound.

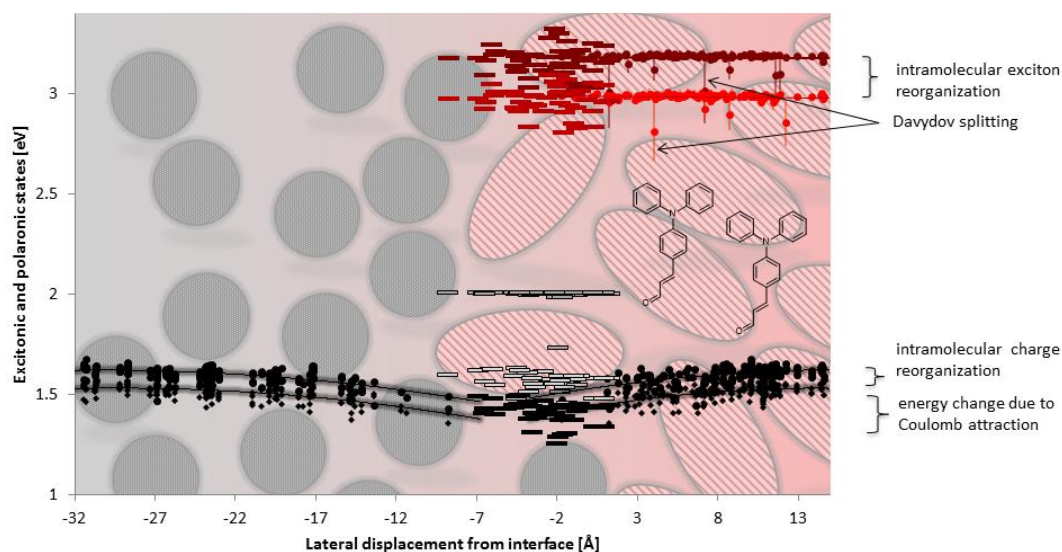Figure 79: "Triamine-aldehyde"::fullerene system (b-c-crystallographic face). For an explanation of the symbols see Table 23.

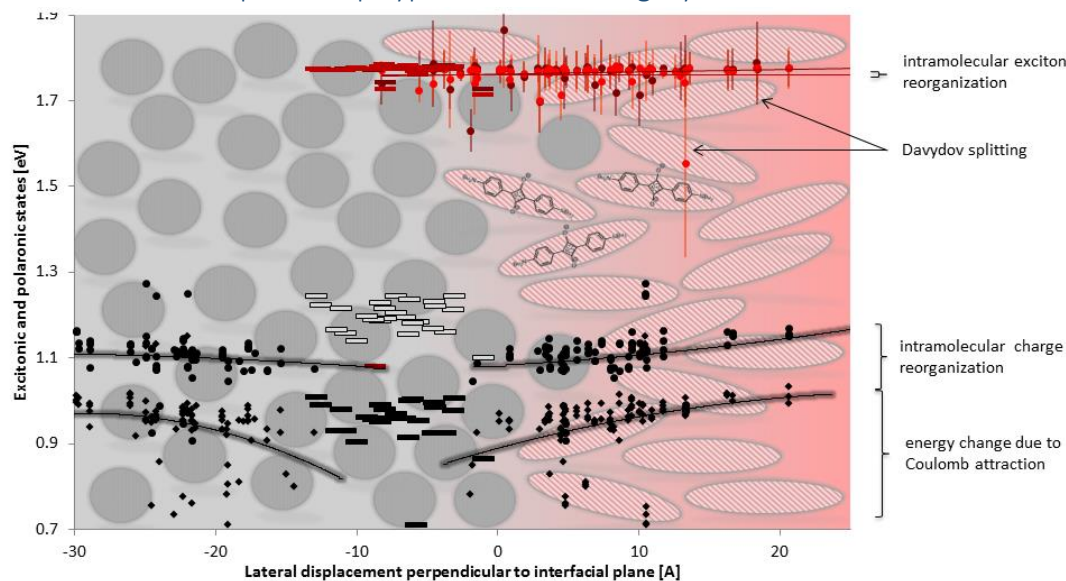### 5.8.5   Polaron traps in the p-type semiconducting layer

Figure 80: Squaraine::fullerene interface (a-b-crystallographic plane). Please note that a singlet exciton in the squaraine bulk phase is energetically below a fullerene singlet exciton. For an explanation of the symbols see Table 23.

Figure 80 shows the energetic profile of the squaraine::fullerene interface. It indicates that pronounced differences between exciton and polaron transport exist in the squaraine bulk phase. The excitonic DOS is very narrow (red circles, Figure 80). Furthermore, intramolecular relaxation is virtually negligible. This results because the rigid electron-rich squaraine core, where the excitation is localized, shows hardly any excited-state reorganization.[623] Thus exciton diffusion through the squaraine thin film can be expected to be efficient, which is indeed reflected in experimental findings about fast exciton transport in squaraine-based devices.[690] Moreover, narrow and red-shifted absorption properties due to the tight J-aggregation of squaraine molecules also in thin-film environments were experimentally found.[691,690] This is in line with the absence of trap states and disorder in the excitonic DOS in Figure 80.

The energetically very narrow exciton transport levels in the squaraine system (Figure 80) contrast with the polaronic states that spread considerably in energy. The latter are thus subject to a significant amount of disorder, which usually results in rather poor hole transport properties. Indeed, comparably low hole mobilities were experimentally found in squaraine thin films.[653,691] According to the calculations and the subsequent visual inspection of squaraine dimers with different polaronic energies, the disorder of the polaronic states is due to the quite strong charge-charge interactions between individual squaraine molecules in the tightly packed but slightly disordered J-aggregate. In squaraine crystals, charge-charge interactions between the adjacent aggregated squaraine molecules are equal because all sites are equivalent. However, in the subsequent MD simulations used to generate the interfaces, adjacent squaraine molecules were somewhat shifted with respect to each other. Then, upon ionization, they may experience differently stabilizing or destabilizing interactions with neighboring charges, leading to variations of polaronic transport energies.

5.8.6 Interfacial charge-transfer traps

Numerous investigations have addressed the intimate relationship between the open-circuit voltage of the device and the charge-transfer state energies at the underlying donor-acceptor interface.[439,955,934,956,440] It has been already analyzed in the literature how individual molecular properties like the polarity and the orientation of molecular aggregates profoundly influence these interfacial charge-transfer states.[26,454] Nevertheless, especially the interplay of the individual molecular properties has to be taken into account to understand in detail their impact on the charge-transfer energies at the interface. For this purpose, the combined influence of molecular orientation, polarity, and size is discussed in the following.

The relationship between the orientation of DIP aggregates, either standing/tip-on or lying/face-on with respect to the interface, and resulting charge-transfer states at the donor-acceptor interface was thoroughly experimentally studied, among others, by Brütting et al.,[957] by Barrena et al.,[958] and by Chen

et al.[959] As already addressed by Beljonne and Heremans and coworkers[597] for the pentacene::fullerene interface, larger couplings and rates are found for the face-on orientation. However, the tip-on/edge-on orientations result in energetically higher charge-transfer states and, concomitantly, in higher open-circuit voltages.
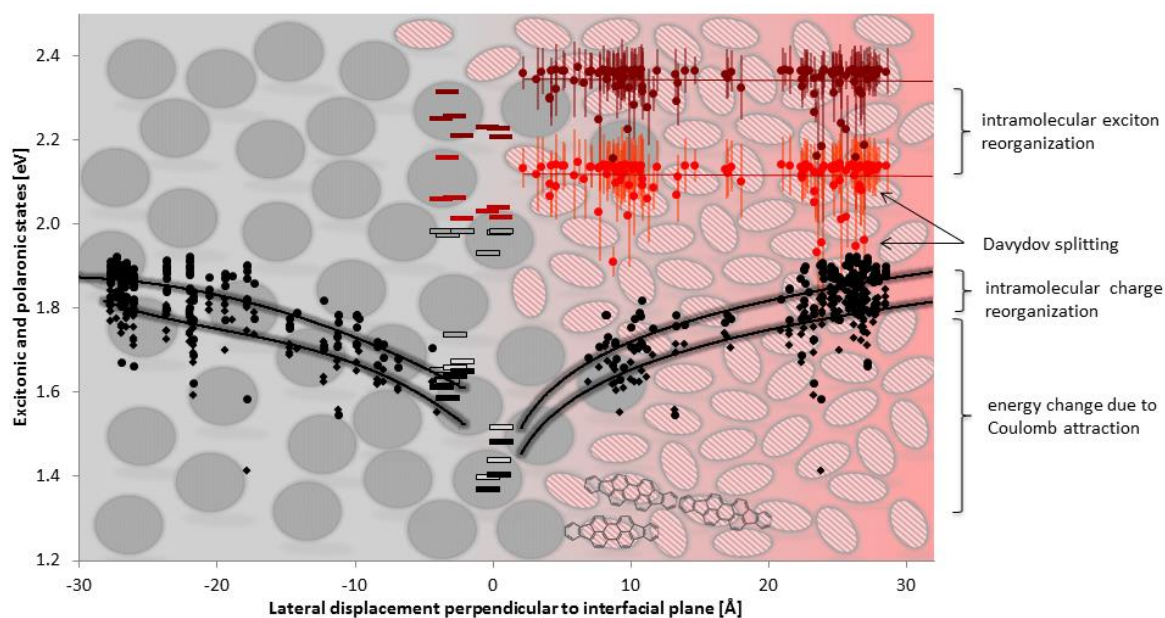
Figure 81: Energetic profile of the DIP::fullerene interface (a-b-crystallographic orientation). DIP molecules are oriented tip-on with respect to the fullerene interface. There are exciton self-trapping sites in the bulk DIP phase (see low-lying red points).

Figure 81 shows the energetic profile of the DIP::fullerene interface where the DIP molecules take on a standing orientation with respect to the fullerenes C_{60}. The lowermost interfacial charge-transfer states are found at energies around 1.40 eV. This contrasts with minimal charge-transfer state energies of approximately 1.20 eV for the lying DIP orientation on C_{60} molecules (Figure 76). It has been emphasized that the numerical values of the charge-transfer state energies cannot be directly translated into an open-circuit voltage, which is influenced by additional parameters such as the minimal driving force required for exciton dissociation. Nevertheless, the decrease of 0.20 eV in the interfacial charge-transfer states (Figure 81 vs. Figure 76) compares well with an equal morphology-dependent decrease of the open-circuit voltage of 0.20 eV observed by Brütting et al.[957] In the calculations, the dependence of the interfacial charge-transfer energies on the morphology at the DIP::fullerene interface results from a two-fold effect:

1. As stated above, couplings are larger for the lying orientation (= face-on). This induces a larger ground-state charge transfer in the face-on heterodimer, thereby decreasing the structural and electronic differences between the ground state and the excited charge-transfer state.

2. The electron-hole separation between the geminate electron and the hole is smaller in the lying orientation because it allows for a closer contact between the DIP molecule and fullerene C_{60}. This increases the Coulomb binding energy and consistently lowers the overall charge-transfer energy.

In addition to its morphology dependence, the initial electron-hole separation is also a function of the molecular size. Lower Coulomb binding energies and higher charge-transfer energies can be expected for larger molecules that enforce higher initial electron-hole separations. This size effect becomes already apparent from the energetic profile of the squaraine molecule (Figure 80). Due to its long linear shape, the squaraine molecules guarantee large initial electron-hole separations and small Coulomb binding energies. In line with this, no deep interfacial charge-transfer states are found at the squaraine::C_{60} interface although the ionization potential of the squaraine molecule is rather low. The average energy of 1.0 eV for the interfacial charge-transfer states in the squaraine system should be compared to the energies found for triphenylamine-based compounds, which are considerably lower (TBA: 0.9 eV; TAM: 0.6 eV). This results from the smaller, spherical shapes of the triphenylamine molecules. These compact molecular shapes lead to small electron-hole separations and comparably high Coulomb binding energies of the interfacial charge-transfer states. Please note that additionally, in the squaraine::fullerene system, the rather high-lying interfacial charge-transfer states are not lower in energy than the polaronic transport levels (black circles and squares, Figure 80). This implies that cold exciton dissociation should be possible at this interface, at least from an energetic point of view.

Throughout the previous sections, a plethora of results has given proof of the structurally and electronically similar behavior of the diketopyrrolopyrrole and the squaraine, the two donor-acceptor-donor compounds comprised in the set of model compounds (Figure 5). In accordance with this observation, the comparable molecular shape and electronic structure of DPP result in an interfacial energetics of the diketopyrrolopyrrole::fullerene system much alike to the squaraine system (Figure 82). No interfacial charge-transfer traps exist. Since the interfacial charge-transfer states are almost isoenergetic with the polaronic transport states in the DPP bulk phase, cold exciton breakup could occur. Again, this is among others a consequence of the large and linear molecular shape of DPP, ensuring large initial electron-hole separations with an average value of 14 Å. In comparison with the anthracene::fullerene system (average initial electron-hole separation: 7 Å), electron-hole pairs at the DPP::fullerene interface experience consequently only half the Coulomb binding energy. It is worth emphasizing that in the DPP bulk phase, both excitonic and polaronic transport levels are rather narrow. This results from the small amount of structural disorder in the tight DPP aggregates. Moreover, in contrast to squaraine disposing large atomic charges, local electron density variations

are smaller in DPP, resulting in reduced interactions of an ionized molecule with its environment and narrower polaronic levels.
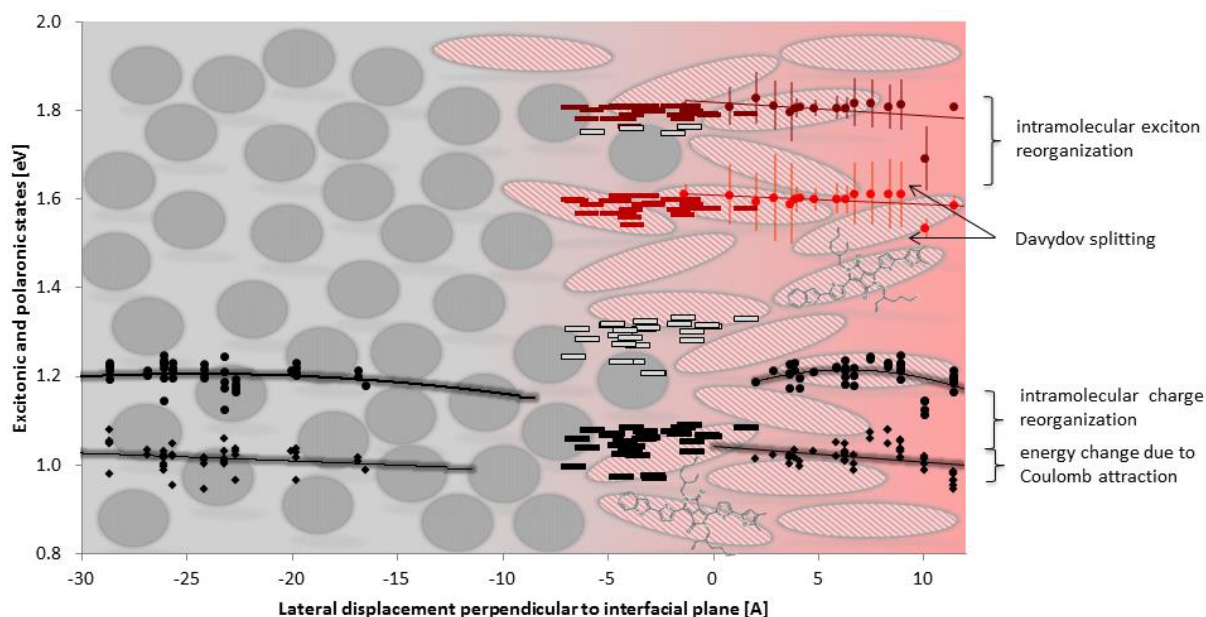
Figure 82: Energetic profile of the diketopyrrolopyrrole::fullerene interface (a-b-crystallographic plane).

It has already been pointed out in several investigations that molecular polarity is crucial for the energetics at a donor::acceptor interface. According to Vandewal, McGehee, and Neher et al.,[960] well-performing OSCs are obtained whenever the process from interfacial charge-transfer states to complete charge separation is isoenergetic. An isoenergetic character is guaranteed by high-lying charge-transfer states that are only weakly bound and thus readily dissociate into separate charges. As also pointed out by Koster[428] in an extension of Scharber's seminal work on the open-circuit voltage,[432] a high effective epsilon of the environment screens charge-charge interactions. It reduces the Coulomb binding energy of geminate electron-hole pairs, raises consequently charge-transfer energies and thereby reduces/removes possible barriers to complete charge separation. Seki et al.[599] outlined further benefits if a generally high effective epsilon in the bulk phases is accompanied by a lower epsilon at the interface. In such a case, the low dielectric constant destabilizes charges and electron-hole pairs selectively at the interface. The charge carriers become in turn more stable whenever they migrate into bulk phase areas with a larger effective epsilon. The combination drives charge separation.

Merocyanines are a class of particularly polar molecular semiconductors.[27] In fact, the effective epsilon for the bulk phase of merocyanines was predicted to be quite high.[645] Furthermore, compared with the typical range of $\varepsilon = 3 - 4$ for most organic semiconductors,[418] the highly polarizable fullerene phase possesses also a rather large effective epsilon.[939,961] Because of the less dense packing at the interface between the merocyanine and the fullerene phase, the effective epsilon can be expected to

drop to a minimum in the interfacial region. Therefore, the donor-acceptor system composed of a merocyanine donor and fullerene C_{60} exactly corresponds to the dielectric environment discussed by Seki et al.[599]
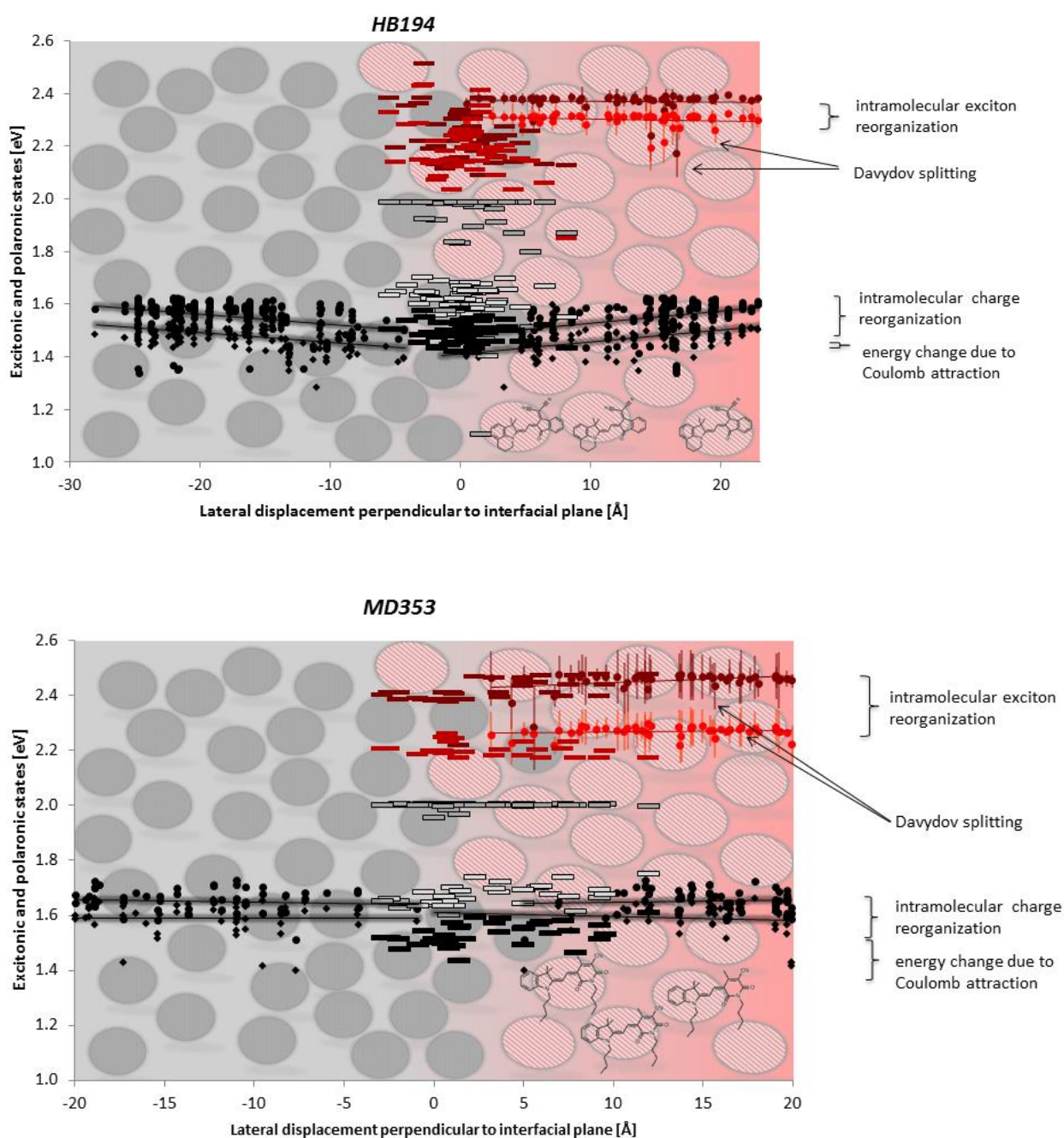
Figure 83: Energy profiles of the interfaces of two different merocyanines (a-b-crystallographic planes). First panel: HB194; second panel: MD353.

Figure 83 shows the energetic profiles of interfaces between two merocyanines, HB194 and MD353, and fullerene. They reflect nicely the effects outlined by Seki et al. because the transition from an interfacial charge-transfer state (black bars) to separate charges (black circles and squares) is isoenergetic. Moreover, the Coulomb attraction between the separating charges is effectively

screened by the highly dipolar environment so that the polaronic states do not feature any r^{-1} dependence. Therefore, charge separation should be efficient, and cold exciton breakup is definitely possible from an energetic point of view. Furthermore, a more detailed comparison of the positions of the interfacial charge-transfer states (black bars, Figure 83) of the HB194 and MD353 systems reveals that almost no interfacial trap states are to be expected for HB194 whereas some trap states exist in MD353 – a few charge-transfer states at the MD353::fullerene interface are situated clearly below the polaronic transport levels. From these calculations, one would assume higher device performances for HB194, which is actually the case. The experimentally determined power conversion efficiencies amount to 0.87%[655] (MD353) and to 2.49%[962] (HB194). These findings could additionally explain the surprisingly high device performances of optoelectronic devices based on merocyanine dyes, which actually contrast with predictions of the Bässler model[548] of charge transport. The high efficiencies have so far been mainly rationalized by the dimerization of merocyanine dyes to centrosymmetric dimers in the solid state, resulting in a zero net dipole moment.[27] Consequently, following the rationale of Würthner and Meerholz, no dipolar disorder exists for the bulk phases of merocyanines so that efficient charge transport is again possible within the Bässler model.[27] However, this rationale is not totally in line with the calculated results (Figure 83). As already found for squaraine aggregates (Figure 80), some charge trap states exist in the polaronic transport levels of merocyanines. In fact, the formation of centrosymmetric dimers cannot completely remove the efficiency limits to charge transport set by the dipolar environment. Even if all merocyanines formed perfect dimers in amorphous thin films, considerable quadrupole moments of these centrosymmetric dimers would still create a certain amount of dipolar disorder. Consequently, in line with Bässler et al.,[548] charge transport properties deteriorate, and charge trap states necessarily emerge. Nevertheless, with regard to the observed high device efficiencies, this underlines the possible significance of the above-described efficient exciton dissociation even more.

To conclude from this section, the dimer method combined with a continuum solvation approach and local electric fields was employed to study the charge generation mechanism in OSCs from a thermodynamic perspective. The good accordance of the results with a number of experimental findings, for instance the exciton self-trapping in perylene-based dyes,[745] high hole mobilities in triphenylamine-based compounds,[682] efficient exciton diffusion in squaraines,[623] excimer formation in donor-acceptor compounds,[953,954] and the morphology-dependent open-circuit voltage[957] in devices based on DIP, suggests that the ansatz is sufficient to cover many important effects. The energetic profiles highlight the influence of diverse loss mechanisms on the charge generation process in OSCs.

A comparison of the existing loss mechanisms for molecules of different shape and electronic structure allows to identify important structure-property relationships. Exciton traps, interfacial charge-transfer traps, and charge traps can be distinguished.

1. Exciton self-trapping occurs in amorphous thin films of DIP. Various dimer conformations exist in such disordered films. For specific dimer arrangements, very low-energy excitonic states result so that dynamic relaxation like in PTCDA or PBI crystals is not necessary for exciton trapping anymore. In bulk phases of medium to large-size triphenylamines, excimer formation is responsible for trapping. J-aggregation effectively prevents the formation of exciton traps. Hence, exciton diffusion should be most efficient in the bulk phases of squaraines, diketopyrrolopyrroles, and merocyanines.

2. In contrast to these favorable effects of J-aggregation on exciton diffusion, it simultaneously tends to impede charge transport. The tightly packed squaraine and merocyanine molecules with significant atomic charges on their donating and accepting moieties lead to disordered polaronic levels and trap states. Charge transport becomes less efficient. Charge traps are on the contrary almost inexistent in isotropic thin films composed of less polar molecules, most notably in phases of triphenylamine-based compounds.

3. It was discussed in detail that for high open-circuit voltages and efficient charge separation, interfacial charge-transfer states should be isoenergetic with the polaronic transport levels. The dielectric properties at the interface, the molecular size and shape, and the morphology are decisive for the energies of these interfacial charge-transfer states. While the dielectric properties of the environment determine to what extent the Coulomb binding energy of the initially formed geminate electron-hole pair is screened, the electron-hole separation in the geminate pair is similarly decisive for its binding energy and depends on the molecular size and morphology. Large and polar molecules, tip-on orientated if possible, most efficiently prevent the formation of interfacial charge-transfer trap states.

As a summary, final structure-property relationships defined for the herein treated molecules are given in Table 24.

Table 24: Summary of the importance of identified trap mechanisms for the selected molecular p-type semiconductors (green bars: no trap states; yellow crosses: some trap states; red crosses: many trap states).

compound class	polarity	model compound	trap states			particularities
			exciton traps	interfacial charge-transfer traps	polaron traps	
aromatic		anthracene				*no functional OSC*

hydrocarbons	no local/no net dipole moments	DIP	−	+	−	*exciton self-trapping* *interfacial traps depend on morphology*
		rubrene	−	−	−	*influence of bulky substituents (vs. anthracene)*
	low polarity					
triphenyl-amines/ D-A-D compounds	*no net but local dipole moments*	TBA „triamine"	+	−	−	*excimer formation: exciton traps* *isotropic efficient polaron transport*
		TAM „triamine-methoxy"	+	−	−	*excimer formation: exciton traps* *isotropic efficient polaron transport*
		TAA „triamine-aldehyde"	+	−	+	*higher interfacial charge-transfer states due to accepting groups*
	intermediate polarity	squaraine	−	−	+	*polaron traps in aggregates* *very efficient exciton transport*
		diketopyrrolo-pyrrole	−	−	+	*polaron traps in aggregates* *isoenergetic charge separation (large size)*
mero-cyanines	*large net dipole moments*	HB194	−	−	+	*polaron traps in aggregates* *isoenergetic charge separation (polarity)*
	high polarity	MD353	−	−	+	*polaron traps in aggregates* *few interfacial trap states (close contact)*

After analyzing thermodynamic aspects of the optoelectronic processes in the vicinity of organic::organic interfaces in this section, the next section complements the discussion by addressing kinetic effects.

5.9 Kinetics of the exciton dissociation and charge separation processes in the vicinity of the organic::organic interfaces

The following discussion parallels [930].

Kinetic aspects of the light-to-energy conversion process in OSCs are complementarily investigated to the above discussed energetics. The same five-step process is reused to organize the discussion.[424] For reasons of completeness, it is briefly repeated:

1. Light absorption: Upon photon absorption, an exciton is created. In view of the poor absorption of fullerene, it is usually assumed that light absorption takes place in the donor phase only.[5]

2. Exciton diffusion: The created exciton diffuses through the donor phase and may reach the interface.

3. Exciton dissociation: Upon exciton dissociation at the interface in a photoinduced charge-transfer step, an interfacial charge-transfer state, i.e., a (bound) geminate electron-hole pair is created. In the following, cold exciton breakup is assumed to be the only relevant mechanism for exciton dissociation (see previous section "Energetics of the exciton dissociation and charge separation processes in the vicinity of the organic::organic interfaces").[460]

4. Charge separation: If a gradient in the free energy landscape exists,[26] the geminate electron-hole pair dissociates to form separate charges.

5. Charge recollection: The freely migrating charges are finally recollected at the electrodes.

Only Steps 2-4 are addressed in this thesis as they are intimately related to the nature of the organic::organic interface (see above). To investigate kinetic aspects, kinetic Monte Carlo (KMC) simulations employing Marcus hopping rates obtained from quantum-chemical calculations are used to model the steps in the vicinity of the organic::organic interfaces. While many "macroscopic" KMC simulations using fit parameters from experiments exist,[963] combined simulations of all interfacial processes with rates and further input parameters obtained from *ab initio* calculations are rare. Moreover, the computational approach chosen to generate the interfacial model systems

permits to investigate the influence of different amorphous thin-film morphologies on the rates of Steps 2-4. In contrast, most literature investigations focus entirely on crystallographic morphologies,[456,575] which might be insufficient to describe the interplay between morphology, disorder, and kinetics. Furthermore, the diverse set of molecular p-type semiconductors (Figure 5) is employed along with the fullerene C_{60} acceptor, allowing for comparisons between different donors and the identification of structure-property relationships.

The simulations comprise not only exciton diffusion and dissociation at the interface, but also the subsequent charge separation up to the point where the migrating charges have almost overcome their mutual Coulomb binding energy. As loss mechanisms, fluorescence, exciton trapping, and recombination of interfacial charge-transfer states are taken into account. Due to the limited size of the interfacial model systems, pure charge transport phenomena of completely independent charges are not included, but ample literature investigations[964,965,464] on charge transport in organic semiconductors exist. Please note that this discussion focusses entirely on the rates, i.e., energetic restrictions to the processes are not taken into account.

It should be emphasized that some approximations are intrinsic to the chosen approach, i.e., KMC simulations based on Marcus hopping rates. Marcus theory is an equilibrium theory so that contributions from vibrationally[591]/electronically[593] excited states as well as coherence phenomena are necessarily disregarded.[5] Exciton delocalization across oligomeric aggregates fundamental to mechanisms like long-range exciton dissociation is not included either.[966,594]

Table 25: Color code used to indicate the positions of the p-type semiconductors and the fullerenes (corresponding to the grid of the KMC simulations) and the exciton couplings and rates. The same color code is used for the corresponding charge couplings and rates.

Position	Symbol
centers of mass of p-type semiconductors	■
centers of mass of fullerenes	●
Coupling/Rate	Symbol
exciton transport coupling/rate Excitons diffuse in the p-type semiconducting phase.	←
hole transport coupling/rate Holes are transported in the p-type semiconducting phase.	→
electron transport coupling/rate (fullerene) Electrons are transported in the fullerene phase.	←
photoinduced charge-transfer coupling/rate An exciton dissociates at the interface into a geminate electron-hole pair.	←
recombination coupling/rate An electron-hole pair at the interface recombines to the ground state.	→

All simulated processes are summarized in Table 25. In the following figures, they are indicated with the displayed symbols (Table 25). It should be noted that the same symbols are used to designate both exciton and charge transport in the bulk donor phase.

The discussion of the kinetic aspects is organized as follows. In a first step, the underlying theoretical approach is presented in detail. Then, results are discussed for selected donor molecules. They are additionally compared to available experimental data, which furthermore permits to critically evaluate the physical soundness of the adopted approach. Finally, all obtained results are summarized to deduce structure-property relationships and to elucidate important trends.

5.9.1 Description of the Theoretical Approach

Figure 84 presents an overview of the adopted approach. It was implemented in C++ using the input extracted from Gaussian[718] by bash scripts. A large number of approximations has to be introduced. This certainly questions the numerical predictability of the results. Yet, the aim of the approach is rather to gain insight and understanding of the microscopic charge generation processes than quantitatively accurate results.

In a first step, the methods to calculate the rates (red box, "Rates", grey boxes, Figure 84) are discussed. Marcus transfer rates k_{if} between an initial state i and a final state f are obtained from the coupling V_{if} between the two diabatic states, the reorganization energy λ (see above), and the driving force ΔG:

$$k_{if} = \frac{{V_{if}}^2}{\hbar} \sqrt{\frac{\pi}{\lambda k_B T}} \cdot e^{-\frac{(\lambda + \Delta G)^2}{4\lambda k_B T}} \tag{453}$$

$\hbar$ is the Planck constant, T the (ambient) temperature and k_B the Boltzmann constant. In hopping processes between localized hopping sites in organic thin films, the initial and final states correspond to two adjacent monomers. Next-neighbor dimers were cut out based on a threshold value for the distance between their centers of mass. The reader is referred to [930] for detailed values. Couplings were calculated between the monomers. In line with literature investigations,[532] no dielectric shielding was included in the calculation of the couplings (because these couplings between next-neighbor monomers can be assumed to be unaffected by the bulk permittivity/dielectric shielding). Exciton couplings between adjacent monomers V_{ex} were calculated from the adiabatic splitting[519,166] of the first two excitations $\{E_1, E_2\}$ of the dimer. Using ZINDO[209,210,772] excitation energies shown to be both reliable and low-cost (see section "Benchmarking vertical excitation energies of molecular semiconductors" for an evaluation of monomer excitations),[702] these exciton couplings were calculated as:

$$V_{ex} = \frac{1}{2}(E_2 - E_1) \tag{454}$$

In a similar procedure, charge transport couplings between neighboring monomers for hole (V_{hole}) (electron ($V_{electron}$)) transport are obtained as the adiabatic splitting of the orbital energies of the HOMO ε_{HOMO} and the HOMO-1 ε_{HOMO-1} (the LUMO ε_{LUMO} and the LUMO+1 ε_{LUMO+1}) of the neutral dimer:[166,967]

$$V_{hole} = \frac{1}{2}(\varepsilon_{HOMO} - \varepsilon_{HOMO-1}) \tag{455}$$

$$V_{electron} = \frac{1}{2}(\varepsilon_{LUMO+1} - \varepsilon_{LUMO}) \tag{456}$$
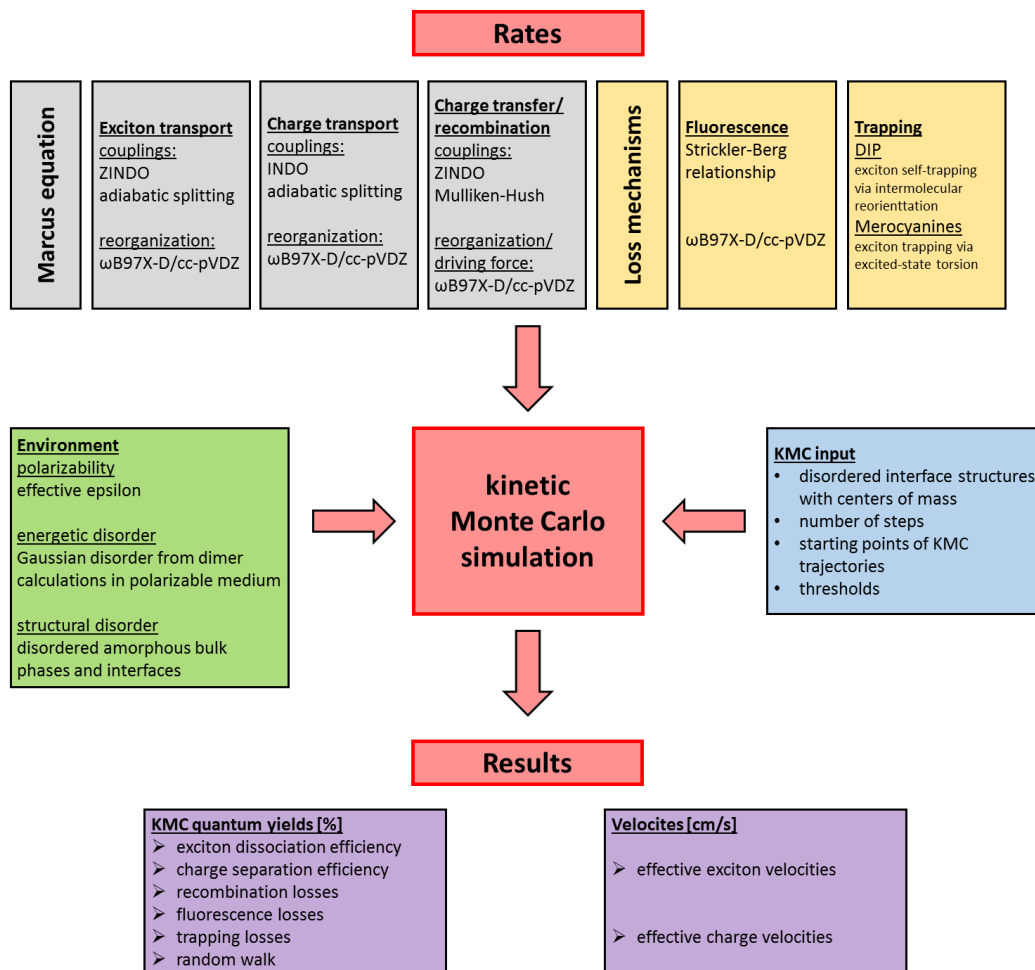
Figure 84: Adopted theoretical approach for the analysis of the interfacial kinetics using diverse molecular p-type semiconductors in heterojunction with fullerene C_{60}. KMC simulations based on Marcus hopping rates are conducted.

As discussed by Coropceanu et al.,[544] using INDO[968] for the calculation of the orbital energies delivers sufficiently accurate charge transport couplings. It is, however, very important to keep in mind that obtaining exciton/charge transport couplings as the adiabatic splitting of dimer excitations/orbital energies is only physically justified as long as the excitations/orbital energies are well-separated in the underlying monomers.[166] Although this is the case for almost all molecules included in the calculations, it does not hold for the "triamine" compound, possessing a degenerate HOMO, and for fullerene C_{60}, which has a three-fold degenerate LUMO due to its icosahedral symmetry. In order to still determine coupling values for these two molecules from the adiabatic splitting method, an approximate scheme illustrated for fullerene C_{60} in Figure 85 is adopted. Instead of using individual excitation/orbital energies for the calculations of the couplings (Eq. (454), (455), (456)), average values are used. This naturally deteriorates the accuracy of the results. Resulting uncertainties represent only a small problem for fullerene C_{60} because it is used in all interfaces. Errors can be expected to be equal in all simulations. Results for the "trimaine"::fullerene interface are, however, more error-prone and should be discussed with caution.
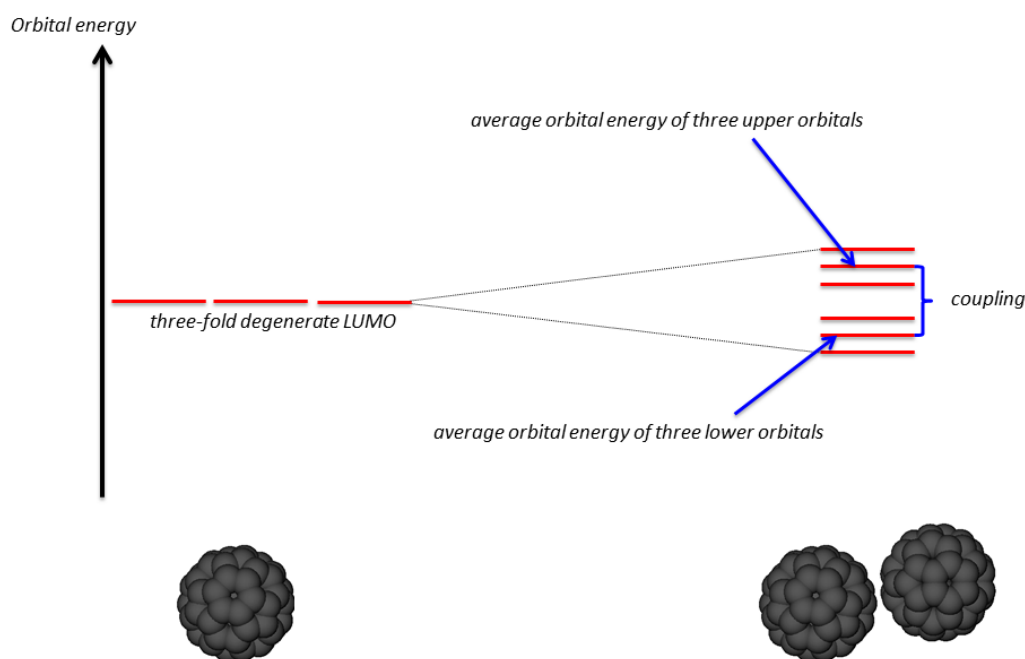
Figure 85: Approximate scheme to determine charge transport couplings from the orbital splitting in fullerene C_{60} dimers.

In addition to exciton and charge transport couplings, charge-transfer and recombination couplings are required as input parameters for the KMC simulations. Utilizing the generalized Mulliken-Hush formalism,[969,970] couplings for photoinduced charge transfer V_{CT} (recombination) are obtained from the energies of the excited and the charge-transfer state $\{E_i\}$ (the charge-transfer state and the ground state), their dipole moments $\{\mu_i\}$ and the transition dipole moment μ_{12}:

$$V_{CT} = \frac{\mu_{12}(E_2 - E_1)}{\sqrt{(\mu_2 - \mu_1)^2 + 4\mu_{12}{}^2}} \qquad (457)$$

In line with most applications of the generalized Mulliken-Hush theory,[971,972] only the projection of the transition dipole moment onto the dipole difference vector is employed to eliminate all locally excited components. The calculation of the excitation energies $\{E_i\}$ in Eq. (457) is somewhat problematic because, as discussed above, the calculation of charge-transfer states is computationally challenging (see Section "Benchmarking vertical excitation energies of molecular semiconductors").[159] Nelson and coworkers[567] pointed out that semiempiric methods are intrinsically unable to capture overlap-dependent contributions to charge-transfer states, while they correctly describe the electrostatic component and reliably incorporate the full Coulomb interaction between the electron and the hole. The inverse is true for TD-DFT,[266] which performs well for overlap-dependent contributions but fails for the electrostatic parts. According to the reasoning of Nelson and coworkers, electrostatic contributions are more important than overlap-dependent terms in most charge-transfer states.[567] Thus ZINDO was employed to extract the excitation energies and transition dipole moments for the calculation of photoinduced charge-transfer couplings (Eq. (457)). ZINDO excited-state dipole moments are, however, not directly accessible with Gaussian. Therefore, the dipole moment of a geminate electron-hole pair situated on the heterodimer, i.e. of a donor$^+$-acceptor$^-$-pair, is calculated with classical electrostatics and used to approximate the excited-state dipole and, assuming a comparably negligible ground-state dipole moment, the difference dipole vector. The electron is assumed to be fully localized on the fullerene while the donor component carries the hole, i.e., the complete positive charge. The electron-hole separation is estimated from the distance between the centers of mass of the underlying monomers.

In line with Brédas and coworkers,[973] reorganization energies λ and driving forces ΔG for photoinduced charge transfer and recombination were obtained from monomer calculations at the ωB97X-D[143]/cc-pVDZ[705] level of theory. The ωB97X-D functional was shown to yield reliable ground-state, excited-state, and ionized-state energies (see previous sections). The effects of Coulomb interactions between the charged monomers on the overall driving forces were disregarded at this point because they were included in the later-on KMC simulations. It should be noted that only internal reorganization energies can be obtained from isolated-monomer calculations. As already mentioned above with regard to external reorganization energies, Troisi et al.[860] and Voityuk et al.[861] presented detailed surveys that the sizes of the external reorganization energies strongly vary with the adopted computational approach to calculate them. Moreover, external reorganization energies are usually approximately one magnitude smaller than internal reorganization energies.[575,864] Therefore, they can be neglected to a first approximation, and their influence is only indirectly included via ΔG (see below).

The yellow boxes ("Loss mechanisms") in Figure 84 indicate that two loss mechanisms in addition to the recombination of charge-transfer states are included in the simulations. Fluorescence rates, i.e., radiative decay rates k_{rad}, were estimated from a simplified version of the Strickler-Berg relationship that approximates the radiative decay rate from the oscillator strength f, the refractive index of the medium n, and the wave number $\tilde{v}$ (assuming equal wave numbers for absorption and fluorescence):[974,418]

$$k_{rad} = n^3 \tilde{v}^2 f \tag{458}$$

Oscillator strengths and wave numbers for the monomer absorption were calculated again at the ωB97X-D/cc-pVDZ of theory because TD-DFT is known to obey the Thomas-Reiche-Kuhn sum rules[975,259]. To treat all molecules on an equal footing, only absorption wave lengths were used because some compounds undergo as gas-phase monomers an excited-state torsion disabled by steric strain in thin films.[645] Such an excited-state torsion results in differing absorption and fluorescence wave lengths. All fluorescence rates (= radiative decay rates) can be found in [930].

As outlined in the section "Energetics of the exciton dissociation and charge separation processes in the vicinity of the organic::organic interfaces", exciton self-trapping mechanisms were investigated for a number of compounds,[745] most notably for perylene-based dyes such as DIP in this thesis. To incorporate self-trapping into the simulations, a self-trapping rate of $10^{12} \ s^{-1}$ was deduced from the time scales found for trapping in PBI (215 fs[878]) and PTCDA (~ 400 fs[745]). Exciton trapping in merocyanines due to a photoinduced torsion[645] was also included. Laser-spectroscopic investigations showed that the photoinduced torsion in merocyanines occurs on femtosecond time scales of approximately 100 fs[851], which translates into an estimated trapping rate of $5 \cdot 10^{12} \ s^{-1}$. It is thereby assumed that the trapping rate is equal for all merocyanines. Furthermore, it is worth emphasizing that although a full torsion of merocyanines is not necessarily possible in a thin-film environment due to steric strain,[645] some twisting around the carbon backbone of merocyanines is already sufficient to effectively prevent further exciton diffusion.

As a suitable description of the environment is decisive for accurate results,[26] (green box, "Environment", Figure 84) a three-fold procedure is adopted to take into account environmental effects:

1. Structural disorder is inherently included since disordered interfacial model systems are employed for the simulations. The disordered model systems translate into a KMC grid with varying distances between adjacent grid points.
2. The polarizability of the environment, particularly fundamental to the energetics and kinetics of the charge separation process[575,601] because it is responsible for the screening of the

Coulomb attraction between migrating electrons and holes, has to be incorporated. The approach already adopted to model effects of the environmental polarizability on energetics – the polarizable continuum model – is also employed for the KMC simulations (Figure 72).

3. Static disorder[425] of site energies, arising from locally varying electric fields and a site-specific polarization and delocalization, needs to be included because it considerably influences the driving forces ΔG. Since resulting rates depend exponentially on these driving forces, static disorder could have a pronounced influence on the outcome of the simulations. In order to take it into account, a Gaussian disorder parameter σ is included in the calculation of driving forces, in line with the Bässler model of disorder.[546,548] All excitonic, polaronic, and charge-transfer state energies are assumed to be normally distributed, distributions which are characterized by this disorder parameters σ. The parameters σ are extracted from the previously conducted dimer calculations (Section "Energetics of the exciton dissociation and charge separation processes in the vicinity of the organic::organic interfaces"; the disorder parameters are calculated as the standard deviations of the distributions of dimer energies). Dimer calculations are perfectly capable of providing an estimate for static disorder because they include variations due to delocalization and intermolecular interactions.[745] The final driving forces are then obtained as sums of the gas-phase ωB97X-D values and contributions from static disorder. These contributions are computed from normally distributed random numbers that are generated with the calculated Gaussian disorder parameters σ. However, it should be noted that the disorder parameters σ for excitonic and polaronic states are assumed to be constant throughout the complete donor/acceptor phase, which is an approximation. Van Voorhis and coworkers[460] thoroughly discussed that the amount of disorder in the direct vicinity of the organic::organic interface can be larger.

The KMC implementation follows Houili et al.[976] (red center box, Figure 84). The centers of mass of the fullerenes and molecular p-type semiconductors of the underlying disordered interfacial model systems constitute the grid points of the KMC simulations (blue box, Figure 84). A particle, an exciton or polaron, reaching the boundary of the interfacial model systems is reflected, i.e., no periodic boundary conditions are used for the disordered systems. At least 15 to 20 starting points were chosen from where an exciton starts diffusing. 100 trajectories were calculated per starting point. To obtain comparable results for all model systems that differ in size, all simulations were conducted with a fixed number of steps, i.e., a fixed number of steps per trajectory was employed. This number was calculated from the number of p-type molecule dimers e and fullerene dimers f for which couplings were computed, i.e., which were selected based on the distance criterion. This has the advantage that the size of the systems and its dimensionality, i.e., its intermixing and interpenetration, is implicitly included in the number of MC steps per trajectory $\#step(MC)$.

$$\#step(MC) = 400 + 2 \cdot (e + f)$$ (459)

To investigate the influence of the number of steps on the KMC results, the simulations were repeated with 1400 instead of 400 steps in Eq. (459) and a higher prefactor of 10, i.e., the number of steps was increased by a factor larger than 6. The resulting changes turned out to be insignificant. This shows that the KMC outcome is generally not predominantly determined by the predefined number of steps. To guarantee the significance of the results and the limited influence of the KMC input parameters (blue box, Figure 84), KMC simulations were additionally conducted for each system and each crystallographic orientation using a slightly larger interfacial model systems.

Figure 86 illustrates further KMC input parameters listed in the blue box of Figure 84. As already mentioned, it is assumed that excitons are only created in the donor phase, with the extinction coefficient of fullerene C_{60} being very low.[977] To be able to also analyze the efficiency of exciton diffusion and its interplay with exciton dissociation and charge separation, no excitons created in the immediate vicinity of the interface are included in the simulations. Instead of this, excitons are randomly generated only in the red box on the right-hand side of Figure 86. This enforces that some exciton diffusion prior to dissociation has to occur. The position of the red box is adjusted to the system size so that it always contains approximately 30% of the donor phase. Notably, since exciton generation occurs randomly and the randomly generated excitons are at first uniformly distributed in the red box, additional effects around exciton creation arising from morphological dependencies or anisotropic light absorption are not considered in the simulations.[978,979] Furthermore, events such as direct excitations of an interfacial charge-transfer states[960] or long-range exciton dissociation[584,457] are disregarded.

To evaluate the results, "KMC quantum yields" are calculated (purple box, Figure 84). The overall KMC quantum yield corresponds to the percentage of generated excitons that successfully dissociate into a charge-separated state[575], thus a quantity intimately related to the experimentally accessible IQE. As above, an electron-hole pair is considered as separate as soon as the Coulomb binding energy has considerably dropped. In fact, it has decreased by at least 80% as soon as the hole has reached the red box in Figure 86 (blue arrow). To clarify the interplay between the individual processes like exciton diffusion, dissociation, and charge transport, and to identify how molecular and aggregate properties influence these processes, quantum efficiencies for all individual processes are additionally calculated (purple box, Figure 84). For instance, fluorescence, recombination, and exciton self-trapping losses can significantly deteriorate the overall quantum yield (green ovals, Figure 86). Nevertheless, a migrating exciton can also simply continue diffusing instead of reaching the interface and dissociating ("exciton migration", green oval, Figure 86). To define the possible bottleneck of the overall light-to-energy conversion, quantum efficiencies for all these processes and others like charge separation and exciton

dissociation are calculated. This allows furthermore to study possible interferences between the processes. For example, if direct and fast exciton diffusion toward the interface is guaranteed, fluorescence and exciton self-trapping become less frequent. In contrast, if random exciton diffusion occurs over long distances, these loss mechanisms can be quite significant. Electron transport in the fullerene phase is not evaluated in detail because fullerene C_{60} is employed in all interfacial model systems. Moreover, the electron transport couplings in the fullerene phase are only approximately estimated (Figure 85). Hence, all mechanisms relying on a predominant role of the fullerenes, such as electron delocalization over fullerene aggregates, are ignored in the simulations. This contrasts for example with investigations of Ratner et al. who suggested an "unequal partnership" between donors and acceptors because electron delocalization in the fullerene phase may play a key role in driving charge separation.[606]
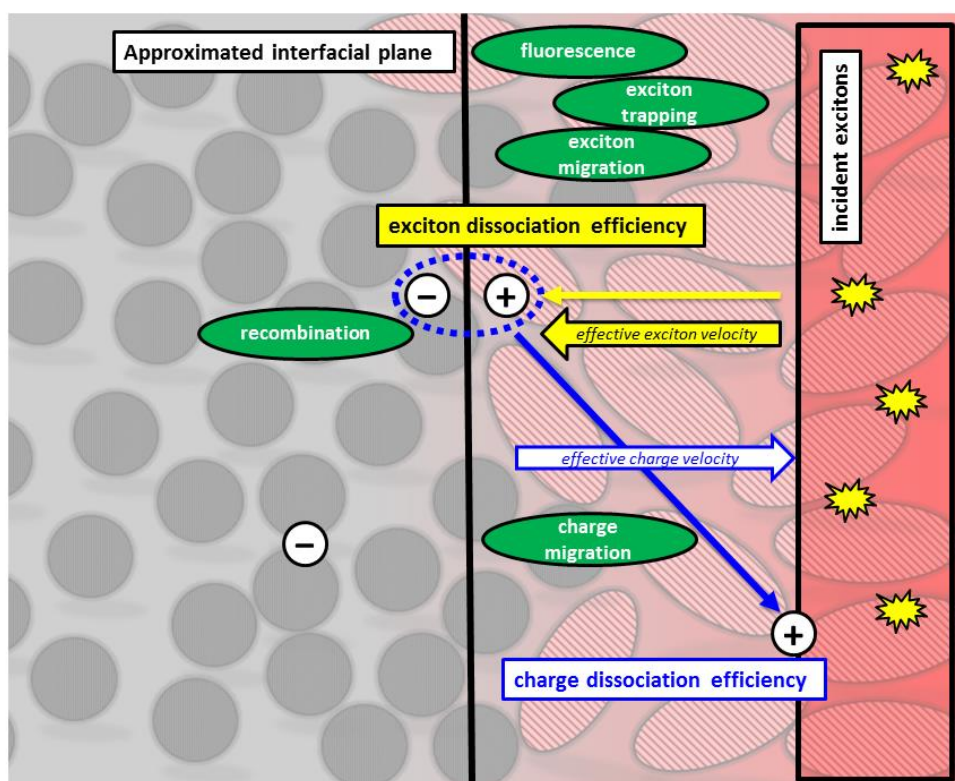
Figure 86: Demonstration of additional parameters used to evaluate the KMC results. The approximated interfacial plane is the center plane between the centers of mass of the p-type semiconducting molecules and the fullerenes.

To gain further insight, effective exciton and charge velocities were calculated for each successful trajectory, i.e., for each successful exciton dissociation or charge separation. In addition to the quantum yields, i.e., the efficiencies of the processes, they provide information about their rates. The velocities are called "effective" because they refer to only one coordinate, i.e., to an "effective" coordinate perpendicular to the interfacial plane. The effective velocity for excitons $|v|_{ex,eff}$ is defined as:

$$|v|_{ex,eff} = \frac{|z_{abs} - z_{CT}|}{t_{ex}} \tag{460}$$

z_{abs} designates the position (perpendicular to the interfacial plane) where absorption took place, i.e., where the exciton was generated. z_{CT} denotes the position of the interfacial charge-transfer state, and t_{ex} is the time between exciton generation and dissociation. The effective charge velocity $|v|_{ch,eff}$ is equivalently defined:

$$|v|_{ch,eff} = \frac{|z_{CT} - z_{sep}|}{t_{ch}} \tag{461}$$

z_{sep} is the position of charge-separated state, i.e., the position of the hole as soon as it has reached the red box in Figure 86. t_{ch} corresponds to the time between the photoinduced charge-transfer step and charge separation. Notably, no electric field is applied in the simulations. This implies that charge carriers move by diffusion, and not by drift. While it is usually assumed that charge transport in organic semiconductors corresponds mostly to drift,[418] applying a constant electric field in all simulations would not change the qualitative trends.

Averaged effective exciton/charge velocities can be *in principle* compared to macroscopic, experimentally accessible counterparts. However, Andrienko and coworker[558] discussed thoroughly that transport parameters obtained from simulations on finite disordered systems suffer from so-called finite-size effects[980] and are thus usually considerably overestimated. Numerous extrapolation schemes[980] exist to correct for finite-size effects. In this thesis, effective velocities and resulting transport parameters, most notably the mobilities, refer exclusively to transport in only one direction. It is well-known that diffusion depends on the square of the average displacement, x^2.[418] It is therefore assumed that the error due to finite-size effects scales with the square of the dimensions of the system. Thus to extrapolate from the calculated mobilities μ_{calc} in model interfaces of a thickness $L_{model\ system}$ to mobilities in a thin-film OSCs with a thickness $L_{solar\ cell}$ of 50 nm, μ_{solar}, a similar quadratic scaling is assumed:

$$\mu_{solar} = \mu_{calc} \cdot \left(\frac{L_{model\ system}}{L_{solar\ cell}}\right)^2 \tag{462}$$

Average effective velocities are employed to deduce theoretical estimates for transport parameters. However, as pointed out by Troisi et al.,[584] average rates are only meaningful if the underlying individual rates have a similar order of magnitude. Otherwise, macroscopic observables (transport parameters) are entirely governed by only the fastest rates. Experiments of Yan et al. led to similar

conclusions.[981] Therefore, the variations of effective charge and exciton velocities were checked before averaging, but they turned out to be rather limited, in contrast to charge-transfer and recombination rates that frequently deviate by several orders of magnitude. Averaging effective exciton and charge velocities should consequently deliver physically meaningful quantities that can be compared to experimental transport parameters.

The same monomer geometries as in the previous section ("Energetics of the exciton dissociation and charge separation processes in the vicinity of the organic::organic interfaces") were used to replace the force-field monomer geometries: ground- and excited state geometries optimized at the SCS-CC2[256,180]/cc-pVDZ[705] level of theory and charged geometries obtained with ωB97X-D[143]/cc-pVDZ[705]. An ultrafine grid was employed for all DFT calculations, including the computations of driving forces and radiative decay rates. ZINDO was employed to compute excitonic, charge-transfer and recombination couplings. As outlined above, INDO was used for charge transport couplings unless no parameters were available, for instance for sulfur-containing molecules. Then, ZINDO was used instead. For the calculation of recombination and charge-transfer couplings, the fullerene C_{60} electrons were frozen. The Gaussian program package was used.[718] Please note that whenever kinetically feasible, endothermic steps are allowed in the simulation to differentiate between purely energetic and purely kinetic effects.

In view of the large number of introduced approximations, it should be kept in mind that the aim of this approach is mainly to gain qualitative insight into the charge generation process and to elucidate important trends.

5.9.2   Discussion of Kinetic Aspects of Organic::Organic Interfaces Obtained From KMC Simulations

The following discussion of the key results on the interfacial kinetics is organized as follows. In a first step, general features of kinetics are discussed on the DIP::fullerene interface system. Three possibly efficiency-limiting kinetic effects are defined that are in a second step generalized by extending the concepts to other molecules. In a third step, to evaluate the reliability of the predictions, transport parameters and quantum efficiencies are compared to available experimental data, i.e., to mobilities and IQE/EQE values. EQE values are only used if IQE data are not available.
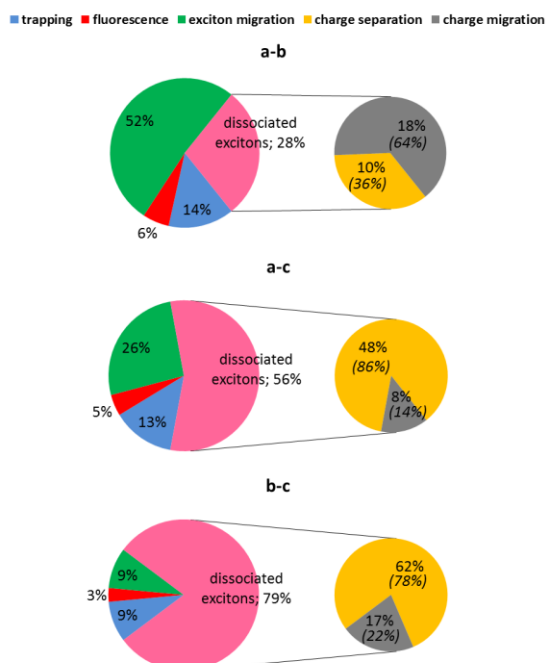
Figure 87: KMC quantum yields (see previous section) for KMC simulations on three different morphologies of the DIP::fullerene interface.

Composite pie charts (Figure 87) display the efficiencies of all processes for the three different morphologies of the DIP::fullerene interface. Left charts illustrate quantum efficiencies up to the process of exciton dissociation whereas right charts refer to processes succeeding exciton dissociation. The efficiencies are referenced to the number of generated excitons, i.e., to the number of KMC trajectories. Values in brackets on the right-hand side are normalized to the number of dissociated excitons instead of the number of generated excitons. It becomes evident from Figure 87 that 28% of the generated excitons reach the interface and dissociate for the a-b-morphology (pink, Figure 87). The remaining 72% of the excitons decay radiatively ("fluorescence", 6%), become trapped ("trapping", 14%) or continue diffusion in the p-type semiconducting phase ("exciton migration", 52%). Turning to the right-hand side, only 36% of the dissociated excitons accomplish the charge separation process for the a-b-morphology ("charge separation") while most of the charges remain bound (64%, "charge migration"). This implies that only 10% of the generated excitons would contribute to the photocurrent. Results differ significantly for the two other morphologies. More excitons dissociate (56% and 79%, respectively), which comes along with fewer radiative decay and trapping processes and a reduced percentage of exciton migration (26% and 9%, respectively). Apparently, fast exciton diffusion and dissociation especially enabled by the b-c-morphology outperforms competing loss channels. Slightly less pronounced differences compared with the a-b-morphology exist also for the number of charge-transfer states (= dissociated excitons) that undergo final charge separation. While

64% of the charge-transfer states formed at the a-b-interface remain bound, this number decreases to 14% at the a-c- and 22% at the b-c-interface.

A more profound understanding for the morphology-dependent efficiencies (Figure 87) is provided by the spatial distributions of the computed couplings and rates for all processes in the vicinity of the three different DIP::fullerene interfaces (Figure 88 - Figure 90). The figures correspond to two-dimensional projections of the three-dimensional interfaces. In all figures in the following, exciton couplings (red arrows) and the couplings of the excitons to interfacial charge-transfer states (= charge-transfer couplings, blue arrows) are shown in the upper left panels, whereas corresponding charge transport (red arrows) and recombination (blue arrows) couplings are displayed in the upper right panels (see Table 25). Corresponding rates that depend on the driving forces and the reorganization energies in addition to the couplings are given in the lower panels. The widths of the arrows indicate the strength of the coupling (linear relationship) and the size of the rates (logarithmic relationship).
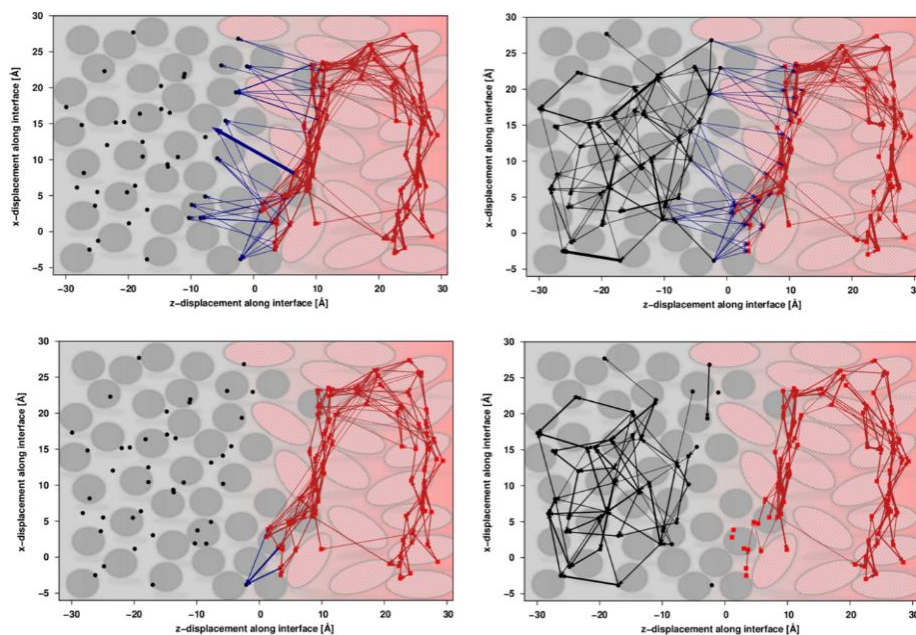
Figure 88: Couplings for excitons (upper left panel) and charges (upper right panel) and the corresponding rates for exciton transport (lower left panel) and charge transport (lower right panel) for the (a-b)-DIP::fullerene interface (standing orientation of DIP molecules on fullerene C_{60}). To calculate charge-transport rates, an image charge on the opposite side of the interface was employed. Moreover, it should be kept in mind that the representations of the interfaces in all figures are two-dimensional projections of the three-dimensional interfacial model systems. Therefore, some molecules might appear closer than they actually are.
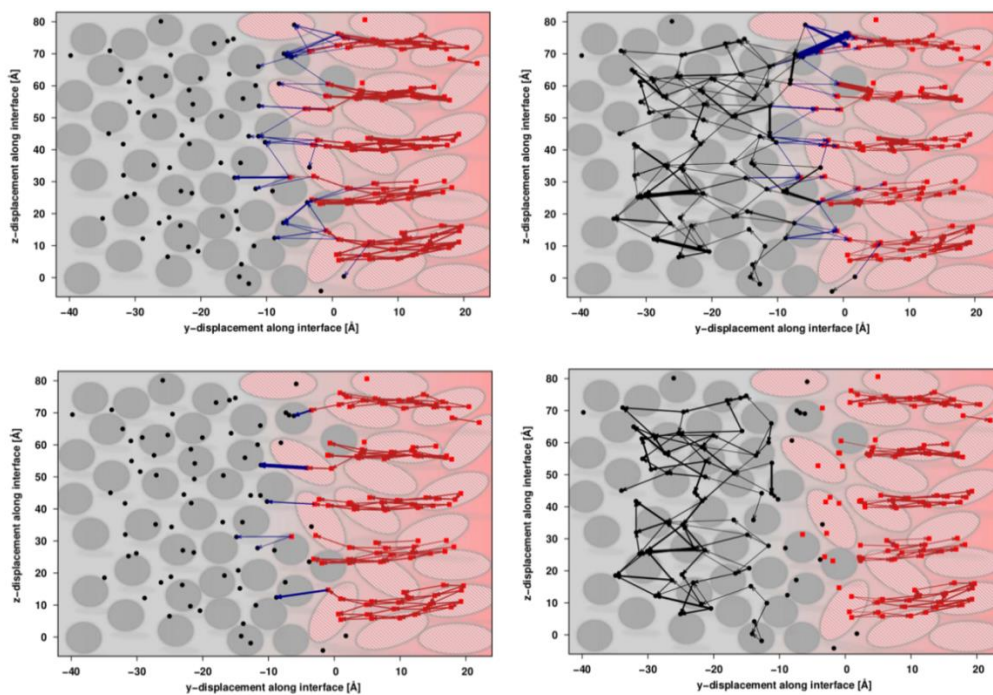
Figure 89: Couplings for excitons (upper left panel) and charges (upper right panel) and the corresponding rates for exciton transport (lower left panel) and charge transport (lower right panel) for the (a-c)-DIP::fullerene interface (lying orientation of DIP molecules on fullerene C_{60}).
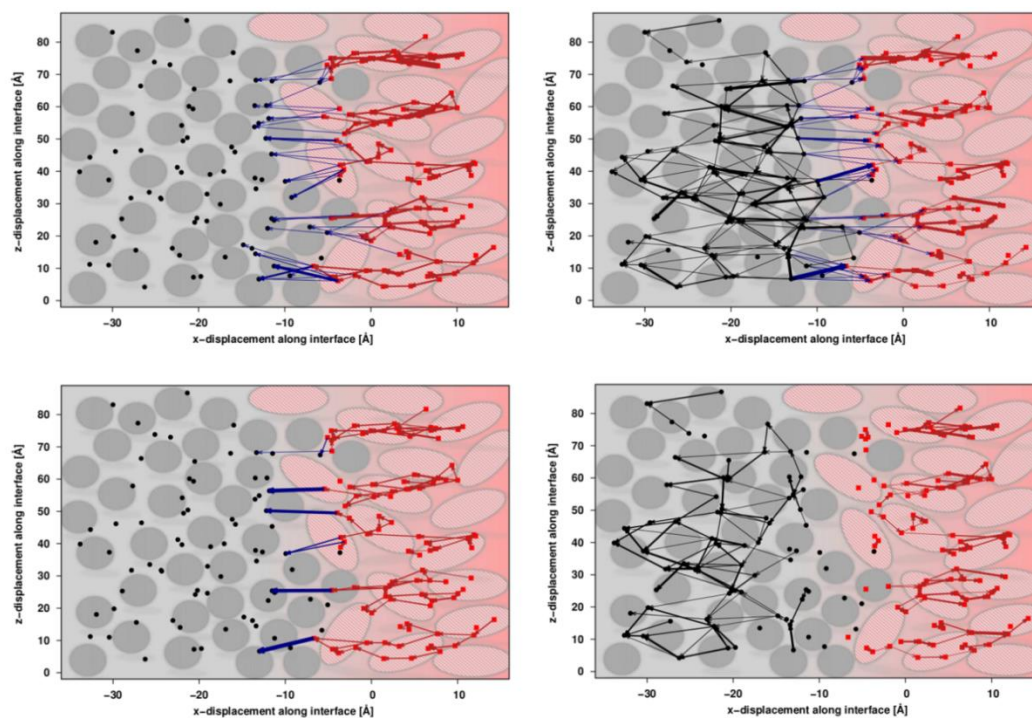
Figure 90: Couplings for excitons (upper left panel) and charges (upper right panel) and the corresponding rates for exciton transport (lower left panel) and charge transport (lower right panel) for the (b-c)-DIP::fullerene interface (lying orientation of DIP molecules on fullerene C_{60}).

Differences in the rates of the three DIP::fullerene morphologies (Figure 88 - Figure 90) directly account for the observed trends in the KMC efficiencies (Figure 87). DIP molecules are standing on top of the fullerene surface in the a-b-morphology. This implies that the exciton and polaron transport along the

336

stack, which is often very fast, goes parallel to the interface (Figure 88, lower panels). In contrast, rather small couplings between adjacent DIP stacks (Figure 88, upper panels) allow only for rather small inter-stack transport. Both other morphologies favor transport rather toward and away from the interface than in parallel directions (Figure 89, Figure 90). This results because in the a-c- as well as in the b-c-morphology, DIP stacks are lying on top of the fullerene phase so that maximum couplings and consequently the fastest transport processes are found toward/away from the interfacial plane.

Nevertheless, it should be noted that irrespective of the exact morphology, charge transport in the direct vicinity of the interface seems to be considerably hampered (Figure 88 to Figure 90, lower right panels). In the following, these regions with reduced charge transport rates will be considered as "charge transport depletion zones". The charge transport depletion zones result from the considerable Coulomb attraction between the geminately formed electron-hole pair. Due to the usually low dielectric constant in organic semiconductors,[418] the charge-charge interactions are only incompletely screened. Moreover, due to its r^{-1}-dependence, the Coulomb attraction between adjacent sites varies most (1) in the immediate vicinity of the organic::organic interface and (2) in hopping processes perpendicular to the interfacial plane. Variations in the Coulomb attraction between the initial and final site account for considerable, endothermic driving forces ΔG for some charge separation pathways. Although thermodynamic aspects are disregarded in the KMC simulations, positive values for ΔG become noticeable via their influence on hopping rates, i.e., they significantly reduce the charge transport rates. As soon as a charge transport depletion zone forms in the vicinity of an organic::organic interface, cold exciton dissociation is *also kinetically* disabled, and vibrationally/electronically excited states must be involved to drive charge separation.[567]

A comparison of the charge transport depletion zones for the different morphologies (Figure 88 to Figure 90) underlines that the depletion zone is least pronounced for the a-b-DIP::fullerene interface. This goes along with the above described finding that no interfacial charge-transfer traps exist for the a-b-morphology where most DIP molecules stand on top of the fullerene layer. This orientation ensures rather large initial electron-hole separations so that the charge separation efficiency is not as inefficient as could be expected from the rather small charge transport coupling values (upper right panel, Figure 88). Moreover, the smaller charge transport depletion zone in the a-b-morphology also accounts for the smaller differences between the morphologies in terms of charge separation efficiency compared to exciton dissociation efficiency. This implies that the effects of driving forces and couplings partially compensate for different morphologies of the DIP system.

In contrast to the largely anisotropic hole transport in the DIP phase, electron transport in the fullerene layer is mostly isotropic for all interfacial model systems. This arises, among others, from the spherical

shape of the icosahedral fullerene molecule, as already discussed by Ratner et al.[606] and by Nelson et al.[567]

Significant differences between the different DIP morphologies exist also in terms of the photoinduced charge-transfer rates. In the photoinduced charge-transfer step, an exciton dissociates at the organic::organic interface into a geminate electron-hole pair (Table 25). At first view, the largely deviating photoinduced charge-transfer rates are surprising because underlying couplings do not differ as much (blue arrows, Figure 88 to Figure 90). However, it should be kept in mind that the rates depend on the square of the couplings, i.e., slightly differing coupling values can translate into considerably differing rates. Photoinduced charge-transfer rates are especially small for the a-b-morphology where they become noticeable only in one region of the organic::organic interface (lower left panel, Figure 88). Analyzing this region by visual inspection reveals that slip-stacked conformations of DIP molecules on fullerene C_{60} exist that give rise to the non-negligible coupling strengths and larger rates. Standing orientations of DIP on fullerenes dominate all other parts of the interface, leading to very low rates. This agrees nicely with findings of Heremans et al.[568] who investigated the crystalline pentacene::fullerene interface and predicted only very low charge-transfer rates for an edge-on orientation of pentacene on top of the fullerene layer. In contrast to the a-b-morphology, considerably more pathways for fast photoinduced charge-transfer processes exist for the a-c- and the b-c-morphology (see the number of blue arrows in the lower left panel of Figure 89 and Figure 90). The very limited number of fast photoinduced charge-transfer trajectories along the interface of the a-b-morphology can also in parts explain the poor exciton dissociation quantum yield of this system (Figure 87).

It is worth emphasizing that large charge-transfer couplings do not necessarily induce very high charge-transfer rates. This results from the additional influence of the driving force on the rates and becomes evident from the distribution of couplings and rates for both the a-c- and the b-c-morphology (Figure 89, Figure 90). Couplings for the photoinduced charge-transfer process are largest for heterodimers with a very close contact between the DIP molecule and the fullerene acceptor. As was discussed in the previous section "Energetics of the exciton dissociation and charge separation processes in the vicinity of the organic::organic interfaces", low-lying interfacial charge-transfer states, i.e., trap states, are found precisely on these heterodimers because their conformations ensure a small initial electron-hole separation and a correspondingly high Coulomb binding energy. As a consequence, the driving force for the photoinduced charge-transfer step to such a low-lying charge-transfer state is so high that the step is situated in the Marcus inverted region. It is thus kinetically hampered in spite of large coupling strengths. This result is quite significant also from a device perspective: it suggests that the influence of interfacial charge-transfer might not be as decisive as one could assume. If Marcus theory

applies, i.e., in the weak coupling limit,[601] the population of deep interfacial charge-transfer state is kinetically unfavorable, which limits their negative impact.

For all DIP::fullerene interfaces, recombination rates virtually vanish (Figure 88 to Figure 90), being always smaller than $5 \cdot 10^7 s^{-1}$. Recombination rates are often inferior to corresponding charge-transfer rates, a fact already discussed by Troisi et al.[584] and by Castet et al.[601] In a Marcus-based description, this is again a direct consequence of the Marcus-inverted region where the majority of the usually very exothermic recombination processes are located. There is also experimental evidence[982] for the Marcus-inverted behavior of recombination processes. In line with these literature results, the driving force for most recombination processes along the DIP::fullerene interface exceeds 1-1.5 eV, which explains the negligible rates.

Please note that disorder of site energies σ was not included in the visual representation of the rates in Figure 88 through Figure 90 to provide a balanced description of all rates (evidently, the disorder of site positions was taken into account). It was, however, taken into account in the computation of the KMC quantum efficiencies (Figure 87). In general, increasing the disorder parameter in the KMC simulations deteriorates exciton dissociation and charge separation efficiencies. Consistently, effective charge and exciton velocities decrease. Moreover, Gennett and coworkers[552] outlined that the effects of disorder are especially pronounced for intrinsically slow rates. Fast processes are naturally also affected by disorder. However, in contrast to them, slow processes can be effectively suppressed because due to the additional deceleration exerted by disorder, they become so small that other competing processes take over.

To summarize this discussion of general aspects of interfacial kinetics, three important kinetic effects were defined at the DIP::fullerene system:

1. Random exciton and charge migration can effectively prevent the completion of exciton dissociation or charge separation processes. Certain morphologies of the DIP::fullerene system were shown to favor random exciton/charge migration due to the intrinsically anisotropic transport. If fast transport pathways parallel the interface, efficient exciton diffusion toward and fast charge separation away from the interface are improbable.

2. In the immediate vicinity of organic::organic interfaces, "charge transport depletion zones" are formed, i.e., areas with slow charge transport rates. The slow rates result from the significant Coulomb attraction between the geminate electron-hole pair that gives rise to a large endothermic contribution to the overall driving force of charge separation. As Marcus charge transport rates depend exponentially on the driving force, they significantly decrease.

Although it is well-known that charge separation can be an energetic uphill process,[423] the kinetic implications of the endothermic nature of the process were mostly disregarded.

3. Loss mechanisms like fluorescence or exciton self-trapping only become competitive if alternative processes are slow. Since charge-transfer steps at the DIP::fullerene interface are sometimes kinetically hampered, fluorescence can outcompete exciton dissociation and becomes noticeable for long exciton diffusion times.

In the following sections, these aspects will be generalized by analyzing the charge generation kinetics at interfaces of fullerene C_{60} with other molecular p-type semiconductors.

Random exciton migration caused by fast exciton/charge transport rates combined with slow charge-transfer steps

If exciton/charge transport is anisotropic and follow-up processes like exciton dissociation/charge separation are slow, charge generation can be effectively suppressed. Instead, excitons (charges) migrate randomly in the donor phase (donor and acceptor phases). To illustrate this, in a first step, two different morphologies, the a-b- and the b-c-orientation, of the rubrene::fullerene system are compared. The KMC yields for the a-b-system are given in Figure 91. Notably, the probability for exciton dissociation is unity. In contrast, barely any excitons dissociate at the b-c-interface (*not shown*), with 0.3 % being the corresponding quantum yield for exciton dissociation. Moreover, no charge separation occurs for this b-c-morphology. No losses due to radiative decay were found in either system.
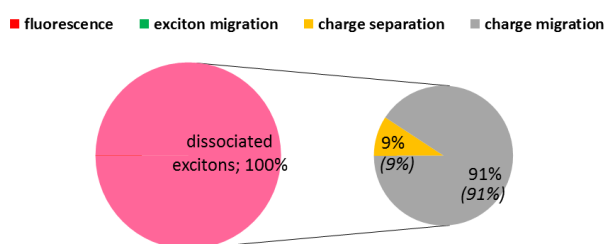
Figure 91: KMC quantum yields for the KMC simulations on the (a-b)-rubrene::fullerene morphology.

To understand these contrasting findings, the distribution of rates and underlying couplings is given in Figure 92 for the a-b-morphology and in Figure 93 for the b-c-morphology. It is well-known from a plethora of experiments[983,489] that exciton diffusion is fast in pristine rubrene crystals. In line with this, fluorescence cannot compete with the high exciton diffusion rates in the KMC simulations so that it is quasi-inexistent within the simulation time scales (Figure 91). Similar to the different morphologies of the DIP::fullerene-donor-acceptor system, the spatial distribution of exciton and charge transport rates differs for the two rubrene::fullerene morphologies (Figure 92 and Figure 93). However, the

pronounced differences in KMC yields (Figure 91) arise primarily from the combination of the very efficient exciton diffusion in rubrene and morphology-dependent, different photoinduced charge-transfer rates. Considerable charge-transfer rates resulting from high couplings and small absolute driving forces are observed for the a-b-orientation (Figure 92). In contrast, in spite of non-negligible charge-transfer couplings in the b-c-system (Figure 93), corresponding charge-transfer rates decline due to the contributions of the driving forces. It is worth emphasizing that these charge-transfer rates are not exceptionally low, but they are very small compared with the fast exciton diffusion processes. Therefore, instead of dissociating, an incoming exciton rather continues diffusing.

Figure 92: Couplings for excitons (upper left panel) and charges (upper right panel) and the corresponding rates for exciton transport (lower left panel) and charge transport (lower right panel) for the (a-b)-rubrene::fullerene interface (face-on orientation of rubrene molecules on fullerene C_{60}).

Endothermic driving forces due to the significant Coulomb binding energy between geminate electron-hole pairs also account for the low charge separation efficiencies in the a-b-system, which amount to only 9% (Figure 91). It is evident from Figure 92 that despite considerable charge-transport couplings (upper right panel), corresponding rates vanish particularly in the immediate vicinity of the organic::organic interface because of the rate-limiting effect of endothermic driving forces. Similar to the DIP::fullerene system, a charge-transport depletion zone is formed that is more pronounced for the face-on orientation of donors (Figure 92) on the fullerene layer than for the edge-on orientation (Figure 93). This area of low charge-transport rates impedes efficient charge separation. Furthermore, also alike to the DIP::fullerene systems, the influence of anisotropic transport due to the presence of stacks is demonstrated by the spatial distribution of rates at the b-c-interface (Figure 93): fast exciton and charge transport take place along the stack. This means for the b-c-orientation that fast transport

parallels the interfacial plane, thereby prohibiting directed exciton/charge transport toward/away from the interface. Therefore, even if excitons were split at the b-c-interface, final charge separation would be highly improbable due to the unfavorable anisotropy of charge-transport rates.

Figure 93: Couplings for excitons (upper left panel) and charges (upper right panel) and the corresponding rates for exciton transport (lower left panel) and charge transport (lower right panel) for the (b-c)-rubrene::fullerene interface (edge-on orientation of rubrene molecules on fullerene C_{60}).

Influence of molecular characteristics on the charge transport depletion zone

It was outlined above that a "charge transport depletion zone" arises in the vicinity of organic::organic interfaces, i.e., an area of very slow charge-transport processes. Its extension is critically influenced by molecular properties, as demonstrated in the following for the HB194::fullerene and the squaraine::fullerene system.
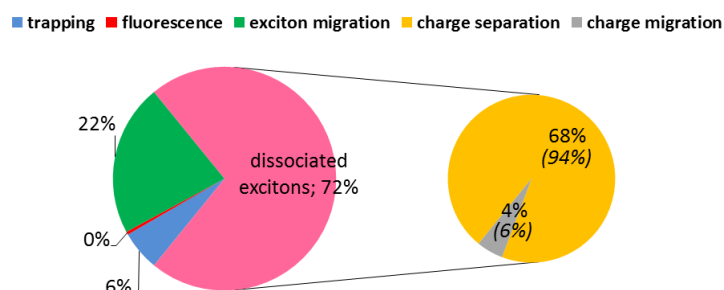
Figure 94: KMC quantum yields for the KMC simulations on the (a-c)-HB194::fullerene morphology.

The KMC efficiencies for the (a-c)-HB194::fullerene system are shown in Figure 94. The vast majority of generated excitons (72%) dissociate at the HB194::fullerene interface (Figure 94). Some random

exciton migration occurs (22%) that is comparable with the amount of exciton migration calculated for the (a-c)-DIP::fullerene system (26%). It is particularly noticeable from Figure 94 that the HB194::fullerene system shows unusually high charge separation efficiencies, amounting to 68% when referenced to the number of generated excitons and to 94% when referenced to the number of dissociated excitons. These numbers even exceed corresponding yields for the (b-c)-DIP::fullerene system where 86% of the dissociated excitons accomplish charge separation. The very high efficiencies for the HB194::fullerene system are in good accordance with high experimental device performances.[962]
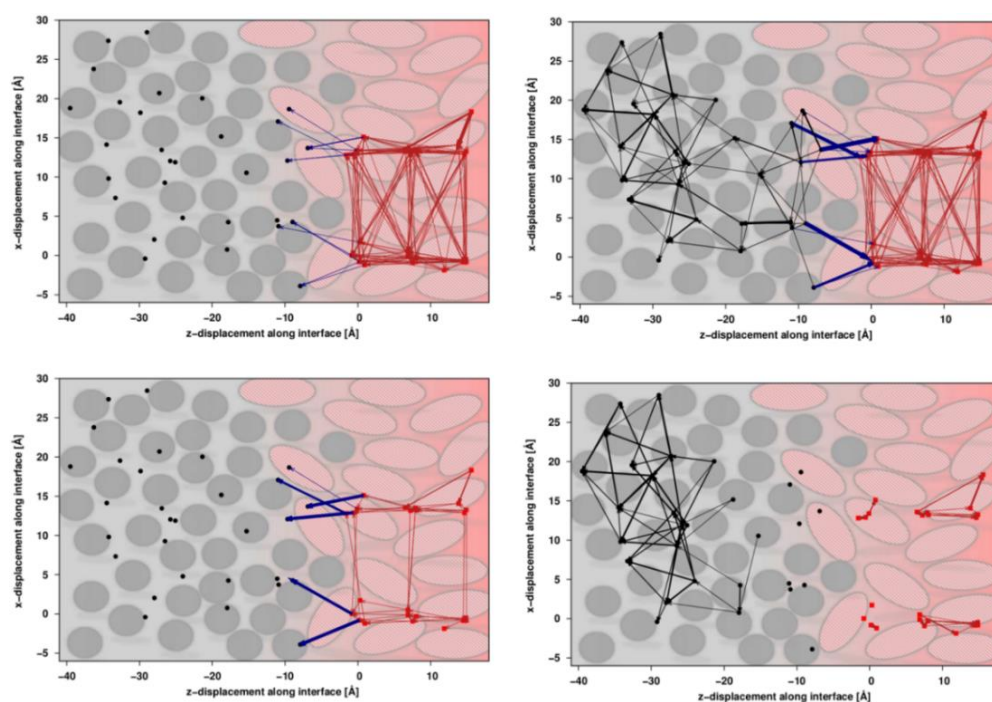

Figure 95: Couplings for excitons (upper left panel) and charges (upper right panel) and the corresponding rates for exciton transport (lower left panel) and charge transport (lower right panel) for the (a-c)-HB194::fullerene interface.

To gain more insight, Figure 95 displays the rates and couplings of the HB194::fullerene system. In contrast to a significantly anisotropic distribution of rates in the DIP and rubrene systems, rates are rather uniformly spread for HB194. The fact that no specific direction of exciton diffusion is favored explains why some exciton migration occurs. High exciton dissociation efficiencies are to some extent due to comparably fast charge-transfer processes (blue arrows, lower left panel, Figure 95). The latter ensure that exciton dissociation occurs with a sufficient probability compared with the competing further diffusion. This contrasts with findings for the rubrene::fullerene system. Nevertheless, above all the quasi-inexistence of a charge-transport depletion zone, the most obvious feature of the HB194::fullerene system (lower right panel, Figure 95), contributes to the high efficiency of charge separation. The endothermic driving forces of charge separation due to the significant Coulomb

binding energy in the DIP and rubrene systems were responsible for the formation of charge-transport depletion zone. At the HB194::fullerene interface, the rates change only to a minor extent, which results from the more efficient screening of the Coulomb attraction by the polar environment. This leads to less pronounced variations of the Coulomb binding energy between different hopping sites and, concomitantly, to a smaller value of the driving force for a given charge transport process. This implies that the polarity of the merocyanine bulk phase does not only reduce the number of interfacial charge-transfer trap states, but it prevents also the formation of a charge-transport depletion zone in the vicinity of the organic::organic interface. Rather fast charge transport processes are possible also in the immediate surroundings of the interface, thereby allowing for fast charge separation and explaining the high charge dissociation yields in Figure 94. These effects could also be partially responsible for the good performances of OSCs based on merocyanine dyes.
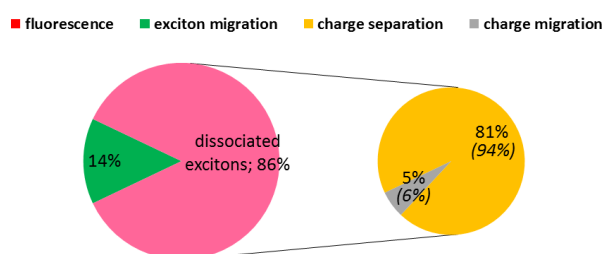
Figure 96: KMC quantum yields for the KMC simulations on the (a-b)-squaraine::fullerene morphology.

The squaraine::fullerene system behaves similarly to the HB194::fullerene system (Figure 96, Figure 97). Strong exciton couplings, correspondingly high exciton transport rates and significant charge-transfer rates result in high exciton dissociation efficiencies (86%, Figure 96). With 81% when referenced to the number of generated excitons or 94% when referenced to the number of dissociated excitons, charge dissociation efficiencies are also very high (Figure 96). Similar to the HB194::fullerene system, this can be explained by the near-absence of a charge transport depletion zone at the squaraine::fullerene interface (Figure 97). On the one hand, this results from the comparably high effective epsilon in a polar and polarizable squaraine environment, which reduces the Coulomb binding energy. On the other hand, the charge separation process is further promoted by the long linear molecular shape of the squaraine molecule that guarantees rather large initial electron-hole separation irrespective of the exact heterodimer conformation. As already discussed, a large initial electron-hole separation decreases the Coulomb binding energy and also its variation along the charge separation pathway. It should be noted that the molecular shape of rubrene is also rather linear and longitudinal. The fact that charge separation efficiencies for the rubrene::fullerene system are low despite this seemingly favorable molecular shape underlines the profound influence of the screening ability of the environment.
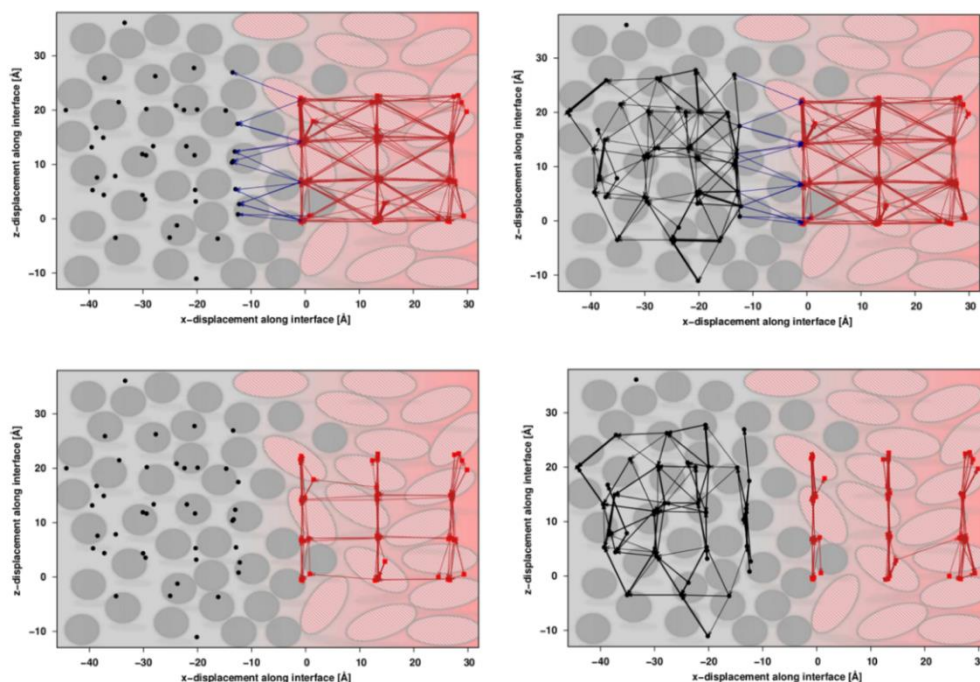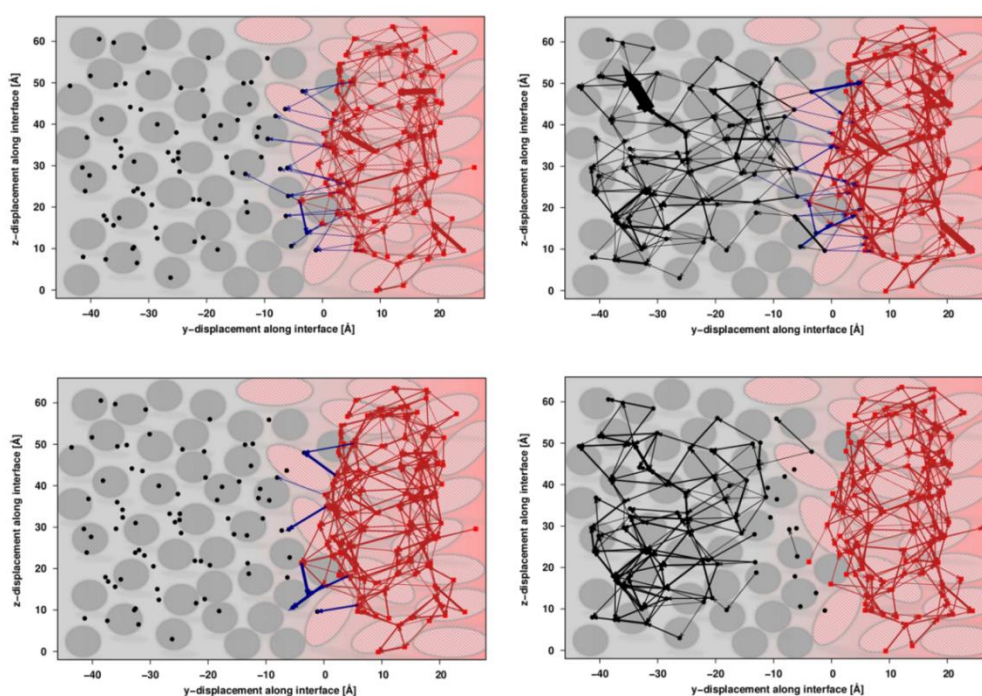
Figure 97: Couplings for excitons (upper left panel) and charges (upper right panel) and the corresponding rates for exciton transport (lower left panel) and charge transport (lower right panel) for the (a-b)-squaraine::fullerene interface.

Structure-property relationships for further loss mechanisms such as fluorescence

Donor-acceptor systems composed of fullerene C_{60} and triphenylamine-based compounds are analyzed to gain further insight into the importance of loss mechanisms such as fluorescence and exciton trapping. Figure 98 shows the KMC quantum yields for the "triamine-methoxy"::fullerene system while Figure 99 displays the spatial distribution of the underlying couplings and rates ("triamine-methoxy"=TAM). It becomes evident from the KMC quantum yields (Figure 98) that fluorescence occurs surprisingly often (23%). This fluorescence efficiency is considerably larger than all previously found values although the absolute radiative decay rate in "triamine-methoxy" is on the same order as other fluorescence rates. Furthermore, the overall exciton dissociation efficiency (30%, Figure 98) is rather poor, the more so as almost half of the generated excitons continue diffusing through the p-type semiconducting layer (50% of exciton migration, Figure 98). Moreover, simulation times are long. Please keep in mind that the number of KMC steps was predefined, not the simulation time.

Figure 98: KMC quantum yields for the KMC simulations on the (a-b)-"triamine-methoxy"::fullerene morphology.

Figure 99: Couplings for excitons (upper left panel) and charges (upper right panel) and the corresponding rates for exciton transport (lower left panel) and charge transport (lower right panel) for the (a-b)-"triamine-methoxy"::fullerene interface.

As charge-transfer rates (lower left panel, Figure 99) are not particularly small, they are not responsible for the low exciton dissociation efficiencies. The latter result rather from slow exciton transport rates, which are reflected in the comparably high fluorescence yields as well. As discussed above, fluorescence can only compete with exciton diffusion if exciton diffusion is slow or if diffusing excitons do not reach the interface, and long diffusion times result. It was discussed in the section "Energetics of the exciton dissociation and charge separation processes in the vicinity of the organic::organic interfaces" that excimers are formed in the bulk "triamine-methoxy" phase because the molecular structure promotes intermolecular charge transfer. In fact, it becomes apparent from the distribution of rates and couplings (Figure 99) that strongly coupled dimers exist in the "triamine-methoxy" layer that barely interact with their surroundings. Any exciton localized on such a dimer hops back and forth between the underlying monomers, while its probability to hop further to a neighboring monomer is almost negligible. As a consequence, the exciton remains for long times on the same dimer, and at

346

some point in time in long simulations, fluorescence becomes competitive with the ongoing back and forth hops. This explains the high fluorescence yields. Furthermore, disorder is significant in the "triamine-methoxy"::fullerene system because, albeit slowing down all rates, it suppresses inter-dimer hops that become diminishingly small and are successively outperformed by fluorescence, in accordance with the above-addressed analysis Gennett et al.[552] Although exciton dissociation efficiencies were poor for some DIP/rubrene::fullerene systems as well, fluorescence is not competitive with fast exciton diffusion in these systems, even in the presence of disorder.
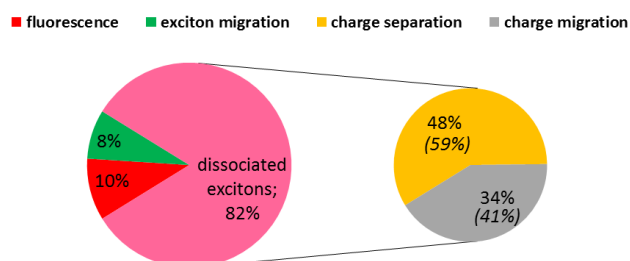
Figure 100: KMC quantum yields for the KMC simulations on the (a-b)-"triamine-aldehyde"::fullerene morphology.
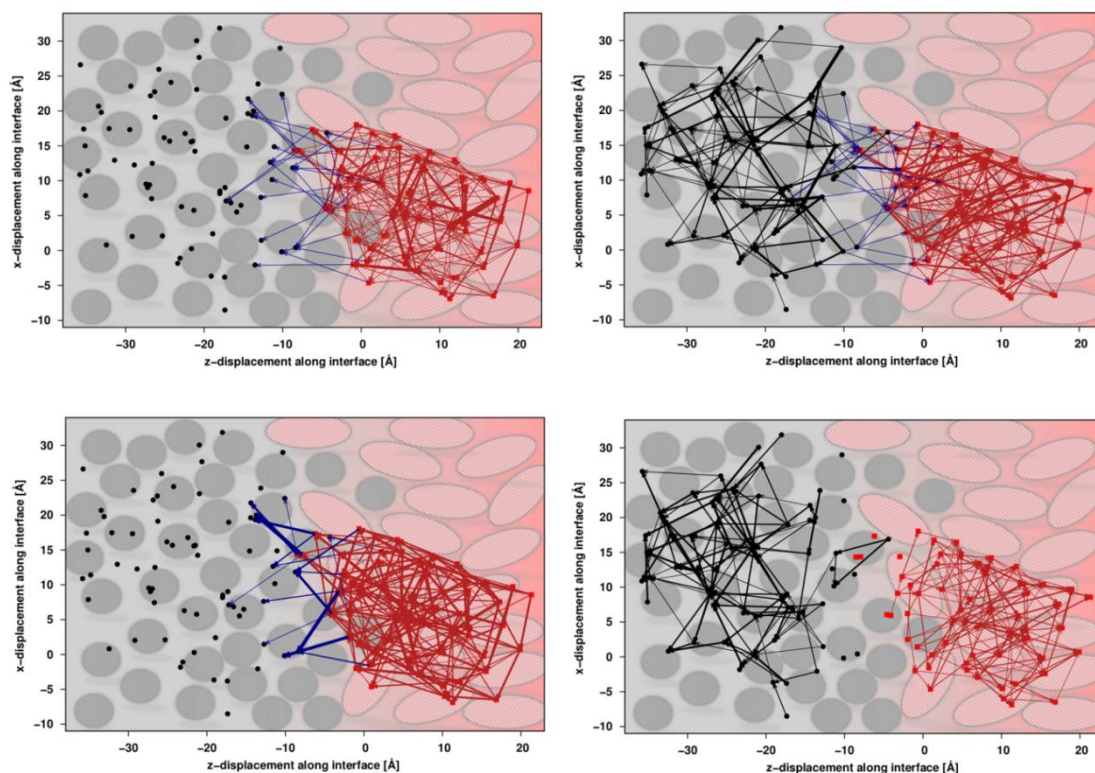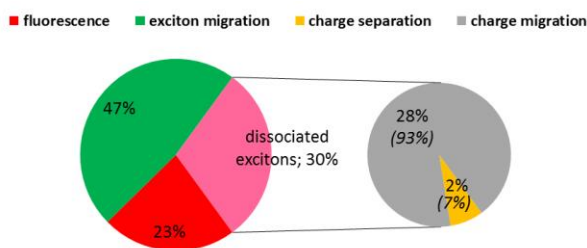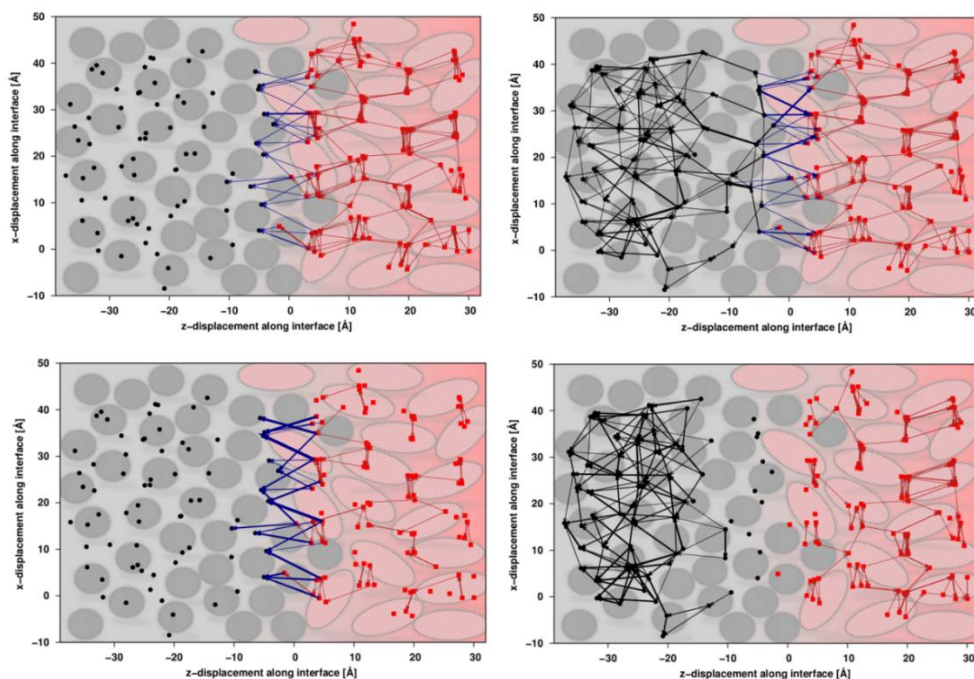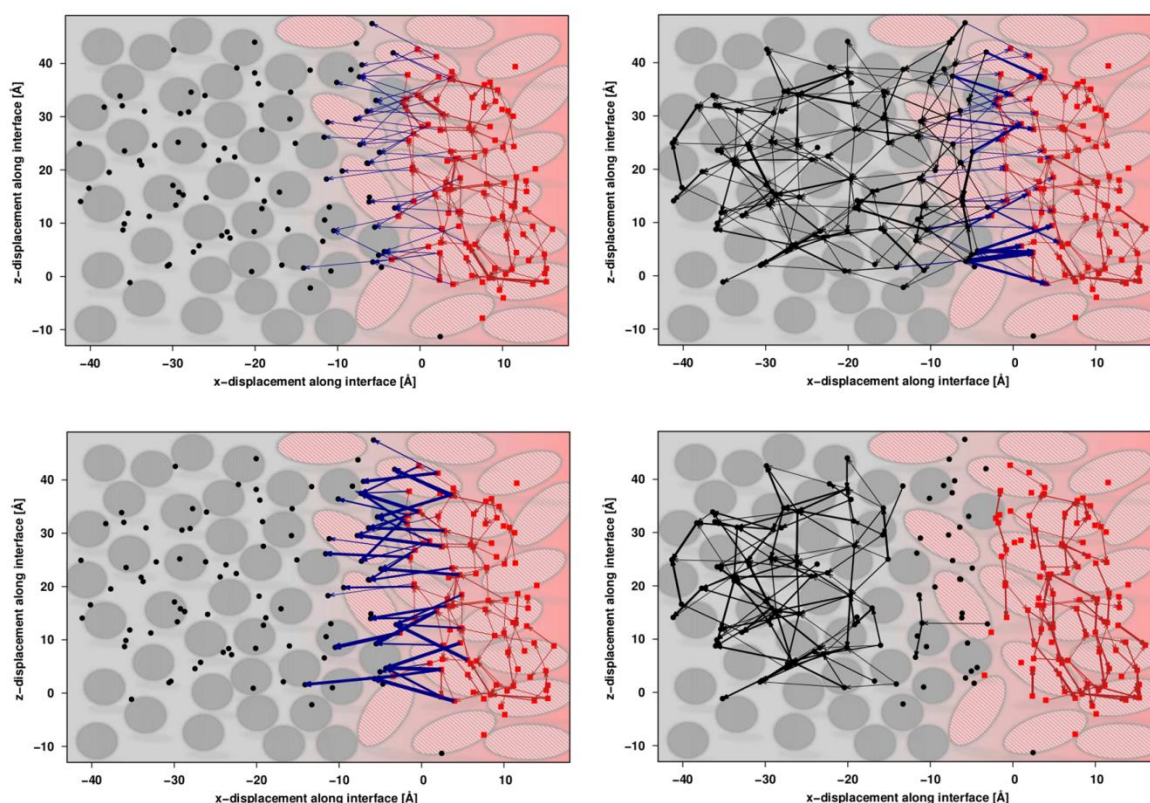

Figure 101: Couplings for excitons (upper left panel) and charges (upper right panel) and the corresponding rates for exciton transport (lower left panel) and charge transport (lower right panel) for the (a-b)-"triamine-aldehyde"::fullerene interface.

Since relative rates rather than absolute rates are important for high quantum yields, high exciton dissociation efficiencies can also be achieved in systems with rather low exciton transport couplings as long as fluorescence is slower and exciton dissociation is sufficiently rapid so that excitons reaching the donor-acceptor interface dissociate immediately. The "triamine-aldehyde"::fullerene system represents such a scenario ("triamine-aldehyde"=TAA). Its quantum yields are shown in Figure 100 with the corresponding rates and couplings displayed in Figure 101. The high exciton dissociation efficiency of 82% (Figure 100) contrasts with rather low diffusion rates (Figure 101, lower left panel). Furthermore, the efficiency for final charge separation of almost 50% (Figure 100) is quite satisfying. These good results compare well with experiments demonstrating the sound optoelectronic performances of related acceptor-substituted star-shaped oligomers.[685,624] The results in Figure 101 imply that the electron-withdrawing groups are not only important for an improved overlap of the donor absorption with the solar spectrum,[984] but also for aligned transport levels.[684,985] The aligned transport levels ensure that the photoinduced charge-transfer is almost isoenergetic or only slightly exothermic so that corresponding charge-transfer rates are very fast. High exciton dissociation efficiencies result. Moreover, the more polar environment due to the introduction of the accepting groups (compared with simple triphenylamines) increases the screening of Coulomb interactions, facilitating charge separation. These results are well line with experimentally found improved EQE values upon introducing accepting groups into triphenylamine derivatives.[685]

Comparison of effective charge and exciton velocities obtained in KMC simulations and resulting transport parameters to macroscopic experimental data

In the last subsections, the impact of kinetics on the quantum yields of exciton dissociation and charge separation was investigated for a number of systems, and three general kinetic effects were defined (random exciton migration due to anisotropic transport and slow follow-up processes, formation of a "charge transport depletion zone", fluorescence losses and similarly further trapping processes like in DIP). The analysis focused on the molecular and aggregate scale, and a number of molecular and aggregate properties were found to be somewhat influential. Nevertheless, from a device perspective, it would be desirable to identify individual molecular or aggregate properties that, when optimized, result in improved device performances. To do so, transport parameters calculated from the KMC effective velocities are compared with macroscopic device properties, most notably, with hole mobilities. This permits also to critically evaluate the adopted approach, which relies on numerous approximations. Effective exciton and charge velocities computed in the KMC simulations are listed in Table 26 for the largest employed model interface per donor-acceptor combination. Although velocities for the same donor-acceptor combination in different morphologies differ quantitatively, no significant qualitative differences were found.

Table 26: Simulated velocities for the discussed systems in heterojunction with fullerene C_{60}. It should be kept in mind that charge velocities refer only to positive charges in the p-type semiconducting layer. Furthermore, all velocities include transport in only one, i.e, the effective direction.

	exciton velocity [cm/s]	charge velocity [cm/s]
HB194	451.25	95.55
squaraine	2501.07	107.41
rubrene	98.05	1.01
DIP	38.65	8.20
MD353	95.15	56.39
DPP (= diketopyrrolopyrrole)	712.47	118.84
TAM („triamine-methoxy")	1.57	0.90
TAA („triamine-aldehyde")	28.10	8.72

Evidently, charge velocities are in the order of $1 - 100 \frac{cm}{s}$ (Table 26). This compares well with frequently encountered experimental values, having maximum values of $10^6 \frac{cm}{s}$ as addressed by Karl et al.[986,987], but ranging usually around $1 - 10^3 \frac{cm}{s}$. The good accordance justifies the approach although it is certainly surprisingly good, especially with regard to the introduced approximations.

Standard device parameters, i.e. a built-in voltage of 0.5 V[988,989] and a thin-film thickness of 50 nm[990] are used to convert calculated effective charge (drift) velocities into experimentally accessible hole mobilities of blends. It should be kept in mind, however, that no electric field was applied in the simulation, i.e., the charge carriers move by diffusion rather than drift.

The hole mobility μ can be obtained from the charge drift velocity $\vec{v}_D$ and the electric field $\vec{E}$:

$$\mu = \frac{|\vec{v}_D|}{|\vec{E}|}$$

(463)

Resulting hole mobilities are correlated with experimental counterparts in Table 27. Please note that if experimental reference data were not available for blends, bulk mobilities are instead employed.

Table 27: Experimental values for hole mobilities. Amorphous/average values are used.

	hole mobility [10^4 cm²/Vs]	Source
squaraine	1.90	[690]
rubrene	0.08	[991]
DIP	0.30	[986] large variations[911]
DPP	2.50	[654]

The correlation is displayed in Figure 102. Expectedly and in line with the findings of Andrienko,[992] predicted values are overestimated compared with experimental data. More importantly, however, is the rather accurate prediction of the trends, with a coefficient of determination R² of almost 1. This provides further support for the adopted model.
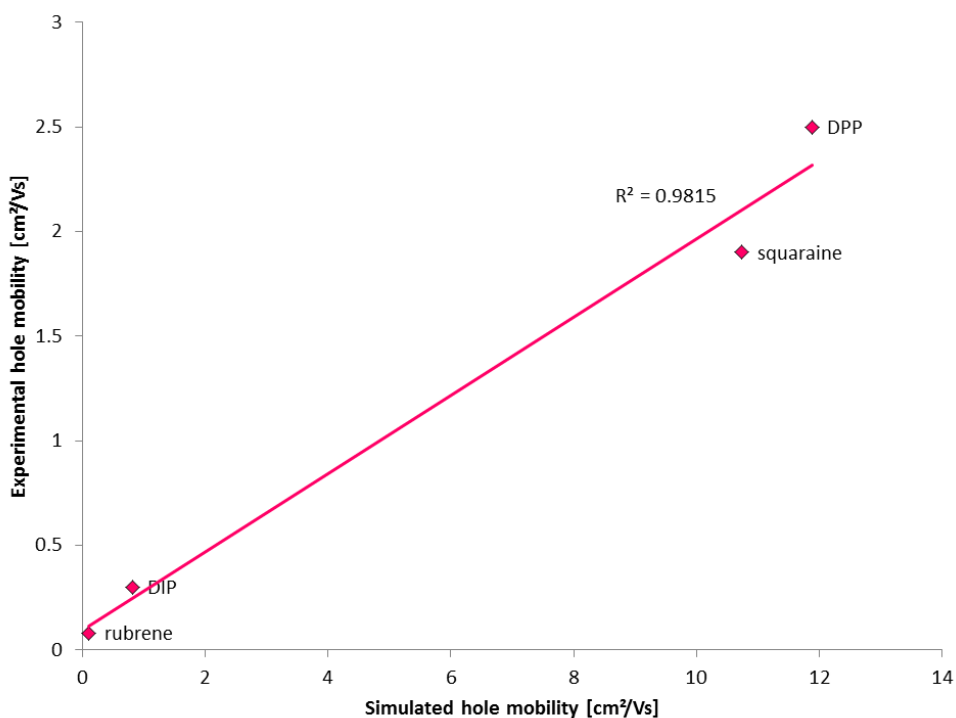
Figure 102: Correlation of experimental and simulated hole mobilities.

Taking the average of the exciton velocities in Table 26 ($100 \frac{cm}{s}$) together with an average exciton lifetime in the nanosecond regime ($5ns$) yields an approximate exciton diffusion length of $5nm$, which

certainly constitutes a reasonable estimate for disordered organic thin films.[952] Therefore, also exciton velocities in Table 26 seem to be plausible.

Upon comparing exciton and charge velocities in Table 26, it becomes evident that exciton velocities are about one to two orders of magnitudes larger than corresponding charge velocities. This arises from the isoenergetic nature of exciton diffusion where disorder represents the only source for non-zero driving forces. In contrast, the Coulomb binding energy dominating driving forces and rates for charge transport is responsible for the generally lower rates because it significantly decreases charge velocities notably in the direct vicinity of the organic::organic interfaces.

The short-circuit current in OSCs depends on the EQE, which is in turn the product of the efficiencies of the individual processes.[418] Therefore, the short-circuit current should be dominated by the least efficient process, i.e., by the rate-limiting step of the outlined multistep light-to-energy conversion. The discussed results suggest that the most efficiency-limiting process corresponds to slow charge transport near the organic::organic interface. Thus if charge transport is indeed efficiency-limiting, its efficiency should correlate with experimental open-circuit currents. To verify whether this holds, experimental short-circuit currents listed in Table 28 are correlated with the computed charge velocities (Figure 103).[aaaa]

Table 28: Experimental values for OSC short-circuit currents. Either fullerene C_{60} or PCBM were used as acceptors in the experimental devices.

	short-circuit current [mA/cm²]	Source
HB194	8.24	[656]
MD353	4.00	[655]
squaraine	6.48	[690]
rubrene	2.35	[511]
DIP	0.80	[671]
DPP	9.85	[654]

[aaaa] Please keep in mind that thermodynamic considerations were disregarded.
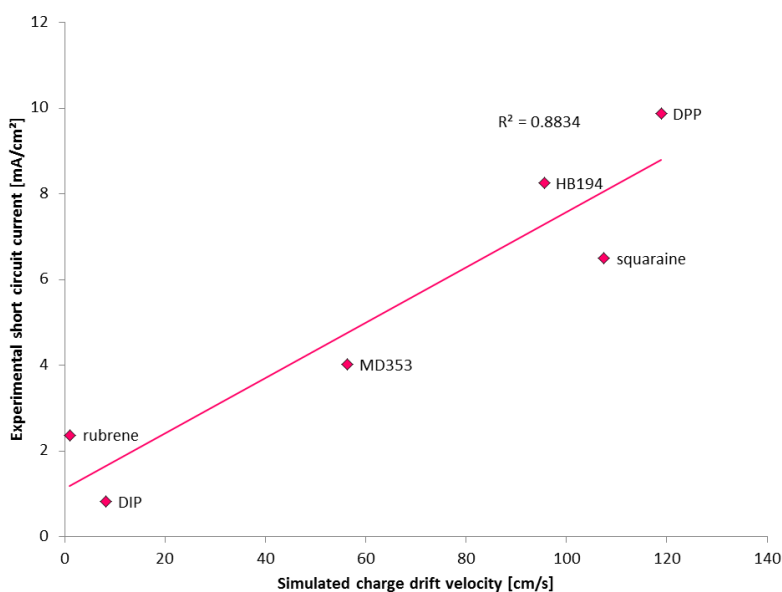
Figure 103: Correlation of simulated charge drift velocities with experimental short-circuit currents.

The rather large R²-value (88%) in Figure 103 underlines that experimental short-circuit currents are indeed somewhat related to the simulated charge velocities. This effectively implies that slow charge transport processes at organic::organic interfaces could constitute a major bottleneck for overall device efficiencies, and that high charge carrier mobilities are absolutely mandatory to obtain high short-circuit currents and good device performances. This key outcome of the presented results is completely in accordance with conclusions from macroscopic simulation models employed for example by Blom et al.,[993] Dyakonov et al.,[994] Riede et al.,[990] Albrecht et al.[498] and Resendiz et al.[995] Experimental data providing further support of the importance of charge carrier mobilities was delivered among others by Nguyen et al.[996] and by Samuel et al.[997]

To conclude from this section, KMC simulations with Marcus hopping rates obtained from *ab initio* calculations were used to model the light-to-energy conversion process in the vicinity of organic donor-acceptor interfaces. KMC quantum yields and velocities were computed that compare well with experimental findings although a number of significant approximations had to be introduced to set up the simulations.

The analysis of the quantum efficiencies and of the spatial distribution of rates and couplings led to the identification of three very important kinetic effects. (1) The significant Coulomb attraction within geminate electron-hole pairs does not only affect the energetics of the charge separation process, but also reduces the rates of the underlying successive charge transport steps. In addition to the energetic penalty, it gives therefore also rise to a considerable kinetic barrier for charge separation. (2) Random exciton and charge migration impede high exciton dissociation and charge separation efficiencies. Both a morphologically imposed unfavorably anisotropy of exciton/charge transport and slow rates of

potential follow-up processes of exciton transport can explain the existence of random exciton/charge migration. For instance, especially in materials where exciton transport is fast, photoinduced charge transfer needs to be fast as well. Otherwise, exciton dissociation becomes highly improbable compared with ongoing exciton diffusion. (3) Loss channels such as radiative decay, exciton trapping, and recombination can only be competitive if alternative exciton or charge transport processes are exceptionally slow. Radiative decay (recombination) is therefore less important (negligible).

It has already been mentioned in this and in the last section ("Energetics of the exciton dissociation and charge separation processes in the vicinity of the organic::organic interfaces") that disorder profoundly influences both the energetics and the kinetics of all optoelectronic processes around the interface. The Gaussian disorder parameters σ were calculated from the energetic distributions of dimer energies, which take into account variations in delocalization and intermolecular interactions. However, the environment was included in the dimer calculations only in an average way, i.e., by an effective epsilon combined with local electric fields. Therefore, the computed Gaussian disorder parameters do not incorporate any effects arising from different interfacial morphologies or environmental discontinuities at the interface if these do not translate into differences at the stage of dimers. However, Yost and van Voorhis pointed out that precisely such interface-related phenomena significantly affect the disorder at organic::organic interfaces so that the interfacial disorder is most accurately modeled by explicitly considering the atomistic details of the surrounding interface.[460,26] Therefore, a more thorough discussion of disorder around organic::organic interfaces is presented in the following section.

5.10 QM/MM Calculations Combined With the Dimer Approach to Investigate the Static Disorder at Disordered Donor-Acceptor Interfaces

This section presents a more detailed analysis of the disorder in the vicinity of organic::organic interfaces. The environment is atomistically taken into account to include as many interface-related phenomena that might affect the disorder as possible. Such phenomena comprise among others the environmental discontinuity between the donor and the acceptor phase or the looser packing density around the interface. It should be noted that the Bässler model has shaped the notion of disorder as employed in the following.

In the Bässler model, charge transport in disordered organic semiconductors is described with successive hopping processes between energetically distributed sites. The model assumes that the underlying DOS (density of states) has a Gaussian shape. Like any other normal distribution, the DOS can be characterized by its standard deviation, i.e., by the Gaussian disorder parameter σ.[425] The Bässler model was extensively employed to explain experimental field- and temperature-dependent charge carrier mobilities.[548] Albeit originally derived for charge transport, it was equally applied to exciton transport. In support of the model, ample experimental evidence was especially provided for the Gaussian shape of the excitonic DOS, for example by means of optical probing of excitonic transitions[545] and time-resolved measurements of dispersive exciton transport.[998,999]

The disorder parameter σ, which governs transport efficiencies, was shown to be related to the polarity and the polarizability of the transport material.[546,548] To further optimize transport properties, more detailed structure-property relationships would still be desirable. Moreover, it has been outlined above that charge carrier mobilities in the vicinity of organic::organic interfaces profoundly influence resulting device performances, and that the probability for exciton dissociation depends considerably on the rates for exiton diffusion. Both charge carrier mobilities and exciton diffusion can be critically influenced by disorder. Therefore, the extent of disorder at the interfaces seems to be quite decisive, and the interfacial parameters σ might differ from their corresponding bulk values.[460,26] While experimental measurements of disorder parameters at interfaces are problematic, an *in silico* extension of the disorder concept to the interfacial region and direct computations of the corresponding parameters σ are straightforward.

To investigate the disorder in the vicinity of organic::organic interfaces in more detail, QM/MM calculations are presented in this section. Excitonic/polaronic states in the donor phase, their DOSs and corresponding Gaussian disorder parameters σ are calculated. The discussion of the approach and the results is organized as follows. In a first step, the theoretical approach is outlined. Then, DOSs of state energies (ground, excited, cationic states) and state energy differences (ionization potentials, excitation energies) are presented. It is verified whether the DOSs have Gaussian shapes and whether

these are sufficiently broad so that transport is disorder-limited (which is usually assumed).[548] Only then, the Gaussian disorder parameters σ are physically meaningful. In a third step, computed disorder parameters are correlated with molecular properties, and several structure-property relationships are identified.

5.10.1 Theoretical Approach

The generated disordered interfacial model systems are again used. It should be noted that these model systems are disordered even for molecules like anthracene or DIP that experimentally readily crystallize.[671] Hence later-on computed disorder parameters σ constitute an upper bound to the actual disorder present at the interfaces.
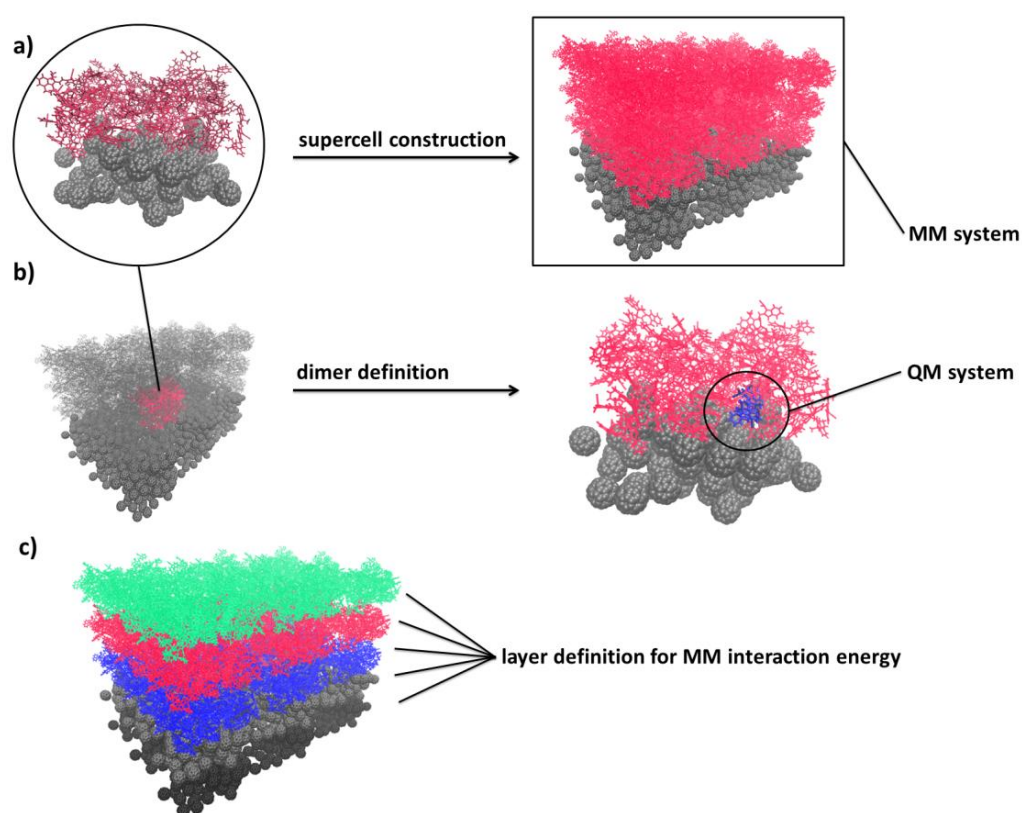
Figure 104: a) Construction of the supercell of sufficient size from the generated disordered interface models highlighted in pink in the supercell. b) Dimers cut out from the center cell. Only one dimer is highlighted, but the procedure was repeated for all dimers of the underlying original model system. c) Definition of layers for the decomposition of the computed MM interaction energy.

It is well-known that charge-charge interactions are of long-range character (see also Section "Interactions between the π-systems of molecular organic semiconductors").[340] Hence large model systems are needed to obtain converged values for charge-charge interactions. Therefore, the disordered interface structures are used to construct supercells (Figure 104a). All possible homodimers composed of donor molecules are cut out in the underlying original disordered interface part (Figure 104b, similar procedure to the previous two sections). These dimers are used as the QM parts of

subsequent QM/MM calculations, thereby incorporating the above discussed advantages of dimer calculations (see Section "Energetics of the exciton dissociation and charge separation processes in the vicinity of the organic::organic interfaces").[745]

The supercell construction process is further illustrated in Figure 105. The underlying disordered interfacial model system is replicated, and resulting identical cells are aligned. Moreover, only the disordered donor (acceptor) phase of the underlying disordered model system is used to extend the supercell in a perpendicular direction above (below) the interfacial plane (Figure 105). The resulting system (100 000 – 400 000 atoms) is too large to be equilibrated in subsequent MD simulations. Therefore, the displacements between the replicas (highlighted in blue, green, and orange in Figure 105) are a very critical point of the supercell construction process. To analyze how much they influence final results, three different values for each displacement were used. It turned out that they do not significantly impact results as long as steric strain does not occur.
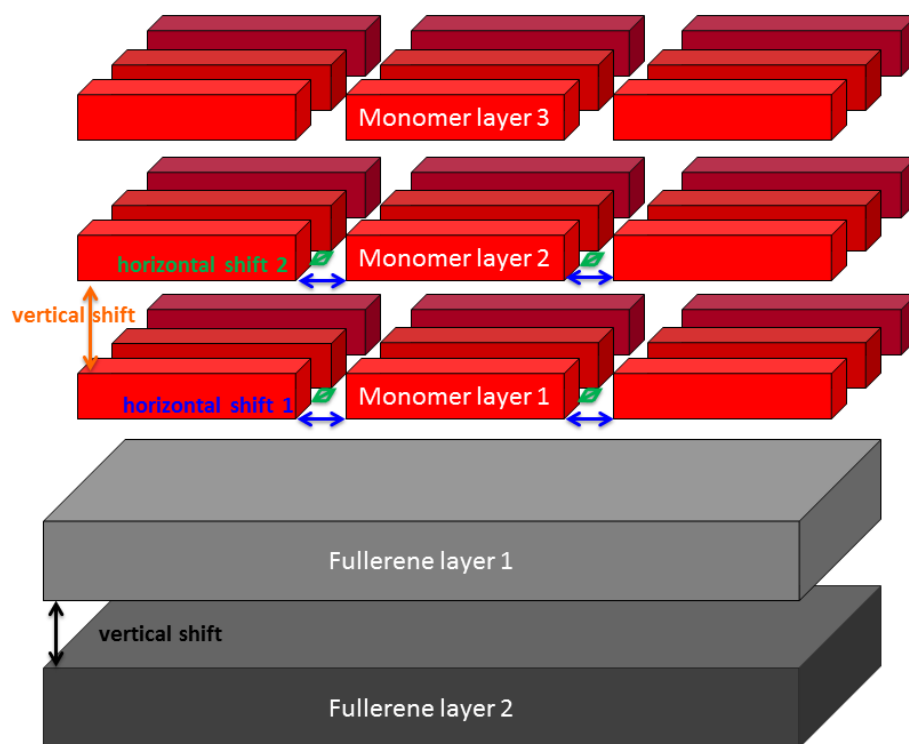
Figure 105: Demonstration of the supercell construction process.

In a subtractive QM/MM scheme, the QM system, i.e., the dimer, is electrostatically embedded into the environment.[410] The dimer interacts with the partial charges on all molecules in the surrounding MM part that were beforehand calculated in ESP fits[892] using the ωB97X-D/cc-pVDZ electronic density. This has the major advantage that the electrostatic interaction energy of a given dimer with its environment is treated quantum-mechanically, which is important because the polarization of the electron densities of the organic π-systems by the surrounding charges might be significant.[645] Back-

polarization is naturally not taken into account in an electrostatic embedding scheme. Due to its acceptable accuracy for the interactions between organic π-systems (see Section "Interactions between the π-systems of molecular organic semiconductors"), the AMOEBA force field is employed to calculate all remaining contributions to the interaction energy of the QM dimer with the environment, most notably the van-der-Waals component.

In the subtractive scheme, final energies $E^{QM/MM}$ are calculated from the dimer QM energies $E^{QM}(dimer)$ (which include the electrostatic interaction energies with the environment) and the difference of the force field energies of the total system and the QM system $E^{MM}(total) - E^{MM}(dimer)$ without the otherwise double-counted electrostatic force field interaction energy $E^{MM,el}(total) - E^{MM,el}(dimer)$.

$$E^{QM/MM} = E^{QM}(dimer) + \left(E^{MM}(total) - E^{MM}(dimer) - \left(E^{MM,el}(total) - E^{MM,el}(dimer) \right) \right) \qquad (464)$$

To analyze whether long-range charge-charge and charge-quadrupole are sufficiently converged in the supercells and to keep the calculations computationally feasible, the constructed supercells are subdivided into layers (Figure 104c) that naturally arise from the construction process. Interaction energies between the QM dimer and each individual layer are separately calculated and subsequently added. This comes at the expense of not correctly including three-body interactions, namely polarization and induction. However, the induction and polarization components were found to be negligible, in line with above-discussed results (see Section "Interactions between the π-systems of molecular organic semiconductors"). Furthermore, the layer-by-layer calculations of interaction energies reveal that the interaction energy between the QM dimer and the outermost fullerene/donor layer is always smaller than 0.1 kcal/mol, (Table 29) thus considerably smaller than the accuracy of the method. These results allow for the conclusion that the sizes of the supercells are sufficient to obtain converged charge-charge interactions. It should be noted that these findings contrast with results of Andrienko et al.[28] who concluded that correct charge transport bands cannot be obtained when using a cutoff for charge-quadrupole interactions.

Table 29: Change of the total intermolecular potential energy when the outermost layers – either the third donor layer ("monomer layer 3") or the second fullerene layer ("fullerene layer 2") are taken into account. Please note the abbreviations used for the triphenylamine-based compounds in the following.

Change intermolecular potential energy due to inclusion of additional layers [kcal/mol]		
Molecule	monomer layer 3	fullerene layer 2
anthracene	0.05	0.10
diketopyrrolopyrrole	-0.11	-0.28

DIP	0.04	0.14
dithiophene	0.04	0.26
HB194	0.00	-0.01
MD353	-0.02	-0.10
rubrene	0.01	0.11
squaraine	-0.03	-0.21
TBA „triamine"	0.01	0.00
TAA „triamine-aldehyde"	0.00	-0.02
TAM „triamine-methoxy"	0.00	-0.05

The GDMA analysis of Stone[353] was employed to generate AMOEBA parameters that were used in the QM/MM calculations for all MM molecules and – in ground-state calculations – for the QM part as well. It should be noted that this is somewhat inconsistent with the ESP charges employed to polarize the QM system. Nevertheless, including all multipole moments in the QM calculations was computationally not feasible. It is assumed that the effects of the ESP charges or the multipole moments on the QM system differ little. Due to the adopted subtractive scheme, additional AMOEBA parameters for cationic and excited dimers are required. It is often assumed that interactions between neutrally excited states (contrary to charge-transfer excitations) and the environment are similar to corresponding interactions of the ground state with the environment. To analyze whether this assumption holds, solvent shifts for the ground and the first excited state in different solvents are calculated for all molecules at the ωB97X-D/cc-pVDZ level of theory using the state-specific solvation model by Improta et al.[344,1000] and the perturbative state-specific solvation of Mennucci et al.[1001] Please note that the ground-state energy difference between the gas-phase and solvated monomer is designated as the "solvent shift". Results are shown in Table 30. Aside from a few exceptions, solvent shifts for the ground and the first excited state are almost identical. To further elaborate this aspect, two different parameter sets are generated for HB194, a push-pull dye for which ground-state and excited-state solvent shifts differ (Table 30). One parameter set is the "regular" set of ground-state parameters. The other set is obtained from GDMA analyses separately conducted for the excited-state electron density of each individual dimer. Interaction energies calculated with each parameter set barely differ. Therefore, ground-state force-field parameters can also be employed for excited states, in line with other investigations.[745]

Table 30: Solvent shifts (= energy differences) of ground states (GS) and excited states (ES) when a gas-phase monomer is solvated in DMSO (dimethylsulfoxide).

gas phase DMSO	solvent shift (perturbative, Mennucci[1001])		solvent shift (state-specific, Improta[344,1000])	
Molecule	GS [eV]	ES [eV]	GS [eV]	ES [eV]
anthracene	0.15	0.15	0.15	0.15
DIP	0.30	0.30	0.30	0.29
diketopyrrolopyrrole	0.36	0.34	0.36	0.33
HB194	0.45	0.55	0.46	0.66
MD353	0.61	0.65	0.61	0.63
rubrene	0.26	0.26	0.26	0.27
squaraine	0.56	0.57	0.56	0.57
TBA	0.31	0.35	0.31	0.39
TAA	0.29	0.44	0.32	0.62
TAM	0.31	0.40	0.31	0.58

Table 31: Solvent shifts (= energy differences) of ground states (GS) and cationic states (CS) when a gas-phase monomer is solvated in DMSO (dimethylsulfoxide).

gas phase DMSO	solvent shift (linear response[317])		solvent shift (state-specific, Improta[344,1000])	
Molecule	GS [eV]	CS [eV]	GS [eV]	ECS [eV]
anthracene	0.15	1.75	0.15	0.89
DIP	0.30	1.33	0.30	0.81
diketopyrrolopyrrole	0.36	1.33	0.36	0.71
HB194	0.45	1.79	0.45	1.09
MD353	0.61	1.85	0.61	1.14
rubrene	0.26	1.34	0.26	0.67
squaraine	0.56	1.40	0.56	0.95
TBA	0.32	1.51	0.32	0.83

TAA	0.30	1.78	0.30	1.04
TAM	0.31	1.46	0.31	0.77

In contrast, interactions of a cationic compound with its environment can be expected to deviate considerably from the interactions of the corresponding ground state with the environment. This is also reflected in the state-specific solvent shifts of cationic compounds that largely differ from their ground-state counterparts (Table 31). For comparison, linear-response solvent shifts are listed as well in Table 31. In order to still be able to calculate interaction energies of cationic compounds with the environment, electron densities of all ionized dimers were calculated using ωB97X-D/cc-pVDZ. As the amount of charge delocalization is different for all dimers, GDMA analyses were individually conducted for all cationic dimers. Dimer-specific force field parameters of the cationic states were obtained and subsequently used to calculate QM/MM energies.

Only one interfacial model system was selected among the generated three different morphologies. In all QM/MM calculations, all site energies are referenced to their joint energy minimum, i.e., they are referenced to 0. All force field calculations were performed with the Tinker program package.[899] No cutoff for van-der-Waals or electrostatic interactions was used. Monomer geometries optimized at the ωB97X-D/cc-pVDZ level of theory were superimposed onto the force field geometries. Dynamic disorder is hence not included. ωB97X-D/cc-pVDZ was also used for the computations of ESP charges, polarizabilities, excitation energies, and ionization potentials. Relaxed dipole moments for the molecular ground states were obtained with SCS-MP2/cc-pVTZ[70,703,704,705]. Excited-state dipole moments were computed using SCS-CC2/cc-pVDZ[256,180,705]. All quantum-mechanical DFT calculations were conducted with the Gaussian program package.[718] Turbomole was used for the calculation of molecular properties.[179]

5.10.2 Analyses of Computed QM/MM DOS

Ground-, excited- and cationic-state DOSs of the electrostatically embedded dimers are presented. Although all DOSs were calculated for all molecules, only the computed ground-state DOSs of three representative molecules, a triphenylamine ("triamine-aldehyde" = TAA), a merocyanine (MD353), and a traditional molecular semiconductor (DIP) are shown in Figure 106. It is evident that they have approximately Gaussian shapes, similar to cationic and excited-state DOSs (not shown). The diamonds in Figure 106 correspond to the energy distributions obtained from the QM/MM calculations that are discretized for the representation. Solid lines are Gaussian fits of the discretized distributions.
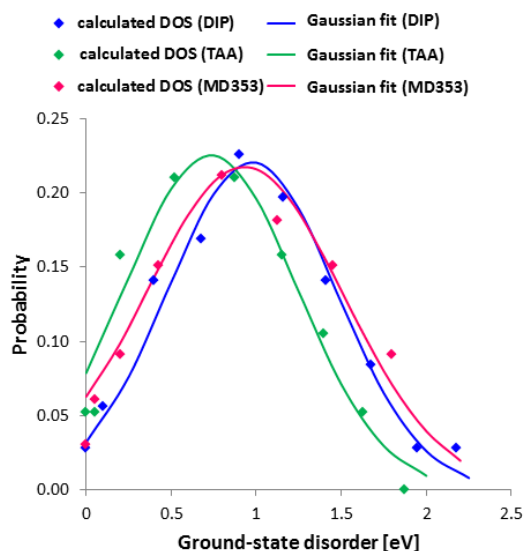
Figure 106: Distribution of QM/MM ground-state energies (squares). Gaussian normal distributions obtained from the mean and the standard deviation of the ground-state energies (solid lines).
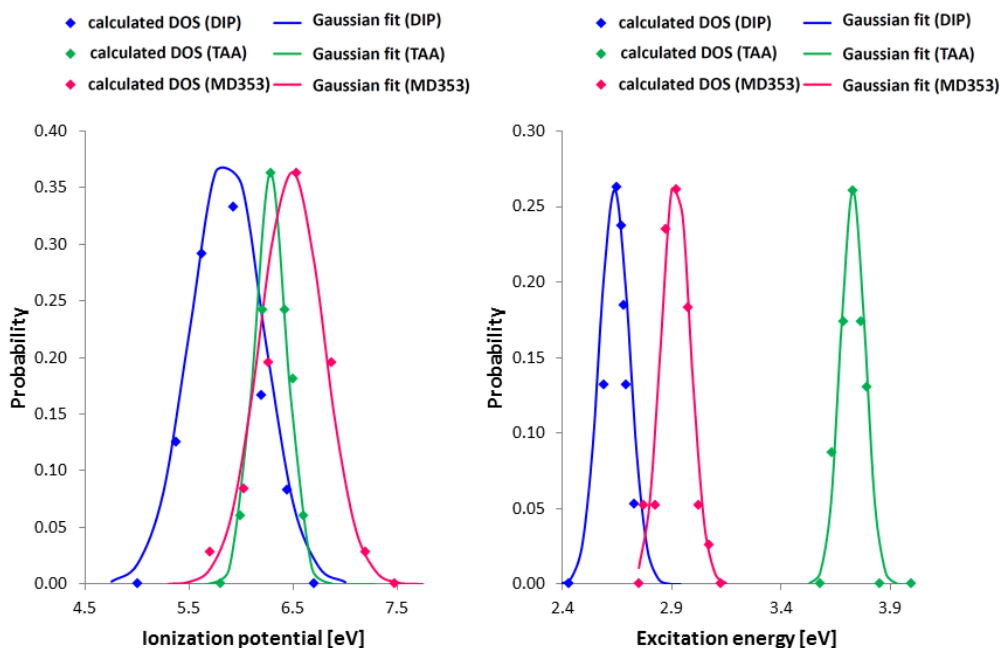
Figure 107: Gaussian distribution of ionization potentials (left) and excitation energies (right). Squares are QM/MM energies, the solid lines correspond to Gaussian fits.

Furthermore, excitonic and polaronic DOSs are calculated, i.e. the distribution of excitation energies and ionization potentials. These distributions of ionization potentials (polaronic states) and excitation energies (excitonic states) are equally Gaussian-shaped (Figure 107), which is to be expected since energy differences between Gaussian distributions are normally distributed as well.

The findings indicate that state energies and their differences are normally distributed even in the presence of an environmental discontinuity such as an organic::organic interface. Therefore, two important conclusions result from the computed DOSs in Figure 106 and Figure 107:

1. As all DOSs have approximately Gaussian shapes, the definition of the disorder parameter σ for the following analysis can be left as is.
2. The profiles are broad so that resulting disorder parameters are large. The latter are in fact on the order of the previously discussed intramolecular reorganization energies ("Benchmarking exciton reorganization energies", "Benchmarking charge reorganization energies"). Transport is therefore certainly also disorder-limited. Understanding and eliminating the origin of this disorder is thus important to improve transport properties.

The effects responsible for the broadening of ground-state, excited-state, and cationic-state energies are discussed next.

5.10.3 Structure-Property Relationships for Energetic Broadening of Ground-State, Excited-State, and Cationic-State Energies

A comparison of the ground-state DOS (Figure 106) with the polaronic and excitonic DOS (Figure 107) clearly shows that the distribution of ground-state energies is significantly broader. Especially packing density fluctuations and resulting variations in the van-der-Waals energies are responsible for the spread in ground-state energies. It was thoroughly discussed above (see Section "Interactions between the π-systems of molecular organic semiconductors") that van-der-Waals energies are extremely distance-dependent compared with their electrostatic counterparts. They thus show stronger variations as soon as the packing density fluctuates. In contrast to the bulk phases, local packing density fluctuations exist particularly in the interfacial region: there are still spatially confined areas with dense molecular packing but grain boundaries, vacancies, and defects accumulate as well. Local packing density fluctuations are illustrated in Figure 108 for two anthracene dimers. Concomitantly, due the different packing, the dimers undergo considerably different interactions with their environment. While the first anthracene dimer is rather stable (left-hand side, Figure 108), the second one (right-hand side, Figure 108) experiences only a much reduced van-der-Waals stabilization – being located just on top of the fullerene layer where the packing is less dense. This dimer is in fact located at the high-energy limit of the DOS.
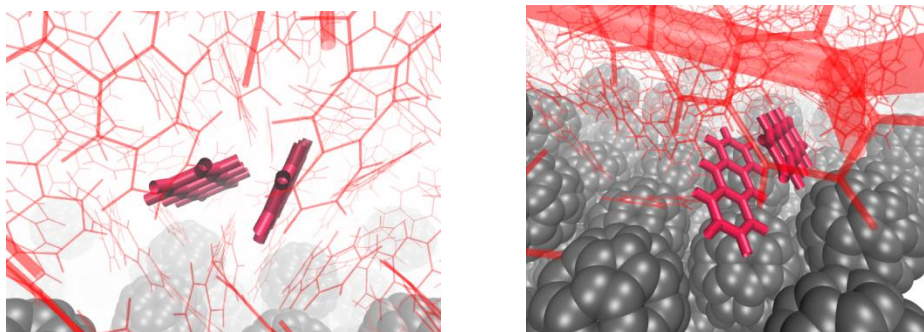
Figure 108: Anthracene dimer stabilized by intermolecular interactions (left-hand side) and a second higher-energy dimer. The intermolecular interaction energy differs by 31 kcal/mol.

Moreover, van-der-Waals interaction energies constitute the main part of total potential intermolecular interaction energies and of the overall site energies as well. To illustrate this, AMOEBA intermolecular interaction energies are decomposed, and corresponding van-der-Waals contributions in percent are given in Figure 109 for potential intermolecular energies of dimers at the DIP::fullerene interface (left panel) and at the HB194::fullerene interface (right panel). The values underline that van-der-Waals interactions contribute approximately 90% to the total interaction energies of ground-state dimers and nearly as much (70% - 80%) to potential intermolecular energies of cationic dimers. Due to this dominance of van-der-Waals interactions (Figure 109), their variations similarly determine variations of total intermolecular potential energies and resulting ground-state energies, producing the considerable amount of disorder σ. Since underlying packing density fluctuations are a distinctly interfacial effect, one can furthermore assume that broad ground-state DOSs are a distinctly interfacial effect as well. In line with this, it has been often pointed out that the less dense packing in the vicinity of organic::organic interfaces profoundly influences the interfacial energy landscapes.[457,26]
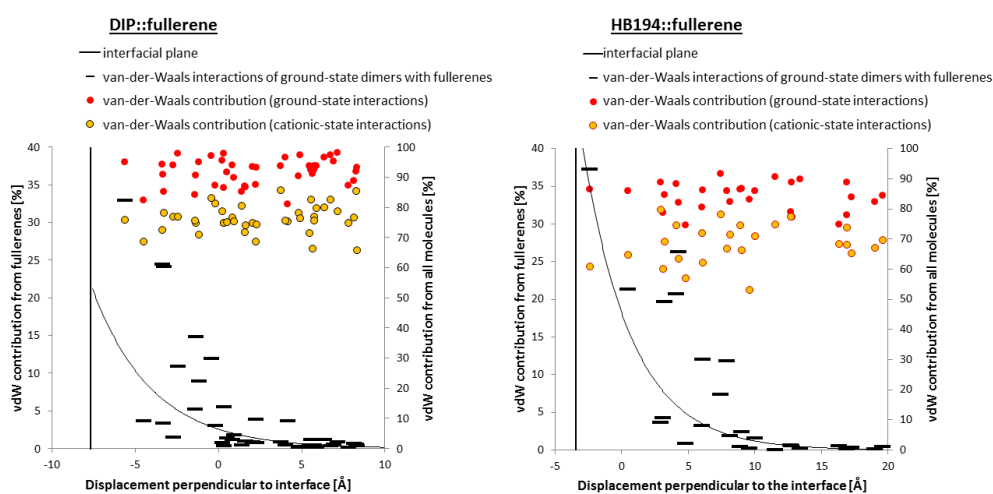
Figure 109: Decomposition of the AMOEBA potential intermolecular energies of dimers along the DIP::fullerene interface (left panel) and the HB194::fullerene interface (right panel). The contribution of the van-der-Waals energy is indicated on the right axis while the fullerene contribution is additionally given on the left axis. The

decline of the influence of the fullerene phase on the site energies is visualized by an exponential fit that serves as a guide to the eye.
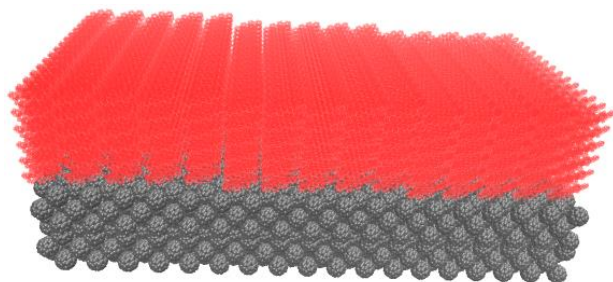
Figure 110: Crystalline supercell for the DIP::fullerene interface. The underlying crystalline interfacial model system is created by aligning a number of crystalline DIP and fullerene unit cells. This number is calculated as the least common multiple of the crystallographic axes of the two crystal structures.
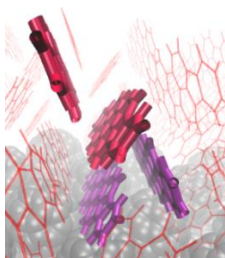
Figure 111: Two different DIP dimers (red, purple) in the crystalline supercell of the DIP::fullerene system (Figure 108). The potential intermolecular energy of the red dimer is 41 kcal/mol lower than the one of the purple dimer. This results from the position of the purple dimer at the interface.

It is worth emphasizing that the ground-state energy broadening due to variations of the van-der-Waals interactions is not directly related to the existence of disorder in the vicinity of the organic::organic interfaces. This becomes evident when crystalline supercells are created, simply by aligning crystalline slabs of fullerene C_{60} and the p-type semiconductor, and used instead of disordered ones. This is illustrated in Figure 110, which shows a crystalline supercell of the DIP::fullerene system. Similar to the disordered supercells (Figure 105), intermolecular interaction energies are calculated for all DIP dimers. In pristine crystals, all DIP dimers have exactly equal intermolecular potential energies. Yet, as soon as the interface is created, albeit without any additional disorder, intermolecular energies of the DIP dimers differ. Figure 111 presents two DIP dimers with potential intermolecular interaction energies that differ by 41 kcal/mol. The pronounced difference in intermolecular interaction energies arises again primarily from the position of the purple dimer directly on top of the fullerene layer, i.e. at the surface of the crystalline DIP layer. At this position, i.e., at the edge of the DIP layer, the dimer undergoes fewer stabilizing van-der-Waals interactions with its environment. Although it interacts with the fullerenes, intermolecular distances are not as optimal as those to other DIP molecules in the crystal structure. As a consequence, the intermolecular potential energy of the purple dimer rises compared with dimers occupying a more central position within the DIP layer (like the red dimer, Figure 111).

The energetic disorder of the excited states is considered next. It differs from the ground-state disorder due to the influence of electrostatics on the excitation energies. Disorder parameters σ calculated for the QM/MM excited dimer states are correlated in Figure 112 with corresponding ground-state values for σ (upper panel). The large coefficient of determination (R^2: 88%) underlines the relationship between the two disorder parameters. Similar to the ground-state disorder, the large excited-state disorder arises from local variations in the van-der-Waals interaction energies. This follows also from the fact that the same AMOEBA van-der-Waals parameters were used in ground- and excited-state calculations. It is nevertheless usually assumed that empirical parameterizations for van-der-Waals interactions are rather state-independent,[1002] and this assumption was shown to be quite reasonable at least for valence excited states.[1003]
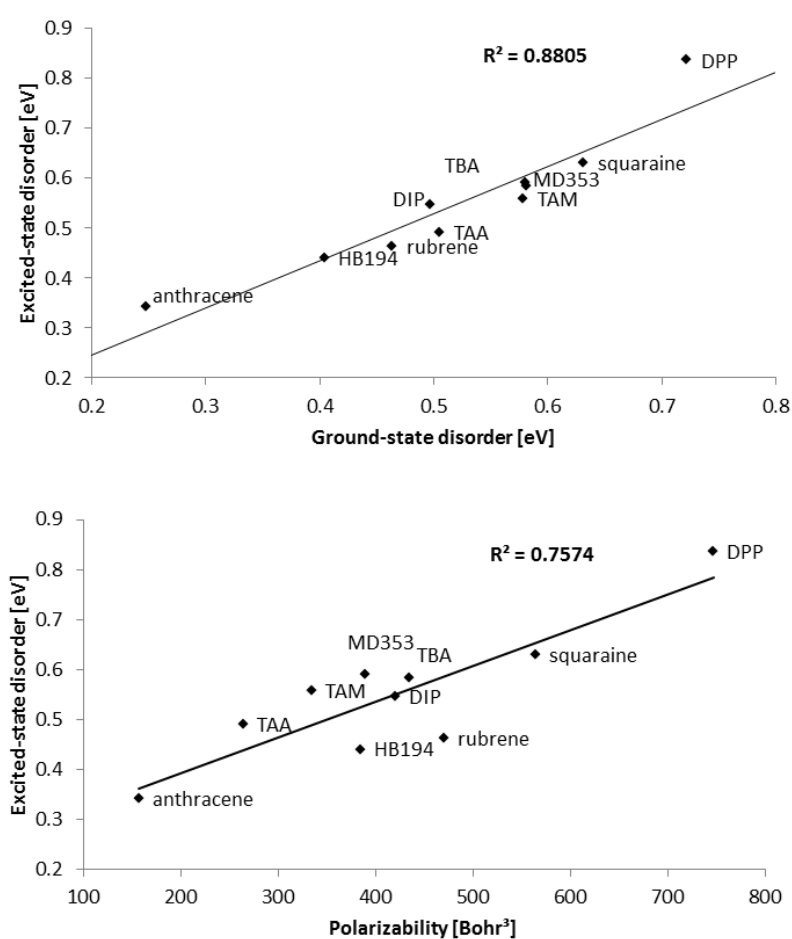
Figure 112: Upper panel: correlation of disorder parameters σ for excited- and ground-state DOSs. Lower panel: dependence of the excited-state disorder parameters on the molecular polarizability.

The dependence of the ground-state and excited-state disorder of dimer states in the vicinity of organic::organic interfaces on variations of the van-der-Waals interactions can be put on a more quantitative basis. It is well-known from London's theory of dispersion forces[1004] that stabilizing van-der-Waals interactions (and with this also their variations) are related to the molecular polarizability. Hence as could be expected, the ground-state disorder (*not shown*) and the excited-state disorder

(lower panel, Figure 112) correlate with the molecular polarizability. Molecular polarizabilities were calculated with ωB97X-D/cc-pVDZ. One common assumption is that the molecular polarizability depends on the number of electrons and thus on the system size.[1005] In line with this assumption, large molecules like the diketopyrrolopyrrole and the squaraine in particular possess very disordered ground- and excited-state DOSs (Figure 112). From a molecular perspective this seems reasonable because a large molecule surrounded by a diffuse electron density has a larger probability of feeling local packing density variations at the interfaces and responds more strongly than smaller molecules.
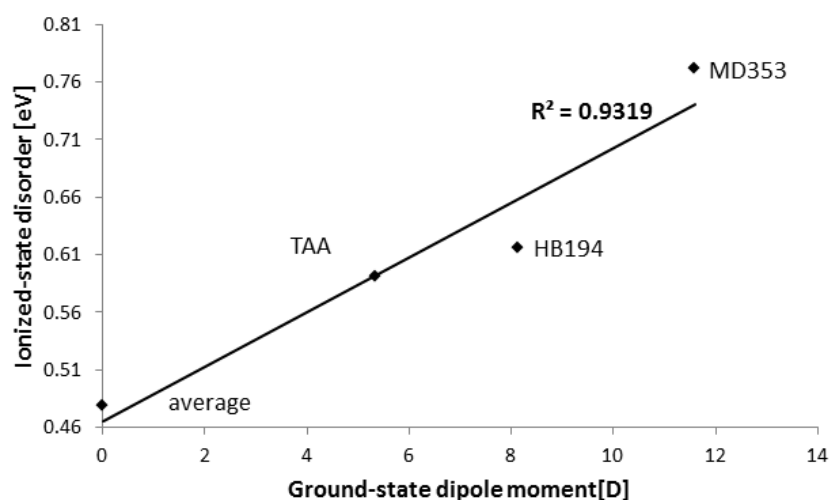
Figure 113: Correlation of the disorder parameters σ of the cationic DOSs with the ground-state dipole moment.

Due to the considerable van-der-Waals contribution to the total intermolecular potential energies of cationic dimers (Figure 109), cationic DOSs naturally also depend on molecular polarizabilities, much alike to ground states and excited states (Figure 112). However, the net charge of cationic dimers additionally increases the importance of electrostatic interactions with the environment at least for some interface systems. In line with this, Figure 113 establishes a clear-cut relationship (R^2: 93%) between the width of the cationic DOS and the size of the molecular ground-state dipole moments present in the environment, the MM part. Only molecules with significant ground-state dipole moments are included in the analysis, whereas all other molecules are averaged. Evidently, the larger the dipole moments in the environment, the larger the disorder of cationic energies, this is, the broader the cationic DOS (Figure 113) and the larger the parameter σ. This agrees nicely with the findings of Bässler and coworkers[548] who argued that environmental dipole moments engender varying local electric fields that affect ground and excited states only to a small extent, but significantly influence cationic states. Furthermore, Bässler et al.[548] similarly concluded from different experiments that more polarizable molecules/polymers also increase the disorder of the DOS.

After this discussion of the DOS of dimer ground, excited, and cationic states, ionization potentials and excitation energies are addressed in the next subsection.

5.10.4 Analysis of The Disorder of Excitation Energies and Ionization Potentials

For exciton and charge transport, the disorders of excitation energies and ionization potentials are decisive.[552] Although intramolecular relaxation (local electron-phonon coupling) processes are disregarded in this QM/MM investigation, an excitation (hole) accompanied by the surrounding lattice polarization can be still considered as an exciton (a polaron). It seems thus consistent to use the notions "excitation energies" and "(vertical) excitons" as well as "ionization potentials" and "(vertical) polarons" interchangeably (see also Table 23). Doing so highlights the intimate relationship between exciton/polaron transport and the disorder of the system, i.e., the fact that disorder considerably deteriorates transport efficiencies.[425] Furthermore, as comprehensively discussed in the previous section ("Kinetics of the exciton dissociation and charge separation processes in the vicinity of the organic::organic interfaces"), efficient exciton and charge transport processes are particularly important in the interfacial region because only then exciton dissociation within the limited exciton lifetime and charge separation can occur.[452] Table 32 shows the disorder parameters σ for ionization potentials and excitation energies in the donor phase in the vicinity of the interface with fullerene C_{60}.[bbbb] At first view, it might be surprising that these disorder parameters are considerably smaller than those found for ground-state, excited-state, and cationic-state DOSs (Figure 112, Figure 113). However, this results from the above-discussed effects that (1) the disorder parameters σ of ground-state, excited-state, and cationic-state DOSs are dominated by variations of van-der-Waals interactions, and that (2) these van-der-Waals variations are state-independent. Consequently, they cancel for state-energy differences. This implies that depending on the position of a given dimer, all of its states are either equally stabilized or equally destabilized by van-der-Waals interactions with the surrounding. Hence, the disorder of exciton and polaron transport levels (of excitation energies and ionization potentials) originates from effects other than local density variations and varying van-der-Waals energies. This result is important because in numerous experimental investigations, percolation pathways were shown to significantly improve OSC charge separation efficiencies[504,1006] although they necessarily introduce considerable differences in the local packing density. This is thus necessarily accompanied by variations of van-der-Waals energies and significant disorder parameters σ for ground, excited, and cationic states.

[bbbb] It should be kept in mind that the disorder parameters σ were calculated from the energies of all dimers contained in the original interfacial model system, i.e., the dimensions of the original model system defines the "vicinity of the interface".

An average disorder σ(EE) of 53 meV is found for excitation energies (Table 32) while ionization potentials spread more with a mean disorder parameter σ(IP) of 227 meV. Both parameters σ(EE) and σ(IP) reach maximal values at the HB194::fullerene interface, with 169 meV for the excitonic DOS and 656 meV for the polaronic DOS. These maximum values agree well with calculated disorder parameters of 660 meV for the hole DOS in polar polymers.[552] However, most experimentally determined values in semiconducting bulk phases are usually in the order of 50-150 meV,[548] which implies that predicted disorder parameters for organic::organic interfaces (Table 32) are on the high-end side of the experimental range. On the one hand, polar push-pull molecules like HB194, MD353, and TAM are certainly to some extent responsible for the rather high predicted disorder parameters but large values are on the other hand also obtained for traditional molecular semiconductors[640] like DIP (σ(IP) = 348 meV). This suggests that especially the disorder σ of polaron transport levels can be considerable in the vicinity of organic::organic interfaces, in line with common assumptions.[26] As a number of recent investigations highlight the importance of long-range order and interfacial charge delocalization for efficient charge generation,[452,596,591] the findings indicate that the potentially significant polaronic disorder at organic::organic interfaces can be an efficiency-limiting parameter.

Table 32: Disorder parameters σ calculated for excitation energies EE (exciton transport levels) and ionization potentials IP (polaron transport levels) in the vicinity of the interfaces composed of fullerene C_{60} and a p-type molecular semiconductor.

molecule	σ(EE) [meV]	σ(IP) [meV]
anthracene	49	129
rubrene	2	82
DIP	53	348
HB194	169	656
MD353	108	306
TBA	9	82
TAA	56	155
TAM	61	264
diketopyrrolopyrrole	17	178
squaraine	7	71
average	53	227

Figure 114 shows the correlation of σ(EE) with σ(IP). Molecules are subdivided into structurally similar groups (Figure 5) to reveal possible structure-property relationships in the vicinity of the organic::organic interfaces. It is again evident that the polaronic disorder is considerably larger than the excitonic disorder: σ(IP) is roughly four times larger than σ(EE). It should be furthermore noted that in contrast to findings about the disorder of ground, excited, and cationic states, excitonic and polaronic disorder parameters for highly polarizable molecules like the squaraine or the diketopyrrolopyrrole are comparably small (Figure 114).

QM/MM energies can be decomposed into the energy of the QM part and its interaction energy with the MM environment. In electrostatic embedding, electrostatic interactions are already included in the QM energy. Comparing this QM energy to the QM energy calculated for the same QM system, i.e., for the same dimer, yet in the gas-phase, delivers the contribution of the electrostatic energy to the final QM/MM energy. Moreover, gas-phase QM energies provide an estimate of how much energies can already vary solely due to the variations in delocalization and intermolecular dimer interactions. To gain further insight, the disorder of excitonic/polaronic QM/MM energies (Figure 114) is decomposed into these contributions (Figure 115):

- The disorder already present in the excitonic/polaronic DOS of gas-phase dimers, which results from different intermolecular interactions and a dimers-dependent exciton/polaron delocalization, is indicated as the "QM disorder (delocalization, dimer interaction)" in Figure 115.

- Additional disorder is created if the dimer is placed in a point-charge environment, which is denoted as the "electrostatic contribution" in Figure 115.

- Including the interactions with the MM part yields the overall disorder, shown as the total "IP disorder" or "EE disorder" in Figure 115. As identical force-field parameters are used for dimer ground and excited states, the QM/MM disorder does not differ from the electrostatic disorder for excitonic states.

- The excitonic disorder is addressed first (right-hand side, Figure 115). To elucidate structure-property relationships, the molecules are again arranged into molecular subgroups (see also Figure 114). For the majority of molecules, the total amount of excitonic disorder (grey bars, Figure 115) basically corresponds to the excitonic disorder already found in gas-phase dimers (ruby bars, Figure 115). Values are almost equal (anthracene: 49 meV//54 meV; rubrene: 2 meV//2meV; DIP: 53 meV//49 meV; MD353: 108 meV//106 meV; TBA: 9 meV/7meV; DPP: 17 meV//16 meV; squaraine: 7 meV//10 meV). This implies that (1) electrostatics does not significantly contribute to excitonic disorder and that (2) exciton delocalization is the main source of excitonic disorder in most systems. The degree of exciton delocalization depends

369

on the precise details of the dimer conformation.[166] It can vary significantly, thus causing a potentially broad distribution of excitation energies (see section "Energetics of the exciton dissociation and charge separation processes in the vicinity of the organic::organic interfaces").
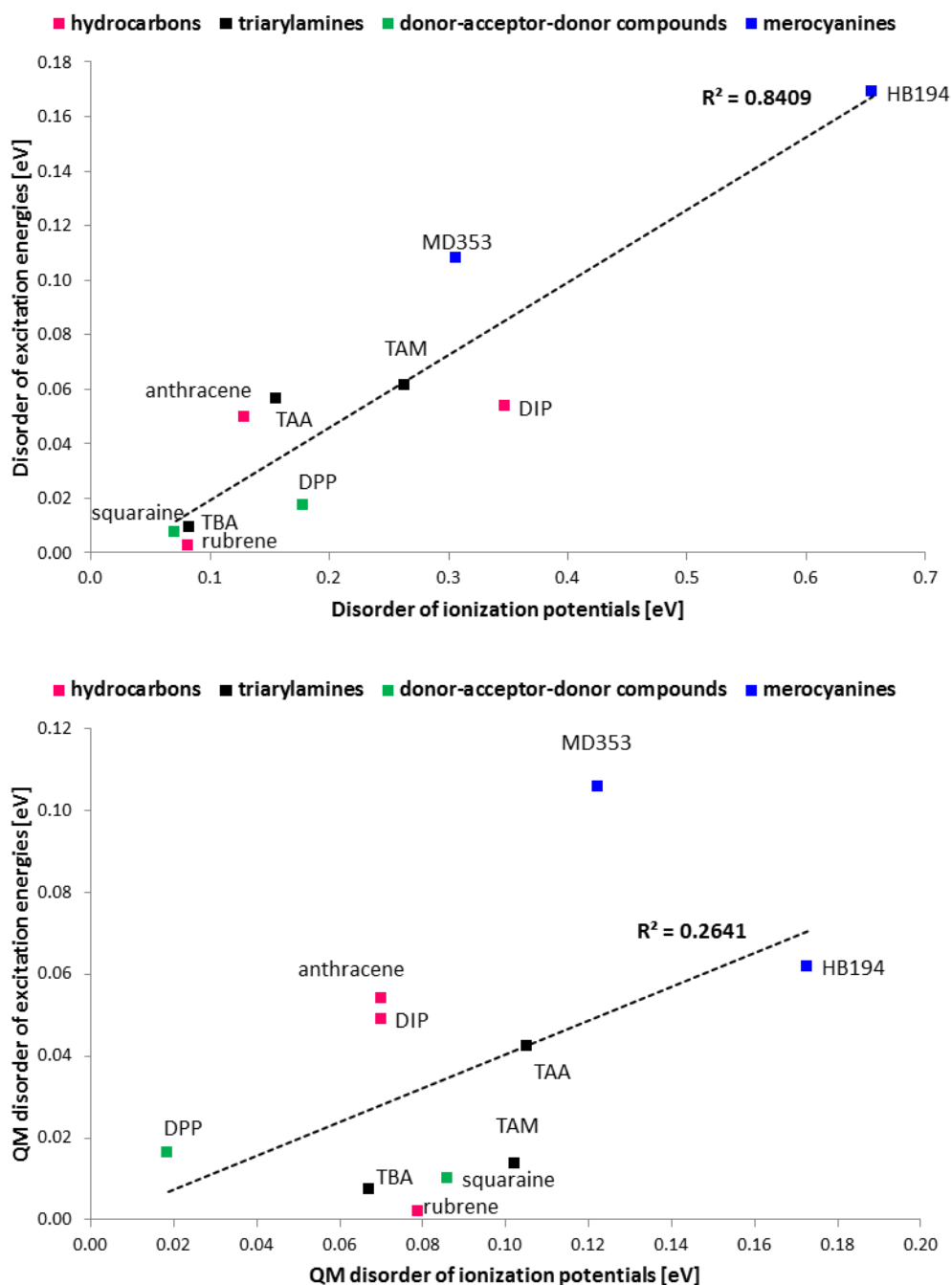
Figure 114: Upper panel: Correlation of the disorder of ionization potentials σ(IP) with the disorder of excitation energies σ(EE). Lower panel: Correlation of the disorder of ionization potentials and excitation energies calculated for gas-phase dimers. Their energetic distributions result only from differences in delocalization and intermolecular interactions.
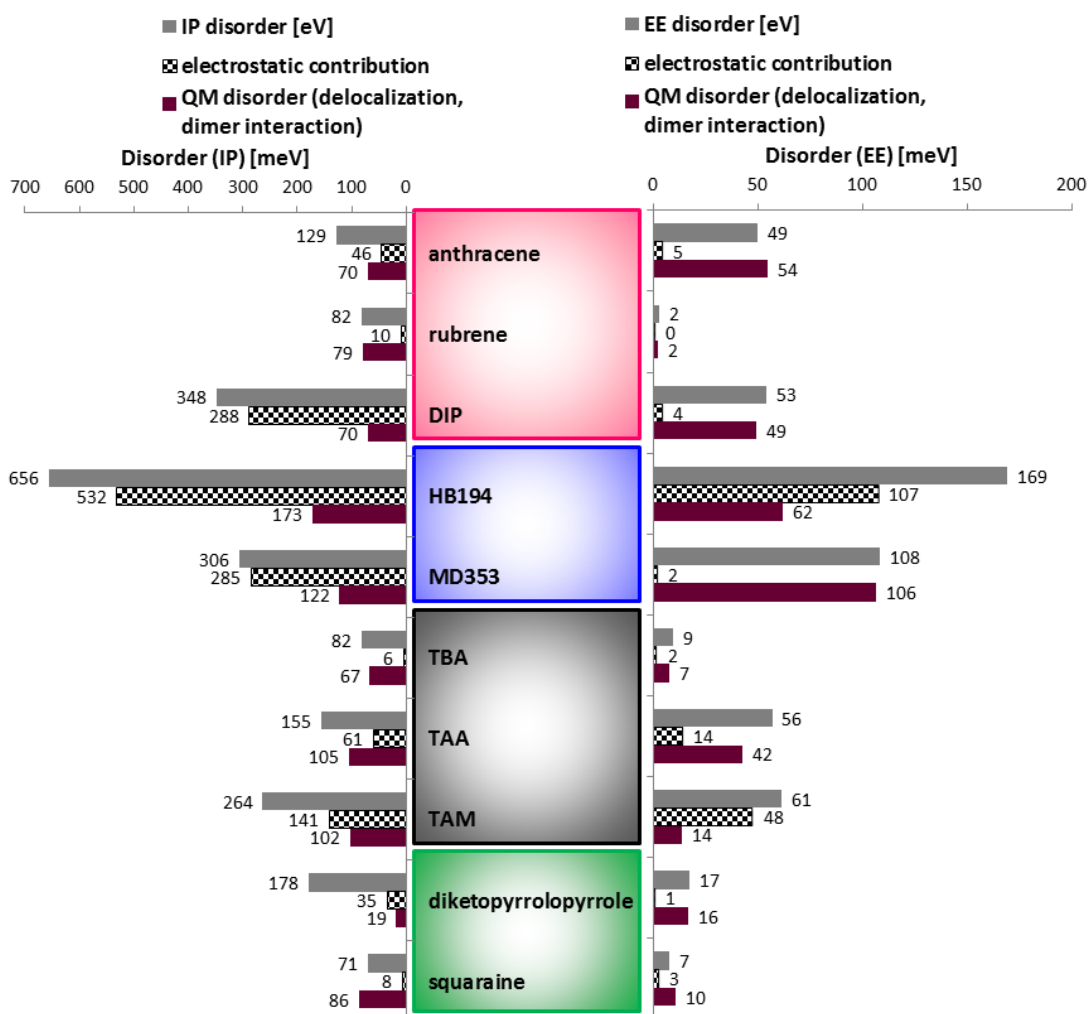
Figure 115: Analysis of the physical origin of the disorder of ionization potentials σ(IP) and of excitation energies σ(EE).

In contrast, electrostatics produces a noticeable increase of the excitonic disorder for three molecules, namely HB194 and the substituted triphenylamines TAA and TBA (checkered bars, Figure 115, HB194: 107 meV; TAA: 14 meV; TAM: 48 meV). To understand this result, Table 33 lists relaxed ground- and excited-state dipole moments of the three molecules and additionally of MD353.

Table 33: Ground- and excited-state dipole moments calculated as relaxed properties on the SCS-CC2[256,180]/cc-pVDZ[705] level of theory. The corresponding values for MD353 are additionally given. Please note that its excited-state dipole moment is smaller than the ground-state one.

	ground-state dipole moment [D]	excited-state dipole moment [D]
HB194	8.32	13.75
TAA	5.37	16.54
TAM	0.50	9.68
MD353	*11.56*	*6.66*

Obviously, the molecular dipole moments of HB194, TAA, and TAM significantly increase upon electronic excitation (Table 33). This behavior is frequently observed for molecules featuring a low-lying intramolecular charge-transfer excitation, and it is reflected in the comparably high solvent shifts of precisely those three molecules as well (Table 30, especially for the state-specific solvation by Improta et al.[344]). Hence the change of the molecular dipole moment upon electronic excitation explains why excited dimers of HB194, TAA, and TAM interact differently with their environment compared with the corresponding ground states. This accounts for the additional electrostatic contribution to excitonic disorder. Albeit being also a push-pull dye, the excitonic DOS of MD353 is not affected by electrostatics, potentially because electronic excitation induces a dipole moment decrease. In a similar way, corresponding solvent shifts of excitation energies are small for MD353 (Table 30). In contrast to these molecules and as addressed above, electronic excitation does not induce pronounced density rearrangements in most organic compounds, which results in a limited disorder contribution of electrostatics (Figure 115).

Contrary to this observation on excitonic disorder, electrostatics leads to a quite significant additional amount of polaronic disorder (Figure 115, left-hand panel) at most interfaces, especially at the interface of DIP, HB194, MD353, TAA, TAM, and of DPP with fullerene C_{60}. This fully agrees with the expectation that as soon as a dimer with a net charge forms, the structurally disordered amorphous thin film gives rise to locally varying electrostatic interactions that broaden the distribution of polaron transport levels. No direct correlation between the molecular structure and the influence of electrostatics is found. However, in general, the disorder of the polaronic transport levels is larger for polar molecules (HB194, MD353, TAA, TAM) compared with their apolar counterparts. This is well in line with findings of Bässler.[25]

Nevertheless, apart from electrostatics, a varying degree of polaron delocalization (ruby bars, Figure 115) plays a role in the formation of the overall polaronic disorder as well. Its average contribution amounts to 90 meV. The lower panel in Figure 114 correlates the contribution of exciton delocalization to the excitonic disorder σ(EE) with the amount of polaronic disorder σ(IP) caused by variations of polaron delocalization. Interestingly, the correlation is poor (R^2: 26%). Consequently, the *same* gas-phase dimers result in *different* disorder parameters for excitons and charges. It seems thus possible that, leaving aside electrostatic effects, a given morphology results in a rather ordered excitonic DOS and a considerably disordered polaronic DOS and *vice versa*. To further elaborate this aspect, exciton and polaron transport levels are calculated for 20 arbitrarily chosen gas-phase dimers of MD353 and DIP located in the vicinity of the interfaces (Figure 116). It becomes evident from the results that variations of excitation energies/exciton transport levels do not necessarily parallel corresponding variations of ionization potentials/polaronic transport levels.
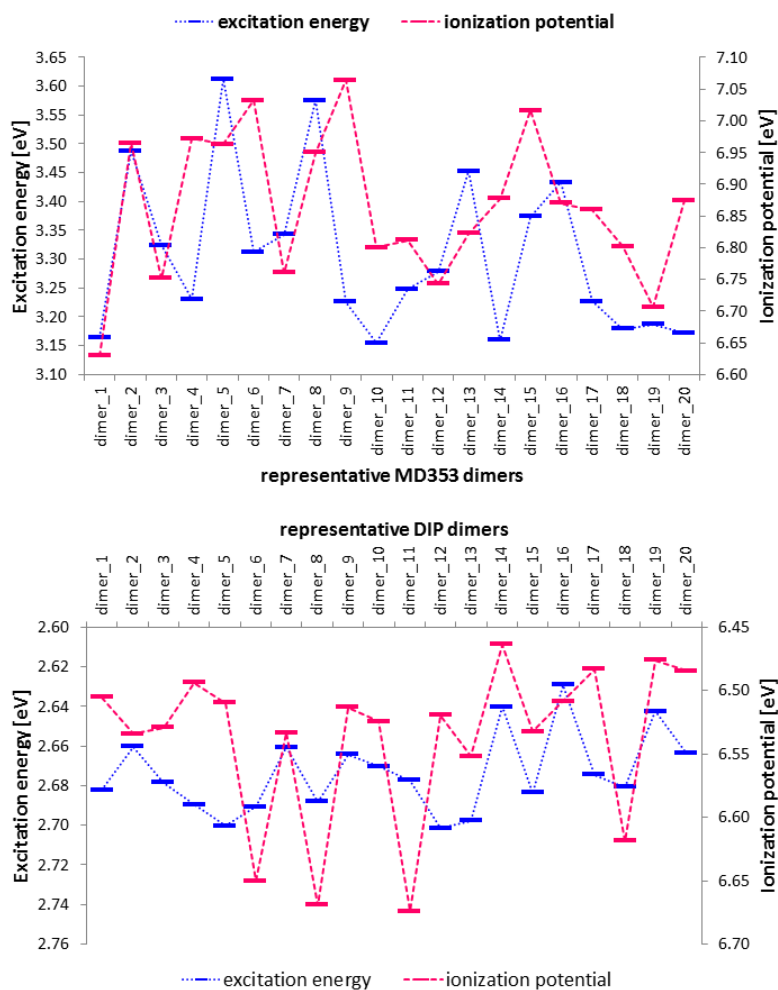
Figure 116: Exciton transport levels (excitation energies, blue bars) and polaron transport levels (ionization potentials, pink bars) for 20 randomly selected gas-phase dimers of MD353 (upper panel) and DIP (lower panel).

Yet, these findings (Figure 116) can be readily understood in terms of the different underlying coupling mechanisms between exciton/polarons that determine the amount of exciton/polaron delocalization. Charge transport couplings[855] primarily depend on the overlap between the relevant orbitals (i.e., either the HOMOs or the LUMOs).[1007] In contrast, the long-range component of singlet excitation energy coupling corresponds essentially to a dipole-dipole interaction between the transition dipole moments.[166] Evidently, a given dimer arrangement may allow for large charge transport couplings due to a significant orbital overlap while simultaneously disabling exciton coupling by impairing the underlying dipole-dipole interaction. The excitation energy/exciton transport levels deviate for such a dimer due to the small coupling only little from the monomer value. In contrast, the ionization potential/polaron transport levels considerably split. Naturally, the inverse situation is also possible. Figure 116 contains numerous examples. Furthermore, while the two energy intervals covered by excitonic and polaronic states are very similar at the MD353::fullerene interface (~ 0.5 eV), they considerably differ for DIP (~ 0.1 eV for excitonic states, ~ 0.25 eV for polaronic states). This implies that for some reason, at the DIP::fullerene interface, DIP conformations that result in energetically

373

broad polaron transport levels and narrower exciton transport states are especially frequent. Otherwise stated, existing DIP conformations at the interface allow for larger variations of the couplings and the resulting delocalization of polarons compared with excitons. This results in more disordered polaronic transport levels.

It is well-known that the disorder parameter σ for transport in disordered organic semiconductors depends on the morphology.[548,552] However, the presented results in Figure 114 and Figure 116 suggest that a further specification is required as the disorders of excitonic and polaronic states differ for the same morphology. Nevertheless, it should be kept in mind that the dominant electrostatic disorder contribution dampens the impact of delocalization effects on the final polaronic disorder to a certain extent. Therefore, the effect is less obvious for overall disorder parameters.

To summarize the results on static disorder from the QM/MM approach, it was found that ground, excited, and cationic states indeed possess broad Gaussian-shaped densities of states (DOSs) and that the distribution of the relevant transport levels, i.e. of ionization potentials and excitation energies, are also broad (i.e., on the order of the intramolecular reorganization energy) and of similar Gaussian shapes.[548] The energetic distributions of all states and transport levels can thus be described in terms of the Gaussian disorder parameter σ. Variations in van-der-Waals interaction energies resulting from differences in the local packing density account for the spread of ground-, excited-, and cationic-state energies. Molecular polarity is especially important for cationic-state energies, and also influences polaronic transport levels that are consistently more disordered in thin films composed of polar semiconductors. Excitonic disorder is dominated by delocalization phenomena, which are also significant for the disorder of polaronic states. Due to the different underlying coupling mechanisms, polaron and exciton delocalization might differ for the same morphology. Expectedly, electrostatics delivers the dominant contribution to the overall polaronic disorder.

From a device perspective, the presented results emphasize especially the importance of specifically optimizing charge transport in the interfacial region because the polaronic DOS can be subject to a significant amount of disorder, which could reduce the charge generation efficiency. Nevertheless, very well-defined structure-property relationships in terms of individual molecular properties could not be identified. The final excitonic and polaronic disorder parameters σ seem to result rather from the combined effects of molecular, intermolecular, and aggregate properties. They are thus highly specific for a given donor-acceptor combination and morphology.

6 Conclusion

Describing the light-to-energy conversion in OSCs requires a multiscale understanding of the involved optoelectronic processes, i.e., an understanding from the molecular, intermolecular, and aggregate perspective.[27] This thesis presents such a multiscale description to provide insight into the processes in the vicinity of the organic::organic interface, which are crucial for the overall performance of OSCs. Light absorption, exciton diffusion, photoinduced charge transfer at the donor-acceptor interface, and charge separation are included. In order to establish structure-property relationships, a variety of different molecular p-type semiconductors are combined at the organic donor-acceptor heterojunction with fullerene C_{60}, one of the most common acceptors in OSCs. Starting with a comprehensive analysis of the accuracy of diverse *ab initio*, DFT, and semiempiric methods for the properties of the individual molecules, the intermolecular, and aggregate/device stage are subsequently addressed. At all stages, both methodological concepts and physical aspects in OSCs are discussed to extend the microscopic understanding of the charge generation processes.

The molecular perspective: ground-, excited- and charged-state description

From the molecular perspective, the light-to-energy conversion is described in terms of individual molecules undergoing light absorption and charge transfer. Intramolecular relaxation processes need to be taken into account, and electronically excited and charged states of the molecules are involved.[19] Suitable methods are required that accurately predict the complex electronic structure of these molecular states and relaxation processes.

Using ground-state geometries optimized at the SCS-MP2/cc-pVTZ level of theory as the reference, a comprehensive benchmark of **molecular ground-state geometries** obtained with diverse DFT, *ab initio*, and semiempiric methods was conducted. To identify methods that are both reliable and efficient, cc-pVDZ basis sets were employed. In contrast to most literature investigations, the evaluation of the quality of the geometries was based on a two-fold criterion. RMSD values were used on the one hand, while MAE values of important geometric parameters such as torsional angles or bond length alternations were employed on the other hand. It was shown that especially long-range corrected functionals, in particular ωB97X-D, predict very accurate ground-state geometries. The good performance of long-range corrected functionals was found to result especially from their reduced basis set sensitivity compared with high-level *ab initio* methods and from their capability to correctly treat different electron correlation regimes, in contrast to simpler DFT functionals or semiempiric methods. In fact, although all of the herein employed molecular semiconductors feature extended π-systems, the computational investigation of their electronic ground-state density revealed that the extent of ground-state electron delocalization, particularly the importance of long- and intermediate-range electron correlation, still deviates considerably among the molecular semiconductors. This result

explains the observed unprecedented importance of the long-range correction for accurate electronic ground-state geometries.[702]

Singlet excitation energies obtained with a variety of *ab initio*, first principle, and semiempiric methods were evaluated with respect to MS-CASPT2 reference values. To keep the calculations of the reference values also for large molecules computationally feasible, a composite approach based on MS-CASPT2 calculations with smaller model systems and a subsequent correction for substituent effects was proposed. The benchmark results led to the conclusion that similar to the ground-state delocalization, the charge-transfer character of the (always bright) first excited state varies significantly among the molecular semiconductors. This has important implications for its computational description. While *ab initio* methods always deliver quite accurate values, the performance of DFT functionals depends critically on their amount of exact exchange. Therefore, long-range corrected functionals like LC-BLYP or LC-ωPBE are required in some cases, whereas hybrid functionals like SOGGA11X or even B3LYP are sufficient in others. Very pronounced performance differences were observed for semiempiric methods, a fact largely disregarded in the current literature. In fact, compared with AM1, PM3, and the OMx methods, ZINDO yielded excitation energies of DFT-like quality at an almost negligible computational cost. In average, it was demonstrated that ωB97X-D and CAM-B3LYP deliver the most accurate excitation energies, especially if higher-lying excited states of the molecules including some full charge-transfer states are taken into account in the evaluation.[702]

In contrast to singlet excited states, the energetic positions of **triplet excitations** are not predominantly influenced by their partial charge-transfer character. A decisive role is rather ascribed to the correct computation of the differential correlation between the triplet excited states and the ground state. It was discussed that this special significance of correlation for accurate triplet excitation energies leads to different errors of DFT functionals containing a comparable amount of exact exchange. It was furthermore demonstrated that DFT triplet excitation energies are usually underestimated, especially within the standard adiabatic linear-response TD-DFT treatment (also due to triplet instabilities). Both the Δ-SCF method and the Tamm-Dancoff approximation were shown to be more accurate alternatives although they tend to provide too low excitation energies as well. Moreover, in the Δ-SCF or the Tamm-Dancoff framework, either hybrid functionals with a significant amount of exact exchange or long-range corrected functionals performed well. However, general guidelines for the computation of accurate triplet excitation energies with DFT are not as clearcut as those for singlet excited states. In contrast, all correlated *ab initio* methods yielded quite accurate triplet excitation energies, potentially because, as commonly outlined, they accurately cover differential correlation. The possibility to calculate both singlet and triplet excitation energies with several DFT schemes (Δ-SCF, TDA, standard TD-DFT) leads to a number of different protocols (for instance TD-DFT singlets and Δ-SCF triplets) when

calculating **singlet-triplet gaps**, i.e., the S_1-T_1 difference, to identify promising singlet fission candidates. The first comprehensive evaluation of these protocols was presented, including an approach to obtain very accurate singlet-triplet gaps with DFT functionals where the amount of exact exchange and local correlation had been fitted beforehand to a set of reference data.[758]

Since Marcus hopping rates depend exponentially on molecular reorganization energies, methods are needed that predict **exciton and charge reorganization energies** to a very high degree of precision. Alike to triplet excitations, somewhat unsystematic performances of different DFT functionals were found for exciton and charge reorganization energies. A particular challenge in the benchmark of **charge reorganization energies** consists in the choice of the reference method, which could explain why no benchmark investigations exist in the literature. In this thesis, a combination of high-level IP-EOM-CCSD single-point calculations and geometries optimized with IP-tuned functionals was proposed to obtain benchmark values for charge reorganization energies. It was revealed that charge reorganization energies, similar to singlet excitation energies, are very sensitive to the amount of exact exchange included in a functional. This suggests that the self-interaction error of DFT functionals influences the description of intramolecular relaxation processes induced by ionization. Consistently, only long-range corrected functionals provided charge reorganization energies of acceptable accuracy. Owing to the well-known excessive charge smearing of pure functionals and hybrids, significantly underestimated charge reorganization energies were obtained with these types of functionals.[854] Using SCS-CC2/cc-pVDZ reference values, **exciton reorganization energies** were furthermore analyzed because corresponding investigations are also missing in the literature. The analysis particularly highlighted the accuracy limits of long-range corrected functionals. Indeed, while these functionals still performed best, they were not always reliable in terms of excited-state structures.

The intermolecular perspective: intermolecular interactions between the π-systems of organic semiconductors

From the intermolecular perspective, the precise details of the conformations between the molecular semiconductors, i.e., their relative orientations with respect to each other, determine coupling pathways as well as underlying excitonic and polaronic transport energies. For a rationally guided device design, it is desirable (1) to understand which physical effects lead to the formation of distinct dimer conformations and (2) to have tools at hand to model them. While a plethora of computational investigations exist that discuss intermolecular interactions in general and/or propose approaches to model them, no analysis specifically dedicated to molecular semiconductors has been conducted. By means of SAPT and LMO-EDA calculations, it could be shown that although dispersion contributes most to intermolecular binding energies, it does not specifically favor distinct dimer conformations. In contrast, spatially constrained **short-range repulsion** forces were found to determine the details of

intermolecular potentials between molecular organic semiconductors irrespective of the exact nature of the semiconductors. These short-range repulsion forces account for the preferential existence of some dimer conformations while simultaneously inhibiting the occurrence of others. Many DFT-D scans using different intermolecular coordinates of stacked homodimers composed of diverse semiconducting molecules were presented in support of this interpretation. While particularly the exchange-repulsion constitutes the short-range repulsion, the latter can still be folded into electrostatic **quadrupole-quadrupole interactions**. Alternatively, a number of **empirical van-der-Waals potentials** with beforehand generated parameters reproduced the intermolecular potentials quite accurately.[875] The similarity of the results obtained with these conceptually different modeling approaches has not been discussed in detail in the literature.

The aggregate/device perspective: energetics and kinetics of the charge generation process

From the aggregate or device perspective, the charge generation at organic::organic interfaces in OSCs can be understood only from the *combination* of energetic and kinetic effects. Suitable atomistic model systems of the organic::organic interfaces are a prerequisite. In this thesis, an *in silico* MM procedure was developed to generate such model systems in a number of successive MD steps. In order to analyze the energetic and kinetic effects based on these interfacial model systems, a three-fold approach was chosen. The energetics in the vicinity of organic::organic interfaces was analyzed by means of dimers that are embedded into a polarizable continuum environment with additional local electric fields, i.e., the dimer method[745] was adapted to the interfacial region.[638] A model of the transport processes in the vicinity of the interface based on KMC simulations and Marcus hopping rates without empirical parameters was proposed and implemented to investigate the kinetics of the optoelectronic processes.[930] QM/MM calculations with electrostatic embedding provided insight into the amount of interfacial disorder of excitonic and polaronic transport levels. All these investigations are dedicated to provide qualitative insight and understanding of the charge generation mechanisms at the interfaces in OSCs. Yet, despite a variety of introduced approximations, many results were found to agree nicely with experimental findings, which emphasizes the soundness of the theoretical models and approaches.

From the energetic profiles retracing the exciton dissociation and charge separation processes at the *in silico* generated model interfaces, **important energy loss channels** could be identified that do not exist if excitons are assumed to be localized on isolated molecules. Exciton losses in the donor phase result from excimer formation and exciton self-trapping, whereas charge trapping was found to be rather disorder-driven, i.e., it occurs in the energetically broad landscapes of polaron levels characteristic for some donor phases. The occurrence and energies of interfacial charge-transfer traps,

which are responsible for reduced open-circuit voltages,[435] critically depend on the dielectric screening of the environment, on the molecular size, and on precise details of the interfacial morphology.[638]

Nevertheless, although the impact of these trap states on the energetics of charge generation might appear rather profound, their population is often kinetically hampered. For instance, the driving forces to reach energetically deep interfacial charge-transfer states are usually so high that the corresponding rates lie in the Marcus-inverted region. Similarly, whereas exciton trapping certainly limits the efficiency of exciton diffusion, it was observed to be only significant when the competing ongoing exciton transport processes are slow. In contrast, the kinetic investigations complementary to the energetic profiles suggest that **slow charge transport processes** in the vicinity of the organic::organic interfaces are a major device efficiency-limiting parameter. The predicted charge transport parameters at the interfaces, which are in accordance with several experimental measurements, arise mainly from slow rates due to the formation of interfacial "charge transport depletion zones", i.e. of regions with only very slow charge transport rates also due to the significant Coulomb attraction between the geminately formed electron and the hole.[930] The additional QM/MM investigations on the disorder of polaronic and excitonic transport levels demonstrated furthermore that the **disorder of the charge transport levels** at organic::organic interfaces is considerable and results especially from electrostatic interactions as well as from a varying degree of delocalization of the charge carriers. In contrast, excitonic transport is only subject to a much smaller degree of disorder.

Hence, as the concluding combined statement from these investigations, a large amount of evidence was provided that **slow charge transport in the vicinity of organic::organic interfaces is a major efficiency-limiting process that requires further optimization**.[498]

7 Zusammenfassung

Um die Umwandlung von Licht zu Strom in organischen Solarzellen zu verstehen, müssen die beteiligten optoelektronischen Prozesse sowohl auf molekularem als auch auf intermolekularem und auf dem Aggregatniveau beschrieben werden.[27] Diese Arbeit stellt eine solche mehrstufige Beschreibung dar, um zum grundlegenden Verständnis derjenigen Prozesse am organisch::organischen *Interface* beizutragen, die für die finale Gesamtleistung der Zelle ausschlaggebend sind. Dabei werden die wesentlichen Schritte von der Lichtabsorption und Exzitonendiffusion über den photoinduzierte *Charge-Transfer*-Schritt am Donor-Akzeptor-*Interface* bis hin zur endgültigen Ladungstrennung berücksichtigt. Um auf Struktur-Eigenschafts-Beziehungen rückschließen zu können, wurden verschiedene molekulare p-Halbleiter in der *heterojunction* mit Fulleren C_{60} kombiniert, einem der gängigsten Akzeptoren in organischen Solarzellen. Nach einer umfangreichen Bewertung der Eignung verschiedener *ab initio* und semiempirischer Methoden sowie diverser DFT-Funktionale für die Beschreibung der molekularen Eigenschaften wurden intermolekulare und Aggregataspekte diskutiert. Auf allen Ebenen, d.h. auf der molekularen, intermolekularen und auf der Aggregatebene, stehen sowohl methodische Ansätze als auch grundlegendende photophysikalische Überlegungen im Mittelpunkt, um das mikroskopische Verständnis der Ladungsträgererzeugung in organischen Solarzellen zu erweitern.

Die molekulare Perspektive: eine Beschreibung des Grundzustands und der angeregten und geladenen elektronischen Zuständen

Aus molekularer Hinsicht werden während der Stromerzeugung in organischen Solarzellen einzelne Moleküle elektronisch angeregt. Zudem entstehen durch die Ladungstransferprozesse Kationen und Anionen. An allen Prozessen sind intramolekulare Relaxationsprozesse beteiligt. Daher werden geeignete Methoden benötigt, die die komplexe elektronische Struktur der beteiligten elektronischen Zustände und die Relaxationsprozesse richtig beschreiben.

In einem umfangreichen Benchmark gegenüber SCS-MP2/cc-pVTZ-Referenzgeometrien wurde die Genauigkeit der **Grundzustandsgeometrien** evaluiert, die mit DFT-Funktionalen oder mit semiempirischen und wellenfunktionsbasierten Methoden erhalten wurden. Um diejenigen Methoden zu identifizieren, die sowohl verlässlich als auch effizient sind, wurde ein eher kleiner Basissatz (cc-pVDZ) verwendet. Zwei verschiedene Kriterien dienten als Maß für die Qualität der Geometrien. Einerseits wurden RMSD-Werte verwendet, während andererseits absolute Abweichungen wichtiger molekularer Parameter wie Torsionswinkel oder die Bindungslängen-alternanz in konjugierten Systemen hinzugezogen wurden. Die Ergebnisse zeigten, dass Funktionale mit *long-range correction*, insbesondere ωB97X-D, sehr gute Grundzustandsgeometrien liefern. Das folgt vor allem aus ihrer geringen Basissatzabhängigkeit, die sie von wellenfunktionsbasierten

Methoden unterscheidet, aber auch aus ihrer Fähigkeit, die verschiedenen Dimensionen von Elektronenkorrelation vollständig zu erfassen, was reinen Funktionalen und semiempirischen Methoden nicht auf vergleichbarem Niveau gelingt. Obwohl nämlich alle verwendeten molekularen Halbleiter aus großen konjugierten π-Systemen bestehen, zeigte sich im Rahmen der Rechnungen, dass sich das Ausmaß der Elektronendelokalisierung im Grundzustand – und damit einhergehend die Bedeutung von lang- bis mittelreichweitiger Elektronenkorrelation – von Molekül zu Molekül nichtsdestotrotz erheblich unterscheidet. Das erklärt die unerwartete und bislang eher vernachlässigte Bedeutung der *long-range correction* für richtige Grundzustandsgeometrien.[702]

Singulettanregungsenergien, die ebenfalls mit *ab initio*-, semiempirischen und DFT-Ansätzen berechnet wurden, wurden anhand von MS-CASPT2-Referenzwerten evaluiert. Um den Rechenaufwand der Referenzrechnungen auch für große Moleküle im Rahmen zu halten, wurden in einem neuen Ansatz zunächst die MS-CASPT2-Rechnungen an kleineren Modellsystemen durchgeführt. Daraufhin wurde der Substituenteneinfluss durch eine nachträgliche Korrektur der Anregungsenergien berücksichtigt. Das Benchmark zeigte, dass analog zur Elektronendelokalisierung im Grundzustand auch der *Charge-Transfer*-Charakter des (immer hellen) ersten angeregten Zustands der molekularen Halbleiter stark variiert. Für die theoretische Beschreibung dieses Zustands hat das wichtige Konsequenzen. Während die verwendeten *ab initio*-Methoden fast immer sehr akkurate Anregungsenergien liefern, hängt die Genauigkeit von DFT-Funktionalen für Singulettanregungsenergien entscheidend von ihrem *Hartree-Fock*-Anteil ab. Deshalb sind manchmal Funktionale mit *long-range correction* wie LC-BLYP oder LC-ωPBE nötig, während Hybridfunktionale, etwa B3LYP oder SOGGA11X, in anderen Fällen bereits ausreichen. Signifikante Unterschiede in der Genauigkeit wurden auch bei den semiempirischen Methoden beobachtet. Im Vergleich zu AM1, PM3 und den OMx-Methoden waren ZINDO-Anregungsenergien bei vernachlässigbaren Rechenzeiten fast ebenso gut wie DFT. Insgesamt waren die Anregungsenergien von ωB97X-D und CAM-B3LYP am genauesten, insbesondere wenn zusätzlich höherangeregte Zustände wie unter anderem einige richtige *Charge-Transfer*-Zustände berücksichtigt wurden.[702]

Im Gegensatz zu den angeregten Singulettzuständen werden die Energien von **Triplettanregungen** nicht vorwiegend durch deren partiellen *Charge-Transfer*-Charakter beeinflusst. Eine entscheidende Rolle scheint eher der richtigen Beschreibung der differenziellen Korrelation zwischen den angeregten Triplettzuständen und dem Grundzustand zuzukommen. Diese besondere Bedeutung der differenziellen Korrelation erklärt auch, warum sich die Fehler von DFT-Funktionalen mit ähnlichem *Hartree-Fock*-Anteil teilweise stark unterscheiden. Als weiteres wichtiges Ergebnis wurde gezeigt, dass DFT Triplettanregungsenergien normalerweise erheblich unterschätzt, vor allem im Rahmen des Standard-*adiabatic linear response TD-DFT*-Formalismus. Das folgt natürlich teilweise auch aus den

bekannten Triplettinstabilitäten. Es stellte sich heraus, dass sowohl die Δ-SCF-Methode als auch die Tamm-Dancoff-Näherung zuverlässiger sind, obwohl auch sie latent zu niedrige Anregungsenergien ergeben. Die besten Werte lieferten sie für Hybridfunktionale mit einem erheblichen *Hartree-Fock*-Anteil oder für Funktionale mit *long-range correction* und einem nur moderaten *range-separation parameter*. Insgesamt sind die Richtlinien für die genaue Berechnung von Triplettanregungsenergien mit DFT verglichen zu den Singuletts allerdings weit weniger klar. Im Gegensatz zu den DFT-Ansätzen waren *ab initio*-Triplettenergien fast immer sehr genau, möglicherweise weil alle *ab initio*-Methoden die differenzielle Korrelation sehr ausgewogen beschreiben. Die Möglichkeiten, die zur Berechnung von Singulett- und Triplettanregungsenergien offen stehen (TD-DFT, Tamm-Dancoff, etc.), führen bei der Berechnung von **Singulett-Triplett-Gaps**, d.h. von S_1-T_1-Energiedifferenzen, zu einer Reihe von Kombinationen (TD-DFT-Singuletts + Δ-SCF-Tripletts, etc.). Ein erstes umfangreiches Benchmark ihrer Genauigkeit zeigte das Potenzial auf, *in silico* vielversprechende *singlet-fission*-Moleküle auszuwählen, insbesondere weil sehr genaue Singulett-Triplett-Gaps mit DFT-Funktionalen erhalten wurden, in denen sowohl der Hartree-Fock-Anteil als auch der Koeffizient der lokalen Korrelation gegenüber einem Referenzdatensatz gefittet wurden.[758]

Weil Marcus-Raten exponentiell von molekularen Reorganisationsenergien abhängen, braucht man Methoden, die **Exzitonen- und Ladungsreorganisationsenergien** sehr genau vorhersagen. Ähnlich wie bei den Tripletts wurden unsystematische Fehler für verschiedene DFT-Funktionale gefunden. Beim Benchmark der **Ladungsreorganisationsenergien** stellt die Wahl der Referenzmethode eine besondere Herausforderung dar, was auch erklären könnte, warum es in der Literatur keine derartigen Benchmarks gibt. In dieser Arbeit wurden Referenzwerte für Ladungsreorganisationsenergien aus einer Kombination von aufwändigen IP-EOM-CCSD-Energieberechnungen und Geometrien bestimmt, die mit IP-getunten Funktionalen berechnet wurden. Es zeigte sich, dass die Werte der Ladungsreorganisationsenergien analog zu den Singulettanregungsenergien sehr stark vom *Hartree-Fock*-Anteil der verwendeten DFT-Funktionale abhängen. Das legt die Schlussfolgerung nahe, dass der Selbstwechselwirkungsfehler von DFT die Beschreibung der beteiligten intramolekularen Relaxationsprozesse beeinflusst, die durch Ionisierung induziert werden. Daher lieferten nur Funktionale mit *long-range correction* Ladungsreorganisationsenergien von akzeptabler Genauigkeit. Im Gegensatz dazu waren entsprechende Werte von Hybridfunktionalen und reinen Funktionalen viel zu klein, was auf deren intrinsisch überschätzte Ladungsdelokalisation zurückzuführen ist.[854] **Exzitonenreorganisationsenergien**, für die ebenfalls keine Benchmarkdaten vorliegen, wurden gegenüber SCS-CC2/cc-pVDZ-Referenzwerten evaluiert. Dabei machten sich vor allem die Grenzen der Genauigkeit der Funktionale mit *long-range correction* bemerkbar: Obwohl diese immer noch die besten Werte lieferten, waren die optimierten Geometrien der angeregten Zustände weit weniger verlässlich.

Die intermolekulare Perspektive: eine Beschreibung der intermolekularen Wechselwirkungen zwischen den π-Systemen der organischen Halbleiter

Die genauen intermolekularen Konformationen zwischen molekularen organischen Halbleiter sind ausschlaggebend für Kopplungen und Energien von Exzitonen- und Ladungstransport. Um bestimmte intermolekulare Konformationen gezielt zu erzeugen, wäre es wünschenswert, (1) die zugrunde liegenden **physikalischen Effekte** zu verstehen, die zur Ausbildung bestimmter Dimerorientierungen führen, und (2) **Ansätze** zu entwickeln, wie man die Wechselwirkungen **modellieren/simulieren** kann. Obwohl sehr viele Literaturuntersuchungen existieren, die intermolekulare Wechselwirkungen allgemein diskutieren oder Ansätze für ihre Berechnung vorstellen, sind Analysen, die sich spezifisch molekularen Halbleitern widmen, nicht bekannt.

Mit Hilfe von SAPT- und LMO-EDA-Rechnungen konnte gezeigt werden, dass die Dispersion zwar den Hauptteil zur intermolekularen Bindungsenergie beiträgt, dabei aber nicht bestimmte Dimerkonformationen spezifisch begünstigt. Im Gegensatz dazu scheinen vor allem sehr lokalisierte, **kurzreichweitige Abstoßungskräfte**, die zudem nicht von den molekularen Eigenschaften der Halbleiter abhängen, für die Details der intermolekularen Potenzialflächen verantwortlich zu sein. Diese kurzreichweitigen Abstoßungskräfte begünstigen manche Dimerkonformationen energetisch, während sie andere stark destabilisieren. Zahlreiche DFT-D-Potenzialflächen von verschiedenen intermolekularen Dimerkoordinaten in diversen *gestackten* Homodimeren stützen diese Interpretation. Während vor allem der Austausch-Repulsions-Term die kurzreichweitige Abstoßung darstellt, kann letztere dennoch durch elektrische **Quadrupol-Quadrupol-Wechselwirkungen** simuliert werden. Alternativ kann auch eine Reihe von **empirischen van-der-Waals-Potenzialen** mit zuvor generierten Parametern verwendet werden, um die intermolekularen Potenzialflächen recht genau zu reproduzieren.[875] Die Ähnlichkeit dieser konzeptionell unterschiedlichen Modellansätze wurde in diesem Detail in der Literatur noch nicht diskutiert.

Die Aggregatebene: eine Beschreibung der Energetik und Kinetik der Ladungsträgererzeugung

Auf der Aggregat-/Zellenebene kann die Ladungsträgererzeugung an den organisch::organischen *Interfaces* in organischen Solarzellen nur als Kombination von energetischen und kinetischen Aspekten verstanden werden. In dieser Arbeit wurde eine *in silico*-MM-Methode entwickelt, um geeignete Modelle der *Interfaces* in einer Reihe von Molekulardynamikschritten zu erzeugen. Ein dreistufiger Ansatz wurde gewählt, um die energetischen und kinetischen Aspekte anhand dieser *Interface*-Modellsysteme zu analysieren. Die Dimermethode[745] wurde auf die *Interfaces* angepasst, so dass mit Hilfe von Dimeren in einem polarisierbaren Kontinuum und zusätzlichen lokalen elektrischen Feldern

der **energetische Verlauf der Ladungstrennung** berechnet wurde.[638] Ein **Modell der Transportprozesse** am *Interface* wurde auf der Grundlage von kinetischen Monte-Carlo-Simulationen und Marcusraten ohne empirische Inputparameter entwickelt und implementiert, um die **Kinetik der optoelektronischen Prozesse** zu untersuchen.[930] QM/MM-Berechnungen mit *electrostatic embedding* ermöglichten weitere Rückschlüsse über die Unordnung der Exzitonen- und Ladungstransportniveaus am *Interface*. Insgesamt sollte im Rahmen dieser Berechnungen vor allem ein qualitatives Verständnis der Mechanismen zur Ladungsträgererzeugung an den *Interfaces* in organischen Solarzellen entwickelt werden. Trotz zahlreicher Näherungen stimmten dennoch etliche Vorhersagen auch quantitativ gut mit experimentellen Werten überein, was unterstreicht, dass die Modelle die wesentlichen Effekte ausreichend berücksichtigen.

Mit Hilfe der energetischen Profilen, die den Prozess von der Exzitonendiffusion bis hin zur Ladungstrennung an den *in silico* erzeugten *Interface*-Modellen darstellen, konnten wichtige **Energiedissipationsmechanismen** identifiziert werden, die nur im Aggregatansatz sichtbar werden. Exzitonenverluste in der Donorphase sind vor allem auf Exzimerbildung und Exzitonenselbsttrapping zurückzuführen, während Ladungsträgertrapping vorwiegend durch energetische Unordnung in den Ladungstransportniveaus hervorgerufen wird. Sehr breite Zustandsdichten der Ladungstransportniveaus sind für einige Donorphasen charakteristisch. Trapzustände an der Grenzfläche, die insbesondere für niedrige *open-circuit voltages* verantwortlich sind, hängen stark von der Permittivität der Umgebung, der Größe der beteiligten Moleküle und der Morphologie am *Interface* ab.[638]

Obwohl der Einfluss dieser Energiedissipationsmechanismen auf den energetischen Verlauf der Ladungstrennung gravierend erscheint, ist die Population von Trapzuständen kinetisch oft gehemmt. Häufig liegen die Raten vor allem für den photoinduzierten Ladungsübertrag auf Trapzustände am *Interface* im Marcus-invertieren Bereich. Ebenso ist die Existenz von Exzitonentrapzuständen nur dann entscheidend, wenn die Exzitonendiffusion ohnehin langsam ist. Die kinetischen Untersuchungen legten komplementär zur Energetik eher die Schlussfolgerung nahe, dass langsame **Ladungstransportprozesse am *Interface*** ein wesentlicher, limitierender Prozess für die gesamte Zellleistung ist. Die simulierten Ladungsträgermobilitäten am *Interface*, die gut mit experimentellen Werten übereinstimmen, sind die Folge einer *„charge transport depletion zone"* am *Interface*, d.h. eines Bereichs, in dem alle Ladungstransportprozesse unter anderem aufgrund der Coulomb-Anziehung zwischen den Ladungsträgern sehr langsam sind.[930] Hinzu kommt, dass die QM/MM-Rechnungen **sehr ungeordnete Ladungstransportniveaus** vorhersagen, was vorwiegend durch elektrostatische Wechselwirkungen und ein unterschießliches Ausmaß von Ladungsträger-

delokalisation hervorgerufen wird. Die Zustandsdichte der Exzitonentransportniveaus ist hingegen energetisch weit weniger breit.

Insgesamt deuten die Rechnungen darauf hin, dass vor allem langsamer Ladungstransport in der Umgebung organisch::organischer *Interfaces* ein limitierender Parameter für die Gesamtleistung organischer Solarzellen ist, so dass an dieser Stelle Optimierungsbedarf besteht.

8 References

(1)   Darling, S. B.; You, F. *RSC Adv.* **2013**, *3* (39), 17633.

(2)   *Multiscale Modelling of Organic and Hybrid Photovoltaics*; Beljonne, D., Cornil, J., Eds.; Topics in Current Chemistry; Springer Berlin Heidelberg: Berlin, Heidelberg, 2014; Vol. 352.

(3)   Forrest, S. R. *Nature* **2004**, *428* (6986), 911–918.

(4)   Brabec, C. J.; Gowrisanker, S.; Halls, J. J. M.; Laird, D.; Jia, S.; Williams, S. P. *Adv. Mater.* **2010**, *22* (34), 3839–3856.

(5)   Pelzer, K. M.; Darling, S. B. *Mol. Syst. Des. Eng.* **2016**, *1* (1), 10–24.

(6)   Green, M. A. *Sol. Energy* **2004**, *76* (1), 3–8.

(7)   Grossiord, N.; Kroon, J. M.; Andriessen, R.; Blom, P. W. M. *Org. Electron.* **2012**, *13*, 432–456.

(8)   Jørgensen, M.; Norrman, K.; Krebs, F. C. *Sol. Energy Mater. Sol. Cells* **2008**, *92* (7), 686–714.

(9)   Giannouli, M.; Drakonakis, V. M.; Savva, A.; Eleftheriou, P.; Florides, G.; Choulis, S. A. *ChemPhysChem* **2015**, *16* (6), 1134–1154.

(10)   Zimmermann, B.; Würfel, U.; Niggemann, M. *Sol. Energy Mater. Sol. Cells* **2009**, *93* (4), 491–496.

(11)   Galagan, Y.; de Vries, I. G.; Langen, A. P.; Andriessen, R.; Verhees, W. J. H.; Veenstra, S. C.; Kroon, J. M. *Chem. Eng. Process. Process Intensif.* **2011**, *50* (5), 454–461.

(12)   Søndergaard, R.; Hösel, M.; Angmo, D.; Larsen-Olsen, T. T.; Krebs, F. C. *Mater. Today* **2012**, *15* (1), 36–49.

(13)   Yan, J.; Saunders, B. R. *RSC Adv.* **2014**, *4* (82), 43286–43314.

(14)   Grätzel, M. *J. Photochem. Photobiol. C Photochem. Rev.* **2003**, *4* (2), 145–153.

(15)   O'Regan, B.; Grätzel, M. *Nature* **1991**, *353* (6346), 737–740.

(16)   Armaroli, N.; Balzani, V. *Chem. - A Eur. J.* **2016**, *22* (1), 32–57.

(17)   Burschka, J.; Pellet, N.; Moon, S.-J.; Humphry-Baker, R.; Gao, P.; Nazeeruddin, M. K.; Grätzel, M. *Nature* **2013**, *499* (7458), 316–319.

(18)   Green, M. A.; Ho-Baillie, A.; Snaith, H. J. *Nat. Photonics* **2014**, *8* (7), 506–514.

(19)   Brédas, J.-L.; Norton, J. E.; Cornil, J.; Coropceanu, V. *Acc. Chem. Res.* **2009**, *42* (11), 1691–1699.

(20)   Braun, S.; Salaneck, W. R.; Fahlman, M. *Adv. Mater.* **2009**, *21* (14–15), 1450–1472.

(21)   Milián-Medina, B.; Gierschner, J. *WIREs Comput. Mol .Sci.* **2012**, *2* (4), 513–524.

(22)   Vázquez, H.; Gao, W.; Flores, F.; Kahn, A. *Phys. Rev. B* **2005**, *71* (4), 41306.

(23)   Vázquez, H.; Flores, F.; Kahn, A. *Org. Electron.* **2007**, *8* (2), 241–248.

(24)   Labat, F.; Le Bahers, T.; Ciofini, I.; Adamo, C. *Acc. Chem. Res.* **2012**, *45* (8), 1268–1277.

(25)   Bässler, H. *Phys. status solidi* **1993**, *175* (1), 15–56.

(26)   Yost, S. R.; Hontz, E.; McMahon, D. P.; Van Voorhis, T. *Top. Curr. Chem.* **2014**, *352*, 103–150.

(27) Würthner, F.; Meerholz, K. *Chem. Eur. J.* **2010**, *16* (31), 9366–9373.

(28) Poelking, C.; Tietze, M.; Elschner, C.; Olthof, S.; Hertel, D.; Baumeier, B.; Würthner, F.; Meerholz, K.; Leo, K.; Andrienko, D. *Nat. Mater.* **2015**, *14* (4), 434–439.

(29) Mishra, A.; Bäuerle, P. *Angew. Chemie Int. Ed.* **2012**, *51* (9), 2020–2067.

(30) Baumeier, B.; May, F.; Lennartz, C.; Andrienko, D. *J. Mater. Chem.* **2012**, *22* (22), 10971.

(31) Jensen, F. *Introduction to Computational Chemistry*, Second Edition; John Wiley & Sons Ltd: Chichester, 2007.

(32) Lewars, E. G. *Computational Chemistry Introduction to the Theory and Applictions of Molecular and Quantum Mechanics*, Second Edition; Springer: Heidelberg, London, New York, 2011.

(33) Born, M.; Oppenheimer, R. *Ann. Phys.* **1927**, *389* (20), 457–484.

(34) de Broglie, L. *Found. Phys.* **1970**, *1* (1), 5–15.

(35) Domcke, W.; Yarkony, D. R. *Annu. Rev. Phys. Chem.* **2012**, *63* (1), 325–352.

(36) Szabo, A.; Ostlund, N. S. *Modern Quantum Chemistry*, First Edition; McGraw-Hill Publishing Company: New York, 1989.

(37) Davidson, E. R. *J. Comput. Phys.* **1975**, *17* (1), 87–94.

(38) Siegbahn, P. E. M. *Chem. Phys. Lett.* **1984**, *109* (5), 417–423.

(39) Helgaker, T.; Jorgensen, P.; Olsen, J. *Molecular Electronic-Structure Theory*; John Wiley & Sons, Inc.: Chichester, 2012.

(40) Møller, C.; Plesset, M. S. *Phys. Rev.* **1934**, *46* (7), 618–622.

(41) Goldstone, J. *Proc. R. Soc. A Math. Phys. Eng. Sci.* **1957**, *239* (1217), 267–279.

(42) Vahtras, O.; Almlöf, J.; Feyereisen, M. W. *Chem. Phys. Lett.* **1993**, *213* (5), 514–518.

(43) Grimme, S.; Goerigk, L.; Fink, R. F. *WIREs Comput. Mol .Sci.* **2012**, *2* (6), 886–906.

(44) Ren, X.; Rinke, P.; Blum, V.; Wieferink, J.; Tkatchenko, A.; Sanfilippo, A.; Reuter, K.; Scheffler, M. *New J. Phys.* **2012**, *14* (5), 53020.

(45) Feyereisen, M.; Fitzgerald, G.; Komornicki, A. *Chem. Phys. Lett.* **1993**, *208* (5), 359–363.

(46) Weigend, F.; Köhn, A.; Hättig, C. *J. Chem. Phys.* **2002**, *116* (8), 3175.

(47) Pulay, P. *Chem. Phys. Lett.* **1983**, *100* (2), 151–154.

(48) Schütz, M.; Hetzer, G.; Werner, H.-J. *J. Chem. Phys.* **1999**, *111* (13), 5691.

(49) Hetzer, G.; Schütz, M.; Stoll, H.; Werner, H.-J. *J. Chem. Phys.* **2000**, *113* (21), 9443.

(50) Köppl, C.; Werner, H.-J. *J. Chem. Phys.* **2015**, *142* (16), 164108.

(51) Polly, R.; Werner, H.-J.; Dahle, P.; Taylor, P. R. *J. Chem. Phys.* **2006**, *124* (23), 234107.

(52) Usvyat, D.; Maschio, L.; Schütz, M. *J. Chem. Phys.* **2015**, *143* (10), 102805.

(53) Jung, Y.; Shao, Y.; Head-Gordon, M. *J. Comput. Chem.* **2007**, *28* (12), 1953–1964.

(54)   Lee, M. S.; Maslen, P. E.; Head-Gordon, M. *J. Chem. Phys.* **2000**, *112* (8), 3592.

(55)   Liakos, D. G.; Sparta, M.; Kesharwani, M. K.; Martin, J. M. L.; Neese, F. *J. Chem. Theory Comput.* **2015**, *11* (4), 1525–1539.

(56)   Riplinger, C.; Neese, F. *J. Chem. Phys.* **2013**, *138* (3), 34106.

(57)   Neese, F. *Magn. Reson. Chem.* **2004**, *42* (S1), S187–S198.

(58)   Kutzelnigg, W.; Klopper, W. *J. Chem. Phys.* **1991**, *94* (3), 1985.

(59)   Kato, T. *Commun. Pure Appl. Math.* **1957**, *10* (2), 151–177.

(60)   Tew, D. P.; Hättig, C. *Int. J. Quantum Chem.* **2013**, *113* (3), 224–229.

(61)   Klopper, W.; Samson, C. C. M. *J. Chem. Phys.* **2002**, *116* (15), 6397.

(62)   Wang, Y. M.; Hättig, C.; Reine, S.; Valeev, E.; Kjærgaard, T.; Kristensen, K. *J. Chem. Phys.* **2016**, *144* (20), 204112.

(63)   Hättig, C.; Tew, D. P.; Helmich, B. *J. Chem. Phys.* **2012**, *136* (20), 204105.

(64)   Shiozaki, T.; Hirata, S. *J. Chem. Phys.* **2010**, *132* (15), 151101.

(65)   Höfener, S.; Klopper, W. *Mol. Phys.* **2010**, *108* (13), 1783–1796.

(66)   Hättig, C.; Tew, D. P.; Köhn, A. *J. Chem. Phys.* **2010**, *132* (23), 231102.

(67)   Noga, J.; Kedžuch, S.; Šimunek, J.; Ten-no, S. *J. Chem. Phys.* **2008**, *128* (17), 174103.

(68)   Krause, C.; Werner, H.-J. *Phys. Chem. Chem. Phys.* **2012**, *14* (21), 7591.

(69)   Adler, T. B.; Werner, H.-J. *J. Chem. Phys.* **2011**, *135* (14), 144117.

(70)   Grimme, S. *J. Chem. Phys.* **2003**, *118* (20), 9095.

(71)   Gerenkamp, M.; Grimme, S. *Chem. Phys. Lett.* **2004**, *392* (1), 229–235.

(72)   Piacenza, M.; Hyla-Kryspin, I.; Grimme, S. *J. Comput. Chem.* **2007**, *28* (14), 2275–2285.

(73)   Distasio, R. A.; Steele, R. P.; Head-Gordon, M. *Mol. Phys.* **2007**, *105* (19–22), 2731–2742.

(74)   Rigby, J.; Barrera Acevedo, S.; Izgorodina, E. I. *J. Chem. Theory Comput.* **2015**, *11* (8), 3610–3616.

(75)   Hill. J. Grant; Platts, J. A. *J. Chem. Theory Comput.* **2007**, *3* (1), 80–85.

(76)   Goldey, M. B.; Belzunces, B.; Head-Gordon, M. *J. Chem. Theory Comput.* **2015**, *11* (9), 4159–4168.

(77)   Lochan, R. C.; Yousung, J.; Head-Gordon, M. *J. Phys. Chem. A* **2005**, *109* (33), 7598.

(78)   Cybulski, S. M.; Lytle, M. L. *J. Chem. Phys.* **2007**, *127* (14), 141102.

(79)   Jung, Y.; Lochan, R. C.; Dutoi, A. D.; Head-Gordon, M. *J. Chem. Phys.* **2004**, *121* (20), 9793.

(80)   Limacher, P. A.; Ayers, P. W.; Johnson, P. A.; De Baerdemacker, S.; Van Neck, D.; Bultinck, P. *J. Chem. Theory Comput.* **2013**, *9* (3), 1394–1401.

(81)   Chan, G. K.-L.; Sharma, S. *Annu. Rev. Phys. Chem.* **2011**, *62* (1), 465–481.

(82) Johnson, P. A.; Limacher, P. A.; Baerdemacker, S. De; Neck, D. Van; Bultinck, P. *Comput. Theor. Chem.* **2013**, *1003*, 101–113.

(83) Bardeen, J.; Cooper, L. N.; Schrieffer, J. R. *Phys. Rev.* **1957**, *108* (5), 1175–1204.

(84) Boguslawski, K.; Tecmer, P.; Ayers, P. W.; Bultinck, P.; De Baerdemacker, S.; Van Neck, D. *Phys. Rev. B* **2014**, *89* (20), 201106.

(85) Knowles, P. J.; Werner, H.-J. *Chem. Phys. Lett.* **1985**, *115* (3), 259–267.

(86) Roos, B. O.; Taylor, P. R.; Siegbahn, P. E. M. *Chem. Phys.* **1980**, *48* (2), 157–173.

(87) Malmqvist, P.-Å.; Roos, B. O. *Chem. Phys. Lett.* **1989**, *155* (2), 189–194.

(88) Malmqvist, P. A.; Rendell, A.; Roos, B. O. *J. Phys. Chem.* **1990**, *94* (14), 5477–5482.

(89) Stårling, J.; Bernhardsson, A.; Lindh, R. *Mol. Phys.* **2001**, *99* (2), 103–114.

(90) Widmark, P.-O.; Malmqvist, P.-A.; Roos, B. O. *Theor. Chim. Acta* **1990**, *77* (5), 291–306.

(91) Andersson, K.; Malmqvist, P. A.; Roos, B. O.; Sadlej, A. J.; Wolinski, K. *J. Phys. Chem.* **1990**, *94* (14), 5483–5488.

(92) Andersson, K.; Malmqvist, P.-A.; Roos, B. O. *J. Chem. Phys.* **1992**, *96* (2), 1218.

(93) Finley, J.; Malmqvist, P.-Å.; Roos, B. O.; Serrano-Andrés, L. *Chem. Phys. Lett.* **1998**, *288* (2), 299–306.

(94) Ghigo, G.; Roos, B. O.; Malmqvist, P.-Å. *Chem. Phys. Lett.* **2004**, *396* (1), 142–149.

(95) Roos, B. O.; Andersson, K. *Chem. Phys. Lett.* **1995**, *245* (2–3), 215–223.

(96) Roos, B. O.; Andersson, K.; Fülscher, M. P.; Serrano-Andrés, L.; Pierloot, K.; Merchán, M.; Molina, V. *J. Mol. Struct. THEOCHEM* **1996**, *388*, 257–276.

(97) Koch, W.; Holthausen, M. C. *A Chemist's Guide to Density Functional Theory*, 2nd Edition; Wiley-VCH Verlag: Weinheim, 2001.

(98) Hohenberg, P.; Kohn, W. *Phys. Rev.* **1964**, *136* (3B), B864–B871.

(99) Capelle, K. *Cornell University Library* **2002**, arXiv: cond-mat/0211443.

(100) Levy, M. *Proc. Natl. Acad. Sci.* **1979**, *76* (12), 6062–6065.

(101) Burke, K.; Wagner, L. O. *Int. J. Quantum Chem.* **2013**, *113* (2), 96–101.

(102) Gilbert, T. L. *Phys. Rev. B* **1975**, *12* (6), 2111–2120.

(103) Harriman, J. E. *Phys. Rev. A* **1981**, *24* (2), 680–682.

(104) Kohn, W. *Phys. Rev. Lett.* **1983**, *51* (17), 1596–1598.

(105) Lieb, E. H. *Int. J. Quantum Chem.* **1983**, *24* (3), 243–277.

(106) Scuseria, G. E.; Staroverov, V. N. In *Theory and Application of Computational Chemistry: The First 40 Years*; Dykstra, C. E., Frenking, G., Kim, K. S., Scuseria, G. E., Eds.; Elsevier: Amsterdam, 2005; pp 669–724.

(107) Kohn, W.; Sham, L. J. *Phys. Rev.* **1965**, *140* (4A), A1133–A1138.

(108) Langreth, D. C.; Perdew, J. P. *Solid State Commun.* **1975**, *17* (11), 1425–1429.

(109) Langreth, D. C.; Perdew, J. P. *Phys. Rev. B* **1977**, *15* (6), 2884–2901.

(110) Gunnarsson, O.; Lundqvist, B. I. *Phys. Rev. B* **1976**, *13* (10), 4274–4298.

(111) Cohen, A. J.; Mori-Sánchez, P.; Yang, W. *Science* **2008**, *321* (5890).

(112) Gritsenko, O. V.; Schipper, P. R. T.; Baerends, E. J. *J. Chem. Phys.* **1997**, *107* (13), 5007.

(113) Levy, M.; Perdew, J. P. *Int. J. Quantum Chem.* **1994**, *49* (4), 539–548.

(114) Perdew, J. P.; Tao, J.; Staroverov, V. N.; Scuseria, G. E. *J. Chem. Phys.* **2004**, *120* (15), 6898.

(115) Mori-Sánchez, P.; Cohen, A. J.; Yang, W. *J. Chem. Phys.* **2006**, *125* (20), 201102.

(116) Ruzsinszky, A.; Perdew, J. P.; Csonka, G. I.; Vydrov, O. A.; Scuseria, G. E. *J. Chem. Phys.* **2007**, *126* (10), 104102.

(117) Lieb, E. H.; Oxford, S. *Int. J. Quantum Chem.* **1981**, *19* (3), 427–439.

(118) Levy, M.; Perdew, J. P. *Phys. Rev. A* **1985**, *32* (4), 2010–2021.

(119) Levy, M. *Int. J. Quantum Chem.* **2009**, *36* (S23), 617–619.

(120) Hui Ou-Yang, H.; Levy, M. *Phys. Rev. A* **1990**, *42* (1), 155–160.

(121) Levy, M.; Ou-Yang, H. *Phys. Rev. A* **1990**, *42* (1), 651–652.

(122) Levy, M. *Phys. Rev. A* **1991**, *43* (9), 4637–4646.

(123) Görling, A.; Levy, M. *Phys. Rev. A* **1992**, *45* (3), 1509–1517.

(124) Levy, M.; Perdew, J. P. *Phys. Rev. B* **1993**, *48* (16), 11638–11645.

(125) Truhlar, D. G.; Zhao, Y. *Theor. Chem. Acc.* **2008**, *120* (1), 215–241.

(126) Perdew, J. P.; Schmidt, K. In *AIP Conference Proceedings*; AIP, 2001; Vol. 577, pp 1–20.

(127) Körzdörfer, T.; Brédas, J.-L. *Acc. Chem. Res.* **2014**, *47* (11), 3284–3291.

(128) Bahmann, H.; Rodenberg, A.; Arbuznikov, A. V.; Kaupp, M. *J. Chem. Phys.* **2007**, *126* (1), 11103.

(129) Autschbach, J.; Srebro, M. *Acc. Chem. Res.* **2014**, *47* (8), 2592–2602.

(130) Tsuneda, T.; Hirao, K. *WIREs Comput. Mol .Sci.* **2014**, *4* (4), 375–390.

(131) Leininger, T.; Stoll, H.; Werner, H.-J.; Savin, A. *Chem. Phys. Lett.* **1997**, *275* (3), 151–160.

(132) Iikura, H.; Tsuneda, T.; Yanai, T.; Hirao, K. *J. Chem. Phys.* **2001**, *115* (8), 3540.

(133) Yanai, T.; Tew, D. P.; Handy, N. C. *Chem. Phys. Lett.* **2004**, *393* (1–3), 51–57.

(134) Görling, A.; Levy, M. *Phys. Rev. B* **1993**, *47* (20), 13105–13113.

(135) Görling, A.; Levy, M. *Phys. Rev. A* **1994**, *50* (1), 196–204.

(136) Grimme, S. *J. Chem. Phys.* **2006**, *124* (3), 34108.

(137) Schwabe, T.; Grimme, S. *Phys. Chem. Chem. Phys.* **2006**, *8* (38), 4398.

(138) Schwabe, T.; Grimme, S. *Phys. Chem. Chem. Phys.* **2007**, *9* (26), 3397.

(139) Sure, R.; Grimme, S. *J. Chem. Theory Comput.* **2015**, *11* (8), 3785–3801.

(140) Grimme, S.; Antony, J.; Ehrlich, S.; Krieg, H. *J. Chem. Phys.* **2010**, *132* (15), 154104.

(141) Grimme, S. *J. Comput. Chem.* **2004**, *25* (12), 1463–1473.

(142) Grimme, S. *J. Comput. Chem.* **2006**, *27* (15), 1787–1799.

(143) Chai, J.-D.; Head-Gordon, M. *Phys. Chem. Chem. Phys.* **2008**, *10* (44), 6615–6620.

(144) Baer, R.; Livshits, E.; Salzner, U. *Annu. Rev. Phys. Chem.* **2010**, *61* (1), 85–109.

(145) Cohen, A. J.; Mori-Sánchez, P.; Yang, W. **2008**.

(146) Perdew, J. P.; Parr, R. G.; Levy, M.; Balduz, J. L. *Phys. Rev. Lett.* **1982**, *49* (23), 1691–1694.

(147) Kronik, L.; Stein, T.; Refaely-Abramson, S.; Baer, R. *J. Chem. Theory Comput.* **2012**, *8* (5), 1515–1531.

(148) Almbladh, C.-O.; von Barth, U. *Phys. Rev. B* **1985**, *31* (6), 3231–3244.

(149) Janak, J. F. *Phys. Rev. B* **1978**, *18* (12), 7165–7168.

(150) Chan, G. K.-L. *J. Chem. Phys.* **1999**, *110* (10), 4710.

(151) Allen, M. J.; Tozer, D. J. *Mol. Phys.* **2002**, *100* (4), 433–439.

(152) Cohen, A. J.; Mori-Sánchez, P.; Yang, W. *Phys. Rev. B* **2008**, *77* (11), 115123.

(153) Seidl, A.; Görling, A.; Vogl, P.; Majewski, J. A.; Levy, M. *Phys. Rev. B* **1996**, *53* (7), 3764–3774.

(154) Becke, A. D. *J. Chem. Phys.* **1993**, *98* (2), 1372.

(155) Vydrov, O. A.; Scuseria, G. E. *J. Chem. Phys.* **2006**, *125* (23), 234109.

(156) Vydrov, O. A.; Heyd, J.; Krukau, A. V.; Scuseria, G. E. *J. Chem. Phys.* **2006**, *125* (7), 74106.

(157) Livshits, E.; Baer, R. *Phys. Chem. Chem. Phys.* **2007**, *9* (23), 2932.

(158) Stein, T.; Eisenberg, H.; Kronik, L.; Baer, R. *Phys. Rev. Lett.* **2010**, *105* (26), 266802.

(159) Stein, T.; Kronik, L.; Baer, R. *J. Am. Chem. Soc.* **2009**, *131* (8), 2818–2820.

(160) Refaely-Abramson, S.; Baer, R.; Kronik, L. *Phys. Rev. B* **2011**, *84* (7), 75144.

(161) Vydrov, O. A.; Scuseria, G. E.; Perdew, J. P. *J. Chem. Phys.* **2007**, *126* (15), 154109.

(162) Tsuneda, T.; Song, J.-W.; Suzuki, S.; Hirao, K. *J. Chem. Phys.* **2010**, *133* (17), 174101.

(163) Wu, Q.; Van Voorhis, T. *Phys. Rev. A* **2005**, *72* (2), 24502.

(164) Wu, Q.; Van Voorhis, T. *J. Chem. Phys.* **2006**, *125* (16), 164105.

(165) Difley, S.; Van Voorhis, T. *J. Chem. Theory Comput.* **2011**, *7* (3), 594–601.

(166) Hsu, C.-P. *Acc. Chem. Res.* **2009**, *42* (4), 509–518.

(167) Seeger, R.; Pople, J. A. *J. Chem. Phys.* **1977**, *66* (7), 3045.

(168) Čížek, J.; Paldus, J. *J. Chem. Phys.* **1967**, *47* (10), 3976.

(169) Paldus, J.; Čížek, J. *J. Chem. Phys.* **1970**, *52* (6), 2919.

(170) Bauernschmitt, R.; Ahlrichs, R. *J. Chem. Phys.* **1996**, *104* (22), 9047.

(171) Foresman, J. B.; Head-Gordon, M.; Pople, J. A.; Frisch, M. J. *J. Phys. Chem.* **1992**, *96* (1), 135–149.

(172) Prlj, A.; Sandoval-Salinas, M. E.; Casanova, D.; Jacquemin, D.; Corminboeuf, C. *J. Chem. Theory Comput.* **2016**, *12* (6), 2652–2660.

(173) Head-Gordon, M.; Rico, R. J.; Oumi, M.; Lee, T. J. *Chem. Phys. Lett.* **1994**, *219* (1–2), 21–29.

(174) Goerigk, L.; Grimme, S. *J. Chem. Phys.* **2010**, *132* (18), 184103.

(175) Silva-Junior, M. R.; Thiel, W. *J. Chem. Theory Comput.* **2010**, *6* (5), 1546–1564.

(176) Head-Gordon, M.; Oumi, M.; Maurice, D. *Mol. Phys.* **1999**, *96* (4), 593–602.

(177) Grimme, S.; Izgorodina, E. I. *Chem. Phys.* **2004**, *305* (1), 223–230.

(178) Rhee, Y. M.; Head-Gordon, M. *J. Phys. Chem. A* **2007**, *111* (24), 5314–5326.

(179) TURBOMOLE V6.2 2010, a development of University of Karlsruhe and Forschungszentrum Karlsruhe GmbH, 1989-2007, TURBOMOLE GmbH, since 2007; available from http://www.turbomole.com.

(180) Hellweg, A.; Grün, S. A.; Hättig, C. *Phys. Chem. Chem. Phys.* **2008**, *10* (28), 4119–4127.

(181) Grimme, S.; Neese, F. *J. Chem. Phys.* **2007**, *127* (15), 154116.

(182) Bredow, T.; Jug, K. *Theor. Chem. Acc.* **2005**, *113* (1), 1–14.

(183) Dewar, M. J. S.; Thiel, W. *J. Am. Chem. Soc.* **1977**, *99* (15), 4899–4907.

(184) Pariser, R.; Parr, R. G. *J. Chem. Phys.* **1953**, *21* (3), 466.

(185) Pariser, R.; Parr, R. G. *J. Chem. Phys.* **1953**, *21* (5), 767.

(186) Pople, J. A. *Trans. Faraday Soc.* **1953**, *49* (0), 1375.

(187) Pople, J. A.; Santry, D. P.; Segal, G. A. *J. Chem. Phys.* **1965**, *43* (10), S129.

(188) Bingham, R. C.; Dewar, M. J. S.; Lo, D. H. *J. Am. Chem. Soc.* **1975**, *97* (6), 1285–1293.

(189) Dewar, M. J. S.; Zoebisch, E. G.; Healy, E. F.; Stewart, J. J. P. *J. Am. Chem. Soc.* **1985**, *107* (13), 3902–3909.

(190) Stewart, J. J. P. *J. Comput. Chem.* **1989**, *10* (2), 209–220.

(191) Thiel, W.; Voityuk, A. A. *J. Phys. Chem.* **1996**, *100* (2), 616–626.

(192) Thiel, W. In *Advances in Chemical Physics: New Methods in Computational Quantum Mechanics, Volume 93*; Prigogine, I., Rice, S. A., Eds.; John Wiley & Sons, Inc., 1996; pp 703–757.

(193) Kolb, M.; Thiel, W. *J. Comput. Chem.* **1993**, *14* (7), 775–789.

(194) Löwdin, P. *J. Chem. Phys.* **1950**, *18* (3), 365–275.

(195) Weber, W.; Thiel, W. *Theor. Chem. Acc.* **2000**, *103* (6), 495–506.

(196) Scholten, M. Semiempirische Verfahren mit Orthogonalisierungskorrekturen: Die OM3 Methode, Universität Düsseldorf, Germany, 2003.

(197) Tuttle, T.; Thiel, W. *Phys. Chem. Chem. Phys.* **2008**, *10* (16), 2159.

(198) McNamara, J. P.; Hillier, I. H. *Phys. Chem. Chem. Phys.* **2007**, *9*, 2362–2370.

(199) Řezáč, J.; Fanfrlík, J.; Salahub, D.; Hobza, P. *J. Chem. Theory Comput.* **2009**, *5* (7), 1749–1760.

(200) Korth, M.; Pitoňák, M.; Řezáč, J.; Hobza, P. *J. Chem. Theory Comput.* **2010**, *6* (1), 344–352.

(201) Winget, P.; Selçuki, C.; Horn, A. H. C.; Martin, B.; Clark, T. *Theor. Chem. Acc.* **2003**, *110* (4), 254–266.

(202) Jurečka, P.; Černý, J.; Hobza, P.; Salahub, D. R. *J. Comput. Chem.* **2007**, *28* (2), 555–569.

(203) Repasky, M. P.; Chandrasekhar, J.; Jorgensen, W. L. *J. Comput. Chem.* **2002**, *23* (16), 1601–1622.

(204) Repasky, M. P.; Chandrasekhar, J.; Jorgensen, W. L. *J. Comput. Chem.* **2002**, *23* (4), 498–510.

(205) Stewart, J. J. P. *J. Mol. Model.* **2007**, *13* (12), 1173–1213.

(206) Stewart, J. J. P. *J. Mol. Model.* **2013**, *19* (1), 1–32.

(207) Rocha, G. B.; Freire, R. O.; Simas, A. M.; Stewart, J. J. P. *J. Comput. Chem.* **2006**, *27* (10), 1101–1111.

(208) Voityuk, A. A. *WIREs Comput. Mol .Sci.* **2013**, *3* (5), 515–527.

(209) Ridley, J.; Zerner, M. *Theor. Chim. Acta* **1973**, *32* (2), 111–134.

(210) Ridley, J. E.; Zerner, M. C. *Theor. Chim. Acta* **1976**, *42* (3), 223–236.

(211) Zerner, M. C.; Loew, G. H.; Kirchner, R. F.; Mueller-Westerhoff, U. T. *J. Am. Chem. Soc.* **1980**, *102* (2), 589–599.

(212) Karlsson, G.; Zerner, M. C. *Int. J. Quantum Chem.* **1973**, *7* (1), 35–49.

(213) Voityuk, A. A. *J. Chem. Theory Comput.* **2014**, *10* (11), 4950–4958.

(214) Da Motta Neto, J. D.; Zerner, M. C. *Int. J. Quantum Chem.* **2001**, *81* (3), 187–201.

(215) Koslowski, A.; Beck, M. E.; Thiel, W. *J. Comput. Chem.* **2003**, *24* (6), 714–726.

(216) Gadaczek, I.; Krause, K.; Hintze, K. J.; Bredow, T. *J. Chem. Theory Comput.* **2011**, *7* (11), 3675–3685.

(217) Frauenheim, T.; Seifert, G.; Elsterner, M.; Hajnal, Z.; Jungnickel, G.; Porezag, D.; Suhai, S.; Scholz, R. *Phys. status solidi* **2000**, *217* (1), 41–62.

(218) Slater, J. C.; Koster, G. F. *Phys. Rev.* **1954**, *94* (6), 1498–1524.

(219) Elstner, M. *Theor. Chem. Acc.* **2006**, *116* (1–3), 316–325.

(220) Pecchia, A.; Di Carlo, A.; Gagliardi, A.; Sanna, S.; Frauenheim, T.; Gutierrez, R. *Nano Lett.* **2004**, *4* (11), 2109–2114.

(221) Niehaus, T. A.; Suhai, S.; Della Sala, F.; Lugli, P.; Elstner, M.; Seifert, G.; Frauenheim, T. *Phys. Rev. B* **2001**, *63* (8), 85108.

(222) Koskinen, P.; Mäkinen, V. *Comput. Mater. Sci.* **2009**, *47* (1), 237–253.

(223) Brandenburg, J. G.; Grimme, S. *J. Phys. Chem. Lett.* **2014**, *5* (11), 1785–1789.

(224) Foulkes, W. M. C.; Haydock, R. *Phys. Rev. B* **1989**, *39* (17), 12520–12536.

(225) Porezag, D.; Frauenheim, T.; Köhler, T.; Seifert, G.; Kaschner, R. *Phys. Rev. B* **1995**, *51* (19), 12947–12957.

(226) Di Carlo, A.; Pecchia, A.; Latessa, L.; Frauenheim, T.; Seifert, G. In *Introducing Molecular Electronics*; Springer Berlin Heidelberg, 2006; pp 153–184.

(227) Yang, Y.; Yu, H.; York, D.; Elstner, M.; Cui, Q. *J. Chem. Theory Comput.* **2008**, *4* (12), 2067–2084.

(228) Heck, A.; Kranz, J. J.; Elstner, M. *J. Chem. Theory Comput.* **2016**, *12* (7), 3087–3096.

(229) Oddershede, J.; Jørgensen, P.; Yeager, D. L. *Comput. Phys. Reports* **1984**, *2* (2), 33–92.

(230) Oddershede, J. In *Methods in Computational Molecular Physics*; Springer US, 1992; pp 303–324.

(231) González, L.; Escudero, D.; Serrano-Andrés, L. *ChemPhysChem* **2012**, *13* (1), 28–51.

(232) Dyson, F. J. *Phys. Rev.* **1949**, *75* (11), 1736–1755.

(233) Kubo, R. *J. Phys. Soc. Japan* **1957**, *12* (6), 570–586.

(234) Lehmann, H. *Nuovo Cim.* **1954**, *11* (4), 342–357.

(235) Goscinski, O.; Lukman, B. *Chem. Phys. Lett.* **1970**, *7* (6), 573–576.

(236) Löwdin, P.-O. *Phys. Rev.* **1965**, *139* (2A), A357–A372.

(237) Toulouse, J. *Introduction to the calculation of molecular properties by response theory*; Paris, 2015.

(238) Maruhn, J. A.; Reinhard, P. G.; Suraud, E. *Simple Models of Many-Fermion Systems*; Springer: Heidelberg, London, New York, 2010.

(239) Dreuw, A.; Wormit, M. *WIREs Comput. Mol .Sci.* **2015**, *5* (1), 82–95.

(240) Schirmer, J. *Phys. Rev. A* **1982**, *26* (5), 2395–2416.

(241) Tuna, D.; Lefrancois, D.; Wolański, Ł.; Gozem, S.; Schapiro, I.; Andruniów, T.; Dreuw, A.; Olivucci, M. *J. Chem. Theory Comput.* **2015**, *11* (12), 5758–5781.

(242) Ruberti, M.; Yun, R.; Gokhberg, K.; Kopelke, S.; Cederbaum, L. S.; Tarantelli, F.; Averbukh, V. *J. Chem. Phys.* **2014**, *140* (18), 184107.

(243) Barth, A.; Cederbaum, L. S. *Phys. Rev. A* **1981**, *23* (3), 1038–1061.

(244) Wenzel, J.; Wormit, M.; Dreuw, A. *J. Comput. Chem.* **2014**, *35* (26), 1900–1915.

(245) Wenzel, J.; Dreuw, A. *J. Chem. Theory Comput.* **2016**, *12* (3), 1314–1330.

(246) Christiansen, O.; Koch, H.; Jørgensen, P. *Chem. Phys. Lett.* **1995**, *243* (5–6), 409–418.

(247) Christiansen, O.; Jorgensen, P.; Hättig, C. *Int. J. Quantum Chem.* **1998**, *68* (1), 1–52.

(248) Christiansen, O.; Koch, H.; Jørgensen, P. *J. Chem. Phys.* **1995**, *103* (17), 7429.

(249) Baudin, P.; Marín, J. S.; Cuesta, I. G.; Sánchez de Merás, A. M. J. *J. Chem. Phys.* **2014**, *140* (10), 104111.

(250) Monkhorst, H. J. *Int. J. Quantum Chem.* **2009**, *12* (S11), 421–432.

(251) Head-Gordon, M.; Lee, T. J. In *Modern Ideas in Coupled Cluster Theory*; Bartlett, R. J., Ed.; Singapore: World Sci., 1997; pp 221–253.

(252) Krylov, A. I. *Acc. Chem. Res.* **2006**, *39* (2), 83–91.

(253) Sekino, H.; Bartlett, R. J. *Int. J. Quantum Chem.* **1984**, *26* (S18), 255–265.

(254) Stanton, J. F.; Bartlett, R. J. *J. Chem. Phys.* **1993**, *98* (9), 7029.

(255) Krylov, A. I. *Annu. Rev. Phys. Chem.* **2008**, *59*, 433–462.

(256) Hättig, C. *J. Chem. Phys.* **2003**, *118* (17), 7751.

(257) Stanton, J. F.; Gauss, J. *J. Chem. Phys.* **1994**, *101* (10), 8938.

(258) Ferré, N.; Filatov, M.; Huix-Rotllant, M. *Density-Functional Methods for Excited States*; Springer-Verlag: Heidelberg, London, New York, 2016.

(259) Dreuw, A.; Head-Gordon, M. *Chem. Rev.* **2005**, *105* (11), 4009–4037.

(260) Runge, E.; Gross, E. K. U. *Phys. Rev. Lett.* **1984**, *52* (12), 997–1000.

(261) Maitra, N. T. *J. Chem. Phys.* **2016**, *144* (22), 220901.

(262) Maitra, N. T.; Burke, K.; Woodward, C. *Phys. Rev. Lett.* **2002**, *89* (2), 23002.

(263) *Fundamentals of Time-Dependent Density Functional Theory*; Marques, M. A. L., Maitra, N. T., Nogueira, F. M. S., Gross, E. K. U., Rubio, A., Eds.; Springer-Verlag: Berlin, Heidelberg, 2012.

(264) Petersilka, M.; Gossmann, U. J.; Gross, E. K. U. *Phys. Rev. Lett.* **1996**, *76* (8), 1212–1215.

(265) Casida, M. E. In *Recent Developments and Applications of Modern Density Functional Theory*; Seminario, J. M., Ed.; Elsevier Science: Amsterdam, 1996; p 391.

(266) Dreuw, A.; Head-Gordon, M. *J. Am. Chem. Soc.* **2004**, *126* (12), 4007–4016.

(267) Fuks, J. I.; Luo, K.; Sandoval, E. D.; Maitra, N. T. *Phys. Rev. Lett.* **2015**, *114* (18), 183002.

(268) Levine, B. G.; Ko, C.; Quenneville, J.; MartÍnez, T. J. *Mol. Phys.* **2006**, *104* (5–7), 1039–1051.

(269) Herbert, J. M.; Zhang, X.; Morrison, A. F.; Liu, J. *Acc. Chem. Res.* **2016**, *49* (5), 931–941.

(270) Shao, Y.; Head-Gordon, M.; Krylov, A. I. *J. Chem. Phys.* **2003**, *118* (11), 4807.

(271) Maitra, N. T.; Zhang, F.; Cave, R. J.; Burke, K. *J. Chem. Phys.* **2004**, *120* (13), 5932.

(272) Hirata, S.; Head-Gordon, M. *Chem. Phys. Lett.* **1999**, *314* (3), 291–299.

(273) Casida, M. E.; Gutierrez, F.; Guan, J.; Gadea, F.-X.; Salahub, D.; Daudey, J.-P. *J. Chem. Phys.* **2000**, *113* (17), 7062.

(274) Ziegler, T.; Seth, M.; Krykunov, M.; Autschbach, J.; Wang, F. *J. Chem. Phys.* **2009**, *130* (15), 154102.

(275) Ziegler, T.; Krykunov, M.; Cullen, J. *J. Chem. Phys.* **2012**, *136* (12), 124107.

(276) Cullen, J.; Krykunov, M.; Ziegler, T. *Chem. Phys.* **2011**, *391* (1), 11–18.

(277) Krykunov, M.; Grimme, S.; Ziegler, T. *J. Chem. Theory Comput.* **2012**, *8* (11), 4434–4440.

(278) Martin, R. L. *J. Chem. Phys.* **2003**, *118* (11), 4775.

(279) Ziegler, T.; Seth, M.; Krykunov, M.; Autschbach, J. *J. Chem. Phys.* **2008**, *129* (18), 184114.

(280) Hedin, L. *Phys. Rev.* **1965**, *139* (3A), A796–A823.

(281) Salpeter, E. E.; Bethe, H. A. *Phys. Rev.* **1951**, *84* (6), 1232–1242.

(282) Leng, X.; Jin, F.; Wei, M.; Ma, Y. *WIREs Comput. Mol .Sci.* **2016**, *6* (5), 532–550.

(283) Jacquemin, D.; Duchemin, I.; Blase, X. *J. Chem. Theory Comput.* **2015**, *11* (7), 3290–3304.

(284) Faber, C.; Boulanger, P.; Attaccalite, C.; Duchemin, I.; Blase, X. *Phil. Trans. R. Soc. A* **2014**, *372*, 20130271.

(285) Rohlfing, M.; Krüger, P.; Pollmann, J. *Phys. Rev. B* **1995**, *52* (3), 1905–1917.

(286) Körbel, S.; Boulanger, P.; Duchemin, I.; Blase, X.; Marques, M. A. L.; Botti, S. *J. Chem. Theory Comput.* **2014**, *10* (9), 3934–3943.

(287) Blase, X.; Attaccalite, C.; Olevano, V. *Phys. Rev. B* **2011**, *83* (11), 115103.

(288) Rohlfing, M.; Louie, S. G. *Phys. Rev. B* **2000**, *62* (8), 4927–4944.

(289) Chandross, M.; Hicks, J. C. *Phys. Rev. B* **1999**, *59* (15), 9699–9702.

(290) Schollwöck, U. *Rev. Mod. Phys.* **2005**, *77* (1), 259–315.

(291) Phipps, M. J. S.; Fox, T.; Tautermann, C. S.; Skylaris, C.-K. *Chem. Soc. Rev.* **2015**, *44* (10), 3177–3211.

(292) Morokuma, K. *J. Chem. Phys.* **1971**, *55* (3), 1236.

(293) Su, P.; Li, H. *J. Chem. Phys.* **2009**, *131* (1), 14102.

(294) Su, P.; Jiang, Z.; Chen, Z.; Wu, W. *J. Phys. Chem. A* **2014**, *118* (13), 2531–2542.

(295) Misquitta, A. J.; Jeziorski, B.; Szalewicz, K. *Phys. Rev. Lett.* **2003**, *91* (3), 33201.

(296) Misquitta, A. J.; Podeszwa, R.; Jeziorski, B.; Szalewicz, K. *J. Chem. Phys.* **2005**, *123* (21), 214103.

(297) Heßelmann, A.; Jansen, G. *Chem. Phys. Lett.* **2003**, *367* (5–6), 778–784.

(298) Heßelmann, A.; Jansen, G.; Schütz, M. *J. Chem. Phys.* **2005**, *122* (1), 14103.

(299) Jeziorski, B.; Moszynski, R.; Szalewicz, K. *Chem. Rev.* **1994**, *94* (7), 1887–1930.

(300) Szalewicz, K.; Patkowski, K.; Jeziorski, B. In *Intermolecular Forces and Clusters II*; Springer-Verlag: Berlin/Heidelberg; pp 43–117.

(301) Hirschfelder, J. O. *Chem. Phys. Lett.* **1967**, *1* (8), 325–329.

(302) Bloch, C. *Nucl. Phys.* **1958**, *6*, 329–347.

(303) Szalewicz, K. *WIREs Comput. Mol .Sci.* **2012**, *2* (2), 254–272.

(304) Adams, W. H. *Int. J. Quantum Chem.* **1990**, *38* (S24), 531–547.

(305) Tang, K. T.; Toennies, J. P.; Yiu, C. L. *J. Chem. Phys.* **1993**, *99* (1), 377.

(306) Klein, D. J. *Int. J. Quantum Chem.* **1987**, *32* (3), 377–396.

(307) Jeziorski, B.; Szalewicz, K.; Chałasiński, G. *Int. J. Quantum Chem.* **1978**, *14* (3), 271–287.

(308) Ćwiok, T.; Jeziorski, B.; Kołos, W.; Moszynski, R.; Szalewicz, K. *J. Chem. Phys.* **1992**, *97* (10), 7555.

(309) Szalewicz, K.; Jeziorski, B. *Mol. Phys.* **1979**, *38* (1), 191–208.

(310) Patkowski, K.; Szalewicz, K.; Jeziorski, B. *Theor. Chem. Acc.* **2010**, *127* (3), 211–221.

(311) Chalasinski, G.; Szczesniak, M. M. *Chem. Rev.* **1994**, *94* (7), 1723–1765.

(312) Patkowski, K.; Szalewicz, K. *J. Chem. Phys.* **2010**, *133* (9), 94304.

(313) Patkowski, K.; Cencek, W.; Jeziorska, M.; Jeziorski, B.; Szalewicz, K. *J. Phys. Chem. A* **2007**, *111* (31), 7611–7623.

(314) Williams, H. L.; Chabalowski, C. F. *J. Phys. Chem. A* **2001**, *105* (3), 646–659.

(315) Misquitta, A. J.; Szalewicz, K. *Intermolecular forces from asymptotically corrected density functional description of monomers*; 2002; Vol. 357.

(316) Longuet-Higgins, H. C. *Discuss. Faraday Soc.* **1965**, *40* (0), 7.

(317) Tomasi, J.; Mennucci, B.; Cammi, R. *Chem. Rev.* **2005**, *105* (8), 2999–3093.

(318) Tomasi, J.; Persico, M. *Chem. Rev.* **1994**, *94* (7), 2027–2094.

(319) Bondi, A. *J. Phys. Chem.* **1964**, *68* (3), 441–451.

(320) Connolly, M. *Science (80-.).* **1983**, *221* (4612).

(321) Connolly, M. L. *J. Appl. Cryst* **1983**, *16*, 548–558.

(322) Foresman, J. B.; Keith, T. A.; Wiberg, K. B.; Snoonian, J.; Frisch, M. J. *J. Phys. Chem.* **1996**, *100* (40), 16098–16104.

(323) Born, M. *Z. Phys.* **1920**, *45*, 1.

(324) Uhlig, H. H. *J. Phys. Chem.* **1937**, *41* (9), 1215–1226.

(325) Reiss, H.; Frisch, H. L.; Lebowitz, J. L. *J. Chem. Phys.* **1959**, *31* (2), 369.

(326) Reiss, H.; Frisch, H. L.; Helfand, E.; Lebowitz, J. L. *J. Chem. Phys.* **1960**, *32* (1), 119.

(327) Amovilli, C.; Mennucci, B. *J. Phys. Chem. B* **1997**, *101* (6), 1051–1057.

(328) Floris, F. M.; Tomasi, J.; Ahuir, J. L. P. *J. Comput. Chem.* **1991**, *12* (7), 784–791.

(329)   Tomasi, J. *Theor. Chem. Acc.* **2004**, *112* (4), 184–203.

(330)   Onsager, L. *J. Am. Chem. Soc.* **1936**, *58* (8), 1486–1493.

(331)   Miertuš, S.; Scrocco, E.; Tomasi, J. *Chem. Phys.* **1981**, *55* (1), 117–129.

(332)   Cossi, M.; Rega, N.; Scalmani, G.; Barone, V. *J. Comput. Chem.* **2003**, *24* (6), 669–681.

(333)   Barone, V.; Cossi, M. *J. Phys. Chem. A* **1998**, *102* (11), 1995–2001.

(334)   Scalmani, G.; Frisch, M. J. *J. Chem. Phys.* **2010**, *132* (11), 114110.

(335)   Klamt, A.; Schüürmann, G. *J. Chem. Soc. Perkin Trans. 2* **1993**, No. 5, 799.

(336)   Cossi, M.; Barone, V. *J. Chem. Phys.* **2001**, *115* (10), 4708.

(337)   Chipman, D. M. *J. Chem. Phys.* **2000**, *112* (13), 5558.

(338)   Cossi, M.; Rega, N.; Scalmani, G.; Barone, V. *J. Chem. Phys.* **2001**, *114* (13), 5691.

(339)   Atkins, P. W.; MacDermott, A. J. *J. Chem. Educ.* **1982**, *59* (5), 359.

(340)   Israelachvili, J. N. *Intermolecular and Surface Forces*, Third Edition; Elsevier Inc.: Waltham, 2011.

(341)   Scalmani, G.; Frisch, M. J.; Mennucci, B.; Tomasi, J.; Cammi, R.; Barone, V. *J. Chem. Phys.* **2006**, *124* (9), 94107.

(342)   Cammi, R.; Corni, S.; Mennucci, B.; Tomasi, J. *J. Chem. Phys.* **2005**, *122* (10), 104513.

(343)   Corni, S.; Cammi, R.; Mennucci, B.; Tomasi, J. *J. Chem. Phys.* **2005**, *123* (13), 134512.

(344)   Improta, R.; Barone, V.; Scalmani, G.; Frisch, M. J. *J. Chem. Phys.* **2006**, *125* (5), 54103.

(345)   Caricato, M.; Mennucci, B.; Tomasi, J.; Ingrosso, F.; Cammi, R.; Corni, S.; Scalmani, G. *J. Chem. Phys.* **2006**, *124* (12), 124520.

(346)   Halgren, T. A. *J. Am. Chem. Soc.* **1992**, *114* (20), 7827–7843.

(347)   Halgren, T. A. *J. Comput. Chem.* **1996**, *17* (5–6), 490–519.

(348)   Ren, P.; Ponder, J. W. *J. Phys. Chem. B* **2003**, *107* (24), 5933–5947.

(349)   Jorgensen, W. L.; Tirado-Rives, J. *J. Am. Chem. Soc.* **1988**, *110* (6), 1657–1666.

(350)   Morse, P. M. *Phys. Rev.* **1929**, *34* (1), 57–64.

(351)   Hodges, M. P.; Stone, A. J.; Xantheas, S. S. *J. Phys. Chem. A* **1997**, *101* (48), 9163–9168.

(352)   Dixon, R. W.; Kollman, P. A. *J. Comput. Chem.* **1997**, *18* (13), 1632–1646.

(353)   Stone, A. J. *J. Chem. Theory Comput.* **2005**, *1* (6), 1128–1132.

(354)   Lipkowitz, K. B.; Boyd, D. B. *Rev. Comput. Chem.* **2002**, *18*, 89.

(355)   Thole, B. T. *Chem. Phys.* **1981**, *59* (3), 341–350.

(356)   Ren, P.; Ponder, J. W. *J. Comput. Chem.* **2002**, *23* (16), 1497–1506.

(357)   Ren, P.; Wu, C.; Ponder, J. W. *J. Chem. Theory Comput.* **2011**, *7* (10), 3143–3161.

(358) Vanommeslaeghe, K.; Guvench, O.; MacKerell, A. D.; Jr. *Curr. Pharm. Des.* **2014**, *20* (20), 3281–3292.

(359) Lemkul, J. A.; Huang, J.; Roux, B.; MacKerell, A. D. *Chem. Rev.* **2016**, *116* (9), 4983–5013.

(360) Jorgensen, W. L.; Maxwell, D. S.; Tirado-Rives, J. *J. Am. Chem. Soc.* **1996**, *118* (45), 11225–11236.

(361) Weiner, S. J.; Kollman, P. A.; Nguyen, D. T.; Case, D. A. *J. Comput. Chem.* **1986**, *7* (2), 230–252.

(362) Weiner, S. J.; Kollman, P. A.; Case, D. A.; Singh, U. C.; Ghio, C.; Alagona, G.; Profeta, S.; Weiner, P. *J. Am. Chem. Soc.* **1984**, *106* (3), 765–784.

(363) Allinger, N. L.; Yuh, Y. H.; Lii, J. H. *J. Am. Chem. Soc.* **1989**, *111* (23), 8551–8566.

(364) Lii, J. H.; Allinger, N. L. *J. Am. Chem. Soc.* **1989**, *111* (23), 8566–8575.

(365) Lii, J. H.; Allinger, N. L. *J. Am. Chem. Soc.* **1989**, *111* (23), 8576–8582.

(366) Thomas, H. D.; Chen, K.; Allinger, N. L. *J. Am. Chem. Soc.* **1994**, *116* (13), 5887–5897.

(367) Allinger, N. L.; Chen, K.; Katzenellenbogen, J. A.; Wilson, S. R.; Anstead, G. M. *J. Comput. Chem.* **1996**, *17* (5–6), 747–755.

(368) Sprague, J. T.; Tai, J. C.; Yuh, Y.; Allinger, N. L. *J. Comput. Chem.* **1987**, *8* (5), 581–603.

(369) Allinger, N. L. *J. Am. Chem. Soc.* **1977**, *99* (25), 8127–8134.

(370) Nosé, S. *Mol. Phys.* **1984**, *52* (2), 255–268.

(371) Alder, B. J.; Wainwright, T. E. *J. Chem. Phys.* **1959**, *31* (2), 459.

(372) Boltzmann, L. *Vorlesungen über Gastheorie,*; J.A. Barth: Leipzig, 1896.

(373) Adcock, S. A.; McCammon, J. A. *Chem. Rev.* **2006**, *106* (5), 1589–1615.

(374) Ni, Z.; Zhang, X. *Sci. China Ser. E Technol. Sci.* **2009**, *52* (2), 484–490.

(375) Roney, A. B.; Space, B.; Castner, E. W.; Napoleon, R. L.; Moore, P. B. *J. Phys. Chem. B* **2004**, *108* (22), 7389–7401.

(376) Andersen, H. C. *J. Comput. Phys.* **1983**, *52* (1), 24–34.

(377) Ryckaert, J.-P.; Ciccotti, G.; Berendsen, H. J. . *J. Comput. Phys.* **1977**, *23* (3), 327–341.

(378) Tobias, D. J.; Brooks, C. L. *J. Chem. Phys.* **1988**, *89* (8), 5115.

(379) Verlet, L. *Phys. Rev.* **1967**, *159* (1), 98–103.

(380) Hairer, E.; Lubich, C.; Wanner, G. *Acta Numer.* **2003**, *12*, 399–450.

(381) Swope, W. C.; Andersen, H. C.; Berens, P. H.; Wilson, K. R. *J. Chem. Phys.* **1982**, *76* (1), 637.

(382) Lagrange, J. L. *Mécanique analytique*; Courcier: Paris, 1811.

(383) Berendsen, H. J. C.; Postma, J. P. M.; van Gunsteren, W. F.; DiNola, A.; Haak, J. R. *J. Chem. Phys.* **1984**, *81* (8), 3684.

(384) Schneider, T.; Stoll, E. *Phys. Rev. B* **1976**, *13* (3), 1216–1237.

(385) Evans, D. J. *Mol. Phys.* **1979**, *37* (6), 1745–1754.

(386) Broughton, J. Q.; Gilmer, G. H.; Weeks, J. D. *J. Chem. Phys.* **1981**, *75* (10), 5128.

(387) Andersen, H. C. *J. Chem. Phys.* **1980**, *72* (4), 2384.

(388) Ponder, J. W.; Richards, F. M. *J. Comput. Chem.* **1987**, *8* (7), 1016–1024.

(389) Nosé, S. *J. Chem. Phys.* **1984**, *81* (1), 511.

(390) Hoover, W. G. *Phys. Rev. A* **1985**, *31* (3), 1695–1697.

(391) Steinbach, P. J.; Brooks, B. R. *J. Comput. Chem.* **1994**, *15* (7), 667–683.

(392) Ewald, P. *Ann. Phys.* **1921**, *64*, 253–287.

(393) Natoli, V.; Ceperley, D. M. *J. Comput. Phys.* **1995**, *117* (1), 171–178.

(394) Chen, Z.-M.; Cagin, T.; Goddard, W. A. *J. Comput. Chem.* **1997**, *18* (11), 1365–1370.

(395) Greengard, L.; Rokhlin, V. *J. Comput. Phys.* **1997**, *135* (2), 280–292.

(396) Petersen, H. G.; Soelvason, D.; Perram, J. W.; Smith, E. R. *J. Chem. Phys.* **1994**, *101* (10), 8870.

(397) Hutter, J. *WIREs Comput. Mol .Sci.* **2012**, *2* (4), 604–612.

(398) Car, R.; Parrinello, M. *Phys. Rev. Lett.* **1985**, *55* (22), 2471–2474.

(399) Tse, J. S. *Annu. Rev. Phys. Chem.* **2002**, *53* (1), 249–290.

(400) Pastore, G.; Smargiassi, E.; Buda, F. *Phys. Rev. A* **1991**, *44* (10), 6334–6347.

(401) Marx, D.; Hutter, U. In *Modern Methods and Algorithms of Quantum Chemistry*; Grotendorst, J., Ed.; John von Neumann Institute for Computing: Jülich, 2000; Vol. 1, pp 301–449.

(402) Tuckerman, M. E.; Parrinello, M. *J. Chem. Phys.* **1994**, *101* (2), 1302.

(403) Niklasson, A. M. N. *Phys. Rev. Lett.* **2008**, *100* (12), 123004.

(404) Niklasson, A. M. N.; Tymczak, C. J.; Challacombe, M. *Phys. Rev. Lett.* **2006**, *97* (12), 123001.

(405) Schlegel, H. B. *Bull. Korean Chem. Soc* **2003**, *24* (6), 1.

(406) Warshel, A.; Levitt, M. *J. Mol. Biol.* **1976**, *103* (2), 227–249.

(407) van der Kamp, M. W.; Mulholland, A. J. *Biochemistry* **2013**, *52* (16), 2708–2728.

(408) Canuto, S. *Solvation Effects on Molecules and Biomolecules: Computational Methods and Applications*; Springer Science & Business Media: Heidelberg, 2010.

(409) Field, M. J.; Bash, P. A.; Karplus, M. *J. Comput. Chem.* **1990**, *11* (6), 700–733.

(410) Senn, H. M.; Thiel, W. *Angew. Chem. Int. Ed.* **2009**, *48* (7), 1198–1229.

(411) Brunk, E.; Rothlisberger, U. *Chem. Rev.* **2015**, *115* (12), 6217–6263.

(412) Svensson, M.; Humbel, S.; Froese, R. D. J.; Matsubara, T.; Sieber, S.; Morokuma, K. *J. Phys. Chem.* **1996**, *100* (50), 19357–19363.

(413) Dapprich, S.; Komáromi, I.; Byun, K. S.; Morokuma, K.; Frisch, M. J. *J. Mol. Struct. THEOCHEM* **1999**, *461*, 1–21.

(414) Murphy, R. B.; Philipp, D. M.; Friesner, R. A. *J. Comput. Chem.* **2000**, *21* (16), 1442–1457.

(415) Adamovic, I.; Gordon *, M. S. *Mol. Phys.* **2005**, *103* (2–3), 379–387.

(416) Gurunathan, P. K.; Acharya, A.; Ghosh, D.; Kosenkov, D.; Kaliman, I.; Shao, Y.; Krylov, A. I.; Slipchenko, L. V. *J. Phys. Chem. B* **2016**, *120* (27), 6562–6574.

(417) Gordon, M. S.; Freitag, M. A.; Bandyopadhyay, P.; Jensen, J. H.; Kairys, V.; Stevens, W. J. *J. Phys. Chem. A* **2001**, *105* (2), 293–307.

(418) Köhler, A.; Bässler, H. *Electronic Processes in Organic Semiconductors*; Wiley-VCH Verlag: Weinheim, 2015.

(419) Knupfer, M. *Appl. Phys. A* **2003**, *77* (5), 623–626.

(420) Tang, C. W. *Appl. Phys. Lett.* **1986**, *48* (2), 183.

(421) Halls, J. J. M.; Walsh, C. A.; Greenham, N. C.; Marseglia, E. A.; Friend, R. H.; Moratti, S. C.; Holmes, A. B. *Nature* **1995**, *376* (6540), 498–500.

(422) Yu, G.; Gao, J.; Hummelen, J. C.; Wudl, F.; Heeger, A. J. *Science* **1995**, *270* (5243), 1789–1791.

(423) Clarke, T. M.; Durrant, J. R. *Chem. Rev.* **2010**, *110* (11), 6736–6767.

(424) Borges, I.; Aquino, A. J. A.; Köhn, A.; Nieman, R.; Hase, W. L.; Chen, L. X.; Lischka, H. *J. Am. Chem. Soc.* **2013**, *135* (49), 18252–18255.

(425) Schwoerer, M.; Wolf, H. C. *Organic Molecular Solids*; WILEY-VCH Verlag GmbH: Weinheim, 2007.

(426) Shockley, W.; Queisser, H. J. *J. Appl. Phys.* **1961**, *32* (3), 510.

(427) Shockley, W. *Noble Lect.* **1956**.

(428) Koster, L. J. A.; Shaheen, S. E.; Hummelen, J. C. *Adv. Energy Mater.* **2012**, *2* (10), 1246–1253.

(429) Foertig, A.; Rauh, J.; Dyakonov, V.; Deibel, C. *Phys. Rev. B* **2012**, *86* (11), 115302.

(430) Giebink, N. C.; Wiederrecht, G. P.; Wasielewski, M. R.; Forrest, S. R. *Phys. Rev. B* **2010**, *82* (15), 155305.

(431) He, C.; Zhong, C.; Wu, H.; Yang, R.; Yang, W.; Huang, F.; Bazan, G. C.; Cao, Y. *J. Mater. Chem.* **2010**, *20* (13), 2617.

(432) Scharber, M. C.; Mühlbacher, D.; Koppe, M.; Denk, P.; Waldauf, C.; Heeger, A. J.; Brabec, C. J. *Adv. Mater.* **2006**, *18* (6), 789–794.

(433) Tayebjee, M. J. Y.; Hirst, L. C.; Ekins-Daukes, N. J.; Schmidt, T. W. *J. Appl. Phys.* **2010**, *108* (12), 124506.

(434) Tayebjee, M. J. Y.; McCamey, D. R.; Schmidt, T. W. *J. Phys. Chem. Lett.* **2015**, *6* (12), 2367–2378.

(435) Deibel, C.; Strobel, T.; Dyakonov, V. *Adv. Mater.* **2010**, *22* (37), 4097–4111.

(436) Veldman, D.; Meskers, S. C. J.; Janssen, R. A. J. *Adv. Funct. Mater.* **2009**, *19* (12), 1939–1948.

(437) Rau, U. *Phys. Rev. B* **2007**, *76* (8), 85303.

(438) Kirchartz, T.; Rau, U. *Phys. status solidi* **2008**, *205* (12), 2737–2751.

(439) Vandewal, K.; Tvingstedt, K.; Gadisa, A.; Inganäs, O.; Manca, J. V. *Nat. Mater.* **2009**, *8* (11), 904–909.

(440) Zou, Y.; Holmes, R. J. *ACS Appl. Mater. Interfaces* **2015**, *7* (33), 18306–18311.

(441) Kirchartz, T.; Taretto, K.; Rau, U. *J. Phys. Chem. C* **2009**, *113* (41), 17958–17966.

(442) Vandewal, K.; Tvingstedt, K.; Inganäs, O. In *Semiconductors and Semimetals*; 2011; Vol. 85, pp 261–295.

(443) Scharber, M. C.; Sariciftci, N. S. *Prog. Polym. Sci.* **2013**, *38* (12), 1929–1940.

(444) Giebink, N. C.; Wiederrecht, G. P.; Wasielewski, M. R.; Forrest, S. R. *Phys. Rev. B* **2011**, *83* (19), 195326.

(445) Liao, S.-H.; Jhuo, H.-J.; Yeh, P.-N.; Cheng, Y.-S.; Li, Y.-L.; Lee, Y.-H.; Sharma, S.; Chen, S.-A. *Sci. Rep.* **2014**, *4*, 6813.

(446) Liu, Y.; Zhao, J.; Li, Z.; Mu, C.; Ma, W.; Hu, H.; Jiang, K.; Lin, H.; Ade, H.; Yan, H.; Yu, G.; Gao, J.; Hummelen, J. C.; Wudl, F.; Heeger, A. J.; Halls, J. J. M. *Nat. Commun.* **2014**, *5*, 5293.

(447) Zhou, H.; Zhang, Y.; Mai, C.-K.; Collins, S. D.; Bazan, G. C.; Nguyen, T.-Q.; Heeger, A. J. *Adv. Mater.* **2015**, *27* (10), 1767–1773.

(448) You, J.; Dou, L.; Yoshimura, K.; Kato, T.; Ohya, K.; Moriarty, T.; Emery, K.; Chen, C.-C.; Gao, J.; Li, G.; Yang, Y. *Nat. Commun.* **2013**, *4*, 1446.

(449) Schlenker, C. W.; Thompson, M. E. *Chem. Commun.* **2011**, *47* (13), 3702.

(450) Ohkita, H.; Cook, S.; Astuti, Y.; Duffy, W.; Tierney, S.; Zhang, W.; Heeney, M.; McCulloch, I.; Nelson, J.; Bradley, D. D. C.; Durrant, J. R. *J. Am. Chem. Soc.* **2008**, *130* (10), 3030–3042.

(451) Gregg, B. A. *J. Phys. Chem. Lett.* **2011**, *2* (24), 3013–3015.

(452) Nayak, P. K.; Narasimhan, K. L.; Cahen, D. *J. Phys. Chem. Lett.* **2013**, *4* (10), 1707–1717.

(453) Akaike, K.; Koch, N.; Heimel, G.; Oehzelt, M. *Adv. Mater. Interfaces* **2015**, *2* (13), 1500232.

(454) Yost, S. R.; Wang, L.-P.; Van Voorhis, T. *J. Phys. Chem. C* **2011**, *115* (29), 14431–14436.

(455) Zhu, X.-Y.; Yang, Q.; Muntwiler, M. *Acc. Chem. Res.* **2009**, *42* (11), 1779–1787.

(456) Linares, M.; Beljonne, D.; Cornil, J.; Lancaster, K.; Brédas, J.-L.; Verlaak, S.; Mityashin, A.; Heremans, P.; Fuchs, A.; Lennartz, C.; Idé, J.; Méreau, R.; Aurel, P.; Ducasse, L.; Castet, F. *J. Phys. Chem. C* **2010**, *114* (7), 3215–3224.

(457) McMahon, D. P.; Cheung, D. L.; Troisi, A. *J. Phys. Chem. Lett.* **2011**, *2* (21), 2737–2741.

(458) Shen, X.; Han, G.; Fan, D.; Xie, Y.; Yi, Y. *J. Phys. Chem. C* **2015**, *119* (21), 11320–11326.

(459) Schulze, M.; Hänsel, M.; Tegeder, P. *J. Phys. Chem. C* **2014**, *118* (49), 28527–28534.

(460) Yost, S. R.; Van Voorhis, T. *J. Phys. Chem. C* **2013**, *117* (11), 5617–5625.

(461) Li, W.; Roelofs, W. S. C.; Wienk, M. M.; Janssen, R. A. J. *J. Am. Chem. Soc.* **2012**, *134* (33), 13787–13795.

(462) Lu, L.; Zheng, T.; Wu, Q.; Schneider, A. M.; Zhao, D.; Yu, L. *Chem. Rev.* **2015**, *115* (23), 12666–12731.

(463) Laquai, F.; Andrienko, D.; Mauer, R.; Blom, P. W. M. *Macromol. Rapid Commun.* **2015**, *36* (11), 1001–1025.

(464) Troisi, A. *Chem. Soc. Rev.* **2011**, *40* (5), 2347.

(465) Xue, J.; Rand, B. P.; Uchida, S.; Forrest, S. R. *Adv. Mater.* **2005**, *17* (1), 66–71.

(466) Warnan, J.; El Labban, A.; Cabanetos, C.; Hoke, E. T.; Shukla, P. K.; Risko, C.; Brédas, J.-L.; McGehee, M. D.; Beaujuge, P. M. *Chem. Mater.* **2014**, *26* (7), 2299–2306.

(467) Meager, I.; Ashraf, R. S.; Mollinger, S.; Schroeder, B. C.; Bronstein, H.; Beatrup, D.; Vezie, M. S.; Kirchartz, T.; Salleo, A.; Nelson, J.; McCulloch, I. *J. Am. Chem. Soc.* **2013**, *135* (31), 11537–11540.

(468) Yang, L.; Tumbleston, J. R.; Zhou, H.; Ade, H.; You, W. *Energy Environ. Sci.* **2013**, *6* (1), 316–326.

(469) Lou, S. J.; Szarko, J. M.; Xu, T.; Yu, L.; Marks, T. J.; Chen, L. X. *J. Am. Chem. Soc.* **2011**, *133* (51), 20661–20663.

(470) Park, C.-D.; Fleetham, T. A.; Li, J.; Vogt, B. D. *Org. Electron.* **2011**, *12* (9), 1465–1470.

(471) Earmme, T.; Hwang, Y.-J.; Subramaniyan, S.; Jenekhe, S. A. *Adv. Mater.* **2014**, *26* (35), 6080–6085.

(472) Savenije, T. J.; Kroeze, J. E.; Yang, X.; Loos, J. *Adv. Funct. Mater.* **2005**, *15* (8), 1260–1266.

(473) Sharma, G. D.; Suresh, P.; Sharma, S. S.; Vijay, Y. K.; Mikroyannidis, J. A. *ACS Appl. Mater. Interfaces* **2010**, *2* (2), 504–510.

(474) Kim, S.-S.; Na, S.-I.; Jo, J.; Kim, D.-Y.; Nah, Y.-C. *Appl. Phys. Lett.* **2008**, *93* (7), 73307.

(475) Notarianni, M.; Vernon, K.; Chou, A.; Aljada, M.; Liu, J.; Motta, N. *Sol. Energy* **2014**, *106*, 23–37.

(476) Schünemann, C.; Wynands, D.; Eichhorn, K.-J.; Stamm, M.; Leo, K.; Riede, M. *J. Phys. Chem. C* **2013**, *117* (22), 11600–11609.

(477) Guskova, O.; Schünemann, C.; Eichhorn, K.-J.; Walzer, K.; Levichkova, M.; Grundmann, S.; Sommer, J.-U. *J. Phys. Chem. C* **2013**, *117* (33), 17285–17293.

(478) Currie, M. J.; Mapel, J. K.; Heidel, T. D.; Goffri, S.; Baldo, M. A. *Science (80-.).* **2008**, *321* (5886), 226–228.

(479) Heremans, P.; Cheyns, D.; Rand, B. P. *Acc. Chem. Res.* **2009**, *42* (11), 1740–1747.

(480) Ehrenreich, P.; Birkhold, S. T.; Zimmermann, E.; Hu, H.; Kim, K.-D.; Weickert, J.; Pfadler, T.; Schmidt-Mende, L. *Sci. Rep.* **2016**, *6*, 32434.

(481) Boudreault, P.-L. T.; Najari, A.; Leclerc, M. *Chem. Mater.* **2011**, *23* (3), 456–469.

(482) Dou, L.; Liu, Y.; Hong, Z.; Li, G.; Yang, Y. *Chem. Rev.* **2015**, *115* (23), 12633–12665.

(483) Liu, C.; Wang, K.; Gong, X.; Heeger, A. J. *Chem. Soc. Rev.* **2016**, *45* (17), 4825–4846.

(484) Zhou, H.; Yang, L.; You, W. *Macromolecules* **2012**, *45* (2), 607–632.

(485) Cheng, Y.-J.; Yang, S.-H.; Hsu, C.-S. *Chem. Rev.* **2009**, *109* (11), 5868–5923.

(486) Ameri, T.; Khoram, P.; Min, J.; Brabec, C. J. *Adv. Mater.* **2013**, *25* (31), 4245–4266.

(487) Yang, L.; Yan, L.; You, W. *J. Phys. Chem. Lett.* **2013**, *4* (11), 1802–1810.

(488) Ameri, T.; Dennler, G.; Lungenschmied, C.; Brabec, C. J. *Energy Environ. Sci.* **2009**, *2* (4), 347.

(489) Akselrod, G. M.; Deotare, P. B.; Thompson, N. J.; Lee, J.; Tisdale, W. A.; Baldo, M. A.; Menon, V. M.; Bulović, V. *Nat. Commun.* **2014**, *5*, 3646.

(490) Yost, S. R.; Hontz, E.; Yeganeh, S.; Van Voorhis, T. *J. Phys. Chem. C* **2012**, *116* (33), 17369–17377.

(491) Najafov, H.; Lee, B.; Zhou, Q.; Feldman, L. C.; Podzorov, V. *Nat. Mater.* **2010**, *9* (11), 938–943.

(492) Chen, L.-M.; Hong, Z.; Li, G.; Yang, Y. *Adv. Mater.* **2009**, *21* (14–15), 1434–1449.

(493) Oosterhout, S. D.; Wienk, M. M.; van Bavel, S. S.; Thiedmann, R.; Jan Anton Koster, L.; Gilot, J.; Loos, J.; Schmidt, V.; Janssen, R. A. J.; Koster, L. J. A.; Gilot, J.; Loos, J.; Schmidt, V.; Janssen, R. A. J. *Nat. Mater.* **2009**, *8* (10), 818–824.

(494) Xu, Z.; Chen, L.-M.; Yang, G.; Huang, C.-H.; Hou, J.; Wu, Y.; Li, G.; Hsu, C.-S.; Yang, Y. *Adv. Funct. Mater.* **2009**, *19* (8), 1227–1234.

(495) Bartelt, J. A.; Beiley, Z. M.; Hoke, E. T.; Mateker, W. R.; Douglas, J. D.; Collins, B. A.; Tumbleston, J. R.; Graham, K. R.; Amassian, A.; Ade, H.; Fréchet, J. M. J.; Toney, M. F.; McGehee, M. D. *Adv. Energy Mater.* **2013**, *3* (3), 364–374.

(496) Bartelt, J. A.; Lam, D.; Burke, T. M.; Sweetnam, S. M.; McGehee, M. D. *Adv. Energy Mater.* **2015**, *5* (15), 1500577.

(497) van Franeker, J. J.; Heintges, G. H. L.; Schaefer, C.; Portale, G.; Li, W.; Wienk, M. M.; van der Schoot, P.; Janssen, R. A. J. *J. Am. Chem. Soc.* **2015**, *137* (36), 11783–11794.

(498) Würfel, U.; Neher, D.; Spies, A.; Albrecht, S. *Nat. Commun.* **2015**, *6*, 6951.

(499) Pingree, L. S. C.; MacLeod, B. A.; Ginger, D. S. *J. Phys. Chem. C* **2008**, *112* (21), 7922–7927.

(500) Hu, X.; Chen, L.; Chen, Y. *J. Phys. Chem. C* **2014**, *118* (19), 9930–9938.

(501) Bejbouji, H.; Vignau, L.; Miane, J. L.; Dang, M.-T.; Oualim, E. M.; Harmouchi, M.; Mouhsen, A. *Sol. Energy Mater. Sol. Cells* **2010**, *94* (2), 176–181.

(502) Boix, P. P.; Ajuria, J.; Etxebarria, I.; Pacios, R.; Garcia-Belmonte, G.; Bisquert, J. *J. Phys. Chem. Lett.* **2011**, *2* (5), 407–411.

(503) Steim, R.; Ren Kogler, ab F.; Brabec, C. J. *J. Mater. Chem.* **2010**, *20*, 2499–2512.

(504) Liu, Y.; Chen, C.-C.; Hong, Z.; Gao, J.; Yang, Y. M.; Zhou, H.; Dou, L.; Li, G.; Yang, Y. *Sci. Rep.* **2013**, *3*, 3356.

(505) Blouin, N.; Michaud, A.; Gendron, D.; Wakim, S.; Blair, E.; Neagu-Plesu, R.; Belletête, M.; Durocher, G.; Tao, Y.; Leclerc, M. *J. Am. Chem. Soc.* **2008**, *130* (2), 732–742.

(506) Li, W.; Hendriks, K. H.; Wienk, M. M.; Janssen, R. A. J. *Acc. Chem. Res.* **2016**, *49* (1), 78–85.

(507) de Gier, H. D.; Jahani, F.; Broer, R.; Hummelen, J. C.; Havenith, R. W. A. *J. Phys. Chem. A* **2016**, *120* (27), 4664–4671.

(508) Yang, B.; Yuan, Y.; Sharma, P.; Poddar, S.; Korlacki, R.; Ducharme, S.; Gruverman, A.; Saraf, R.; Huang, J. *Adv. Mater.* **2012**, *24* (11), 1455–1460.

(509) Yuan, Y.; Reece, T. J.; Sharma, P.; Poddar, S.; Ducharme, S.; Gruverman, A.; Yang, Y.; Huang, J. *Nat. Mater.* **2011**, *10* (4), 296–302.

(510) Vandewal, K.; Oosterbaan, W. D.; Bertho, S.; Vrindts, V.; Gadisa, A.; Lutsen, L.; Vanderzande, D.; Manca, J. V. *Appl. Phys. Lett.* **2009**, *95* (12), 123303.

(511) Perez, M. D.; Borek, C.; Forrest, S. R.; Thompson, M. E. *J. Am. Chem. Soc.* **2009**, *131* (26), 9281–9286.

(512) Zhang, G.; Clarke, T. M.; Mozer, A. J. *J. Phys. Chem. C* **2016**, *120* (13), 7033–7043.

(513) Jortner, J. *J. Chem. Phys.* **1976**, *64* (12), 4860.

(514) Marcus, R. A. *J. Chem. Phys.* **1956**, *24* (5), 966.

(515) Barbara, P. F.; Meyer, T. J.; Ratner, M. A. *J. Phys. Chem.* **1996**, *100* (31), 13148–13168.

(516) Bardeen, C. J. *Annu. Rev. Phys. Chem.* **2014**, *65* (1), 127–148.

(517) Fornari, R. P.; Aragó, J.; Troisi, A. *J. Phys. Chem. C* **2016**, *120* (15), 7987–7996.

(518) Aragó, J.; Troisi, A. *Adv. Funct. Mater.* **2016**, *26* (14), 2316–2325.

(519) Stehr, V.; Engels, B.; Deibel, C.; Fink, R. F. *J. Chem. Phys.* **2014**, *140* (2), 24503.

(520) Förster, T. *Ann. Phys.* **1948**, *437* (1–2), 55–75.

(521) Hsu, C.-P.; You, Z.-Q.; Chen, H.-C. *J. Phys. Chem. C* **2008**, *112* (4), 1204–1212.

(522) Dexter, D. L. *J. Chem. Phys.* **1953**, *21* (5), 836.

(523) You, Z.-Q.; Hsu, C.-P. *Int. J. Quantum Chem.* **2014**, *114* (2), 102–115.

(524) Brédas, J.-L.; Beljonne, D.; Coropceanu, V.; Cornil, J. *Chem. Rev.* **2004**, *104* (11), 4971–5004.

(525) Madigan, C.; Bulović, V. *Phys. Rev. Lett.* **2006**, *96* (4), 46404.

(526) Fishchuk, I. I.; Kadashchuk, A.; Hoffmann, S. T.; Athanasopoulos, S.; Genoe, J.; Bässler, H.; Köhler, A. *Phys. Rev. B* **2013**, *88* (12), 125202.

(527) Yao, Y.; Si, W.; Hou, X.; Wu, C.-Q. *J. Chem. Phys.* **2012**, *136* (23), 234106.

(528) Zhang, X.; Li, Z.; Lu, G. *Phys. Rev. B* **2011**, *84* (23), 235208.

(529) Bjorgaard, J. A.; Köse, M. E. *J. Phys. Chem. C* **2014**, *118* (11), 5756–5761.

(530) Tamai, Y.; Ohkita, H.; Benten, H.; Ito, S. *J. Phys. Chem. Lett.* **2015**, *6* (17), 3417–3428.

(531) Papadopoulos, T. A.; Muccioli, L.; Athanasopoulos, S.; Walker, A. B.; Zannoni, C.; Beljonne, D. *Chem. Sci.* **2011**, *2* (6), 1025.

(532) Stehr, V.; Fink, R. F.; Engels, B.; Pflaum, J.; Deibel, C. *J. Chem. Theory Comput.* **2014**, *10* (3), 1242–1255.

(533) Smith, M. B.; Michl, J. *Chem. Rev.* **2010**, *110* (11), 6891–6936.

(534) Smith, M. B.; Michl, J. *Annu. Rev. Phys. Chem.* **2013**, *64*, 361–386.

(535) Johnson, J. C.; Nozik, A. J.; Michl, J. *Acc. Chem. Res.* **2013**, *46* (6), 1290–1299.

(536) Zimmerman, P. M.; Bell, F.; Casanova, D.; Head-Gordon, M. *J. Am. Chem. Soc.* **2011**, *133* (49), 19944–19952.

(537) Musser, A. J.; Liebel, M.; Schnedermann, C.; Wende, T.; Kehoe, T. B.; Rao, A.; Kukura, P. *Nat. Phys.* **2015**, *11* (4), 352–357.

(538) Baldo, M. A.; Adachi, C.; Forrest, S. R. *Phys. Rev. B* **2000**, *62* (16), 10967–10977.

(539) Luo, Y.; Aziz, H. *Adv. Funct. Mater.* **2010**, *20* (8), 1285–1293.

(540) Trupke, T.; Green, M. A.; Würfel, P. *J. Appl. Phys.* **2002**, *92* (7), 4117.

(541) Schulze, T. F.; Schmidt, T. W. *Energy Environ. Sci.* **2015**, *8* (1), 103–125.

(542) Holstein, T. *Ann. Phys.* **1959**, *8* (3), 325–342.

(543) Holstein, T. *Ann. Phys.* **1959**, *8* (3), 343–389.

(544) Coropceanu, V.; Cornil, J.; da Silva Filho, D. A.; Olivier, Y.; Silbey, R.; Brédas, J.-L. *Chem. Rev.* **2007**, *107* (4), 926–952.

(545) Kador, L. *J. Chem. Phys.* **1991**, *95* (8), 5574.

(546) Dieckmann, A.; Bässler, H.; Borsenberger, P. M. *J. Chem. Phys.* **1993**, *99* (10), 8136.

(547) Miller, A.; Abrahams, E. *Phys. Rev.* **1960**, *120* (3), 745–755.

(548) Hertel, D.; Bässler, H. *ChemPhysChem* **2008**, *9* (5), 666–688.

(549) Vehoff, T.; Chung, Y. S.; Johnston, K.; Troisi, A.; Yoon, D. Y.; Andrienko, D. *J. Phys. Chem. C* **2010**, *114* (23), 10592–10597.

(550) Vehoff, T.; Baumeier, B.; Troisi, A.; Andrienko, D. *J. Am. Chem. Soc.* **2010**, *132* (33), 11702–11708.

(551) Vehoff, T.; Baumeier, B.; Andrienko, D. *J. Chem. Phys.* **2010**, *133* (13), 134901.

(552) Kemper, T. W.; Larsen, R. E.; Gennett, T. *J. Phys. Chem. C* **2015**, *119* (37), 21369–21375.

(553) Li, H.; Duan, L.; Sun, Y.; Zhang, D.; Wang, L.; Qiu, Y. *J. Phys. Chem. C* **2013**, *117* (32), 16336–16342.

(554) Kwiatkowski, J. J.; Frost, J. M.; Nelson, J. *Nano Lett.* **2009**, *9* (3), 1085–1090.

(555) Kirkpatrick, J.; Marcon, V.; Nelson, J.; Kremer, K.; Andrienko, D. *Phys. Rev. Lett.* **2007**, *98* (22), 227402.

(556) Marcon, V.; Breiby, D. W.; Pisula, W.; Dahl, J.; Kirkpatrick, J.; Patwardhan, S.; Grozema, F.; Andrienko, D. *J. Am. Chem. Soc.* **2009**, *131* (32), 11426–11432.

(557) Rühle, V.; Lukyanov, A.; May, F.; Schrader, M.; Vehoff, T.; Kirkpatrick, J.; Baumeier, B.; Andrienko, D. *J. Chem. Theory Comput.* **2011**, *7* (10), 3335–3345.

(558) Lukyanov, A.; Andrienko, D. *Phys. Rev. B* **2010**, *82* (19), 193202.

(559) Kwiatkowski, J. J.; Nelson, J.; Li, H.; Bredas, J. L.; Wenzel, W.; Lennartz, C. *Phys. Chem. Chem. Phys.* **2008**, *10* (14), 1852.

(560) Difley, S.; Wang, L.-P.; Yeganeh, S.; Yost, S. R.; Van Voorhis, T. *Acc. Chem. Res.* **2010**, *43* (7), 995–1004.

(561) Su, W. P.; Schrieffer, J. R.; Heeger, A. J. *Phys. Rev. B* **1980**, *22* (4), 2099–2111.

(562) Troisi, A.; Orlandi, G. *J. Phys. Chem. A* **2006**, *110* (11), 4065–4070.

(563) Troisi, A.; Orlandi, G. *Phys. Rev. Lett.* **2006**, *96* (8), 86601.

(564) Troisi, A. *J. Chem. Phys.* **2011**, *134* (3), 34702.

(565) Tummala, N. R.; Zheng, Z.; Aziz, S. G.; Coropceanu, V.; Brédas, J.-L. *J. Phys. Chem. Lett.* **2015**, *6* (18), 3657–3662.

(566) Zou, Y.; Holmes, R. J. *Adv. Energy Mater.* **2015**, *5* (12), 1500019.

(567) Few, S.; Frost, J. M.; Nelson, J. *Phys. Chem. Chem. Phys.* **2015**, *17* (4), 2311–2325.

(568) Cornil, J.; Verlaak, S.; Martinelli, N.; Mityashin, A.; Olivier, Y.; Van Regemorter, T.; D'Avino, G.; Muccioli, L.; Zannoni, C.; Castet, F.; Beljonne, D.; Heremans, P. *Acc. Chem. Res.* **2013**, *46* (2), 434–443.

(569) Mityashin, A.; Olivier, Y.; Van Regemorter, T.; Rolin, C.; Verlaak, S.; Martinelli, N. G.; Beljonne, D.; Cornil, J.; Genoe, J.; Heremans, P. *Adv. Mater.* **2012**, *24* (12), 1535–1539.

(570) Onsager, L. *Phys. Rev.* **1938**, *54* (8), 554–557.

(571) Smoluchowski, M. von. *Phys. Zeitschrift* **1917**, *17*, 537–571.

(572) Langevin, M. P. *Ann. Chim. PHys.* **1903**, *28*, 433.

(573) Chance, R. R.; Braun, C. L. *J. Chem. Phys.* **1976**, *64* (9), 3573.

(574) Braun, C. L. *J. Chem. Phys.* **1984**, *80* (9), 4157.

(575) Beljonne, D.; Cornil, J.; Muccioli, L.; Zannoni, C.; Brédas, J.-L.; Castet, F. *Chem. Mater.* **2011**, *23* (3), 591–609.

(576) Muccioli, L.; D'Avino, G.; Berardi, R.; Orlandi, S.; Pizzirusso, A.; Ricci, M.; Roscioni, O. M.; Zannoni, C. *Top. Curr. Chem.* **2014**, *352*, 39–102.

(577) Martinelli, N. G.; Olivier, Y.; Athanasopoulos, S.; Ruiz Delgado, M.-C.; Pigg, K. R.; da Silva Filho, D. A.; Sánchez-Carrera, R. S.; Venuti, E.; Della Valle, R. G.; Brédas, J.-L.; Beljonne, D.; Cornil, J. *ChemPhysChem* **2009**, *10* (13), 2265–2273.

(578) Martinelli, N. G.; Idé, J.; Sánchez-Carrera, R. S.; Coropceanu, V.; Brédas, J.-L.; Ducasse, L.; Castet, F.; Cornil, J.; Beljonne, D. *J. Phys. Chem. C* **2010**, *114* (48), 20678–20685.

(579) Martinelli, N. G.; Savini, M.; Muccioli, L.; Olivier, Y.; Castet, F.; Zannoni, C.; Beljonne, D.; Cornil, J. *Adv. Funct. Mater.* **2009**, *19* (20), 3254–3261.

(580) Fu, Y.-T.; Risko, C.; Brédas, J.-L. *Adv. Mater.* **2013**, *25* (6), 878–882.

(581) Song, Y.; Clafton, S. N.; Pensack, R. D.; Kee, T. W.; Scholes, G. D. *Nat. Commun.* **2014**, *5*, 4933.

(582) Vithanage, D. A.; Devižis, A.; Abramavičius, V.; Infahsaeng, Y.; Abramavičius, D.; MacKenzie, R. C. I.; Keivanidis, P. E.; Yartsev, A.; Hertel, D.; Nelson, J.; Sundström, V.; Gulbinas, V. *Nat. Commun.* **2013**, *4*, 87–95.

(583) Kanai, Y.; Grossman, J. C. *Nano Lett.* **2007**, *7* (7), 1967–1972.

(584) Liu, T.; Cheung, D. L.; Troisi, A. *Phys. Chem. Chem. Phys.* **2011**, *13* (48), 21461–21470.

(585) Few, S.; Frost, J. M.; Kirkpatrick, J.; Nelson, J. *J. Phys. Chem. C* **2014**, *118* (16), 8253–8261.

(586) Lee, J.; Vandewal, K.; Yost, S. R.; Bahlke, M. E.; Goris, L.; Baldo, M. A.; Manca, J. V; Van Voorhis, T. *J. Am. Chem. Soc.* **2010**, *132* (34), 11878–11880.

(587) He, S.-J.; Wang, D.-K.; Jiang, N.; Lu, Z.-H. *J. Phys. Chem. C* **2016**, *120* (38), 21325–21329.

(588) Coffey, D. C.; Larson, B. W.; Hains, A. W.; Whitaker, J. B.; Kopidakis, N.; Boltalina, O. V.; Strauss, S. H.; Rumbles, G. *J. Phys. Chem. C* **2012**, *116* (16), 8916–8923.

(589) Izawa, S.; Nakano, K.; Suzuki, K.; Hashimoto, K.; Tajima, K. *Adv. Mater.* **2015**, *27* (19), 3025–3031.

(590) Jailaubekov, A. E.; Willard, A. P.; Tritsch, J. R.; Chan, W.-L.; Sai, N.; Gearba, R.; Kaake, L. G.; Williams, K. J.; Leung, K.; Rossky, P. J.; Zhu, X.-Y. *Nat. Mater.* **2013**, *12* (1), 66–73.

(591) Bakulin, A. A.; Rao, A.; Pavelyev, V. G.; van Loosdrecht, P. H. M.; Pshenichnikov, M. S.; Niedzialek, D.; Cornil, J.; Beljonne, D.; Friend, R. H. *Science* **2012**, *335* (6074), 1340–1344.

(592) Vázquez, H.; Troisi, A. *Phys. Rev. B* **2013**, *88* (20), 205304.

(593) D'Avino, G.; Muccioli, L.; Olivier, Y.; Beljonne, D. *J. Phys. Chem. Lett.* **2016**, *7* (3), 536–540.

(594) Caruso, D.; Troisi, A. *Proc. Natl. Acad. Sci.* **2012**, *109* (34), 13498–13502.

(595) Ma, H.; Troisi, A. *Adv. Mater.* **2014**, *26* (35), 6163–6167.

(596) Tamura, H.; Burghardt, I. *J. Am. Chem. Soc.* **2013**, *135* (44), 16364–16367.

(597) Verlaak, S.; Beljonne, D.; Cheyns, D.; Rolin, C.; Linares, M.; Castet, F.; Cornil, J.; Heremans, P. *Adv. Funct. Mater.* **2009**, *19* (23), 3809–3814.

(598) Idé, J.; Mothy, S.; Savoyant, A.; Fritsch, A.; Aurel, P.; Méreau, R.; Ducasse, L.; Cornil, J.; Beljonne, D.; Castet, F. *Int. J. Quantum Chem.* **2013**, *113* (4), 580–584.

(599) Akaike, K.; Kanai, K.; Ouchi, Y.; Seki, K. *Adv. Funct. Mater.* **2010**, *20* (5), 715–721.

(600) Mothy, S.; Guillaume, M.; Idé, J.; Castet, F.; Ducasse, L.; Cornil, J.; Beljonne, D. *J. Phys. Chem. Lett.* **2012**, *3* (17), 2374–2378.

(601) Castet, F.; D'Avino, G.; Muccioli, L.; Cornil, J.; Beljonne, D. *Phys. Chem. Chem. Phys.* **2014**, *16* (38), 20279–20290.

(602) D'Avino, G.; Mothy, S.; Muccioli, L.; Zannoni, C.; Wang, L.; Cornil, J.; Beljonne, D.; Castet, F. *J. Phys. Chem. C* **2013**, *117* (25), 12981–12990.

(603) Norton, J. E.; Brédas, J.-L. *J. Am. Chem. Soc.* **2008**, *130* (37), 12377–12384.

(604) Ryno, S. M.; Risko, C.; Brédas, J.-L. *ACS Appl. Mater. Interfaces* **2016**, *8* (22), 14053–14062.

(605) Poelking, C.; Andrienko, D. *J. Am. Chem. Soc.* **2015**, *137* (19), 6320–6326.

(606) Savoie, B. M.; Rao, A.; Bakulin, A. A.; Gelinas, S.; Movaghar, B.; Friend, R. H.; Marks, T. J.; Ratner, M. A. *J. Am. Chem. Soc.* **2014**, *136* (7), 2876–2884.

(607) Xu, L.; Wang, J.; Villa, M. de A.; Daunis, T. B.; Lee, Y.-J.; Malko, A. V.; Hsu, J. W. P. *J. Phys. Chem. C* **2016**, *120* (30), 16470–16477.

(608) Rand, B. P.; Cheyns, D.; Vasseur, K.; Giebink, N. C.; Mothy, S.; Yi, Y.; Coropceanu, V.; Beljonne, D.; Cornil, J.; Brédas, J.-L.; Genoe, J. *Adv. Funct. Mater.* **2012**, *22* (14), 2987–2995.

(609) Holcombe, T. W.; Norton, J. E.; Rivnay, J.; Woo, C. H.; Goris, L.; Piliego, C.; Griffini, G.; Sellinger, A.; Brédas, J.-L.; Salleo, A.; Fréchet, J. M. J. *J. Am. Chem. Soc.* **2011**, *133* (31), 12106–12114.

(610) Idé, J.; Méreau, R.; Ducasse, L.; Castet, F.; Bock, H.; Olivier, Y.; Cornil, J.; Beljonne, D.; D'Avino, G.; Roscioni, O. M.; Muccioli, L.; Zannoni, C. *J. Am. Chem. Soc.* **2014**, *136* (7), 2911–2920.

(611) Groves, C.; Greenham, N. C. *Top. Curr. Chem.* **2014**, *352*, 257–278.

(612) Volpi, R.; Nassau, R.; Nørby, M. S.; Linares, M. *ACS Appl. Mater. Interfaces* **2016**, acsami.6b06645.

(613) Bouhassoune, M.; Mensfoort, S. L. M. van; Bobbert, P. A.; Coehoorn, R. *Org. Electron.* **2009**, *10* (3), 437–445.

(614) Huang, Y.; Westenhoff, S.; Avilov, I.; Sreearunothai, P.; Hodgkiss, J. M.; Deleener, C.; Friend, R. H.; Beljonne, D. *Nat. Mater.* **2008**, *7* (6), 483–489.

(615) Watkins, P. K.; Walker, A. B.; Verschoor, G. L. B. *Nano Lett.* **2005**, *5* (9), 1814–1818.

(616) Marsh, R. A.; Groves, C.; Greenham, N. C. *J. Appl. Phys.* **2007**, *101* (8), 83509.

(617) Schmechel, R. *Phys. Rev. B* **2002**, *66* (23), 235206.

(618) Kallmann, H.; Pope, M. *J. Chem. Phys.* **1959**, *30* (2), 585–586.

(619) Lin, Y.; Li, Y.; Zhan, X. *Chem. Soc. Rev.* **2012**, *41* (11), 4245.

(620) Bendikov, M.; Wudl, F.; Perepichka, D. F. *Chem. Rev.* **2004**, *104* (11), 4891–4946.

(621) Anthony, J. E. *Chem. Rev.* **2006**, *106* (12), 5028–5048.

(622) Li, Z.; Li, X.; Li, J.; Hu, Y. *Chinese J. Org. Chem.* **2013**, *33* (5), 891.

(623) Chen, G.; Sasabe, H.; Igarashi, T.; Hong, Z.; Kido, J. *J. Mater. Chem. A* **2015**, *3* (28), 14517–14534.

(624) Lin, Y.; Zhan, X. *Acc. Chem. Res.* **2016**, *49* (2), 175–183.

(625) Li, C.-Z.; Yip, H.-L.; Jen, A. K.-Y. *J. Mater. Chem.* **2012**, *22* (10), 4161.

(626) Mi, D.; Kim, J.-H.; Kim, H. U.; Xu, F.; Hwang, D.-H. *J. Nanosci. Nanotechnol.* **2014**, *14* (2), 1064–1084.

(627) Sariciftci, N. S.; Smilowitz, L.; Heeger, A. J.; Wudl, F. *Science* **1992**, *258* (5087), 1474–1476.

(628) Ross, R. B.; Cardona, C. M.; Guldi, D. M.; Sankaranarayanan, S. G.; Reese, M. O.; Kopidakis, N.;

Peet, J.; Walker, B.; Bazan, G. C.; Van Keuren, E.; Holloway, B. C.; Drees, M. *Nat. Mater.* **2009**, *8* (3), 208–212.

(629) Lin, Y.; Zhan, X. *Mater. Horizons* **2014**, *1* (5), 470.

(630) Sonar, P.; Fong Lim, J. P.; Chan, K. L. *Energy Environ. Sci.* **2011**, *4* (5), 1558.

(631) Nielsen, C. B.; Holliday, S.; Chen, H.-Y.; Cryer, S. J.; McCulloch, I. *Acc. Chem. Res.* **2015**, *48* (11), 2803–2812.

(632) Li, H.; Earmme, T.; Ren, G.; Saeki, A.; Yoshikawa, S.; Murari, N. M.; Subramaniyan, S.; Crane, M. J.; Seki, S.; Jenekhe, S. A. *J. Am. Chem. Soc.* **2014**, *136* (41), 14589–14597.

(633) Dang, M. T.; Hirsch, L.; Wantz, G. *Adv. Mater.* **2011**, *23* (31), 3597–3602.

(634) Hummelen, J. C.; Knight, B. W.; LePeq, F.; Wudl, F.; Yao, J.; Wilkins, C. L. *J. Org. Chem.* **1995**, *60* (3), 532–538.

(635) Troshin, P. A.; Hoppe, H.; Renz, J.; Egginger, M.; Mayorova, J. Y.; Goryachev, A. E.; Peregudov, A. S.; Lyubovskaya, R. N.; Gobsch, G.; Sariciftci, N. S.; Razumov, V. F. *Adv. Funct. Mater.* **2009**, *19* (5), 779–788.

(636) Brabec, C.; Scherf, U.; Dyakonov, V. *Organic Photovoltaics: Materials, Device Physics, and Manufacturing Technologies*, First Edition; WILEY-VCH Verlag GmbH: Weinheim, 2008.

(637) Pfuetzner, S.; Meiss, J.; Petrich, A.; Riede, M.; Leo, K. *Appl. Phys. Lett.* **2009**, *94* (22), 223307.

(638) Brückner, C.; Würthner, F.; Meerholz, K.; Engels, B. Atomistic approach to simulate processes relevant for the efficiencies of organic solar cells as a function of molecular properties. I. Thermodynamic aspects *(submitted)*.

(639) Coehoorn, R.; Bobbert, P. A. *Phys. status solidi* **2012**, *209* (12), 2354–2377.

(640) Gsänger, M.; Bialas, D.; Huang, L.; Stolte, M.; Würthner, F. *Adv. Mater.* **2016**, *28* (19), 3615–3645.

(641) Würthner, F. *Acc. Chem. Res.* **2016**, *49* (5), 868–876.

(642) Mennucci, B.; Cappelli, C.; Guido, C. A.; Cammi, R.; Tomasi, J. *J. Phys. Chem. A* **2009**, *113* (13), 3009–3020.

(643) Muniz-Miranda, F.; Pedone, A.; Battistelli, G.; Montalti, M.; Bloino, J.; Barone, V. *J. Chem. Theory Comput.* **2015**, *11* (11), 5371–5384.

(644) Preat, J.; Jacquemin, D.; Wathelet, V.; André, J.-M.; Perpète, E. A. *J. Phys. Chem. A* **2006**, *110* (26), 8144–8150.

(645) Brückner, C.; Walter, C.; Stolte, M.; Braïda, B.; Meerholz, K.; Würthner, F.; Engels, B. *J. Phys. Chem. C* **2015**, *119* (31), 17602–17611.

(646) Brock, C. P.; Dunitz, J. D. *Acta Crystallogr. Sect. B Struct. Sci.* **1990**, *46* (6), 795–806.

(647) Heinrich, M. A.; Pflaum, J.; Tripathi, A. K.; Frey, W.; Steigerwald, M. L.; Siegrist, T. *J. Phys. Chem. C* **2007**, *111* (51), 18878–18881.

(648) Pappenfus, T. M.; Seidenkranz, D. T.; Reinheimer, E. W. *Heterocycles* **2012**, *85* (2), 355–364.

(649) Jurchescu, O. D.; Meetsma, A.; Palstra, T. T. M. *Acta Crystallogr. B.* **2006**, *62* (Pt 2), 330–334.

(650) Inada, H.; Ohnishi, K.; Nomura, S.; Higuchi, A.; Nakano, H.; Shirota, Y. *J. Mater. Chem.* **1994**, *4* (2), 171.

(651) Chudomel, J. M.; Yang, B.; Barnes, M. D.; Achermann, M.; Mague, J. T.; Lahti, P. M. *J. Phys. Chem. A* **2011**, *115* (30), 8361–8368.

(652) Coe, B. J.; Fielden, J.; Foxon, S. P.; Helliwell, M.; Brunschwig, B. S.; Asselberghs, I.; Clays, K.; Olesiak, J.; Matczyszyn, K.; Samoc, M. *J. Phys. Chem. A* **2010**, *114* (45), 12028–12041.

(653) Ashwell, G. J.; Bahra, G. S.; Brown, C. R.; Hamilton, D. G.; Kennard, C. H. L.; Lynch, D. E. *J. Mater. Chem.* **1996**, *6* (1), 23.

(654) Liu, J.; Walker, B.; Tamayo, A.; Zhang, Y.; Nguyen, T.-Q. *Adv. Funct. Mater.* **2013**, *23* (1), 47–56.

(655) Kronenberg, N. M.; Deppisch, M.; Würthner, F.; Lademann, H. W. A.; Deing, K.; Meerholz, K. *Chem. Commun.* **2008**, No. 48, 6489–6491.

(656) Bürckstümmer, H.; Tulyakova, E. V.; Deppisch, M.; Lenze, M. R.; Kronenberg, N. M.; Gsänger, M.; Stolte, M.; Meerholz, K.; Würthner, F. *Angew. Chem. Int. Ed.* **2011**, *50* (49), 11628–11632.

(657) Hains, A. W.; Liang, Z.; Woodhouse, M. A.; Gregg, B. A. *Chem. Rev.* **2010**, *110* (11), 6689–6735.

(658) Ando, S.; Nishida, J.; Fujiwara, E.; Tada, H.; Inoue, Y.; Tokito, S.; Yamashita, Y. *Chem. Mater.* **2005**, *17* (6), 1261–1264.

(659) Valentini, L.; Bagnis, D.; Marrocchi, A.; Seri, M.; Taticchi, A.; Kenny, J. M. *Chem. Mater.* **2008**, *20* (1), 32–34.

(660) Teng, C.; Yang, X.; Yang, C.; Li, S.; Cheng, M.; Hagfeldt, A.; Sun, L. *J. Phys. Chem. C* **2010**, *114* (19), 9101–9110.

(661) Sundar, V. C.; Zaumseil, J.; Podzorov, V.; Menard, E.; Willett, R. L.; Someya, T.; Gershenson, M. E.; Rogers, J. A. *Science* **2004**, *303* (5664), 1644–1646.

(662) Li, G.; Shinar, J. *Appl. Phys. Lett.* **2003**, *83* (26), 5359.

(663) Pandey, A. K.; Nunzi, J.-M. *Adv. Mater.* **2007**, *19* (21), 3613–3617.

(664) Sarangerel, K.; Ganzorig, C.; Fujihira, M.; Sakomura, M.; Ueda, K. *Chem. Lett.* **2008**, *37* (7), 778–779.

(665) Sutton, C.; Marshall, M. S.; Sherrill, C. D.; Risko, C.; Brédas, J.-L. *J. Am. Chem. Soc.* **2015**, *137* (27), 8775–8782.

(666) da Silva Filho, D. A.; Kim, E.-G.; Brédas, J.-L. *Adv. Mater.* **2005**, *17* (8), 1072–1076.

(667) Bergantin, S.; Moret, M. *Cryst. Growth Des.* **2012**, *12* (12), 6035–6041.

(668) Jo, P. S.; Duong, D. T.; Park, J.; Sinclair, R.; Salleo, A. *Chem. Mater.* **2015**, *27* (11), 3979–3987.

(669) Yu, S.; Opitz, A.; Grob, S.; Resel, R.; Oehzelt, M.; Brütting, W.; Salzmann, I.; Koch, N. *Org. Electron.* **2014**, *15* (10), 2210–2217.

(670) Gruber, M.; Rawolle, M.; Wagner, J.; Magerl, D.; Hörmann, U.; Perlich, J.; Roth, S. V.; Opitz, A.; Schreiber, F.; Müller-Buschbaum, P.; Brütting, W. *Adv. Energy Mater.* **2013**, *3* (8), 1075–1083.

(671) Wagner, J.; Gruber, M.; Hinderhofer, A.; Wilke, A.; Bröker, B.; Frisch, J.; Amsalem, P.; Vollmer, A.; Opitz, A.; Koch, N.; Schreiber, F.; Brütting, W. *Adv. Funct. Mater.* **2010**, *20* (24), 4295–4303.

(672) Grob, S.; Bartynski, A. N.; Opitz, A.; Gruber, M.; Grassl, F.; Meister, E.; Linderl, T.; Hörmann, U.; Lorch, C.; Moons, E.; Schreiber, F.; Thompson, M. E.; Brütting, W. *J. Mater. Chem. A* **2015**, *3* (30), 15700–15709.

(673) Meiss, J.; Hermenau, M.; Tress, W.; Schuenemann, C.; Selzer, F.; Hummert, M.; Alex, J.; Lackner, G.; Leo, K.; Riede, M. *Phys. Rev. B* **2011**, *83* (16), 165305.

(674) Günes, S.; Neugebauer, H.; Sariciftci, N. S. *Chem. Rev.* **2007**, *107* (4), 1324–1338.

(675) Garcia-Belmonte, G.; Boix, P. P.; Bisquert, J.; Sessolo, M.; Bolink, H. J. *Sol. Energy Mater. Sol. Cells* **2010**, *94* (2), 366–375.

(676) Kim, Y.; Choulis, S. A.; Nelson, J.; Bradley, D. D. C.; Cook, S.; Durrant, J. R. *Appl. Phys. Lett.* **2005**, *86* (6), 63502.

(677) Lungenschmied, C.; Dennler, G.; Neugebauer, H.; Sariciftci, S. N.; Glatthaar, M.; Meyer, T.; Meyer, A. *Sol. Energy Mater. Sol. Cells* **2007**, *91* (5), 379–384.

(678) Risko, C.; McGehee, M. D.; Brédas, J.-L. *Chem. Sci.* **2011**, *2* (7), 1200–1218.

(679) Zhou, H.; Yang, L.; Stuart, A. C.; Price, S. C.; Liu, S.; You, W. *Angew. Chem. Int. Ed.* **2011**, *50* (13), 2995–2998.

(680) Son, H. J.; Wang, W.; Xu, T.; Liang, Y.; Wu, Y.; Li, G.; Yu, L. *J. Am. Chem. Soc.* **2011**, *133* (6), 1885–1894.

(681) Zhang, J.; Deng, D.; He, C.; He, Y.; Zhang, M.; Zhang, Z.-G.; Zhang, Z.; Li, Y. *Chem. Mater.* **2011**, *23* (3), 817–822.

(682) Shirota, Y. *J. Mater. Chem.* **2000**, *10* (1), 1–25.

(683) Shirota, Y. *J. Mater. Chem.* **2005**, *15* (1), 75–93.

(684) Leliège, A.; Blanchard, P.; Rousseau, T.; Roncali, J. *Org. Lett.* **2011**, *13* (12), 3098–3101.

(685) Roquet, S.; Cravino, A.; Leriche, P.; Alévêque, O.; Frère, P.; Roncali, J. *J. Am. Chem. Soc.* **2006**, *128* (10), 3459–3466.

(686) Lin, L.-Y.; Chen, Y.-H.; Huang, Z.-Y.; Lin, H.-W.; Chou, S.-H.; Lin, F.; Chen, C.-W.; Liu, Y.-H.; Wong, K.-T. *J. Am. Chem. Soc.* **2011**, *133* (40), 15822–15825.

(687) Deing, K. C.; Mayerhöffer, U.; Würthner, F.; Meerholz, K. *Phys. Chem. Chem. Phys.* **2012**, *14* (23), 8328–8334.

(688) Würthner, F.; Kaiser, T. E.; Saha-Möller, C. R. *Angew. Chem. Int. Ed.* **2011**, *50* (15), 3376–3410.

(689) Ajayaghosh, A.; Chithra, P.; Varghese, R.; Divya, K. P. *Chem. Commun.* **2008**, No. 8, 969–971.

(690) Chen, G.; Sasabe, H.; Sasaki, Y.; Katagiri, H.; Wang, X.-F.; Sano, T.; Hong, Z.; Yang, Y.; Kido, J. *Chem. Mater.* **2014**, *26* (3), 1356–1364.

(691) Chen, G.; Sasabe, H.; Lu, W.; Wang, X.-F.; Kido, J.; Hong, Z.; Yang, Y. *J. Mater. Chem. C* **2013**, *1* (40), 6547.

(692) Arjona-Esteban, A.; Krumrain, J.; Liess, A.; Stolte, M.; Huang, L.; Schmidt, D.; Stepanenko, V.; Gsänger, M.; Hertel, D.; Meerholz, K.; Würthner, F. *J. Am. Chem. Soc.* **2015**, *137* (42), 13524–13534.

(693) Arjona-Esteban, A.; Stolte, M.; Würthner, F. *Angew. Chem. Int. Ed.* **2016**, *55* (7), 2470–2473.

(694) Kronenberg, N. M.; Steinmann, V.; Bürckstümmer, H.; Hwang, J.; Hertel, D.; Würthner, F.; Meerholz, K. *Adv. Mater.* **2010**, *22* (37), 4193–4197.

(695) Qu, S.; Tian, H. *Chem. Commun.* **2012**, *48* (25), 3039–3051.

(696) Dou, L.; Gao, J.; Richard, E.; You, J.; Chen, C.-C.; Cha, K. C.; He, Y.; Li, G.; Yang, Y. *J. Am. Chem. Soc.* **2012**, *134* (24), 10071–10079.

(697) Qu, S.; Wu, W.; Hua, J.; Kong, C.; Long, Y.; Tian, H. *J. Phys. Chem. C* **2010**, *114* (2), 1343–1349.

(698) Walker, B.; Tamayo, A. B.; Dang, X.-D.; Zalar, P.; Seo, J. H.; Garcia, A.; Tantiwiwat, M.; Nguyen, T.-Q. *Adv. Funct. Mater.* **2009**, *19* (19), 3063–3069.

(699) Tamayo, A. B.; Tantiwiwat, M.; Walker, B.; Nguyen, T.-Q. *J. Phys. Chem. C* **2008**, *112* (39), 15543–15552.

(700) Shin, W.; Yasuda, T.; Watanabe, G.; Yang, Y. S.; Adachi, C. *Chem. Mater.* **2013**, *25* (12), 2549–2556.

(701) Grimme, S.; Parac, M. *ChemPhysChem* **2003**, *4* (3), 292–295.

(702) Brückner, C.; Engels, B. *J. Phys. Chem. A* **2015**, *119* (51), 12876–12891.

(703) Hättig, C.; Hellweg, A.; Köhn, A. *Phys. Chem. Chem. Phys.* **2006**, *8* (10), 1159–1169.

(704) Weigend, F.; Häser, M. *Theor. Chem. Acc.* **1997**, *97* (1–4), 331–340.

(705) Dunning, T. H. *J. Chem. Phys.* **1989**, *90* (2), 1007.

(706) Häser, M.; Ahlrichs, R. *J. Comput. Chem.* **1989**, *10* (1), 104–111.

(707) Becke, A. D. *Phys. Rev. A* **1988**, *38* (6), 3098–3100.

(708) Lee, C.; Yang, W.; Parr, R. G. *Phys. Rev. B* **1988**, *37* (2), 785–789.

(709) Miehlich, B.; Savin, A.; Stoll, H.; Preuss, H. *Chem. Phys. Lett.* **1989**, *157* (3), 200–206.

(710) Zhao, Y.; Truhlar, D. G. *J. Chem. Phys.* **2006**, *125* (19), 194101.

(711) Austin, A.; Petersson, G. A.; Frisch, M. J.; Dobek, F. J.; Scalmani, G.; Throssell, K. *J. Chem. Theory Comput.* **2012**, *8* (12), 4989–5007.

(712) Becke, A. D. *J. Chem. Phys.* **1996**, *104* (3), 1040.

(713) Becke, A. D. *J. Chem. Phys.* **1993**, *98* (7), 5648.

(714) Peverati, R.; Zhao, Y.; Truhlar, D. G. *J. Phys. Chem. Lett.* **2011**, *2* (16), 1991–1997.

(715) Goerigk, L.; Grimme, S. *J. Chem. Theory Comput.* **2011**, *7* (2), 291–309.

(716) Grimme, S.; Ehrlich, S.; Goerigk, L. *J. Comput. Chem.* **2011**, *32* (7), 1456–1465.

(717) Stewart, J. J. P. *J. Comput. Chem.* **1989**, *10* (2), 221–264.

(718) Gaussian09, Revision D.01; Frisch, M. J.; Trucks, G. W.; Schlegel, H. B.; Scuseria, G. E.; Robb, M. A.; Cheeseman, J. R.; Scalmani, G.; Barone, V.; Mennucci, B.; Petersson, G. A.; Nakatsuji, H.; Caricato, M.; Li, X.; Hratchian, H. P.; Izmaylov, A. F.; Bloino, J.; Zheng, G.; Sonnenberg, J. L.; Hada,

M.; Ehara, M.; Toyota, K.; Fukuda, R.; Hasegawa, J.; Ishida, M.; Nakajima, T.; Honda, Y.; Kitao, O.; Nakai, H.; Vreven, T.; Montgomery, J. A., J.; Peralta, J. E.; Ogliaro, F.; Bearpark, M.; Heyd, J. J.; Brothers, E.; Kudin, K. N.; Staroverov, V. N.; Kobayashi, R.; Normand, J.; Raghavachari, K.; Rendell, A.; Burant, J. C.; Iyengar, S. S. .; Tomasi, J.; Cossi, M.; Rega, N.; Millam, J. M.; Klene, M.; Knox, J. E.; Cross, J. B.; Bakken, V.; Adamo, C.; Jaramillo, J.; Gomperts, R.; Stratmann, R. E.; Yazyev, O.; Austin, A. J.; Cammi, R.; Pomelli, C.; Ochterski, J. W.; Martin, R. L.; Morokuma., K.; Zakrzewski, V. G.; Voth, G. A.; Salvador, P.; Dannenberg, J. J.; Dapprich, S.; Daniels, A. D.; Farkas, Ö.; Foresman, J. B.; Ortiz, J. V.; Cioslowski, J.; Fox, D. J. Gaussian, Inc.: Wallingford CT 2009.

(719) Stewart, J. J. P. MOPAC2012, Stewart Computational Chemistry, Colorado Springs, CO, USA, HTTP://OpenMOPAC.net (2012).

(720) Tirado-Rives, J.; Jorgensen, W. L. *J. Chem. Theory Comput.* **2008**, *4* (2), 297–306.

(721) Kozuch, S.; Bachrach, S. M.; Martin, J. M. L. *J. Phys. Chem. A* **2014**, *118* (1), 293–303.

(722) Wodrich, M. D.; Corminboeuf, C.; Schreiner, P. R.; Fokin, A. A.; Schleyer, P. von R. *Org. Lett.* **2007**, *9* (10), 1851–1854.

(723) Bousquet, D.; Fukuda, R.; Jacquemin, D.; Ciofini, I.; Adamo, C.; Ehara, M. *J. Chem. Theory Comput.* **2014**, *10* (9), 3969–3979.

(724) Guido, C. A.; Knecht, S.; Kongsted, J.; Mennucci, B. *J. Chem. Theory Comput.* **2013**, *9* (5), 2209–2220.

(725) Peverati, R.; Truhlar, D. G. *Philos. Trans. A. Math. Phys. Eng. Sci.* **2014**, *372* (2011), 20120476.

(726) Kruse, H.; Goerigk, L.; Grimme, S. *J. Org. Chem.* **2012**, *77* (23), 10824–10834.

(727) Le Guennic, B.; Jacquemin, D. *Acc. Chem. Res.* **2015**, *48* (3), 530–537.

(728) Gieseking, R. L.; Ravva, M. K.; Coropceanu, V.; Brédas, J.-L. *J. Phys. Chem. C* **2016**, *120* (18), 9975–9984.

(729) Kuprievich, V. A. *Theor. Exp. Chem.* **1986**, *22* (3), 245–252.

(730) Minenkov, Y.; Singstad, Å.; Occhipinti, G.; Jensen, V. R. *Dalt. Trans.* **2012**, *41* (18), 5526.

(731) Linder, M.; Brinck, T. *Phys. Chem. Chem. Phys.* **2013**, *15* (14), 5108.

(732) Jacquemin, D.; Femenias, A.; Chermette, H.; Ciofini, I.; Adamo, C.; André, J.-M.; Perpète, E. A. *J. Phys. Chem. A* **2006**, *110* (17), 5952–5959.

(733) Jacquemin, D.; Adamo, C. *J. Chem. Theory Comput.* **2011**, *7* (2), 369–376.

(734) Sancho-García, J. C.; Pérez-Jiménez, A. J. *Phys. Chem. Chem. Phys.* **2007**, *9* (44), 5874.

(735) Jacquemin, D.; Femenias, A.; Chermette, H.; André, J.-M.; Perpète, E. A. *J. Phys. Chem. A* **2005**, *109* (25), 5734–5741.

(736) Jacquemin, D.; Perpète, E. A.; Scalmani, G.; Frisch, M. J.; Kobayashi, R.; Adamo, C. *J. Chem. Phys.* **2007**, *126* (14), 144105.

(737) Körzdörfer, T.; Parrish, R. M.; Sears, J. S.; Sherrill, C. D.; Brédas, J.-L. *J. Chem. Phys.* **2012**, *137* (12), 124305.

(738) Wykes, M.; Su, N. Q.; Xu, X.; Adamo, C.; Sancho-García, J.-C. *J. Chem. Theory Comput.* **2015**, *11*

(2), 832–838.

(739) Sonar, P.; Singh, S. P.; Williams, E. L.; Li, Y.; Soh, M. S.; Dodabalapur, A. *J. Mater. Chem.* **2012**, *22* (10), 4425–4435.

(740) Malagoli, M.; Brédas, J. L. *Chem. Phys. Lett.* **2000**, *327* (1), 13–17.

(741) Liang, M.; Xu, W.; Cai, F.; Chen, P.; Peng, B.; Chen, J.; Li, Z. *J. Phys. Chem. C* **2007**, *111* (11), 4465–4472.

(742) Xu, J.; Wang, L.; Liang, G.; Bai, Z.; Wang, L.; Xu, W.; Shen, X. *Spectrochim. Acta Part A Mol. Biomol. Spectrosc.* **2011**, *78* (1), 287–293.

(743) Send, R.; Kühn, M.; Furche, F. *J. Chem. Theory Comput.* **2011**, *7* (8), 2376–2386.

(744) Schreiber, M.; Silva-Junior, M. R.; Sauer, S. P. A.; Thiel, W. *J. Chem. Phys.* **2008**, *128* (13), 134110.

(745) Settels, V.; Schubert, A.; Tafipolski, M.; Liu, W.; Stehr, V.; Topczak, A. K.; Pflaum, J.; Deibel, C.; Fink, R. F.; Engel, V.; Engels, B. *J. Am. Chem. Soc.* **2014**, *136* (26), 9327–9337.

(746) Autschbach, J. *ChemPhysChem* **2009**, *10* (11), 1757–1760.

(747) Jacquemin, D.; Perpète, E. A.; Ciofini, I.; Adamo, C. *J. Chem. Theory Comput.* **2010**, *6* (5), 1532–1537.

(748) Silva-Junior, M. R.; Schreiber, M.; Sauer, S. P. A.; Thiel, W. *J. Chem. Phys.* **2010**, *133* (17), 174318.

(749) Schäfer, A.; Huber, C.; Ahlrichs, R. *J. Chem. Phys.* **1994**, *100* (8), 5829.

(750) Laurent, A. D.; Blondel, A.; Jacquemin, D. *Theor. Chem. Acc.* **2015**, *134* (6), 76.

(751) Laurent, A. D.; Jacquemin, D. *Int. J. Quantum Chem.* **2013**, *113* (17), 2019–2039.

(752) Levine, B. F.; Bethea, C. G.; Wasserman, E.; Leenders, L. *J. Chem. Phys.* **1978**, *68* (11), 5042.

(753) Marder, S. R.; Gorman, C. B.; Tiemann, B. G.; Perry, J. W.; Bourhill, G.; Mansour, K. *Science* **1993**, *261* (5118), 186–189.

(754) Furche, F.; Rappoport, D. In *Computational Photochemistry*; Olivucci, M., Ed.; Elsevier: Amsterdam, 2005; pp 93–128.

(755) Sándorfy, C. *The Role of Rydberg States in Spectroscopy and Photochemistry - Low and High Rydberg States*; Kluwer Academic Publishers: New York, Boston, Dordrecht, London, Moscow, 2002.

(756) Deotare, P. B.; Chang, W.; Hontz, E.; Congreve, D. N.; Shi, L.; Reusswig, P. D.; Modtland, B.; Bahlke, M. E.; Lee, C. K.; Willard, A. P.; Bulović, V.; Van Voorhis, T.; Baldo, M. A. *Nat. Mater.* **2015**, *14* (11), 1130–1134.

(757) Rohrdanz, M. A.; Martins, K. M.; Herbert, J. M. *J. Chem. Phys.* **2009**, *130* (5), 54112.

(758) Brückner, C.; Engels, B. *Chem. Phys.* **2016**.

(759) Trofimov, A. B.; Schirmer, J. *J. Phys. B At. Mol. Opt. Phys.* **1995**, *28* (12), 2299–2324.

(760) Hättig, C.; Weigend, F. *J. Chem. Phys.* **2000**, *113* (13), 5154.

(761) Hättig, C.; Hald, K.; Hald, K. *Phys. Chem. Chem. Phys.* **2002**, *4* (11), 2111–2118.

(762) Hättig, C.; Köhn, A.; Hald, K. *J. Chem. Phys.* **2002**, *116* (13), 5401.

(763) Jacquemin, D.; Perpète, E. A.; Scuseria, G. E.; Ciofini, I.; Adamo, C. *J. Chem. Theory Comput.* **2008**, *4* (1), 123–135.

(764) Tian, B.; Eriksson, E. S. E.; Eriksson, L. A. *J. Chem. Theory Comput.* **2010**, *6* (7), 2086–2094.

(765) Jacquemin, D.; Perpète, E. A.; Ciofini, I.; Adamo, C.; Valero, R.; Zhao, Y.; Truhlar, D. G. *J. Chem. Theory Comput.* **2010**, *6* (7), 2071–2085.

(766) Jacquemin, D.; Perpète, E. A.; Ciofini, I.; Adamo, C. *J. Chem. Theory Comput.* **2010**, *6* (5), 1532–1537.

(767) Peach, M. J. G.; Tozer, D. J. *J. Phys. Chem. A* **2012**, *116* (39), 9783–9789.

(768) Aquilante, F.; De Vico, L.; Ferré, N.; Ghigo, G.; Malmqvist, P.; Neogrády, P.; Pedersen, T. B.; Pitonák, M.; Reiher, M.; Roos, B. O.; Serrano-Andrés, L.; Urban, M.; Veryazov, V.; Lindh, R. *J. Comput. Chem.* **2010**, *31* (1), 224–247.

(769) Veryazov, V.; Widmark, P.-O.; Serrano-Andrés, L.; Lindh, R.; Roos, B. O. *Int. J. Quantum Chem.* **2004**, *100* (4), 626–635.

(770) Karlström, G.; Lindh, R.; Malmqvist, P.-Å.; Roos, B. O.; Ryde, U.; Veryazov, V.; Widmark, P.-O.; Cossi, M.; Schimmelpfennig, B.; Neogrady, P.; Seijo, L. *Comput. Mater. Sci.* **2003**, *28* (2), 222–239.

(771) Forsberg, N.; Malmqvist, P.-Å. *Chem. Phys. Lett.* **1997**, *274* (1–3), 196–204.

(772) Bacon, A. D.; Zerner, M. C. *Theor. Chim. Acta* **1979**, *53* (1), 21–54.

(773) Dral, P. O.; Wu, X.; Spörkel, L.; Koslowski, A.; Thiel, W. *J. Chem. Theory Comput.* **2016**, *12* (3), 1097–1120.

(774) Dral, P. O.; Wu, X.; Spörkel, L.; Koslowski, A.; Weber, W.; Steiger, R.; Scholten, M.; Thiel, W. *J. Chem. Theory Comput.* **2016**, *12* (3), 1082–1096.

(775) Lischka, H.; Shepard, R.; Brown, F. B.; Shavitt, I. *Int. J. Quantum Chem.* **2009**, *20* (S15), 91–100.

(776) Jacquemin, D.; Zhao, Y.; Valero, R.; Adamo, C.; Ciofini, I.; Truhlar, D. G. *J. Chem. Theory Comput.* **2012**, *8* (4), 1255–1259.

(777) Kanis, D. R.; Ratner, M. A.; Marks, T. J. *J. Am. Chem. Soc.* **1992**, *114* (26), 10338–10357.

(778) Breitung, E. M.; Shu, C.-F.; McMahon, R. J. *J. Am. Chem. Soc.* **2000**, *122* (6), 1154–1160.

(779) Moore, B.; Sun, H.; Govind, N.; Kowalski, K.; Autschbach, J. *J. Chem. Theory Comput.* **2015**, *11* (7), 3305–3320.

(780) Lu, J.; Zheng, Y.; Zhang, J. *RSC Adv.* **2015**, *5* (24), 18588–18592.

(781) Peach, M. J. G.; Benfield, P.; Helgaker, T.; Tozer, D. J. *J. Chem. Phys.* **2008**, *128* (4), 44118.

(782) Autschbach, J.; Srebro, M. *Acc. Chem. Res.* **2014**, *47* (8), 2592–2602.

(783) Hagfeldt, A.; Boschloo, G.; Sun, L.; Kloo, L.; Pettersson, H. *Chem. Rev.* **2010**, *110* (11), 6595–6663.

(784) Hasanein, A. A.; Elmarassi, Y. R.; Ramadan, A. M. *J. Theor. Comput. Chem.* **2014**, *13* (8),

1450064(1-23).

(785) Hasanein, A. A.; Elmarassi, Y. R.; Kassem, E. N. *J. Mol. Model.* **2016**, *22* (5), 115.

(786) Parac, M.; Grimme, S. *Chem. Phys.* **2003**, *292* (1), 11–21.

(787) Hoffmann, S. T.; Schrögel, P.; Rothmann, M.; Albuquerque, R. Q.; Strohriegl, P.; Köhler, A. *J. Phys. Chem. B* **2011**, *115* (3), 414–421.

(788) Bagnich, S. A.; Athanasopoulos, S.; Rudnick, A.; Schroegel, P.; Bauer, I.; Greenham, N. C.; Strohriegl, P.; Köhler, A. *J. Phys. Chem. C* **2015**, *119* (5), 2380–2387.

(789) Salman, S.; Kim, D.; Coropceanu, V.; Brédas, J.-L. *Chem. Mater.* **2011**, *23* (23), 5223–5230.

(790) Jacquemin, D.; Duchemin, I.; Blase, X. *J. Chem. Theory Comput.* **2015**, *11* (11), 5340–5359.

(791) Mooore II, B.; Autschbach, J. *J. Chem. Theory Comput.* **2013**, *9* (11), 4991–5003.

(792) Krauter, C. M.; Pernpointner, M.; Dreuw, A. *J. Chem. Phys.* **2013**, *138* (4), 44107.

(793) Lee, J.; Jadhav, P.; Reusswig, P. D.; Yost, S. R.; Thompson, N. J.; Congreve, D. N.; Hontz, E.; Van Voorhis, T.; Baldo, M. A. *Acc. Chem. Res.* **2013**, *46* (6), 1300–1311.

(794) Wilson, M. W. B.; Rao, A.; Ehrler, B.; Friend, R. H. *Acc. Chem. Res.* **2013**, *46* (6), 1330–1338.

(795) Ehrler, B.; Walker, B. J.; Böhm, M. L.; Wilson, M. W. B. B.; Vaynzof, Y.; Friend, R. H.; Greenham, N. C. *Nat. Commun.* **2012**, *3*, 1019.

(796) Musser, A. J.; Al-Hashimi, M.; Maiuri, M.; Brida, D.; Heeney, M.; Cerullo, G.; Friend, R. H.; Clark, J. *J. Am. Chem. Soc.* **2013**, *135* (34), 12747–12754.

(797) Sanders, S. N.; Kumarasamy, E.; Pun, A. B.; Steigerwald, M. L.; Sfeir, M. Y.; Campos, L. M. *Angew. Chem. Int. Ed.* **2016**, *55* (10), 3373–3377.

(798) Korovina, N. V.; Das, S.; Nett, Z.; Feng, X.; Joy, J.; Haiges, R.; Krylov, A. I.; Bradforth, S. E.; Thompson, M. E. *J. Am. Chem. Soc.* **2016**, *138* (2), 617–627.

(799) Sanders, S. N.; Kumarasamy, E.; Pun, A. B.; Appavoo, K.; Steigerwald, M. L.; Campos, L. M.; Sfeir, M. Y. *J. Am. Chem. Soc.* **2016**, *138* (23), 7289–7297.

(800) Sears, J. S.; Koerzdoerfer, T.; Zhang, C.-R.; Brédas, J.-L. *J. Chem. Phys.* **2011**, *135* (15), 151103.

(801) Perdew, J. P.; Burke, K.; Ernzerhof, M. *Phys. Rev. Lett.* **1997**, *78* (7), 1396–1396.

(802) Perdew, J. P.; Burke, K.; Ernzerhof, M. *Phys. Rev. Lett.* **1996**, *77* (18), 3865–3868.

(803) Adamo, C.; Barone, V. *J. Chem. Phys.* **1999**, *110* (13), 6158.

(804) Burke, K.; Werschnik, J.; Gross, E. K. U. *J. Chem. Phys.* **2005**, *123* (6), 62206.

(805) Casida, M. E.; Huix-Rotllant, M. *Annu. Rev. Phys. Chem.* **2012**, *63* (1), 287–323.

(806) Peach, M. J. G.; Warner, N.; Tozer, D. J. *Mol. Phys.* **2013**, *111* (9–11), 1271–1274.

(807) Peach, M. J. G.; Williamson, M. J.; Tozer, D. J. *J. Chem. Theory Comput.* **2011**, *7* (11), 3578–3585.

(808) Nguyen, K. A.; Kennel, J.; Pachter, R. *J. Chem. Phys.* **2002**, *117* (15), 7128.

(809) Isegawa, M.; Truhlar, D. G. *J. Chem. Phys.* **2013**, *138* (13), 134111.

(810) Wang, Y.-L.; Wu, G.-S. *Int. J. Quantum Chem.* **2008**, *108* (3), 430–439.

(811) Leang, S. S.; Zahariev, F.; Gordon, M. S. *J. Chem. Phys.* **2012**, *136* (10), 104101.

(812) Hait, D.; Zhu, T.; McMahon, D. P.; Van Voorhis, T. *J. Chem. Theory Comput.* **2016**, *12* (7), 3353–3359.

(813) Köhler, A.; Bässler, H. *Mater. Sci. Eng. R Reports* **2009**, *66* (4), 71–109.

(814) Fang, C.; Oruganti, B.; Durbeej, B. *J. Phys. Chem. A* **2014**, *118* (23), 4157–4171.

(815) Zhao, Y.; Truhlar, D. G. *J. Phys. Chem. A* **2005**, *109* (25), 5656–5667.

(816) Zhao, Y.; Lynch, B. J.; Truhlar, D. G. *J. Phys. Chem. A* **2004**, *108* (14), 2715–2719.

(817) Adamo, C.; Barone, V. *J. Chem. Phys.* **1998**, *108* (2), 664.

(818) Becke, A. D. *J. Chem. Phys.* **2000**, *112* (9), 4020.

(819) Krieger, J. B.; Chen, J.; Iafrate, G. J.; Savin, A. In *Electron Correlations and Materials Properties*; Springer US: Boston, MA, 1999; pp 463–477.

(820) Rey, J.; Savin, A. *Int. J. Quantum Chem.* **1998**, *69* (4), 581–590.

(821) Toulouse, J.; Savin, A.; Adamo, C. *J. Chem. Phys.* **2002**, *117* (23), 10465.

(822) Zhao, Y.; González-García, N.; Truhlar, D. G. *J. Phys. Chem. A* **2005**, *109* (9), 2012–2018.

(823) Jacquemin, D.; Moore, B.; Planchat, A.; Adamo, C.; Autschbach, J. *J. Chem. Theory Comput.* **2014**, *10* (4), 1677–1685.

(824) Penfold, T. J. *J. Phys. Chem. C* **2015**, *119* (24), 13535–13544.

(825) Chen, T.; Zheng, L.; Yuan, J.; An, Z.; Chen, R.; Tao, Y.; Li, H.; Xie, X.; Huang, W. *Sci. Rep.* **2015**, *5*, 10923.

(826) Aryanpour, K.; Shukla, A.; Mazumdar, S. *J. Phys. Chem. C* **2015**, *119* (13), 6966–6979.

(827) Sun, H.; Zhong, C.; Bredas, J.-L. *J. Chem. Theory Comput.* **2015**, *11* (8), 3851–3858.

(828) Huang, S.; Zhang, Q.; Shiota, Y.; Nakagawa, T.; Kuwabara, K.; Yoshizawa, K.; Adachi, C. *J. Chem. Theory Comput.* **2013**, *9* (9), 3872–3877.

(829) Milián-Medina, B.; Gierschner, J. *Org. Electron.* **2012**, *13* (6), 985–991.

(830) Tao, Y.; Yuan, K.; Chen, T.; Xu, P.; Li, H.; Chen, R.; Zheng, C.; Zhang, L.; Huang, W. *Adv. Mater.* **2014**, *26* (47), 7931–7958.

(831) Niehaus, T. A.; Hofbeck, T.; Yersin, H. *RSC Adv.* **2015**, *5* (78), 63318–63329.

(832) Kociper, B.; Niehaus, T. A. *Cornell University Library*; **2013**; p arXiv:1308.1053.

(833) Becke, A. D. *J. Chem. Phys.* **2013**, *138* (7), 74109.

(834) Fuchs, M.; Niquet, Y.-M.; Gonze, X.; Burke, K. *J. Chem. Phys.* **2005**, *122* (9), 94116.

(835) Sutton, C.; Körzdörfer, T.; Coropceanu, V.; Brédas, J.-L. *J. Phys. Chem. C* **2014**, *118* (8), 3925–3934.

(836) Körzdörfer, T.; Sears, J. S.; Sutton, C.; Brédas, J. L. *J. Chem. Phys.* **2011**, *135* (20).

(837) Becke, A. D. *J. Chem. Phys.* **1988**, *88* (2), 1053.

(838) Becke, A. D. *J. Chem. Phys.* **1997**, *107* (20), 8554.

(839) Zhao, Y.; Schultz, N. E.; Truhlar, D. G. *J. Chem. Theory Comput.* **2006**, *2* (2), 364–382.

(840) Perdew, J. P.; Burke, K. *Int. J. Quantum Chem.* **1996**, *57* (3), 309–319.

(841) Zhang, I. Y.; Xu, X.; Jung, Y.; Goddard, W. A. *Proc. Natl. Acad. Sci.* **2011**, *108* (50), 19896–19900.

(842) Chan, B.; Song, J.-W.; Kawashima, Y.; Hirao, K. *J. Comput. Chem.* **2016**, *37* (14), 1306–1312.

(843) Goerigk, L.; Moellmann, J.; Grimme, S. *Phys. Chem. Chem. Phys.* **2009**, *11* (22), 4611.

(844) Shuai, Z.; Geng, H.; Xu, W.; Liao, Y.; André, J.-M. *Chem. Soc. Rev.* **2014**, *43* (8), 2662.

(845) Zhang, C.-R.; Coropceanu, V.; Sears, J. S.; Brédas, J.-L. *J. Phys. Chem. C* **2014**, *118* (1), 154–158.

(846) Pastore, M.; Mosconi, E.; De Angelis, F.; Grätzel, M. *J. Phys. Chem. C* **2010**, *114* (15), 7205–7212.

(847) Adamo, C.; Jacquemin, D.; Huix-Rotllant, M. *Chem. Soc. Rev.* **2013**, *42* (3), 845–856.

(848) Bernini, C.; Zani, L.; Calamante, M.; Reginato, G.; Mordini, A.; Taddei, M.; Basosi, R.; Sinicropi, A. *J. Chem. Theory Comput.* **2014**, *10* (9), 3925–3933.

(849) Liu, W.; Settels, V.; Harbach, P. H. P.; Dreuw, A.; Fink, R. F.; Engels, B. *J. Comput. Chem.* **2011**, *32* (9), 1971–1981.

(850) Walter, C.; Ruetzel, S.; Diekmann, M.; Nuernberger, P.; Brixner, T.; Engels, B. *J. Chem. Phys.* **2014**, *140* (22), 224311.

(851) Ruetzel, S.; Diekmann, M.; Nuernberger, P.; Walter, C.; Engels, B.; Brixner, T. *Proc. Natl. Acad. Sci. U. S. A.* **2014**, *111* (13), 4764–4769.

(852) Ruetzel, S.; Diekmann, M.; Nuernberger, P.; Walter, C.; Engels, B.; Brixner, T. *J. Chem. Phys.* **2014**, *140* (22), 224310.

(853) Réal, F.; Vallet, V.; Marian, C.; Wahlgren, U. *J. Chem. Phys.* **2007**, *127* (21), 214302.

(854) Brückner, C.; Engels, B. *J. Comput. Chem.* **2016**, *37* (15), 1335–1344.

(855) Stehr, V.; Pfister, J.; Fink, R. F.; Engels, B.; Deibel, C. *Phys. Rev. B* **2011**, *83* (15), 155208.

(856) Asaoka, S.; Takeda, N.; Iyoda, T.; Cook, A. R.; Miller, J. R. *J. Am. Chem. Soc.* **2008**, *130* (36), 11912–11920.

(857) Duhm, S.; Xin, Q.; Hosoumi, S.; Fukagawa, H.; Sato, K.; Ueno, N.; Kera, S. *Adv. Mater.* **2012**, *24* (7), 901–905.

(858) Koch, N.; Vollmer, A.; Duhm, S.; Sakamoto, Y.; Suzuki, T. *Adv. Mater.* **2007**, *19* (1), 112–116.

(859) D'Souza, F.; Maligaspe, E.; Ohkubo, K.; Zandler, M. E.; Subbaiyan, N. K.; Fukuzumi, S. *J. Am. Chem. Soc.* **2009**, *131* (25), 8787–8797.

(860) Liu, T.; Troisi, A. *J. Phys. Chem. C* **2011**, *115* (5), 2406–2415.

(861) Martínez, J. P.; Solà, M.; Voityuk, A. A. *J. Comput. Chem.* **2016**, *37* (15), 1396–1405.

(862) Siriwong, K.; Voityuk, A. A.; Newton, M. D.; Rösch, N. *J. Phys. Chem. B* **2003**, *107* (11), 2595–2601.

(863) Kocherzhenko, A. A.; Whaley, K. B.; Sforazzini, G.; Anderson, H. L.; Wykes, M.; Beljonne, D.; Grozema, F. C.; Siebbeles, L. D. A. *J. Phys. Chem. C* **2012**, *116* (48), 25213–25225.

(864) McMahon, D. P.; Troisi, A. *J. Phys. Chem. Lett.* **2010**, *1* (6), 941–946.

(865) Ge, Y.; Gordon, M. S.; Battaglia, F.; Fox, R. O. *J. Phys. Chem. A* **2007**, *111* (8), 1475–1486.

(866) Bromley, S. T.; Illas, F.; Mas-Torrent, M. *Phys. Chem. Chem. Phys.* **2008**, *10* (1), 121–127.

(867) Angus, J. G.; Morris, G. C. *J. Mol. Spectrosc.* **1966**, *21* (1–4), 310–324.

(868) Debies, T. P.; Rabalais, J. W. *Inorg. Chem.* **1974**, *13* (2), 308–312.

(869) webbook.nist.gov http://webbook.nist.gov/chemistry/name-ser.html.

(870) Valiev, M.; Bylaska, E. J.; Govind, N.; Kowalski, K.; Straatsma, T. P.; Van Dam, H. J. J.; Wang, D.; Nieplocha, J.; Apra, E.; Windus, T. L.; de Jong, W. A. *Comput. Phys. Commun.* **2010**, *181* (9), 1477–1489.

(871) Golubeva, A. A.; Krylov, A. I. *Phys. Chem. Chem. Phys.* **2009**, *11* (9), 1303–1311.

(872) Pieniazek, P. A.; Arnstein, S. A.; Bradforth, S. E.; Krylov, A. I.; Sherrill, C. D. *J. Chem. Phys.* **2007**, *127* (16), 164110.

(873) Moore, B.; Charaf-Eddin, A.; Planchat, A.; Adamo, C.; Autschbach, J.; Jacquemin, D. *J. Chem. Theory Comput.* **2014**, *10* (10), 4599–4608.

(874) Refaely-Abramson, S.; Sharifzadeh, S.; Govind, N.; Autschbach, J.; Neaton, J. B.; Baer, R.; Kronik, L. *Phys. Rev. Lett.* **2012**, *109* (22), 226405.

(875) Brückner, C.; Walter, C.; Engels, B. *Int. J. Quantum Chem.* **2016**, *116* (15), 1138–1152.

(876) Brédas, J.-L.; Beljonne, D.; Coropceanu, V.; Cornil, J. *Chem. Rev.* **2004**, *104* (11), 4971–5004.

(877) Fink, R. F.; Seibt, J.; Engel, V.; Renz, M.; Kaupp, M.; Lochbrunner, S.; Zhao, H.-M.; Pfister, J.; Würthner, F.; Engels, B. *J. Am. Chem. Soc.* **2008**, *130* (39), 12858–12859.

(878) Schubert, A.; Settels, V.; Liu, W.; Würthner, F.; Meier, C.; Fink, R. F.; Schindlbeck, S.; Lochbrunner, S.; Engels, B.; Engel, V. *J. Phys. Chem. Lett.* **2013**, *4* (5), 792–796.

(879) Martinez, C. R.; Iverson, B. L. *Chem. Sci.* **2012**, *3* (7), 2191.

(880) Salonen, L. M.; Ellermann, M.; Diederich, F. *Angew. Chem. Int. Ed.* **2011**, *50* (21), 4808–4842.

(881) Hunter, C. A.; Sanders, J. K. M. *J. Am. Chem. Soc.* **1990**, *112* (14), 5525–5534.

(882) Sinnokrot, M. O.; Sherrill, C. D. *J. Phys. Chem. A* **2006**, *110* (37), 10656–10668.

(883) Lee, E. C.; Kim, D.; Jurecka, P.; Tarakeshwar, P.; Hobza, P.; Kim, K. S. *J. Phys. Chem. A* **2007**, *111* (18), 3446–3457.

(884) Grimme, S. *Angew. Chem. Int. Ed. Engl.* **2008**, *47* (18), 3430–3434.

(885) Wheeler, S. E.; Houk, K. N. *J. Am. Chem. Soc.* **2008**, *130* (33), 10854–10855.

(886) Wheeler, S. E. *J. Am. Chem. Soc.* **2011**, *133* (26), 10262–10274.

(887) Rybak, S.; Jeziorski, B.; Szalewicz, K. *J. Chem. Phys.* **1991**, *95* (9), 6576.

(888) Korona, T.; Williams, H. L.; Bukowski, R.; Jeziorski, B.; Szalewicz, K. *J. Chem. Phys.* **1997**, *106* (12), 5109.

(889) Tafipolsky, M.; Engels, B. *J. Chem. Theory Comput.* **2011**, *7* (6), 1791–1803.

(890) Ansorg, K.; Tafipolsky, M.; Engels, B. *J. Phys. Chem. B* **2013**, *117* (35), 10093–10102.

(891) Wirz, L. N.; Tonner, R.; Hermann, A.; Sure, R.; Schwerdtfeger, P. *J. Comput. Chem.* **2016**, *37* (1), 10–17.

(892) Singh, U. C.; Kollman, P. A. *J. Comput. Chem.* **1984**, *5* (2), 129–145.

(893) Besler, B. H.; Merz, K. M.; Kollman, P. A. *J. Comput. Chem.* **1990**, *11* (4), 431–439.

(894) Werner, H.-J.; Knowles, P. J.; Knizia, G.; Manby, F. R.; Schütz, M.; Celani, P.; Györffy, W.; Kats, D.; Korona, T.; Lindh, R.; Mitrushenkov, A.; Rauhut, G.; Shamasundar, K. R.; Adler, T. B.; Amos, R. D.; Bernhardsson, A.; Berning, A.; Cooper, D. L.; Deegan, M. J. O.; Dobbyn, A. J.; Eckert, F.; Goll, E.; Hampel, C.; Hesselmann, A.; Hetzer, G.; Hrenar, T.; Jansen, G.; Köppl, C.; Liu, Y.; Lloyd, A. W.; Mata, R. A.; May, A. J.; McNicholas, S. J.; Meyer, W.; Mura, M. E.; Nicklaß, A.; O'Neill, D. P.; Palmieri, P.; Peng, D.; Pflüger, K.; Pitzer, R.; Reiher, M.; Shiozaki, T.; Stoll, H.; Stone, A. J.; Tarroni, R.; Thorsteinsson, T.; Wang, M.; MOLPRO, version 2015.

(895) Werner, H.-J.; Knowles, P. J.; Knizia, G.; Manby, F. R.; Schütz, M. *WIREs Comput. Mol .Sci.* **2012**, *2* (2), 242–253.

(896) Kendall, R. A.; Dunning, T. H.; Harrison, R. J. *J. Chem. Phys.* **1992**, *96* (9), 6796.

(897) Woon, D. E.; Dunning, T. H. *J. Chem. Phys.* **1993**, *98* (2), 1358.

(898) Ditchfield, R. *J. Chem. Phys.* **1971**, *54* (2), 724.

(899) TINKER Molecular Modeling Package http://dasher.wustl.edu/tinker/.

(900) Zhao, H.-M.; Pfister, J.; Settels, V.; Renz, M.; Kaupp, M.; Dehm, V. C.; Würthner, F.; Fink, R. F.; Engels, B. *J. Am. Chem. Soc.* **2009**, *131* (43), 15660–15668.

(901) Fink, R. F.; Pfister, J.; Zhao, H. M.; Engels, B. *Chem. Phys.* **2008**, *346* (1–3), 275–285.

(902) Boys, S. F.; Bernardi, F. *Mol. Phys.* **1970**, *19* (4), 553–566.

(903) Simon, S.; Duran, M.; Dannenberg, J. J. *J. Chem. Phys.* **1996**, *105* (24), 11024.

(904) Jurečka, P.; Šponer, J.; Černý, J.; Hobza, P.; Muller-Dethlefs, K.; Hobza, P.; Vondrášek, J.; Bendová, L.; Klusák, V.; Hobza, P. *Phys. Chem. Chem. Phys.* **2006**, *8* (17), 1985–1993.

(905) Jung, Y.; Head-Gordon, M. *Phys. Chem. Chem. Phys.* **2006**, *8* (24), 2831–2840.

(906) Wang, F.-F.; Jenness, G.; Al-Saidi, W. A.; Jordan, K. D. *J. Chem. Phys.* **2010**, *132* (13), 134303.

(907) Hill, J. G.; Das, A. *Phys. Chem. Chem. Phys.* **2014**, *16* (23), 11754–11762.

(908) Khaliullin, R. Z.; Cobar, E. A.; Lochan, R. C.; Bell, A. T.; Head-Gordon, M. *J. Phys. Chem. A* **2007**, *111* (36), 8753–8765.

(909) Chen, Z.; Lohr, A.; Saha-Möller, C. R.; Würthner, F. *Chem. Soc. Rev.* **2009**, *38* (2), 564–584.

(910) *Reviews in Computational Chemistry*; Lipkowitz, K. B., Boyd, D. B., Eds.; Reviews in Computational Chemistry; John Wiley & Sons, Inc.: Hoboken, NJ, USA, 2000; Vol. 16.

(911) Dürr, A. C.; Schreiber, F.; Ritley, K. A.; Kruppa, V.; Krug, J.; Dosch, H.; Struth, B. *Phys. Rev. Lett.* **2003**, *90* (1), 16104.

(912) Rivnay, J.; Mannsfeld, S. C. B.; Miller, C. E.; Salleo, A.; Toney, M. F. *Chem. Rev.* **2012**, *112* (10), 5488–5519.

(913) Hinderhofer, A.; Schreiber, F. *ChemPhysChem* **2012**, *13* (3), 628–643.

(914) Wilke, A.; Endres, J.; Hörmann, U.; Niederhausen, J.; Schlesinger, R.; Frisch, J.; Amsalem, P.; Wagner, J.; Gruber, M.; Opitz, A.; Vollmer, A.; Brütting, W.; Kahn, A.; Koch, N. *Appl. Phys. Lett.* **2012**, *101* (23), 233301.

(915) Kramer, C.; Gedeck, P.; Meuwly, M. *J. Comput. Chem.* **2012**, *33* (20), 1673–1688.

(916) Stone, A. J. *The Theory of Intermolecular Forces*, Oxford Uni.; New York, 1996.

(917) Kim, Y. S.; Kim, S. K.; Lee, W. D. *Chem. Phys. Lett.* **1981**, *80* (3), 574–575.

(918) Söderhjelm, P.; Karlström, G.; Ryde, U. *J. Chem. Phys.* **2006**, *124* (24), 244101.

(919) Walter, C. Excitonic States and Optoelectronic Properties of Organic Semiconductors - A Quantum-Chemical Study Focusing on Merocyanines and Perylene-Based Dyes Including the Influence of the Environment, Universität Würzburg, 2015.

(920) Fu, Y.-T.; da Silva Filho, D. A.; Sini, G.; Asiri, A. M.; Aziz, S. G.; Risko, C.; Brédas, J.-L. *Adv. Funct. Mater.* **2014**, *24* (24), 3790–3798.

(921) Price, S. S. L. *Acc. Chem. Res.* **2009**, *42* (1), 117–126.

(922) Dunitz, J. D.; Gavezzotti, A. *Chem. Soc. Rev.* **2009**, *38* (9), 2622–2633.

(923) Idé, J.; Mothy, S.; Savoyant, A.; Fritsch, A.; Aurel, P.; Méreau, R.; Ducasse, L.; Cornil, J.; Beljonne, D.; Castet, F. *Int. J. Quantum Chem.* **2013**, *113* (4), 580–584.

(924) David, W. I. F.; Ibberson, R. M.; Matthewman, J. C.; Prassides, K.; Dennis, T. J. S.; Hare, J. P.; Kroto, H. W.; Taylor, R.; Walton, D. R. M. *Nature* **1991**, *353* (6340), 147–149.

(925) Riedel, E.; Janiak, C. *Anorganische Chemie*, 7. Auflage; de Gruyter: Berlin, New York, 2007.

(926) Zakhidov, A. A.; Baughman, R. H.; Iqbal, Z.; Cui, C.; Khayrullin, I.; Dantas, S. O.; Marti, J.; Ralchenko, V. G. *Science (80-.).* **1998**, *282* (5390), 897–901.

(927) Krakow, W.; Rivera, N. M.; Roy, R. A.; Ruoff, R. S.; Cuomo, J. J. *Appl. Phys. A* **1993**, *56* (3), 185–192.

(928) Hirshfeld, F. L. *Theor. Chim. Acta* **1977**, *44* (2), 129–138.

(929) Marenich, A. V; Jerome, S. V; Cramer, C. J.; Truhlar, D. G. *J. Chem. Theory Comput.* **2012**, *8* (2), 527–541.

(930) Brückner, C.; Würthner, F.; Meerholz, K.; Engels, B. Atomistic approach to simulate processes relevant for the efficiencies of organic solar cells as a function of molecular properties II. Kinetic aspects *(submitted)*.

(931)   Risko, C.; Brédas, J.-L. Springer Berlin Heidelberg, 2013; pp 1–38.

(932)   Mikhnenko, O. V; Kuik, M.; Lin, J.; van der Kaap, N.; Nguyen, T.-Q.; Blom, P. W. M. *Adv. Mater.* **2014**, *26* (12), 1912–1917.

(933)   Deschler, F.; Da Como, E.; Limmer, T.; Tautz, R.; Godde, T.; Bayer, M.; von Hauff, E.; Yilmaz, S.; Allard, S.; Scherf, U.; Feldmann, J. *Phys. Rev. Lett.* **2011**, *107* (12), 127402.

(934)   Vandewal, K.; Gadisa, A.; Oosterbaan, W. D.; Bertho, S.; Banishoeib, F.; Van Severen, I.; Lutsen, L.; Cleij, T. J.; Vanderzande, D.; Manca, J. V. *Adv. Funct. Mater.* **2008**, *18* (14), 2064–2070.

(935)   Mandoc, M. M.; Kooistra, F. B.; Hummelen, J. C.; de Boer, B.; Blom, P. W. M. *Appl. Phys. Lett.* **2007**, *91* (26), 263505.

(936)   Salzmann, I.; Heimel, G.; Oehzelt, M.; Winkler, S.; Koch, N. *Acc. Chem. Res.* **2016**, *49* (3), 370–378.

(937)   Bandyopadhyay, P.; Gordon, M. S.; Mennucci, B.; Tomasi, J. *J. Chem. Phys.* **2002**, *116* (12), 5023.

(938)   Mennucci, B. *Int. J. Quantum Chem.* **2015**, *115* (18), 1202–1208.

(939)   Hebard, A. F.; Haddon, R. C.; Fleming, R. M.; Kortan, A. R. *Appl. Phys. Lett.* **1991**, *59* (17), 2109.

(940)   Hamann, C. H.; Hamnett, A.; Vielstich, W. *Electrochemistry*, Second Edition; WILEY-VCH Verlag GmbH: Weinheim, 2007.

(941)   Eichkorn, K.; Treutler, O.; Öhm, H.; Häser, M.; Ahlrichs, R. *Chem. Phys. Lett.* **1995**, *242* (6), 652–660.

(942)   Eichkorn, K.; Weigend, F.; Treutler, O.; Ahlrichs, R. *Theor. Chem. Acc.* **1997**, *97* (1–4), 119–124.

(943)   Sierka, M.; Hogekamp, A.; Ahlrichs, R. *J. Chem. Phys.* **2003**, *118* (20), 9136.

(944)   Lunt, R. R.; Giebink, N. C.; Belak, A. A.; Benziger, J. B.; Forrest, S. R. *J. Appl. Phys.* **2009**, *105* (5), 53711.

(945)   van Hal, P. A.; Janssen, R. A. J.; Lanzani, G.; Cerullo, G.; Zavelani-Rossi, M.; De Silvestri, S. *Phys. Rev. B* **2001**, *64* (7), 75206.

(946)   Hukka, T. I.; Toivonen, T.; Hennebicq, E.; Brédas, J.-L.; Janssen, R. A. J.; Beljonne, D. *Adv. Mater.* **2006**, *18* (10), 1301–1306.

(947)   Becker, H. D. *Chem. Rev.* **1993**, *93* (1), 145–172.

(948)   Hertel, D.; Meerholz, K. *J. Phys. Chem. B* **2007**, *111* (42), 12075–12080.

(949)   Gesquiere, A. J.; Park, S.-J.; Barbara, P. F. *J. Am. Chem. Soc.* **2005**, *127* (26), 9556–9560.

(950)   Hung, R. R.; Grabowski, J. J. *J. Phys. Chem.* **1991**, *95* (16), 6073–6075.

(951)   Yang, L.; Zhou, H.; You, W. *J. Phys. Chem. C* **2010**, *114* (39), 16793–16800.

(952)   Kurrle, D.; Pflaum, J. *Appl. Phys. Lett.* **2008**, *92* (13), 133306.

(953)   Chen, C.-Y.; Ho, J.-H.; Wang, S.-L.; Ho, T.-I. *Photochem. Photobiol. Sci.* **2003**, *2* (11), 1232–1236.

(954)   Shigeta, M.; Morita, M.; Konishi, G. *Molecules* **2012**, *17* (4), 4452–4459.

(955) Lee, C.-C.; Su, W.-C.; Chang, W.-C.; Huang, B.-Y.; Liu, S.-W. *Org. Electron.* **2015**, *16*, 1–8.

(956) Vandewal, K.; Tvingstedt, K.; Manca, J. V.; Inganäs, O. *IEEE J. Sel. Top. Quantum Electron.* **2010**, *16* (6), 1676–1684.

(957) Hörmann, U.; Lorch, C.; Hinderhofer, A.; Gerlach, A.; Gruber, M.; Kraus, J.; Sykora, B.; Grob, S.; Linderl, T.; Wilke, A.; Opitz, A.; Hansson, R.; Anselmo, A. S.; Ozawa, Y.; Nakayama, Y.; Ishii, H.; Koch, N.; Moons, E.; Schreiber, F.; Brütting, W. *J. Phys. Chem. C* **2014**, *118* (46), 26462–26470.

(958) Aghamohammadi, M.; Fernández, A.; Schmidt, M.; Pérez-Rodríguez, A.; Goñi, A. R.; Fraxedas, J.; Sauthier, G.; Paradinas, M.; Ocal, C.; Barrena, E. *J. Phys. Chem. C* **2014**, *118* (27), 14833–14839.

(959) Zhong, J. Q.; Mao, H. Y.; Wang, R.; Qi, D. C.; Cao, L.; Wang, Y. Z.; Chen, W. *J. Phys. Chem. C* **2011**, *115* (48), 23922–23928.

(960) Vandewal, K.; Albrecht, S.; Hoke, E. T.; Graham, K. R.; Widmer, J.; Douglas, J. D.; Schubert, M.; Mateker, W. R.; Bloking, J. T.; Burkhard, G. F.; Sellinger, A.; Fréchet, J. M. J.; Amassian, A.; Riede, M. K.; McGehee, M. D.; Neher, D.; Salleo, A. *Nat. Mater.* **2014**, *13* (1), 63–68.

(961) Zope, R. R.; Baruah, T.; Pederson, M. R.; Dunlap, B. I. *Phys. Rev. B* **2008**, *77* (11), 115452.

(962) Bürckstümmer, H.; Kronenberg, N. M.; Gsänger, M.; Stolte, M.; Meerholz, K.; Würthner, F. *J. Mater. Chem.* **2010**, *20* (2), 240–243.

(963) Tress, W. *Organic Solar Cells*; Springer International Publishing Switzerland: Heidelberg, 2014.

(964) Troisi, A. *Adv. Mater.* **2007**, *19* (15), 2000–2004.

(965) Cheung, D. L.; Troisi, A. *Phys. Chem. Chem. Phys.* **2008**, *10* (39), 5941.

(966) Troisi, A. *Faraday Discuss.* **2013**, *163* (0), 377.

(967) Lin, B. C.; Cheng, C. P.; You, Z.-Q.; Hsu, C.-P. *J. Am. Chem. Soc.* **2005**, *127* (1), 66–67.

(968) Pople, J. A.; Beveridge, D. L.; Dobosh, P. A. *J. Chem. Phys.* **1967**, *47* (6), 2026.

(969) Cave, R. J.; Newton, M. D. *Chem. Phys. Lett.* **1996**, *249* (1–2), 15–19.

(970) Subotnik, J. E.; Yeganeh, S.; Cave, R. J.; Ratner, M. A. *J. Chem. Phys.* **2008**, *129* (24), 244101.

(971) Chen, H.-C.; Hsu, C.-P. *J. Phys. Chem. A* **2005**, *109* (51), 11989–11995.

(972) You, Z.-Q.; Hung, Y.-C.; Hsu, C.-P. *J. Phys. Chem. B* **2015**, *119* (24), 7480–7490.

(973) Yi, Y.; Coropceanu, V.; Brédas, J.-L. *J. Mater. Chem.* **2011**, *21* (5), 1479.

(974) Strickler, S. J.; Berg, R. A. *J. Chem. Phys.* **1962**, *37* (4), 814.

(975) Wang, S. *Phys. Rev. A* **1999**, *60* (1), 262–266.

(976) Houili, H.; Tutiš, E.; Batistić, I.; Zuppiroli, L. *J. Appl. Phys.* **2006**, *100* (3), 33702.

(977) Ebbesen, T. W.; Tanigaki, K.; Kuroshima, S. *Chem. Phys. Lett.* **1991**, *181* (6), 501–504.

(978) Grote, R. R.; Brown, S. J.; Driscoll, J. B.; Osgood, R. M.; Schuller, J. A. *Opt. Express* **2013**, *21 Suppl 5* (105), A847-63.

(979) Jo, S. B.; Kim, H. H.; Lee, H.; Kang, B.; Lee, S.; Sim, M.; Kim, M.; Lee, W. H.; Cho, K. *ACS Nano* **2015**, *9* (8), 8206–8219.

(980) Binder, K. *Introduction:Theory and "Technical" Aspects of Monte Carlo Simulations*, Springer.; Berlin, Heidelberg, 1986.

(981) Xie, Y.; Li, Y.; Xiao, L.; Qiao, Q.; Dhakal, R.; Zhang, Z.; Gong, Q.; Galipeau, D.; Yan, X. *J. Phys. Chem. C* **2010**, *114* (34), 14590–14600.

(982) Ghirotti, M.; Chiorboli, C.; You, C.-C.; Würthner, F.; Scandola, F. *J. Phys. Chem. A* **2008**, *112* (15), 3376–3385.

(983) Gieseking, B.; Schmeiler, T.; Müller, B.; Deibel, C.; Engels, B.; Dyakonov, V.; Pflaum, J. *Phys. Rev. B* **2014**, *90* (20), 205305.

(984) Gautam, P.; Misra, R.; Siddiqui, S. A.; Sharma, G. D. *ACS Appl. Mater. Interfaces* **2015**, *7* (19), 10283–10292.

(985) Patil, Y.; Jadhav, T.; Dhokale, B.; Misra, R. *European J. Org. Chem.* **2016**, *2016* (4), 733–738.

(986) Karl, N. *Synth. Met.* **2003**, *133–134*, 649–657.

(987) Karl, N.; Marktanner, J.; Stehle, R.; Warta, W. *Synth. Met.* **1991**, *42* (3), 2473–2481.

(988) Siebert-Henze, E.; Lyssenko, V. G.; Fischer, J.; Tietze, M.; Brueckner, R.; Schwarze, M.; Vandewal, K.; Ray, D.; Riede, M.; Leo, K. *AIP Adv.* **2014**, *4* (4), 47134.

(989) Li, C.; Credgington, D.; Ko, D.-H.; Rong, Z.; Wang, J.; Greenham, N. C. *Phys. Chem. Chem. Phys.* **2014**, *16* (24), 12131–12136.

(990) Tress, W.; Leo, K.; Riede, M. *Phys. Rev. B* **2012**, *85* (15), 155201.

(991) Seo, S.; Park, B.-N.; Evans, P. G. *Appl. Phys. Lett.* **2006**, *88* (23), 232114.

(992) Feng, X.; Marcon, V.; Pisula, W.; Hansen, M. R.; Kirkpatrick, J.; Grozema, F.; Andrienko, D.; Kremer, K.; Müllen, K. *Nat. Mater.* **2009**, *8* (5), 421–426.

(993) Mandoc, M. M.; Koster, L. J. A.; Blom, P. W. M. *Appl. Phys. Lett.* **2007**, *90* (13), 133504.

(994) Deibel, C.; Wagenpfahl, A.; Dyakonov, V. *Phys. status solidi - Rapid Res. Lett.* **2008**, *2* (4), 175–177.

(995) Ramírez, O.; Cabrera, V.; Reséndiz, L. M. *Opt. Quantum Electron.* **2014**, *46* (10), 1291–1296.

(996) Proctor, C. M.; Love, J. A.; Nguyen, T.-Q. *Adv. Mater.* **2014**, *26* (34), 5957–5961.

(997) Ebenhoch, B.; Thomson, S. A. J.; Genevičius, K.; Juška, G.; Samuel, I. D. W. *Org. Electron.* **2015**, *22*, 62–68.

(998) Meskers, S. C. J.; Hübner, J.; Oestreich, M.; Bässler, H. *Chem. Phys. Lett.* **2001**, *339* (3–4), 223–228.

(999) Meskers, S. C. J.; Hübner, J.; Oestreich, M.; Bässler, H. *J. Phys. Chem. B* **2001**, *105* (38), 9139–9149.

(1000) Improta, R.; Scalmani, G.; Frisch, M. J.; Barone, V. *J. Chem. Phys.* **2007**, *127* (7), 74504.

(1001) Chibani, S.; Laurent, A. D.; Blondel, A.; Mennucci, B.; Jacquemin, D. *J. Chem. Theory Comput.*

2014, *10* (5), 1848–1851.

(1002) Barone, V.; Biczysko, M.; Pavone, M. *Chem. Phys.* **2008**, *346* (1), 247–256.

(1003) Briggs, E. A.; Besley, N. A. *Phys. Chem. Chem. Phys.* **2014**, *16* (28), 14455.

(1004) London, F. *Trans. Faraday Soc.* **1937**, *33*, 8b–26.

(1005) Wang, J.; Xie, X.-Q.; Hou, T.; Xu, X. *J. Phys. Chem. A* **2007**, *111* (20), 4443–4448.

(1006) Liu, Y.; Wan, X.; Wang, F.; Zhou, J.; Long, G.; Tian, J.; Chen, Y. *Adv. Mater.* **2011**, *23* (45), 5387–5391.

(1007) Li, H.; Brédas, J.-L.; Lennartz, C. *J. Chem. Phys.* **2007**, *126* (16), 164704.

(1008) Garashchuk, S.; Light, J. C.; Rassolov, V. A. *The diagonal Born–Oppenheimer correction to molecular dynamical properties*; 2001; Vol. 333.

(1009) Thomas, L. H. *Math. Proc. Cambridge Philos. Soc.* **1927**, *23* (5), 542.

(1010) Fermi, E. *Rend. Accad. Naz. Lincei.* **1927**, *6*, 602–607.

(1011) Chong, D. P.; Gritsenko, O. V.; Baerends, E. J. *J. Chem. Phys.* **2002**, *116* (5), 1760.

(1012) Raghavachari, K. *Annu. Rev. Phys. Chem.* **1991**, *42*, 615–642.

(1013) Cossi, M.; Rega, N.; Scalmani, G.; Barone, V. *J. Comput. Chem.* **2003**, *24*, 669–681.

(1014) Klamt, A.; Jonas, V. *J. Chem. Phys.* **1996**, *105* (22), 9972.

(1015) Tolbert, L. M.; Zhao, X. *J. Am. Chem. Soc.* **1997**, *119* (14), 3253–3258.